Transactions of the ASME, Journal of Fluids Engineering (ISSN 0098-2202) is published bimonthly (Jan., Mar., May, July, Sept., Nov.) by The American Society of Mechanical Engineers, Three Park Avenue, New York, NY 10016. Periodicals postage paid at New York, NY and additional mailing offices.
POSTMASTER: Send address changes to Transactions of the ASME, Journal of Fluids Engineering, c/o THE AMERICAN SOCIETY OF MECHANICAL ENGINEERS, 22 Law Drive, Box 2300, Fairfield, NJ 07007-2300.
CHANGES OF ADDRESS must be received at Society headquarters seven weeks before they are to be effective. Please send old label and new address.
STATEMENT from By-Laws. The Society shall not be responsible for statements or opinions advanced in papers or ... printed in its publications (B7.1, Par. 3).

INDEXED by Applied Mechanics Reviews and Engineering Information, Inc. Canadian Goods & Services Tax Registration #126148 048.

Journal of Fluids Engineering

Published Bimonthly by ASME

VOLUME 127 • NUMBER 1 • JANUARY 2005

TECHNICAL PAPERS

(Contents continued on inside back cover)

This journal is printed on acid-free paper, which exceeds the ANSI Z39.48-1992 specification for permanence of paper and library materials. ♾™
♻ 85% recycled content, including 10% post-consumer fibers.

Journal of Fluids Engineering Volume 127, Number 1 JANUARY 2005

TECHNICAL BRIEFS

The ASME Journal of Fluids Engineering is abstracted and indexed in the following:

Applied Science & Technology Index, Chemical Abstracts, Chemical Engineering and Biotechnology Abstracts (Electronic equivalent of Process and Chemical Engineering), Civil Engineering Abstracts, Computer & Information Systems Abstracts, Corrosion Abstracts, Current Contents, Ei EncompassLit, Electronics & Communications Abstracts, Engineered Materials Abstracts, Engineering Index, Environmental Engineering Abstracts, Environmental Science and Pollution Management, Excerpta Medica, Fluidex, Index to Scientific Reviews, INSPEC, International Building Services Abstracts, Mechanical & Transportation Engineering Abstracts, Mechanical Engineering Abstracts, METADEX (The electronic equivalent of Metals Abstracts and Alloys Index), Petroleum Abstracts, Process and Chemical Engineering, Referativnyi Zhurnal, Science Citation Index, SciSearch (The electronic equivalent of Science Citation Index), Shock and Vibration Digest, Solid State and Superconductivity Abstracts, Theoretical Chemical Engineering

Masahide Inagaki
Researcher,
Digital Engineering Laboratory, Toyota Central Research & Development Laboratories, Inc.,
Nagakute, Aichi 480-1192, Japan

Tsuguo Kondoh
Principal Researcher,
System Engineering & Electronics Department, Toyota Central Research & Development Laboratories, Inc.,
Nagakute, Aichi 480-1192, Japan

Yasutaka Nagano
Vice-President,
Nagoya Institute of Technology,
Gokiso-cho, Showa-ku, Nagoya 466-8555, Japan

A Mixed-Time-Scale SGS Model With Fixed Model-Parameters for Practical LES

A new subgrid-scale (SGS) model for practical large eddy simulation (LES) is proposed. The model is constructed with the concept of mixed time-scale, which makes it possible to use fixed model-parameters and to dispense with the distance from the wall. The model performance is tested in plane channel flows, and the results show that this model is able to account for near-wall turbulence without an explicit damping function as in the dynamic Smagorinsky model. The model is also evaluated in a backward-facing step flow and in a flow around a circular cylinder. The calculated results using the consistent model-parameters show good agreement with experimental data, while the results obtained using the dynamic Smagorinsky model show less accuracy and less computational stability. Furthermore, to confirm the validity of the present model in practical applications, the three-dimensional complex flow around a bluff body (Ahmed et al., SAE paper no. 840300) is also calculated with the model. The agreement between the calculated results and the experimental data is quite satisfactory. These results suggest that the present model is a refined SGS model suited for practical LES to compute flows in a complicated geometry. [DOI: 10.1115/1.1852479]

1 Introduction

Computational fluid dynamics (CFD) has been strenuously applied in engineering predictions of turbulent fluid flow for about two decades. Together with the advances in computers, numerical methods, and turbulence modeling, CFD has become one of the most useful tools for investigating engineering application problems and designing fluid machinery. Above all, turbulence modeling is very important for predicting the performance of fluid machines with sufficient reliability since most of them involve complex turbulent phenomena. So far, the approach based on Reynolds averaged Navier–Stokes equation (RANS) has been most frequently used to predict various engineering turbulent flows with a certain degree of success (e.g., Gatski and Rumsey [1]).

On the other hand, the unsteadiness of the turbulent flow itself is also important in some engineering applications, e.g., aerodynamic noise prediction, turbulent mixing, and turbulent combustion in an engine. For resolving such unsteadiness over a broad range of scales, large eddy simulation (LES) based on the space-filtered Navier–Stokes equation is considered to be a more suitable approach. With the recent remarkable advances in computers, large eddy simulation has also become applicable to engineering predictions, although there is no doubt that the RANS approach will continue to be a popular and profitable tool for design and development of fluid machinery because of its robustness and high cost-effectiveness.

The key to the success of LES in its practical use is to accurately represent the effect of SGS components in complex geometries. The Smagorinsky model is one of the SGS models in wide use so far. When applied to simple flow fields, this model is acknowledged to yield good results. At the same time, the following defects of the model have been pointed out in many studies:

1. The model must be supplemented with a wall-damping function of van Driest's type;
2. The model parameter needs to be adjusted according to the type of flow field;
3. The SGS effect does not disappear in the laminar flow region.

The first is an especially important issue. A wall-unit coordinate used in a wall-damping function of van Driest's type is defined using the wall friction velocity. Near a flow separation point or a flow reattachment point, the friction velocity vanishes or becomes very small, which unreasonably expands the effective region of a wall-damping function. For engineering-relevant practical LES, it is important to use a SGS model free from the use of a wall-unit coordinate in order to prevent the inaccuracy.

The dynamic Smagorinsky model developed by Germano et al. [2] has been proven to be a SGS model that overcomes those defects of the conventional Smagorinsky model and dispenses with a wall-damping function. In spite of the remarkable success of the dynamic Smagorinsky model, some problems have occurred in its practical use. First, the SGS eddy viscosity obtained by using the dynamic procedure is not guaranteed to be positive, which leads to numerical instability. To avoid this, the averaging in a homogeneous plane or direction is often performed to obtain the model parameter. However, Akselvoll and Moin [3] have pointed out that the one-directional averaging was not sufficient to stabilize their calculation of a backward-facing step flow. Moreover, this approach is not feasible in complicated engineering flows. Clipping, which sets the negative SGS eddy viscosity to zero, and volume average are alternative approaches to avoid this numerical instability. Nevertheless, the stabilizing effect is still insufficient. The numerical instability restricts the time step, allowing a stable calculation, which brings about an increase in computational cost. This is considered to be a great disadvantage in practical use. Although Meneveau et al. [4] have proposed a Lagrangian-path averaging method as a more general averaging procedure, the results using the method heavily depend on the averaging time-scale at least in complicated engineering flows. The appropriate averaging time-scale has not been defined in a general manner. Second, the accuracy of the dynamic Smagorinsky model is lower than the Smagorinsky model with the model parameter intentionally optimized for the relevant flow field, at least using those artificial approaches, i.e., the clipping or the volume average.

Thus, in this paper we propose a new SGS model to improve

Contributed by the Fluids Engineering Division for publication in the JOURNAL OF FLUIDS ENGINEERING. Manuscript received by the Fluids Engineering Division May 16, 2003; revised manuscript received July 30, 2004. Review Conducted by: K. Squires.

the accuracy and computational stability of practical LES. We suppose that the computational instability of the dynamic Smagorinsky model originates in the dynamical adjustment of the model parameters. The present model avoids this problem since it is based on fixed model-parameters and is constructed with the concept of the mixed time-scale in order to dispense with a wall-damping function of van Driest's type. In the present model, the SGS kinetic energy estimated by means of filtering a grid-filtered velocity field is regarded as the velocity scale. Since we intend to expand the practical use of LES, we must also pay attention to the filtering procedure. Filtering is ordinarily done in the streamwise and spanwise directions, but not in the wall-normal direction. However, it is difficult to define the wall-normal direction in complex geometries. Thus, in this study the filtering is done in all spatial directions. This filtering procedure is also adopted in the dynamic Smagorinsky model to assess the model performance.

On the other hand, LES has another well-known problem near the wall when applied to high Reynolds number flows. This is because the number of grid points required near the wall for LES is proportional to $\mathrm{Re}^{1.8}$ (e.g., [5]) while that away from the wall is $\mathrm{Re}^{0.5}$. In such conditions, LES becomes prohibitively expensive. To circumvent the near-wall problem, some hybrid LES/RANS methods including the best-known DES method of Spalart et al. [6] have been proposed and appraised, where a RANS-type representation of the near-wall flow is combined with an LES solution in the outer region. It should be noted that the new SGS model proposed in this paper is not a type of the hybrid models. The present model, as well as the existing SGS models such as the Smagorinsky model, the dynamic model, and scale similarity models, assumes that the large-scale motions containing most of the turbulent energy are resolved to a certain degree. Accordingly, the advantage of the present model over the existing SGS models is expected to be observed except in the near-wall region in high Reynolds number flows where the energy-containing motions are difficult to be resolved with an admissible computational cost.

We consider that the improvement of the SGS model, based on the assumption previously mentioned, is still as important as the near-wall modeling. First of all, the medium Reynolds number flows ($\mathrm{Re}=10^4-10^5$) are frequently encountered in engineering applications. With the recent advances in computers, even at such Reynolds numbers, LES calculation resolving turbulent boundary layer has become possible. Because the hybrid LES/RANS models also have some defects in common, e.g., the double buffer, the theoretical ambiguity around the interface between RANS and LES regions (i.e., switching from space-averaging to time-averaging), and the incapability in predicting separation bubbles, the LES method is a better choice in such conditions with sufficient grid resolution. Moreover, for aerodynamic noise predictions, for example, the accurate pressure fluctuations on the wall surface are essential, so that LES without a RANS-type wall modeling is a more suitable approach. Secondly, in calculation of high Reynolds number flows ($\mathrm{Re}=10^6$), the methodology to treat the near-wall region is certainly important, but most of the computational domain is solved using the LES method with a SGS model. It may be convinced that the performance of the SGS model employed in the LES region also has a great influence on the whole prediction accuracy.

Thus, in this paper, we have chosen various types of fundamental flows at low to medium Reynolds numbers, i.e., the plane channel flow, the rotating channel flow, the backward-facing step flow, and the flow around a circular cylinder, as test cases to examine the model performance. In addition, the present model is applied to the flow around an *Ahmed model* [7] as a high Reynolds number test case, where, in taking account of the near-wall problem on such Reynolds number condition, we employed a conventional artificial wall condition. The performance of the proposed model is elucidated in comparison with the existing SGS models.

2 Governing Equations

The basic equations are the filtered Navier–Stokes and continuity equations for an incompressible fluid given as follows:

$$\frac{\partial \overline{u_j}}{\partial x_j}=0, \tag{1}$$

$$\frac{\partial \overline{u_i}}{\partial t}+\frac{\partial \overline{u_j}\,\overline{u_i}}{\partial x_j}+\frac{\partial \tau_{ij}}{\partial x_j}=-\frac{1}{\rho}\frac{\partial \overline{p}}{\partial x_i}+\nu\frac{\partial^2 \overline{u_i}}{\partial x_j^2}, \tag{2}$$

where the overline denotes the grid-filtering operator and $\tau_{ij}=\overline{u_iu_j}-\overline{u_i}\,\overline{u_j}$ is the SGS stress, which should be modeled. All the SGS models tested in this paper are based on the eddy viscosity concept. Thus,

$$\tau_{ij}^{*}=-2\nu_t\overline{S}_{ij}, \tag{3}$$

$$\overline{S}_{ij}=\frac{1}{2}\left(\frac{\partial \overline{u_i}}{\partial x_j}+\frac{\partial \overline{u_j}}{\partial x_i}\right), \tag{4}$$

where $\tau_{ij}^{*}=\tau_{ij}-(1/3)\,\delta_{ij}\tau_{kk}$.

3 Representative Subgrid-Scale Models

3.1 Smagorinsky Model. The widely used Smagorinsky model is based on the assumption of the balance between the energy production and dissipation effects in the equation for SGS kinetic energy. It is described as follows:

$$\nu_t=(Cs\overline{\Delta}f)^2|\overline{S}|,\quad |\overline{S}|=\sqrt{2\overline{S_{ij}S_{ij}}}, \tag{5}$$

where $\overline{\Delta}=(\Delta x\Delta y\Delta z)^{1/3}$. As a wall-damping function, f, van Driest's function is commonly used:

$$f_{VD}=1-\exp(-y^{+}/25). \tag{6}$$

In this paper, the following wall-damping function [8] that improves the near-wall asymptotic behavior of the SGS eddy viscosity is also used in the channel flow calculation mentioned later:

$$f_{PFM}=\sqrt{1-\exp[-(y^{+}/25)^3]}. \tag{7}$$

3.2 Dynamic Smagorinsky Model. In the dynamic Smagorinsky model proposed by Germano et al. [2], the test filter is applied to the grid-filtered flow field. The sub-test-scale stress is defined as $T_{ij}=\widetilde{\overline{u_iu_j}}-\widetilde{\overline{u_i}}\,\widetilde{\overline{u_j}}$, where $(\widetilde{\ })$ denotes the test-filtering operator. Using the "Germano identity," a stress tensor, L_{ij}, is defined as follows:

$$L_{ij}=T_{ij}-\widetilde{\tau}_{ij}=\widetilde{\overline{u_iu_j}}-\widetilde{\overline{u_i}}\,\widetilde{\overline{u_j}}. \tag{8}$$

By assuming the Smagorinsky model for both T_{ij} and τ_{ij}, the following relation is obtained:

$$L_{ij}^{*}=-2C\widetilde{\overline{\Delta}}^2M_{ij}, \tag{9}$$

$$M_{ij}=\alpha^2\widetilde{|\overline{S}|\overline{S}_{ij}}-\widetilde{|\overline{S}|\overline{S}_{ij}}, \tag{10}$$

where $C=(Csf)^2$ and $\alpha=\widetilde{\overline{\Delta}}/\overline{\Delta}$. $\widetilde{\overline{\Delta}}$ is evaluated as $\sqrt{\overline{\Delta}^2+\widetilde{\overline{\Delta}}^2}$. The parameter C is computed by applying a least-square approach suggested by Lilly [9] as follows:

$$C=-\frac{1}{2}\frac{L_{ij}^{*}M_{ij}}{\overline{\Delta}^2M_{ij}M_{ij}}. \tag{11}$$

Consequently, there is no need to give the model parameter or a wall-damping function beforehand. Thus, the defects of the Smagorinsky model are formally settled. In this study, we set $\alpha=2$. The ratio of the test filter width to the grid filter width, $\gamma=\widetilde{\overline{\Delta}}/\overline{\Delta}$, is set to $\sqrt{3}$. We adopt the following formula elaborated by Taniguchi [10] for the test filtering operation:

Table 1 Computational conditions for plane channel flows

Case no.	Re_τ	Grid points	Δx^+	Δy^+	Δz^+
1	180	64×62×64	18.0	0.5–14.1	4.5
2	395	64×62×64	39.5	1.1–30.9	9.9
3	395	32×62×32	79.0	1.1–30.9	19.8
4	395	32×62×32	79.0	1.1–30.9	39.5
5	395	32×62×32	316.0	1.1–30.9	79.0

$$\tilde{\overline{g}}_i=\overline{g}_i+\frac{1}{4}(\overline{g}_{i+1}-2\overline{g}_i+\overline{g}_{i-1})-\frac{\gamma^2-6}{96}(\overline{g}_{i+2}-2\overline{g}_i+\overline{g}_{i-2}), \tag{12}$$

where suffix i denotes the location in the i direction of the computational space. This filtering operation is performed in each direction. Using this formula, the effects of the aliasing and truncation errors on the L_{ij} and M_{ij} are reduced.

4 Proposal of a Mixed-Time-Scale SGS Model

The SGS eddy viscosity is generally expressed as follows:

$$\nu_t \propto (\text{Velocity Scale}) \times (\text{Length Scale}), \tag{13}$$

or

$$\nu_t \propto (\text{Velocity Scale})^2 \times (\text{Time Scale}). \tag{14}$$

The Smagorinsky model obeys the former expression, where the velocity scale is $\overline{\Delta}|\overline{S}|$ and the length scale is $\overline{\Delta}$. The velocity scale can be replaced with $\sqrt{k}$, where k is the SGS turbulent energy which is often estimated solving the modeled k-equation. We can also estimate k by filtering a velocity field (e.g., [11–13]):

$$k_{es}=(\overline{u}_k-\hat{\overline{u}}_k)^2. \tag{15}$$

The notation, $\hat{(\ )}$, denotes the filtering operator, for which the Simpson rule is adopted. This estimation procedure is based on an idea similar to the scale similarity proposed by Bardina [14] and is employed in the present modeling. One of the merits of this estimation procedure is that ν_t is consistently guaranteed to approach zero in the laminar-flow region because k_{es} approaches zero by itself there. According to these models, the following relation can be obtained:

$$\nu_t=(Cs\overline{\Delta}f)^2|\overline{S}|=C_\nu\overline{\Delta}f\sqrt{k}. \tag{16}$$

This equation implies $f\propto\sqrt{k}/(\overline{\Delta}|\overline{S}|)$. By assuming this relation, we can construct an alternative expression for SGS eddy viscosity without a wall-damping function f:

$$\nu_t \propto k/|\overline{S}|. \tag{17}$$

This expression is identical to Eq. (14), where the velocity scale is $\sqrt{k}$, and the time-scale is $1/|\overline{S}|$. To examine the validity of this expression, we have performed an a priori test in a channel flow (case 1, see Table 1). Figure 1 shows the SGS eddy viscosity distribution calculated from each expression using the data from an instantaneous flow field. In this figure, S-VD represents the Smagorinsky model with the wall-damping function, f_{VD}, given by Eq. (6), and S-PFM is the corresponding revised version with f_{PFM} as Eq. (7), where Cs is set to 0.1. Although the expression $k_{es}/|\overline{S}|$ is free from a damping function, it agrees well with other SGS models incorporated with a damping function. This result reveals that $1/|\overline{S}|$ is a proper time scale near the wall. Tsubokura [15] proposed a revised dynamic model where the same expression of the SGS eddy viscosity as Eq. (17) was employed. However, we consider that the introduction of a dynamic procedure is not necessary, at least near the wall when using this expression.

Away from the wall, this expression $k_{es}/|\overline{S}|$ probably suffers from the zero-divide problem when $|\overline{S}|$ approaches zero. On the other hand, the expression $\nu_t\approx\overline{\Delta}\sqrt{k_{es}}$, where the time-scale is $\overline{\Delta}/\sqrt{k_{es}}$, has been already studied in some papers (e.g., [13]), and its performance has been shown to be quite good in their test cases of the plane channel flows, although it needs a wall-damping function supplemented. Then, in order to utilize the property of the time-scale $1/|\overline{S}|$ in the expression $\nu_t\approx\overline{\Delta}\sqrt{k_{es}}$, we introduce the concept of the mixed-time-scale, whose effectiveness is ascertained in RANS models (e.g., [16]), and propose a new SGS model as follows:

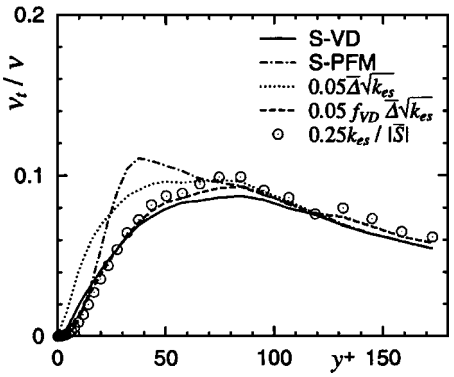

Fig. 1 A priori test for the SGS eddy viscosity in the channel flow (case 1)

$$\nu_t=C_{MTS}k_{es}T_S, \tag{18}$$

$$T_S^{-1}=\left(\frac{\overline{\Delta}}{\sqrt{k_{es}}}\right)^{-1}+\left(\frac{C_T}{|\overline{S}|}\right)^{-1}. \tag{19}$$

The model parameters, C_{MTS} and C_T, are set to 0.05 and 10, respectively, which are optimized considering the results of an a priori test in the channel flow and those of some test studies in the backward-facing step flow mentioned later. Note that, in the present model, the time-scale is defined as the harmonic average of $\overline{\Delta}/\sqrt{k_{es}}$ and $1/|\overline{S}|$. $\overline{\Delta}/\sqrt{k_{es}}$ stands for the characteristic time-scale of the small-scale turbulence corresponding to the cut-off scale, whereas $1/|\overline{S}|$ stands for that of the large scales. Because the harmonic average gives weight to a shorter scale, the time-scale in the present model approaches $1/|\overline{S}|$ near the wall, which is easily found by comparing the difference between the results using the two time-scales as shown in Fig. 1. Thus, the proposed model does not require a wall-damping function to be supplemented. In the region away from the wall, if $|\overline{S}|$ becomes nearly zero, ν_t approaches $C_{MTS}\overline{\Delta}\sqrt{k_{es}}$. This is because $\overline{\Delta}/\sqrt{k_{es}}$ becomes much smaller than $1/|\overline{S}|$ in such a condition. Therefore, the present model does not suffer from the zero-divide problem.

The present model can be rewritten as follows:

$$\nu_t=\frac{C_{MTS}}{1+(RC_T)^{-1}}\overline{\Delta}\sqrt{k_{es}}, \tag{20}$$

where $R=\sqrt{k_{es}}/(\overline{\Delta}|\overline{S}|)$. This means that the present model corresponds to a single time-scale model, $\nu_t\approx\overline{\Delta}\sqrt{k_{es}}$, with the model parameter dependent on R. The damping effect near the wall is attributed to the significant decrease in R there. Yoshizawa et al. [13] have suggested that R may be constant on the assumption of the local equilibrium of SGS turbulence. If this is true, the R-dependent model parameter of the present model remains constant in such a condition. In contrast, where the local equilibrium of SGS turbulence is not satisfied, the model parameter of the present model is adjusted according to the resultant change of R. Hence, the present model is expected to be more universal than

the SGS model (e.g., the Smagorinsky model) that is based on the equilibrium assumption. In this paper, the behavior of R is also examined in some test cases.

5 Numerical Methods

We employ a second-order collocated grid system, which is modified from the original one (Rhie and Chow [17] or Morinishi et al. [18]). The modification has two points. One is the interpolation method of the auxiliary flux velocity components, U_i, at the center of the cell faces. We use a fourth-order interpolation instead of a second-order one. The other is the discretization method for the pressure gradient at the center of the cells. We use the combination of three-fourths of a fourth-order central difference scheme and one-fourth of a second-order central difference scheme. Owing to this modification, the present grid system has almost the same numerical accuracy as the second-order staggered grid system and is readily applicable to curvilinear grids. It should be noted that the Poisson equation for pressure is discretized in the same way as in the original collocated grid system using the auxiliary flux velocity components, U_i. The stencil of the left-hand side of the Poisson equation is the same as in the original one, and thus the increase in computational cost using the present grid system is negligible.

The convection terms are advanced explicitly using the second-order Adams–Bashforth method, whereas the viscous terms are advanced implicitly using the Crank–Nicolson method.

6 Results

6.1 Plane Channel Flow. To verify the present SGS model in wall-bounded flows, we apply it to plane channel flows. To examine the grid-dependency at the same time, we conduct several computations varying the Reynolds number, the number of grid points, or the size of the computational domain (Table 1). In every case, the grid resolution in the wall-normal direction is sufficiently high. The periodic boundary condition is applied in the streamwise and spanwise directions. The no-slip condition is applied at the wall surface. Four kinds of SGS models are used: the present model, the S-VD model, the S-PFM model and the dynamic Smagorinsky model (DS model). In the S-VD and S-PFM models, Cs is set to 0.1. In DS model, the parameter C is calculated by taking the average over the plane parallel to the wall. Therefore, the results for the DS model are not expected to show the numerical instability nor inferior accuracy.

Figure 2 shows the profiles of mean velocity, turbulent intensities, and SGS eddy viscosity in case 1, where the substantial grid resolution is highest in all cases. The mean velocity obtained by the S-PFM model or DS model agrees quite well with the DNS data [19]. Although the mean velocity obtained with the present or S-VD model is slightly lower in the logarithmic region, the underestimation is trivial at least for practical use. As shown in Fig. 2(c), the present model gives the SGS eddy viscosity properly damped near the wall like the other SGS models. Figure 3 shows the near-wall behavior of the SGS eddy viscosity in case 2. The S-PFM and DS models follow the correct near-wall asymptotic behavior. The present model does not conform to it as well as the S-VD model. However, this shortcoming is considered not to be important in LES because the grid-scale components directly computed contain most of the turbulent effects. Taking into account that the S-VD model has been widely used with success in simple flows, the present model is expected to account for near-wall turbulence without an explicit damping function as in the DS model.

Figure 4 shows the results in case 4 in which the grid resolution is considerably low. Overestimation of the mean velocity in the logarithmic region is seen in any model result. Figure 5 shows the computational error in total mass flux in the channel, which assesses the grid-dependency quantitatively. In Fig. 5, $E_{DNS}=(Q_{calc.}-Q_{DNS})/Q_{DNS}$, where $Q_{calc.}$ is the total mass flux obtained from the computational result and Q_{DNS} is that obtained from the DNS data [20]. Although, in the result of any model, the total mass flux is underestimated with fine grids and is overestimated with coarse grids, the grid-dependency of the present model is improved in comparison with the DS model. Figure 6 shows the variation of the SGS eddy viscosity according to the change in grid resolution. In the dynamic models results, the region where the SGS eddy viscosity is damped extends farther from the wall in

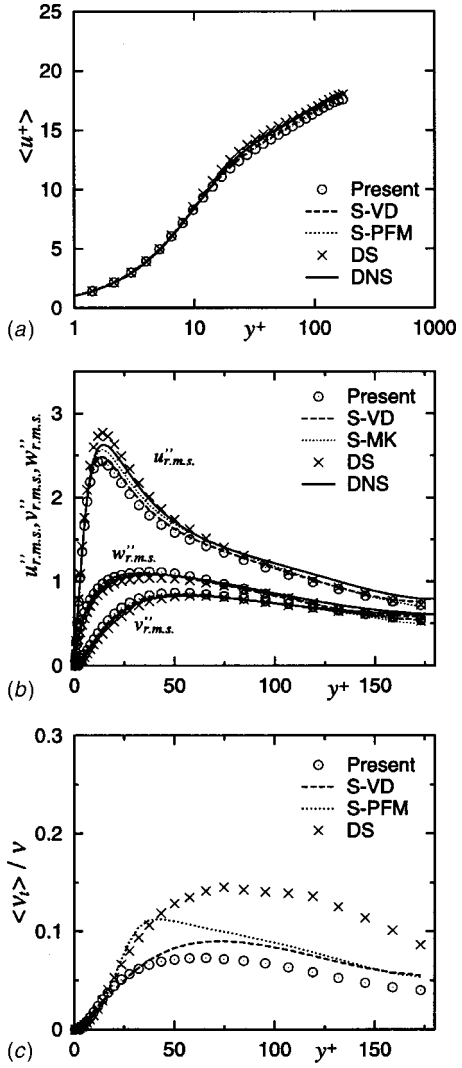

Fig. 2 Predictions of channel flow (case 1): (*a*) mean velocity, (*b*) turbulent intensities, and (*c*) SGS eddy viscosity

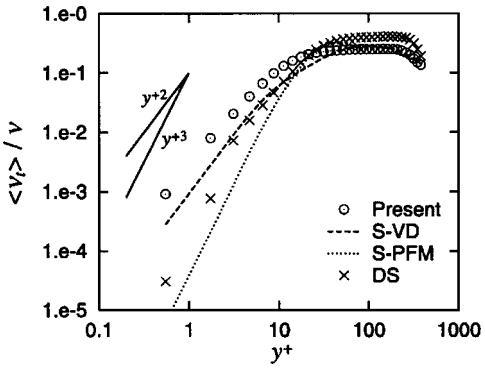

Fig. 3 Near-wall behavior of the SGS eddy viscosity (case 2)

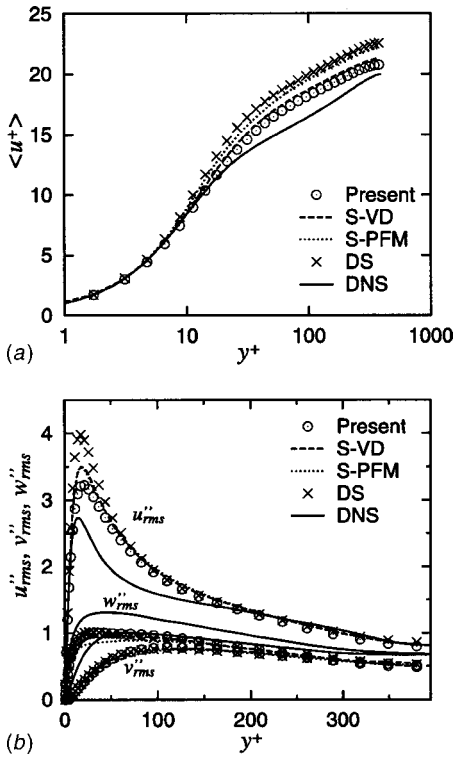

Fig. 4 Predictions of channel flow (case 4): (*a*) mean velocity and (*b*) turbulent intensities

a coarse grid case, which is considered to be a reason for the DS models high grid dependency. In contrast, the region of the damped SGS eddy viscosity in the present model does not extend so much with the change in grid resolution, which seems to be a preferable property.

Figure 7 shows the profiles of the ratio of two time-scales in the present model, R. It is found that R is approximately constant away from the wall and is independent of the grid resolution. Consequently, it is obvious that, in this flow field, the ratio R affects the SGS eddy viscosity only in the near-wall region as the representation of the wall-damping effects. The grid-independence of R results in the consistent damped region.

6.2 Rotating Channel Flow. To examine the behavior of the two time-scales, R, in more complicated shear layers, we apply the present SGS model to the rotating channel flows. The computational domain and the coordinate system are demonstrated in Fig. 8. The momentum transport equation is replaced by

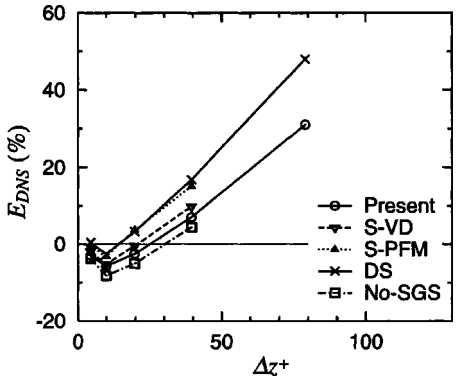

Fig. 5 Computational error in the total mass flux in the channel

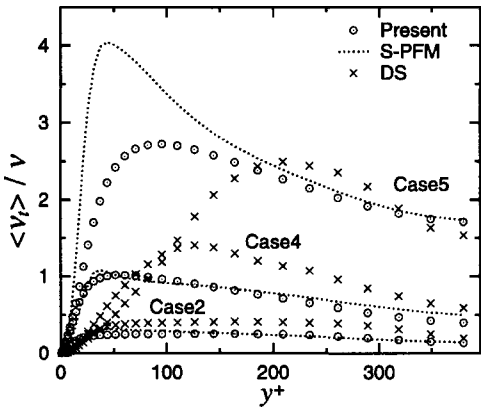

Fig. 6 Variation of SGS eddy viscosity according to the change of grid resolution

the following equation using a rotating frame of reference:

$$\frac{\partial \overline{u_i}}{\partial t}+\frac{\partial \overline{u_j}\,\overline{u_i}}{\partial x_j}+\frac{\partial \tau_{ij}}{\partial x_j}=-\frac{1}{\rho}\frac{\partial}{\partial x_i}\left(\overline{p}-\frac{\rho}{2}\Omega^2 r^2\right)+\nu\frac{\partial^2 \overline{u_i}}{\partial x_j^2}-2\Omega_m \varepsilon_{ijk}\overline{u_j}, \tag{21}$$

where Ω and r denote the angular velocity of the rotating frame of reference and the distance from the axis of rotation, respectively. The Reynolds number, Re_τ^*, based on a channel half-width, δ, and the friction velocity averaged on the pressure and suction sides, u_τ^*, is set to be 194. The grid resolution is $48\times64\times48$ grid points in the x, y and z directions, respectively, and the grid widths in the wall-unit coordinates are 32.3, 1.0–12.3, and 16.2 in each direction. The periodic boundary condition is applied in the streamwise and spanwise directions. The no-slip condition is applied on the wall surface.

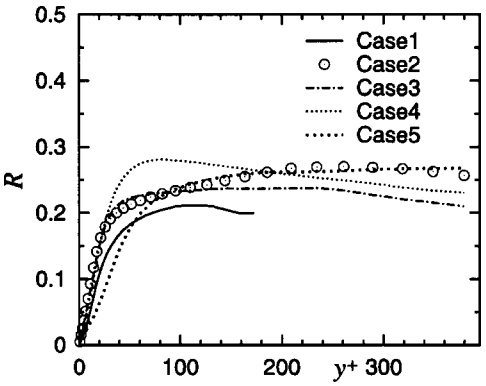

Fig. 7 Ratio of two time-scales used in the present model in the channel flow

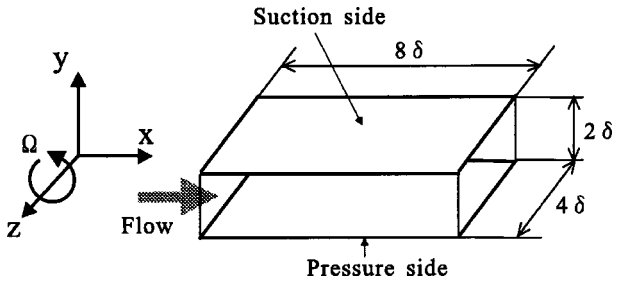

Fig. 8 Computational domain and coordinate system for rotating channel flow

Table 2 Computational conditions and results for rotating channel flows

Ro_τ	$\mathrm{Re}(=2u_{\max}\delta/\nu)$	$\mathrm{Ro}=2\Omega\delta/u_b$	$u_{\tau p}/u_\tau^*$	$u_{\tau s}/u_\tau^*$
0.0	7070	0.0	1.0	1.0
0.15	7190	0.0093	1.046	0.952
0.75	7220	0.0455	1.168	0.798
3.0	6920	0.1983	1.210	0.732
7.5	8010	0.4845	1.226	0.706

The computational conditions and results are summarized in Table 2. The nondimensional rotation number, Ro_τ, is defined as $2\Omega\delta/u_\tau^*$. $u_{\max}$ and u_b denote the maximum velocity in the mean velocity profile and the bulk velocity, respectively. $u_{\tau p}$ and $u_{\tau s}$ are the friction velocities on the pressure side and on the suction side, respectively. Figure 9 shows the calculated profiles of the mean velocity and the velocity fluctuations. As the rotation number increases, the mean velocity profile becomes asymmetric. The turbulence is intensified on the pressure side, while relaminarization occurs on the suction side. For that reason, the mean velocity on the pressure side lies below the log-law, whereas the mean veloc-

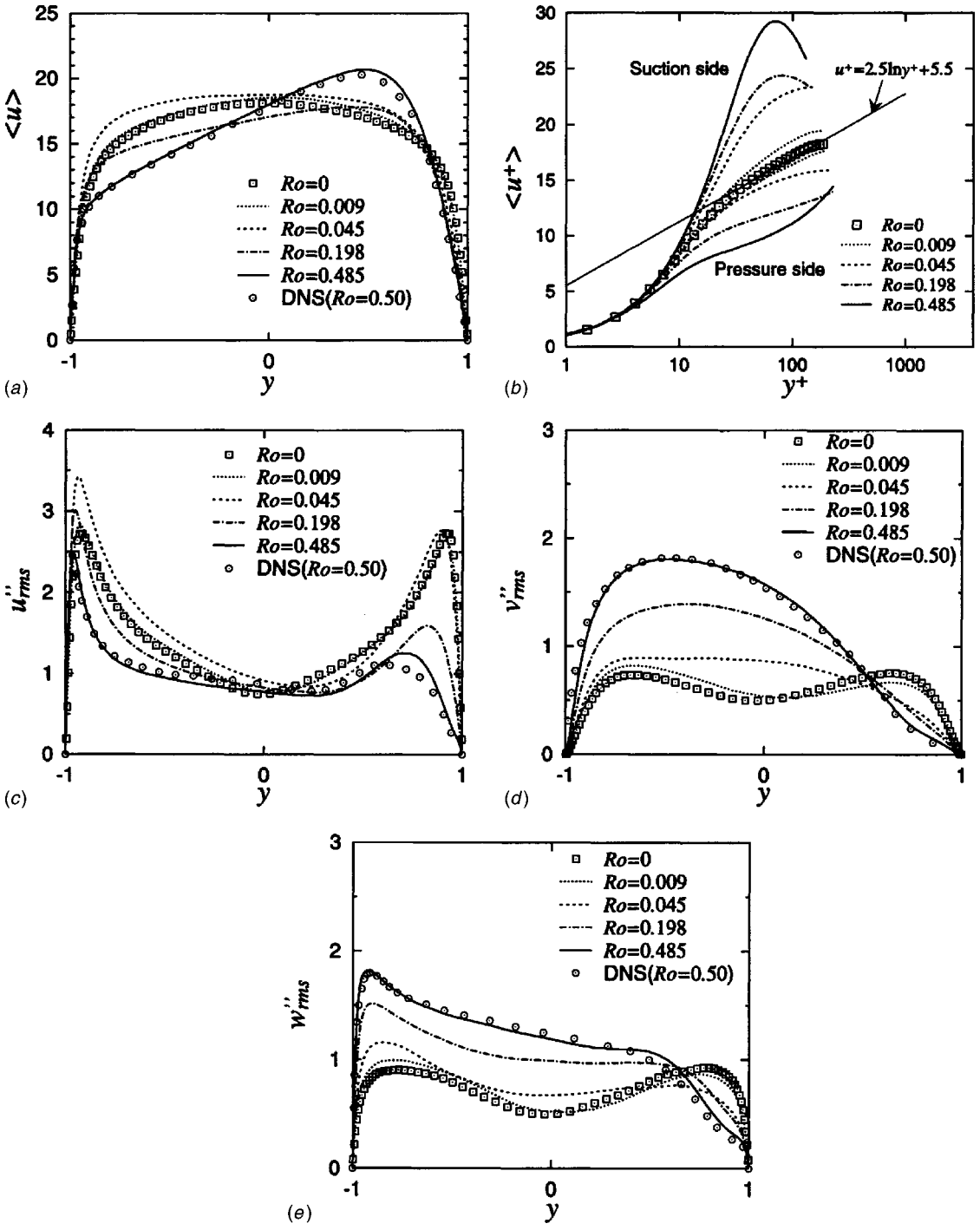

Fig. 9 Predictions of rotating channel flows using the present model: (*a*) mean velocity in global coordinate, (*b*) mean velocity in wall coordinate, (*c*) streamwise turbulent intensity, (*d*) wall-normal turbulent intensity, and (*e*) spanwise turbulent intensity

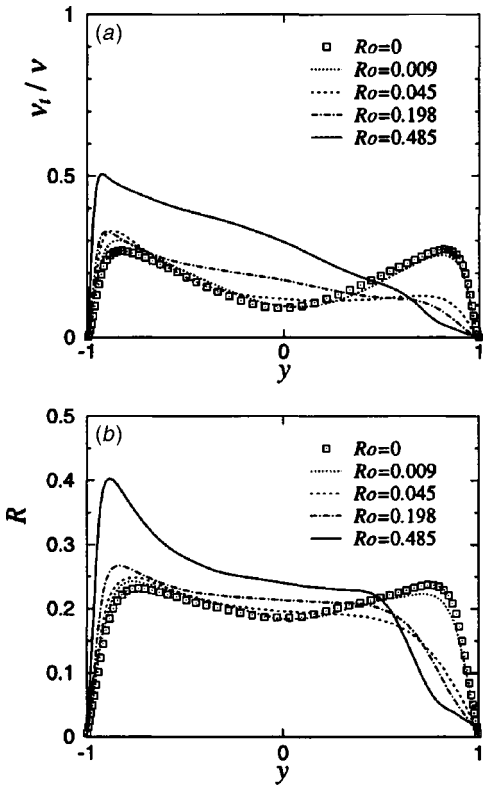

Fig. 10 Behavior of the present model in response to the change of rotation number: (*a*) SGS eddy viscosity, and (*b*) ratio of two time-scales

ity on the suction side lies above it. The results in the case of $Ro_\tau = 7.5$ agree well quantitatively with the DNS data [21].

Figure 10 shows the profiles of the SGS eddy viscosity and the ratio of two time-scales in the present model, *R*. On the suction side, *R* decreases with an increase in the rotation number, while it increases on the pressure side. On the suction side, for example, the shear rate, $|\bar{S}|$, decreases due to the relaminarization, but *R* given as $\sqrt{k_{es}}/(\Delta|\bar{S}|)$ also decreases, because the estimated SGS turbulent energy, k_{es}, decreases more rapidly in those conditions. Consequently, ν_t also decreases with an increase in the rotation number on the suction side and increases on the pressure side, which conforms to the physical development there.

6.3 Backward-Facing Step Flow. To verify the present SGS model in separating flows, we apply it to the backward-facing step flow ($Re_H = 5500$) corresponding to the experiment by Kasagi and Matsunaga [22]. Figure 11 shows the computational domain. Since the inflow condition upstream of the step was established as a fully developed turbulent channel flow in the experiment, the inflow boundary condition in the present calculation is given from the computational results of the driver part at each time step, where the independent calculation of a plane channel flow is performed with the same Reynolds number and time step. The convective boundary condition is applied at the outflow boundary. A no-slip boundary condition is applied on the all solid walls, and a periodic boundary condition is imposed in the spanwise direction. The grid resolution is $134 \times 55 \times 60$ grid points in the *x*, *y* and *z* directions, respectively, excluding the driver part. The grid resolutions in wall coordinates at the upper corner of the step are 11.6, 1.2 and 14.5 in the *x*, *y* and *z* directions, respectively.

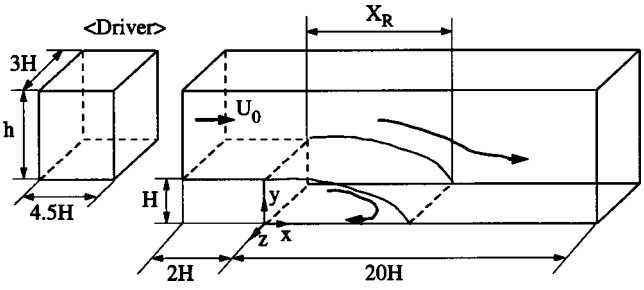

Fig. 11 Computational domain and coordinate system for backward-facing step flow

In the Smagorinsky model (S model), Cs is set to 0.1, and the value of the wall friction velocity used in the definition of the wall-damping function, f_{VD}, is fixed to that at the driver part throughout the flow field so as to mitigate the decrease in accuracy caused by the inadequate wall-damping function near the reattachment point. In the DS model, the parameter *C* is calculated by taking the average over the spanwise direction and is set to zero at those locations where *C* is calculated to be negative. For comparison of the standard DS model (DS1 model) with $\gamma = \sqrt{3}$, the calculation using $\gamma = \sqrt{6}$ (DS2 model) is also made. While we apply the filtering operator in all directions as already mentioned, the calculation using DS1 model without filtering in the wall-normal direction (DSf model) is also performed.

Figure 12 shows the profiles of mean streamwise velocity, streamwise turbulent intensity, Reynolds shear stress, and SGS eddy viscosity. The dimensionless time step, Δt, allowing for a stable calculation, and the calculated flow reattachment length, X_R, are shown in Table 3. The computational results obtained using the present model agree well with the experimental data, while the results obtained using the DS1 model show less accuracy and less computational stability. Owing to the computational instability, the time step in the calculation using DS1 model must be set to about one-fourth of that using the S model. On the other hand, the calculation using the present model is successfully performed with the same time step as in the calculation using the S model. This computational stability of the present model is due to the fixed model-parameters employed instead of the dynamically adjusted ones adopted in the DS1 model. By using the DS2 model, the restriction on the time step is somewhat relaxed in comparison with the DS1 model, but the disagreement of X_R becomes larger. These results prove that the present model is a practically useful SGS model that satisfies both the accuracy and the computational stability.

Figure 13 shows the ratio of two time-scales in the present model, *R*. As in the results of the plane channel flows, *R* is approximately constant away from the wall, though its value (around 0.4) is somewhat higher, i.e., 0.2–0.3 in the plane channel flows. It should be noted that *R* remains nearly constant despite the stretch of grid spacing in the streamwise direction. It is also found that *R* is about 0.3 at the maximum in the $x/H = -1$ plane where the property of the flow is almost the same as that in the plane channel flow. That is, *R* may change according to the flow property. The cusps are observed around $y/H = 1$ where the grid in the *y* direction is highly condensed. These cusps result in the smoother change of ν_t there, which is similar to the effect of the cusps in the calculated parameter Cs in the DS model shown later (see Fig. 14).

One of the reasons why the DS model is considered to be not always accurate in our study, despite so many previous studies demonstrating the excellent property of the dynamic approach, is that the direction-independent filtering procedure is employed in our calculations as mentioned previously. Figure 14 shows the effect of *y*-direction filtering in the DS model. As shown in Fig. 14(*b*), the distributions of the SGS eddy viscosity obtained using the DSf model almost coincide with those obtained using the S model with the exception of the region of separating shear layer. On the other hand, those obtained using the DS1 model do not coincide with those obtained using the DSf model except for the

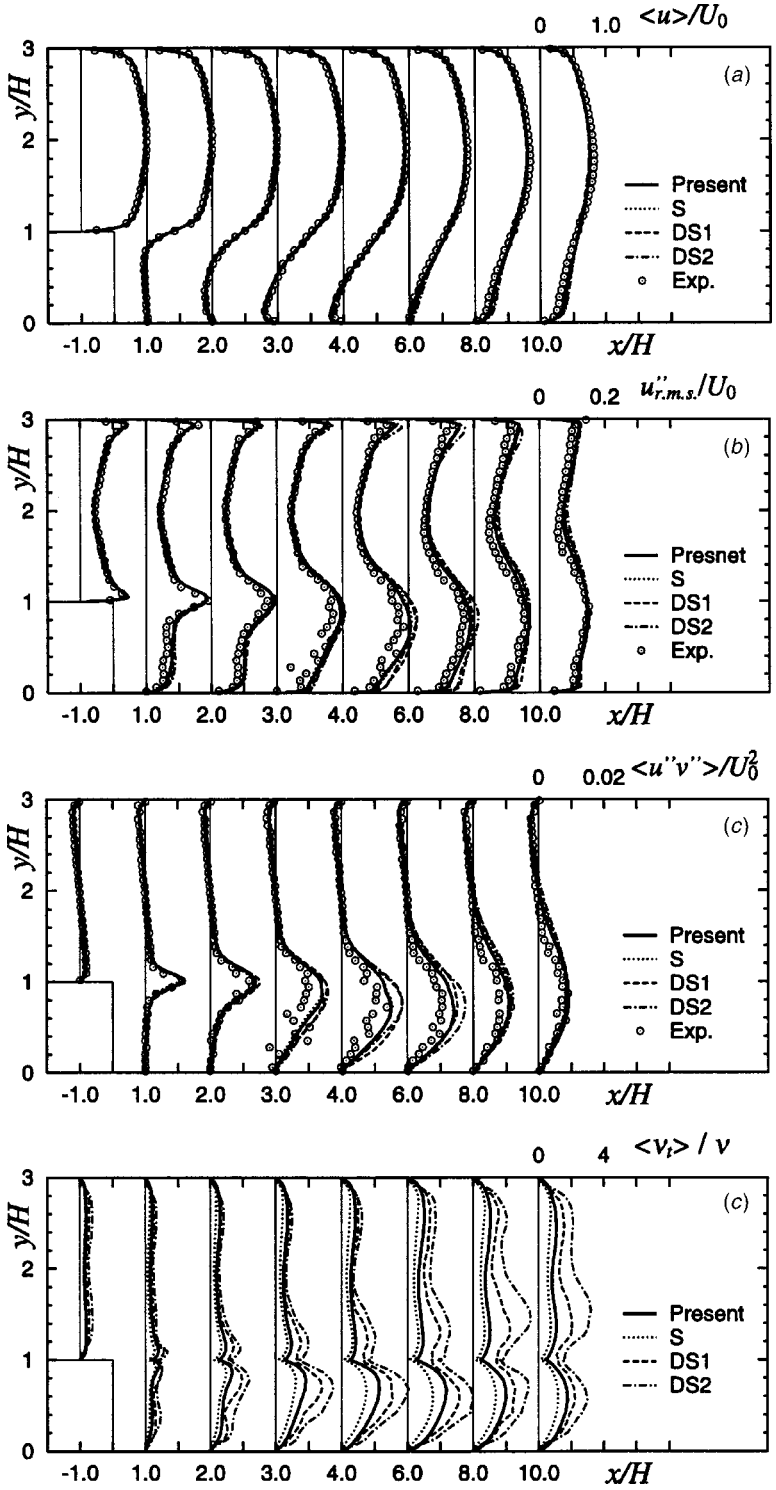

Fig. 12 Predictions of backward-facing step flow: (*a*) mean streamwise velocity, (*b*) streamwise turbulent intensity, (*c*) Reynolds shear stress, and (*d*) SGS eddy viscosity

regions with fine grid spacing in the y direction, where the y-direction filtering has very little influence. This discrepancy in the SGS eddy viscosity is owed to the different Cs calculated as shown in Fig. 14(*a*). The DS1 model gives an over 30% higher Cs value than the DSf model. This discrepancy possibly leads to a different evaluation of the accuracy of DS model from other studies. Although little improvement is seen in the prediction of X_R using the DSf model, the improvement in the Reynolds shear

Table 3 Computational time step and flow reattachment length in calculation of backward-facing step flow

	X_R/H	Δt	Time step ratio
Present	6.44	4×10^{-4}	1.0
S	6.40	4×10^{-4}	1.0
DS1($\gamma=\sqrt{3}$)	6.25	1×10^{-4}	0.25
DS2($\gamma=\sqrt{6}$)	6.06	2×10^{-4}	0.50
DSf	6.28	1×10^{-4}	0.25
Exp.	6.51	···	···

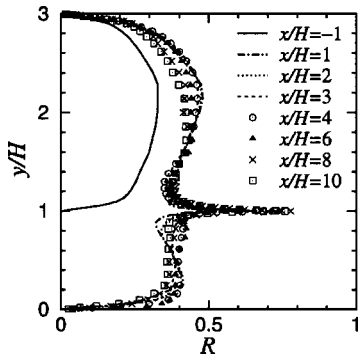

Fig. 13 Ratio of two time-scales used in present model in backward-facing step flow

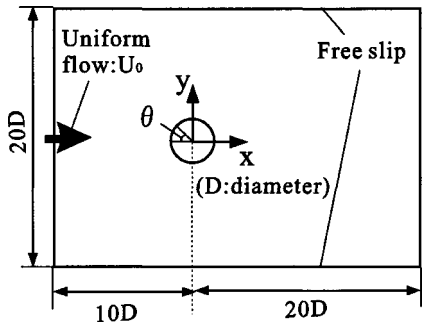

Fig. 15 Computational domain and coordinate system for flow around the circular cylinder

stress is clearly observed around the location of $x/H=4$ in Fig. 14(*c*). For the practical use of LES, however, the use of all-directional filtering is considered inevitable. In other words, the assessment of the dynamic model on the assumption that the filtering is not done in the wall-normal direction is not valid for engineering application problems. From this standpoint, the present model is a refined SGS model suited for practical LES.

6.4 Flow Around Circular Cylinder. We also apply the present model to flow around a circular cylinder, which is a typical outer flow. The Reynolds number based on the diameter of the circular cylinder and the mean inflow velocity, $\mathrm{Re}=DU_0/\nu$, is set to 10,000. Figure 15 shows the computational domain. We employ an overlaid grid system (e.g., [23]) to reduce the computational cost. The computational domain is divided into two subdomains. Subdomain 1 surrounds the circular cylinder with the radial extent of about $1.7D$, while subdomain 2 covers the whole computational domain. The number of grid points in subdomain 1 is $160\times56\times20$ in the circumferential, radial, and spanwise directions, respectively; that in subdomain 2 is $96\times60\times20$ in the *x*, *y*, and *z* directions, respectively. The minimum grid spacing is $4\times10^{-3}D$. The spanwise extent of the domain is set to $2D$, and a periodic condition is imposed on that direction. A no-slip boundary condition is applied on the wall, and a no-stress condition is imposed at the upper and lower boundaries. A uniform flow condition is imposed at the inflow boundary. At the outflow boundary, the convective boundary condition is applied.

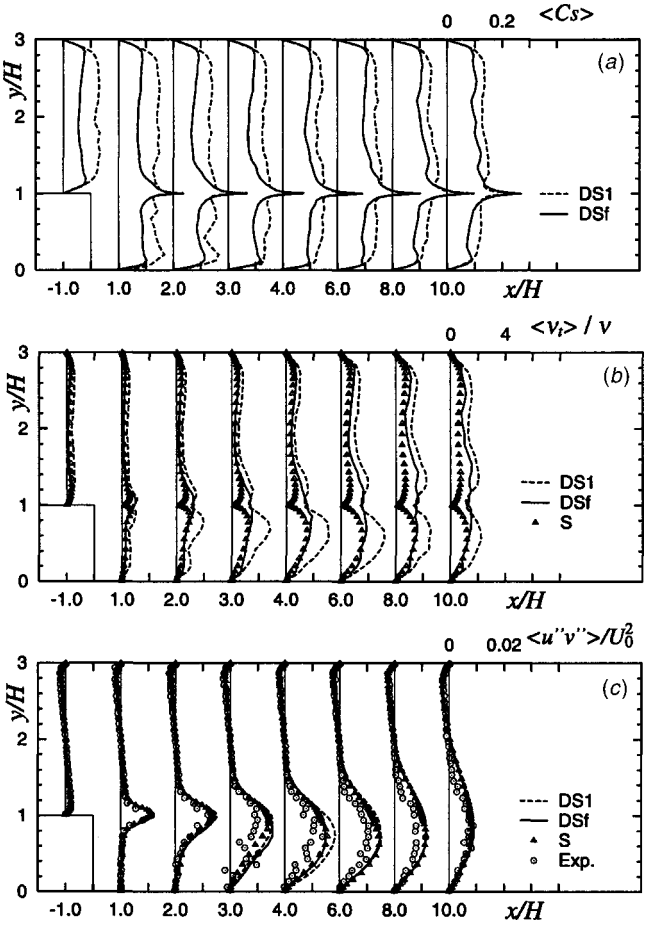

Fig. 14 Effect of *y*-direction filtering in the dynamic Smagorinsky model: (*a*) model parameter *Cs*, (*b*) SGS eddy viscosity, and (*c*) Reynolds shear stress

In the Smagorinsky model, Cs is set to 0.1 (S1 model) and 0.15 (S2 model). The former is the value used in the previous test cases, while the latter is the value generally used in outer flow calculations. As for the wall-damping function, the same problem as in the backward-facing step flow occurs if that of van Driest's type is adopted. Namely, the effective region of a wall-damping function is unreasonably expanded near the flow separation point and reattachment point. Moreover, there is another problem in the region before the separation point, where the flow is laminar at the current Reynolds number. To represent this flow field, the wall-damping function must be equal to zero. However, it is impossible for the damping function of van Driest's type to represent this relation. Thus, to evade the decrease in accuracy and the ambiguity caused by the wall-damping function in this study, the following wall-damping function, the validity of which in this flow field is ascertained by Kato and Ikegawa [24], is employed:

$$f=\min(1,\sqrt{5n/D}), \tag{22}$$

where n indicates the distance from the wall surface. In the DS model, the parameter C is obtained in the same manner as in the calculation of the backward-facing step flow.

Table 4 shows the calculated drag coefficient, C_D, which is the most important characteristic of bluff bodies, the root mean square of the lift coefficient fluctuation, C_{Lrms}, the angle of the flow separation point, θ_{SP}, the length of the recirculating region on the centerline, X_R, Strouhal number, St, and the time step allowing for a stable calculation, Δt. In this table, C_{Dp} and C_{Df} indicate the pressure and friction drag coefficient, respectively. These calculated results are compared with some experimental results [25–28]. Figure 16 shows the pressure distribution on the cylinder surface. The present model and the S2 model predict the C_D to be in fair agreement with the experimental data, while the DS model shows less accuracy in pressure distribution on the cylinder surface (especially $\theta>100$ deg) and less computational stability, similar to the previous test case. The S1 model underpredicts the base pressure, while the present model predicts it accurately even though the same model parameter as in the previous test cases is

Table 4 Results of flow around a circular cylinder and the computational time step

	$C_D(C_{Dp},C_{Df})$	C_{Lrms}	θ_{SP}	X_R	St	Δt	Time step ratio
Present	1.17(1.142,0.030)	0.44	86 deg	0.83D	0.21	4×10^{-3}	1.0
S1($Cs=0.1$)	1.32(1.286,0.032)	0.61	86 deg	0.75D	0.21	4×10^{-3}	1.0
S2($Cs=0.15$)	1.19(1.162,0.032)	0.39	85 deg	0.95D	0.21	4×10^{-3}	1.0
DS	1.08(1.054,0.029)	0.39	86 deg	0.91D	0.21	2×10^{-3}	0.50
Exp.	1.1–1.2	0.3–0.5	⋯	$\approx1.0D$	0.20–0.21	⋯	⋯

used. Thus, the present model is considered to be more universal than the Smagorinsky model. Figure 17 shows the ratio of two time-scales, R, used in the present model. In contrast to the results in the channel flow and the backward-facing step flow, it varies from 0.4 to 0.8 in the wake region of this flow field. If R rises from 0.225 to 0.6, ν_t increases by 24%. This property of the present model may be one reason why it gives accurate results with the consistent model parameters.

Figure 18 shows the profiles of the mean streamwise velocity, streamwise turbulent intensity, mean pressure coefficient, and SGS eddy viscosity along the radial lines. Although we do not have corresponding experimental data, it is found that the present model gives results closer to those of the S2 model than the DS model. Taking into account that the model parameter used in the S2 model is an artificially optimized one for this flow field, the accuracy of the present model is presumably higher than that of the DS model. Figure 18(d) shows that at $\theta=0°$ where flow is laminar, ν_t given by the present model becomes nearly zero as in the DS model since $\sqrt{k_{es}}$ approaches zero. Figure 19 shows the mean velocity and turbulent intensity distributions in the $x=D$ plane in quantitative comparison with experimental data by Norberg [28]. In this figure, any results except for the S1 model's agree well with the experimental data. It can be seen that the calculated maximum value of the turbulent intensity is lower than the experi-

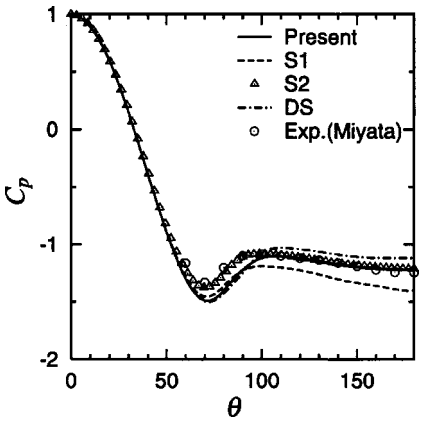

Fig. 16 Pressure distribution on the cylinder surface

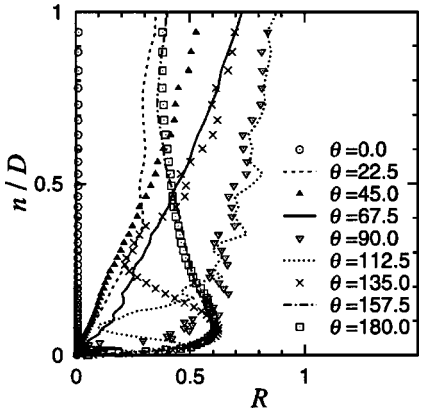

Fig. 17 Ratio of two time-scales used in the present model in flow around the circular cylinder

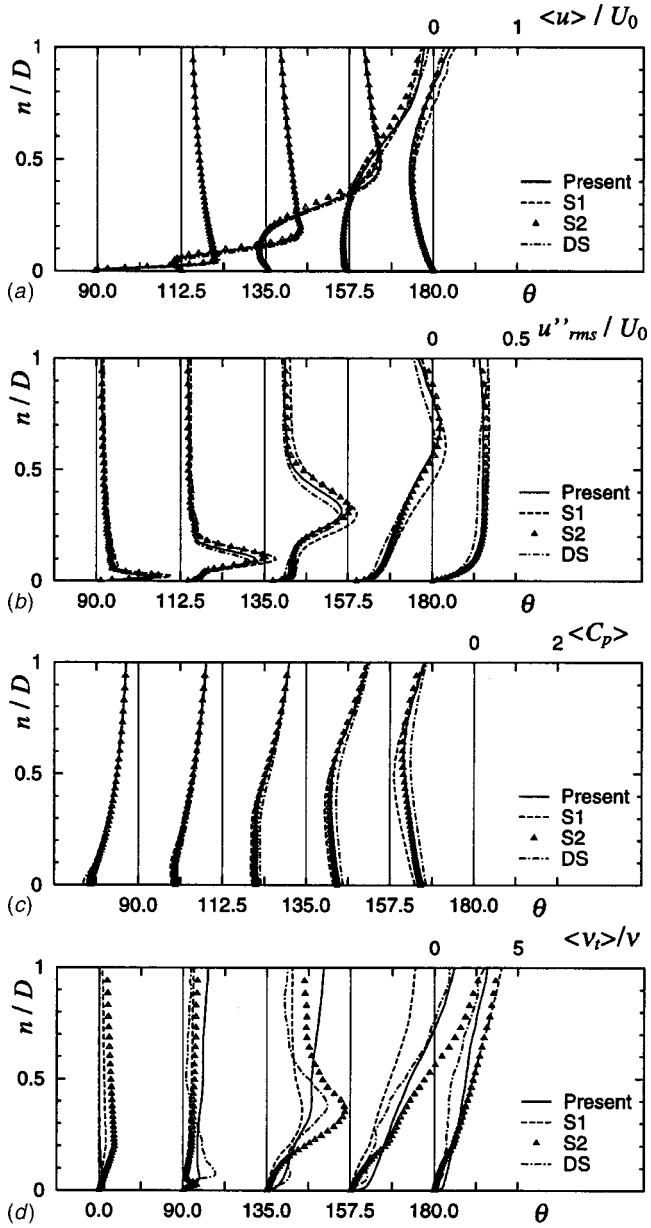

Fig. 18 Comparison of results of flow around the circular cylinder along radial lines: (a) mean streamwise velocity, (b) streamwise turbulent intensity, (c) mean pressure coefficient, and (d) SGS eddy viscosity

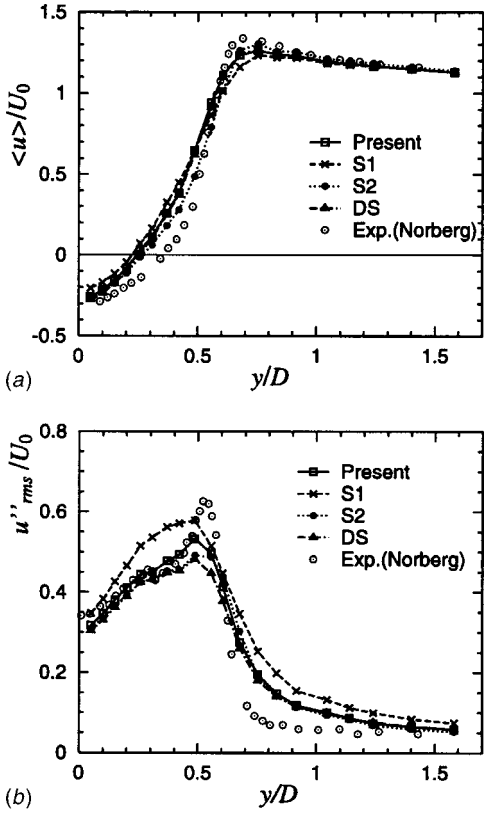

Fig. 19 Comparison of results of flow around the circular cylinder with experimental data: (*a*) mean streamwise velocity and (*b*) streamwise turbulent intensity

mental data, probably due to the insufficient grid resolution around the separating shear layer. Another reason is that the results do not include the SGS components, which also become nontrivial in the region of low grid resolution.

6.5 Flow Around the Ahmed Model. We also apply the present SGS model to the three-dimensional flow around an Ahmed model (Ahmed et al. [7]) that is a typical engineering application on high Reynolds number condition. The coordinate system is illustrated in Fig. 20. The rear body slant angle is 25 deg and the incoming flow velocity is 40 m/s. Taking account of the previously mentioned near-wall problem on such high Reynolds number conditions, we employ a conventional artificial wall condition on the wall surface, and select a test problem in which the locations of the flow separation points are apparent and little influenced by the conceivable disparity in the property of turbulent boundary layer before the separation.

The computational domain is divided into two subdomains. The number of grid points is 197×127×132 in subdomain 1 that surrounds the Ahmed model and 122×59×62 in subdomain 2 that covers the whole computational domain. The minimum grid spacing is 0.05 mm. In the DS model, the parameter C is calculated locally with the clipping that sets the negative SGS eddy viscosity to zero. In the S model, Cs is set to 0.15, and the following wall-damping function is adopted: $f=\min(1,\sqrt{n/L_d})$, where L_d is set to 10 mm.

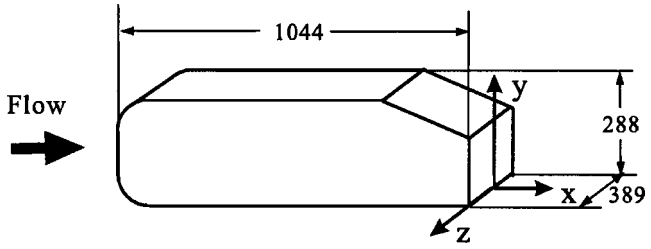

Fig. 20 Appearance of the Ahmed body and dimensions

Table 5 Drag coefficient of the Ahmed model and the computational time step

	C_D (Error %)	Δt	Time step ratio
Present	0.289 (+2)	5×10^{-5}	1.0
S	0.326 (+15)	5×10^{-5}	1.0
DS	0.262 (−7)	2.5×10^{-5}	0.50
Exp.	0.283	···	···

In the wall condition, we assume the following three-layer wall function modified from the two-layer one proposed by Werner and Wengle [29] on the instantaneous velocity distribution:

$$\begin{aligned} u^+&=y^+ \quad (y^+\leqslant y^+_{C1}),\\ u^+&=A1y^{+B1} \quad (y^+_{C1}<y^+\leqslant y^+_{C2}),\\ u^+&=A2y^{+B2} \quad (y^+_{C2}<y^+),\\ y^+_{C1}&=A1^{1/(1-B1)},\quad y^+_{C2}=(A2/A1)^{1/(B1-B2)}, \end{aligned} \tag{23}$$

where $A1=2.7$, $A2=8.6$, $B1=1/2$, and $B2=1/7$. Using the three-layer wall function may prevent a decrease in accuracy around $y^+=10$. According to Eq. (23), the wall shear stress, τ_w, is estimated as follows:

$$\begin{aligned} \tau_w&=\frac{\overline{u}_p}{\mathrm{Re}\,y_p} \quad (\overline{u}_p\leqslant\overline{u}_{C1}),\\ \tau_w&=\left[\frac{1+B1}{A1}\left(\frac{1}{2\,\mathrm{Re}\,y_p}\right)^{B1}\overline{u}_p+\frac{1-B1}{2}\left(\frac{y^+_{C1}}{2\,\mathrm{Re}\,y_p}\right)^{1+B1}\right]^{2/1+B1}\\ &\quad(\overline{u}_{C1}<\overline{u}_p\leqslant\overline{u}_{C2}),\\ \tau_w&=\left[\frac{1+B2}{A2}\left(\frac{1}{2\,\mathrm{Re}\,y_p}\right)^{B2}\overline{u}_p+\frac{B1-B2}{1+B1}\left(\frac{y^+_{C2}}{2\,\mathrm{Re}\,y_p}\right)^{1+B2}\right.\\ &\quad\left.+\frac{(1-B1)(1+B2)}{2A2(1+B1)}\left(\frac{1}{2\,\mathrm{Re}\,y_p}\right)^{1+B2}y^+_{C1}\right]^{2/1+B1}\\ &\quad(\overline{u}_{C2}<\overline{u}_p),\\ \overline{u}_{C1}&=\frac{1}{4\,\mathrm{Re}\,y_p}(y^+_{C1})^2,\quad \overline{u}_{C2}=\frac{1}{4\,\mathrm{Re}\,y_p(B1+1)}\{(B1-1)(y^+_{C1})^2\\ &\quad+2A2(y^+_{C2})^{(1+B2)}\}, \end{aligned} \tag{24}$$

where $\overline{u}_p$ and y_p indicate the filtered velocity component parallel to the wall and the distance from the wall at the center of the grid cells next to the wall, respectively. However, τ_w itself does not appear explicitly in the discretized equation in the generalized curvilinear coordinates. Thus, we define the effective viscosity on the wall as follows:

$$\nu_{\mathrm{eff}}=\frac{\tau_w y_p}{\overline{u}_p}. \tag{25}$$

By using ν_{eff} instead of ν in evaluating the viscous stress on the wall, the present wall condition is embedded. In the LES calculation using the present model, the wall coordinates at the center of the grid cells adjacent to the upper surface of the body in the symmetry plane vary approximately from 0.2 to 6.

The calculated drag coefficient, C_D, and the time step allowing for a stable calculation are shown in Table 5. The drag coefficient obtained using the present model agrees well with the experimental result, while the results using the DS model continue to show

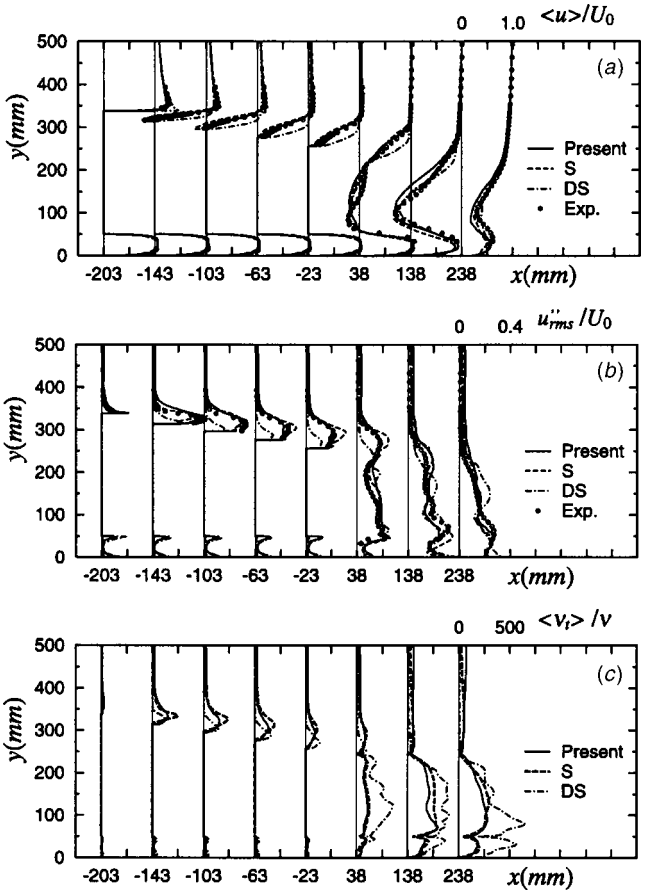

Fig. 21 Comparison of results of flow around the Ahmed body in symmetry plane: (*a*) mean streamwise velocity, (*b*) streamwise turbulent intensity, and (*c*) SGS eddy viscosity

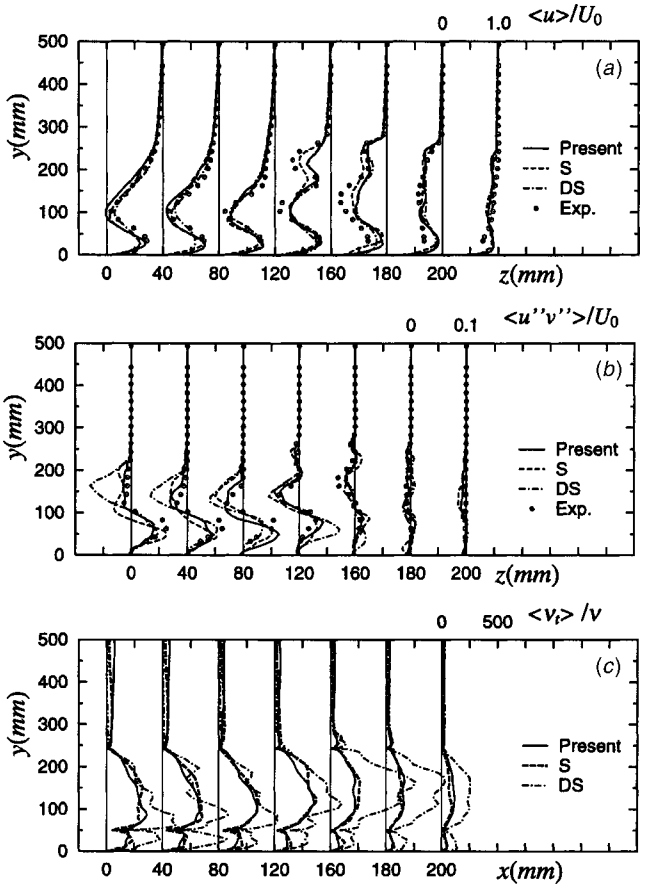

Fig. 22 Comparison of results of flow around the Ahmed body in $x=200$ mm plane: (*a*) mean streamwise velocity, (*b*) Reynolds shear stress, and (*c*) SGS eddy viscosity

less accuracy and less computational stability. Figure 21 shows the mean velocity, the turbulent intensity distribution, and the SGS eddy viscosity in the symmetry plane, while Fig. 22 shows those in the $x=200$ mm plane. The agreement between the computational results using the present model and the experimental data [30] is quite satisfactory. The DS model does not predict these quantities adequately, especially in the separation region over the rear slant face. The DS model predicts a shorter separation length whereas the S model predicts a longer one, which results in the disagreement in C_D. As shown in Figs. 21(*c*) and 22(*c*), the ratio of the calculated SGS eddy viscosity to the molecular viscosity is more than 100. Thus, the role of the SGS eddy viscosity is extraordinarily large. The present model gives the similar distributions calculated with the S model in the wake region behind the body, while the DS model gives two or three times larger values there. The same tendency has been found in the results of the backward-facing step flow, i.e., the higher SGS eddy viscosity is given by the DS model. The overestimation of the SGS eddy viscosity in the DS model should be enhanced in the calculation of this flow, because the Reynolds number is very high. Hence, the present model can be expected to work well in various three-dimensional engineering applications. However, when the present model is applied to the high Reynolds number flow in which the locations of the flow separation points are difficult to predict, it might be combined with more proper wall modeling (e.g., hybrid LES/RANS modeling) as already mentioned.

7 Conclusions

We proposed a new SGS model that is suited for practical large eddy simulation. Being constructed with the concept of the mixed-time-scale, the present model enables us to use a set of consistent model-parameters and to dispense with a wall-damping function of van Driests type as in the dynamic Smagorinsky model. The accuracy of the present model is as good as that of the Smagorinsky model with the model parameter optimized for the relevant flow field, and is higher than the dynamic Smagorinsky model using the all-direction filtering procedure. The usage of fixed model-parameters provides computational stability in contrast to the dynamic Smagorinsky model. Furthermore, the present model is easily applied to flows with complex geometries because no artificial averaging procedure is needed to stabilize the computation. Thus, it is concluded that the present model is a refined SGS model suited for engineering-relevant practical LES.

References

[1] Gatski, T. B., and Rumsey, C. L., 2002, "Linear and Nonlinear Eddy Viscosity Models," in *Closure Strategies for Turbulent and Transitional Flows* (edited by B. Launder and N. Sandham), Cambridge University Press, Cambridge, pp. 9–46.

[2] Germano, M., Piomelli, U., Moin, P., and Cobat, W. H., 1991, "A Dynamic Subgrid-Scale Eddy Viscosity Model," Phys. Fluids A, **3**(7), pp. 1760–1765.

[3] Akselvoll, K., and Moin, P., 1993, "Large Eddy Simulation of a Backward Facing Step Flow," Proc. 2nd International Symposium on Engineering Turbulence Modeling and Measurements, May 21–June 2, Florence, Italy.

[4] Meneveau, C., Lund, T. S., and Cabot, W. H., 1996, "A Lagrangian Dynamic Subgrid-Scale Model of Turbulence," J. Fluid Mech., **319**, pp. 353–385.

[5] Chapman, D. R., 1979, "Computational Aerodynamics Development and Outlook," AIAA J., **17**(12), pp. 1293–1313.

[6] Spalart, P. R., Jou, W.-H., Strelets, M., and Allmaras, S. R., 1997, "Comments

on the Feasibility of LES for Wings, and on a Hybrid RANS/LES Approach,'' First AFOSR Int. Conf. on DNS/LES, August 4–8, Ruston, LA.
[7] Ahmed, S. R., Ramm, G., and Faltin, G., 1984, ''Some Salient Features of the Time-Averaged Ground Vehicle Wake,'' SAE Paper no. 840300.
[8] Piomelli, U., Ferziger, J. H., and Moin, P., 1987, ''Models for Large Eddy Simulations of Turbulent Channel Flows Including Transpiration,'' Report TF-32, Department of Mechanical Engineering, Stanford University, Stanford, CA.
[9] Lilly, D. K., 1992, ''A Proposed Modification of the Germano Subgrid-Scale Closure Method,'' Phys. Fluids A, **4**, pp. 633–635.
[10] Taniguchi, N., 1995, ''Dynamic SGS Model by Finite Difference Method,'' Mon. J. Inst. Ind. Sci. (University of Tokyo), **47**(2), pp. 42–45.
[11] Horiuti, K., 1993, ''A Proper Velocity Scale for Modeling Subgrid-Scale Eddy Viscosities in Large Eddy Simulation,'' Phys. Fluids A, **5**(1), pp. 146–157.
[12] Sagaut, P., Comte, P., and Ducros, F., 2000, ''Filtered Subgrid-Scale Models,'' Phys. Fluids, **12**(1), pp. 233–236.
[13] Yoshizawa, A., Kobayashi, K., Kobayashi, T., and Taniguchi, N., ''A Nonequilibrium Fixed-Parameter Subgrid-Scale Model Obeying the Near-Wall Asymptotic Constraint,'' Phys. Fluids, **12**(9), pp. 2338–2344.
[14] Bardina, J., Ferziger, J. H., and Reynolds, W. C., 1983, ''Improved Turbulence Models Based on Large Eddy Simulation of Homogenous, Incompressible, Turbulent Flows,'' Report TF-10, Thermosciences Division, Department of Mechanical Engineering, Stanford University, Stanford, CA.
[15] Tsubokura, M., 2001, ''Proper Representation of the Subgrid-Scale Eddy Viscosity for the Dynamic Procedure in Large Eddy Simulation Using Finite Difference Method,'' Phys. Fluids, **13**(2), pp. 500–504.
[16] Abe, K., Kondoh, T., and Nagano, Y., 1995, ''A New Turbulence Model for Predicting Fluid Flow and Heat Transfer in Separating and Reattaching Flows—II. Thermal Field Calculations,'' Int. J. Heat Mass Transfer, **38**, pp. 1467–1481.
[17] Rhie, C. M., and Chow, W. L., 1983, ''Numerical Study of the Turbulent Flow Past an Airfoil With Trailing Edge Separation,'' AIAA J., **21**, pp. 1525–1532.
[18] Morinishi, Y., Lund, T. S., Vasilyev, O. V., and Moin, P., 1998, ''Fully Conservative Higher Order Finite Difference Schemes for Incompressible Flow,'' J. Comput. Phys., **143**, pp. 90–124.
[19] Kim, J., Moin, P., and Moser, R., 1987, ''Turbulence Statistics in Fully Developed Channel Flow at Low Reynolds Number,'' J. Fluid Mech., **177**, pp. 133–166.
[20] Kim, J., 1990, ''The Collaborative Testing of Turbulence Models,'' organized by P. Bradshaw, Data disk no. 4.
[21] Kristoffersen, R., and Andersson, H., 1993, ''Direct Simulation of Low-Reynolds-Number Turbulent Flow in a Rotating Channel,'' J. Fluid Mech., **256**, pp. 163–197.
[22] Kasagi, N., and Matsunaga, A., 1995, ''Three-Dimensional Particle-Tracking Velocimetry Measurement of Turbulence Statistics and Energy Budget in a Backward-Facing Step Flow,'' Int. J. Heat Fluid Flow, **16**, pp. 477–485.
[23] Horinouchi, N., Kato, Y., Shinano, S., Kondoh, T., and Tagayashi, Y., 1995, ''Numerical Investigation of Vehicle Aerodynamics With Overlaid Grid System,'' SAE paper no. 950628.
[24] Kato, C., and Ikegawa, M., 1991, ''Large Eddy Simulation of Unsteady Turbulent Wake of a Circular Cylinder Using the Finite Element Method,'' ASME FED-Vol. 117, Advances in Numerical Simulation of Turbulent Flows.
[25] Schlichting, H., *Boundary Layer Theory*, McGraw-Hill Series in Mechanical Engineering, McGraw–Hill, New York.
[26] Norberg, C., and Sundén, B., 1987, ''Turbulence and Reynolds Number Effects on the Flow and Fluid Forces on a Single Cylinder in Cross Flow,'' J. Fluids Struct., **1**, pp. 337–357.
[27] Mityata, M., and Okuyama, T., 1997, ''Some Methods for Drag Reduction of Circular Cylinder in Uniform Flow,'' Proc. JSFM Symposium on Turbulent Flows (in Japanese), pp. 147–148.
[28] Norberg, C., 1998, ''LDV-Measurements in the Near Wake of a Circular Cylinder,'' ASME Fluids Engineering Division Summer Conference Paper FEDSM98-5202.
[29] Werner, H., and Wengle, H., 1991, ''Large Eddy Simulation of Turbulent Flow Over and Around a Cube in a Plane Channel,'' Proc. 8th Symposium on Turbulent Shear Flows, pp. 19-4-1–19-4-6.
[30] Lienhart, H., Stoots, C., and Becker, S., 2000, ''Flow and Turbulence Structures in the Wake of a Simplified Car Model (Ahmed Model),'' DGLR Fach Symp. der AG STAB, pp. 15–17.

K. Ghorbanian
Assistant Professor

M. R. Soltani
Associate Professor

M. R. Morad
Ph.D. Student

Department of Aerospace Engineering,
Sharif University of Technology,
Tehran, Iran

M. Ashjaee
Associate Professor,
Department of Mechanical Engineering,
University of Tehran,
Tehran, Iran

Velocity Field Reconstruction in the Mixing Region of Swirl Sprays Using General Regression Neural Network

A general regression neural network technique is proposed for design optimization of pressure-swirl injectors. Phase doppler anemometry measurements for velocity distributions are used to train the neural network. An overall optimized value for the width of the probability is determined. The velocity field in the extrapolation regime is reconstructed with an accuracy of 93%. Excellent agreement between the predicted values and the measurements is obtained. The results indicate that the capability of performing design- and optimization studies for pressure-swirl injectors with sufficient accuracy exists by applying modest amount of data in conjunction with an overall optimized value for the width of the probability. [DOI: 10.1115/1.1852472]

1 Introduction

Atomization processes are inherently complex involving close coupling of both thermodynamic state of the fluid, as well as the design of the injector. The fragmentation of the injected liquid into smaller fluid elements, its mixing, evaporation, and combination at the molecular level with other species in chemical reaction is of critical importance. Today, new propulsion systems require practically new injector developments. Hence, research programs are launched toward a better phenomenological understanding of atomization phenomena in terms of breakup behavior of the spray in the near-field, drop size, and velocity characteristics in the far-field of the injector.

Historically, pressure-swirl injectors are designed based on experience, empirical design tools derived from subscale databases, and personal intuition. However, in general, empirical design methodologies are limited to test conditions and range of variables for which the tests are performed. Design improvements are achieved through extensive sub- and full-scale cold and hot test programs. Furthermore, due to the lack of an optimization scheme for pressure-swirl injectors, a large number of studies are performed for a better assessment of impacts of the geometrical parameters, operating conditions, and propellant properties on the spray and the resulting flow characteristics. Specifically, state-of-the-art computers and CFD algorithms, as well as laser-based nonintrusive diagnostics are utilized. As a result, required data from test programs, for the purpose of injector design, as well as the performance optimization task, make the design procedure expensive and time consuming.

On the other hand, in both experimental and CFD studies, flow fields are often illustrated as a distribution of discrete points. While experimental measurements provide local and instantaneous information, CFD methods exploit continuous differential equations on a discrete environment called numerical grid. Thus, interpolation schemes are usually employed to determine unknown values at desired positions. Nevertheless, in common interpolation methods, it is required to assume a function with some unknown parameters. Thus, if the flow becomes complex or has a great spatial dependency, common interpolation methods are challenged since a large number of data is required to represent the entire flow field. Recognition of this has direct implications for pressure-swirl atomizer design methodologies.

In addition, tight and lower budget programs as well as aggressive schedules will no longer allow either an extensive test program as in the past or a thorough experimental investigation on the effect of new determined design variables on the overall performance characteristics. Thus, the introduction of an alternative tool, enabling to foresee the effect of modification of design variables, as well as to guide the design optimization procedure in a short time frame, will be of great importance to the designer. A different approach to capture the flow field is by means of neural networks.

Among the scientific communities, the application of neural networks is growing owing to their fast, reliable, and computationally inexpensive response. Several attempts have been made to apply artificial neural networks to problems in fluid dynamics and sprays. Amir et al. [1] used CFD calculations to train artificial neural network (ANN) methodology for the propane spray development. Their results indicated that ANN modeling could be superior to CFD techniques if the model is sufficiently trained. In another study, Schulte et al. [2] applied neural network to model the structure of a fan atomizer. Measurements from phase doppler anemometer (PDA) are used to train the neural network. Further, Pruvost et al. [3] used a neural network algorithm based on radial basis functions (RBF) to investigate three-dimensional velocity field of a swirl jet flow. This technique appeared to be an efficient tool to accurately represent any hydro-dynamical characteristics of complex flows.

The present work attempts to develop a fast, reliable, and robust neural network tool for pressure-swirl atomizer design optimization when a limited amount of design data exist. Two different atomizer configurations are considered: A single swirl atomizer and a double swirl atomizer. As a first step, the spray behavior at various pressures, as well as various spatial arrangements, is experimentally investigated for both configurations using a high-speed CCD camera and phase doppler anemometry (PDA) technique. PDA results are used to train a general regression neural network (GRNN) [4]. Critical parameters to the GRNN training are also evaluated and discussed. Finally, the degree of the accuracy of the predicted results by GRNN is presented and compared using additional data from PDA.

Contributed by the Fluids Engineering Division for publication on the JOURNAL OF FLUIDS ENGINEERING. Manuscript received by the Fluids Engineering Division December 17, 2002; revised manuscript received September 27, 2004. Review Conducted by: M. Plesniak.

2 General Regression Neural Network

ANN is a wide class of flexible nonlinear regression and discriminant models, data reduction models, and nonlinear dynamical systems [5]. ANN consists of an often large number of "neurons"—that is, simple linear or nonlinear computing elements, interconnected in some complex ways and normally structured into layers.

Many ANN models are similar or identical to popular statistical techniques, such as generalized linear models, polynomial regression, nonparametric regression, discriminant analysis, projection pursuit regression, principal components, and cluster analysis. ANN models are capable of processing vast amount of data and making predictions of complicated phenomenon beyond conditions examined during testing, computations, etc. This paper is concerned with general regression neural networks (GRNN) for data analysis, and predictions at various situations.

The GRNN is a memory-based feed forward network that is based on the assessment of probability density function. Assume that $f(\vec{x},y)$ represents the known joint continuous probability density function of a vector random variable, $\vec{x}$, and a scalar random variable, y. The expected value of y given X (also called the regression of y on X) can be computed by

$$E[y|X]=\frac{\int_{-\infty}^{+\infty} y f(X,y)dy}{\int_{-\infty}^{+\infty} f(X,y)dy} \tag{1}$$

In practice, the probability density function is usually not known and, therefore, has to be estimated by sample of observations of $\vec{x}$ and y. The probability estimator $\hat{f}(X,Y)$ is based on sample values X_i and Y_i

$$\hat{f}(X,Y)=\frac{1}{(2\pi)^{(p-1)/2}\sigma^{(p+1)}}\cdot\frac{1}{n}\sum_{i=1}^{n}\exp\left[-\frac{(X-X_i)^T(X-X_i)}{2\sigma^2}\right]\exp\left[-\frac{(Y-Y_i)^2}{2\sigma^2}\right] \tag{2}$$

Substituting the probability estimator $\hat{f}$ from Eq. (2) into the conditional mean in Eq. (1), gives the desired conditional mean of y for a given X as

$$\hat{Y}(X)=\frac{\Sigma_{i=1}^{n} Y_i \exp\left[-\frac{D_i^2}{2\sigma^2}\right]}{\Sigma_{i=1}^{n}\exp\left[-\frac{D_i^2}{2\sigma^2}\right]} \tag{3}$$

where the scalar function D_i^2 is defined as:

$$D_i^2=(X-X_i)^T(X-X_i) \tag{4}$$

Parzen [6] and Cacoullos [7] have shown that the probability estimator in the form of equation (2), used in estimating (1) by (3), provides consistent estimators (that is, asymptotically converging to the underlying probability density function $f(\vec{x},y)$) at all points $(\vec{x},y)$ where the density function is continuously by given as $\sigma=\sigma(n)$, and is a decreasing function of n such that

$$\lim_{n\to\infty}\sigma(n)=0 \tag{5}$$

$$\lim_{n\to\infty} n\sigma^n(n)=\infty \tag{6}$$

The topology of a GRNN, shown in Fig. 1, consists of four layers: The input layer, the hidden layer, the summation layer, and the output layer. The function of the input layer is to pass the input vector variables X to all the units in the hidden layer which consist of all the training samples $X_1\cdots X_n$. Further, the scalar function D_i^2 between the unknown pattern and the training sample is calculated and passed through the kernel function. As illustrated in

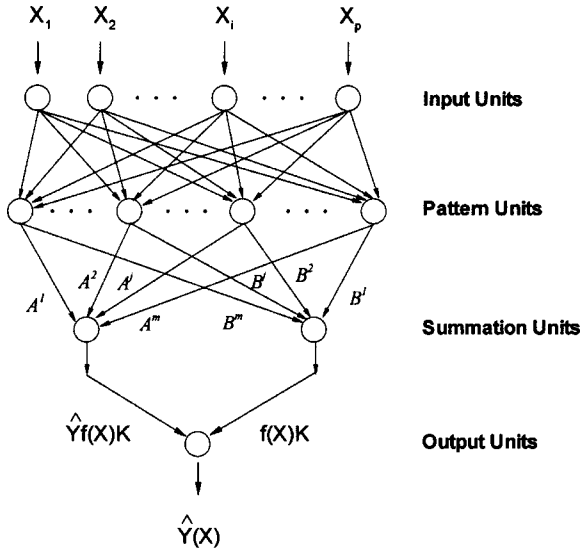

Fig. 1 GRNN block diagram

Fig. 1, the summation layer has two units A and B. While the unit A computes the summation of $\exp[-D_i^2/2\sigma^2]$ multiplied by the Y_i associated with X_i, the unit B computes the summation $\exp[-D_i^2/2\sigma^2]$. Finally, the output unit divides A by B to provide the prediction result as

$$\hat{Y}(X)=\frac{\sum_{i=1}^{m} A^i \exp\left[-\frac{D_i^2}{2\sigma^2}\right]}{\sum_{i=1}^{m} B^i \exp\left[-\frac{D_i^2}{2\sigma^2}\right]} \tag{7}$$

with $A^i(k)$ and $B^i(k)$ are defined as

$$A^i(k)=A^i(k-1)+Y_i \tag{8}$$

$$B^i(k)=B^i(k-1)+1 \tag{9}$$

where $A^i(k)$ and $B^i(k)$ are the values of the coefficients for cluster i after k observations and are the sum of the Y values and the number of samples assigned to cluster i, respectively. For a more detailed description on GRNN, the reader is referred to Specht [8].

3 Experimental Approach

A selected number of experimental investigations found in the literature were used to document the general spray characteristics. High-resolution photography was used in the early investigations and still remains a reliable tool [9]. An experimental investigation was conducted by Lee and Tankin on the study of water spray in air [10]. In their experiments, holography was used to study the spray pattern, as well as the droplet size distribution. In another study, jet and swirl spray pattern of water in steam was explored by using the aforementioned methods [11]. Further, a high-speed CCD camera was used to capture the modes of instabilities in a coaxial air-blast injector [12]. In addition to flow visualization, laser doppler anemometry was used to study the mixing process of a pressure-atomized spray [13]. It was found that mixing is strongly influenced by the degree of flow development at the injector exit and the breakup regime. In another study, PDA and Malvern instruments were used to predict the atomization process for solid-cone pressure swirl sprays [14]. Further, PDA was also used to explore the effect of viscosity and liquid surface tension on the mean diameter [15]. It is found that mean diameter increases as viscosity and surface tension increase.

The present authors have also conducted a series of experimental studies on various governing parameters of a liquid spray pat-

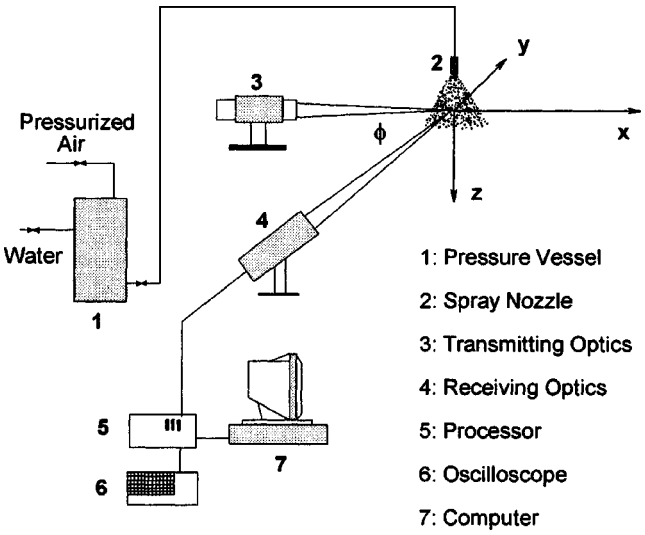

Fig. 2 Experimental setup

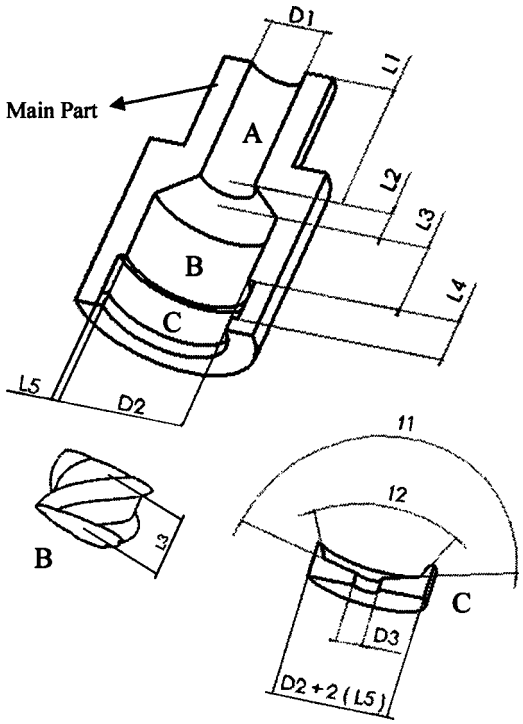

Fig. 3 Atomizer close-up

tern of swirl type injectors. The spray formation at various injection pressures, spray cone angles, breakup lengths, and velocity components were obtained as a function of pressure drop. At low injection pressures, CCD camera was used for visualization of the liquid sheets and breakup processes whereas at higher pressures, PDA was used to measure the droplet size, as well as the axial and radial velocities at each point. For a detailed description on the experimental setup, the reader is referred to Refs. [16–20].

3.1 Experimental Setup. As illustrated in Fig. 2, the experimental setup consists of a high-speed, 640×480 pixel CCD camera, a PDA system, a Stroboscope, a data acquisition system (DAS), an injector block, and the working fluid supply system. The spray images, as well as PDA measurements, are stored in DAS for off-line analysis. Further, the injector nozzle is mounted on a test rig and water is used as the working fluid. In order to be able to vary the feed pressure to the injector, water is supplied from a pressure vessel under pressurized air. Water is injected vertically downstream through the atomizer at atmospheric temperature and pressure conditions.

As illustrated in Fig. 3, the liquid enters the injector section A with diameter D1. Further downstream, the liquid gains on angular momentum due to the helical path in section B with diameter D2 and is ultimately accelerated through a nozzle and discharges from the orifice in section C. As a result, continuous liquid is discharged through the nozzle in the form of a hollow conical liquid sheet and the disintegration into droplets occurs by the liquid sheet instability processes that may happen at various modes for different injection pressures or discharge velocities.

Finally, as previously indicated, two different injector settings are investigated: A single injector and a double injector. While for the double injector the resulting spray pattern is the product of the intersection of two single spray patterns, the spray pattern for the single injector remains unaffected.

4 Case 1: Single Injector

4.1 PDA Measurements. PDA measurements are performed along five parallel lines but in two different modes: A trajectory mode and a planar mode as illustrated in Figs. 4 and 5, respectively. All lines are in one plane and are perpendicular to the injector center of axis. The first line is at a distance of $Z = 20$ mm downstream of the nozzle and the remaining lines are spaced at an increment of 3 mm—that is, at $Z = 20$, 23, 26, 29, and 32 mm downstream of the nozzle, respectively.

It should be noted that Z locations smaller than 20 mm—that is, closer to the nozzle exit of the injector—are omitted due to the dense spray region and the resulting inaccuracy of the PDA measurements. Further, Z locations beyond 32 mm are not of practical importance in this research.

In the trajectory mode, as illustrated in Fig. 4, each line contains 13 measurement points regardless of the Z location. However, the measurement points are positioned in such a way to keep the spray cone angle of respected measurement points from one line to another line as constant. As a result, the length of the lines and the spacing between equally spaced measurement points increase from the first line ($Z = 20$ mm) to the last line ($Z = 32$ mm).

In the planar mode, as illustrated in Fig. 5, each line contains 19 measurement points regardless of Z location. However, in contrast to the trajectory mode, the length of the lines and the spacing between equally spaced measurement points are not changed from

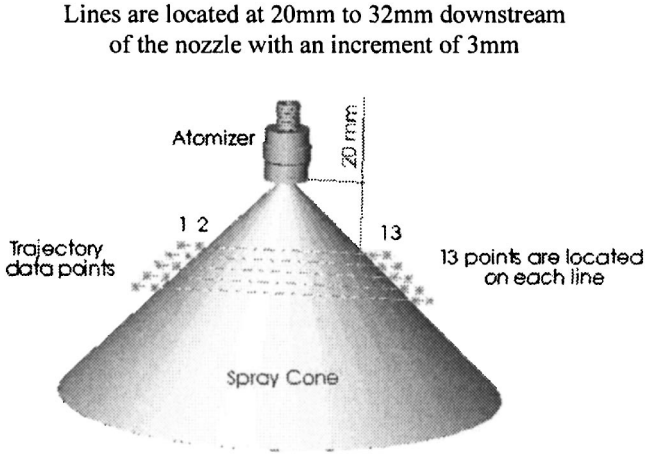

Fig. 4 Trajectory mode. Measurements are used for GRNN training.

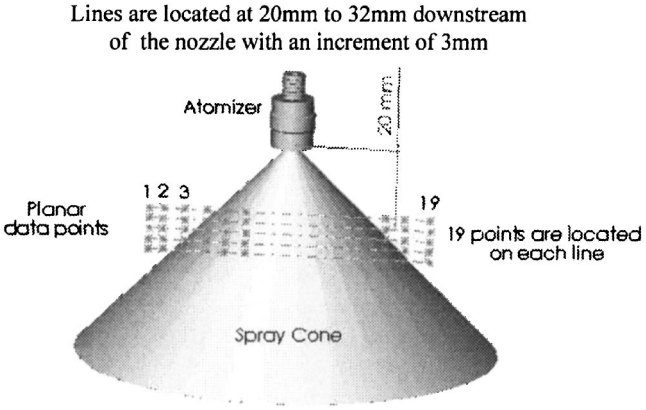

Fig. 5 Planar mode. Measurements are used for evaluation of the GRNN predictions.

the first line ($Z=20$ mm) to the last line ($Z=32$ mm). Finally, regardless of the measurement mode (trajectory or planar), two different components of the velocity are measured at each point, namely the radial velocity and the axial velocity.

It should be emphasized that data by the PDA measurements from the trajectory mode are exclusively applied for GRNN training and data by the PDA measurements from the planar mode are kept reserved for evaluation of the predicted data by GRNN. In other words, data by the PDA measurements from the trajectory mode are used as an input to train the GRNN. Subsequently, the trained GRNN is employed to predict data for the planar mode. Finally, the predicted data for the planar mode by the GRNN is then compared with those obtained from the PDA measurements for the planar mode.

4.2 GRNN Training. As a preprocessing step, the width of the estimating kernel, σ, in the GRNN needs to be determined [21,22]. In order to pinpoint the optimized value for the width of the probability σ, a systematic investigation is performed as follows: data by the PDA measurements for the trajectory mode at a particular position downstream of the injector nozzle (i.e., $Z=20$, 23, 26, 29, or 32 mm) for a specific value of the probability (i.e., $\sigma=0.01$, 0.05, 0.2, 0.4, or 3) are used as input to train the GRNN. Further, it should be kept in mind that for each set of probability, σ, and measurement position Z, GRNN training is performed two times—one for the axial velocity and one for the radial velocity. It should be emphasized that while each GRNN is trained with 13 samples (measured data points), the number of predictions for the same flow field are 19.

4.3 Results. Due to the excessive amount of the experimental and GRNN results, only one set out of the previously mentioned results is selected for illustration. A more comprehensive description of the results may be found in Ref. [23]. Results for the axial and radial velocities at $Z=26$ mm are summarized in Figs. 6(*a*) and 6(*b*), respectively. While the bold solid line shows data obtained by the PDA measurements, the dashed lines represent data predicted by the GRNN. For both velocities, axial and radial, the deviation between the PDA measurements and those predicted by the GRNN becomes larger as the probability σ increases. Therefore, in order to identify the optimized value of the probability σ, a mean error is defined, as follows:

$$E_{\text{mean}}=\frac{\Sigma_{i=1}^{k}|\hat{Y}(X^i)-Y^i|}{k} \tag{10}$$

Hence, the mean error for different values of the probability σ at particular Z-locations is calculated. Figure 7 shows the optimized value of the probability σ at each Z-location, $23\text{ mm}\leqslant Z\leqslant 32$ mm, for both radial and axial velocities.

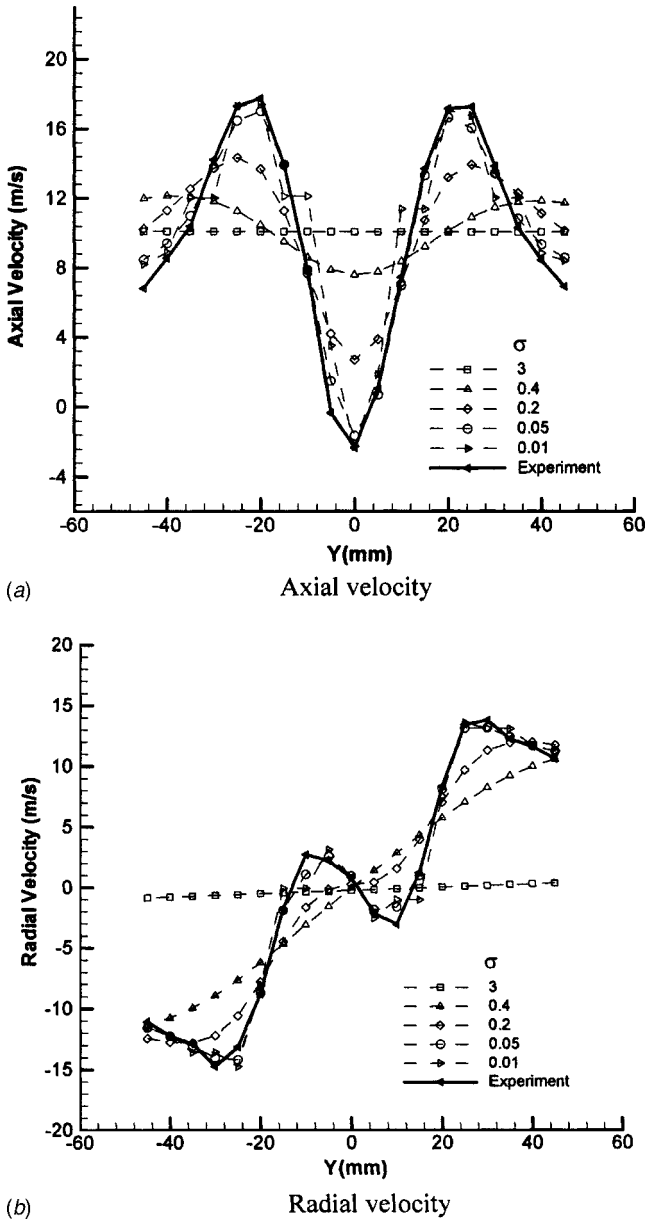

Fig. 6 Effect of σ on the velocity prediction at $Z=26$ mm: (*a*) Axial velocity; (*b*) Radial velocity

It can be seen by inspection that for $Z=20$, 23, 26, 29, and 32 mm, the optimized value of the probability σ is almost identical for both types of velocities and is independent of the Z-location. For the present GRNN model, the authors opt the value $\sigma=0.05$ as the overall optimized value of the probability, $\sigma_{\text{opt,overall}}$. In order to investigate the sensitivity of $\sigma_{\text{opt,overall}}=0.05$ to the accuracy of GRNN prediction, $\sigma_{\text{opt,overall}}=0.05$ is used to train the GRNN at all Z-locations for the trajectory mode. The corresponding GRNN is called $\text{GRNN}_{\text{opt,overall}}$ in this paper and is used to predict data at the planar mode for both types of velocities. Finally, the predicted results are then compared with those from a GRNN that is trained with a locally optimized value of the probability σ, called $\text{GRNN}_{\text{opt,local}}$. It should be mentioned that locally optimized value of the probability σ are referred to a probability σ which minimizes the mean prediction error, Eq. (10).

Figure 8 shows the mean velocity errors of $\text{GRNN}_{\text{opt,overall}}$ and $\text{GRNN}_{\text{opt,local}}$ with respect to PDA measurements as a function of Z-location. Three different values of the mean velocity errors are indicated: The local maximum error, the local minimum error, and

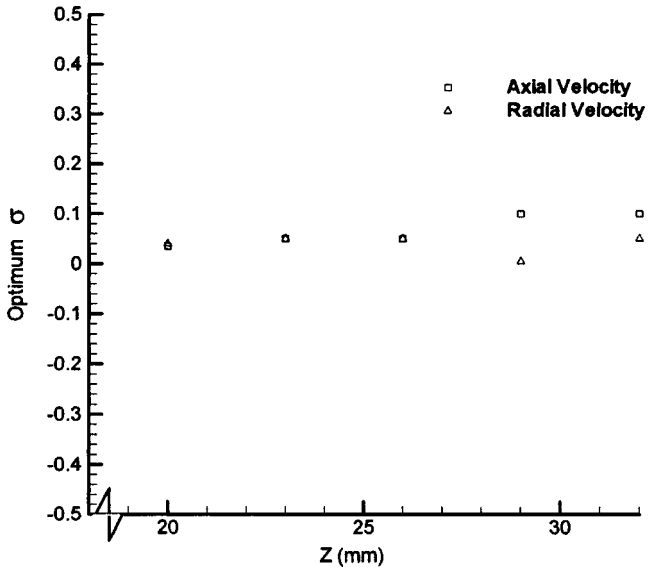

Fig. 7 Variation of $\sigma_{opt.}$ for data lines at different Z

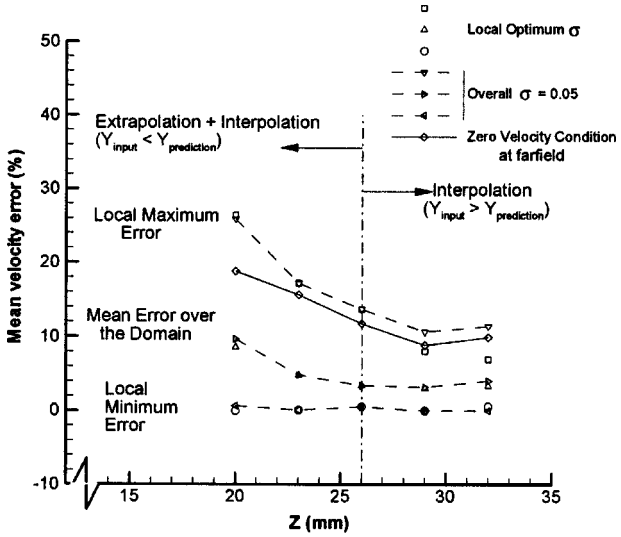

Fig. 8 Mean velocity error for the planar mode

the mean error over the whole domain. While the local maximum (minimum) error present the largest (smallest) deviation between any similar points of $GRNN_{opt,overall}$ and $GRNN_{opt,local}$, the mean error over the whole domain reflects the error over the full data set—that is, 19 test points.

The local minimum error of both $GRNN_{opt,overall}$ and $GRNN_{opt,local}$ are almost identical and their deviation with the PDA measurements are less than 1% everywhere, for both interpolation and extrapolation regions. Further, the mean error over the whole domain of both $GRNN_{opt,overall}$ and $GRNN_{opt,local}$ is also in extreme good accordance. However, the deviation from the PDA measurements is between 4% and 10% at $Z=32$ and 20 mm, respectively. Finally, the local maximum error of both $GRNN_{opt,overall}$ and $GRNN_{opt,local}$ is in good agreement except at $Z=29$ and 32 mm with a difference of about 2% to 3%. Nevertheless, the deviation to the PDA measurements is between 13% and 27% at $Z=32$ and 20 mm, respectively.

On the other hand, a dash–dotted line is plotted in Fig. 8 which represents the boundary between the regions of the pure interpolation and the combination of interpolation and extrapolation. A further inspection of the data set about the local maximum errors of 27% at $Z=20$ mm confirms that the error corresponds to the last point of the data set—that is, the extrapolation region. However, in order to minimize the magnitude of the local maximum errors in the extrapolation region, one may provide the zero velocity condition at the far field as an extra input to the GRNN training. This methodology is also investigated and the result is plotted in Fig. 8 as a solid line. It is apparent that by this method the deviation to the PDA measurements is lowered by up to 8%.

5 Case 2: Double Injector

5.1 PDA Measurements. Phase Doppler measurements were carried out with two pressure-swirl injectors placed side by side at a distance d_i. The geometrical parameters, as well as a schematic illustration of the setup, are shown in Fig. 9. Both injectors are of the same configuration as that investigated for the case of the single injector. PDA measurements are carried out for four different d_i settings of 18, 22, 26, and 30 mm. It is apparent from Fig. 9 that by varying the distance between the injectors, the remaining geometrical parameters will also be altered. However, in this investigation, the distance L_m is kept constant while the distance L_i is adjusted for changes in d_i. This approach enabled us to perform the PDA measurements on a plane at a fixed distance to the intersection point of the two spray patterns independent of the distance, d_i, between the injectors. Further, PDA measurements are performed for a plane as opposed to a line used for the case of the single injector. In addition, the PDA measurement plane, illustrated in Fig. 10, is made of measurement points that are 5 mm apart from each other; in other words, an equally spaced

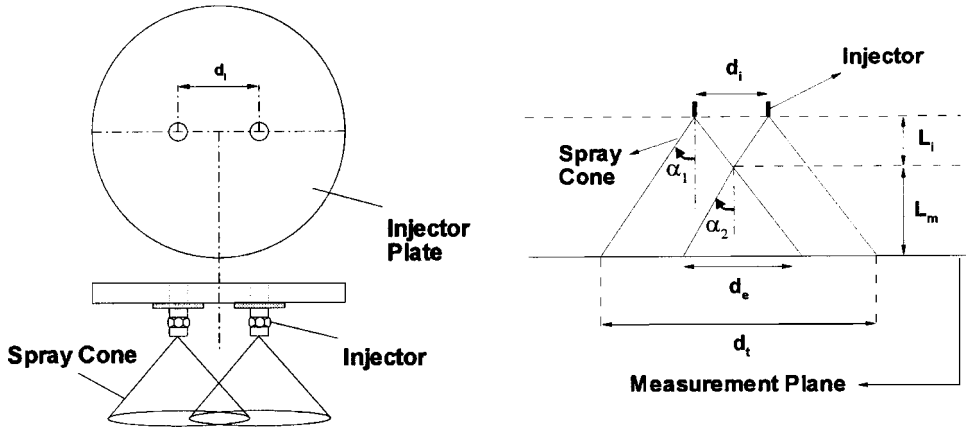

Fig. 9 Geometrical setup and the corresponding parameters

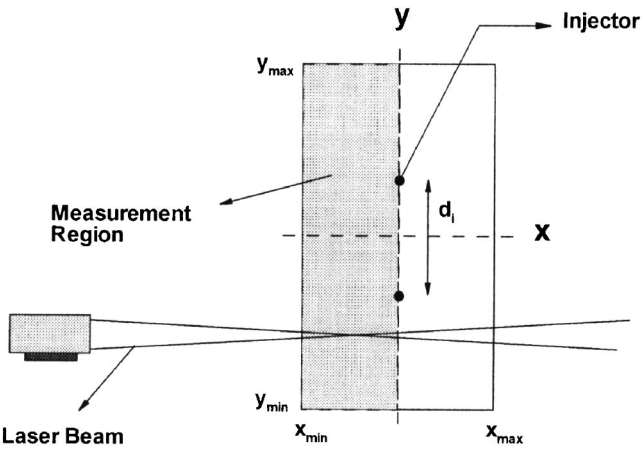

Fig. 10 Measurement region for the side-by-side injector setup

measurement grid of 5×5 mm was performed. In order to capture the full spray cones, the measurement plane is enlarged from 9 by 19 cells at $d_i = 18$ mm to 9 by 23 cells at $d_i = 30$ mm. Measurements are performed for both axial and radial velocity distributions at different d_i settings, Figs. 11 and 12, respectively. The results indicate that due to the impingement of the two spray cones, a secondary maximum velocity is developed at the center of the inner spray. As d_i increases, this secondary maximum velocity grows in magnitude. A comprehensive discussion on the experimental results is found in Ref. [23].

5.2 GRNN Training. Considering the results from the single injector case, the GRNN training for the double injector is focused on the extrapolation regime. In other words, data by the PDA measurements at $d_i = 22$, 26, and 30 mm for the axial- and radial velocities are used as an input to train the GRNN with an adopted optimized value of the probability $\sigma_{opt,overall} = 0.05$. Subsequently, this GRNN algorithm is used to predict data for the axial- and radial velocities at $d_i = 18$ mm, shown in Figs. 13 and 14, respectively. The results shown in Figs. 13 and 14 indicate that the predicted values for both axial and radial velocities are in excellent agreement with the PDA measurements indicating the capability and accuracy of the trained network. Further, as illustrated in Fig. 15, the mean prediction error over the whole domain of $GRNN_{opt,overall}$ (relative to the PDA measurements) is also calculated for both axial- and radial velocities at different injector spacing d_i. The values are also compared with the mean prediction error based on the local optimized value of the probability, $GRNN_{opt,local}$. The mean prediction error for both $GRNN_{opt,overall}$ and $GRNN_{opt,local}$ are found to be in a good agreement. Finally, the mean error for the GRNN prediction of the axial velocities is less than the corresponding radial velocities. While the mean error for the GRNN prediction of the axial velocities at $d_i = 18$, 22, 26, and 30 mm is about 5%, 3%, 3%, and 4%, respectively, the corresponding mean error for the radial velocities at the same injector spacing is about 6%, 5%, 4%, and 8%, respectively.

Finally, an assessment is made on the sensitivity of the $GRNN_{opt,overall}$ on the number of training samples for both axial- and radial velocity predictions. Again, attention is focused on the extrapolation regime of the $GRNN_{opt,overall}$ rather than the interpolation regime. In other words, data by the PDA measurements at $d_i = 22$, 26, and 30 mm for the axial- and radial velocities are randomly selected and used as an input to train the $GRNN_{opt,overall}$. The trained network is subsequently used to predict data for the axial- and radial velocities at $d_i = 18$ mm. Figures 16(*a*) and 16(*b*) show the mean prediction error of the $GRNN_{opt,overall}$ at $d_i = 18$ mm as a function a number of randomly selected training samples for both axial- and radial velocity prediction, respectively. It should be noted that each measurement plane has approximately 225 measurement points (samples). Both curves are similar and reach an asymptote for a mean prediction error of 5% at about 200 randomly selected samples. However, as illustrated in Fig. 16, if one reduces the number of samples to about 120 (that is, ~20% of the available samples on the $d_i = 22$, 26, and 30 mm measurement planes), one may predict 225 measurement points on the $d_i = 18$ mm measurement plane (extrapolation regime) with an accuracy of approximately 93% (that is, a mean prediction error of 7%).

6 Summary and Conclusion

Neural network technique is applied to the design optimization of a simple pressure-swirl injector. PDA measurements of axial- and radial velocities at different *Z*-locations of the spray cone, for different measurement modes (trajectory and planar), and for different injector setups (single and double) are performed. While the PDA measurements for the single injector are performed on a line, the PDA measurements for the double injector are performed on a plane.

Further, PDA measurements from the trajectory mode are exclusively used to train the GRNN. However, GRNN predictions are made for the planar mode. It should be noted that the number of training samples from the trajectory mode is kept always smaller than the number of predictions for the planar mode—making the GRNN an interpolation, as well as an extrapolation algorithm.

It is observed that the GRNN predictions for both axial- and radial velocities are very sensitive to the width of the probability σ. Thus, PDA measurements for a single pressure-swirl injector are used as a reference for GRNN predictions to pinpoint an optimized value for the probability σ. The optimized value was found to be 0.05 ($\sigma_{opt,overall} = 0.05$). A GRNN algorithm based on $\sigma_{opt,overall}$ is developed, $GRNN_{opt,overall}$. The accuracy and robustness of $GRNN_{opt,overall}$ is examined for design optimization of pressure-swirl atomizers when limited amount of design data exists. For a single pressure-swirl injector, $GRNN_{opt,overall}$ is found to be capable of predicting the axial- and radial velocities at *Z*-locations of 20, 23, 26, 29, and 32 mm with a mean velocity error of approximately 10%, 5%, 4%, 4%, and 4%, respectively.

Furthermore, the determined $\sigma_{opt,overall}$ from the PDA measurements for the single pressure-swirl injector is used to train the GRNN for a double injector at d_i settings of 22, 26, and 30 mm. However, attention is given to the extrapolation regime rather than interpolation regime. Subsequently, the developed GRNN is used to predict values for the axial- and radial velocities at d_i settings of 18 mm (extrapolation), as well as at 22, 26, and 30 mm. The mean prediction error for the reconstructed axial (radial) velocity field of the impinging spray pattern at d_i settings of 18, 22, 26, and 30 mm is found to be 5% (6%), 3% (5%), 3% (4%), and 4% (8%), respectively.

In addition, an investigation is made on the sensitivity of the GRNN on the number of the training samples for both axial- and radial velocity predictions. It is observed that as one reduces the number of samples to about 120 (that is, ~20% of the available samples on the $d_i = 22$, 26, and 30 mm measurement planes), one may predict the 225 measurement points on the $d_i = 18$ mm measurement plane (extrapolation regime) with an accuracy of approximately 93% (that is, a mean prediction error of 7%).

In conclusion, the preceding observations indicate that the GRNN is capable of performing design approaches, as well as optimization studies of sufficient accuracy with modest amount of data for pressure-swirl injectors. It has been determined that the GRNN model, which was dependent to the width of probability σ, could be modified into a nonparametric model by adopting an overall optimum value of the width of probability $\sigma_{opt,overall}$. The application and the high accuracy of the GRNN model for reconstructing the velocity flow field of a single swirl spray, as well as the interaction of two swirl sprays, is demonstrated. Finally, tak-

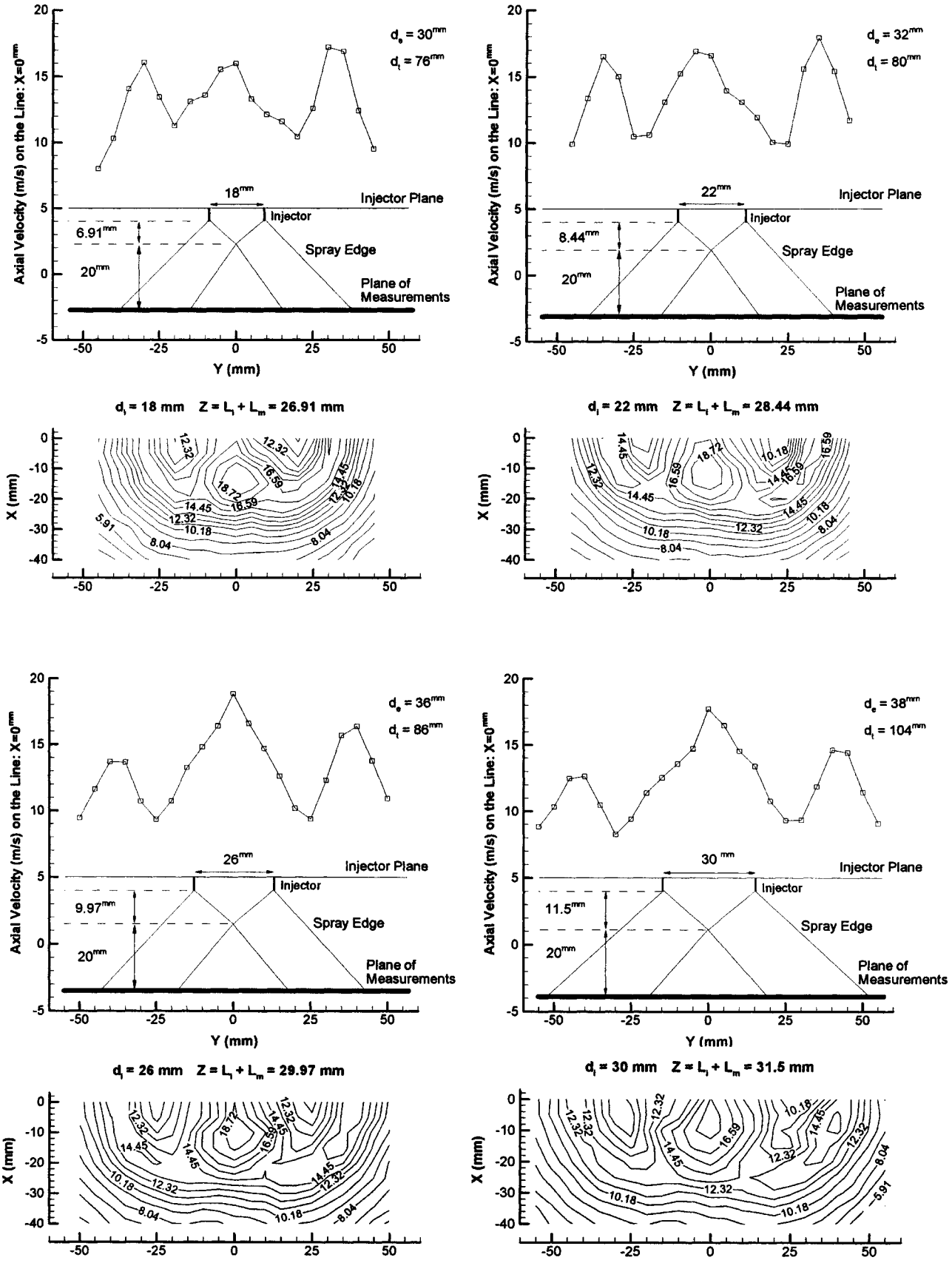

Fig. 11 Axial velocity distribution for different injector spacing

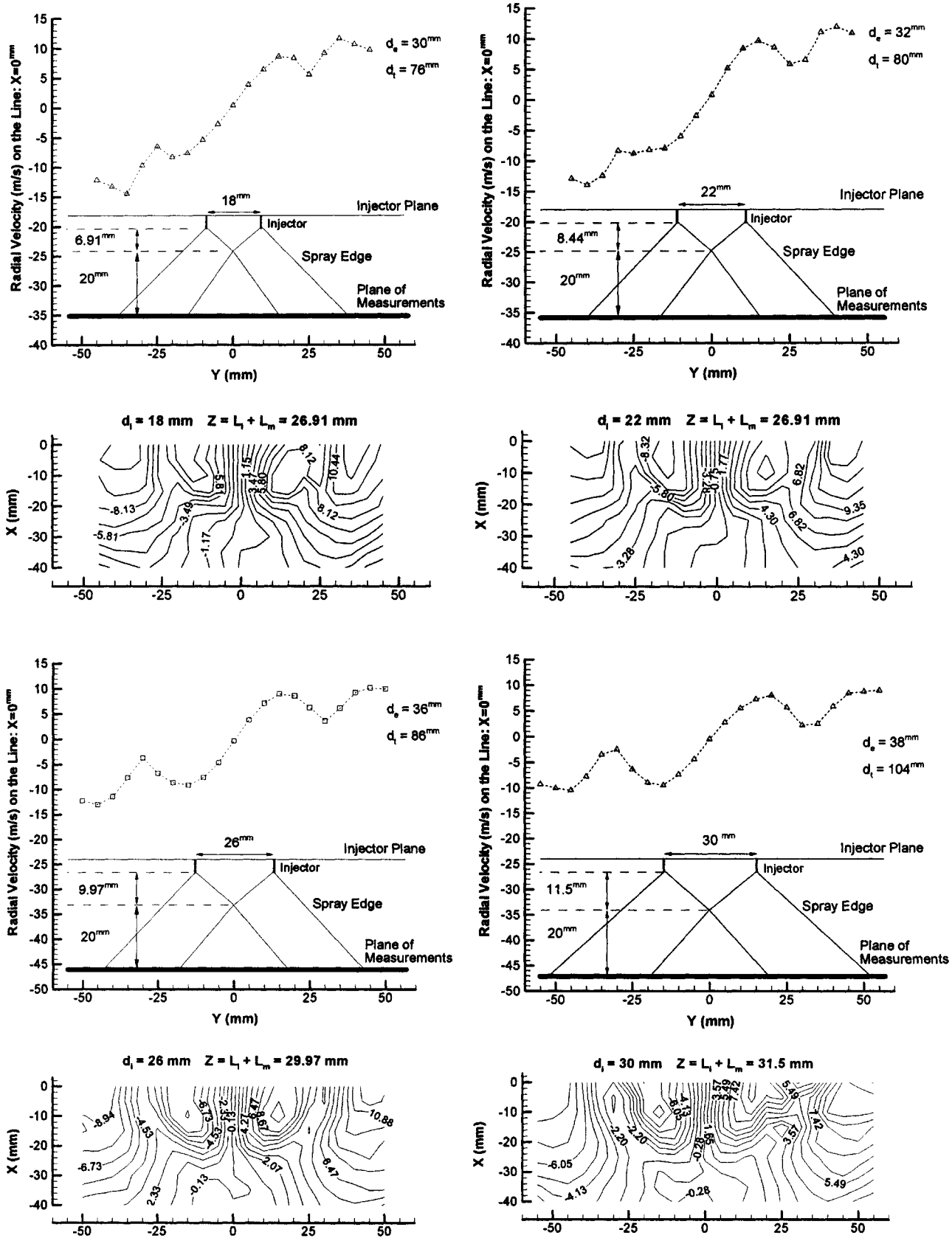

Fig. 12 Radial velocity distribution for different injector spacing

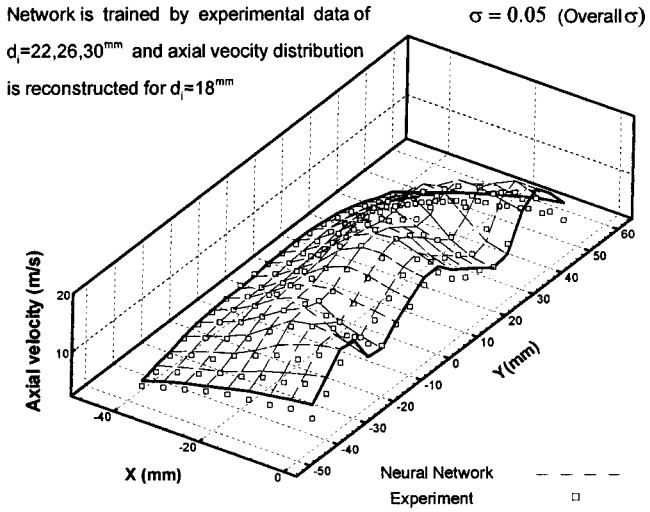

Fig. 13 Axial velocity reconstruction

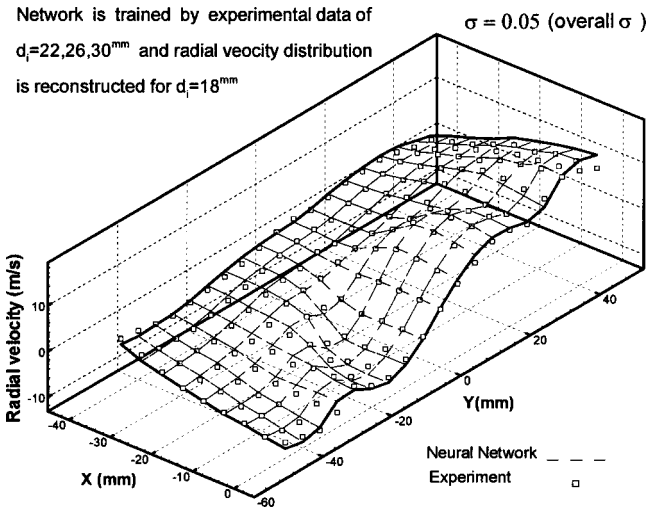

Fig. 14 Radial velocity reconstruction

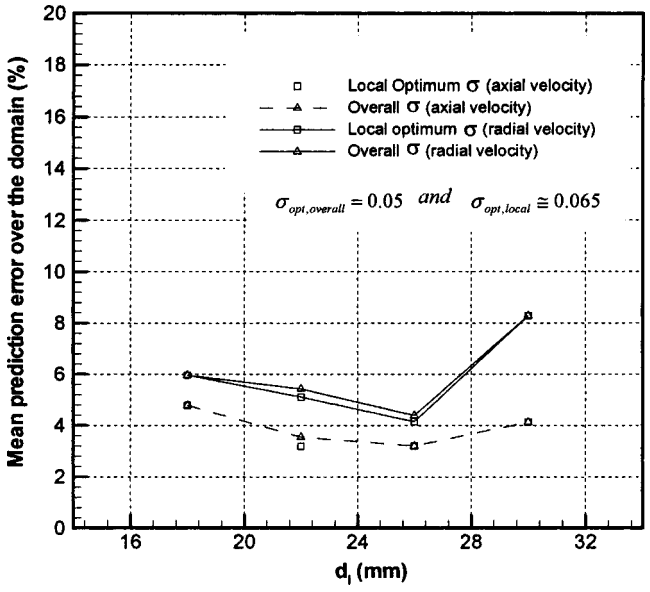

Fig. 15 Mean prediction error over the domain for different injector spacing

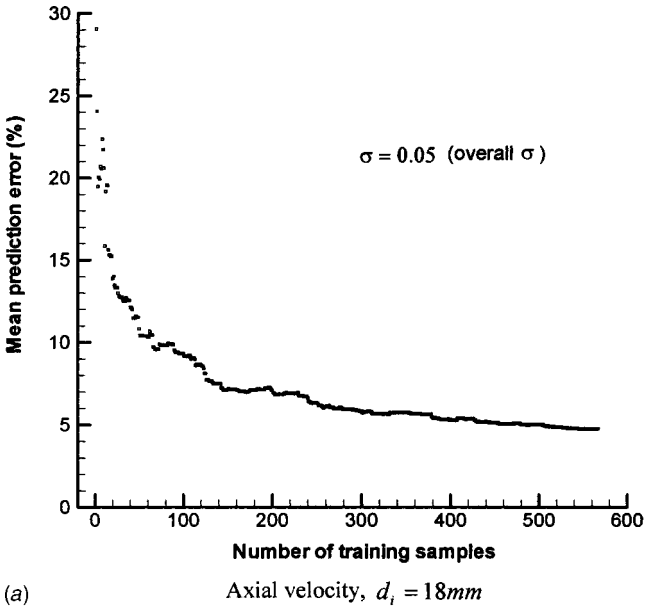

(*a*) Axial velocity, $d_i = 18mm$

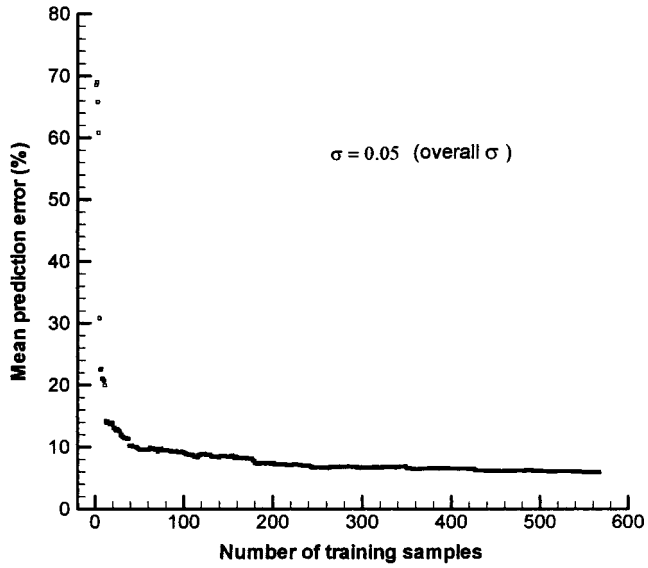

(*b*) Radial velocity, $d_i = 18mm$

Fig. 16 Mean prediction error for different number of training samples: (*a*) Axial velocity, d_i=18 mm; (*b*) Radial velocity, d_i =18 mm

ing into account that accurate data are time consuming and expensive to obtain for swirl injectors, a better communication between the GRNN and nonintrusive diagnostic techniques would benefit both.

Acknowledgment

The present work has been supported in part by the office of research at Sharif University of Technology.

Nomenclature

A^i = first coefficient of cluster i
B^i = second coefficient of cluster i
d_i = the distance between two injectors
d_e = envelope width
d_t = total width
E_{mean} = mean prediction error

$E[y|X]$ = regression of y on X
$f(\vec{x},y)$ = probability density function
$\hat{f}(\vec{x},y)$ = estimator
m = number of clusters
n = number of samples available
l_i = from nozzle to intersection point
l_m = intersection to measurement point
p = dimension of the vector variable x
T = transpose of vector
$\vec{x}$ = random vector variable (input)
y = random scalar variable (output)
X = system's input (measured value)
Y = system's output (measured value)
$\hat{Y}$ = conditional mean of y
X_i = sample value of the variable x
Y_i = sample value of the variable y
Z = axial distance downstream of nozzle
σ = width of probability
$\sigma_{\text{opt,local}}$ = optimum width of probability
$\sigma_{\text{opt,overall}}$ = overall optimum width of probability
α_1 = half spray angle
α_2 = half envelope angle

References

[1] Amir, M. A., Awais, M. M., Watkins, A. P., and Lockwood, F. C., 1999, ''CFD and Neural Network Modeling of Dense Propane Spray,'' Atomization Conference, ILASS-Europe'99, Toulouse, France, July 5–7.

[2] Schulte, G., Guardani, R., and Oller do Nascimento, C. A., 1999, ''Study of the Spray Structure of a Fan Atomizer by Means of a Neural Network-Based Mathematical Model,'' Atomization Conference, ILASS-Europe'99, Toulouse, France, July 5–7.

[3] Pruvost, J., Legrand, J., and Legentilhomme, P., 2001, ''Three-Dimensional Swirl Flow Velocity-Field Reconstruction Using a Neural Network With Radial Basis Function,'' J. Fluids Eng., **123**, pp. 920–927.

[4] Wasserman, P. D., 1993, *Advanced Methods in Neural Computing*, Van Nostrand Reinhold.

[5] Cichocki, A., and Unbehauen, R., 1993, *Neural Networks for Optimization and Signal Processing*, Wiley, New York.

[6] Parzen, E., 1962, ''On Estimation of a Probability Density Function and Mode,'' Ann. Math., **33**, pp. 1065–1076.

[7] Cacoullos, T., 1966, ''Estimation of a Multivariable Density,'' Ann. Inst. Stat. Math., **18**, No. 2, pp. 179–189.

[8] Specht, D. F., 1991, ''A General Regression Neural Network,'' IEEE Trans. Neural Netw., **2**, No. 6, pp. 568–576.

[9] Bachalo, W. D., 2000, ''Spray Diagnostics for the Twenty-First Century,'' Atomization Sprays, **10**, pp. 439–474.

[10] Lee, S. Y., and Tankin, R. S., 1984, ''Study of Liquid Spray (Water) in a Non-Condensable Environment (Air),'' Int. J. Heat Mass Transfer, **27**, No. 3, pp. 351–361.

[11] Lee, S. Y., and Tankin, R. S., 1984, ''Study of Liquid Spray (Water) in a Condensable Environment (Steam),'' Int. J. Heat Mass Transfer, **27**, No. 3, pp. 363–374.

[12] Adzic, M., Carvalho, I. S., and Heitor, M. V., 2001, ''Visualization of the Disintegration of an Annular Liquid Sheet in a Coaxial Airblast Injector at Low Atomizing Air Velocities,'' Opt. Diagnostics Eng., **5**, No. 1, pp. 27–38.

[13] Ruff, G. A., Sagar, A. D., and Faeth, G. M., 1989, ''Structure and Mixing Properties of Pressure-Atomized Sprays,'' AIAA J., **27**, No. 7, pp. 901–908.

[14] Yule, A. J., Sharief, R. A., Jeong, J. R., Nasr, G. G., and James, D. D., 2000, ''The Performance Characteristics of Solid-Cone- Spray Pressure Swirl Atomizers,'' Atomization Sprays, **10**, pp. 627–646.

[15] Dorfner, V., Domnick, J., Durst, F., and Kohler, R., 1996, ''Viscosity and Surface Tension Effects in Pressure Swirl Atomization,'' Atomization Sprays, **5**, pp. 261–285.

[16] Ghorbanian, K., Ashjaee, M., Soltani, M. R., Mesbahi, M. H., and Morad, M. R., 2003, ''Experimental Flow Visualization of Single Swirl Spray Pattern at Various Pressure Drops,'' AIAA-2003-4758, AIAA 39th Joint Propulsion Conference and Exhibit, Huntsville, Alabama, USA, 20–23 July.

[17] Ghorbanian, K., Ashjaee, M., Soltani, M. R., Mesbahi, M. H., and Morad, M. R., 2003, ''Experimental Study of the Spray of a Liquid-Liquid Coaxial Swirl Injector for Different Injection Pressures,'' 9th International Conference on Liquid Atomization and Spray Systems, ICLASS 2003, Sorrento, Italy.

[18] Ghorbanian, K., Ashjaee, M., Soltani, M. R., Mesbahi, M. H., and Morad, M. R., 2002, ''PDA Droplet Size and Velocity Measurement of a Swirl Atomized Spray,'' 9th Asian Congress of Fluid Mechanics, Isfahan, Iran.

[19] Ashjaee, M., Soltani, M. R., Ghorbanian, K., and Morad, M. R., 2002, ''PDA Study of Two Phase Flow in a Spray Field of a Jet-Swirl Type Injector,'' 3rd Australian Conference on Laser Diagnostics in Fluid Mechanics and Combustion, Australia.

[20] Ashjaee, M., Ghorbanian, K., Soltani, M. R., Mesbahi, M. H., and Morad, M. R., 2002, ''PDA Measurements of Droplet Size and Velocity In Mixing Region of Two Sprays,'' 9th Conference of Iranian Society of Mechanical Engineers, Tehran, Iran.

[21] Soltani, M. R., Ghorbanian, K., Ashjaee, M., and Morad, M. R., 2003, ''Neural Network Analysis of Single Swirl Spray Pattern at Various Pressure Drops,'' AIAA-2003-4757, AIAA 39th Joint Propulsion Conference and Exhibit, Huntsville, Alabama, USA, 20–23 July.

[22] Soltani, M. R., Ghorbanian, K., Ashjaee, M., Mesbahi, M. H., and Morad, M. R., 2003, ''Prediction of Velocity Distribution in the Mixing Region of Swirl Sprays Using Neural Network Implementation,'' AIAA-2003-4270, AIAA 33rd Fluid Dynamics Conference, Orlando, Florida, USA, 23–26 June.

[23] Morad, M. R., 2005, ''Determination of the Spray Characteristics of a Liquid–Liquid Coaxial Injector Utilizing PDA and Neural Network Analysis,'' Sharif University of Technology, Tehran, Iran, January.

E. J. Soares
M. S. Carvalho
P. R. Souza Mendes[1]
e-mail: pmendes@mec.puc-rio.br

Department of Mechanical Engineering, Pontifícia Universidade Católica do Rio de Janeiro, Rua Marquês de São Vicente 225, Rio de Janeiro, RJ 22453-900, Brazil

Immiscible Liquid-Liquid Displacement in Capillary Tubes

We analyze the liquid-liquid displacement in capillary tubes. The goal is to determine the amount of displaced liquid that remains attached to the tube wall and the configuration of the liquid-liquid interface at different operating parameters. The study encompasses both numerical and experimental approaches. The finite element method is used to solve the governing equations and, in order to validate the predictions, visualization experiments are performed to capture images of the interface. The numerical results were obtained for the assumption of negligible inertia, and the effects of viscosity ratio and capillary number are investigated. The predictions and experimental observations are in good agreement. [DOI: 10.1115/1.1852484]

1 Introduction

The present paper deals with the displacement of a liquid, initially occupying the interior of a tube, by another liquid which is immiscible with the first. Practical applications include the flow through porous media during enhanced oil recovery [e.g., [1–4]] and the cementation process of production and injection wells. Comprehensive reviews on this subject are available in the literature [5,6]. In these processes, it is important to understand the mechanism of liquid displacement and to determine the amount of liquid that is left behind adjacent to the wall. The configuration of the interface between the two liquids depends on the force balance near the interface, which is the focus of the present study.

Most of the related work found in the literature deals with the case of a gas displacing a viscous liquid, going back to the pioneer work of Fairbrother and Stubbs [7] and Taylor [8]. In the experiments reported in these early papers, the Reynolds number was kept small enough to assure negligible inertial effects. The main goal was to determine the fraction of mass deposited on the tube wall m, which, with the aid of the mass conservation principle, can be written as a function of the velocity of the tip of the interface U and the mean velocity $\overline{u}$ of the liquid ahead of the gas-liquid interface, viz.,

$$m = \frac{U - \overline{u}}{U} \tag{1}$$

Taylor [8] studied the dependence of the mass fraction on the *capillary number* $Ca \equiv \mu U/\sigma$, where μ and σ are the liquid viscosity and surface tension, respectively. His analysis indicated that the amount of liquid deposited on the wall rises with the interface speed, and that m tends asymptotically to a value of 0.56 as Ca approaches 2. Working on the same problem, Cox [9] studied the mass fraction over a wider range of the capillary number, and also observed that m reaches an asymptotic value at a high capillary number. However, he showed that this asymptotic value was 0.60 as Ca approached 10. Using the lubrication approximation, Bretherton [10] derived a theoretical correlation between the mass fraction and the Capillary number, and the agreement between his predictions and Cox's experiments is good in the range of $10^{-3} < Ca < 10^{-2}$.

Some contributions found in the literature deal with the theoretical modeling of gas-liquid displacement in the small gap between two parallel plates. Giavedoni and Saita [11] reviewed these articles and presented a theoretical analysis of the steady displacement of a viscous liquid by a semi-infinite gas bubble using the finite element method. They extended the range of the Capillary number of the analysis from 5×10^{-5} up to 10. Lee et al. [12] used a finite-element method to study the steady gas displacement of a polymeric liquid confined between two parallel plates. The non-Newtonian behavior of the liquid was modeled by three different differential constitutive equations.

Articles dealing with the analysis of liquid-liquid displacement are much scarcer. One of these few papers is given by Goldsmith and Mason [13], who report experimental results on the amount of displaced liquid left on the tube wall as a function of different parameters. In their experiments, the displacing material is a long drop of a viscous liquid. The results showed that the mass fraction rises as the viscosity ratio $N_\mu = \mu_2/\mu_1$ is decreased, where the index 1 refers to the displacing fluid and μ_2, to the displaced fluid. This trend agrees with the theoretical predictions and experimental data presented in this work.

Teletzke et al. [14], using a perturbation method, analyzed the wetting hydrodynamics problem. They extended the work of Bretherton [10] to account for a viscous (rather than inviscid) displacing fluid, and the effects of intermolecular forces in submicroscopically thin films. Their computations agreed with the observation of Goldsmith and Mason [13], who showed that the film thickness of the displaced fluid left on the wall rises with the viscosity of the displacing fluid. However, their results were limited to small capillary numbers, namely, $Ca < 10^{-4}$.

Petitjeans and Maxworthy [15] analyzed the situation of liquid-liquid displacement with miscible liquids. They studied the effect of the Péclet number, defined as $\mathrm{Pe} = V_m D/D_m$, where V_m is the maximum velocity far from the tip of the interface, D the tube diameter, and D_m is the diffusion coefficient. The high Péclet number regime should correspond to the case of immiscible fluids and infinite capillary number.

In the present work, the steady displacement of a viscous liquid by a long drop of another viscous liquid in a capillary tube is analyzed by simulations and experiments for a wide range of the governing parameters. A thin layer of the displaced liquid is left behind on the tube walls, as illustrated in Fig. 1. In the figure, R_o is the radius of the tube and R_b, the radius of the cylindrical portion of the interface. The theoretical approach consisted of the solution of the governing equations of this free surface problem using the finite element method. The flow field variables and the position of the interface between the two liquids are all solved simultaneously and the formulation is not limited to low capillary numbers. The theoretical predictions show the effect of different parameters on the interface configuration and on the thickness of the layer of the displaced liquid left on the walls. The experiments

[1] To whom correspondence should be addressed.

Contributed by the Fluids Engineering Division for publication on the JOURNAL OF FLUIDS ENGINEERING. Manuscript received by the Fluids Engineering Division June 9, 2003; revised manuscript received August 13, 2004. Review Conducted by: S. Balachandar.

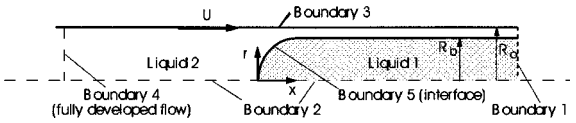

Fig. 1 Schematics of the problem

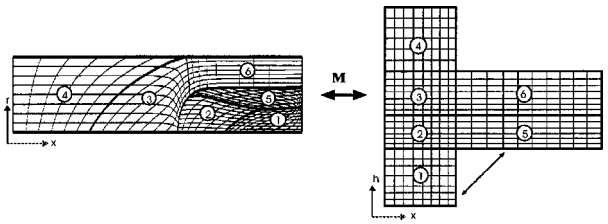

Fig. 2 Mapping between the physical and reference domains

consisted of visualization of the tip of the interface to examine the shape of the free surface and the amount of displaced liquid left on the tube wall.

2 Mathematical Formulation

The physical model to describe the displacement of a Newtonian liquid of viscosity μ_2 by a long drop of a second Newtonian liquid of viscosity μ_1 is now presented. The displacing drop (Liquid 1) is translating steadily with speed U. To simplify the analysis, the governing equations are written with respect to a moving frame of reference located at the tip of the interface. In this frame of reference, the flow is steady and the walls are moving with velocity U.

The geometry analyzed is an axisymmetric tube of radius R_o. The liquids are assumed to be incompressible, and the flow is laminar and inertialess. The velocity and pressure fields are governed by the continuity and momentum equations. In cylindrical coordinates, these governing equations are written as (the subscript $k=1, 2$ labels the two liquids)

$$0=\frac{1}{r}\frac{\partial}{\partial r}(rv_k)+\frac{\partial}{\partial x}(u_k) \tag{2}$$

$$0=\left[\frac{1}{r}\frac{\partial}{\partial r}(r\tau_{(rx)_k})+\frac{\partial}{\partial x}(\tau_{(xx)_k})\right]-\frac{\partial p_k}{\partial x} \tag{3}$$

$$0=\left[\frac{1}{r}\frac{\partial}{\partial r}(r\tau_{(rr)_k})-\frac{\tau_{(\theta\theta)_k}}{r}+\frac{\partial}{\partial x}(\tau_{(rx)_k})\right]-\frac{\partial p_k}{\partial r} \tag{4}$$

In these equations, x and r are the axial and radial coordinates, u and v are the axial and radial components of the velocity vector ($\mathbf{u}=u\hat{\mathbf{e}}_x+v\hat{\mathbf{e}}_r$), p is the pressure, τ_{xx}, τ_{xr}, τ_{rx}, τ_{rr}, and $\tau_{\theta\theta}$ are components of the extra-stress tensor, $\boldsymbol{\tau}$ ($\boldsymbol{\tau}\equiv\mathbf{T}+p\mathbf{1}$, where $\mathbf{T}$ is the stress tensor and $\mathbf{1}$ is the unit tensor).

As mentioned above, the two liquids are Newtonian, i.e., the extra-stress tensor $\boldsymbol{\tau}$ is proportional to the rate-of-deformation tensor $\dot{\boldsymbol{\gamma}}\equiv\nabla\mathbf{u}+\nabla\mathbf{u}^T$

$$\boldsymbol{\tau}_k=\boldsymbol{\mu}_k\dot{\boldsymbol{\gamma}},\quad k=1,2 \tag{5}$$

As indicated in Fig. 1, far enough upstream of the interface (Boundary 4) the flow is assumed to be fully developed and hence the pressure is uniform on the cross section

$$\mathbf{n}\cdot\nabla\mathbf{u}_2=0,\quad p_2=p_{\text{in}} \tag{6}$$

where $\mathbf{n}$ is the unit vector normal to the boundary and p_{in} is a constant. Far enough downstream of the interface (Boundary 1), the flow is also assumed to be fully developed, but the pressure is not imposed

$$\mathbf{n}\cdot\nabla\mathbf{u}_1=0 \tag{7}$$

The symmetry axis (Boundary 2) is a streamline of the flow, and there the shear stress vanishes

$$\mathbf{t}\cdot[\mathbf{n}\cdot\boldsymbol{\tau}_k]=\tau_{(rx)_k}=0,\quad \mathbf{n}\cdot\mathbf{u}_k=0 \tag{8}$$

where $\mathbf{t}$ is the unit vector tangent to the boundary. The no-slip and impermeability conditions are applied along the tube wall (Boundary 3)

$$\mathbf{u}=U\mathbf{e}_x \tag{9}$$

The liquid-liquid interface (Boundary 5) is also a streamline of the flow. There is no velocity jump, while a normal stress jump occurs at the interface, which is balanced by the capillary pressure

$$(\mathbf{u}_1-\mathbf{u}_2)=0 \tag{10}$$

$$\mathbf{n}(p_1-p_2)+\mathbf{n}(\boldsymbol{\tau}_2-\boldsymbol{\tau}_1)=\frac{\sigma}{R_m}\mathbf{n} \tag{11}$$

where $1/R_m$ is the local mean curvature of the interface, given by

$$\frac{1}{R_m}\mathbf{n}=\frac{1}{\sqrt{x_s^2+r_s^2}}\frac{\partial\mathbf{t}}{\partial s}-\frac{x_s}{r\sqrt{x_s^2+r_s^2}}\mathbf{n} \tag{12}$$

where s is the arc-length curvilinear coordinate along the interface.

The relevant dimensionless parameters are

$$\text{Capillary Number:}\quad Ca\equiv\frac{\mu_2 U}{\sigma} \tag{13}$$

$$\text{Viscosity Ratio:}\quad N_\mu\equiv\frac{\mu_2}{\mu_1} \tag{14}$$

3 Solution Method

Because of the liquid-liquid interface, the flow domain for each set of parameter values is unknown a priori. In order to solve this free boundary problem by means of standard techniques for boundary value problems, the set of differential equations and boundary conditions posed in the unknown domain has to be transformed into an equivalent set, defined in a known reference domain. This transformation is made by a mapping $\underline{x}=\underline{x}(\xi)$ that connects the two domains (Fig. 2). The unknown physical domain is parametrized by the position vector $\underline{x}$, and the reference domain by ξ. The mapping used here is the one presented by de Santos [16]. He showed that a functional of weighted smoothness can be used successfully to construct the type of mapping involved here. The inverse of the mapping that minimizes the functional is governed by a pair of elliptic differential equations identical to those governing diffusional transport with variable diffusion coefficients. The coordinates ξ and η of the reference domain satisfy

$$\nabla(D_\xi\nabla\xi)=0 \tag{15}$$

$$\nabla(D_\eta\nabla\eta)=0 \tag{16}$$

D_ξ and D_η are diffusion coefficients used to control the element spacing. Equations (15) and (16) describe the inverse mapping $\boldsymbol{\xi}=\boldsymbol{\xi}(x)$. To evaluate $\mathbf{x}=\mathbf{x}(\boldsymbol{\xi})$, the diffusion equations that describe the mapping also have to be transformed to the reference configuration. The gradient of mapping $\mathbf{x}=\mathbf{x}(\boldsymbol{\xi})$ in a two-dimensional domain is defined as $\nabla_\xi\mathbf{x}\equiv\mathbf{J}$. $\|J\|=\det\mathbf{J}$ is the Jacobian of the transformation.

Boundary conditions are needed in order to solve the second-order partial differential Eqs. (15) and (16). Along the solid walls and at the synthetic inlet and outlet planes, the boundary is located by imposing a relation between the coordinates x and r from the equation that describes the shape of the boundary, and stretching functions are used to distribute the points along the boundaries.

The liquid-liquid interface is located by imposing the kinematic condition (10). The discrete version of the mapping equations are generally referred to as mesh generation equations.

Spatial derivatives with respect to coordinates of the physical domain $\mathbf{x}$ can be written in terms of derivatives with respect to coordinates of the reference domain $\boldsymbol{\xi}$ by using the inverse of the gradient of the mapping

$$\begin{pmatrix} \frac{\partial}{\partial x} \\ \frac{\partial}{\partial y} \end{pmatrix} = \mathbf{J}^{-1} \begin{pmatrix} \frac{\partial}{\partial \xi} \\ \frac{\partial}{\partial \eta} \end{pmatrix} \tag{17}$$

The differential equations that govern the problem were solved simultaneously with the aid of the finite element/Galerkin's method. The velocity, pressure, and node position are represented in terms of basis functions

$$u = \sum_{j=1}^{n} U_j \phi_j ; \quad v = \sum_{j=1}^{n} V_j \phi_j ; \quad p = \sum_{j=1}^{m} P_j \chi_j ;$$
$$x = \sum_{j=1}^{n} X_j \phi_j ; \quad y = \sum_{j=1}^{n} Y_j \phi_j . \tag{18}$$

Biquadratic basis functions (ϕ_j) were used to represent the velocity and nodal coordinates and linear discontinuous functions (χ_j) to expand the pressure field. The coefficient of the expansions are the unknowns of the problem

$$\underline{c} = [U_j \;\; V_j \;\; P_j \;\; X_j \;\; Y_j]^T$$

The corresponding weighted residuals of the Galerkin method are

$$R^i_{mx} = \int_{\bar{\Omega}} \left[\frac{\partial \phi_i}{\partial x} T_{(xx)_k} + \frac{\partial \phi_i}{\partial r} T_{(xr)_k} \right] r \|J\| d\bar{\Omega} - \int_{\bar{\Gamma}} \mathbf{e}_x (\mathbf{n} \cdot \mathbf{T}_k) \phi_i r \frac{d\Gamma}{d\Gamma} d\bar{\Gamma} \tag{19}$$

$$R^i_{mr} = \int_{\bar{\Omega}} \left[\frac{\partial \phi_i}{\partial x} T_{(xr)_k} + \frac{\partial \phi_i}{\partial r} T_{(rr)_k} + \frac{\phi}{r} T_{\theta\theta_k} \right] r \|J\| d\bar{\Omega} - \int_{\bar{\Gamma}} \mathbf{e}_r (\mathbf{n} \cdot \mathbf{T}_k) \phi_i r \frac{d\Gamma}{d\Gamma} d\bar{\Gamma} \tag{20}$$

$$R^i_c = \int_{\bar{\Omega}} \left[\frac{1}{r} \frac{\partial}{\partial r} (r v_k) + \frac{\partial u_k}{\partial x} \right] \chi_i r \|J\| d\bar{\Omega} \tag{21}$$

$$R^i_\xi = - \int_{\bar{\Omega}} D_\xi \left(\frac{\partial \phi}{\partial x} \frac{\partial \xi}{\partial x} + \frac{\partial \phi}{\partial r} \frac{\partial \xi}{\partial r} \right) \|J\| d\bar{\Omega} + \int_{\Gamma} D_\xi (\nabla \xi \cdot \mathbf{n}) \phi_i \frac{d\Gamma}{d\Gamma} d\bar{\Gamma} \tag{22}$$

$$R^i_\eta = - \int_{\bar{\Omega}} D_\eta \left(\frac{\partial \phi}{\partial x} \frac{\partial \eta}{\partial x} + \frac{\partial \phi}{\partial r} \frac{\partial \eta}{\partial r} \right) \|J\| d\bar{\Omega} + \int_{\Gamma} D_\eta (\nabla \eta \cdot \mathbf{n}) \phi_i \frac{d\Gamma}{d\Gamma} d\bar{\Gamma} \tag{23}$$

At the elements located along the interface, the boundary integral of the residuals of momentum were calculated with the aid of Eq. (11).

Once all the variables are represented in terms of the basis functions, the system of partial differential equations reduces to simultaneous algebraic equations for the coefficients of the basis function of all the fields. This set of equations is nonlinear and sparse. It was solved by Newton's method, and a quadratic convergence was obtained as the residual approached zero. The linear system of equations at each Newton iteration was solved using a frontal solver.

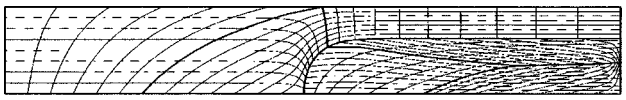

Fig. 3 The finite element mesh, with 362 elements and 7178 degrees of freedom

The overall domain length was equal to 15 inner diameters ($L = 15 D_o$), the interface tip being located in the middle of it. This length was chosen to ensure that the results do not depend on it. The domain was divided into 362 elements that correspond to 1523 nodes and 7178 degrees of freedom. A representative mesh is shown in Fig. 3.

4 Experiments

The experimental setup used in the visualization experiments is sketched in Fig. 4. Initially, the displacing liquid (Liquid 1) is stored in reservoir (A), and the displaced liquid (Liquid 2), in reservoir (E). Collecting Tanks (B) and (C) are auxiliary tanks used in the process of eliminating air bubbles in the system, as explained below.

The flow was controlled by cutoff valves (V1 to V5) and by the gate valve R1. The glass capillary tube was $L = 1.5$ m long, and the inner and outer diameters were $D_o = 5$ mm and $D_{\text{ext}} = 7$ mm, respectively. The tube was mounted inside a plexiglas box (D) filled with glycerin in order to minimize distortions of the interface image. A charge-coupled device (CCD) camera mounted at a right angle to the side wall of the plexiglas box was used to get the image of the interface as it traveled through the glass capillary. The camera was connected to a VCR to record the images.

The selection of the liquids was crucial to the experiments. The pair of liquids used had to be immiscible and with refractive indexes sufficiently different from each other in order to render the interface visible. Furthermore, the densities had to be as close as possible to minimize buoyancy effects. The buoyancy force is proportional to the magnitude of the density difference $\Delta\rho = \rho_1 - \rho_2$, and to the square of the drop diameter, D_b. For gas-liquid displacement, the importance of buoyancy relative to viscous forces is small when [10,9]

$$\frac{(\Delta\rho) g D_b^2}{\mu_2 U} \ll 1 \tag{24}$$

where g is the acceleration due to gravity. This ratio was useful in providing design guidelines for the experiments, although the characteristic viscous force employed is less than satisfactory for liquid-liquid displacement.

The displaced liquid used in the experiments was soybean oil. Its density was $\rho_2 = 915\ \text{kg/m}^3$ and its viscosity $\mu_2 = 50 \times 10^{-3}$ Pa s. Two different types of displacing liquids were used. The first was a mixture of water and ethanol, with $\rho_1 = 915\ \text{kg/m}^3$ and $\mu_1 = 2.5 \times 10^{-3}$ Pa s. The second set of displacing liquids was a solution of PEG (polyethylene glycol, MW = 6000 g/mol) in water. The viscosity level could be selected by changing the polymer concentration, and varied from $\mu_1 = 4 \times 10^{-3}$ Pa s up to $\mu_1 = 27.5 \times 10^{-3}$ Pa s. The density of the PEG aqueous solution was virtually constant over the range of concentration explored, namely, $\rho_1 = 1030\ \text{kg/m}^3$.

Before starting each visualization experiment, the glass capillary has to be filled with the displaced liquid (Liquid 2), stored in Reservoir (E). This is done by opening valves V4, V5, and R1, while keeping valve V3 closed. This causes the liquid to flow from Reservoir (E) to collecting tank (C). This flow is maintained until all the air bubbles are removed from the capillary tube. A similar procedure is followed to fill the line from reservoir (A) to valve V3 with the displacing liquid (Liquid 1). Again, the flow is maintained until all the air bubbles are removed. To start the experiment, reservoir (E) is disconnected from the capillary tube and

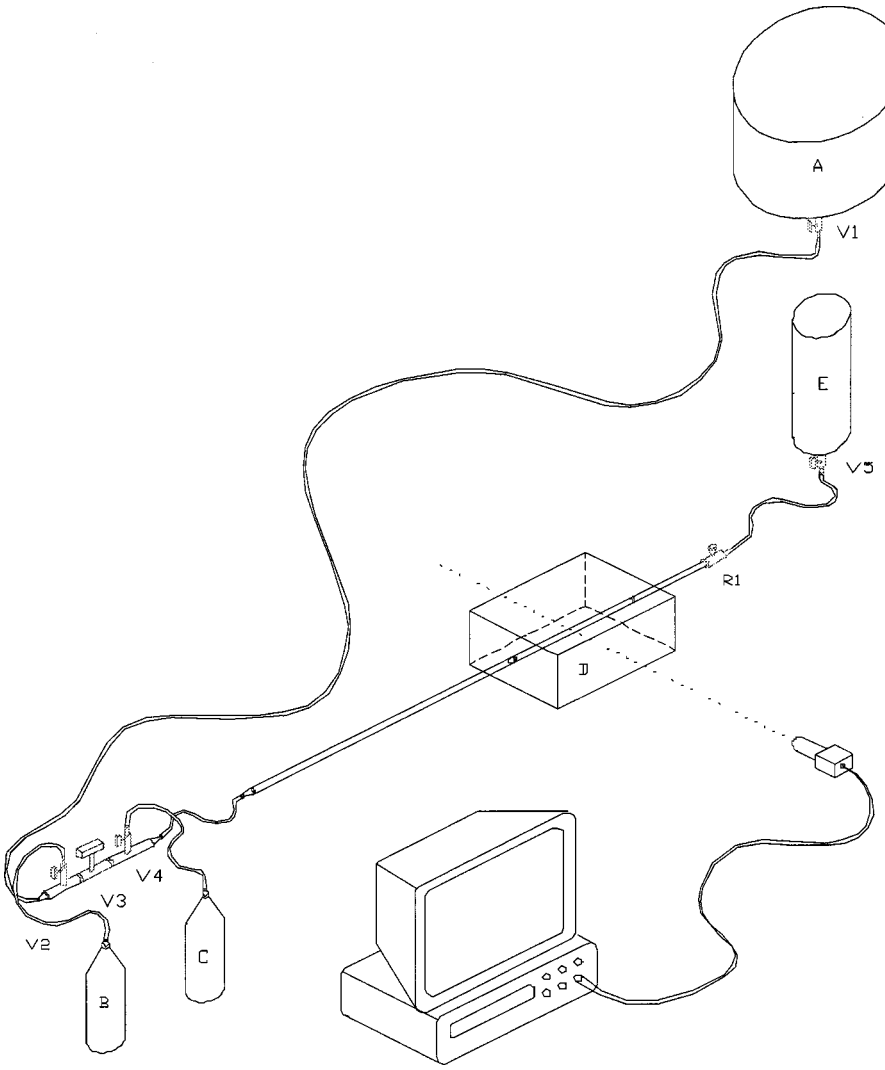

Fig. 4 Schematics of the apparatus

valve V3 is opened, with V2 and V4 closed. The tip of the interface starts traveling through the capillary tube and its velocity is controlled by the gate-valve R1. The CCD camera captures the image of the interface as it passes through the visualization box. The amount of Liquid 2 that remains on the tube wall is determined a posteriori by an image analysis. The level variation at Reservoir (A) during each experiment is negligible because the transversal area of the reservoir is sufficiently large, rendering the pressure gradient essentially constant during each experiment.

Because the liquids had different viscosities, the pressure loss along the capillary changes as Liquid 1 takes over the tube. This change in pressure loss would lead to a change in the drop speed as it travels through the capillary. This is avoided by assuring that most of the overall pressure loss occurs in the gate valve, so that the pressure loss along the capillary is always negligible. Therefore, any variation that occurs in the later causes no appreciable change in the overall pressure loss of the system, and thus the interface always travels with constant speed. The interface velocity U is measured by recording the time that it takes to travel between two axial positions marked on the tube. The maximum interface velocity that could be measured with accuracy was of about 0.15 m/s, which determined the maximum capillary number that could be obtained in the experiments. The surface tension for each pair of liquids is measured by carefully placing a layer of the lighter liquid at the top of the surface of the heavier liquid previously placed in a beaker, and then using a Lauda ring tensiometer to determine the interfacial tension.

After each run, the tube is rigorously cleaned to remove all contaminants. This procedure is needed to avoid changes in surface tension.

5 Results

The amount of Liquid 2 that remains on the capillary wall is usually reported in terms of the mass fraction of liquid that is not displaced m, or simply by the liquid film thickness left on the wall h_∞ (see Fig. 5). The two forms are related by

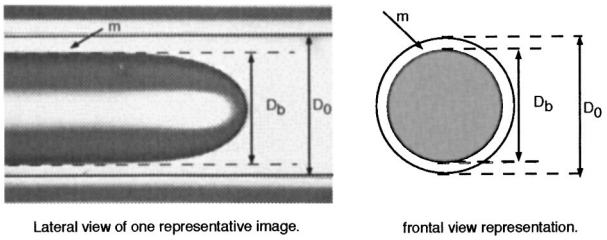

Fig. 5 Representative image of the interface

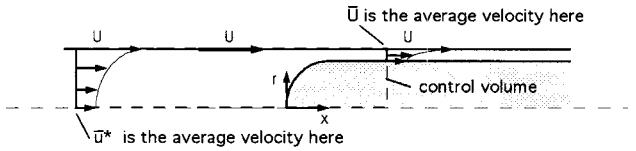

Fig. 6 Velocity profiles as measured from a reference frame located at the tip of the interface

$$m = \frac{\text{mass left on wall}}{\text{total mass}} = 1 - \frac{\text{displaced mass}}{\text{total mass}}$$

$$= 1 - \left(\frac{D_b}{D_o}\right)^2 = 1 - \left(1 - \frac{2h_\infty}{D_o}\right)^2 \tag{25}$$

where $h_\infty = (D_o - D_b)/2$ is the layer thickness of Liquid 2 left on the tube wall.

The mass fraction of Liquid 2 left on the tube wall can be evaluated by employing the mass conservation principle for Liquid 2 in a control volume containing the tip of the interface and attached to it. Figure 6 shows this control volume and the sketch of the velocity profiles at the inlet and outlet planes as seen from a reference frame attached to the tip of the interface. The mass flow rate of Liquid 2 through the control surface upstream of the drop is equal to $\pi R_o^2 \overline{u}^*$ and through the control surface downstream the tip of the interface is $\pi(R_o^2 - R_b^2)\overline{U}$, $\overline{u}^*$ and $\overline{U}$ being the average velocities of Liquid 2 at the two planes with respect to the moving frame of reference. The average velocity $\overline{u}^*$ can be evaluated as a function of the average velocity with respect to a fixed frame of reference, $\overline{u}$: $\overline{u}^* = U - \overline{u}$. Combining the previous relations, the mass fraction m can be expressed in terms of the average velocities

$$m = 1 - \left(\frac{D_b}{D_o}\right)^2 = \frac{U - \overline{u}}{U} \tag{26}$$

It is important to notice that, in the particular case of a rather low-viscosity displacing fluid, as in gas displacement, the velocity profile at the downstream control surface (Fig. 6) is uniform and equal to the wall velocity. The pressure is uniform on the gas phase and the shear stress at the interface vanishes. Therefore, the average velocity $\overline{U}$ is also equal to the wall velocity, i.e., $\overline{U} = U$. Only in this limiting case (viz., as $\mu_1/\mu_2 \to 0$), the mass fraction m can be evaluated via the expression employed by Taylor [8], namely, Eq. (1).

The experimental data were obtained for Reynolds numbers small enough to assure negligible inertial effects. The main goal was to study the effect of the capillary number Ca and of the viscosity ratio N_μ on the flow near the interface. In order to compare our results with the ones of previous works, our results are also reported in terms of the mass fraction m. It was calculated, in both the numerical and the experimental studies, using the diameters of the tube and the drop, as indicated in Eq. (26).

In order to validate the theoretical model, the solution algorithm, and the experimental procedure, the results of Taylor [8] for gas-liquid displacement were employed. Figure 7 shows Taylor's experimental data together with our theoretical predictions obtained for $N_\mu = 1000$ and our experimental results of liquid-liquid displacement for $N_\mu = 20$. The agreement is quite good over the range of capillary numbers explored. The viscosity ratio $N_\mu = 20$ was shown to be large enough to reproduce the limiting case of gas-liquid displacement. The images of the interface at different capillary numbers and $N_\mu = 20$ are shown in Fig. 8. The displacing liquid was a 50% in volume mixture of water and ethanol. Buoyancy effects could not be avoided in the experiments and, therefore, often the observed interface was not exactly axisymmetric. The images show clearly that the film thickness of Liquid 2 left on the wall rises as the capillary number is increased.

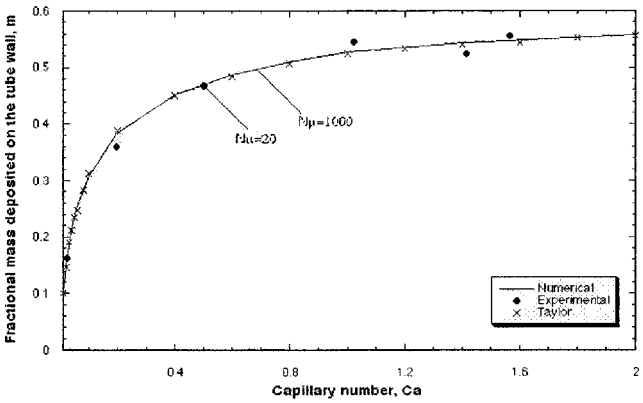

Fig. 7 Fraction of mass deposited on the tube wall as a function of the capillary number. Comparison between the results with high viscosity ratio and Taylor's data for gas-liquid displacement.

Before presenting the numerical results, it is important to emphasize that no stability analysis was performed in the research reported here. Therefore, it may happen that some of the following theoretical results in the large Ca range are not stable. Olbricht and Kung [2] observed experimentally the existence of a critical capillary number beyond which a finite-size drop is not stable, and these observations have later been predicted numerically by Tsai and Miksis [1]. The objective in exploring these large Capillary number values at different viscosity ratios was to look for the asymptotic value for the deposited mass m which is observed experimentally and numerically for infinite viscosity ratio.

Figure 9 shows the streamline pattern as a function of capillary number for the case of liquid-liquid displacement, i.e., finite viscosity ratio. The predictions are for $N_\mu = 4$. The net flow rate of the displacing liquid relative to the frame of reference attached to the interface tip is zero, and therefore a large recirculation is always present in the Liquid 1 region. For large capillary numbers, e.g., $Ca = 5$, there is no recirculation in the displaced liquid. There

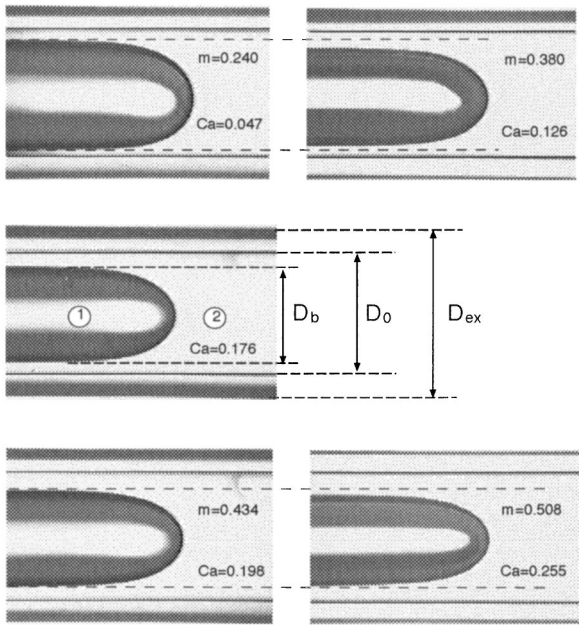

Fig. 8 Images of the tip of the liquid-liquid interface for $N_\mu = 2$. $Ca = 0.047$, 0.126, 0.176, 0.198, and 0.255.

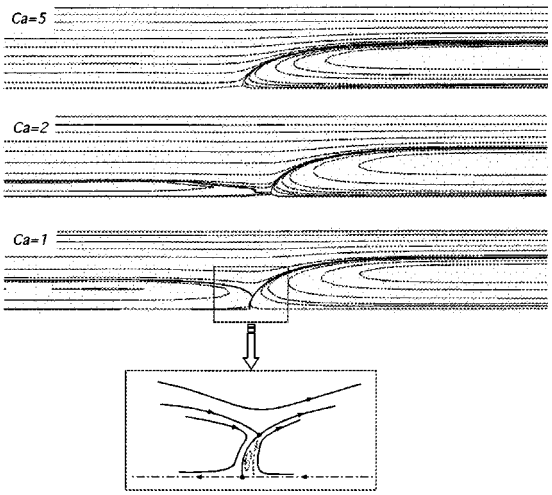

Fig. 9 Streamline patterns near the liquid-liquid interface for $N_\mu=4$. Ca=5, 2, and 1.

is a single stagnation point at the tip of the interface. As the capillary number is decreased, a recirculation near the centerline in Liquid 2 appears. For $Ca=2$, this recirculation is not attached to the interface, and there are two stagnation points located at the symmetry axis, one at the tip of the interface between the two liquids and the other at the tip of the recirculating region in the displaced liquid. As the capillary number is further decreased, e.g., $Ca=1$, the recirculation region grows and becomes attached to the interface. Now there is a stagnation point at the tip of the interface and a stagnation ring, also located at the interface. The existence of these different streamline patterns has been proposed by Taylor [8] and predicted by Giavedoni and Saita [11] for the particular case of a gas displacing a viscous liquid. At capillary numbers at which the stagnation ring is present, there is a rather weak secondary recirculation on the displacing liquid, as sketched in the insert of Fig. 9, that the mesh used to descritize the domain was not fine enough to capture. This recirculation was also observed by Petitjeans and Maxworthy [15] and by Chen and Meiburg [17].

The effect of the viscosity ratio on the streamlines of the flow is shown in Fig. 10, for $Ca=10$. As the displacing liquid becomes more viscous, and consequently the viscosity ratio falls, the thickness of Liquid 2 left behind increases, and a recirculation near the centerline appears on the Liquid 2 region.

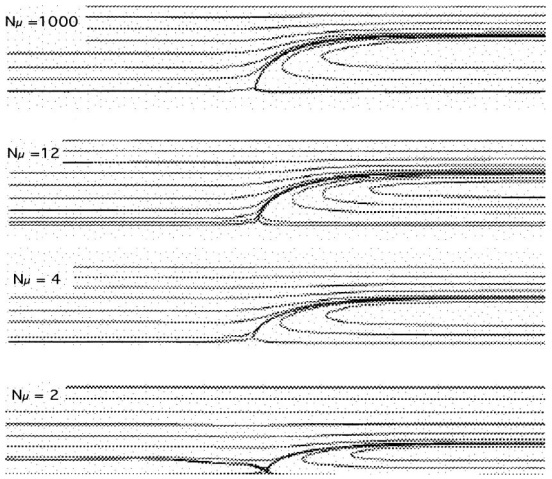

Fig. 10 Streamline patterns near the liquid-liquid interface for $Ca=10$. $N_\mu=1000$, 12, 4, and 2.

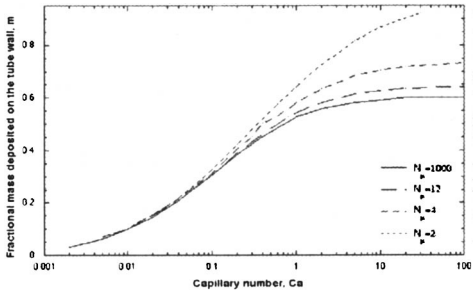

Fig. 11 Fraction of mass deposited on the tube wall as a function of the capillary number. Numerical predictions.

The predictions of mass fraction of Liquid 2 left on the wall m as a function of the capillary number and of the viscosity ratio are summarized in Fig. 11. A wide range of both parameters was investigated, viz., $2\times10^{-3}<Ca<100$ and $2<N_\mu<1000$. It is important to point out that the predictions and experiments discussed here are for the case of a less viscous liquid displacing a more viscous liquid, i.e., $N_\mu>1$. The thickness of displaced liquid left on the tube wall rises with capillary number for all the viscosity ratios explored. In the particular case of gas-liquid displacement ($N_\mu=1000$), the mass fraction m reaches an asymptotic value of $m\approx0.6$, as reported by Cox [18]. For a fixed capillary number, the layer thickness rises as the viscosity ratio is decreased, i.e., as the displacing liquid becomes more viscous. This behavior has been observed in the theoretical predictions of Teletzke et al. [14], limited to very small capillary number values ($Ca\approx10^{-4}$), by the predictions of Schwartz et al. [19], and by the experiments of Goldsmith and Mason [13]. A comparison between some of these experimental results and the theoretical predictions obtained here are presented in Table 1. The table shows data for two different values of the capillary number and of the viscosity ratio. The agreement was quite good, with a discrepancy within 1%.

The experimental study presented here also confirmed the trend of thicker layers of displaced liquid left on the wall as the displacing liquid becomes more viscous, as illustrated by the images of Fig. 12. The images were obtained at the same capillary number $Ca\approx0.2$ and viscosity ratio of $N_\mu=12$, $N_\mu=4$, and $N_\mu=2$. The experimental results are summarized in Fig. 13. The high viscosity ratio curve $N_\mu=1000$ reproduced the results of Taylor [8]. At a fixed capillary number, the mass fraction m left on the wall increases as the viscosity ratio is decreased, as predicted by the theoretical model. The plot also shows the theoretical predictions at the same viscosity ratios, already presented in Fig. 11. The

Table 1 Comparison between the experimental results of Goldsmith and Mason [13] and the present numerical predictions

	Reference [13]	Numerical predictions
$Ca=1.43$; $N_\mu=4.55$	$m=0.590$	$m=0.600$
$Ca=1.30$; $N_\mu=1.00$	$m=0.767$	$m=0.773$

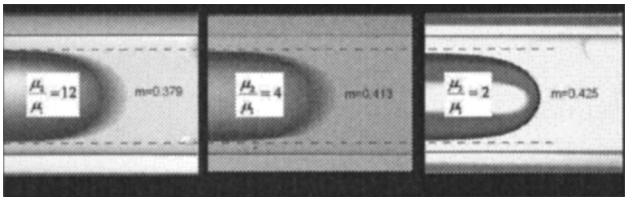

Fig. 12 Images of the tip of the liquid-liquid interface for $Ca=0.2$. $N_\mu=12$, $N_\mu=4$, and $N_\mu=2$.

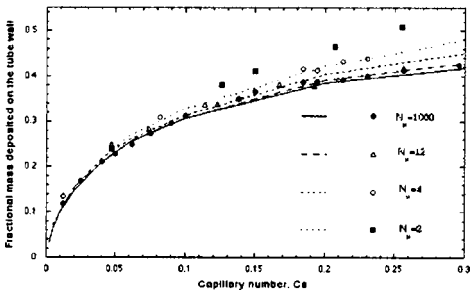

Fig. 13 Fraction of mass deposited on the tube wall as a function of the capillary number. Comparison between the experimental results and the numerical predictions.

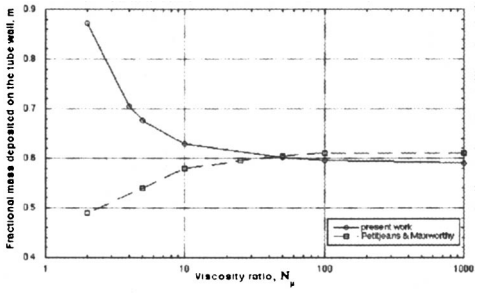

Fig. 15 Fraction of mass deposited on the tube wall as a function of viscosity ratio. Comparison between the present numerical predictions and the experimental results of Petitjeans and Maxworthy [15] for miscible liquid-liquid displacement.

qualitative agreement is good, but the theoretical results underpredict the film thickness on the wall; the typical discrepancy is close to 10%. It is important to notice that the effect of the viscosity ratio on the mass fraction on the wall m over the range of capillary numbers presented in Fig. 13 is rather small, and hence experimental uncertainty may explain the discrepancy in the range of 10%. The experiments could not be done at higher capillary numbers due to limitations of the experimental procedure. The effect of the viscosity ratio becomes more pronounced at $Ca>1$, as shown by the theoretical predictions presented in Fig. 14.

The trend observed in the experimental and theoretical analysis discussed above, namely, that the amount of displaced liquid remaining on the tube wall rises as the displacing liquid becomes more viscous, is in contradiction with the experiments reported by Petitjeans and Maxworthy [15]. They studied the liquid-liquid displacement of miscible liquids at large values of the Péclet number, and suggested that this situation should mimic the case of immiscible liquids at infinite capillary numbers. The comparison between our theoretical predictions and their experiments is shown in Fig. 15, for $Ca=10$. Both curves approach the same asymptotic value of $m\approx 0.6$ as the viscosity ratio becomes very large, recovering the gas-displacement result of Cox [9].

An explanation for this discrepancy is that Petitjeans and Maxworthy [15] evaluated the mass fraction left on the tube wall using the expression proposed by Taylor [8], namely, Eq. (1), based on the average velocity of the displaced liquid ahead of the free surface and on the velocity of the tip of the interface. As discussed before, this expression is valid only for the particular case of gas-liquid displacement, and underestimates the mass fraction if used for liquid-liquid displacement. The error decreases as the viscosity ratio is increased, because the average velocity of the film left on the wall approaches the wall velocity. For the sake of testing the correctness of the above explanation, we have also employed Eq. (1) to evaluate the mass fraction for a representative case, and indeed the thus calculated mass fraction was in agreement with the results presented by Petitjeans and Maxworthy [15].

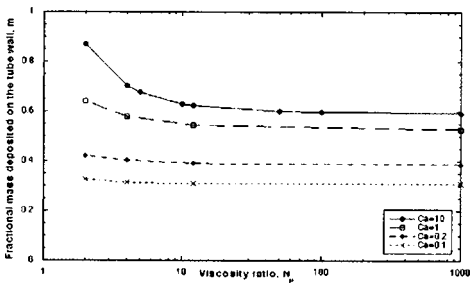

Fig. 14 Fraction of mass deposited on the tube wall as a function of the viscosity ratio. Numerical predictions.

6 Final Remarks

An axisymmetric model of the flow near the upstream liquid-liquid interface of a long drop penetrating through a liquid in a capillary tube was presented. The presence of the interface makes the problem complex, since the domain in which the differential equations are integrated is unknown a priori. A fully coupled formulation was used and the differential equations were solved via the Galerkin finite element method. Some experimental visualizations were done in order to validate the numerical approach. Furthermore, the numerical predictions were confronted with experimental data and predictions of theoretical analyses of other authors, and a good agreement was observed.

Recent articles are found in the literature which analyze liquid displacement in tubes. However, these are limited to gas-liquid displacement or to liquid-liquid displacement at rather small capillary numbers. Thus, the main contribution of the present work was the study of liquid-liquid displacement in tubes for a wider range of the capillary number, focusing also on the influence of the viscosity ratio.

The predictions obtained here for the mass fraction at large viscosity ratios agree well with experimental data of Taylor [8]. Our experimental visualizations for large values of the viscosity ratio agree with Taylor's results as well.

For small values of the viscosity ratio, the theoretical predictions were compared with the experimental data reported by Goldsmith and Mason [13], and a quite good agreement was obtained. The predictions of the viscosity ratio effect also follows the same trend obtained by asymptotic analysis of Teletzke et al. [14], but limited to small capillary numbers.

The analysis of the capillary number effect shows that the interface front becomes flatter as the capillary number decreases. In addition, the recirculations increase in both liquids as the capillary number is reduced. Our analysis also showed that the interface front becomes less flat as the viscosity ratio is decreased. Some recirculations in the displaced liquid appear for low values of the viscosity ratio as well, but for high values of the capillary number only. Finally, it is seen that mass fraction increases as the viscosity ratio is decreased.

Our theoretical predictions and experimental visualization results are in qualitative agreement. However, the range of capillary number studied experimentally was relatively small.

The apparent disagreement to the experimental analysis of Petitjeans and Maxworthy [15] and the theoretical predictions of Chen and Meiburg [17] for miscible liquid-liquid displacement at high Péclet numbers can be explained by an inappropriate definition of the mass fraction of displaced liquid that remains attached to the tube wall.

Acknowledgments

This research was partially funded by the Brazilian Research Council (CNPq), the Research Foundation of the State of Rio de Janeiro (FAPERJ), and the Brazilian National Oil Company (Petrobras).

References

[1] Tsai, T. M., and Miksis, M. J., 1994, ''Dynamics of a Drop in a Constricted Capillary Tube,'' J. Fluid Mech., **292**, pp. 197–217.
[2] Olbricht, W. L., and Kung, D. M., 1992, ''The Deformation and Breakup of Liquid Drops in Low Reynolds Number Flow Through a Capillary,'' Phys. Fluids A, **4**(7), pp. 1347–1354.
[3] Martinez, M. J., and Udell, K. S., 1990, ''Axisymmetric Creeping Motion of Drops Through Circular Tubes,'' J. Fluid Mech., **210**, pp. 565–591.
[4] Westborg, H., and Hassager, O., 1989, ''Creeping Motion of Long Bubbles and Drops in Capillary Tubes,'' J. Colloid Interface Sci., **133**(1), pp. 135–147.
[5] Olbricht, W. L., 1996, ''Pore-Scale Prototypes of Multiphase Flow in Porous Media,'' Annu. Rev. Fluid Mech., **28**, pp. 187–213.
[6] Stark, J., and Manga, M., 2000, ''The Motion of Long Bubbles in a Network of Tubes,'' Transp. Porous Media, **40**, pp. 201–218.
[7] Fairbrother, F., and Stubbs, A. E., 1935, ''Studies in Electroendosmosis. Part VI. The Bubble-Tube Methods of Measurement,'' J. Chem. Soc., **1**, pp. 527–529.
[8] Taylor, G. I., 1961, ''Deposition of a Viscous Fluid on the Wall of a Tube,'' J. Fluid Mech., **10**, pp. 161–165.
[9] Cox, B. G., 1962, ''On Driving a Viscous Fluid Out of a Tube,'' J. Fluid Mech., **14**, pp. 81–96.
[10] Bretherton, F. P., 1961, ''The Motion of Long Bubbles in Tubes,'' J. Fluid Mech., **10**, pp. 166–188.
[11] Giavedoni, M. D., and Saita, F. A., 1997, ''The Axisymmetric and Plane Cases of a Gas Phase Steadily Displacing a Newtonian Liquid: A Simultaneous Solution of the Governing Equations,'' Phys. Fluids, **9**, pp. 2420–2428.
[12] Lee, A. G., Shaqfeh, E. S. G., and Khomami, B., 2002, ''A Study of Viscoelastic Free Surface Flows by the Finite Element Method: Hele-Shaw and Slot Coating Flows,'' J. Non-Newtonian Fluid Mech., **108**, pp. 327–362.
[13] Goldsmith, H. L., and Mason, S. G., 1963, ''The Flow of Suspensions Through Tubes,'' J. Colloid Sci., **18**, pp. 237–261.
[14] Teletzke, G. F., Davis, H. T., and Scriven, L. E., 1988, ''Wetting Hydrodynamics,'' Rev. Phys. Appl., **23**, pp. 989–1007.
[15] Petitjeans, P., and Maxworthy, T., 1996, ''Miscible Displacements in Capillary Tubes,'' J. Fluid Mech., **326**, pp. 37–56.
[16] de Santos, J. M., 1991, *Two-Phase Cocurrent Downflow Through Constricted Pas-Sages*, PhD thesis, University of Minnesota.
[17] Chen, C., and Meiburg, E., 1996, ''Miscible Displacements in Capillary Tubes. Part 2. Numerical Simulation,'' J. Fluid Mech., **326**, pp. 57–90.
[18] Cox, B. G., 1964, ''An Experimental Investigation of the Streamlines in Viscous Fluid Expelled From a Tube,'' J. Fluid Mech., **20**, pp. 193–200.
[19] Schwartz, L. W., Princen, H., and Kiss, A., 1986, ''On the Motion of Bubbles in Capillary Tubes,'' J. Fluid Mech., **172**, pp. 259–275.

Three-Dimensional Vortex Method for Gas-Particle Two-Phase Compound Round Jet

Tomomi Uchiyama
EcoTopia Research Institute,
Nagoya University,
Furo-cho, Chikusa-ku,
Nagoya 464-8603, Japan
Phone/Fax +81-52-789-5187
e-mail: uchiyama@info.human.nagoya-u.ac.jp

Akihito Fukase
Ebara Corporation,
Haneda Asahi-cho, Ohta-ku,
Tokyo 144-8510, Japan

This paper proposes a three-dimensional vortex method for a gas-particle two-phase compound round jet. The method can take account of the interaction between the two phases by calculating the motion of particles and the behavior of gas vortex elements through the Lagrangian approach. In order to discuss the validity of the method, an air jet, loaded with small glass particles, issuing from a round nozzle into the co-flowing air stream is simulated. The simulation demonstrates that the air turbulence modulations due to the particles, such as the relaxation of velocity decay, the decrement of momentum diffusion in the radial direction at the fully developed region, and the reduction of turbulent intensity and Reynolds shear stress, are successfully captured by the method. [DOI: 10.1115/1.1852490]

Introduction

In various industrial equipment, such as pulverized-coal combustors, solid rocket engines, and sand-blasting machines, gas jets containing small solid particles are observed. For the gas-particle two-phase jets issuing from a round nozzle, the mean velocity, the turbulent intensity, and the Reynolds shear stress have been measured [1–3]. By these experimental investigations, the gas turbulence modulations due to the loaded particles, such as the relaxation of velocity decay, the decrement of momentum diffusion in the radial direction at the fully developed region, and the reduction of turbulent intensity and Reynolds shear stress, have been clarified. Some numerical simulations have also been conducted. Elghobashi et al. [4], Shuen et al. [5], and Mostafa-Mongia [6] proposed k-ε turbulent models, and they reported that the mean velocity and the kinetic energy of turbulence for round jets are successfully simulated by the models. But they simulated the steady and axisymmetrical jets by using a number of model constants. Therefore, the simulations do not promise to have high reliability and applicability. To analyze the flow more accurately, Yuu et al. performed the direct numerical simulation on a round jet [7] and the large eddy simulation on a slit nozzle jet [8]. They got valuable results, such as the instantaneous velocity distributions for the two phases in the jet cross-sections. Their simulations demonstrated that the effect of particle on the development and momentum diffusion of the gas-phase can be computed.

Recently, vortex methods have been usefully applied to analyze various flow fields [9–13]. They can calculate directly the development of vortical structure by tracing the motion of the vortex elements having vorticity through the Lagrangian approach. Therefore, they have been favorably applied to free turbulent flows, in which the organized large-scale eddies play a dominant role. The vortex methods are easily adaptable to parallel computing, which can be exploited to solve large-scale problems efficiently. Though the vortex methods have the above-mentioned advantages, they present a problem that the vorticity field represented by the vortex elements does not always satisfy a divergent-free field. To resolve this problem, a few attempts have been conducted, and a relaxation scheme was presented by Winckelmans and Leonard [11].

To extend the applicability of vortex methods, one of the authors has proposed a two-dimensional vortex method for gas-particle two-phase free turbulent flow in a prior paper [14]. In the succeeding papers, the method was applied to a plane mixing layer [15], a slit nozzle jet [16], and a wake flow behind a plate [17] to simulate the effect of particle on the flow development and the relation between the large-scale eddy and the particle motion. The proposed vortex method was also employed to analyze the particulate jet induced by particles falling in an unbounded quiescent air [18]. The air flow having complicated vortical structure was calculated, and the entrained air flow rate agreed with the measurements.

Though a number of simulations on jet flows have been performed by using vortex methods, most of them are two-dimensional ones [19–21]. There are few three-dimensional simulations of jet, except for the analyses of single-phase jets by Kiya and his co-workers [22,23]. But the analyses were performed only for the developing region of an impulsively started jet, and the statistical properties, such as the mean velocity and the turbulent intensity, were not calculated. To discuss the applicability of a three-dimensional vortex method for a single-phase jet, one of the authors [24] simulated a single-phase compound round jet, which issues from a circular nozzle into the co-flowing stream. The simulation revealed that the mean velocity and the turbulent intensity are reasonably computed by the vortex method.

The objective of this study is to propose a three-dimensional vortex method for gas-particle two-phase compound round jet. For the two-way coupling, the two-dimensional method presented in a prior study [14] is extended. The method takes account of the effect of particle on the gas flow through the change of vorticity in the grids resolving the computational domain. In this study, the method is also applied to the simulation of a two-phase compound jet loaded with glass particles with diameter of 100 μm issuing from a round nozzle into the co-flowing air stream. It is confirmed that the numerical result does not contradict the existing knowledge on the two-phase jet issuing into still air.

Basic Equations

Assumptions. The following assumptions are employed for the simulation.

a. The gas-phase is incompressible.
b. The density of the particle is much larger than that of the gas.
c. The particle has a spherical shape with uniform diameter.
d. The collision between the particles is negligible.

Contributed by the Fluids Engineering Division for publication in the JOURNAL OF FLUIDS ENGINEERING. Manuscript received by the Fluids Engineering Division December 30, 2003; revised manuscript received August 25, 2004. Review conducted by: G. Chahine.

Governing Equations for Gas and Particle. The conservation equations for the mass and momentum of the gas-phase are expressed as follows under the assumption (a):

$$\nabla \cdot \mathbf{u}_g = 0 \tag{1}$$

$$\frac{\partial \mathbf{u}_g}{\partial t} + (\mathbf{u}_g \cdot \nabla)\mathbf{u}_g = -\frac{1}{\rho_g}\nabla p + \nu \nabla^2 \mathbf{u}_g - \frac{1}{\rho_g}\mathbf{F}_D \tag{2}$$

where $\mathbf{F}_D$ is the force exerted by the particle acting on the gas-phase per unit volume.

Using the assumption (b), the dominant forces on the particle are the drag and gravitational forces, while the virtual mass force, the Basset force, and the pressure gradient force are negligible [25]. The lift force is neglected with reference to the studies simulating the particle motion in a jet [19], a plane wake [26], and mixing layers [25,27]. Consequently, the equation of motion for a particle (mass m) is written as

$$m\frac{d\mathbf{u}_p}{dt} = \mathbf{f}_D + m\mathbf{g} \tag{3}$$

where the drag force $\mathbf{f}_D$ is given by the following from the assumption (c):

$$\mathbf{f}_D = (\pi d^2 \rho_g/8) C_D |\mathbf{u}_g - \mathbf{u}_p|(\mathbf{u}_g - \mathbf{u}_p) \tag{4}$$

Here, d is the particle diameter, and the drag coefficient C_D is estimated as [28]

$$C_D = (24/\mathrm{Re}_p)(1 + 0.15\,\mathrm{Re}_p^{0.687}) \tag{5}$$

where $\mathrm{Re}_p = d|\mathbf{u}_g - \mathbf{u}_p|/\nu$.

For the simultaneous calculation of Eqs. (1)–(3), a vortex method is used to solve Eqs. (1) and (2), and the Lagrangian approach is applied to Eq. (3).

Numerical Method

Discretization of Gas Vorticity Field by Vortex Element When taking the curl of Eq. (2) and substituting Eq. (1) into the resultant equation, the vorticity equation for the gas is derived:

$$\frac{D\boldsymbol{\omega}}{Dt} = (\boldsymbol{\omega} \cdot \nabla)\mathbf{u}_g + \nu \nabla^2 \boldsymbol{\omega} - \frac{1}{\rho_g}\nabla \times \mathbf{F}_D \tag{6}$$

The gas velocity $\mathbf{u}_g$ at $\mathbf{x}$ is given by the Biot-Savart equation:

$$\mathbf{u}_g(\mathbf{x}) = -\frac{1}{4\pi}\int \frac{(\mathbf{x} - \mathbf{x}') \times \boldsymbol{\omega}(\mathbf{x}')}{|\mathbf{x} - \mathbf{x}'|^3} d^3\mathbf{x}' + \mathbf{u}_{g0} \tag{7}$$

where $\mathbf{u}_{g0}$ stands for the velocity of potential flow.

The vorticity field is discretized by vortex elements. This study employs a blob model [11], which is frequently used to solve single-phase flow. The vortex element has a cylindrical shape as illustrated in Fig. 1, while the vorticity distribution is spherical with a finite core radius.

When the vortex element α at $\mathbf{x}^\alpha$ is supposed to have a core radius σ_α, the vorticity at $\mathbf{x}$ induced by the vortex element is expressed by the following equation:

$$\boldsymbol{\omega}^\alpha(\mathbf{x}) = \frac{\boldsymbol{\gamma}^\alpha}{\sigma_\alpha^3} f\left(\frac{|\mathbf{x} - \mathbf{x}^\alpha|}{\sigma_\alpha}\right) \tag{8}$$

Here, $f(\varepsilon)$ is the core distribution function, and $\boldsymbol{\gamma}^\alpha$ is the strength of vortex element expressed as

$$\boldsymbol{\gamma}^\alpha = \Gamma_\alpha \mathbf{l}^\alpha \tag{9}$$

where Γ_α and $\mathbf{l}^\alpha$ are the circulation and length vector of the vortex element, respectively, as indicated in Fig. 1.

For $f(\varepsilon)$, the following equation proposed for single-phase flow analysis [29] is applied:

$$f(\varepsilon) = \frac{3}{4\pi}\exp(-\varepsilon^3) \tag{10}$$

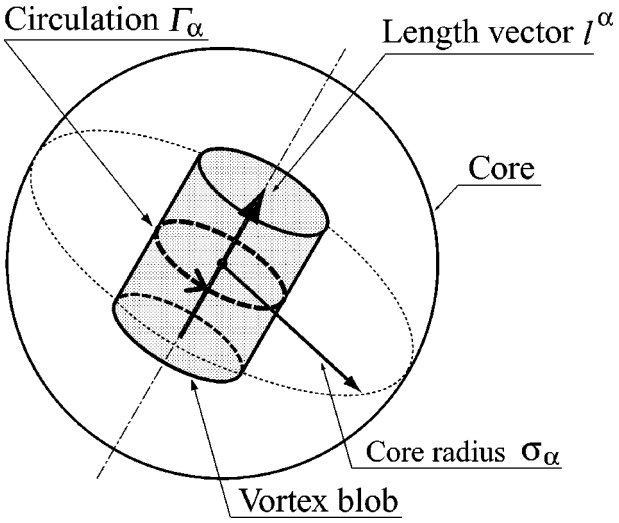

Fig. 1 Vortex element

When the vorticity field is discretized into a set of N vortex elements, the gas velocity $\mathbf{u}_g(\mathbf{x})$ is given by the following equation derived from Eqs. (7) and (8):

$$\mathbf{u}_g(\mathbf{x}) = -\frac{1}{4\pi}\sum_{\alpha=1}^{N} \frac{(\mathbf{x} - \mathbf{x}^\alpha) \times \boldsymbol{\gamma}^\alpha}{|\mathbf{x} - \mathbf{x}^\alpha|^3} g\left(\frac{|\mathbf{x} - \mathbf{x}^\alpha|}{\sigma_\alpha}\right) + \mathbf{u}_{g0} \tag{11}$$

where the function $g(\varepsilon)$ is determined as

$$g(\varepsilon) = 4\pi\int_0^\varepsilon f(\rho)\rho^2\, d\rho = 1 - \exp(-\varepsilon^3) \tag{12}$$

The minimum length scale of flow resolved by the vortex method is equivalent to the core radius. For single-phase flow analyses, a few attempts have been conducted to take account of the eddies, of which scale is smaller than the core radius, by employing turbulent models [23,30,31].

Release and Convection of Vortex Element. The simulation is performed on a gas jet issuing with velocity U_0 from a round nozzle of diameter D into the same gas co-flowing with velocity U_a, as shown in Fig. 2. Solid particles are loaded from the nozzle exit.

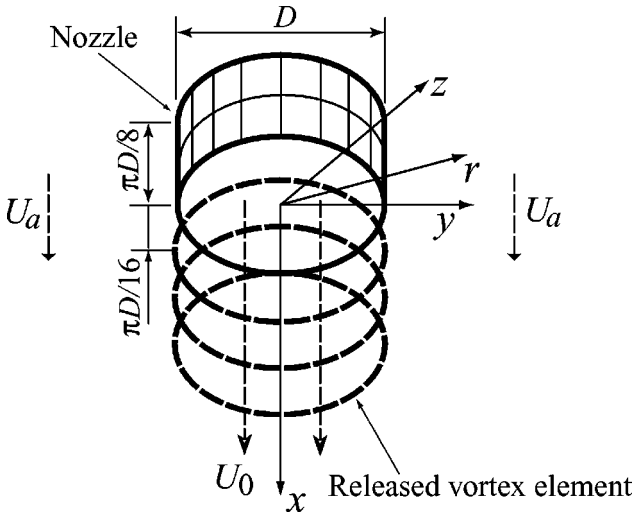

Fig. 2 Round nozzle and released vortex element

The vortex elements are released from the position of $x = \pi D/16$ at a time interval Δt_v. The released vortex element α convects with the gas velocity:

$$\frac{d\mathbf{x}^\alpha}{dt} = \mathbf{u}_g(\mathbf{x}^\alpha) \tag{13}$$

The circulation Γ_0 at the release is given as [24]

$$\Gamma_0 = (U_0^2 - U_a^2)\Delta t_v/2 \tag{14}$$

In this simulation, the strength of vortex element $\boldsymbol{\gamma}$ is employed as one of the dependent variables. The initial value can be given by the circulation and the length vector at the release of the vortex element, as found from Eq. (9). The initial circulation is specified from Eq. (14), while the initial length vector is determined from the geometry of nozzle edge.

When Eq. (6) is rewritten in the Lagrangian co-ordinates, it is found that the vorticity of vortex element varies with the lapse of time due to the changes in the length of vortex element, the viscous diffusion, and the force exerted by the loaded particles. These changes are computed simultaneously with the Lagrangian calculation of Eq. (13), as explained in the following.

Change in Vorticity Due to Stretch and Contraction of Vortex Element. The time evolution in the vorticity owing to the stretch and contraction of the vortex element is calculated from the Lagrangian expression of Eq. (6) omitting the viscous diffusion and particle terms:

$$\frac{d\boldsymbol{\omega}}{dt} = (\boldsymbol{\omega}\cdot\nabla)\mathbf{u}_g \tag{15}$$

When substituting Eqs. (7) and (8) into Eq. (15), the time rate of change in the strength of vortex element $\boldsymbol{\gamma}^\alpha$ is derived:

$$\frac{d\boldsymbol{\gamma}^\alpha}{dt} = \frac{1}{4\pi}\sum_{\beta=1}^{N}\frac{1}{\sigma_\beta^3}\left\{-\frac{g(\rho)}{\rho^3}\boldsymbol{\gamma}^\alpha\times\boldsymbol{\gamma}^\beta + \frac{1}{\sigma_\beta^2}\left[-\frac{1}{\rho}\frac{d}{d\rho}\left(\frac{g(\rho)}{\rho^3}\right)\right]\right.$$
$$\left.\times[\boldsymbol{\gamma}^\alpha\cdot(\mathbf{x}^\alpha-\mathbf{x}^\beta)][(\mathbf{x}^\alpha-\mathbf{x}^\beta)\times\boldsymbol{\gamma}^\beta]\right\}, \tag{16}$$

where $\rho = |\mathbf{x}^\alpha - \mathbf{x}^\beta|/\sigma_\beta$.

The stretch of vortex element, caused by the increment in the vorticity, lowers the spatial resolution. To maintain the resolution, the vortex element, of which strength becomes greater than twice its initial value, is divided into two elements [22,24].

Change in Core Radius Due to Viscosity. The vorticity decreases due to the viscous effect. The decrement is simulated by applying a core spreading method for single-phase flow [9], in which the core radius of the vortex element is made to increase with the lapse of time:

$$\frac{d\sigma_\alpha^2}{dt} = 4\nu \tag{17}$$

There are several other methods to take account of the viscous effect, for example a random walk method [32] and a weighted particle method [33]. These methods require a huge number of vortex elements for high Reynolds number flows. Thus, this study employs the core spreading method by considering the application to engineering problems.

Change in Strength of Vortex Element Due to Particle. When substituting Eq. (6) into an equation, derived from the Reynolds transport theorem and Eq. (1), the time rate of change in the strength of vorticity $\boldsymbol{\gamma}$ in any volume is obtained:

$$\frac{D\boldsymbol{\gamma}}{Dt} = -\frac{1}{\rho_g}\int(\nabla\times\mathbf{F}_D)dV = -\frac{1}{\rho_g}\int(\mathbf{n}\times\mathbf{F}_D)dS \tag{18}$$

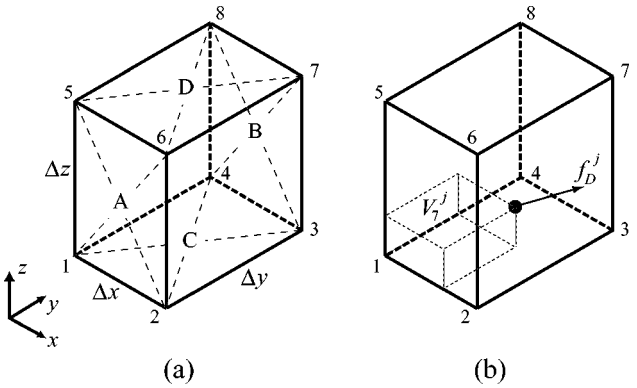

Fig. 3 Computational grid

where $\mathbf{n}$ is the unit vector normal to the volume surface, and the stretch-contraction term and the viscous diffusion term are neglected because they are already considered through Eqs. (16) and (17), respectively.

The computational domain is resolved into hexahedral grids. A grid is shown in Fig. 3(*a*). If the $\mathbf{F}_D$ value is known on every surface of a grid, the time rate of change for $\boldsymbol{\gamma}$, $\Delta\boldsymbol{\gamma}/\Delta t$, in the grid is determined from Eq. (18). For example, the x-component $\Delta\gamma_x/\Delta t$ is written as

$$\frac{\Delta\gamma_x}{\Delta t} = -\frac{1}{\rho_g}[(F_{Dz}^B - F_{Dz}^A)\Delta S_y + (F_{Dy}^C - F_{Dy}^D)\Delta S_z] \tag{19}$$

where F_{Dz}^A is the F_{Dz} value on the surface A, and ΔS_y is the area of a surface normal to the y-axis, $\Delta x\Delta z$.

In the case that the number of vortex elements in a grid is n_v, the change in the strength for each vortex element during Δt is supposed to be $\Delta\boldsymbol{\gamma}/n_v$. In the case that there are no vortex elements in the grid, a vortex element with a strength $\Delta\boldsymbol{\gamma}$ is generated at the grid center.

Since the force $\mathbf{F}_D$ in a grid cell is the reaction of the drag force acting on the particles existing in the cell, $\mathbf{F}_D$ is estimated by the following method. The $\mathbf{F}_D$ value on a grid surface in Eq. (19), such as F_{Dz}^A, is estimated by taking the average for the $\mathbf{F}_D$ values at four grid points on the surface. It is supposed that the number of particles in a grid cell is n_p and that the drag force $\mathbf{f}_D^j$ acts on the jth particle. The $\mathbf{f}_D^j$ value is distributed to every grid point of the cell. When extending the method for a two-dimensional simulation proposed by one of the authors [14], the $\mathbf{F}_D$ value on the grid point β, $\mathbf{F}_D^\beta$, is estimated by a volume weighted scheme as

$$\mathbf{F}_D^\beta = \frac{1}{V}\sum_{j=1}^{n_p}\frac{V_\beta^j}{V}\mathbf{f}_D^j \quad (\beta = 1,2,\ldots,8) \tag{20}$$

where V is the grid volume $\Delta x\Delta y\Delta z$, and V_β^j is the volume concerning to the grid point β and the particle, as shown in Fig. 3(*b*). For example, the force acting on the grid point 7 due to the jth particle is determined by the drag force $\mathbf{f}_D^j$ and the volume V_7^j. When the jth particle approaches the grid point 7, V_7^j becomes larger, and accordingly the contribution of the particle to the force acting on the grid point 7 heightens.

Numerical Procedure. When the flow field at $t = t$ is known, the flow at $t = t + \Delta t$ is simulated by the following procedure.

1. Calculate the particle motion from Eq. (3).
2. Calculate $\mathbf{F}_D$ from Eq. (20).
3. Calculate $\boldsymbol{\gamma}$ from Eqs. (16) and (18).
4. Calculate σ from Eq. (17).
5. Calculate the convection of vortex element from Eq. (13).
6. Calculate $\mathbf{u}_g$ from Eq. (11).

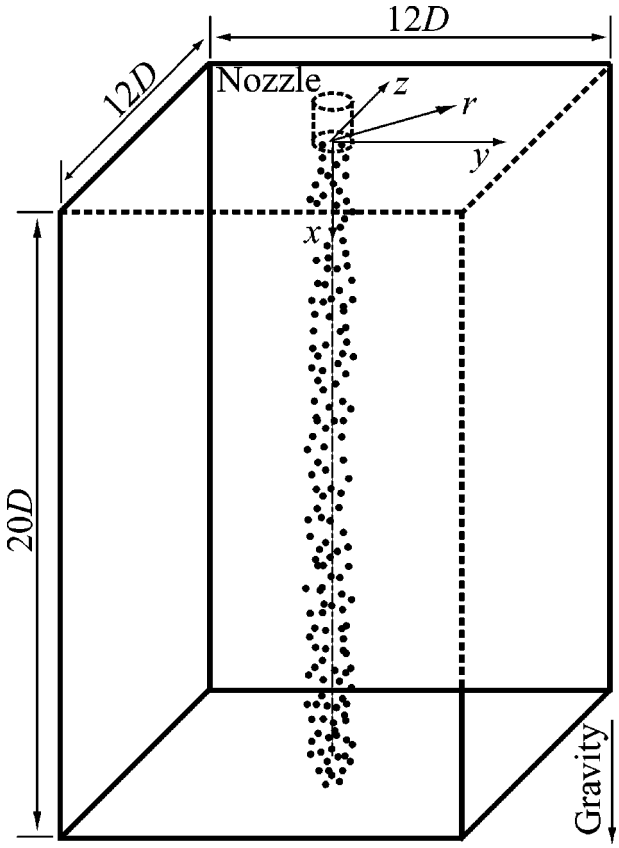

Fig. 4 Configuration of flow field

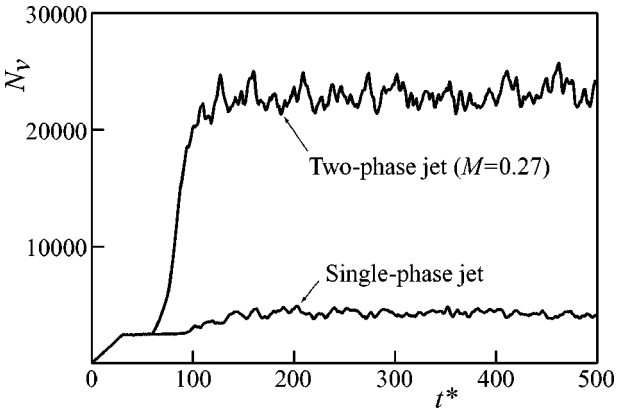

Fig. 5 Time variation for number of vortex elements

Simulation Conditions

Air jet issuing with velocity U_0 from a round nozzle of diameter $D=12$ mm into an air co-flowing with velocity U_a is simulated, where the Reynolds number $U_0D/\nu=2\times10^4$ and the velocity ratio $U_a/U_0=0.27$. The flow direction is vertical downward. Spherical glass particles are loaded from the nozzle exit into the jet. The particle diameter d is 100 μm and the density ρ_p is 2590 kg/m^3, where the mass loading ratio M is 0.27. The particle velocity at the nozzle exit is lower than the air velocity U_0 in most of the experiments on two-phase jets issuing into still air. This calculation sets the velocity at $0.8U_0$ with reference to the experiment by Yuu et al. [8]. The Stokes number, defined as the ratio of the particle response time to the characteristic time of the flow τ_g, is 200 when the relation $\tau_g=D/U_0$ is considered.

The simulation is performed in a hexahedral region $20D\times12D\times12D$ downstream of the nozzle, as shown in Fig. 4. The region is resolved into $80\times48\times48$ hexahedral grids.

The potential flow, of which velocity $\mathbf{u}_{g0}$ appears in Eqs. (7) and (11), is simulated by a panel method [22,24]. The nozzle, of which axial length is $\pi D/8$, has a circular panel at the bottom to supply the gas flow. In the panel, 168 source points are located on the six concentric circles, $r/D=2n/13$ ($n=1,2,\ldots,6$), and the panel center. The strength for each source is determined so that the velocity distributes uniformly at the nozzle exit ($x=0$). The nozzle surface is constructed by 32 square panels; 2 and 16 panels in the axial and circumferential directions, respectively, as shown in Fig. 2. Vortex elements are fixed on the sides of the panels. The strength for such fixed vortex element is determined to satisfy the zero cross-flow at the center of each panel.

To exclude the vortex element leaving the outlet boundary, a circular panel having 168 sink points is located $\pi D/8$ downstream of the domain. The panel is ten times larger than the source panel at the nozzle bottom, and the strength of the sink is 0.01 times larger than that of the source.

The time increment Δt is $0.1D/U_0$, and the second-order Adams–Bashforth method is employed for the Lagrangian calculations for vortex element and particle. The Δt value satisfies the CFL condition, and it is sufficiently small to yield reasonable solution. The time interval to release the vortex element Δt_v is set at $2\Delta t$. The core radius at the release is $0.4D$. To maintain the accuracy of the simulation, the core overlapping between neighboring vortex elements is needed. Such overlapping is realized because the number of vortex elements is sufficiently large in this simulation.

The time interval to load the particle is set at $2\Delta t$, and the loading positions within the nozzle exit section are determined by using random numbers. The number of loading points is determined from the particle mass loading ratio. The single-phase air flow is simulated when the nondimensional time $t^*<60$, and the particles are loaded at $t^*\geqslant60$.

Though Eq. (11) is derived for free space, the core of the vortex element released from the vicinity of the nozzle edge intersects with the nozzle. Therefore, Eq. (11) is not always valid near the nozzle edge. This may be one of the problems that should be improved in the vortex methods employing the Biot–Savart equation.

The core radius at the outlet boundary of the computational domain is at most 1.02 times larger than that at the nozzle exit. Thus, the excessive increment in the core radius deteriorating the computational accuracy does not occur in this simulation.

Results and Discussions

The time variation for the number of vortex elements N_v in the computational domain is shown in Fig. 5. For the single-phase jet, the N_v value slightly fluctuates around 4160 at $t^*\geqslant141$. This indicates that the number of vortex elements generated in the domain balances with that of the vortex elements leaving the domain. Accordingly, it is found that the fully developed flow is established at $t^*\geqslant141$. For the two-phase jet loaded with particles when $t^*\geqslant60$, N_v also fluctuates at $t^*\geqslant141$, demonstrating that the fully developed flow is simulated. Since vortex elements are generated due to the particle motion, N_v for the two-phase jet is much larger than that for the single-phase one.

The distribution of the vortex element at $t^*=220$ for the single-phase jet ($M=0$) is depicted in Fig. 6, where the positions of vortex element are projected onto the x-y plane. The vortex elements flow straight in the axial (x) direction at $x/D\leqslant7.3$, where the potential core exists, but they also move in the lateral (y) direction in the downstream region. There are a lot of vortex elements at $x/D\geqslant14$, and the vortex elements distribute in the wider

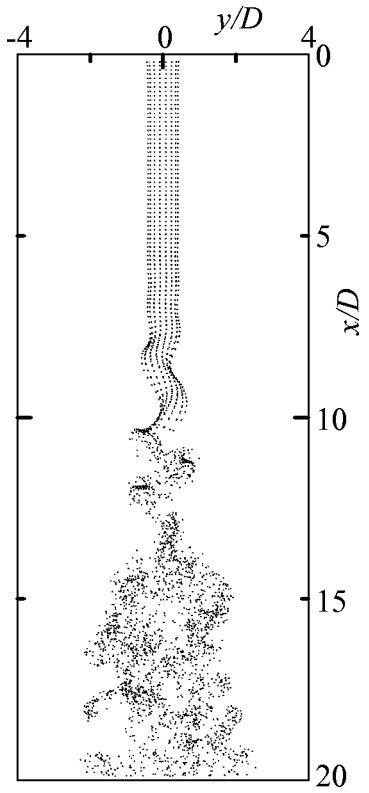

Fig. 6 Instantaneous distribution of vortex element for air single-phase jet

region. This is because the flow changes into the turbulent, and accordingly vortex elements are stretched and frequently divided. An experimental formula by Forstall-Shapiro [34] predicts that the potential core disappears at $x/D=7.2$. It is found that the disappearing point obtained in this simulation is in good agreement with the measured results.

Figure 7 shows the axial evolution of the time-averaged air velocity on the centerline for the single-phase jet. The velocity begins to decrease at $x/D=7.3$, where straight movement of the vortex element breaks and the potential core disappears, as shown in Fig. 6. The disappearing point nearly coincides with the experimental formula by Forstall-Shapiro [34]. But the velocity obtained by the vortex method is higher at $7.3 \leqslant x/D \leqslant 13$. The present simulation imposes no disturbances at the nozzle exit, which exist in the experiments, and accordingly the decay of the centerline velocity is milder. It is very hard to make the numerical disturbance coincide with the experimental one, and a direct numerical simulation [35] have also reported the disagreement due to such causes.

The radial profile of the time-averaged air velocity for the single-phase jet is shown in Fig. 8, where the results on eight

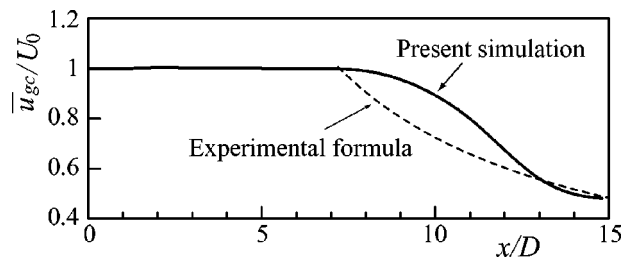

Fig. 7 Axial evolution of air velocity on centerline for single-phase jet

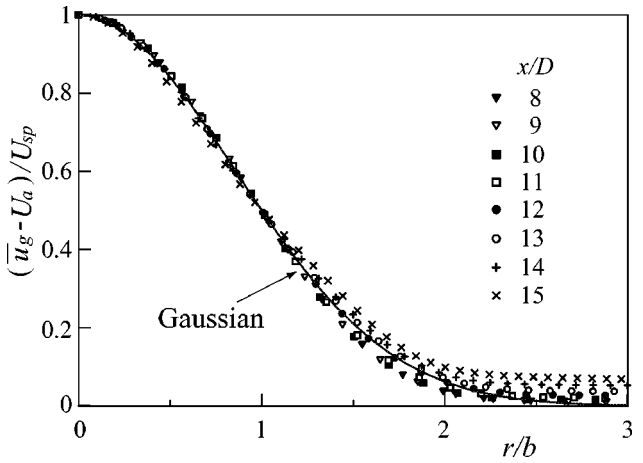

Fig. 8 Radial profile of mean air velocity for single-phase jet

cross-sections at $8 \leqslant x/D \leqslant 15$ are plotted. According to the experiment by Forstall–Shapiro [34], the velocity satisfies the self-preservation distribution at $x/D \geqslant 8$. The simulated velocity is almost in the self-preservation state and nearly approximated with a Gaussian curve.

Figure 9 shows the instantaneous distributions of the vortex element and the particle for the two-phase jet, where the distributions at $t^*=220$ are projected onto the x-y plane. The particles moves almost straight in the vertical downward direction, being less affected by the air flow, because their Stokes number is so large at 200. The number of vortex elements is markedly higher than that for the single-phase jet shown in Fig. 6. The vortex elements distribute not only near the jet centerline, where the loaded particles flow, but also in broader region at $x/D \geqslant 10.9$.

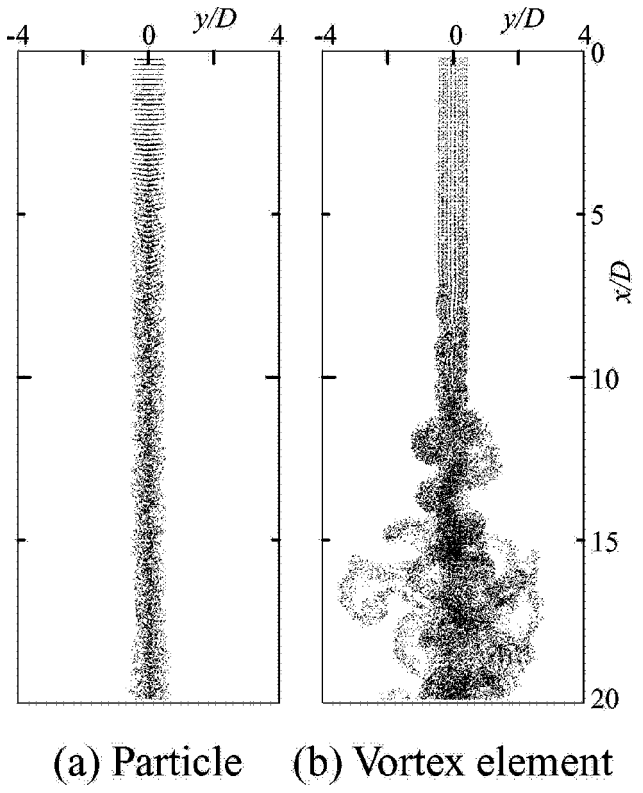

Fig. 9 Distributions of particle and vortex element for $M=0.27$ at $t^*=220$

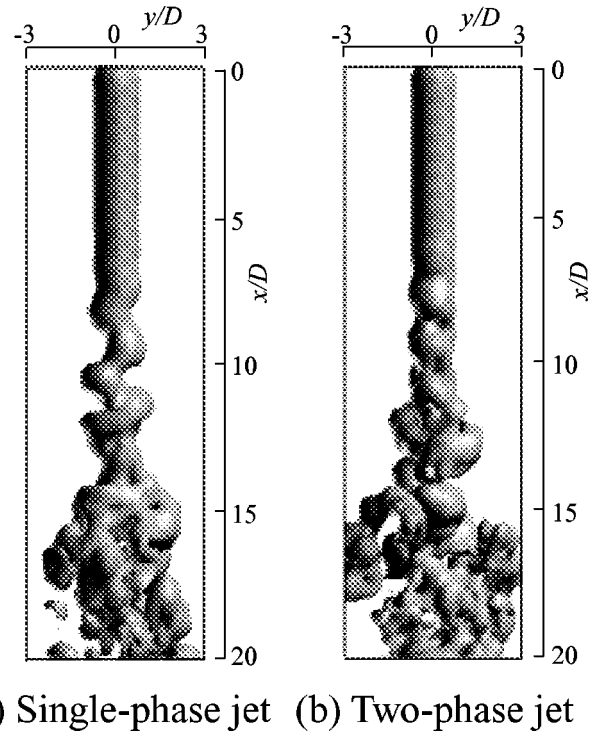

Fig. 10 Surface of constant magnitude for vorticity $|\omega|/|\omega_0| = 0.4$ at $t^* = 220$

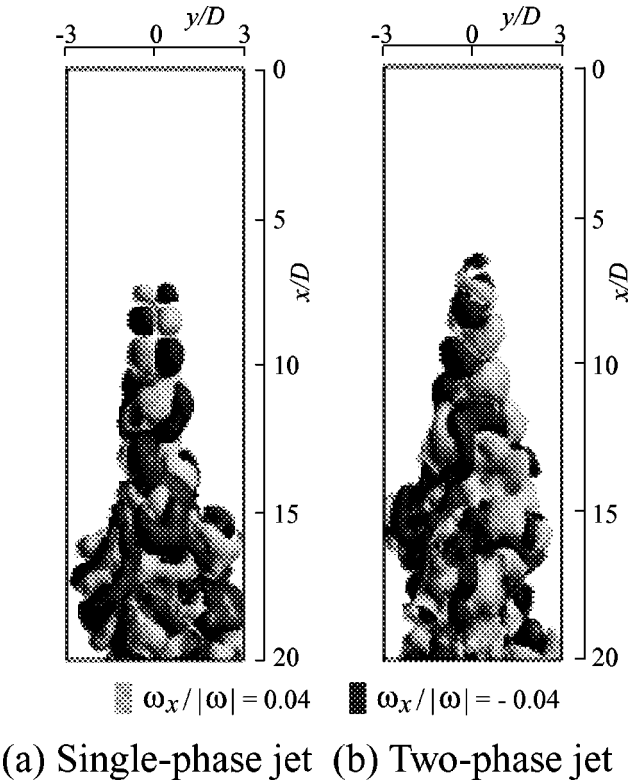

Fig. 11 Surfaces of constant magnitude for streamwise vorticity $\omega_x/|\omega_0| = \pm 0.04$ at $t^* = 220$

The iso-surface for the vorticity of $|\boldsymbol{\omega}|/|\boldsymbol{\omega}_0| = 0.4$ at $t^* = 220$ is presented in Fig. 10, where $\boldsymbol{\omega}_0$ denotes the vorticity at the nozzle exit. For the single-phase jet, a helical structure is clearly found at $7.3 \leqslant x/D \leqslant 12.6$ just downstream of the disappearing point for the potential core. But such structure is not observed clearly in the two-phase jet. This is because more vortex elements exist around the jet centerline in the two-phase jet and the vorticity around the centerline increases, and therefore the iso-surface of the vorticity is smoothed.

Figure 11 shows the iso-surfaces for the axial component of vorticity for $\omega_x/|\boldsymbol{\omega}_0| = \pm 0.04$ at the same instant as Fig. 10. Highly organized vortical structures are observed, in which pairs of positive and negative vortex tubes exist and the tubes entangle. The streamwise vorticity ω_x for the two-phase jet occurs more upstream when comparing with the result for the single-phase jet. This indicates that the loaded particles impose disturbances on the air flow, promoting the transition from the axisymmetrical structure to the three-dimensional one.

The mean velocities for air and particle on the jet centerline change as a function of the axial distance from the nozzle exit as shown in Fig. 12. The particle mean velocity at a fixed location on the jet centerline is obtained by recording the particle velocity at every time when the particles pass the location. The air velocity for the two-phase jet is slightly lower at $6 \leqslant x/D \leqslant 12$ and slightly higher at $x/D > 12$ than that for the single-phase jet. The particle, exiting the nozzle with a lower velocity than the air, is slightly accelerated until $x/D = 11$, where a slow deceleration occurs. The rapid decay of the velocity, observed in the case of air, does not occur. This is attributable to the larger inertia of the particle. The particle velocity is higher than the air at $x/D \geqslant 10.7$. The decrement of the air velocity due to the particle at $6 \leqslant x/D \leqslant 12$ is caused by the drag force of the particle flowing slower than the air. It is also because the momentum diffusion of the air increases due to the increment of the air turbulent intensity, as discussed later. The relaxation of velocity decay for the air at $x/D > 12$ is attributable to the fact that the air gains momentum from the particles flowing faster than it. When calculating the particle terminal velocity u_t, the nondimensional value u_t/U_0 is 0.025. Since the particle velocity $\overline{u}_{pc}/U_0$ is 0.817 at $x/D = 15$, it is found that the particles are still affected by the air flow even at $x/D = 15$.

The mean velocity profile in the radial direction is shown in Fig. 13, where the half-width b and the excess velocity at the centerline for the single-phase jet U_{sp} are used for the nondimensional expressions. Figure 13(a) indicates the result on the section of $x/D = 10$. The particle velocity profile is flatter than the air. The air velocity for the two-phase jet is lower at $r/b \leqslant 0.82$ and slightly higher at $0.82 < r/b \leqslant 2.4$ than the air for the single-phase jet. Such decrement of the air velocity at the jet centerline and the increment of the spread for the air velocity are owed to the drag force exerted by the particle. They are also attributable to the increment of the air momentum diffusion induced by the incre-

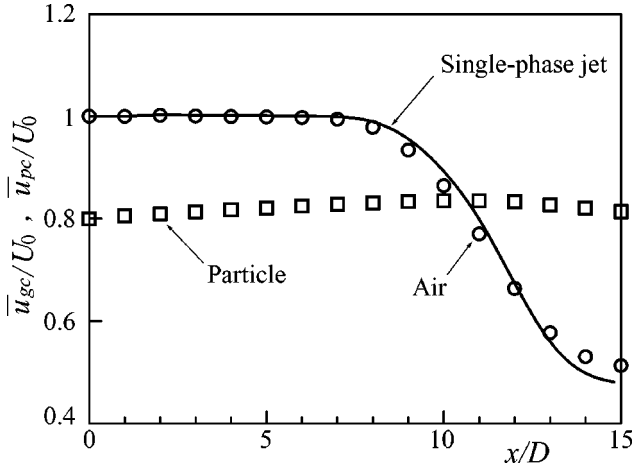

Fig. 12 Change of centerline velocity in axial direction

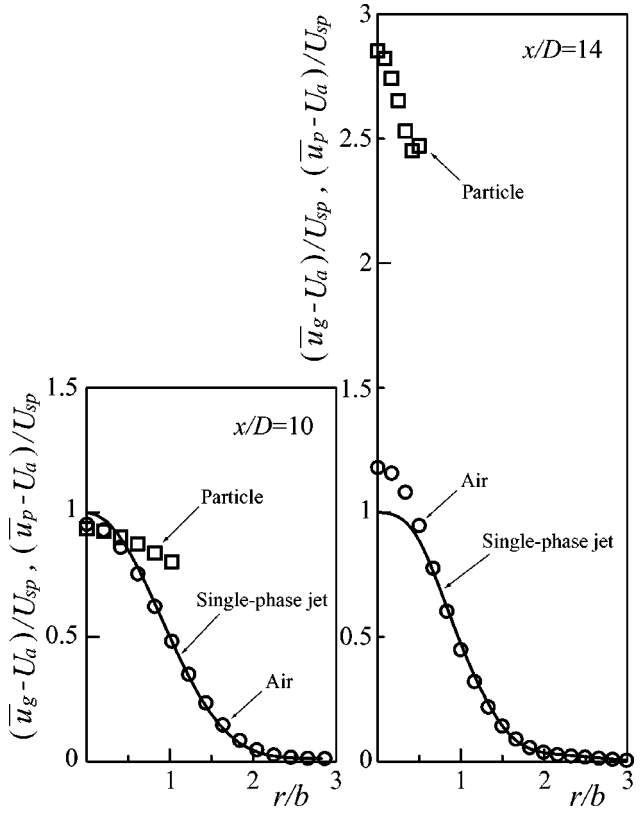

Fig. 13 Radial profile of mean velocity

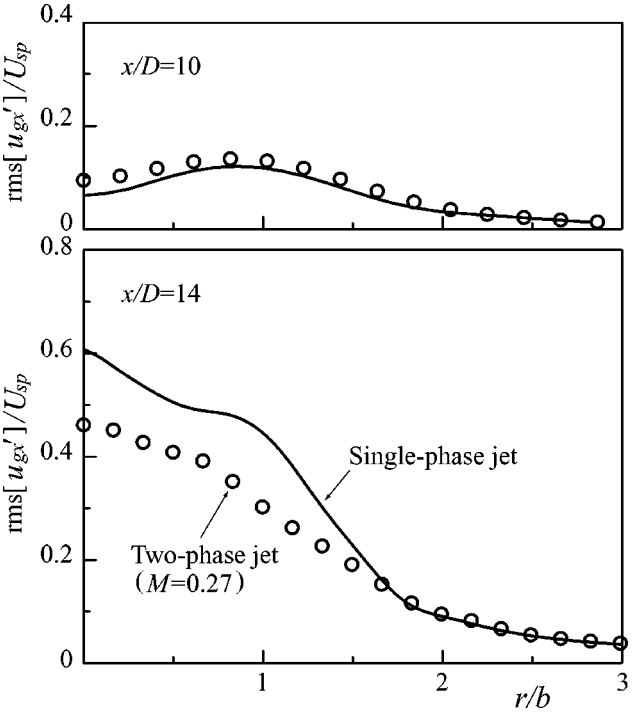

Fig. 14 Axial component of rms velocity fluctuation for air

ment of the turbulent intensity, as mentioned later. On the section of $x/D=14$, the particle velocity is mush higher than the air, and it decreases markedly in the radial direction, as shown in Fig. 13(*b*). This is because Fig. 13 presents the particle velocity in the nondimensional form by using U_{sp}, which decreases with increasing the axial distance x. The air velocity for the two-phase jet is higher than that for the single-phase one at $r/b \leqslant 0.66$. This is because the air is accelerated by the particles. At $0.66 < r/b \leqslant 1.5$, however, the air velocity for the two-phase jet is lower than that for the single-phase jet. Consequently, the velocity gradient in the radial direction is steeper, and the width of velocity profile is narrower because the turbulent intensity reduces, and accordingly the momentum diffusion in the radial direction is damped, as explained later.

Figure 14 shows the radial distribution for the axial component of the air turbulent intensity. On the section of $x/D=10$, the intensity for the two-phase jet is higher than that for the single-phase one at $r/b \leqslant 2.46$. This is because the particles disturb the air flow, as found from the fact that the streamwise vortex appears more upstream in the case of the two-phase jet (Fig. 11). Such increment in the turbulent intensity due to the particle at the developing region has also been reported by the LES [8] on slit nozzle jets, loaded with glass particles having diameters of 65 and 310 μm, issuing into still air. On the section of $x/D=14$, the turbulent intensity for the two-phase jet is lower than that for the single-phase one at $r/b \leqslant 1.66$.

The radial component of the air turbulent intensity is presented in Fig. 15. On the section of $x/D=10$, the marked effect of the particle is not observed. On the section of $x/D=14$, however, the reduction of the intensity due to the particle occurs around $r/b=0.83$, where the intensity for the single-phase jet reaches its maximum value.

The radial profile for the rms velocity fluctuation of the particle is shown in Fig. 16, where the axial and radial components on two sections of $x/D=10$ and 14 are plotted. The velocity fluctuations are higher on the downstream section. But they are markedly lower than those for the air shown in Figs. 14 and 15, demonstrating that the particle cannot fully follow the air turbulent motion. The radial component is especially lower, being about 50% of the axial one.

Figure 17 presents the radial distribution for the Reynolds shear stress. On the section of $x/D=10$, the Reynolds shear stress for the two-phase jet is higher than that for the single-phase one at $r/b \geqslant 0.82$. Therefore, the increment of the air momentum diffu-

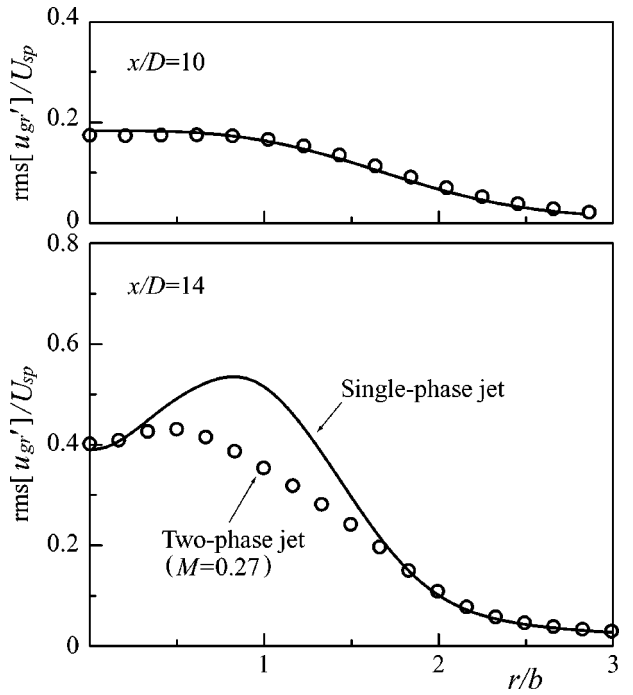

Fig. 15 Radial component of rms velocity fluctuation for air

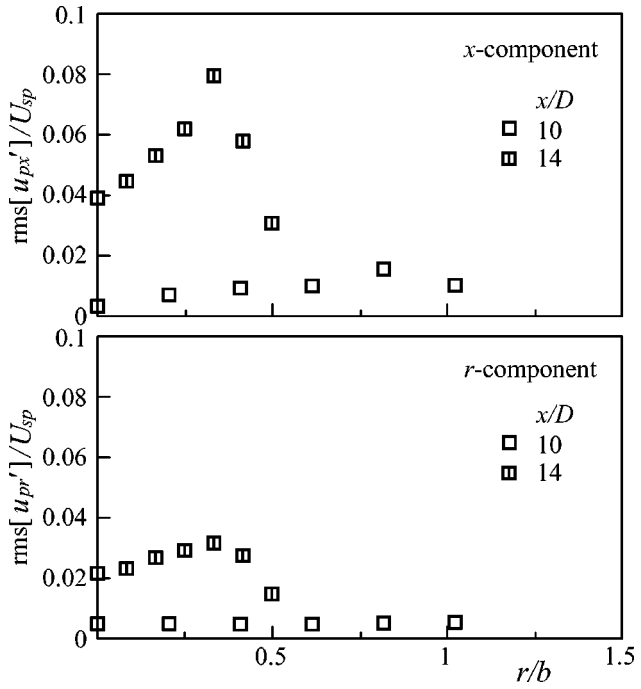

Fig. 16 Distribution of rms velocity fluctuation for particle

sion in the radial direction, observed in Fig. 13(*a*), can also be confirmed from this figure. On the section of $x/D=14$, the maximum value reduces for the two-phase jet, presenting the reduction of the air momentum diffusion found in Fig. 13(*b*).

Few researches have been done on the gas-particle two-phase compound round jet. Thus, there are no data which are available for the comparison with the present result. But the relaxation for air velocity decay, the decrement in the spread of jet at the developed region, and the reduction for air turbulent intensity and Reynolds shear stress obtained by the present vortex method have also been revealed by the measurements [1–3] and DNS [7] on the round jets, loaded with sand or glass particle with diameter less than 132 μm at $M\leqslant 0.85$, issuing into still air. They have also been reported by the LES [8] and the two-dimensional vortex simulation [16] on a two-phase slit nozzle jet issuing into still air. Therefore, the present method is found to yield the reasonable solution for two-phase compound round jets.

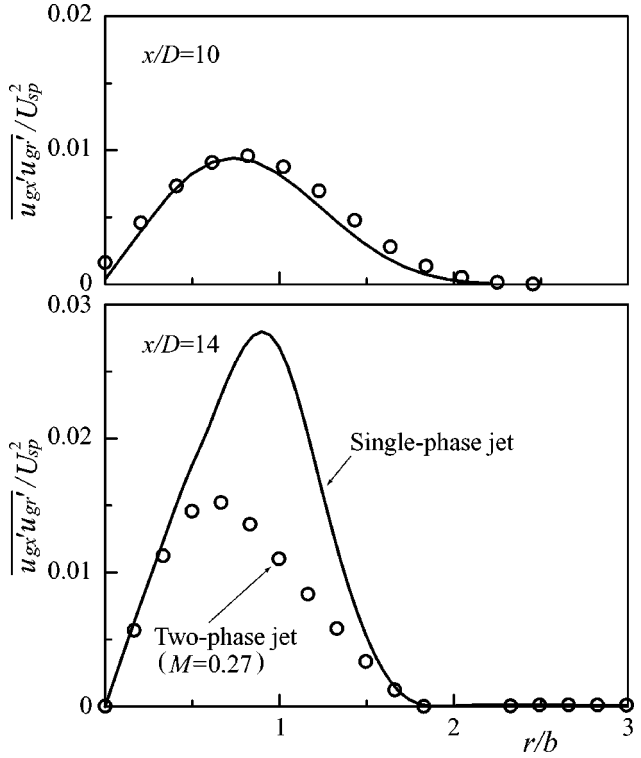

Fig. 17 Distribution of Reynolds shear stress

Conclusions

A three-dimensional vortex method for a gas-particle two-phase compound round jet is proposed. For the two-way coupling, a two-dimensional method presented in a prior paper is extended. The viscous effect is simulated through the core spreading method.

To discuss the applicability of the present vortex method, an air jet issuing with velocity U_0 from a nozzle of diameter D into the air co-flowing with velocity U_a is simulated. The flow direction is vertically downward. The Reynolds number U_0D/ν is 2×10^4, and the velocity ratio U_a/U_0 is 0.27. Spherical glass particles having diameter 100 μm with a Stokes number of 200 are loaded from the nozzle exit. The simulated changes in the air flow due to the particle are confirmed to agree with the existing experimental and numerical results on the two-phase jets issuing into still air. These indicate the validity of the present method.

Nomenclature

b = half-width
D = nozzle diameter
d = particle diameter
$\mathbf{F}_D$ = force exerted by particle acting on gas-phase
$\mathbf{f}_D$ = drag force acting on particle
g = gravitational constant
M = particle mass loading ratio
p = pressure
r = radial coordinate
t = time
t^* = nondimensional time$=U_0t/D$
U_0 = gas velocity at nozzle exit
U_a = co-flowing gas velocity
U_{sp} = excess velocity at centerline for single-phase flow $=\overline{\mathbf{u}}_{gc}-U_a$
$\mathbf{u}$ = velocity
$\mathbf{u}'$ = fluctuating velocity
$\overline{\mathbf{u}}$ = mean velocity
$\mathbf{x}$ = position vector
Δt = time increment
γ = vortex strength
ν = kinematic viscosity of gas
ρ = density
σ = core radius
$\boldsymbol{\omega}$ = vorticity$=\nabla\times\mathbf{u}_g$

Subscripts

0 = nozzle exit or potential flow
c = jet centerline
g = gas
p = particle
r = radial component
x = axial component

References

[1] Shuen, J-S., Solomon, A. S. P., Zhang, Q-F., and Faeth, G. M., 1983, "A theoretical and experimental study of turbulent particle-laden jets," NASA, CR-168293.
[2] Modarress, D., Tan, H., and Elghobashi, S., 1984, "Two-component LDA measurement in a two-phase turbulent jet," AIAA J., **22**(5), pp. 624–630.
[3] Fleckhaus, D., Hishida, K., and Maeda, M., 1987, "Effect of laden solid par-

ticles on the turbulent flow structure of a round free jet,'' Exp. Fluids, **5**, pp. 323–333.
[4] Elghobashi, S., Abou-Arab, T., Rizk, M., and Mostafa, A., 1984, ''Prediction of the particle-laden jet with a two-equation turbulence model,'' Int. J. Multiphase Flow, **10**(6), pp. 697–710.
[5] Shuen, J-S., Solomon, A. S. P., Zhang, Q-F., and Faeth, G. M., 1985, ''Structure of particle-laden jets: measurements and predictions,'' AIAA J., **23**(3), pp. 396–404.
[6] Mostafa, A. A., and Mongia, H. C., 1988, ''On the interaction of particles and turbulent fluid flow,'' Int. J. Heat Mass Transfer, **31**(10), pp. 2063–2075.
[7] Yuu, S., Umekage, S., and Tabuchi, M., 1994, ''Direct numerical simulation for three-dimensional gas-solid two-phase jet using two-way method and experimental verification,'' Trans. Jpn. Soc. Mech. Eng., Ser. B, **60**(572), pp. 1152–1160.
[8] Yuu, S., Ueno, T., and Umekage, T., 2001, ''Numerical simulation of the high Reynolds number slit nozzle gas-particle jet using subgrid-scale coupling large eddy simulation,'' Chem. Eng. Sci., **56**, pp. 4293–4307.
[9] Leonard, A., 1980, ''Vortex methods for flow simulation,'' J. Comput. Phys., **37**, pp. 289–335.
[10] Knio, O., and Ghoniem, A. F., 1992, ''Vortex simulation of a 3-dimensional reacting shear-layer with finite-rate kinetics,'' AIAA J., **30**, pp. 105–116.
[11] Winckelmans, G. S., and Leonard, A., 1993, ''Contribution to vortex particle methods for the computation of three-dimensional incompressible unsteady flows,'' J. Comput. Phys., **109**, pp. 247–273.
[12] Cottet, G.-H., and Koumoutsakos, P. D., 2000, *Vortex Method: Theory and Practice*, Cambridge University Press, Cambridge.
[13] Kamemoto, K., 2000, ''On attractive features of advanced vortex methods and their subjects as a tool of Lagrangian large eddy simulation,'' Proc. 4th Int. Conf. Hydrodynamics, Yokohama, Vol. 1, pp. 37–56.
[14] Uchiyama, T., and Naruse, M., 2001, ''A numerical method for gas-solid two-phase free turbulent flow using a vortex method,'' Powder Technol., **119**, pp. 206–214.
[15] Uchiyama, T., and Naruse, M., 2002, ''Numerical simulation of gas-particle two-phase mixing layer by vortex method,'' Powder Technol., **125**, pp. 111–121.
[16] Uchiyama, T., and Naruse, M., 2003, ''Numerical simulation of gas-particle two-phase jet by vortex method,'' Powder Technol., **131**, pp. 156–165.
[17] Uchiyama, T., and Yagami, H., 2005, ''Numerical analysis of gas-particle two-phase wake flow by vortex method,'' Powder Technol., **149**, pp. 112–120.
[18] Uchiyama, T., 2004, ''Numerical analysis of particulate jet generated by free falling particles,'' Powder Technol., **145**, pp. 123–130.
[19] Chung, J. N., and Troutt, T. R., 1988, ''Simulation of particle dispersion in an axisymmetric jet,'' J. Fluid Mech., **186**, pp. 199–222.
[20] Joia, I. A., Ory, E., and Perkins, R. J., 1998, ''A discrete vortex model of particle laden jets,'' Proc. 3rd Int. Conf. Multiphase Flow, Lyon (on CD-ROM).
[21] Kida, T., Take, T., Toshima, M., and Kurata, M., 1999, ''Pressure distribution on the ground by impinging two-dimensional jet due to a vortex method,'' Proc. 3rd ASME-JSME Joint Fluid Eng. Conf., San Francisco, FEDSM99-6815 (on CD-ROM).
[22] Kiya, M., Nagatomi, M., and Mochizuki, O., 1997, ''Simulating an impulsively started round jets by a 3D vortex method,'' Proc. Int. Conf. Fluid Eng., Tokyo, Vol. 1, pp. 135–140.
[23] Izawa, S., and Kiya, M., 2000, ''A turbulence model for the three-dimensional vortex blob method,'' JSME Int. J., Ser. B, **43**(3), pp. 434–442.
[24] Uchiyama, T., 2003, ''Numerical prediction of the round jet in a co-flowing stream by three-dimensional vortex method,'' Int. J. Turbo Jet Engines, **20**, pp. 235–244.
[25] Chein, R., and Chung, J. N., 1987, ''Effects of vortex pairing on particle dispersion in turbulent shear flows,'' Int. J. Multiphase Flow, **13**(6), pp. 785–802.
[26] Tang, L., Wen. F., Yang, Y., Crowe, C. T., Chung, J. N., and Troutt, T. R., 1992, ''Self-organizing particle dispersion mechanism in a plane wake,'' Phys. Fluids A, **4**(10), pp. 2244–2251.
[27] Wen, F., Kamalu, N., Chung, J. N., Crowe, C. T., and Troutt, T. R., 1992, ''Particle dispersion by vortex structures in plane mixing layers,'' ASME J. Fluids Eng., **114**, pp. 657–666.
[28] Schiller, L., and Naumann, A. Z., 1933, ''Über die grundlegenden Berechnungen bei der Schwerkraftaufbereitung,'' Z. Vereines Deutscher Inge., **77**, pp. 318–321.
[29] Beale, J. T., and Majda, A., 1985, ''High order vortex methods with explicit velocity kernels,'' J. Comput. Phys., **58**, pp. 188–208.
[30] Mansfield, J. R., Knio, O. M., and Meneveau, C., 1999, ''Dynamic LES of colliding vortex rings using a 3D vortex method,'' J. Comput. Phys., **152**, pp. 305–345.
[31] Leonard, A., and Chua, K., 1989, ''Three-dimensional interactions of vortex tubes,'' Phys. Fluids, **37**, pp. 490–496.
[32] Chorin, A. J., 1973, ''Numerical study of slightly viscous flow,'' J. Fluid Mech., **57**, pp. 785–796.
[33] Degond, P., and Mas-Gallic, S., 1989, ''The weighted particle method for convection-diffusion equations,'' Math. Comput., **53**, pp. 485–526.
[34] Forstall, W., and Shapiro, A., 1950, ''Momentum and mass transfer in coaxial gas jets,'' ASME J. Appl. Mech., **17**, pp. 399–408.
[35] Takeuchi, S., Miyake, Y., and Kajishima, T., 1999, ''On the numerical simulation of round jets of incompressible fluid,'' Proc. 3rd ASME-JSME Joint Fluid Eng. Conf., San Francisco, FEDSM99-6957 (on CD-ROM).

Abraham N. Varghese
Naval Undersea Warfare Center Division
Newport, RI

James S. Uhlman

Ivan N. Kirschner

Anteon Corporation Engineering, Engineering Technology Center
Mystic, CT

Numerical Analysis of High-Speed Bodies in Partially Cavitating Axisymmetric Flow

Partial cavitation of high-speed axisymmetric bodies is modeled using a steady potential-flow boundary-element technique. The effects of several key parameters defining the vehicle geometry are examined for configurations consisting of a disk cavitator followed by a conical section and ending in a cylindrical body. A single cavity is assumed to detach at the edge of the disk. A variety of conditions have been studied, including cavity closure on either the conical or cylindrical portions of the vehicle, variations in the cone angle, and variations in the radius of the cylindrical section. The results for the partially cavitating case are also compared with those for the supercavitating case.
[DOI: 10.1115/1.1852473]

Introduction

At sufficiently high-speeds, cavitation will occur on the surface of submerged bodies at the point where the local pressure drops to the value of the vapor pressure of the ambient fluid. If the cavitation number is sufficiently low, a supercavity will form that covers the entire vehicle. Partial cavitation occurs for such bodies at lower speeds, for example, those characterizing a launch transient. Partial cavitation may also occur during flight when maneuvering of the vehicle is necessary. Partial cavities can be created or their extent increased via the use of suitably designed ventilation systems.

Early research on supercavitating flows was performed by Efros [1], who employed conformal mapping techniques. Tulin [2] introduced the use of perturbation methods for examination of two-dimensional supercavitating flows. Cuthbert and Street [3] used sources and sinks along the axis of a slender axisymmetric body-cavity system, along with a Riabouchinski cavity closure model. They solved for the unknown cavity shape, but were successful only for a few cases. Brennan [4] employed a relaxation method in a transformed velocity potential-stream function plane for analyzing axisymmetric cavitating flows behind a disk and a sphere between solid walls. Chou [5] extended the work of Cuthbert and Street [3] to solve axisymmetric supercavitating flows using slender body theory. He solved the problem by locating sources along the body-cavity axis and control points along the body-cavity surface. A nonlinear integro-differential equation was formed by imposing the dynamic condition on the cavity boundary. He assumed a conical cavity profile near closure to simplify the equation.

Vorus [6] addressed the problem of supercavitating flows using a Laurent series for the cavity shape, resulting in a more realistic cavity closure model, being the lowest-order representation of a re-entrant jet. His results showed differences in the predicted drag compared with those of Chou. Kuria [7] attempted to solve the slender body problem in the same way as Chou did, except that he employed a spectral method with modified Chebyshev polynomials. He successfully solved the problem for specific numbers of collocation points.

Nonlinear boundary-element models were developed for cavitating flows about hydrofoils by Uhlman [8,9], and Kinnas and Fine [10,11], among others. They distributed sources and normal dipoles along the body-cavity surface. The unknown values of these sources and dipoles were determined by imposing the dynamic condition on an assumed cavity boundary. The kinematic boundary condition was then used to update the cavity shape.

Beginning in 1994, two numerical hydrodynamics models were developed by the authors for axisymmetric supercavitating high-speed bodies: A slender-body theory model (Varghese et al. [12]) and a boundary-element model (Kirschner et al. [13]; Uhlman et al. [14]). The results of both the slender-body theory model and the boundary-element model have been compared with other numerical and experimental results, with good agreement. Specifically, both models predict the cavity shape and length with good accuracy. The slender-body theory model presented in Varghese et al. [12] is essentially an extension of Chou's method. Viscous drag corrections were incorporated and tested using both the Thwaites and Falkner–Skan approximations along the wet portions of the cavitator, and the effects of subsonic compressible flow were investigated using the compressible Green function. The boundary-element model was employed to examine supercavitating flows past disk-, cone-, and sigma-shaped cavitators. Such predictions are in good agreement with experimental and analytical results, as is summarized, for example, in Savchenko et al. [15].

Several researchers have modeled partially cavitating flows using nonlinear boundary-element techniques (Uhlman [8,9]; Kinnas and Fine [10,11]), but most of this work has addressed only hydrofoils. During preparation of this paper, the authors became aware of boundary-element modeling of axisymmetric flows recently performed in the Former Soviet Union by Krasnov [16]. The formulation of a partial cavitation model for high-speed bodies follows the same methodology used in the supercavitation boundary-element model, wherein sources and normal dipoles are distributed along the body-cavity surface. The unknown values of the source and dipole strengths are then obtained using the mixed Fredholm integral equation that results from the application of Green's third identity. The authors' preliminary formulation and early results of an effort to develop such a method were presented in Varghese [17] and in Varghese and Uhlman [18].

Mathematical Formulation

The physical problem of partial cavitation is shown in Fig. 1. The cavitator shown in this figure is a disk, but the model is capable of handling general axisymmetric cavitator and body geometries. The body length is ℓ_b and the cavity length is ℓ_c. For the partially cavitating case, the body extends beyond the cavity closure point. The bodies considered in this article consist of a truncated circular cone frustum followed downstream by a right circular cylinder. The upstream face of the truncated cone frustum abuts the downstream face of the cavitator. The maximum diam-

Contributed by the Fluids Engineering Division for publication on the JOURNAL OF FLUIDS ENGINEERING. Manuscript received by the Fluids Engineering Division November 2, 2002; revised manuscript received November 20, 2003. Review Conducted by: S. Ceccio.

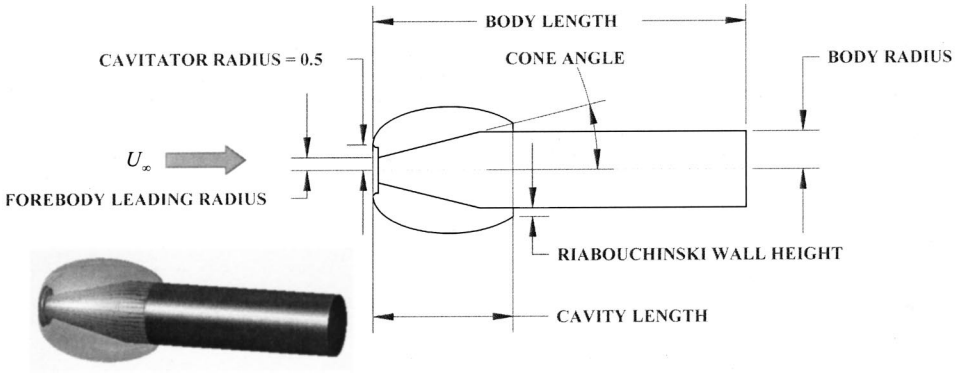

Fig. 1 Partial cavitation problem

eter of the cone frustum is equal to the diameter of the cylinder, which terminates in a flat base. For the bodies discussed herein, the diameter of the upstream face of the truncated cone frustum is equal to the diameter of the cavitator. The edge of the disk cavitator always defines a salient locus of separation. As is discussed below, under certain conditions cavities can originate at points along the body profile other than the cavitator; however, the cavities that have been studied here originate from the edge of the cavitator. The body radius is defined as the radius of the cylindrical portion of the hull. The forebody cone angle is the semiangle of the conical portion of the body and the cone–cylinder intersection is the location where the body changes from a conical to a cylindrical shape.

Much technical literature has been devoted to the conditions at cavity closure, where simultaneous satisfaction of the dynamic and kinematic boundary conditions requires special treatment. (See, for example, Tulin [19].) For the current investigation, the cavity is closed with a modified Riabouchinski cavity termination wall. (Application of this termination model for the axisymmetric boundary-element method is discussed in detail in Kirschner et al. [13]. An improved re-entrant jet closure model is presented in Uhlman et al. [14].)

All quantities in the following formulation have been made dimensionless with respect to fluid density, cavitator diameter, and free-stream velocity. The flow field is governed by Laplace's equation

$$\nabla^2\Phi = 0$$

The total potential, Φ, is the sum of free-stream potential and the disturbance potential, ϕ

$$\Phi = x + \phi$$

The disturbance potential also obeys Laplace's equation.

The disturbance potential satisfies Green's third identity. Thus, with the normal directed out of the fluid, the disturbance potential at any point on the body-cavity surface can be computed from

$$2\pi\phi(\mathbf{x}) = -\iint_S \left[\phi(\mathbf{x}')\frac{\partial}{\partial n}G(\mathbf{x},\mathbf{x}') - G(\mathbf{x},\mathbf{x}')\frac{\partial}{\partial n}\phi(\mathbf{x}')\right]dS(\mathbf{x}') \quad (1)$$

where the Green's function, G, is

$$G(\mathbf{x},\mathbf{x}') = \frac{1}{|\mathbf{x}-\mathbf{x}'|}$$

The dynamic condition on the cavity boundary is derived from Bernoulli's equation, which can be used to derive the following expression for the total velocity along the cavity surface, U_s:

$$U_s = \sqrt{1+\sigma} \quad (2)$$

where σ is the cavitation number. A dynamic condition for the potential on the cavity boundary results by integrating Eq. (2) downstream along the cavity boundary from the cavity detachment point. The kinematic boundary condition specifies that no flow cross the body-cavity boundary

$$\frac{\partial\phi}{\partial n} = -n_x \quad (3)$$

The no net flux condition

$$\iint_S \frac{\partial\phi(x)}{\partial n}dS = 0 \quad (4)$$

is also required to make the problem determinate.

The solution is determined iteratively starting with an initial approximation for the cavity shape, which can be as simple as a straight line from the edge of the cavitator to the outboard end of a small (but otherwise arbitrary) Riabouchinski wall. The panels are distributed along the cavitator, the cavity, the Riabouchinski wall, and the vehicle body aft of the cavity. By imposing the dynamic condition over the cavity boundary [specified as the integration of Eq. (2) downstream along the cavity boundary from the cavity detachment point], applying Green's third identity [Eq. (1)] at all panels along the body-cavity surface, and imposing the no-net-flux condition [Eq. (4)] on all wet surfaces, a system of equations is obtained. This system is solved for the disturbance potential along the wet portions of the boundary and on the Riabouchinski wall, the normal derivative of the disturbance potential along the cavity boundary, and the quantity $\sqrt{1+\sigma}$. Whereas in physical experiments the cavity length is a result of the cavitation number associated with the operating conditions, in the current method it is convenient to specify the cavity length and compute the cavitation number as part of the solution. The cavity length can then be predicted for a specified cavitation number via iteration, if desired. Once the solution is obtained, the cavity shape is updated to satisfy the kinematic condition, Eq. (3), and the Riabouchinski wall height is adjusted accordingly to form a closed profile. The iterations continue until the cavity shape has converged. A flow chart of this computational procedure is presented in Uhlman et al. [14]. Nonuniform panel spacing is used in many locations, in order to reduce the number of panels without reducing the accuracy of the solution. The number of panels along the Riabouchinski wall is allowed to vary as the wall height changes with iteration on cavity geometry. To ensure good accuracy of the results, the distribution of panels along the wet afterbody is modified as well, such that the ratio of neighboring panel lengths is constrained to values between 0.5 and 2.0.

From the converged disturbance potential along the body-cavity surface, the disturbance velocity components are calculated as

$$u_x = \frac{\partial \phi}{\partial x} \quad \text{and} \quad u_r = \frac{\partial \phi}{\partial r}.$$

The total drag coefficient of a partially cavitating body is computed as the sum of the pressure drag and the viscous drag. For the configurations of interest in this article, the pressure drag can be additionally subdivided into two components: (1) A component due to the pressure acting over the cavitator and the body forward of the base; and, (2) the drag due to the pressure acting on the base of the cylinder. With this breakdown, the pressure force is computed by integrating the product of the pressure and the axial component of the local unit normal vector over the cavitator and the body forward of the cylinder–base intersection. For short cavities, the forward part of the body is subject to cavity pressure, and a variable pressure acts downstream of the cavity closure point. For longer cavities, more of the body is subject to cavity pressure. At low enough values of the cavitation number, the cavity is large enough to envelope the entire forebody, so that the forebody is subject to the constant value of cavity pressure over its entire length. Note that, under certain conditions, a second cavity could form at the cone-cylinder intersection. However, for the relatively gentle cone angles considered herein, it is assumed that the flow in this region is more likely to separate than to cavitate, justifying the assumption of a single cavity originating at the cavitator.

The pressure acting at the base of the cylindrical portion of the body depends on the conditions of the flow and the operation of the model under consideration. For an unventilated system, the base flow can cavitate or not, depending on the cavitation number. For example, at high cavitation numbers, the flow will separate at the cylinder–base intersection, allowing the velocity to remain finite in this region without formation of a cavity. In this condition, the time-averaged pressure acting over the base is greater than vapor pressure and relatively constant. The base drag may be approximated from semiempirical formulas available in the technical literature for base-separated flows. (See, for example, Hoerner [20].) To complicate the analysis, cavities can be ventilated; moreover, in the partially cavitating case, the ventilation conditions at the base need not be identical to those at the cavitator. Finally, at very low values of the cavitation number, a supercavity will form that envelopes the entire body, and the pressure acting on the base is simply cavity pressure. Thus, the general flow case requires consideration of a large number of combinations of conditions, an undertaking that was beyond the scope of the current investigation. However, for the important case of nonventilated base flow, for which the base pressure cannot fall below vapor pressure, the base drag is bounded above by its value in the base-cavitating flow condition. Conversely, since pressure recovery over the base is limited by separation, the base drag is bounded below by its value in the base-separated flow condition. For the vaporous base cavitation, as the cavitation number decreases, a ring cavity will form over the outboard region of the base, so there exists a range of the cavitation number over which the base drag will take some intermediate value between the lower bound represented by the value for base-separated flow and the upper bound represented by the value for base-cavitating flow. As the cavitation number continues to decrease, eventually the base cavity will grow to cover the entire base, and the value of the base drag coefficient can be computed by integrating the base cavity pressure over the base. This effect will be discussed in more detail below, in the context of some specific results.

The pressure can be computed from Bernoulli's equation

$$C_p = 1 - q^2$$

where q is the magnitude of the dimensionless local fluid velocity vector. The pressure contribution to the drag coefficient (exclusive of base drag) may then be computed as

$$C_{Dp} = \frac{4}{\pi} \oint_S C_p n_x dS$$

The viscous contribution to the drag coefficient along the wet portions of the conical and cylindrical body areas is calculated using the ITTC equation (see, for example, Newman [21]) for the friction coefficient, c_f. The viscous drag is

$$C_{Dv} = \frac{4}{\pi} \oint_{S_{\text{wetted}}} c_f s_x dS$$

For base-separated flows, the base drag coefficient may be estimated using an empirical formula found in Hoerner [20]

$$C_{Db} = \frac{0.029(2b_{\text{base}})^3}{\sqrt{C_{Dv}}} \tag{5}$$

where b_{base} is the dimensionless body radius at the base. For base-cavitating flows, the base drag coefficient is simply the integral over the base area of the cavity pressure, $p_{c\,\text{base}}$ (which may, in general, be different than the cavity pressure at the cavitator, p_c). This integral can be expressed as

$$C_{Db} = \frac{8 b_{\text{base}}^2 \sigma_{\text{base}}}{\rho U_\infty^2}. \tag{6}$$

With either of these formulas, the total drag coefficient is given by

$$C_D = C_{Dp} + C_{Dv} + C_{Db}.$$

Results

The model described above was exercised to investigate various effects associated with the body geometry. Selected results are discussed, and (where possible) compared with experimental data found in the technical literature.

Cavity Closure on the Cylindrical Portion of the Body. To isolate the basic effect of body length and radius, a profile was selected with a very short conical forebody, such that the cavity always closed on the cylinder (but not so blunt as to intersect the cavity boundary). These results were compared with the baseline case of supercavitation.

Figure 2 shows cavity shapes for a dimensionless body radius of 0.9 for different values of the cavity length. The dimensionless body length in each of these cases was 40. The cavity length for these cases is plotted against cavitation number in Fig. 3, along with two formulas commonly used to predict the length of supercavities. The first of these formulas is Garabedian's well-known result, derived from first principles, which captures the functional dependence of the cavity length on the cavitation number and on the square root of the drag coefficient (Garabedian [22]):

$$\frac{\ell_c}{d_c} = \frac{1}{\sigma} \sqrt{C_{Dc} \ln \frac{1}{\sigma}}$$

where d_c is the cavitator diameter. The second formula plotted in Fig. 3 is a semiempirical result found in May (1975), Eqs. (3)–(13):

$$\frac{\ell_c}{d_c} = \sqrt{C_{Dc}}(1.24\sigma^{-1.123} - 0.60).$$

May's formula also captures the square-root dependence of cavity length on drag, while the dependence on cavitation number is based on a fit of experimental data. For partial cavitation, as in the case of supercavitation, the cavitation number decreases with increasing cavity length. However, it can be seen that, over most of the range, the cavity at a given cavitation number is shorter for the case of partial cavitation than when the flow is not complicated by the presence of the wet afterbody. The difference between the results for partial cavitation and either of the formulas for super-

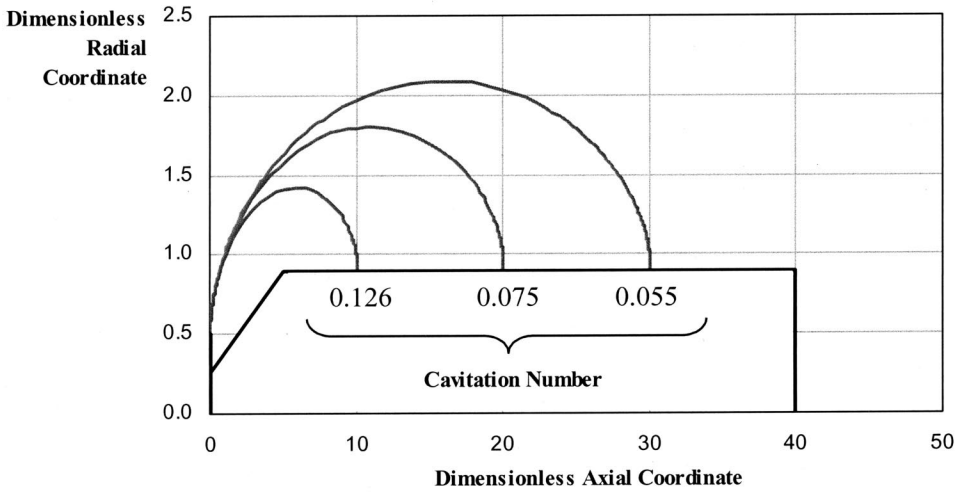

Fig. 2 Cavity shapes for different cavity lengths (dimensionless body radius: 0.9; dimensionless body length: 40)

cavitation is significantly greater than the difference between the two formulas for supercavitation themselves, especially for cavitation numbers greater than $\sigma=0.1$.

An intuitive explanation of the physics underlying this effect is based on the conditions at cavity closure. Although this region is generally unsteady for the axisymmetric flow conditions studied herein, the Riabouchinski wall model approximates the time-averaged cavity behavior by allowing for pressure recovery at the cavity end. In the case of supercavitation, stagnation pressure acts only on the axis of symmetry. For the partially cavitating flow currently considered, however, the locus of stagnation is a circle at the intersection of the Riabouchinski wall and the wet afterbody. Thus, the high-pressure region near cavity closure is more extensive, an effect that leads to shorter cavities.

Further insight concerning these effects can be gleaned from Fig. 4(*a*), which presents surface pressure distributions for a dimensionless body radius of 0.8 for two different values of the partial cavity length and for the case of supercavitation. The plots in Fig. 4(*b*) present the associated body-cavity geometry for the same three flow cases. Figure 4(*a*) also gives an idea of the distribution of panels along the surface. Note the increased panel density where pressure gradients are large. It can be seen that the pressure along the cavitator falls from its value at the stagnation point at the center of the cavitator and is continuous across the edge of the cavitator, at which point the value has dropped to cavity pressure. The pressure rises to its stagnation value at the intersection of the Riabouchinski wall and the body (if the cavity closes on the body) or on the Riabouchinski wall at the axis of symmetry (for a supercavity). For partial cavitation, the pressure coefficient downstream of the cavity closure point gradually approaches zero along the cylindrical body as the flow velocity approaches that of free-stream, then drops rapidly near the base–cylinder intersection. Note that this low-pressure spike should be considered an artifact of the simple model implemented at the base: A more physically realistic approach would properly account for flow separation in that region. The current model is deemed to be acceptable, except when cavity closure occurs very close to the base, at which point the nonphysical localized low pressure at the assumed cylinder-base intersection probably results in cavity lengths that are somewhat overpredicted. Also note that a low-pressure spike is predicted at the cone–cylinder intersection if the cavity closes upstream of this point. In a real flow, viscous effects would lead to a separation bubble at this point, which would tend to mitigate this spike. Alternatively, low pressure in this region

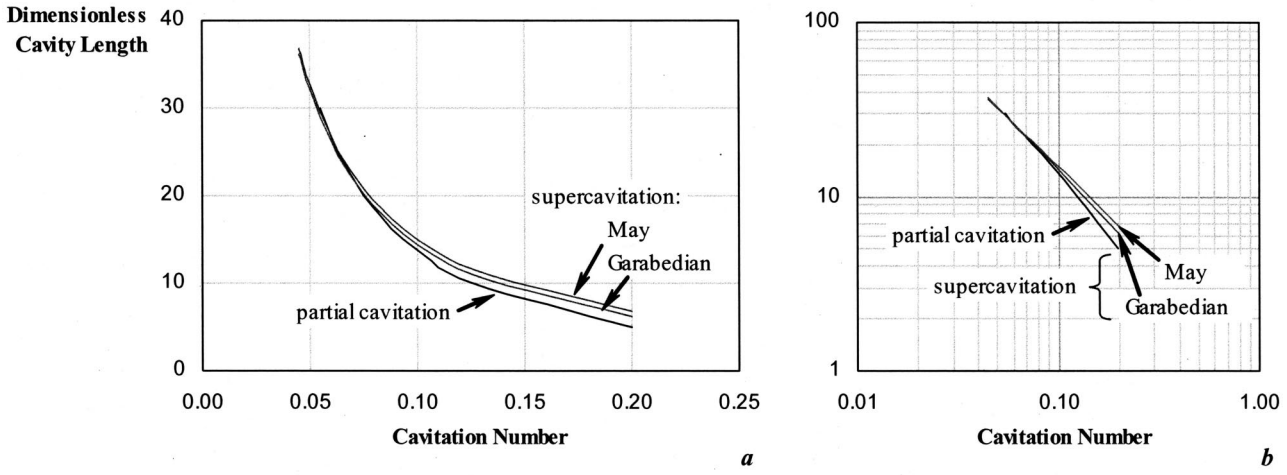

Fig. 3 Cavity length versus cavitation number on (*a*) linear and (*b*) logarithmic scales (dimensionless body radius: 0.9; dimensionless body length: 40)

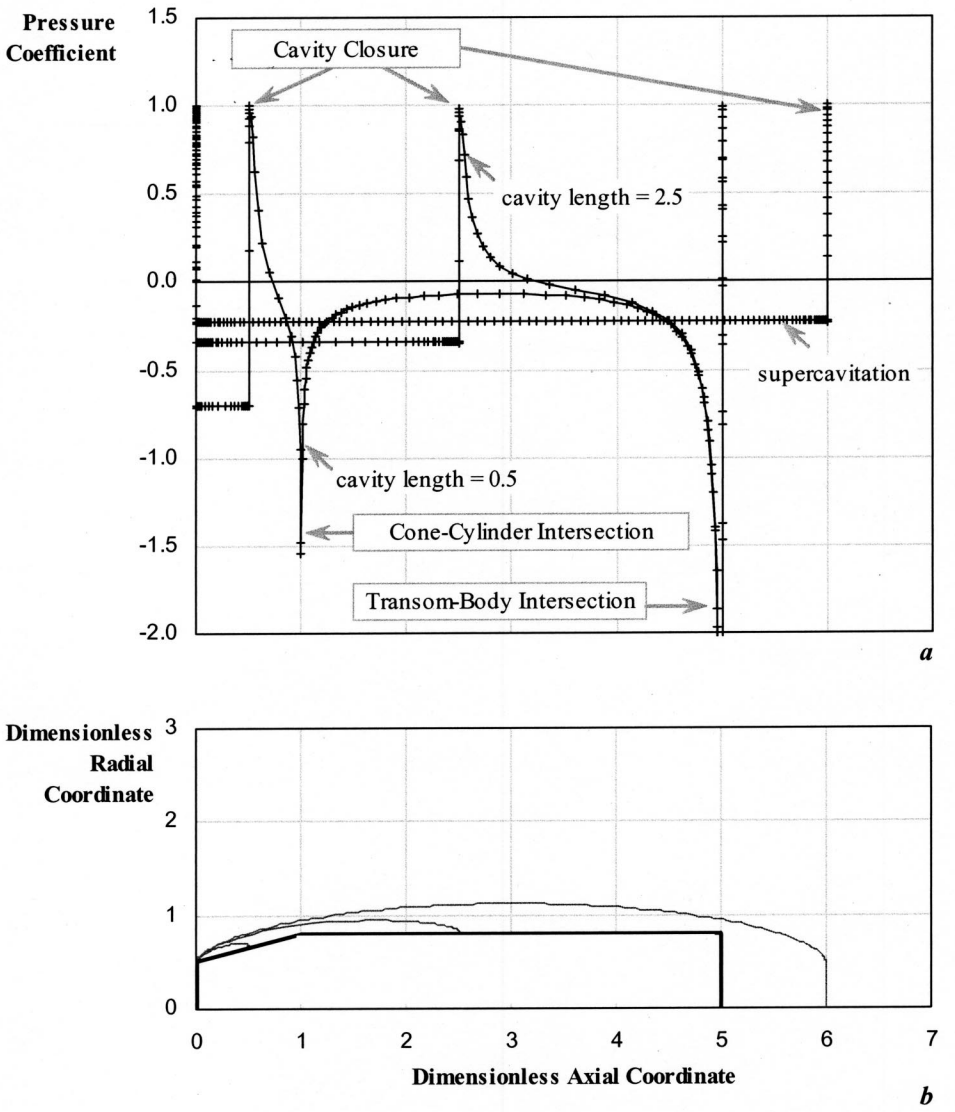

Fig. 4 (*a*) Surface pressure distribution and (*b*) cavity shape for different cavity lengths (dimensionless body length: 5; dimensionless body radius: 0.8); see text for discussion of pressure spikes

could be associated with a second cavity. Neither effect has been addressed with the current model, so it is expected that the cavity length is slightly over-predicted for cases in which closure occurs just upstream of the cone–cylinder intersection.

Figure 5 presents cavity shapes at a constant cavity length for the body radii ranging from 0.5 to 1.3. Here the cavity length is 30 and the body length is 40. Changes in the cavity shape are much more apparent downstream of the point of maximum cavity radius, although significant differences can also be observed somewhat forward of this point.

Figures 6(*a*) and 6(*b*) present the Riabouchinski wall height as a function of the body radius and cavity length, respectively. In Fig. 6(*a*), the Riabouchinski wall height is plotted against the body radius for values of the cavity length of 10, 20, and 30. It can be seen that, for all cavity lengths, the Riabouchinski wall height decreases with increasing body radius. The curves are somewhat jagged, especially for a body radii greater than 1 cavitator diameter. This may be due to discretization error. Figure 6(*b*) shows the variation of Riabouchinski wall height with cavity length for two values of the body radius. The wall height is seen to decrease with increasing cavity length.

The decrease in the Riabouchinski wall height with increasing body radius provides information concerning the maximum body that can be accommodated by a partial cavity for a given cavitation number. With further increase in the body radius, negative values of the Riabouchinski wall height were obtained, so that the converged cavity shape actually intersected the body, suggesting that such a cavity is not physically realizable. Over most of the parameter space studied, this occurred when the body radius was greater than approximately 1.3 times the cavitator diameter (to within the resolution tested; that is, for increments of a dimensionless body radius of 0.1), as is depicted in Fig. 7. When the cavity closure location was very close to the aft end of the body, negative Riabouchinski wall heights occurred at lower values of the body radius; for longer bodies, this effect occurred at lower ratios of the cavity length to the body length. (Note, however, that the results for very long partial cavities—approaching the body length—are not entirely accurate, because cavitation or separation at the base of the cylinder has not been properly modeled. The effects of this deficiency are considered negligible for lower values of the ratio of cavity to body length.)

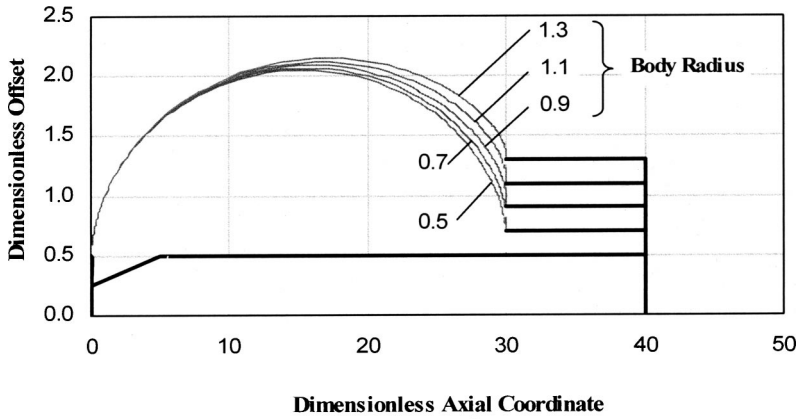

Fig. 5 Cavity shapes for various body radii (dimensionless body length: 40; dimensionless cavity length: 30)

At least from a numerical perspective, limitations also apply to the minimum cavity length for a given body radius. Figure 8 shows the minimum cavity length for which convergence was achieved as a function of the body radius. When the current analysis was applied to flow cases with shorter cavities than this minimum value, nonphysical cavity shapes resulted, characterized by nonconvex profiles. It can be seen that this minimum cavity length increases with increasing body radius.

Figure 9(*a*) presents the cavitation number versus the cavity length for different body radii. The dimensionless body length is again 40. Except for the case of supercavitation (a body radius of zero), the cavity closes on the cylindrical portion of the body. The cavitation number decreases with increasing body radius. As the cavity length increases, each curve asymptotically approaches the supercavitation result, which agrees well with the low-cavitation-number limits of two formulas presented in May [23]. One of these is May's own semiempirical formula, and the other is Garabedian's theoretical formula [22]. A dimensionless body radius of 0.5 is the case where the cavitator and cylinder diameters are the same, the so-called ''zero-caliber ogive'' for which partial cavitation experiments were performed by Billet and Weir [24]. Figure 9(*b*) presents the cavity length versus cavitation number for this case for the current method (labeled ''0.5''), for the curve fit recommended in [24] for their experimental results:

$$\frac{\ell_c}{d_c} = \left(\frac{0.751}{\sigma}\right)^{1/0.75}$$

and for the semiempirical formula for supercavitation recommended in May [23]. It can be seen that, although the current

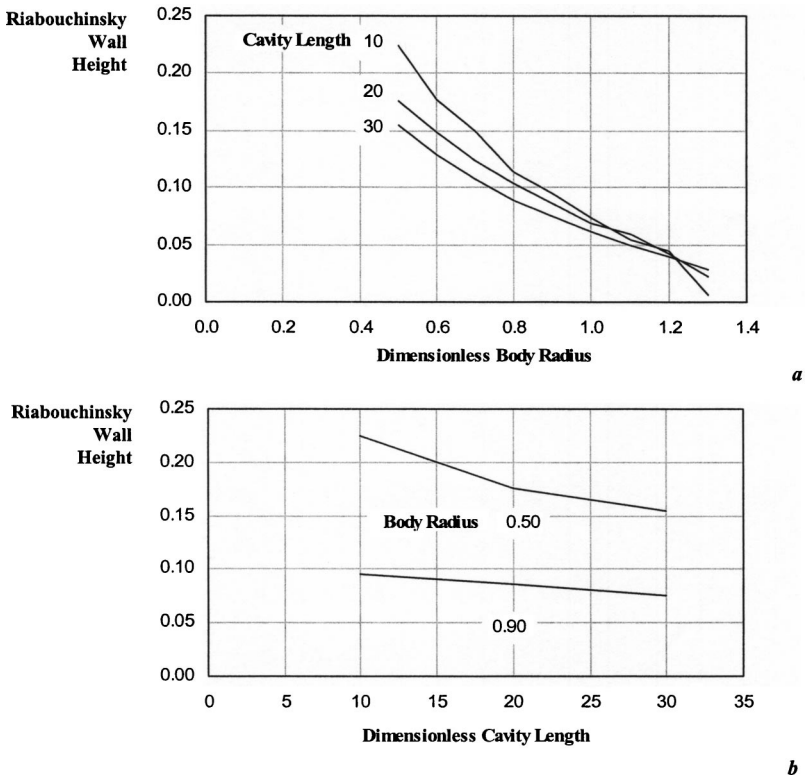

Fig. 6 Riabouchinski wall height versus (*a*) body radius and (*b*) cavity length (dimensionless body length: 40)

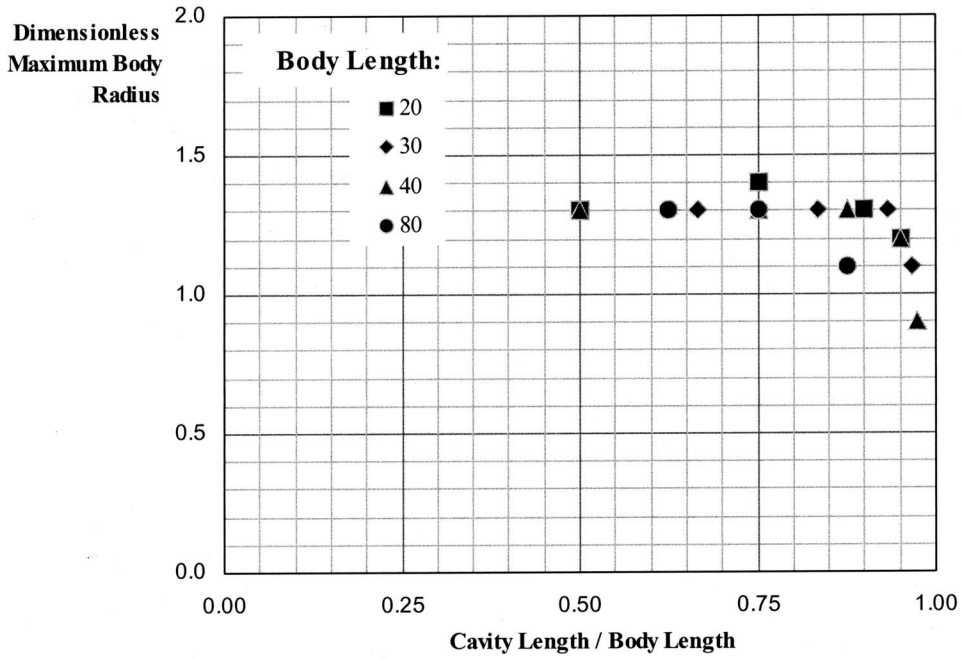

Fig. 7 Maximum body radius (resolved in increments of 0.1) for nonnegative Riabouchinski wall height as a function of cavity length

results fall between the two sets of experimental data, the trend is somewhat closer to the partially cavitating case, suggesting that part of the difference between the data sets presented in [23] and in [24] can be explained by the presence of the body in the latter case. Other differences may be attributable to any difference in body length between the flow case associated with Fig. 9(*b*) and the actual model length of Billet and Weir (1975), which is not stated in their publication. Also, the physical flow conditions at the model base and the presence of a strut and tunnel walls are not accounted for in the current model. Although the presence of a body will be less important for cylinders of the smaller radii, it is suggested that the current method could be used to correct experimental supercavitation data for the presence of a downstream sting.

It is often useful to have available a simple approximate formula relating cavity length to cavitation number. For the case of supercavitation, many such formulas are available, notably Garabedian's theoretical formula [22] and May's semiempirical formula [23] shown in Figs. 3 and 9. Such a formula is proposed in the Appendix for the case of a partial cavity terminating on the cylindrical portion of the body.

Cavity Closure on the Conical Forebody. The pressure distribution for closure on the conical forebody of a selected configuration was discussed above in connection with Fig. 4. Figure 10 presents the effect of the body radius if the cavity closes on the conical portion of the body. It can be seen that a much longer cavity is generated for supercavitation than for the partially cavi-

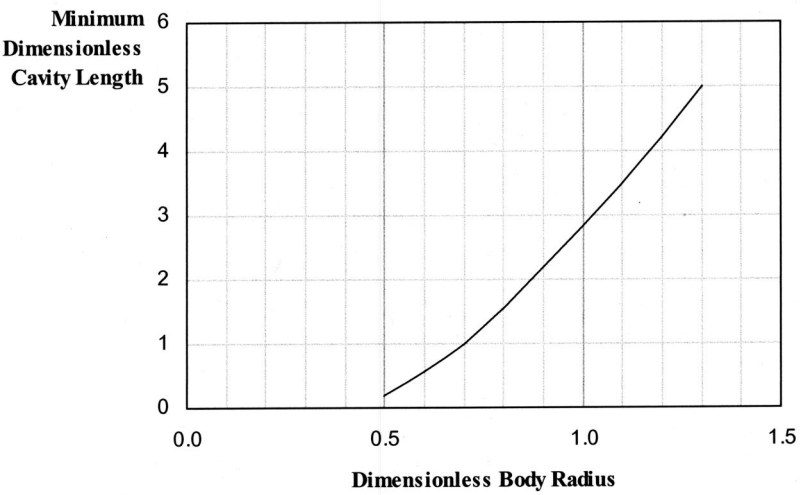

Fig. 8 Minimum cavity length for which convergence was achieved versus body radius (dimensionless body length: 40)

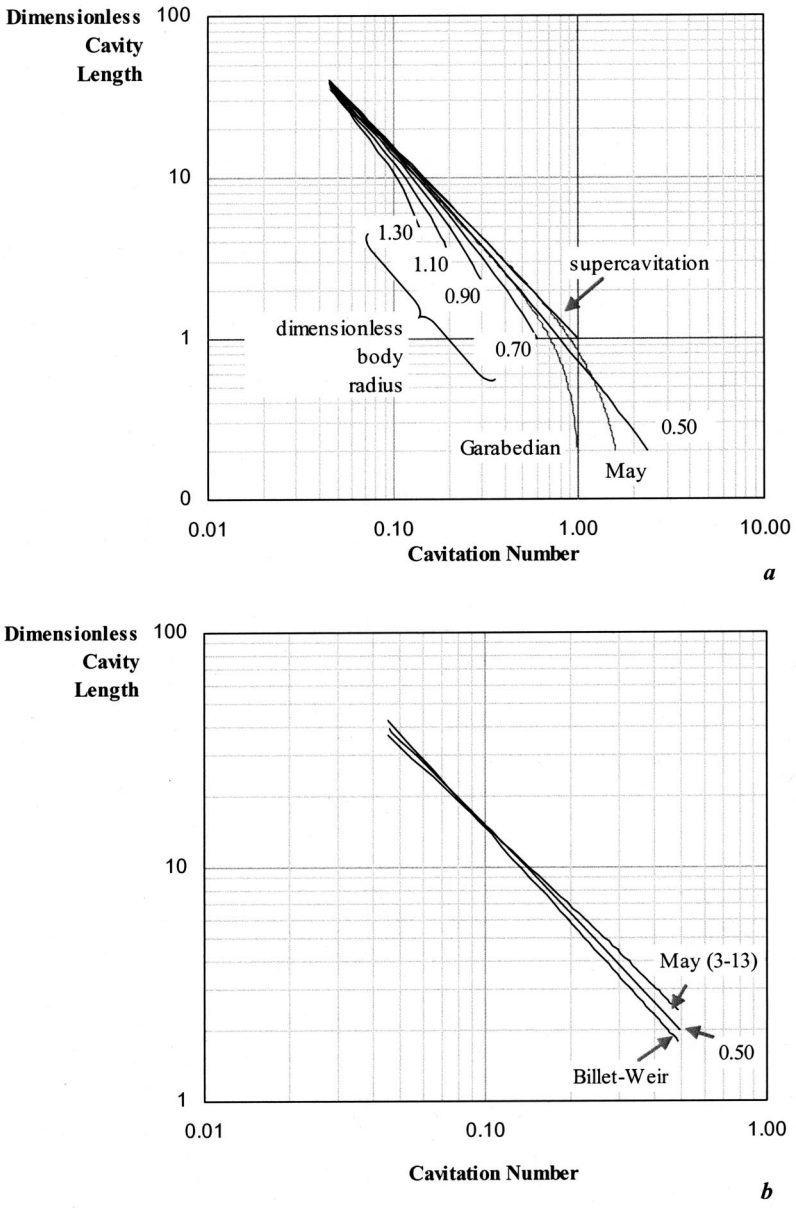

Fig. 9 Cavity length versus cavitation number (*a*) for bodies of different radii (dimensionless body length: 40); (*b*) comparison with the zero-caliber ogive experiments of Billet and Weir (1975)

tating case at the same cavitation number. For a constant cavitation number, the cavity length decreases slightly with increasing body radius, especially at lower cavitation numbers. The semi-empirical results from May [23] are also presented in the figure for purposes of comparison with the case of supercavitation.

In Fig. 11(*a*), the cavitation number versus the cavity length is plotted for three different cone angles: 4.77 deg, 9.55 deg, and 15.92 deg. The dimensionless axial coordinates of the cone–cylinder intersection for each of these bodies are 8.38, 4.16, and 2.46, respectively. The body length is 80 and the cavity closes on either the conical or the cylindrical portion of the body. For cone angles of 4.77 deg and 9.55 deg, a continuous curve is obtained. But for 15.92 deg, the curve is discontinuous for values of the cavity length between approximately 2 and 6.

This can be explained by referring to Fig. 12, where the cavity shapes for different cavitation numbers are shown for this cone angle. The cavity shapes for cavity lengths 4 and 5, even though they are shown in the figure, intersect the body and so are not physically realizable. Hence a jump in the cavity length is required at this point. For the other two cone angles shown in Fig. 11, the cone–cylinder intersection is further downstream, so the cavity is large enough to envelope that point as the cavity length increases continuously with a decrease in the cavitation number; thus continuous curves result. Note, however, the very apparent change in the slopes of the curves, even for the 9.55 deg cone angle, as the cavity closure point moves from the cone to the cylinder in each case. This effect is emphasized in Fig. 11(*b*), where the reciprocal of the cavitation number is plotted versus cavity length for each of the body profiles. This figure clearly shows either discontinuous or slope-discontinuous behavior when the cavity closes at the cone–cylinder intersection, depending on the cone angle.

Although the current analysis does not address ventilation effects, such behavior may be related to the hysteresis effect discussed in Semenenko [25]. This effect, which was discovered and investigated experimentally, involves the behavior of nominally

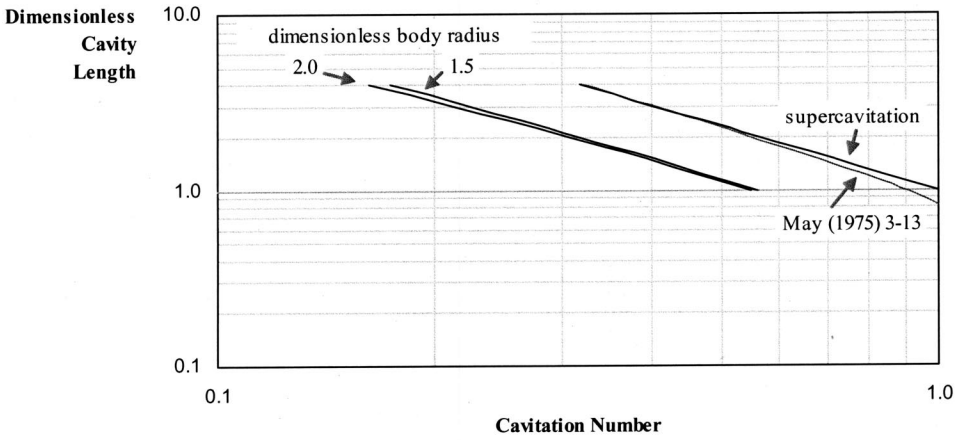

Fig. 10 Cavity length versus cavitation number for cavity termination on the conical forebody, comparing partial cavitation with supercavitation (dimensionless body length: 80; cone angle: 6.96 deg)

axisymmetric ventilated cavities that close on an axisymmetric body profile with slope discontinuities. Specifically, Semenenko claims that the ventilation rate required to maintain a cavity of a given length depends on the angle that the cavity boundary makes with the body profile near closure. Since this quantity depends, in turn, on the slope of the profile and the cavity length, a slope-discontinuous profile is associated with discontinuities in the relationship between the required ventilation rate and the cavity length. Figures 11 and 12 herein provide qualitative evidence of a similar dependence on the angle that the cavity boundary makes with the body profile near closure. This result suggests that the effect discussed in [25] involves the relationship between the cavi-

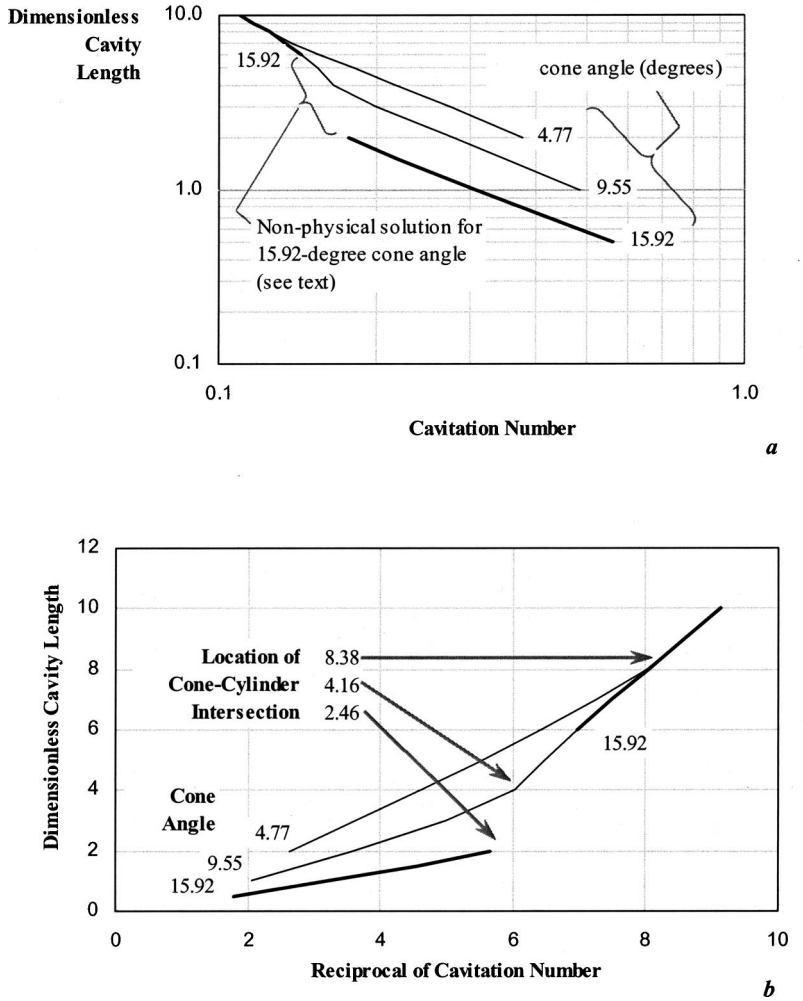

Fig. 11 Cavity length versus (*a*) cavitation number and (*b*) reciprocal of cavitation number for three different cone angles (dimensionless body length: 80; dimensionless body radius: 1.2)

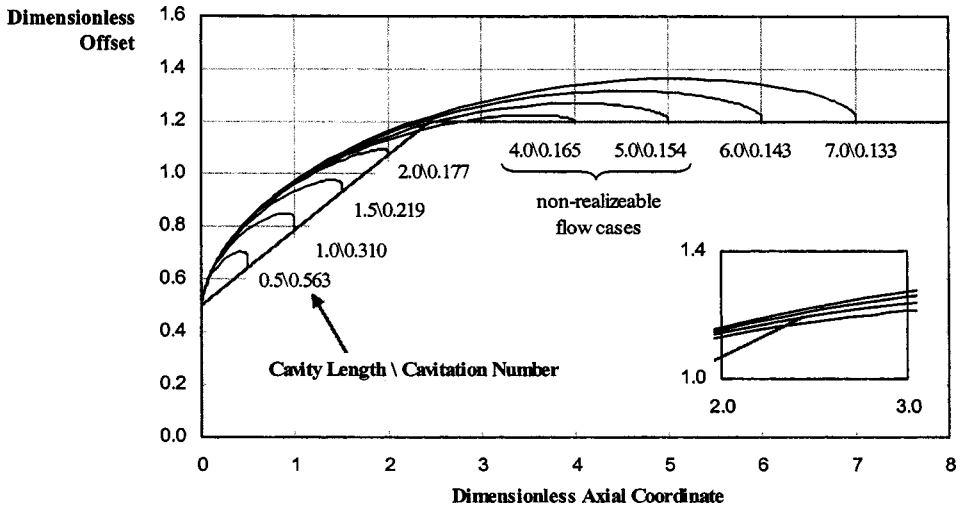

Fig. 12 Numerical analysis of high-speed bodies in partially cavitating flow

tation number and the cavity length directly, although it is clear that the required ventilation rate must also be affected. Application of the current model to the body profiles discussed by Semenenko for purposes of a more direct comparison was beyond the scope of this effort.

Drag coefficients for bodies with cone angles of 9.55 deg and 15.92 deg are plotted in Figs. 13 and 14, respectively, broken down into the components described above. For these examples, it was assumed that the flow at the cylinder base was separated, rather than cavitating, and the base drag component was computed using Eq. (5). The pressure drag in Fig. 13 decreases as the cavity closure point approaches the cone–cylinder intersection and then increases slowly as the cavity length increases. This behavior is reflected in the total drag, since the pressure drag is a significant component, and the other components change only slowly with changes in the cavity length. As is to be expected, the viscous drag decreases with increasing cavity length while the base drag increases. Note that all these computations were performed for a single, arbitrarily selected value of the Reynolds number.

In Fig. 14, the drag associated with the nonphysical solutions for values of the cavity length between 2 and 6 is not shown, although the pressure and total drag coefficients show a tendency toward reduced values just outside this range, so that the qualitative behavior is similar to that described in Fig. 13.

The local minimum in the forebody pressure drag coefficient as the cavity closure point approaches the cone–cylinder intersection represents two primary competing effects: (1) A decrease in the length of the conical forebody that is exposed to elevated pressures downstream of the cavity closure point; and, (2) the increase in cavity pressure relative to ambient as the cavitation number increases, which results in increased drag on the forebody. It can be seen from Fig. 4 that the fraction of the forebody length that is exposed to pressures higher than static pressure is reduced as more of the cone is enveloped by the cavity. Once the cavity

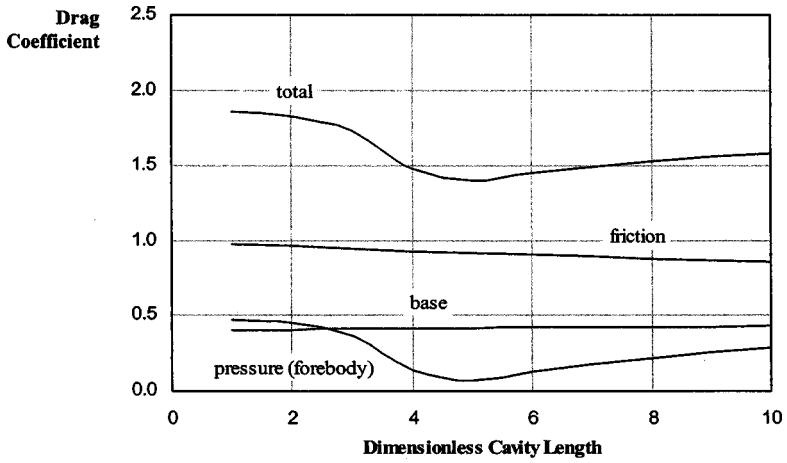

Fig. 13 Drag coefficient versus cavity length (dimensionless body length: 80; dimensionless body radius: 1.2; cone angle: 9.55 deg; Reynolds number: 3.0e7)

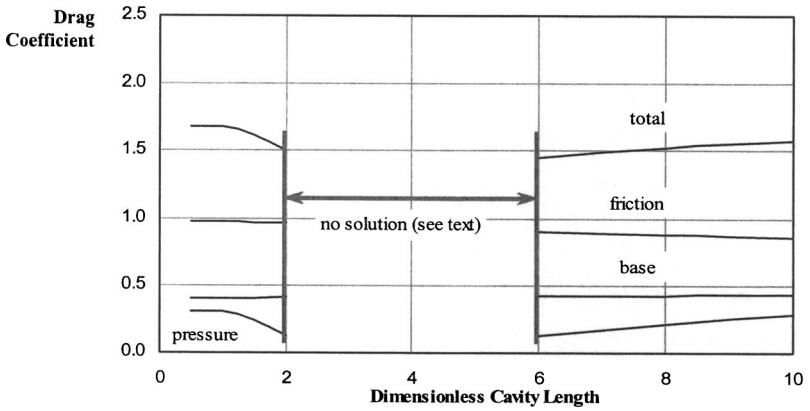

Fig. 14 Drag coefficient versus cavity length (dimensionless body length: 80; dimensionless body radius: 1.2; cone angle: 15.92 deg; Reynolds number: 3.0e7)

closure point reaches the cone–cylinder intersection, no further decrease can occur, since the cone is completely enveloped. The minimum pressure drag should, therefore, be observed when the cavity and cone lengths are equal; the cavity increments used to produce the curves in Fig. 13 were not quite sufficient to resolve the pressure minimum exactly, although the basic behavior is captured. The dip in the total drag coefficient as the cavity closure point approaches the cone–cylinder intersection does not reduce the drag to values associated with supercavitation. In that case, there is no base drag as currently defined, friction drag is negligible, and the total drag is simply the cavitator drag for a disk, so that the total drag coefficient based on cavitator projected area takes a value approaching 0.82–0.84 (see, for example, May [23], Kirschner et al. [13], Uhlman et al. [14], and many others).

Figures 15 and 16 show the effects of body radius when the cavity closes on the conical portion of the body at constant values of the cavitation number. Once again, the base drag was computed using Eq. (5), assuming that the flow is base-separated, rather than base-cavitating. For this example, the cavitation number was fixed at 0.15, the dimensionless body length was 80, and the cone angle was 15.92 deg. As for the case of cavity closure on the cylinder, it can be seen in Fig. 15 that the cavity length decreases with increasing body radius. Figure 16 shows that all the drag components except the pressure drag increase with increasing body radius over the range considered. The increase in friction drag is due to the increase in the ratio of wet area to cavitator area. Similarly, the increase in base drag is associated with the increase in the ratio of base area to cavitator area. The forebody pressure drag varies under the influence of two primary competing effects: (1) The increase in the wet area of the conical forebody that is exposed to elevated pressures downstream of the cavity closure point; and, (2) the increase in the wet area of the conical forebody exposed to the low-pressure spike near the cone–cylinder intersection. At this cavitation number, with the cavity enveloping a fraction of the cone, the first effect leads to a slight increase in the pressure drag coefficient until a dimensionless body radius of approximately 1.8, at which point the effect of the low-pressure spike begins to dominate and the pressure decreases.

The Effect on Drag of Flow Conditions at the Cylinder Base

As discussed above, the base and total drag coefficients depend on the type of flow occurring at the base of the cylinder: Base-separated flow, in which case the base drag is computed using Eq. (5), or the base-cavitating flow, for which Eq. (6) applies. In reality, the base drag coefficient can fall somewhere between these two values, depending on the extent of cavitation over the cylinder base. Thus, the base-separated and base-cavitating flow cases represent limiting values that are useful for the purposes of estimating the total drag on a partially cavitating body.

As an illustration of this behavior, the base and total drag coefficients were predicted for a partially cavitating body with a dimensionless length of 40 and a dimensionless cylinder radius of

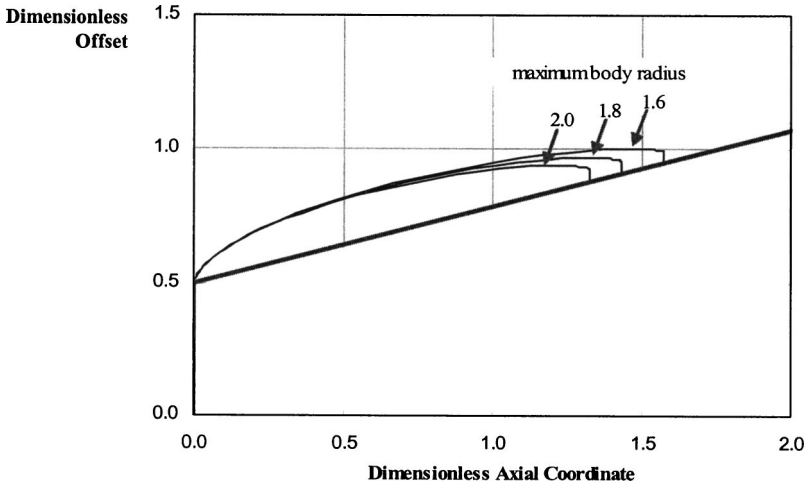

Fig. 15 Cavity shapes for different maximum dimensionless body radii (dimensionless body length: 80; cavitation number: 0.15; cone angle: 15.92 deg)

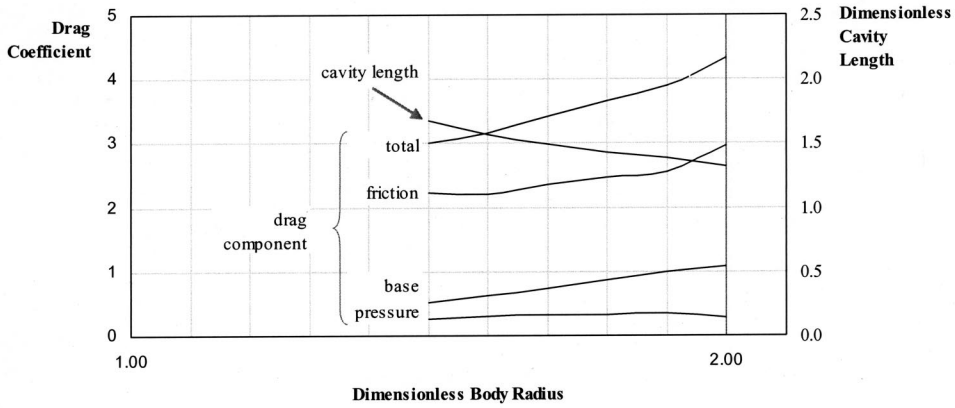

Fig. 16 Dimensionless cavity length and drag components versus dimensionless body radius (dimensionless body length: 80; cavitation number: 0.1; cone angle: 15.92 deg)

0.9, subject to base-separated and base-cavitating flow. For each of these two cases, it was assumed that the forward cavity closed on the cylindrical portion of the body. For the case of the base-cavitating flow, it was assumed that cavity pressure at the base and at the cavitator were equal. The results are presented in Fig. 17.

It can be seen that as the cavitation number decreases with increasing cavity length, the base drag coefficient for the base-cavitating flow case also decreases in accordance with Eq. (6). Assuming that the semiempirical formula, Eq. (5), is applicable, a generally opposite trend applies to the base-separated flow case. These trends are reflected in the total drag coefficients. It is thus apparent from Fig. 17 that the total drag coefficient is very dependent on the base flow conditions. Therefore, in applying these results, several cautions must be noted, as follows:

As discussed above, the pressure in the fluid cannot fall below vapor pressure. Thus, the base drag coefficient cannot achieve a value higher than the value computed for the case of the base-cavitating flow with the cavity pressure equal to vapor pressure. Thus for the example results presented in Fig. 17, the base drag coefficient for the base-separated flow case is nonphysical for dimensionless cavity lengths greater than approximately 13.6. For longer cavities, cavitation would begin to occur over the base, and the base drag coefficient would begin to depart from the curve for base separation shown in Fig. 17, and eventually follow the curve for base cavitation as the base flow became fully cavitated. The total drag coefficient is similarly limited.

If the cavities at the cavitator and at the base are subject to unequal values of cavity pressure, as can occur for a ventilated system, results such as those presented in Fig. 17 must be modified.

The results for the base-separated flow case are presented as an engineering approximation based on a semiempirical formula for the drag coefficient. This formula is a rather simplified expression that does not involve body length as a parameter, nor does it account for the occurrence of cavitation. Such complications warrant additional modeling and experimental validation to improve predictions such as those presented in Fig. 17.

Conclusions

A physics-based model of partial cavitation has been developed for axisymmetric flows. The model has been applied to a disk cavitator with a simple body profile consisting of a conical forebody abutting a cylinder. The effects of the body radius and forebody cone angle on the cavity shape and length, the cavitation number, and the body drag were studied. The model predicts that,

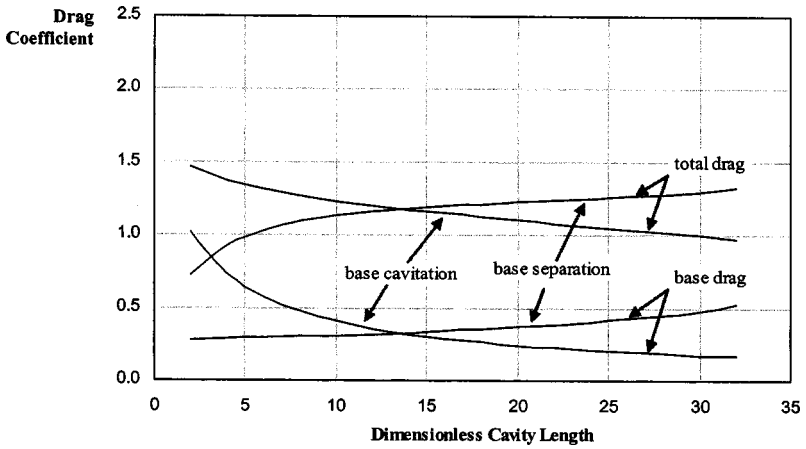

Fig. 17 Base and total drag coefficients versus cavity length (dimensionless body length: 40; dimensionless body radius: 0.9; Reynolds number: 3.0e7) comparing the base-separated and base-cavitating flow cases

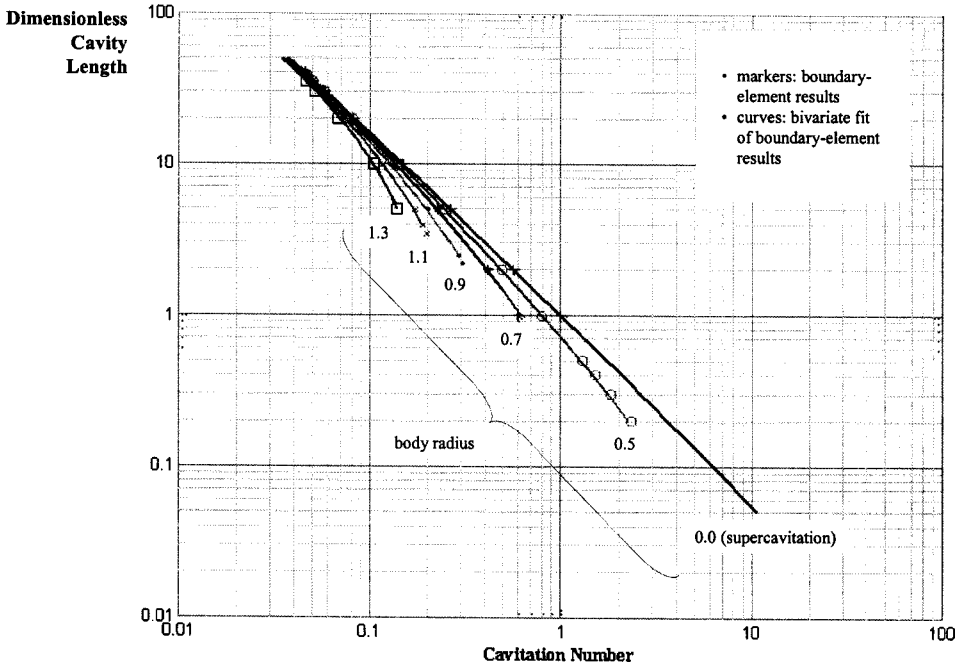

Fig. 18 Bivariate surface fit of cavity length as a function of cavitation number and cylinder radius (results strictly applicable to a dimensionless body length of 40; computed using Eq. (7); original numerical data plotted as markers)

for fixed cavitation number, partial cavities are generally shorter than supercavities for the same cavitation number over the regime investigated. The model also predicts that, for a given cavitation number, cavity length decreases and drag increases with an increase in the body radius over most of the parameter space investigated. A dip in the pressure drag coefficient occurs as the cavitation number decreases and the cavity termination point approaches the cone–cylinder intersection. However, discontinuous cavity behavior can also occur at such an operating point, depending on the forebody cone angle. It is proposed that this effect is related to experimental observations of other researchers involving ventilation hysteresis effects.

Acknowledgments

This work was supported, in part, by the Office of Naval Research (ONR), most recently with the sponsorship of Dr. K. Ng under Program No. 0602747N. Previous support was provided by Mr. J. Fein, then of ONR.

Nomenclature

A_c = cavitator projected area
$b(x)$ = body-cavity radius at axial location x
b_{base} = radius of cylindrical portion of body
b_{ij} = coefficients used in surface fit of computed results
C_D = total drag coefficient, $D/\frac{1}{2}\rho U_\infty^2 A_c$
C_{Db} = base (pressure) drag coefficient, $D_b/\frac{1}{2}\rho U_\infty^2 A_c$
C_{Dc} = cavitator drag coefficient for a supercavity, $D_c/\frac{1}{2}\rho U_\infty^2 A_c$
C_{Dp} = pressure drag coefficient, $D_p/\frac{1}{2}\rho U_\infty^2 A_c$
C_{Dv} = viscous drag coefficient, $D_v/\frac{1}{2}\rho U_\infty^2 A_c$
C_f = friction coefficient, $\tau_w/\frac{1}{2}\rho U_\infty^2$
C_p = pressure coefficient, $(p-p_\infty)/\frac{1}{2}\rho U_\infty^2$
D = total drag on the body
D_b = base drag at the aft end of the body
D_c = cavitator drag for a supercavity
D_p = pressure drag on the body excluding base drag component
D_v = viscous drag on the body
d_c = cavitator diameter
ℓ_b = body length
ℓ_c = cavity length
$\ell_i(b)$ = coefficients used in surface fit of computed results
p_c = cavity pressure at cavitator
$p_{c\ \text{base}}$ = cavity pressure at cylinder base, for base-cavitating flows
p_∞ = free-stream ambient pressure
q = magnitude of local fluid velocity vector
s = arc length coordinate along body-cavity surface
U_∞ = free-stream velocity
x = axial distance
ρ = density of water
σ = cavitation number, $(p_\infty-p_c)/\frac{1}{2}\rho U_\infty^2$, based on cavity pressure at cavitator
σ_{base} = cavitation number, $(p_\infty-p_{c\ \text{base}})/\frac{1}{2}\rho U_\infty^2$, based on cavity pressure at cylinder base
Φ = total potential
ϕ = disturbance potential

Appendix: Parametric Surface Fit of Partial Cavity Characteristics

It is often useful to have available a simple approximate formula relating the cavity length to the cavitation number. For the case of partial cavitation over a cylindrical body of dimensionless length of 40, the following surface is proposed, based on curve fits of the numerical results presented above

$$\ln(\sigma(\ell_c,b)) = \ell_1(b)\ln^2(\ell_c) + \ell_2(b)\ln(\ell_c) + \ell_3(b) \quad (A\text{-}1)$$

where b is the cylinder radius

$$\ell_i(b) = b_{i1}b^2 + b_{i2}b + b_{i3}$$

and

$$b_{ij} = \begin{bmatrix} -0.0648 & 0.5201 & -1.0961 \\ -0.0003 & -0.0210 & 0.0899 \\ -0.0069 & -0.8140 & -0.0031 \end{bmatrix}$$

The minimum cavity length for which the formula is applicable is given as a polynomial regression to the results presented in Fig. 18

$$\ln(\ell_{c\ \min}) = -2.0717\ln^2(b) + 2.4282\ln(b) + 1.0842 \quad (A\text{-}2)$$

The original data computed using the boundary-element method is compared in Fig. 18 with the associated family of curves generated using Eq. (*A*-1). It can be seen that the surface fit is quite satisfactory for values of the cavity length greater than the minimum defined by Eq. (*A*-2).

References

[1] Efros, D. A., 1946, ''Hydrodynamic Theory of Two-Dimensional Flow With Cavitation,'' Dokl. Akad. Nauk SSSR, **51**, pp. 267–270.

[2] Tulin, M. P., 1964, ''Supercavitating Flows—Small Perturbation Theory,'' J. Ship Res., **7**, p. 3.

[3] Cuthbert, J., and Street, R., 1964, ''An Approximate Theory for Supercavitating Flow About Slender Bodies of Revolution,'' LMSC Report, TM81-73/39, Lockheed Missiles and Space Co., Sunnyvale, CA.

[4] Brennan, C., 1969, ''A Numerical Solution of Axisymmetric Cavity Flows,'' J. Fluid Mech., **37**, p. 4.

[5] Chou, Y. S., 1974, ''Axisymmetric Cavity Flows Past Slender Bodies of Revolution,'' J. Hydronautics, **8**, p. 1.

[6] Vorus, W. S., 1991, ''A Theoretical Study of the Use of Supercavitation/Ventilation for Underwater Body Drag Reduction,'' VAI Technical Report, Vorus & Associates, Inc., Gregory, MI.

[7] Kuria, I. M., Kirschner, I. N., Varghese, A. N., and Uhlman, J. S., 1997, ''Compressible Cavity Flows Past Slender Non-Lifting Bodies of Revolution,'' *Proceedings of the ASME & JSME Fluids Engineering Annual Conference & Exhibition, Cavitation and Multiphase Flow Forum*, FEDSM97-3262, Vancouver, BC.

[8] Uhlman, J. S., 1987, ''The Surface Singularity Method Applied to Partially Cavitating Hydrofoils,'' J. Ship Res., **31**, p. 2.

[9] Uhlman, J. S., 1989, ''The Surface Singularity or Boundary Integral Method Applied to Supercavitating Hydrofoils,'' J. Ship Res., **33**, p. 1.

[10] Kinnas, S. A., and Fine, N. E., 1990, ''Nonlinear Analysis of the Flow Around Partially and Super-Cavitating Hydrofoils by a Potential Based Panel Method,'' *Proceedings of the IABEM-90 Symposium*, International Association for Boundary Element Methods, Rome, Italy.

[11] Kinnas, S. A., and Fine, N. E., 1993, ''A Numerical Nonlinear Analysis of the Flow Around Two- and Three-Dimensional Partially Cavitating Hydrofoils,'' J. Fluid Mech., **254**, pp. 151–181.

[12] Varghese, A. N., Uhlman, J. S., and Kirschner, I. N., 1997, ''Axisymmetric Slender-Body Analysis of Supercavitating High-Speed Bodies in Subsonic Flow,'' *Proceedings of the Third International Symposium on Performance Enhancement for Marine Applications*, T. Gieseke, editor, Newport, RI.

[13] Kirschner, I. N., Uhlman, J. S., Varghese, A. N., and Kuria, I. M., 1995, ''Supercavitating Projectiles in Axisymmetric Subsonic Liquid Flows,'' *Proceedings of the ASME & JSME Fluids Engineering Annual Conference & Exhibition, Cavitation and Multiphase Flow Forum*, FED 210, J. Katz and Y. Matsumoto, editors, Hilton Head Island, SC.

[14] Uhlman, J. S., Varghese, A. N., and Kirschner, I. N., 1998, ''Boundary Element Modeling of Axisymmetric Supercavitating Bodies,'' *Proceedings of the 1st Symposium on Marine Applications of Computational Fluid Dynamics, Hydrodynamic/Hydroacoustic Technology Center*, McLean, VA.

[15] Savchenko, Y. N., Semenenko, V. N., Naumova, Y. I., Varghese, A. N., Uhlman, J. S., and Kirschner, I. N., 1997, ''Hydrodynamic Characteristics of Polygonal Contours in Supercavitating Flow,'' *Proceedings of the Third International Symposium on Performance Enhancement for Marine Applications*, T. Gieseke, editor, Newport, RI.

[16] Krasnov, V. K., 2002, ''The Movement of an Axisymmetrical Solid With Formation of a Cavity,'' *Proceedings of the 2002 International Summer Scientific School on High-Speed Hydrodynamics*, Chuvash National Academy of Science and Art, Cheboksary, Russia.

[17] Varghese, A. N., 1999, ''Boundary-Element Modeling of Partial Cavitating and Supercavitating High-Speed Bodies,'' presentation in the *Proceedings of the 1999 ONR Workshop on Supercavitating High-Speed Bodies*, Naval Undersea Warfare Center, Newport, RI.

[18] Varghese, A. N., and Uhlman, J. S., 2000, ''Advanced Physics Modeling of Supercavitating High-Speed Bodies,'' in ''FY99 Annual In-House Laboratory Independent Research Annual Report,'' NUWC-NPT Working Memorandum 8007 dated 17 April, Naval Undersea Warfare Center Division, Newport, RI.

[19] Tulin, M. P., 2001, ''Supercavitation: An Overview,'' *Lecture Notes for the RTO AVT/VKI Special Course on Supercavitating Flows*, von Karman Institute for Fluid Dynamics, Rhode Saint Genèse, Belgium.

[20] Hoerner, S. F., 1965, *Fluid-Dynamic Drag*, Hoerner Fluid Dynamics, Brick Town, NJ.

[21] Newman, J. N., 1980, *Marine Hydrodynamics*, The MIT Press, Cambridge, MA.

[22] Garabedian, P. R., 1956, ''Calculation of Axially Symmetric Cavities and Jets,'' Pac. J. Math., **6**, pp. 611–689.

[23] May, A., 1975, ''Water Entry and the Cavity-Running Behavior of Missiles,'' SEAHAC Technical Report 75-2, Naval Surface Weapons Center, White Oak Laboratory, Silver Spring, MD.

[24] Billet, M. L., and Weir, D. S., 1975, ''The Effect of Gas Diffusion on the Flow Coefficient for a Ventilated Cavity,'' J. Fluids Eng., December issue, American Society of Mechanical Engineers, New York, NY.

[25] Semenenko, V. N., 2001, ''Artificial Supercavitation: Physics and Calculation,'' *Lecture Notes for the RTO AVT/VKI Special Course on Supercavitating Flows*, von Karman Institute for Fluid Dynamics, Rhode Saint Genèse, Belgium.

Scaling of Tip Vortex Cavitation Inception Noise With a Bubble Dynamics Model Accounting for Nuclei Size Distribution

Chao-Tsung Hsiao
e-mail: ctsung@dynaflow-inc.com

Georges L. Chahine
e-mail: glchahine@dynaflow-inc.com

Dynaflow, Inc.
10621-J Iron Bridge Road, Jessup, MD 20794

The acoustic pressure generated by cavitation inception in a tip vortex flow was simulated in water containing a realistic bubble nuclei size distribution using a surface-averaged pressure (SAP) spherical bubble dynamics model. The flow field was obtained by the Reynolds-averaged Navier–Stokes computations for three geometrically similar scales of a finite-span elliptic hydrofoil. An "acoustic" criterion, which defines cavitation inception as the flow condition at which the number of acoustical "peaks" above a pre-selected pressure level exceeds a reference number per unit time, was applied to the three scales. It was found that the scaling of cavitation inception depended on the reference values (pressure amplitude and number of peaks) selected. Scaling effects (i.e., deviation from the classical $\sigma_i \propto R_e^{0.4}$*) increase as the reference inception criteria become more stringent (lower threshold pressures and less number of peaks). Larger scales tend to detect more cavitation inception events per unit time than obtained by classical scaling because a relatively larger number of nuclei are excited by the tip vortex at the larger scale due to simultaneous increase of the nuclei capture area and of the size of the vortex core. The average nuclei size in the nuclei distribution was also found to have an important impact on cavitation inception number. Scaling effects (i.e., deviation from classical expressions) become more important as the average nuclei size decreases.* [DOI: 10.1115/1.1852476]

1 Introduction

Scaling of the results of a propeller tip vortex cavitation inception studies from laboratory to large scales has not always been very successful. Aside from the problems associated with properly scaling the flow field, existing scaling laws as derived or used by previous studies, e.g., [1–6], lack the ingredients necessary to explain sometimes major discrepancies between model and full scale. One of the major aspects which has not been appropriately incorporated in the scaling law is nuclei presence and nuclei size distribution effects. Another issue which may cause scaling problems is the means of detection of cavitation inception. Practically, the flow condition is considered to be at cavitation inception when either an "*acoustic*" criterion or an "*optical*" criterion is met [7,8]. These two detection methods are known to provide different answers in the most practical applications. Furthermore, for practical reasons inception may be detected by one method at model scale and by another at full scale. To address this issue in a more consistent manner for different scales, the present study considers an "*acoustic*" criterion which determines the cavitation inception event by counting the number of acoustical signal peaks that exceed a certain level in unit time.

To theoretically address the above issues in a practical way spherical bubble dynamics models were adopted in many studies in order to simulate the bubble dynamics and to predict tip vortex cavitation inception [8–10]. In our previous studies [8,11], an improved surface-averaged pressure (SAP) spherical bubble dynamics model was developed and applied to predict single bubble trajectory, size variation and resulting acoustic signals. This model was later shown to be much superior than the classical spherical model through its comparison to a two-way fully three-dimensional (3D) numerical model which includes bubble shape deformation and the full interaction between the bubble and the viscous flow field [11]. In the present study we incorporate the SAP spherical bubble dynamics model with a statistical nuclei distribution in order to enable prediction of cavitation inception in a practical liquid flow field with known nuclei size distribution. This is realized by randomly distributing the nuclei in space and time according to the given nuclei size distribution. According to previous studies [12,13] the number of nuclei to use in the computation can be reduced by considering only the nuclei that pass through a so-called "window of opportunity" and are captured by the tip vortex.

In order to study scale effects in a simple vortex flow filed we consider the tip vortex flows generated by a set of three geometrically similar elliptic hydrofoils. The flow fields are obtained by steady-state Navier–Stokes computations which provide the velocity and pressure fields for the bubble dynamics computations. The SAP spherical model is then used to track all nuclei released randomly in time and space from the nuclei release area and to record the acoustic signals generated by their dynamics and volume oscillations.

2 Numerical Models

2.1 Navier–Stokes Computations. To best describe the tip vortex flow field around a finite-span hydrofoil, the Reynolds-averaged Navier–Stokes (RANS) equations with a turbulence model are solved. These have been shown to be successful in addressing tip vortex flows [14] and general propulsor flows [15,16]. The three-dimensional unsteady Reynolds-averaged incompressible continuity and Navier–Stokes equations in nondimensional form and Cartesian tensor notations are written as

$$\frac{\partial u_i}{\partial x_i} = 0 \tag{1}$$

Contributed by the Fluids Engineering Division for publication on the JOURNAL OF FLUIDS ENGINEERING. Manuscript received by the Fluids Engineering Division September 13, 2003; revised manuscript received August 13, 2004. Review Conducted by: S. Ceccio.

$$\frac{\partial u_i}{\partial t}+u_j\frac{\partial u_i}{\partial x_j}=-\frac{\partial p}{\partial x_i}+\frac{\partial \tau_{ij}}{\partial x_j} \tag{2}$$

where $u_i=(u,v,w)$ are the Cartesian components of the velocity, $x_i=(x,y,z)$ are the Cartesian coordinates, p is the pressure, $R_e=\rho u^* L^*/\mu$ is the Reynolds number, u^* and L^* are the characteristic velocity and length selected to be, respectively, the free stream velocity, V_∞ and root chord length, C_0. ρ is the liquid density, and μ is its dynamic viscosity. The effective stress tensor τ_{ij} is given by

$$\tau_{ij}=\frac{1}{R_e}\left[\left(\frac{\partial u_i}{\partial x_j}+\frac{\partial u_j}{\partial x_i}\right)-\frac{2}{3}\delta_{ij}\frac{\partial u_k}{\partial x_k}\right]-\overline{u_i u_j} \tag{3}$$

where δ_{ij} is the Kronecker delta and $\overline{u_i' u_j'}$ is the Reynolds stress tensor resulting from the Reynolds averaging scheme.

To numerically simulate the tip vortex flow around a finite-span hydrofoil, a body-fitted curvilinear grid is generated and Eqs. (1) and (2) are transformed into a general curvilinear coordinate system. The transformation provides a computational domain that is better suited for applying the spatial differencing scheme and the boundary conditions. To solve the transformed equations, we use the three-dimensional incompressible Navier–Stokes flow solver, DF_UNCLE, derived from the code UNCLE developed at Mississippi State University. The DF_UNCLE code is based on the artificial-compressibility method [17] which a time derivative of the pressure multiplied by an artificial-compressibility factor is added to the continuity equation. As a consequence, a hyperbolic system of equations is formed and is solved using a time marching scheme in pseudo-time to reach a steady-state solution.

The numerical scheme in DF_UNCLE uses a finite volume formulation. First-order Euler implicit differencing is applied to the time derivatives. The spatial differencing of the convective terms uses the flux-difference splitting scheme based on Roe's method [18] and van Leer's MUSCL method [19] for obtaining the first-order and the third-order fluxes, respectively. A second-order central differencing is used for the viscous terms which are simplified using the thin-layer approximation. The flux Jacobians required in the implicit scheme are obtained numerically. The resulting system of algebraic equations is solved using the Discretized Newton Relaxation method [20] in which symmetric block Gauss–Seidel sub-iterations are performed before the solution is updated at each Newton interaction. A $k-\varepsilon$ turbulence model is used to model the Reynolds stresses in Eq. (3).

All boundary conditions in DF_UNCLE are imposed implicitly. Here, a free stream constant velocity and pressure condition is specified at all far-field side boundaries. The method of characteristic is applied at the inflow boundary with all three components of velocities specified while a first-order extrapolation for all variables is used at the outflow boundary. On the solid hydrofoil surface, a no-slip condition and a zero normal pressure gradient condition are used. At the hydrofoil root boundary, a plane symmetry condition is specified.

2.2 Statistical Nuclei Distribution Model. In order to address a realistic liquid condition in which a liquid flow field contains a distribution of nuclei with different sizes, a statistical nuclei distribution is used. We consider a liquid with a known nuclei size density distribution function, $n(R)$. $n(R)$ is defined as the number of nuclei per cubic meter having radii in the range $[R, R+\delta R]$. This function has a unit m^{-4} and is given by

$$n(R)=\frac{dN(R)}{dR} \tag{4}$$

where $N(R)$ is the number of nuclei of radius R in a unit volume. This function can be obtained from experimental measurements such as light scattering, cavitation susceptibility meter and ABS Acoustic Bubble Spectrometer® measurements [21] and can be expressed as a discrete distribution of M selected nuclei sizes. Thus, the total void fraction, α, in the liquid can be obtained by

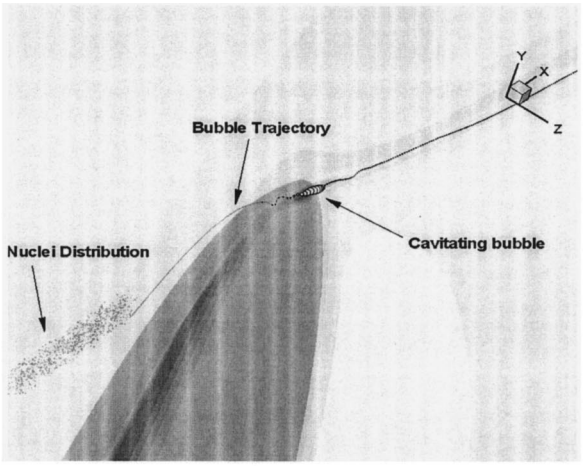

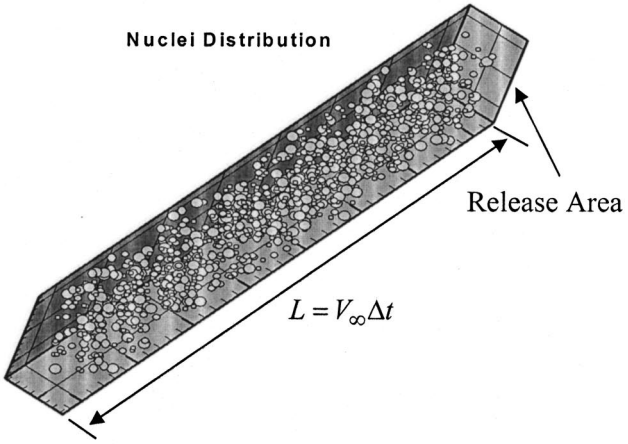

Fig. 1 The location and size of a fictitious volume for randomly distributing the nuclei

$$\alpha=\sum_{i=1}^{M} N_i\frac{4\pi R_i^3}{3} \tag{5}$$

where N_i is the discrete number of nuclei of radius R_i used in the computations. The position and timing of nuclei released in the flow field are obtained using random distribution functions, always ensuring that the local and overall void fraction satisfy the nuclei size distribution function.

From previous studies [12,13], we know that only nuclei that "enter" a given region or "window of opportunity" are actually captured by the vortex and generate strong acoustic signals. Therefore, it is economical to consider only nuclei emitted from this "window of opportunity." This is similar to considering a fictitious volume of cross area equal to the window area and of length equal to $V_\infty \Delta t$, where V_∞ is the free stream velocity and Δt is the total time of signal acquisition (see Fig. 1).

2.3 Bubble Dynamics. The nuclei convected in the flow field are treated using a spherical bubble dynamics model. To do so, we use the Rayleigh–Plesset equation modified to account for a slip velocity between the bubble and the host liquid, and for the nonuniform pressure field along the bubble surface [10]. The resulting modified surface-averaged pressure (SAP) Rayleigh–Plesset equation can be written as:

$$R\ddot{R}+\frac{3}{2}\dot{R}^2=\frac{1}{\rho}\left(p_v+p_{g0}\left(\frac{R_0}{R}\right)^{3k}-P_{\text{encounter}}-\frac{2\gamma}{R}-\frac{4\mu\dot{R}}{R}\right)+\frac{(\mathbf{u}-\mathbf{u}_b)^2}{4} \tag{6}$$

where R is the time varying bubble radius, R_0 is the initial or reference bubble radius, γ is the surface tension parameter, p_v is the vapor pressure. p_{g0} is the initial or reference gas pressure inside the bubble, and k is the polytropic compression law constant. $\mathbf{u}$ is the liquid convection velocity and $\mathbf{u}_b$ is the bubble travel velocity. $P_{\text{encounter}}$ is the ambient pressure "seen" by the bubble during its travel. In the SAP method $P_{\text{encounter}}$ is defined as the average of the liquid pressures over the bubble surface [11].

The bubble trajectory is obtained using the following motion equation [22]

$$\frac{d\mathbf{u}_b}{dt}=\frac{3}{\rho}\nabla P+\frac{3}{4}C_D(\mathbf{u}-\mathbf{u}_b)|\mathbf{u}-\mathbf{u}_b|+\frac{3}{R}(\mathbf{u}-\mathbf{u}_b)\dot{R} \tag{7}$$

where the drag coefficient C_D is given by an empirical equation such as that of Haberman and Morton [23]

$$C_D=\frac{24}{R_{eb}}(1+0.197R_{eb}^{0.63}+2.6\times10^{-4}R_{eb}^{1.38});\quad R_{eb}=\frac{2\rho R|\mathbf{u}-\mathbf{u}_b|}{\mu} \tag{8}$$

The pressure at a distance l from the bubble center generated by the bubble dynamics is given by the expression

$$p=\frac{\rho}{l}[R^2\ddot{R}+2R\dot{R}^2]-\rho\left[\frac{R^4\dot{R}^2}{2l^4}\right] \tag{9}$$

When $l\gg R$, Eq. (9) becomes the expression for the acoustic pressure p_a of Fitzpatrick and Strasberg [24] after introduction of the delayed time t' due to a finite sound speed, c

$$p_a(t')=\frac{R\rho}{l}[R\ddot{R}(t')+2\dot{R}^2(t')],\quad t'=t-\frac{r-R}{c}. \tag{10}$$

To determine the bubble motion and its volume variation, a Runge–Kutta fourth-order scheme is used to integrate Eqs. (6) and (7) through time. The liquid velocity and pressures are obtained directly from the RANS computations. The numerical solution of the RANS equations, however, offers the solution directly only at the grid points. To obtain the values for any specified location (x,y,z) on the bubble we need to interpolate from the background grid. To do so, an interpolation stencil and interpolation coefficients at any specified location are determined at each time step. We use a three-dimensional point-locating scheme based on the fact that the coordinates (x,y,z) of the bubble location are uniquely represented relative to the eight corner points of the background grid stencil by

$$x=\sum_{i=1}^{8}N_i\overline{x_i},\quad y=\sum_{i=1}^{8}N_i\overline{y_i},\quad z=\sum_{i=1}^{8}N_i\overline{z_i}, \tag{11}$$

where

$$\begin{aligned}N_1&=(1-\phi)(1-\psi)(1-\varphi),\quad N_2=\phi(1-\psi)(1-\varphi),\\ N_3&=(1-\phi)\psi(1-\varphi),\quad N_4=\phi\psi(1-\varphi),\\ N_5&=(1-\phi)(1-\psi)\varphi,\quad N_6=\phi(1-\psi)\varphi,\\ N_7&=(1-\phi)\psi\varphi,\quad N_8=\phi\psi\varphi.\end{aligned} \tag{12}$$

ϕ, ψ, φ are the interpolation coefficients, and $(\overline{x_i},\overline{y_i},\overline{z_i})$ are the coordinates of the eight corner points of a grid stencil in the background grid. Equation (11) is solved using a Newton–Raphson method. For a bubble point to be inside the grid stencil requires that the corresponding ϕ, ψ, φ satisfy $0\leq\phi\leq1$, $0\leq\psi\leq1$, $0\leq\varphi\leq1$.

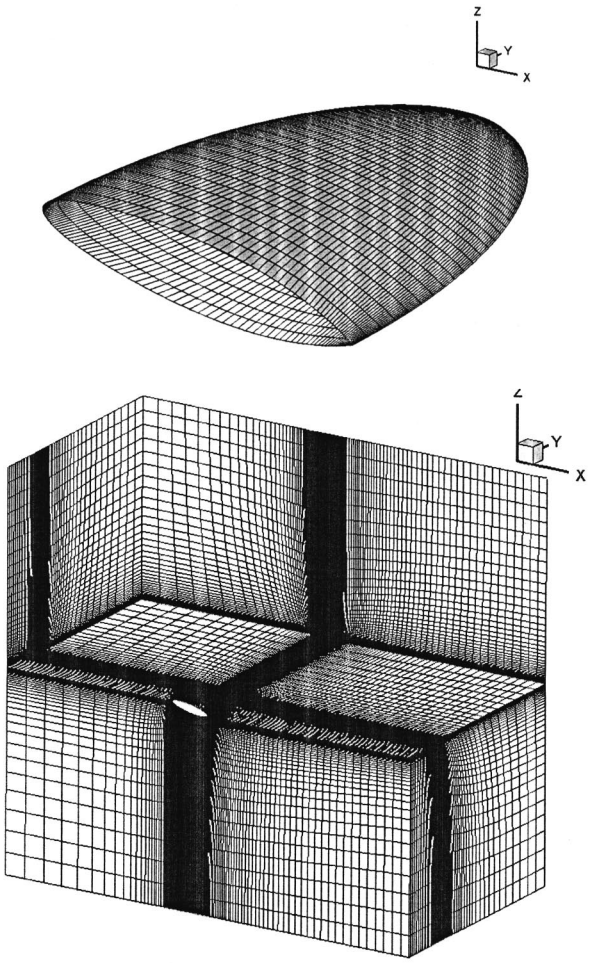

Fig. 2 Computational domain and grid for the current study

Once the interpolation stencil and interpolation coefficients are determined, the pressure and velocities can be obtained by using a similar equation to Eq. (11).

2.4 Computational Domain and Grid Generation. To compute the flow around the finite-span elliptic hydrofoil we generated an H–H type grid with a total of 2.7 million grid points in which $191\times101\times101$ grid points were created in the streamwise, spanwise and normal direction, respectively, and 81×61 grid points were used to discretize the hydrofoil surface. The grid is subdivided into 12 blocks for a computational domain which has all far-field boundaries located six (6) chord lengths away from the hydrofoil surface (see Fig. 2). Grid resolution was determined according to previous numerical studies [14,25] in which extensive investigations of the grid resolution for the tip vortex flow showed that the minimum number of grid points needed for good resolution is at least 15 grid points across the vortex core. Here, the grid resolution for the tip vortex was optimized through repeated computations and regridding to align grid clustering around the tip vortex centerline. The final refined grid selected for the results shown below had at least 16 grid points in the spanwise direction and 19 grid points in the crosswise direction within the vortex core. The first grid above the hydrofoil surface was located such that $y^+\approx1$ in order to properly apply the turbulence model.

3 Results

3.1 3D Steady-State Tip Vortex Flow. The selected finite-span elliptic foil has a NACA16020 cross section with an aspect ratio of 3 (based on semispan). The flow field at an angle of attack

Table 1 Characteristics of the three NACA16020 foil used

	Small scale	Medium scale	Large scale
C_0	0.144 m	0.288 m	0.576 m
V_∞	10 m/s	10 m/s	10 m/s
R_e	1.44×10^6	2.88×10^6	5.76×10^6
$-Cp_{\min}$	3.34	4.34	5.48

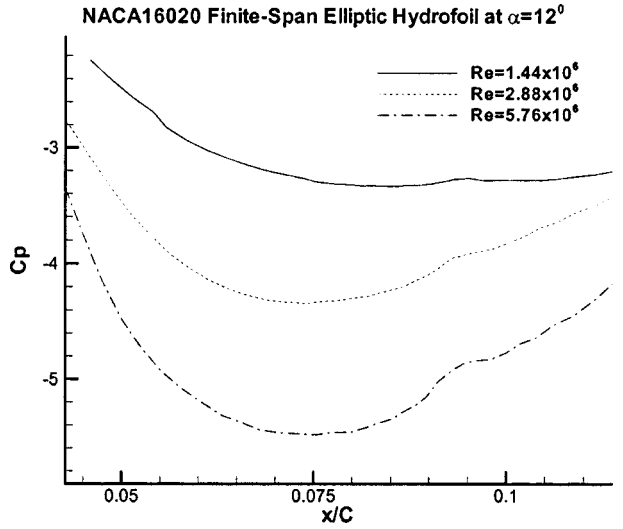

Fig. 3 Pressure coefficient variations along the NACA16020 elliptic foil for three values of the Reynolds number

of 12 deg was computed for three foil sizes or three different Reynolds numbers in order to study cavitation scaling effects. These correspond to the three scales shown in Table 1. In all three cases a steady-state solution was considered achieved when $\nabla \cdot \overline{V} \leqslant 1\times10^{-4}$. The resulting pressure coefficients along the tip vortex centerline are shown in Fig. 3. It is seen that the locations of the minimum pressure for all three cases are very close to the hydrofoil tip and are located at $x/C_0=0.085$, 0.075, and 0.075. The corresponding minimum pressure coefficients are shown in Table 1. If the cavitation inception number is assumed to be $-Cp_{\min}$, then these values correlate with the power formulation: $\sigma_i \propto R_e^{0.36}$.

To validate the steady state computations an additional case was computed at an angle of attack equal to 10° and $R_e=4.75\times10^6$. The results were compared to the available experimental measurements of [2] by considering the tangential and axial velocity components across the tip vortex core at two streamwise locations. As seen in Fig. 4, the comparison indicates that the tip vortex flow is well predicted in the near-field region in which the pressure coefficient along the vortex center reaches its minimum. However, over-diffusion in vortex core size and over-dissipation in velocities are seen for the numerical solution further downstream especially for the axial velocity component whose velocity profile changes from excess to deficit. Notice, however, that this occurs beyond the region of interest here for bubble dynamics studies. Indeed, the bubble dynamics simulations show that the bubble growth and collapse durations are relatively very short (see Fig. 5) and occur before $x/C_0=0.1$. In this region, our numerical solution

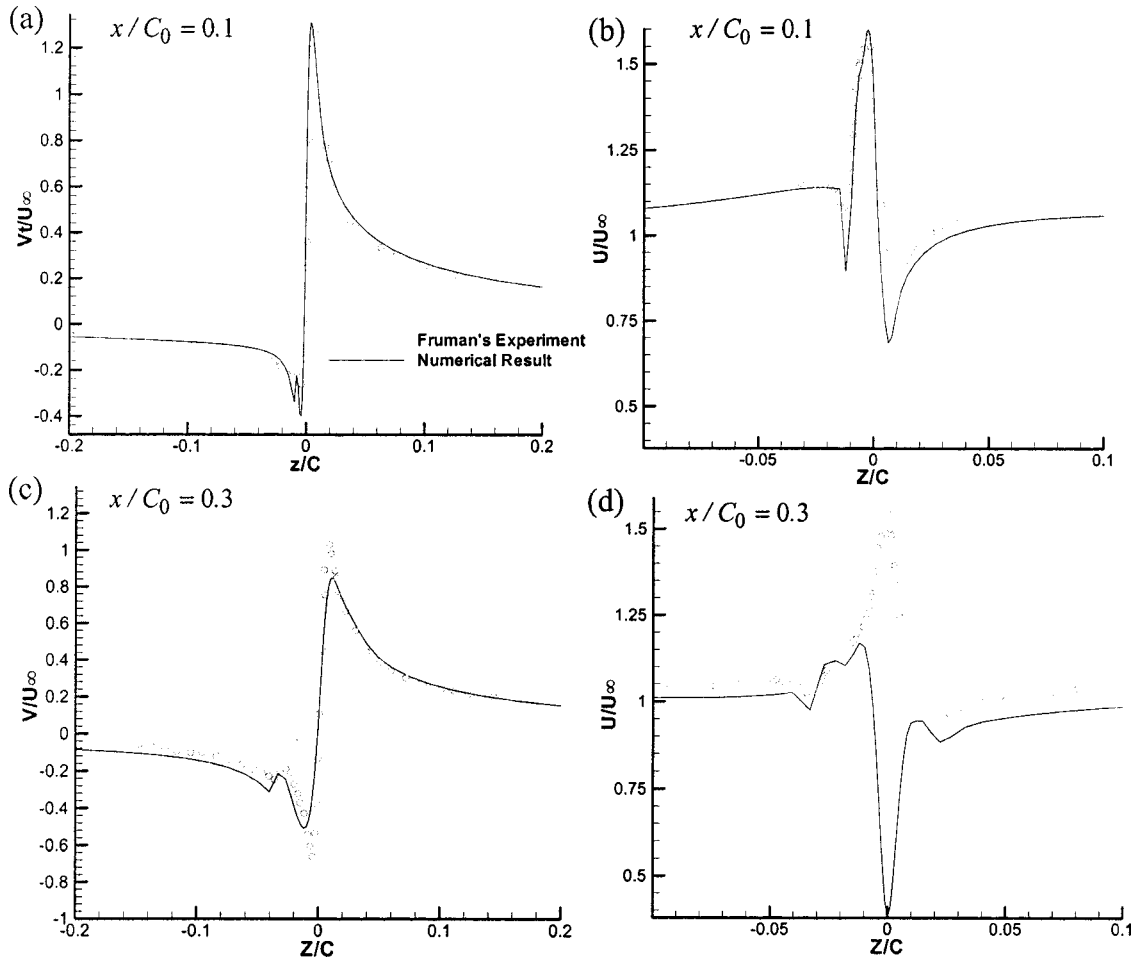

Fig. 4 Comparison of tangential and axial velocity components across the tip vortex core at $x/C_0=0.1$ and 0.3 between present numerical result and experimental measurements (Fruman et al. 1992)

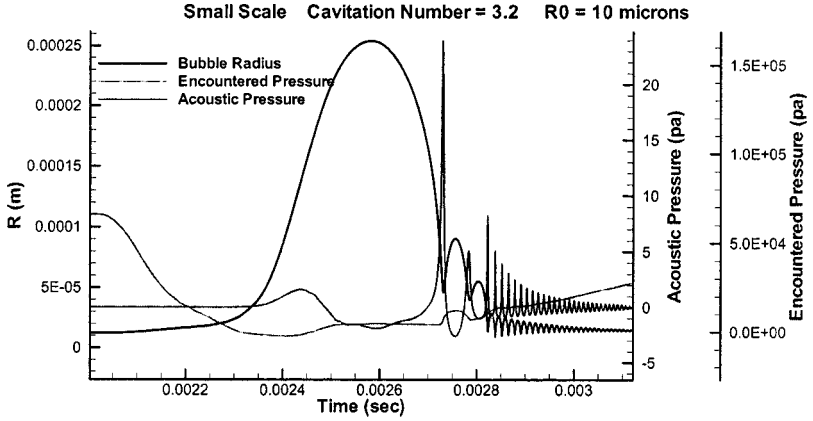

Fig. 5 Example computation of bubble dynamics for bubble radius, encountered pressure, and emitted acoustic pressure versus time during bubble capture in the tip vortex

agrees quite well with the experimental measurements. Therefore, the present Navier–Stokes computations are reliable for studying the bubble behavior in the $Cp_{\min}$ region of interest.

3.2 Window of Opportunity. The ''window of opportunity'' can be determined by releasing nuclei upstream of the foils and tracking their trajectories to see if they enter into the low pressure areas in the tip vortex flow. A release plane located at $x/C_0 = -0.1$ ahead of the hydrofoil tip ($x/C_0 = 0$) was used. Nuclei were released from this plane at various locations, tracked, and the minimum pressure they encountered is recorded at the corresponding release point.

Initially, 300 nuclei of a given size were released from the release plane. All properties are defined at 20°C. The cavitation number was specified high enough such that the maximum growth size of nucleus was less than 10%. Figure 6 shows a contour plot of the minimum pressure coefficient encountered for each release location for different nuclei sizes in the small scale. The contours are blanked out for the release points where the nuclei collide with the hydrofoil surface. It is seen that the size of the ''window of opportunity'' becomes smaller and its location shifts closer to the hydrofoil surface of pressure side when the nuclei sizes decrease. The contours of minimum encounter pressure coefficient for different scales with the same initial nuclei size are shown in Fig. 7. It is seen that the size of the ''window of opportunity'' increases as the scale increases. This implies that larger scales capture more nuclei into the vortex for the same nuclei sizes and duration of observation time when compared to smaller scales.

3.3 Statistical Nuclei Size Distribution. Nuclei size distribution studies in water tunnels, lakes and oceans [26,27] show a power-law distribution for the number density distribution function, with $n(R) \approx 1/R^{\beta}$, where the exponent β lies between 2.5 and 4. In the present study we consider a nuclei size distribution ranging from 10 to 100 μm with a void fraction $\alpha \approx 1 \times 10^{-6}$ as shown in Fig. 8. In order to consider a same bubble population for all scales, we have accounted for the fact that a bubble will change its radius in a static equilibrium fashion when the ambient pressure is changed. Therefore, for the same scaled cavitation number, initial nuclei sizes are reduced for the larger scales where the ambient pressure would be larger. This is not a major change in the values since gas pressure inside the bubble varies like the cube of the radius, while surface tension which is predominant varies like the inverse of the radius. This results in nuclei sizes

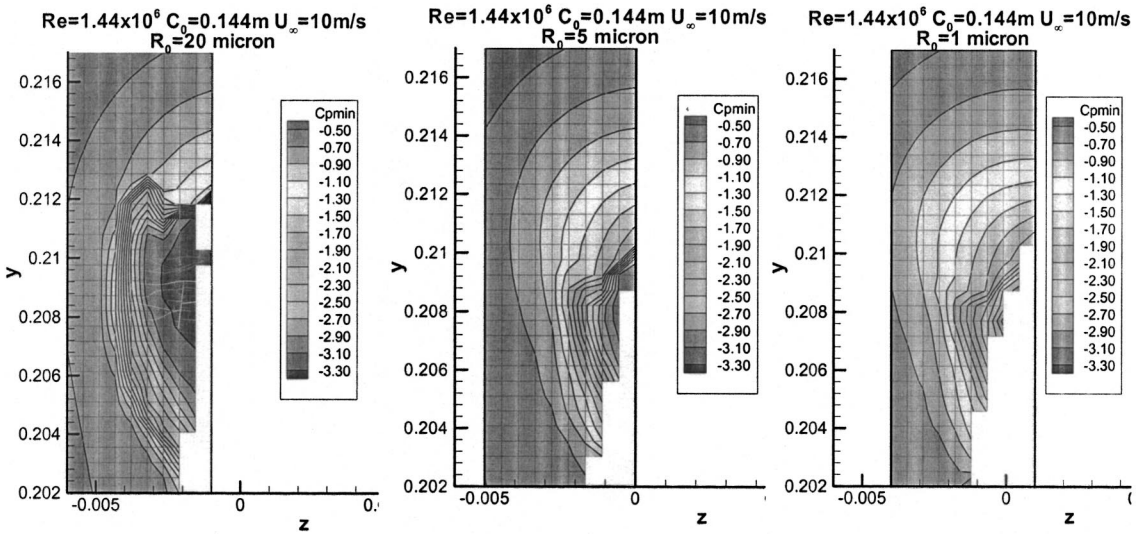

Fig. 6 Contours of the minimum pressure coefficient encountered at high cavitation number for different nuclei size in the small foil scale

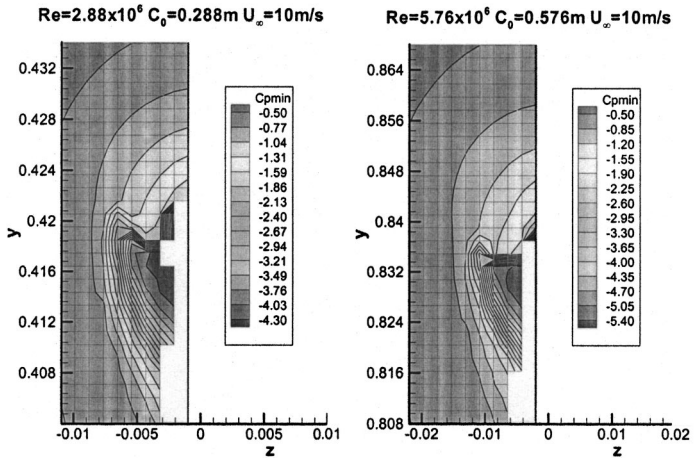

Fig. 7 Contours of the minimum pressure coefficient encountered at high cavitation number for $R_0=20$ μm and for the medium and large foil scale

ranging from 10 to 100 μm for the small scale, 9.2–92 μm for the medium scale, and from 8.5 to 85 μm for the large scale. These curves are used to generate the nuclei field.

With the void fraction and size distribution provided, the total number of nuclei released for each scale is then determined based on the length of signal acquisition time and the size of the release area. To determine an appropriate statistically meaningful observation time we tested two different signal acquisition times $\Delta t = 0.2$ and 1 s. Both cases were conducted for the small scale at cavitation number $\sigma=3.0$. The number of nuclei released and the number of nuclei reaching critical (cavitating) condition versus nuclei size for these two cases are shown in Fig. 9. In this figure a nucleus is considered to be a cavitation bubble when $P_{\text{encounter}} < P_{\text{cr}}$, where the critical pressure is defined as

$$P_{\text{cr}} = p_v - (3k-1)\left(\frac{2\gamma}{3k}\right)^{3k/3k-1}(p_{g0}R_0^{3k})^{-1/3k-1} \qquad (13)$$

with $k=1.4$. Comparison between these two cases shows that the smaller acquisition time only results in a slightly smaller probability for cavitation. Therefore, $\Delta t = 0.2$ second is statistically sufficient and was used for the other tests. For the release window, we consider an area to be large enough to cover the ''windows of opportunity'' for all nuclei sizes released. Here, the size of the release area is specified as 7 mm×5 mm, 14 mm×10 mm, and 28 mm×20 mm for the small, medium, and large scale, respectively. As a result, the number of nuclei in each population is 142, 568, and 2272 for the three scales, respectively.

3.4 Scaling of Cavitation Inception Noise. As nuclei travel in the computational domain, the resulting acoustic pressure is monitored. The acoustic pressure was computed at a location 0.3 m away from the hydrofoil tip for all cases. A series of computa-

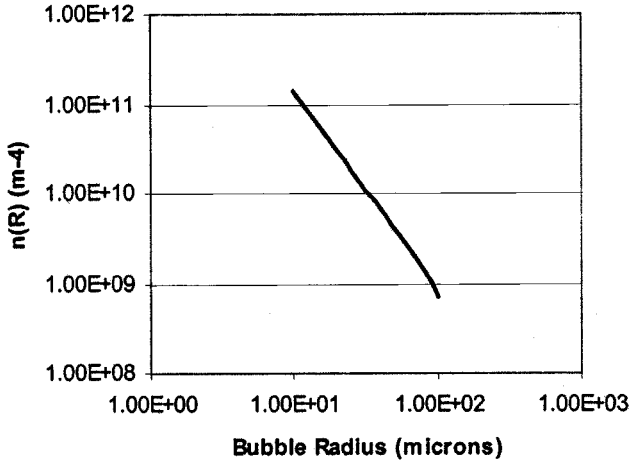

Fig. 8 Nuclei size number density distributions applied at the three scales

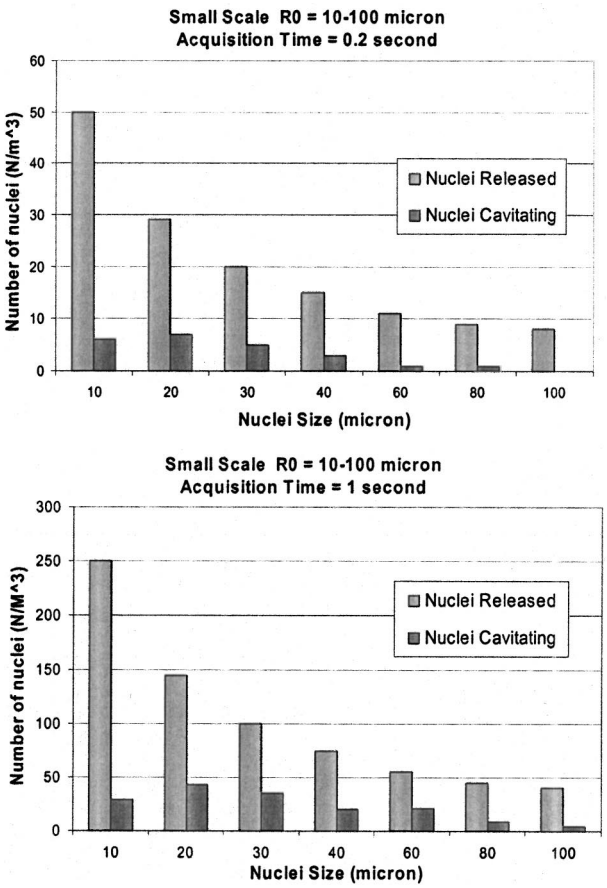

Fig. 9 The number of nuclei released and the number of nuclei reaching critical pressure (cavitating) versus nuclei size obtained at $\sigma=3.0$ for two different acquisition times

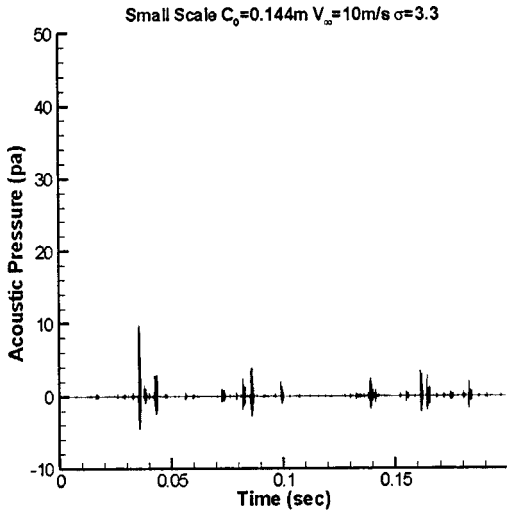

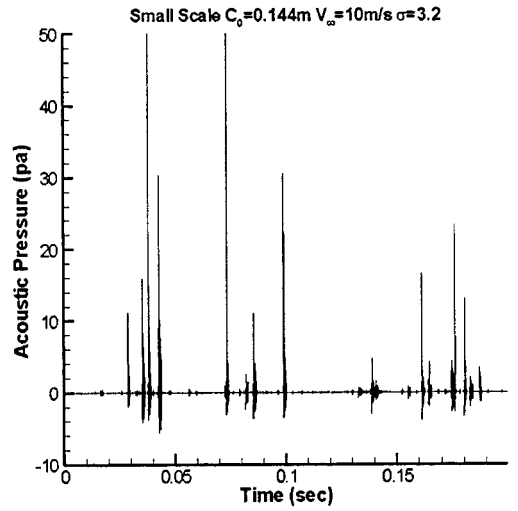

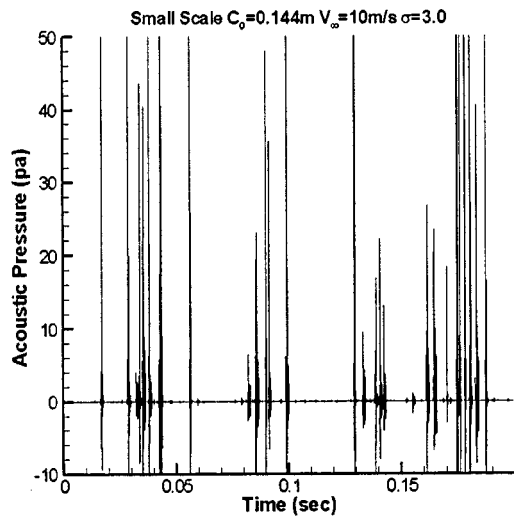

Fig. 10 The acoustic signals for the small scale at three different cavitation numbers

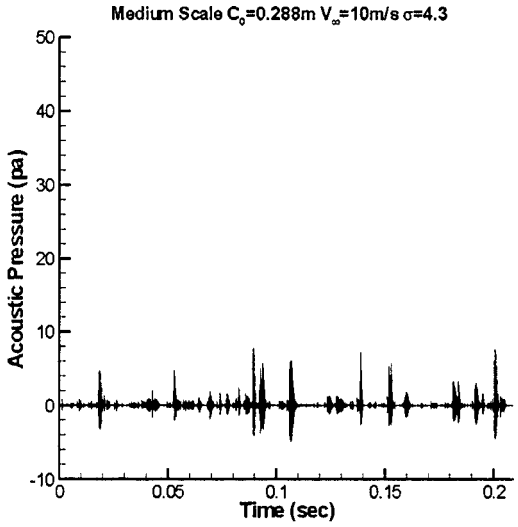

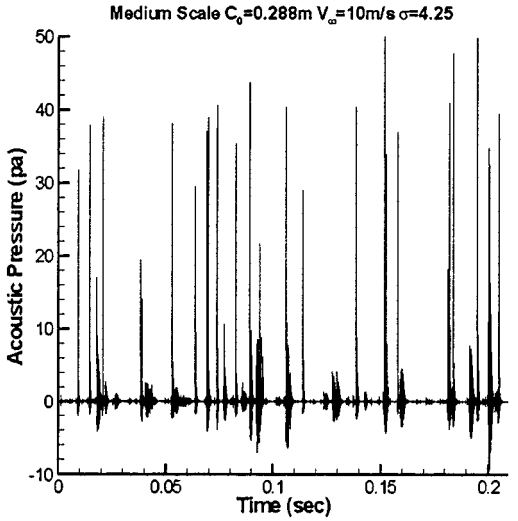

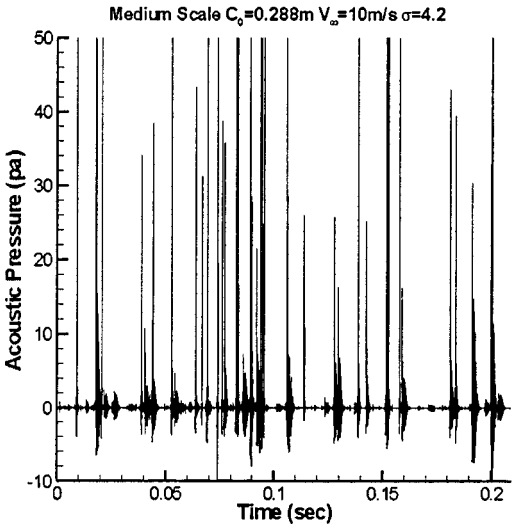

Fig. 11 The acoustic signals for the medium scale at three different cavitation numbers

tions were conducted at different cavitation numbers for the three scales to obtain the acoustic signals for conditions above and below cavitation inception. Figures 10–12 illustrate the acoustic signals for three different scales at three different cavitation numbers. High-level peaks of acoustic signals are clearly seen when the cavitation number is near the cavitation inception number. It is seen that, as expected, for all scales the number of high-level peaks increases as the cavitation number decreases. However, the larger scale is more sensitive to cavitation number changes since

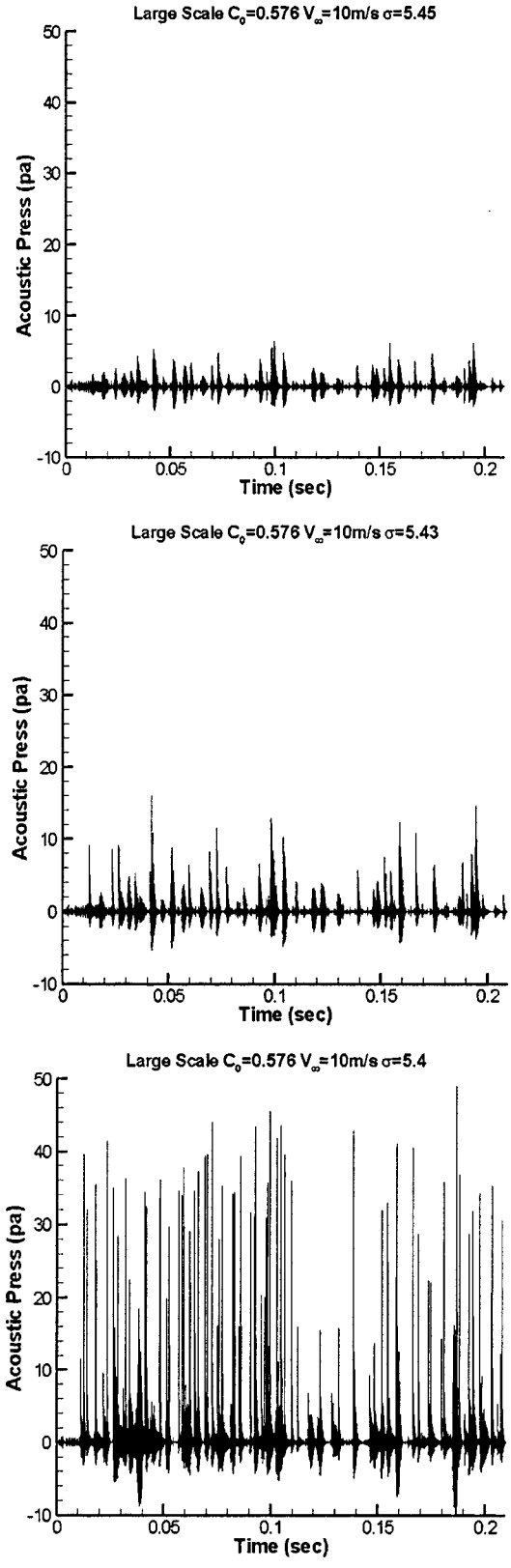

Fig. 12 The acoustic signals for the large scale at three different cavitation numbers

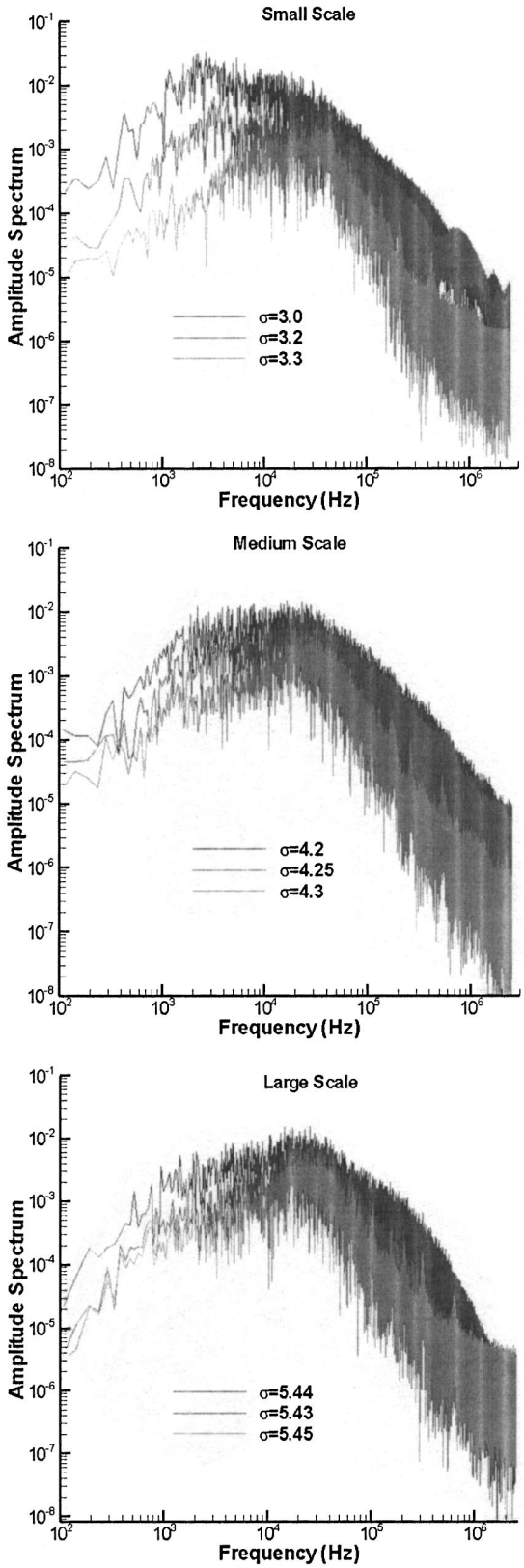

Fig. 13 Amplitude spectra for all three scales at three different cavitation numbers

the number of peaks increases much faster than for the smaller scale as the cavitation number decreases. Figure 13 shows the resulting frequency spectra for the acoustic signals shown in Figs. 10–12. A peak in the frequency range 30–40 kHz is seen at all scales. The amplitude of this peak increases as the cavitation number decreases.

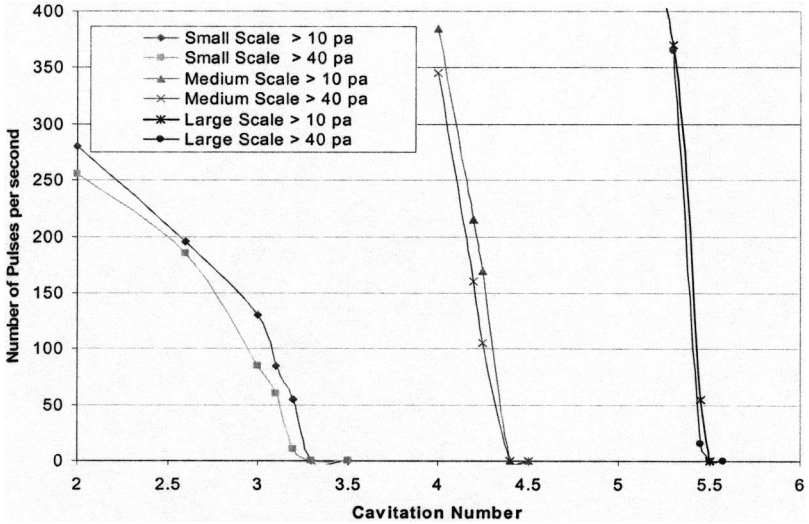

Fig. 14 Number of pressure peaks versus cavitation number deduced at two criteria of acoustic level for the three scales considered

Based on the results shown in Figs. 10–12, we can define a cavitation inception number based on the number of acoustical signal peaks per unit time that exceed a certain level. To deduce the cavitation inception number based on this criterion, a curve for the number of pressure peaks higher than a give acoustic pressure level is created for each cavitation number and for the three scales. Figure 14 shows such curves with two acoustic pressure levels, 10 and 40 Pa, are chosen for each scale. Given a selected criterion based on the number of peaks and acoustic pressure level, one can determine the cavitation inception number from Fig. 14.

The deduced cavitation inception numbers of the three scales for the criteria: 10 peaks/s over 10 Pa and 50 peaks/s over 40 Pa, are shown in Table 2. The deduced cavitation numbers and $-Cp_{\min}$ are fitted with the classical power formula $\sigma_i \propto R_e^{\gamma}$, and the fitted values of γ are also shown in Table 2. It is seen that different criteria for defining the cavitation inception event can lead to different cavitation inception numbers and different scaling laws. The scaling effect due to the nuclei can be demonstrated by comparing the deduced inception number with $-Cp_{\min}$. The results in Table 2 show that cavitation inception scaling deviates more from $-Cp_{\min}$ when the reference inception criterion becomes less stringent (higher reference pressure amplitude and larger number of peaks). Furthermore, the predicted value of γ is closer to the classical value (γ=0.4), as the reference inception criterion becomes less stringent. This agrees with many experimental studies usually established in laboratory conditions where background noise and detection techniques lead to high values of the pressure amplitude for inception detection.

Table 2 Cavitation inception numbers obtained from the numerical study using various criteria, and power law fit deduced from these results

	Numerical computed values for σ_i			R_e^{γ} curve fit	
	Small scale	Medium scale	Large scale	γ	Square of correlation coefficient
$-Cp_{\min}$	3.34	4.34	5.48	0.357	0.999
10 peaks/s over 10 Pa	3.28	4.33	5.47	0.369	0.998
50 peaks/s over 40 Pa	3.12	4.28	5.44	0.401	0.994

3.5 Nuclei Size Distribution Effect. To illustrate how different nuclei size distributions influence the prediction of cavitation inception, a much finer nuclei size distribution ranging from 1 to 10 μm is tested. In the computations the total number of nuclei released in each case was kept the same. This results in a much smaller void fraction ($\alpha \approx 1 \times 10^{-9}$) than in the previous case. Figure 15 shows the acoustical signal obtained at σ=3.0 and the number of nuclei cavitating for each prescribed nuclei size is shown in Fig. 16. It is seen that, as expected, the number of peaks is dramatically reduced for the smaller nuclei size range when comparing the results to those of the larger nuclei size range. That is because as shown in Fig. 16 near inception the nuclei contributing to the high-level peaks are only the larger bubble sizes.

A series of computations were also conducted at different cavitation numbers for the small and the large scale with the smaller

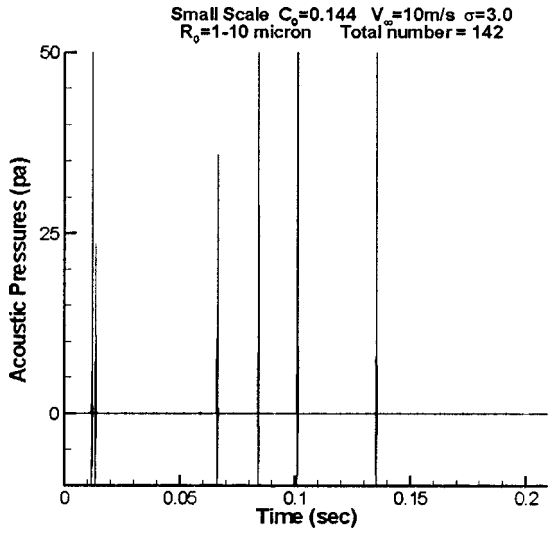

Fig. 15 The acoustic signals for the small scale at σ=3.0 using the smaller nuclei size range (1–10 μm)

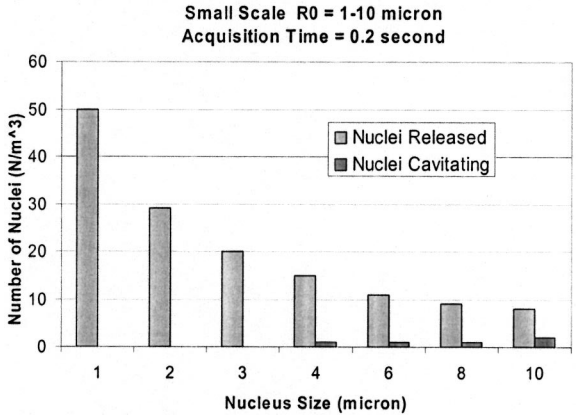

Fig. 16 The number of nuclei released and the number of nuclei cavitating versus nuclei size obtained for the 1–10 μm small nuclei size distribution at σ=3.0

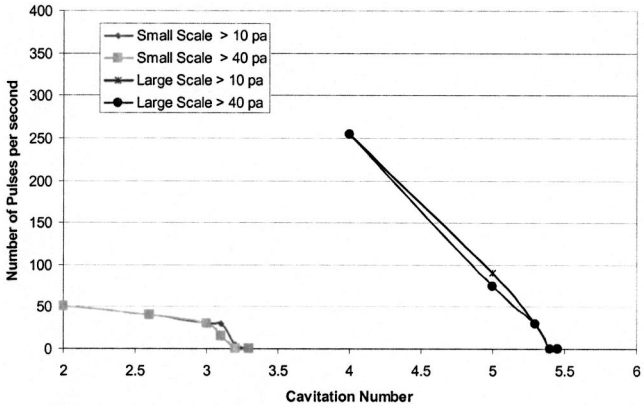

Fig. 17 Number of pressure peaks versus cavitation number deduced at two criteria of acoustic level for the small and large scales considered

Table 3 Cavitation inception numbers obtained from the numerical study using various criteria, and power law fit deduced from these results. For smaller void fraction ($\alpha \approx 1\times10^{-9}$).

	Numerical computed values for σ_i		R_e^γ curve fit γ
	Small Scale	Large Scale	
$-Cp_{\min}$	3.34	5.48	0.357
10 peaks/s over 10 Pa	3.20	5.40	0.377
50 peaks/s over 40 Pa	2.0	5.18	0.687

nuclei size range. Two acoustic pressure levels, 10 and 40 Pa, are also selected to determine the number of pressure peaks for each cavitation number. The resulting curves of number of pressure peaks versus cavitation numbers for the small and large scales are shown in Fig. 17. The deduced cavitation inception numbers are shown in Table 3. By comparing with Table 2 we can see very important differences for the small scale when the cavitation inception criteria are less stringent. Also, scaling effects and deviation from classical formula due to nuclei size distribution are seen to significantly increase when nuclei sizes (or void fraction) decreases.

4 Conclusions

The study of the behavior of a realistic distribution of nuclei in the tip vortex flow field of a NACA16020 foil at three scales has enabled observation of several effects:

1. Comparison of the size of the bubble capture area or ''window of opportunity'' at the various scales shows that the larger scale results in more cavitation events by allowing more nuclei per unit time to be captured by the tip vortex;
2. the numerical results show that different criteria for defining the cavitation inception can lead to a different cavitation inception numbers as well as different scaling laws. By comparing the predicted cavitation inception number with $-Cp_{\min}$, we found that scaling effects (i.e., deviation from $-Cp_{\min}$) due to nuclei increase as the reference inception criteria become less stringent (higher reference pressure amplitude and larger number of peaks);
3. the predicted value of γ in the power formula ($\sigma_i \propto R_e^\gamma$) is closer to the classical value (γ=0.4), as the reference inception criterion becomes less stringent;
4. the range of nuclei sizes was shown to have an important effect on the prediction of cavitation inception. Differences between predicted cavitation inception number and $-Cp_{\min}$ increase as nuclei sizes (or void fractions) decrease. This implies that scaling effects due to nuclei size distribution are stronger when the water contains only small nuclei (or for low void fraction).

Acknowledgments

This work was conducted at Dynaflow, Inc. (www.dynaflow-inc.com) and has been supported by the Naval Surface Warfare Carderock Division and the Office of Naval Research. This support of Dr. Ki-Han Kim, ONR, and Dr. Young Shen, NSWCCD, is greatly appreciated.

References

[1] McCormick, B. W., 1962, ''On Cavitation Produced by a Vortex Trailing From a Lifting Surface,'' ASME J. Basic Eng., **84**, pp. 369–379.
[2] Fruman, D. H., Dugue, C., Pauchel, A., and Cerrutti, P., 1992, ''Tip Vortex Roll-Up and Cavitation,'' *Eighteenth Symposium on Naval Hydrodynamics*, Seoul, Korea.
[3] Arndt, R. E., and Dugue, C., 1992, ''Recent Advances in Tip Vortex Cavitation Research,'' *Proc. International Symposium on Propulsors Cavitation*, Hamburg, Germany, pp. 142–149.
[4] Farrell, K. J., and Billet, M. L., 1994, ''A Correlation of Leakage Vortex Cavitation in Axial-Flow Pumps,'' ASME J. Fluids Eng., **116**, pp. 551–557.
[5] Maines, B., and Arndt, R., 1997, ''Tip Vortex Formation and Cavitation,'' ASME J. Fluids Eng., **119**, pp. 413–419.
[6] Arndt, R. E. A., 2002, ''Cavitation in Vertical Flows,'' Annu. Rev. Fluid Mech., **34**, pp. 143–175.
[7] Copalan, S., Liu, H. L., and Katz, J., 2000, ''On the Flow Structure, Tip Leakage Cavitation Inception and Associated Noise,'' 23rd Symposium on Naval Hydrodynamics.
[8] Hsiao, C.-T., Chahine, G. L., and Liu, H. L., 2003, ''Scaling Effects on Prediction of Cavitation Inception in a Line Vortex Flow,'' ASME J. Fluids Eng., **125**, pp. 53–60.
[9] Ligneul, P., and Latorre, R., 1989, ''Study on the Capture and Noise of Spherical Nuclei in the Presence of the Tip Vortex of Hydrofoils and Propellers,'' Acustica, **68**, pp. 1–14.
[10] Hsiao, C.-T., and Pauley, L. L., 1999, ''Study of Tip Vortex Cavitation Inception Using Navier–Stokes Computation and Bubble Dynamics Model,'' ASME J. Fluids Eng., **121**, pp. 198–204.
[11] Hsiao, C.-T., and Chahine, G. L., 2004, ''Prediction of Vortex Cavitation Inception Using Coupled Spherical and Nonspherical Models and UnRANS Computations,'' J. Marine Sci. Technol., **8**, No. 3, pp. 99–108.
[12] Arndt, R. E. A., and Maines, B. H., 2000, ''Nucleation and Bubble Dynamics in Vortical Flows,'' ASME J. Fluids Eng., **122**, pp. 488–493.
[13] Hsiao, C.-T., and Pauley, L. L., 1999, ''Study of Tip Vortex Cavitation Inception Using Navier–Stokes Computation and Bubble Dynamics Model,'' ASME J. Fluids Eng., **121**, pp. 198–204.
[14] Hsiao, C.-T., and Pauley, L. L., 1998, ''Numerical Study of the Steady-State Tip Vortex Flow Over a Finite-Span Hydrofoil,'' ASME J. Fluids Eng., **120**, pp. 345–349.
[15] Hsiao, C.-T., and Pauley, L. L., 1999, ''Numerical Calculation of Tip Vortex Flow Generated by a Marine Propeller,'' ASME J. Fluids Eng., **121**, pp. 638–645.
[16] Taylor, L. K., Pankajakshan, R., Jiang, M., Sheng, C., Briley, W. R., Whitfield, D. L., Davoudzadeh, F., Boger, D. A., Gibeling, H. J., Gorski, J., Haussling,

H., Coleman, R., and Buley, G., 1998, ''Large-Scale Simulations for Maneuvering Submarines and Propulsors,'' AIAA Paper 98-2930.
[17] Chorin, A. J., 1967, ''A Numerical Method for Solving Incompressible Viscous Flow Problems,'' J. Comput. Phys., **2**, pp. 12–26.
[18] Roe, P. L., 1981, ''Approximate Riemann Solvers, Parameter Vectors, and Difference Schemes,'' J. Comput. Phys., **43**, pp. 357–372.
[19] van Leer, B., 1979, ''Towards the Ultimate Conservative Difference Scheme V. A Second Order Sequel to Godunov's Method,'' J. Comput. Phys., **32**, pp. 101–136.
[20] Vanden, K., and Whitfield, D. L., 1993, ''Direct and Iterative Algorithms for the Three-Dimensional Euler Equations,'' AIAA-93-3378.
[21] Chahine, G. L., Kalumuck, K. M., Cheng, L.-Y., and Frederick, G., 2001, ''Validation of Bubble Distribution Measurements of the ABS Acoustic Bubble Spectrometer With High Speed Video Photography,'' *4th International Symposium on Cavitation*, California Institute of Technology, Pasadena, CA.
[22] Johnson, V. E., and Hsieh, T., 1966, ''The Influence of the Trajectories of Gas Nuclei on Cavitation Inception,'' *Sixth Symposium on Naval Hydrodynamics*, pp. 163–179.
[23] Haberman, W. L., and Morton, R. K., 1953, ''An Experimental Investigation of the Drag and Shape of Air Bubbles Rising in Various Liquids,'' Report 802, DTMB.
[24] Fitzpatrick, N., and Strasberg, M., 1958, ''Hydrodynamic Sources of Sound,'' *2nd Symposium on Naval Hydrodynamics*, pp. 201–205.
[25] Dacles-Mariani, J., Zilliac, G. G., Chow, J. S., and Bradshaw, P., 1995, ''Numerical/Experimental Study of a Wingtip Vortex in the Near Field,'' AIAA J., **33**, No. 9, pp. 1561–1568.
[26] Billet, M. L., 1984, ''Cavitation Nuclei Measurements,'' *International Symposium on Cavitation Inception*, FED-Vol. 16, pp. 33–42.
[27] Franklin, R. E., 1992, ''A Note on the Radius Distribution Function for Microbubbles of Gas in Water,'' *ASME Cavitation and Mutliphase Flow Forum*, FED-Vol. 135, pp. 77–85.

Fundamental Analysis of the Secondary Flows and Jet-Wake in a Torque Converter Pump—Part I: Model and Flow in a Rotating Passage

R. Flack
Mechanical and Aerospace Engineering,
University of Virginia,
Charlottesville, VA 22903-2442
e-mail: rdf@virginia.edu

K. Brun
Southwest Research Institute,
San Antonio, TX 78238
e-mail: klaus.brun@swri.org

Previously, experimental results for the velocity field in a torque converter pump showed strong jet/wake characteristics including backflows and circulatory secondary flows. To understand the fundamental flow behavior simplified analytical/numerical Navier-Stokes flow models were developed herein to independently analyze the pump pressure-to-suction side jet/wake flow, the core-to-shell side jet/wake flow, and the secondary flows. Parametric studies were undertaken to evaluate the effect that operating conditions and geometry had on the characteristics. Two relatively simple models were employed: (i) a rotating two-dimensional straight-walled duct to model the pressure-to-suction side jet/wake flow due to rotational Coriolis forces and (ii) a 180 deg flow bend to model the core-to-shell side jet/wake flow due to rapid radial/axial flow turning. The formation and development of the pump jet/wake flow was studied in detail. Results showed that the suction side wake, which was due to the counter-rotational tangential Coriolis force, was almost only a function of the modified Rossby number and independent of the Reynolds number. Increasing the modified Rossby number increased the pressure-to-suction side jet/wake flow. A geometric parameter that was seen to affect the pump flow was the backsweeping angle for the pressure-to-suction side jet/wake. Results showed that using backswept blades can completely eliminate the pressure-to-suction side jet/wake flow effect. Other geometrical parameters were tested but only a small to moderate influence on the jet/wake flow phenomena was found. Predicted trends compared favorably with experimental results.
[DOI: 10.1115/1.1852485]

Introduction

Torque converters are an important part of automatic transmissions in automobiles and other vehicles. The smooth transmission of torque between the engine and the wheels is provided and torque amplification at low speeds is accomplished with the device. A pump, a turbine, and a stator all are a part of a torque converter. The working fluid in the closed system is light oil. The pump, which in many ways acts as a centrifugal pump energizes the fluid, while the turbine extracts energy from the fluid. Ideally an incidence free flow into the pump inlet blades is provided by the stator.

The design of a torque converter is quite complex due to a number of conditions. First, the torque converter should exhibit high efficiencies over a range of operating conditions. Unfortunately, over the typical operating range, the flow field changes drastically; for example, incidence flow angles to all of the component blades change drastically. Second, the flow is turned in the passages in two directions. The flow is also turned in the transverse direction in both the pump and turbine, usually in a short distance; namely, flow enters these components in the axial direction, rapidly is turned to the radial direction, and rapidly turned into the reverse axial direction, leading to further separation. The torque converter pump is, therefore, a complex mixed-flow variety of hydraulic turbomachine with a variety of forces acting on the fluid particles.

Fister and Adrian [1] used the laser-two-focus method to measure flows in a large-scale industrial water torque converter and used a spark tracer method in an air torque converter. Hot film anemometry was utilized by Browarzik [2] to examine the flow details of the periodic pump-turbine interaction at the inlet and outlet of a pump and turbine of a torque converter. Flow visualization and laser velocimetry was used by Watanabe et al. [3] to study the flow in stator passages for different vane thicknesses. They found that the flow was nonuniform and separated regions were present regardless of the test conditions. Vane thickness was found to affect the flow fields.

Ejiri and Kubo [4] investigated the hydraulic performance of a torque converter using a five-hole Pitot tube. Results indicated that the pump is a major source of loss at the most frequently utilized speed ratio range. Flow visualization and a three-dimensional flow analysis was used to investigate the cause of the losses in the pump.

Average static pressures on the blades of a 230 mm diameter torque converter stator and pump were measured by By and Lakshminarayana [5]. The static pressure distribution was shown to be generally poor at the blade core section and that centrifugal force has a dominant effect on the static pressure rise in the pump. Furthermore, potential flow theory can approximately predict the static pressure distribution at the blade midspan, but not at the core and shell sections. A three-dimensional, incompressible, viscous Navier-Stokes code was developed by By et al. [6] to predict the flow field of this torque converter pump. Pump rotation had an effect on the secondary flow field. Pressures at the inlet and exit of the torque converter stator were measured by Marathe et al. [7] using a fast response five-hole probe and embedded transducers in the stator vanes. Large secondary flows were observed at the stator exit. Also, the separated flow near the stator shell side was

Contributed by the Fluids Engineering Division for publication on the JOURNAL OF FLUIDS ENGINEERING. Manuscript received by the Fluids Engineering Division September 11, 2003; revised manuscript received September 7, 2004. Review Conducted by: J. Lee.

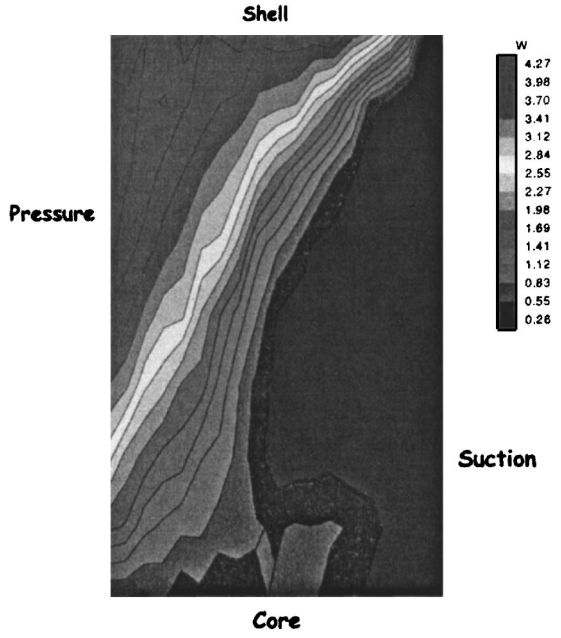

Fig. 1 Midplane through flow velocities, SR=0.800

observed. Predictions from a Navier-Stokes code and the pressure measurements were in good agreement. The five hole probe was used by Dong et al. [8] to investigate the unsteady flow fields at the turbine and pump exits of a larger (245 mm diameter) torque. Jet, wake, secondary flows, and mixing regions were identified.

Bahr et al. [9] employed a complete (pump/turbine/stator) 230 mm diameter torque converter that was designed for optical access and a laser velocimeter to obtain detailed velocity profiles in five planes in the stator. The flow was cavitation and air free. Gruver et al. [10] used the same experimental facility to measure velocities in three planes in the torque converter pump for two turbine/pump speed ratios. In general the flow was measured to be relatively uniform from pressure surface to suction surface at the pump inlet. From shell surface to core surface the flow again was measured to be relatively uniform at the inlet except near the core. Brun and Flack [11] measured velocities in four planes in the torque converter turbine and data was complimented by additional stator data by Ainley and Flack [12]. Whitehead [13], Yermakov [14], and Claudel [15] used a series of larger (245 mm diameter) torque converter to study the average and unsteady flows in the pump, turbine and stator for three speed ratios. Schweitzer and Gandham [16] successfully modeled the characteristics of the flow using a full three-dimensional (3D) CFD solution for the larger converter, but did not identify the fundamental dependence of the flow field on geometric parameters. For all of the earlier efforts strong secondary flows and large jet and separated regions were identified for a variety of operating conditions in particularly the pump and stator.

Motivations and Objectives of the Current Research. Great strides have been made over the past few years in CFD predictions and experimental data, but the analyses as applied to the torque converter has not yet been applied providing fundamental insights into the complex flow behavior. Although the torque converter is one of the most complex turbomachines, the fundamental fluid dynamic aspects of the machine have not received due attention. The current fundamental understanding of the internal flow fields of torque converters over a range of geometries and conditions is inadequate.

For example, in Fig. 1 the pump midplane through flow velocities at a turbine/pump speed ratio of 0.800 are presented from Gruver et al. [10]. As can be seen, a large velocity is present in the pressure-shell corner of the passage. However, a very large separation region is observed in the suction-core corner. Although some success has been demonstrated in prediction such flows, an explanation for the development and variations from section to section has not yet been postulated.

For this paper a CFD analysis was performed in which the different driving mechanisms were separated to provide a better understanding of the complex nature of the secondary flows and separated regions. In particular, the Coriolis and centrifugal forces were independently varied to ascertain the relative importance of such terms. Furthermore, a number of other parameters were varied to determine their importance, including, blade angles, number of blades, passage length, and radius. Previous to this study the different mechanisms had not been separated to ascertain the magnitude and significance of the different effects on the jet-wake and secondary flows.

Modeling

Description of jet/wake flow development was given by Dean and Senoo [17], Eckardt [18], and Johnson and Moore [19] for centrifugal impellers and is applicable to a torque converter pump: (1) Coriolis forces in the counter-rotational tangential direction enhance boundary layer growth on the suction side of the blade passage and suppress boundary layer growth on the pressure side. (2) Flow at the passage core (hub) side separates because of rapid radial/axial flow turning. (3) The expanded suction side boundary layer and the core side separation shift higher kinetic energy fluid toward the pressure/shell sides to form a jet. (4) A large wake forms when the suction side boundary layer and core side separation combine.

The location of the jet and wake are primarily a function of the relative influence of the rotation and turning on the fluid flow. This influence is typically expressed as a function of the Rossby number

$$\mathrm{Ro} = \frac{\text{inertial Force}}{\text{coriolis Force}} \sim \frac{(\rho V^2)/r}{\rho \omega V} = \frac{V}{\omega r}, \tag{1}$$

where r is the radius of curvature of the pump blade passage. Although the force vectors between inertial and Coriolis force are at a 90 deg angle, usage of the Rossby number allows for a generalized analysis of their relative influence on the flow field in the rotating frame as both forces have a direct influence on the development of boundary layer growth jet/wake flow. For example, for low Rossby number impeller flows ($\mathrm{Ro} \ll 1$) the rotational Coriolis force (in the counter-rotational tangential direction) dominates and, thus, the suction side boundary layer growth contributes more to the wake flow than the core separation. The jet and wake will be located directly at the pressure and suction sides, respectively. On the other hand, for very high Rossby numbers ($\mathrm{Ro} \gg 1$) the core side separation due to rapid radial/axial flow turning dominates and the jet and wake will be located directly at the shell and core (hub) sides, respectively. For the efforts here Rossby numbers are relatively close to unity (similar influence of curvature and rotation) and, thus, the jet and wake should be located at the pressure/shell corner and suction/core corner, respectively. This is confirmed by experimental observations in Gruver et al. [10].

Hence, the development of the jet/wake flow can be modeled to be primarily a function of two separate and independent flow phenomena: (i) Suction side separation due to the rotational Coriolis force and (ii) core side separation due to the rapid radial/axial flow turning (see Fig. 2). Each of these simple flow phenomena can be solved individually using a two-dimensional (2D) viscous flow solver. Consequently, a commercially available flow solver was employed to simulate (i) flow in a 2D rotating straight-walled duct to study the suction side separation—part 1 of this paper and (ii) flow in a stationary 180 deg bend to study the coreseparation—part II of this paper. The geometries of the straight-walled duct and the 180 deg bend are shown in Fig. 3 and

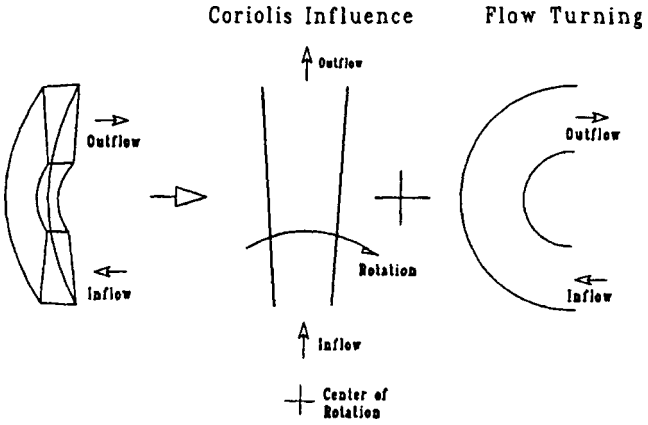

Fig. 2 Two-dimensional flow models

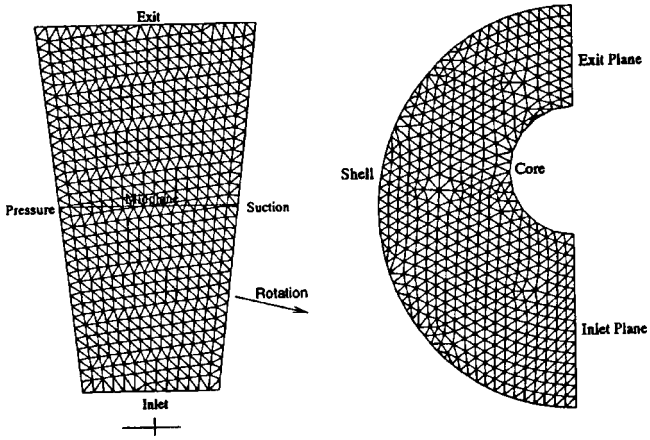

Fig. 4 Finite element mesh

the geometry used by Gruver et al. [10] is used as the nominal geometry. This simplified model is not intended to predict the flow field at high accuracy. Superposition of the two solutions will not accurately predict the total flow field. As noted earlier, Schweitzer and Gandham [16] successfully modeled the characteristics of the flow using a full 3D CFD solution for a larger torque converter. Rather, the solution of the two different geometries and thus division of the contributions of the separate force components allows for an improved fundamental understanding of the individual influences of the forces on the resulting flow field, which is *not* possible with a full 3D solution because all of the forces are present. Separation of the two solutions allows for trend studies to, for example, identify the independent relative contributions of flow turning and rotation on the resulting secondary flows. A number of other trend studies are possible that are not possible with a full 3D solution.

A numerical approach is required to obtain solutions for the two flow models (rotating straight-walled duct and 180 deg stationary bend) described earlier. For the work described in this dissertation, FlowPlus™ [20] a commercially available, finite element, full Navier-Stokes equation solver was employed. A two equation K-ϵ model is used to determine the turbulent flow eddy viscosity and the ''Law of the Wall'' is enforced to obtain the turbulent boundary layer flow profile. The nonlinear advection terms are treated using a monotone streamline upwind method (Rice and Schnipke [21]).

An unstructured finite element mesh with uniform triangular elements was used. For the straight-walled duct flow 600 nodes with 1096 triangular elements and for the 180 deg bend 556 nodes with 2008 triangular elements were employed (Fig. 4). For both models finer meshes with 4024 (3062 nodes) and 6662 (2738 nodes) elements, respectively, were also used to test for a mesh dependence in the solution. The finer mesh yielded the same solutions and, hence, the coarse mesh was used for all subsequent studies. Also, for the stationary 180 deg bend flow, axis-symmetry about the shaft centerline was assumed.

Based on the measurements from Gruver et al. [10] and to maintain the fundamentality of the studies, the boundary conditions that were applied on the inlet and exit nodes were a uniform inlet throughflow profile (vorticity free) and a constant exit pressure, respectively. Inlet velocities were based on the plane-averaged experimental values. Also, the constant pressure boundary condition was applied sufficiently far downstream from the pump exit plane so that it did not affect the pump flow field directly.

The total accuracy of a CFD solution is difficult to determine because of the nonlinear nature of the governing equations, the turbulence model assumptions, and the application of the law of the wall. In general a CFD solver's accuracy is assessed by benchmarking numerical solutions with experimental results. The CFD code employed for the subject study was compared to experimental data from the public domain for a wide range of applications and numerical solution were found to be consistently within 5% of experimental data (Flowplus [20]). Within the total accuracy of the CFD solution the numerical uncertainty is generally small if the solution is properly converged and an adequate mesh density is employed. To limit this numerical uncertainty the following steps were performed: The progress of the solution was monitored by observing the norm of the equation residuals; when the residual norm of the equation was below 10E−4, the solution was considered converged. For each numerical solution the inlet/exit mass balance was checked and the solution was rejected if the balance difference exceeded 0.1%. To test for mesh dependence of the solution a model with a finer mesh of about four times the number of elements was tested. The finer mesh yielded the same solutions and, hence, the coarse mesh was employed for all subsequent studies.

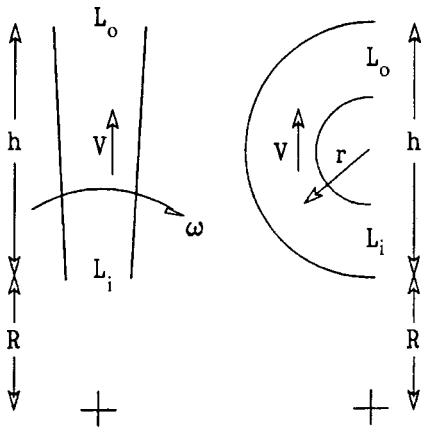

Fig. 3 Model dimensions

Relevant Non-Dimensional Parameters. Dimensional analysis shows that there are two force parameters and three geometrical parameters that are directly relevant for the jet/wake phenomenon in the pump. These parameters can be divided into non-dimensional force parameters, based on viscous, inertial, centrifugal, and Coriolis forces, and nondimensional length scales, based on the geometry of the pump. Table 1 shows the relevant non-dimensional parameters for the two simplified flows (straight-walled rotating duct and 180 deg stationary bend), which are necessary to model the jet/wake phenomena.

In Table 1 V_i is the pump inlet velocity (in the radial direction for the straight-walled duct and in the axial direction for the 180

Table 1 Jet/wake nondimensional parameters

RotatingDuct	180° Stationary Bend
Force Parameters	
Reynolds Number = $\rho V_i R/\mu$	Reynolds Number = $\rho V_i R/\mu$
Modified Rossby Number = $\omega R/2V_i$	
Geometric Parameters	
L_i/R	L_i/R
L_o/R	L_o/R
h/R	h/R = 2r/R

deg bend), r is the radius of curvature of the pump blade-passage centerline, R is the mean radius between pump inlet and the shaft centerline (radius of rotation), L_i is the inlet length, L_o is the outlet length, and h is the passage length. One should note that for the rotating duct flow both the Reynolds number and the modified Rossby number, Ro_m, appear, while for the 180 deg bend flow only the Reynolds number is present. Also, the modified Rossby number ($\omega R/2V_i$) is in actuality the ratio of centrifugal force/coriolis force.

Flow in a Straight-Walled Rotating Section

Pressure-to-Suction Side Separation and Jet/Wake Flow Due To Coriolis Force. The jet/wake phenomenon in the suction-to-pressure side direction of the torque converter pump is primarily driven by boundary layer growth due to rotational Coriolis force. The Coriolis force per volume, F_C, on a moving fluid in a rotating frame is given by

$$F_C = 2\rho\omega V, \tag{2}$$

where F_C acts in the counter-rotational tangential direction. Here V is the outward radial velocity component and ω is the rotation of the reference frame (the pump in this case). Equation (2) shows that, since F_C is a function of V, for a nonuniform radial velocity profile ($\partial V/\partial\theta \neq 0$) the Coriolis force tends to amplify the nonuniformity of the flow ($\partial F_C/\partial\theta \neq 0$). On the other hand if the radial flow is perfectly uniform ($\partial V/\partial\theta = 0$) then the Coriolis force will act uniformly on all the fluid at a fixed radial distance ($\partial F_C/\partial\theta = 0$). Consequently, the more nonuniform the flow enters a rotating element, the stronger will be the jet/wake effect due to the Coriolis force.

As the flow enters the torque converter pump, boundary layer flow develops on both the pressure and suction sidewalls. On the pressure side the Coriolis force tends to suppress boundary layer growth by forcing tangential secondary flow towards the pressure side wall (Fig. 5), while on the suction side the Coriolis force tends to increase the boundary layer growth by forcing tangential secondary flow away from the suction sidewall Hence, a wake forms on the suction side and a jet forms on the pressure side. To quantify this pump pressure-to-suction side jet/wake flow phenomenon, the viscous flow solver was employed to obtain numerical solution for the simple rotating straight-walled duct flow model.

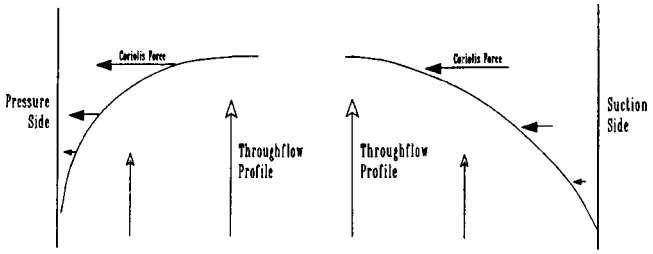

Fig. 5 Pressure and suction side coriolis forces

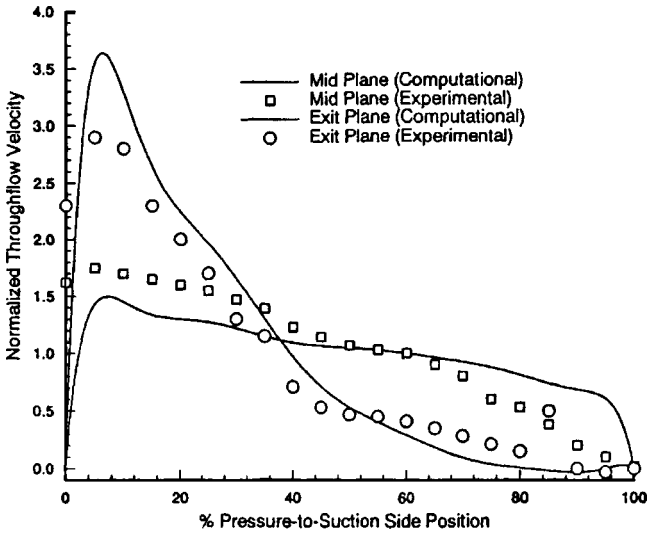

Fig. 6 Mid- and exit plane velocity profiles, SR=0.80

The torque converter pump geometry at the 0.065 and 0.800 speed ratio operating conditions was analyzed but only results for SR=0.800 are presented. Figure 6 shows the nondimensional throughflow profiles (nondimensionalized by the plane-averaged throughflow velocity, V_{ave}) at the mid and exit planes for the 0.800 speed ratio case ($\omega_p = 1100$ rpm$= 115.19$ rad/s, $V_i = 1.442$ m/s, $\mathrm{Ro}_m = 2.661$, $\mathrm{Re} = 5055$). A strong jet with peak velocities of ~ 3.5 (in the exit plane) is located directly at the pressure side and a wake region with reversed flow velocities of ~ -0.1 is located on the suction side. The numerically predicted jet/wake effect is seen to be significantly stronger in the exit plane than in the midplane. As a comparison, the experimental throughflow profiles (nondimensionalized and core-to-shell averaged) for the earlier measurement conditions are also included on the plot. The computational flow solver underpredicts the jet/wake flow in the mid plane and overpredicts it in the exit plane. The wake area for this case is larger than for the 0.065 speed ratio case.

To quantitatively evaluate the influence of the jet/wake phenomenon on the pump flow field a number of relevant jet/wake flow parameters were calculated from the computational rotating straight-walled duct (radial passage) results. For example, the wake area was calculated as a percentage of the entire passage cross-sectional area. The wake area is defined as the area in which the throughflow velocity is below the average passage throughflow velocity. Finally, the normal component of the average flow vorticity, ξ_n, which is necessary for a secondary flow analysis was determined from the results as follows:

$$\xi_n = -\frac{1}{A}\int\int(\nabla\times V)\cdot dA = -\frac{1}{A}\int\int\left(\frac{\partial v}{\partial x}-\frac{\partial u}{\partial y}\right)dA, \tag{3}$$

where V is the total velocity vector, A is the plane area perpendicular to the normal direction, and u and v are the local Cartesian velocity components in the rotating frame. The average vorticity expression can be discretized as follows:

$$\xi_n = -\frac{1}{A}\sum\sum\left(\frac{v_{i+1}-v_i}{x_{i+1}-x_i}-\frac{u_{j+1}-u_j}{y_{j+1}-y_j}\right)\cdot(x_{i+1}-x_i)\cdot(y_{j+1}-y_j), \tag{4}$$

where x and y are the local Cartesian directions. The expression was evaluated by integrating the velocity results across two adjacent computational planes.

Parametric Study of Nondimensional Force Parameters. Computational parametric studies are performed to evaluate the relative influence of the nondimensional quantities on the torque

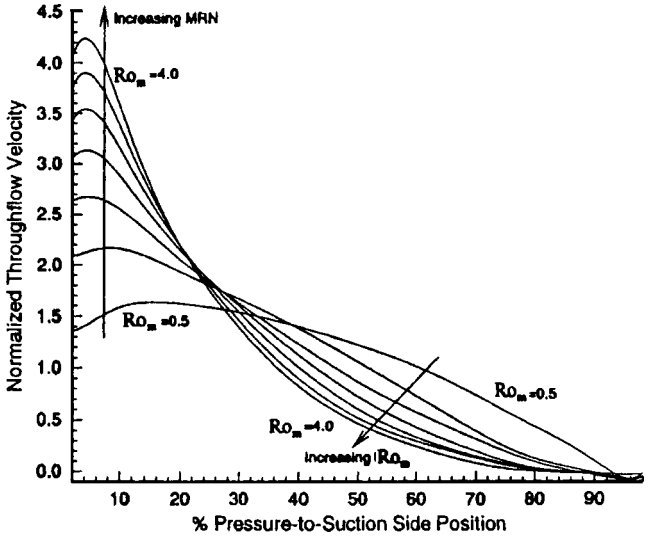

Fig. 7 Nondimensional exit velocity profiles—7 Ro_m's

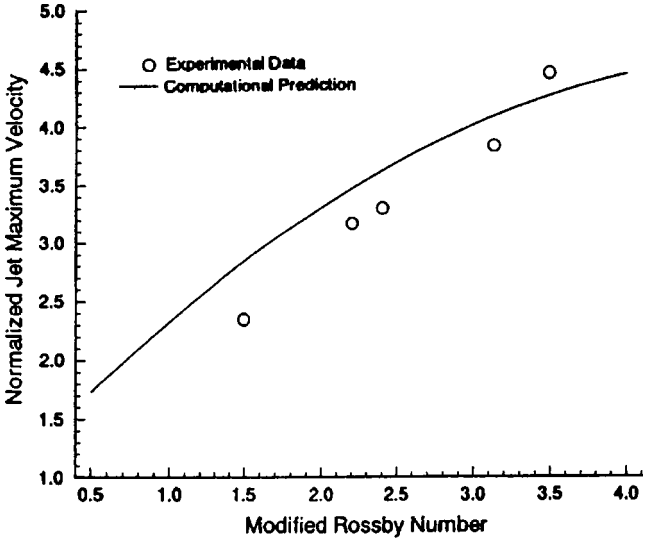

Fig. 8 Nondimensional exit jet velocities

converter pump pressure-to-suction side jet/wake flow from the simplified rotating straight-walled duct flow model. Of particular interest is the effect on the flow field of varying the nondimensional force parameters: the Reynolds number and the modified Rossby number. To vary these two parameters independently, only the rotational speed, ω_p, (for Ro_m) and the working fluid's viscosity, μ, (for Re) are changed.

During an actual automotive torque converter operation these two nondimensional parameters are in a constant state of flux; namely, as the speed ratio and the input speed (pump speed) of the torque converter changes, the modified Rossby number and the Reynolds number will also change significantly. Hence, the influence of these two quantities over a range of realistic operating conditions is discussed.

Modified Rossby Number. The modified Rossby number, Ro_m, given by

$$Ro_m = \frac{\omega R}{2V_i} \tag{5}$$

and is a measure of the relative influence of the centrifugal force (in the outward radial direction) versus the Coriolis force (in the counter-rotational tangential direction). As such, a strong correlation between the modified Rossby number and the rotating straight-walled flow passage jet/wake parameters is expected. To evaluate this correlation, the modified Rossby number was varied between 0.5 and 4.0 (this corresponds approximately to a pump rotational speed range from 140 to 1200 rpm for the 0.800 speed ratio) while the Reynolds number ($Re = \rho V_i R/\mu$) was fixed. This study was repeated for Reynolds numbers ranging from 1000 to 12,000. The geometry used for all parametric studies was the torque converter pump with $R = 0.0661$ m, $h = 0.04061$ m, $L_i = 0.0155$ m, $L_o = 0.02496$, and $r = 0.0203$ m.

Figure 7 shows predicted exit plane non-dimensional throughflow profiles as a function of the modified Rossby number at a Reynolds number of 3000. The trends indicate an increasing pressure-to-suction side jet/wake flow with an increasing modified Rossby number. To quantify this observation, the exit plane jet/wake parameters such as peak jet velocity, wake area, and normal vorticity component are plotted as a function of modified Rossby number in Figs. 8–10. Also, experimental results for these parameters are included on these plots for the limited number of experimental conditions tested.

Figure 8 shows the nondimensionalized peak jet velocity versus the modified Rossby number. The nondimensionalized peak velocity is seen to increase from ~1.7 to ~4.3 as the modified Rossby number increases from 0.5 to 4.0. Experimental results are seen to agree within 25% with the computational predictions. Similarly, Fig. 9 presents the exit plane wake area. The wake area is seen to increase from ~41% to ~63% of the entire passage flow area. Again, experimental results are seen to agree within 18% to the predictions.

Finally, the normal component of the flow vorticity versus modified Rossby number is presented in Fig. 10. Insufficient experimental data was available to calculate the normal vorticity component. The normal vorticity component from −37 to −112 s^{-1} as the modified Rossby number is increased from 0.5 to 4.0.

Hence, the pressure-to-suction side jet/wake flow is seen to significantly increase with an increasing modified Rossby number. This is explained by the streamwise pressure gradient, which is caused by the radial centrifugal force, also becoming more unfavorable when the modified Rossby number is increased. The suction side wake and flow separation is, thus, enhanced by the rising unfavorable pressure gradient. Interestingly, this observation indi-

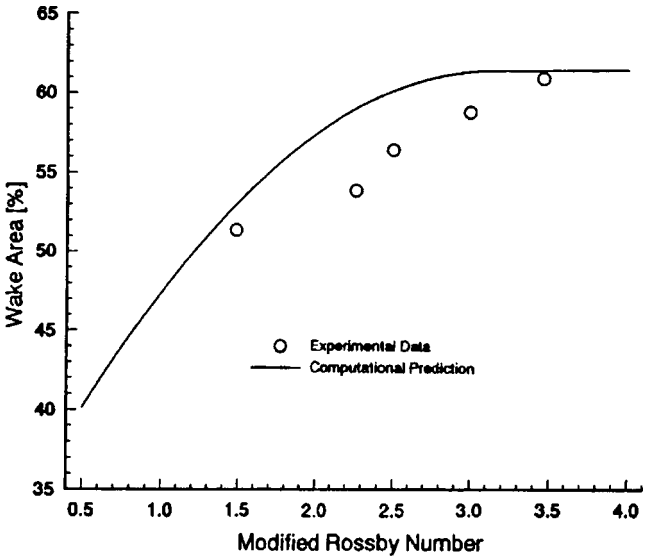

Fig. 9 Exit wake area

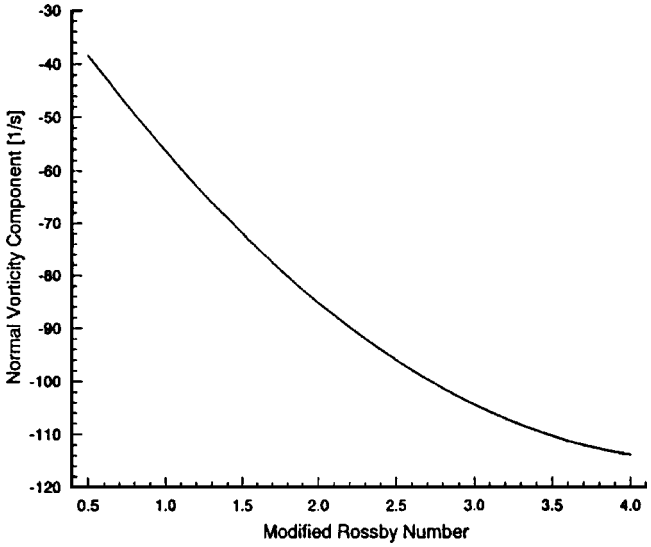

Fig. 10 Exit normal vorticity

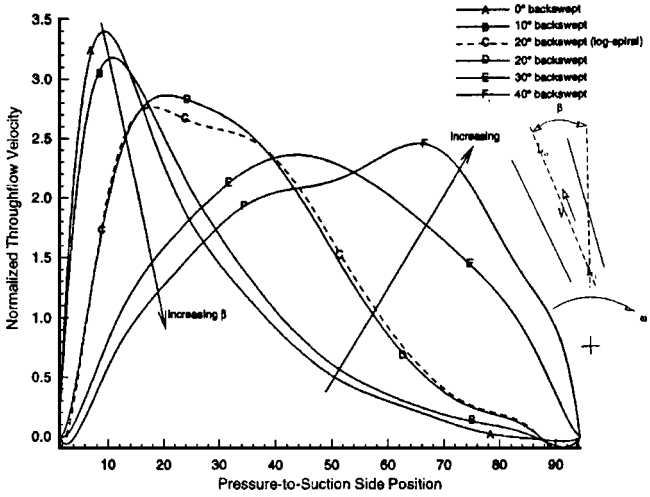

Fig. 11 Nondimensional exit velocity profiles—five angles

cates that the centrifugal force has a stronger magnifying influence on the pressure-to-suction side jet/wake flow than the rotational Coriolis force.

Reynolds Number. The influence of the Reynolds number on the pump pressure-to-suction side (rotating straight-walled duct) jet/wake flow was studied by fixing the modified Rossby number and varying the Reynolds number from 1000 to 12,000. A very weak correlation between the Reynolds number and the pressure-to-suction side jet/wake phenomenon was observed. For example, the exit plane peak jet velocity was seen to vary by only 2% over the entire Reynolds number range (at a modified Rossby number of 3.0). Similarly, the wake area for the same case varied by only 1.5% for different Reynolds numbers. These observation were confirmed for all earlier described jet/wake parameters over the entire range of Reynolds and modified Rossby numbers. Hence, the influence of the Reynolds number on the rotating straight-walled duct jet/wake flow and, thus, the torque converter pump suction side wake, is minimal and the effect can be ignored in the analysis. Experimental results showed a similar flow behavior; namely, even though the wake area at the pump core side was seen to increase with Reynolds number, the suction side separation was not affected by changing the Reynolds number. Thus, the pressure-to-suction side jet/wake flow in the torque converter pump is primarily a function of the modified Rossby number and not significantly affected by the Reynolds number; the Reynolds number can be neglected in the pressure-to-suction side jet/wake parametric studies.

Parametric Study of Geometry. Computational (rotating straight-walled duct) parametric flow studies were performed to analyze the influence of changing the torque converter pump geometry on the pressure-to-suction side jet/wake flow. The pump passage length, h, blade backsweeping angle, β, and number of blades, were varied and the jet/wake parameters were determined from the rotating straight-walled duct model for a range of modified Rossby numbers from 0.5 to 4.0. Results of these parametric studies are discussed later.

Backsweeping Angle. In most modern centrifugal impellers the blades are backswept to achieve a more uniform meridional flow field and, thus, less flow slippage and a higher efficiency, but with a decreased total pressure head. Adler [22] stated that the viscous jet/wake flow phenomenon in a centrifugal impeller is strongly dependent on the backsweeping angle torque converter pumps are similar in geometry to a conventional centrifugal impeller in this respect.

To evaluate the influence of the backsweeping angle on the pump pressure-to-suction side jet/wake flow, parametric studies were performed on the rotating straight-walled duct model for a range of backsweeping angles from 0 deg to 40 deg and modified Rossby numbers from 0.5 to 4.0. Both log-spiral blades and straight backswept blades were tested (the actual torque converter's exit blades are assembled with an almost straight backsweeping angle). Results for this study follow.

Figure 11 shows nondimensionalized pump exit throughflow profiles at a modified Rossby number of 2.5 for straight backsweeping angles of 0 deg, 10 deg, 20 deg, 30 deg, and 40 deg. A log-spiral 20 deg backswept case is also shown (log-spiral and straight angled results are nearly identical). The jet/wake flow behavior is seen to decrease with increasing backsweeping angle; namely, the flow field becomes more uniform for higher backsweeping angles. At the backsweeping angle of 30 deg the flow field is seen to be the most uniform. Beyond that angle, at 40 deg backsweeping angle, the flow field is seen to develop a jet on the suction side and a wake on the pressure side.

The exit plane jet peak velocities and wake areas are presented as a series of curves for the range of backsweeping angles and modified Rossby numbers in Figs. 12 and 13. Again, a decreasing

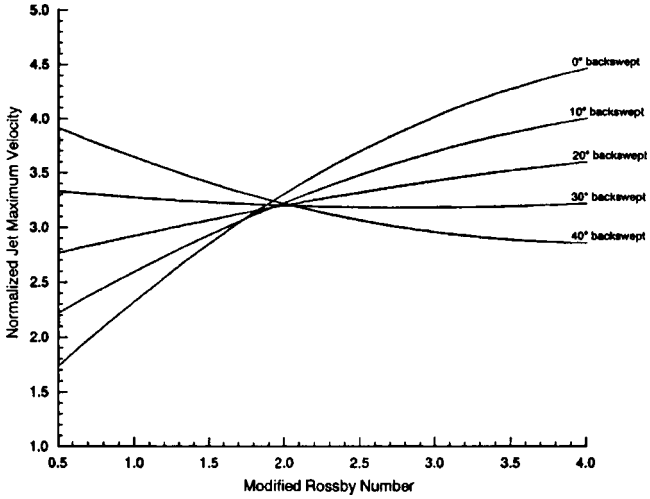

Fig. 12 Nondimensional jet velocities—five angles

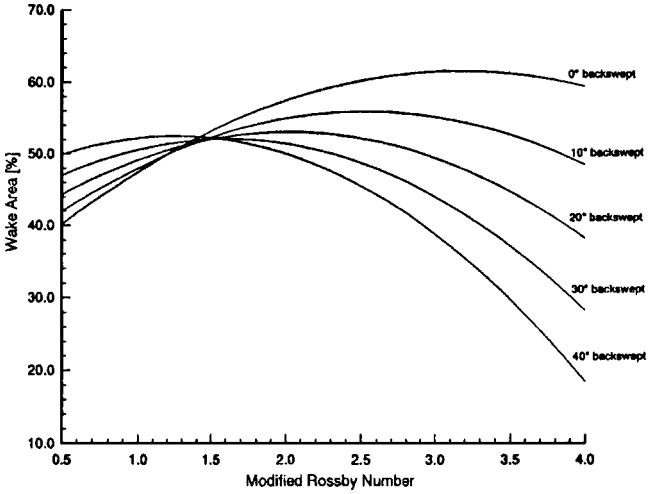

Fig. 13 Exit wake area—five angles

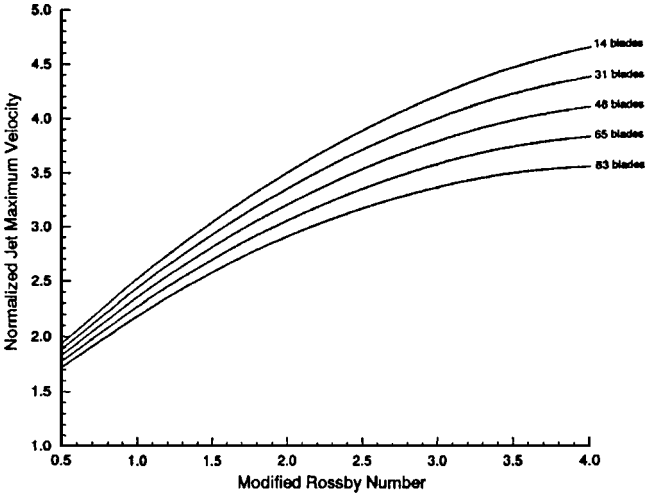

Fig. 14 Nondimensional jet velocities—five solidities

jet/wake effect is observed for increasing backsweeping angles up to an ideal angle (dependent on the modified Rossby number), beyond which the jet/wake flow starts reappearing on the opposite passage sides. Also, for small backsweeping angles the jet/wake phenomenon is seen to increase with the modified Rossby number, while for large backsweeping angles the jet/wake phenomenon decreases with the modified Rossby number; consequently, for large backsweeping angles the tangential blade curvature (backsweeping) dominates over the rotational Coriolis force on the fluid.

Radius of Rotation. The effect on the pressure-to-suction side jet/wake flow of changing the radius from the inlet plane to the center of rotation (pump shaft), R, was studied using the rotating straight-walled duct model. The radius was varied from 0.05 to 0.10 m. No noticeable influence on the nondimensionalized flow profiles was observed when the radius was changed while the modified Rossby number and the Reynolds number were held constant. Since the radius was used to nondimensionalize the geometry, changing the radius only affects the overall size of the rotating straight-walled duct (when Re and Ro_m are fixed) and, thus, does not affect the nondimensional output parameters (the dimensional output parameters, such as maximum and minimum throughflow velocity, were affected).

Inlet and Outlet Areas. Changing the inlet and outlet (lengths) areas, while keeping the area (length) ratio, L_i/L_o, constant, is similar to changing the number of blades in a centrifugal impeller/pump. A study was performed in which the inlet area was varied, the area ratio was fixed, and the modified Rossby number was varied over a range from 0.5 to 4.0. Tested inlet lengths ranged from 0.005 to 0.030 m with $L_i/L_o = 0.621$. This inlet area range corresponded to changing the number of blades from approximately 83 to 14 (the pump has 27 blades).

Figures 14 and 15 show some of the pressure-to-suction side jet/wake parameter results for this study. The jet/wake effect is seen to significantly decrease with increasing number of blades (or decreasing inlet area). For example, the nondimensional jet peak velocity at $\mathrm{Ro}_m = 4.0$ for 14 blades ($L_i = 0.005$ m) is 4.7, while it is only 3.5 for 83 blades ($L_i = 0.030$ m). Hence, narrower blade passages increase the fluid guidance and, thus, suppress flow separation and wake formation. This trend is consistent with experimental observations in radial impellers by Adler [22] and Moore [23].

Passage Length. The effect of changing the passage length, h, on the pressure-to-suction side jet/wake flow was evaluated from the 2D rotating straight-walled duct model. The passage length was varied from 0.02 to 0.10 m and jet/wake parameters were obtained for modified Rossby numbers from 0.5 to 4.0. Results for this parametric study are presented.

Figure 16 shows that the pump exit plane jet peak velocity and thus, the jet/wake phenomenon increases with greater passage length. This is explained by the fact that for a fixed inlet velocity in an elongated passage the tangential Coriolis force acts longer on the fluid and the jet/wake effect has more time to develop. Similar results are seen when observing the wake area relations in Fig. 17; namely, an increasing wake is seen for an increasing passage length. For example, the exit plane wake area at $\mathrm{Ro}_m = 3.0$ for $h = 0.02$ m is 55%, while the wake area for $h = 0.10$ m is 74%. Adler [22] and Moore [23] obtained similar results experimentally for a conventional radial impeller.

Conclusions

The complex three-dimensional velocity field inside the automotive torque converter was previously experimentally determined using laser velocimetry. Results showed strong jet/wake including backflows and circulatory secondary flows in the pump. Particularly interesting was the sign change in rotation as the flow traversed from the midplane to the exit plane. For this paper to understand the fundamental flow behavior simplified analytical/numerical flow models, based on two-dimensional Navier-Stokes

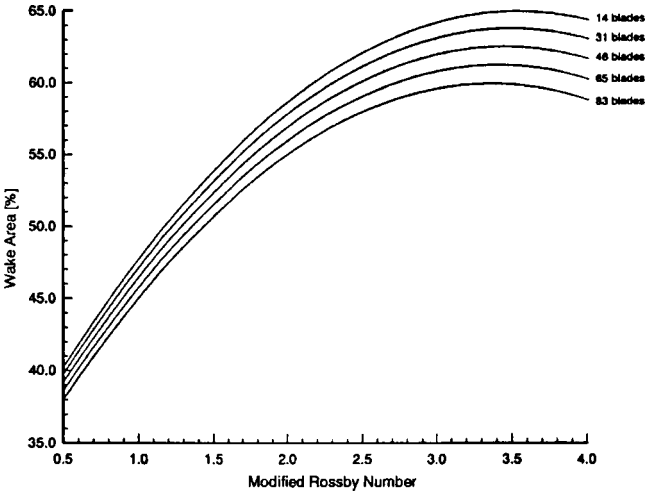

Fig. 15 Exit wake areas—five solidities

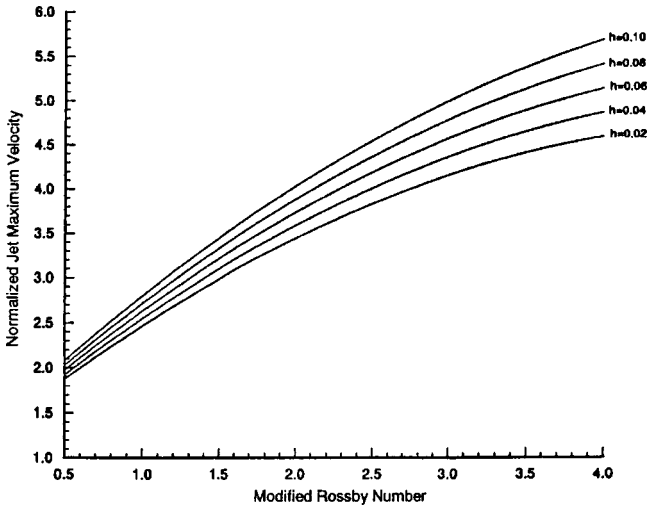

Fig. 16 Nondimensional jet velocities—five lengths

equation solutions and the streamwise vorticity generation equations, were developed to independently analyze the pump pressure-to-suction side jet/wake flow, the core-to-shell side jet/wake flow, and the circulating secondary flow phenomena. Parametric studies, based on the two-dimensional flow models, were undertaken to evaluate the effect that torque converter operating conditions and pump geometry had on the jet/wake flow parameters and the pump secondary velocities. Previous to this study the different mechanisms had not been separated to ascertain the magnitude and significance of the different effects on the jet-wake and secondary flows. Trends seen in the results from these studies compared favorably with experimental results.

To model and analyze the jet/wake phenomena observed in the pump, Navier-Stokes equation solutions for two simple two-dimensional flows (from a commercially available flow solver) were employed: (i) a rotating straight-walled duct to model the pressure-to-suction side jet/wake flow due to rotational Coriolis forces and (ii) a 180 deg flow bend to model the core-to-shell side jet/wake flow due to rapid radial/axial flow turning. Using the first of these two simple models the formation and development of the pump pressure to suction surface jet/wake flow was studied in detail in part I of this paper. In part II the second model will be analyzed and added to the results in part I.

It is very important to recognize that the goal of these two papers is not to accurately predict the total flow field by superimposing the two results. Other authors have used full 3D models have been used to predict the total flow fields but using such models does not allow for the separation of different forces so that the fundamentals can be understood.

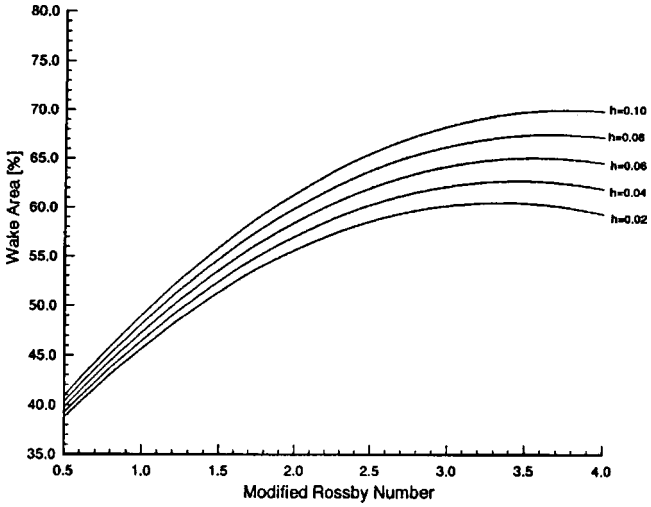

Fig. 17 Exit wake areas—five lengths

Results from the model showed that the suction side wake, which was due to the counter-rotational tangential Coriolis force, was almost only a function of the modified Rossby number ($\mathrm{Ro}_m = \omega R/2V_i$) and independent of the Reynolds number ($\mathrm{Re} = \rho V_i R/\mu$). Increasing the modified Rossby number by, for example, increasing the pump rotational speed, increased the pressure-to-suction side jet/wake flow.

The most significant geometric parameter that was seen to affect the pump flow was the backsweeping angle for the pressure-to-suction side jet/wake. For example, results showed that using backswept blades can eliminate the pressure-to-suction side jet/wake flow effect, giving a very uniform pump exit throughflow profile. Other geometrical parameters such as the radius of rotation (inlet to centerline) and the passage inlet/outlet areas were also tested, but only a small to moderate influence on the jet/wake flow phenomena was found.

Acknowledgments

This research was sponsored by the General Motors Corporation Powertrain Division, the ROMAC Industrial Research Program at the University of Virginia, and by Blue Ridge Numerics, Inc.

References

[1] Fister, W., and Adrian, F. W., 1983, "Experimental Researches of Flow in Hydrodynamic Torque Converters," *Proceedings of the 7th Conference on Fluid Machinery*, September 13–16, Budapest, Hungary, **1**, pp. 210–224.
[2] Browarzik, V., 1994, "Experimental Investigation of Rotor/Rotor Interaction in a Hydrodynamic Torque Converter Using Hot Film Anemometry," 39th International Gas Turbine and Aeroengine Congress and Exposition, The Hague, The Netherlands, June 13–16, ASME paper no. 94-GT-246.
[3] Watanabe, H., Kurahashi, T., and Kojima, M., 1997, "Flow Visualization and Measurement of Torque Converter Stator Blades Using a Laser Sheet Lighting Method and a Laser Velocimeter," SAE International Congress and Exposition, Detroit, Michigan, February 24–27, SAE paper no. 970680.
[4] Ejiri, E., and Kubo, M., 1997, "Performance Analysis of Torque Converter Elements," ASME Fluids Engineering Meeting, Vancouver, B.C., Canada, June 22–26, ASME paper no. FEDSM97-3219.
[5] By, R. R., and Lakshminarayana, B., 1993, "Measurement and Analysis of Static Pressure Fields in a Torque Converter Pump," 2nd ASME Pumping Machinery Symposium, Washington, DC, June 20–24, **154**, pp. 253–264.
[6] By, R. R., Kunz, R. F., and Lakshminarayana, B., 1993, "Navier Stokes Analysis of the Pump of an Automotive Torque Converter," 2nd ASME Pumping Machinery Symposium, Washington, DC, June 20–24, **154**, pp. 264–274.
[7] Marathe, B. V., and Lakshminarayana, B., 1995, "Experimental Investigation of Steady and Unsteady Flow Field Downstream of an Automotive Torque Converter Turbine and Stator," Int. J. Rotating Mach., **2**, pp. 67–84.
[8] Dong, Y., Lakshminarayana, B., and Maddock, D. G., 1997, "Steady and Unsteady Flow Field at Pump and Turbine Exit of a Torque Converter," 1997 ASME Fluid Engineering Division Summer Meeting, Vancouver, June 22–26, ASME paper no. FEDSM97-3351.
[9] Bahr, H. M., Flack, R. D., By, R. R., and Zhang, J. J., 1990, "Laser Velocimeter Measurements in the Stator of a Torque Converter," SAE Trans., **99**, pp. 1625–1634.
[10] Gruver, J. K., Flack, R. D., and Brun, K., 1996, "Laser Velocimeter Measurements in the Pump of a Torque Converter Part I—Average Measurements," ASME J. Turbomach., **118**, pp. 562–569.
[11] Brun, K., and Flack, R. D., 1997, "Laser Velocimeter Measurements in the Turbine of an Automotive Torque Converter, Part I—Average Measurements," ASME J. Turbomach., **119**, pp. 646–654.
[12] Ainley, S. B., and Flack, R. D., 2000, "Laser Velocimeter Measurements in the Stator of an Automotive Torque Converter," Int. J. Rotating Mach., **6**, pp. 417–431.
[13] Whitehead, L. D., 1995, "A Comparison of the Internal Flow Fields of Two Automotive Torque Converters Using Laser Velocimetry," M.S. thesis, University of Virginia, Charlottesville, Virginia.
[14] Yermakov, A., 1998, "A Study of the Internal Flow Fields of Two Automotive Torque Converter Turbines Using Laser Velocimetry," M.S. thesis, University of Virginia, Charlottesville, Virginia.
[15] Claudel, W. D., 1997, "A Comparison of the Internal Flow Fields of Three Automotive Torque Converter Pumps Using Laser Velocimetry," M.S. thesis, University of Virginia, Charlottesville, Virginia.
[16] Schweitzer, J., and Gandham, J., 2002, "Computational Fluid Dynamics on

Torque Converters—Validation and Application,'' Proceedings of the 9th International Symposium on Transport Phenomena and Dynamics of Rotating Machinery (ISROMAC-9), Honolulu, Hawaii, February 10–14, paper No. FD-ABS-046.
[17] Dean, Jr., R. C., and Senoo, Y., 1960, ''Rotating Wakes in Vaneless Diffusers,'' J. Basic Eng., **82**, pp. 563–570.
[18] Eckardt, D., 1976, ''Detailed Flow Investigations Within a High Speed Centrifugal Compressor Impeller,'' ASME J. Fluids Eng., **98**, pp. 390–402.
[19] Johnson, M. W., and Moore, J., 1980, ''The Development of Wake Flow in a Centrifugal Impeller,'' J. Eng. Power, **102**, pp. 382–390.
[20] Flowplus, 1994, *FlowPlus User's Guide—Finite Element CFD Solver Version 1.2–2*, Blue Ridge Numerics, Inc., Charlottesville, Virginia.
[21] Rice, J. G., and Schnipke, R. J., 1985, ''A Monotone Streamline Upwind Finite Element Method for Convection Dominated Flows,'' Comput. Methods Appl. Mech. Eng., **48**, pp. 313–327.
[22] Adler, D., 1980, ''Status of Centrifugal Impeller Internal Aerodynamics Part II: Experiments and Influence of Viscosity,'' J. Eng. Power, **102**, pp. 738–746.
[23] Moore, J., 1967, ''Effects of Coriolis on Turbulent Flow in Rotating Rectangular Channels,'' MIT Gas Turbine Laboratory Report, No. 89, Cambridge, Massachusetts.

Fundamental Analysis of the Secondary Flows and Jet-Wake in a Torque Converter Pump—Part II: Flow in a Curved Stationary Passage and Combined Flows

R. Flack
Mechanical and Aerospace Engineering,
University of Virginia,
Charlottesville, VA 22903-2442
e-mail: rdf@virginia.edu

K. Brun
Southwest Research Institute,
San Antonio, TX 78238
e-mail: klaus.brun@swri.org

Previously, experimental results for the velocity field in a torque converter pump showed strong jet/wake characteristics including backflows and circulatory secondary flows. Navier-Stokes flow models were developed herein to independently analyze the pump pressure-to-suction side jet/wake flow, the core-to-shell side jet/wake flow, and the secondary flows. Two relatively simple models were employed: (i) a rotating two-dimensional straight-walled duct and (ii) a 180 deg flow bend. Parametric studies were undertaken to evaluate the effect that operating conditions and geometry had on the characteristics. Results from the model showed that the core side wake, which was due to flow separation caused by rapid radial flow turning, was primarily a function of the Reynolds number; increasing the Reynolds number increased the core-to-shell side jet/wake flow. The passage length (or curvature) strongly affected the core-to-shell jet/wake. Using the modified equations for the generation of streamwise vorticity and the results from the two-dimensional jet/wake model for the normal and binormal vorticity components, trends for the secondary flows in the torque converter pump were predicted. Predicted secondary flows in the torque converter pump circulated in the counterclockwise direction (positive streamwise vorticity) in the pump midplane and in the clockwise direction (negative streamwise vorticity) in the pump exit plane. These trends agreed with experimental observations. Both the Reynolds number and the modified Rossby number were seen to have a significant influence on the streamwise vorticity and, thus, on the magnitude of the secondary flow velocities. The pump midplane counter-clockwise secondary flow circulation was primarily caused by the interaction of the pressure-to-suction side jet/wake nonuniform flow (and the associated normal vorticity component) with the high radial/axial flow turning angle the flow underwent while passing through blade passage. Similarly, the pump exit plane clockwise secondary flow circulation was caused by the core-to-shell side jet/wake nonuniform flow (and the associated binormal vorticity component) being rotated about a fixed centerline (pump shaft). Thus, the pump streamwise vorticity, which was responsible for the generation circulatory secondary flows, was directly related to the pump jet/wake phenomena. [DOI: 10.1115/1.1852486]

Introduction

Torque converters are an important part of automatic transmissions. The smooth transmission of torque between the engine and the wheels is provided and torque amplification at low speeds is accomplished with the device. The torque converter pump in many ways acts as a centrifugal pump.

In part I of this paper the background literature was reviewed and the basic approach was outlined. Although the torque converter is one of the most complex turbomachines, the fundamental fluid dynamic aspects of the machine have not received due attention. The current fundamental understanding of the internal flow fields of torque converters over a range of geometries and conditions is inadequate.

Krain [1], Moore and Moore [2], Eckardt [3], Howard and Lennemann [4], Gruver et al. [5], and Brun and Flack [6] experimentally determined the secondary flows in mixed-flow centrifugal impellers. Johnson and Moore [7] determined secondary flow mixing losses in a centrifugal impeller from pressure probes installed in the rotating impeller.

For example, in Fig. 1 the pump mid- and exit plane secondary velocities at a speed ratio of 0.800 are presented at a turbine/pump speed ratio of 0.800 from Gruver et al. [5]. As can be seen, at the midplane the flow is counterclockwise, whereas at the exit plane the flow is clockwise. Although some success has been demonstrated in prediction such flows, an explanation has not yet been postulated for the reversal in rotation.

For this paper a CFD analysis was performed in which the different driving mechanisms were separated to provide a better understanding of the complex nature of the secondary flows and separated regions. In particular, the Coriolis and centrifugal forces were independently varied to ascertain the relative importance of such terms. Furthermore, a number of other parameters were varied to determine their importance, including, blade angles, number of blades, passage length, and radius. Previous to this study the different mechanisms had not been separated to ascertain the magnitude and significance of the different effects on the jet-wake and secondary flows.

Contributed by the Fluids Engineering Division for publication on the JOURNAL OF FLUIDS ENGINEERING. Manuscript received by the Fluids Engineering Division September 11, 2003; revised manuscript received September 7, 2004. Review Conducted by: J. Lee.

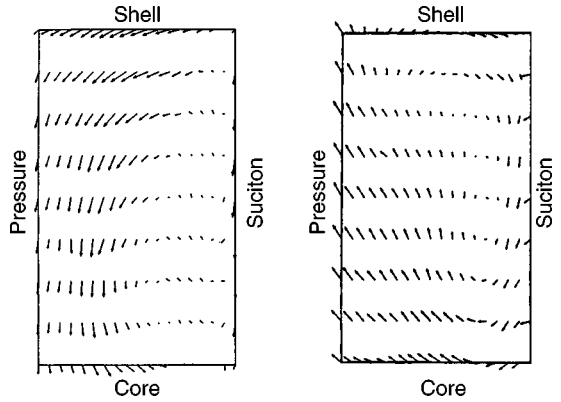

Fig. 1 Mid- and exit plane secondary velocities, SR=0.800

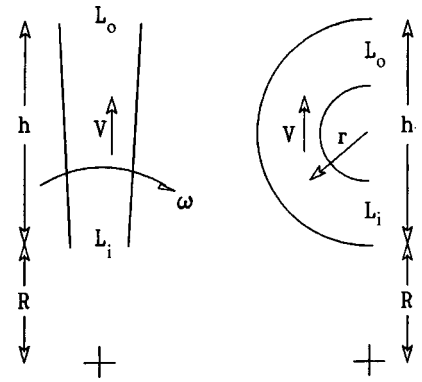

Fig. 3 Model dimensions

Modeling

In part I of this paper, the development of the jet/wake flow was modeled in detail to be primarily a function of two separate and independent flow phenomena: (i) Suction side separation due to the rotational Coriolis force and (ii) core side separation due to the rapid radial/axial flow turning (Fig. 2). Each of these simple flow phenomena can be solved individually using a two-dimensional (2D) viscous flow solver. A commercially available flow solver was employed to simulate (i) flow in a 2D rotating straight-walled duct to study the suction side separation—part I of this paper and (ii) flow in a stationary 2D 180 deg bend to study the core separation—part II of this paper. The geometries are shown in Fig. 3 and grids are presented in part I. This simplified model is not intended to predict the flow field at high accuracy. Rather, the division of the contributions of the separate force components allows for an improved understanding of the individual influences of the forces on the flow.

Table 1 shows the relevant nondimensional parameters for the two simplified flows (straight-walled rotating duct and 180 deg stationary bend), which are necessary to model the jet/wake phenomena.

V_i is the pump inlet velocity (in the radial direction for the straight-walled duct and in the axial direction for the 180 deg bend), r is the radius of curvature of the pump blade-passage centerline, R is the mean radius between pump inlet and the shaft centerline (radius of rotation), L_i is the inlet length, L_o is the outlet length, and h is the passage length. For the rotating duct flow both the Reynolds number and the modified Rossby number, Ro_m, appear, while for the 180 deg bend flow only the Reynolds number is present. Also, the modified Rossby Number ($\omega R/2V_i$) is in actuality the ratio of centrifugal force/coriolis force.

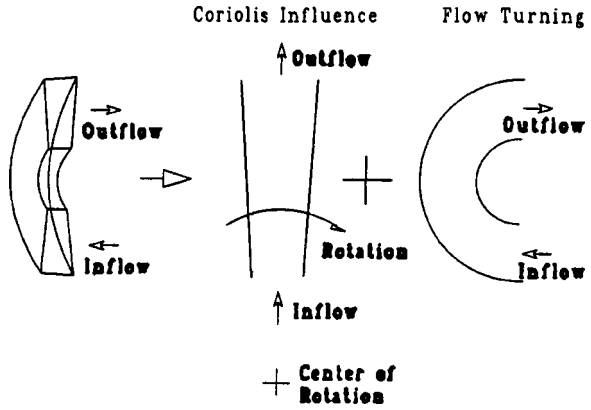

Fig. 2 Two-dimensional flow models

Flow in a Curved Stationary Section

Core-to-Shell Side Separation and Jet/Wake Flow Due to Rapid Flow Turning. The jet/wake phenomenon in the core-to-shell side direction of the torque converter pump is primarily driven by separation due to rapid radial/axial flow turning. Namely, flow on the core side of the passage separates and forms a wake because of an unfavorable boundary layer pressure gradient generated by the diverging curvature of the core side wall. Higher kinetic energy fluid is shifted toward the pressure side of the passage by the wake and a jet forms. The centrifugal force per volume, F_s, on a moving fluid following a passage with a radius of curvature, r, is given by

$$F_s = \rho \frac{V^2}{r}, \tag{1}$$

where F_s acts in the direction normal to the passage curvature (see Fig. 4). Here V is the throughflow velocity component. This centrifugal force is primarily responsible for the generation of the unfavorable pressure gradient in the boundary layer. Equation (1) shows that for higher throughflow velocities or shorter passage lengths ($h=2r$) an increase in the unfavorable pressure gradient

Table 1 Jet/wake nondimensional parameters

Rotating Duct	180° Stationary Bend
Force Parameters	
Reynolds Number = $\rho V_i R/\mu$	Reynolds Number = $\rho V_i R/\mu$
Modified Rossby Number = $\omega R/2V_i$	
Geometric Parameters	
L_i/R	L_i/R
L_o/R	L_o/R
h/R	$h/R = 2r/R$

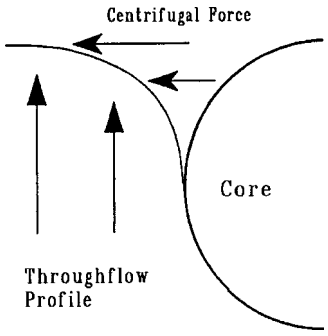

Fig. 4 Separation due to centrifugal force

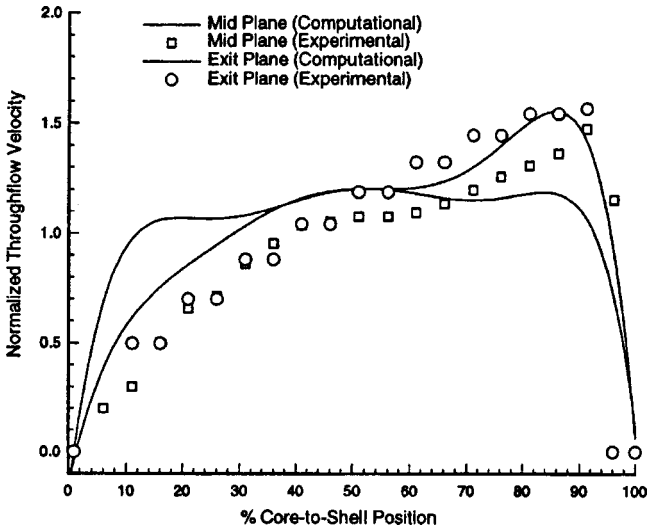

Fig. 5 Mid- and exit plane velocity profiles, SR=0.80

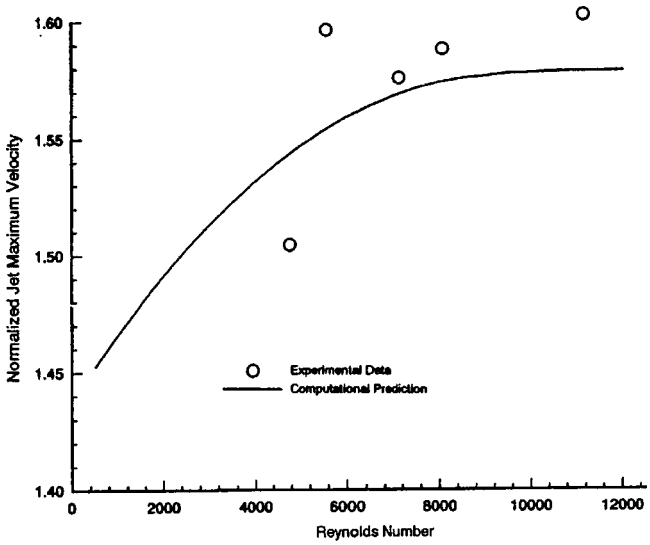

Fig. 6 Exit nondimensional jet velocities

and, thus, in the jet/wake flow behavior is anticipated. Detailed observations of the jet/wake development and the redistribution of the streamwise velocities in simple curved ducts have been reported by Mori et al. [8] and others.

To quantify the core-to-shell jet/wake flow phenomenon in the torque converter pump, the viscous flow solver was employed to obtain numerical solution for the simple stationary 180 deg bend flow model. Initially, the torque converter pump geometry at the 0.065 and 0.800 speed ratio operating conditions was analyzed. Also, the curvature of the bend was assumed to be circular to simplify the geometry.

The 0.800 speed ratio ($V_i = 1.442$ m/s, Re=5055) computationally predicted flow field is presented in Fig. 5. The nondimensional throughflow profiles (nondimensionalized by the plane-averaged throughflow velocity, V_{ave}) at the mid and exit planes are presented. Figure 5 shows that the computational flow solver underpredicts the jet/wake effect in both the mid- and exit planes; this is similar to observations for the rotating straight-walled duct model. The wake area for this case is smaller than for the 0.065 speed ratio case. A jet with peak velocities of ~1.6 (in the exit plane) is located directly at the shell side and a wake region with flow velocities of ~0.5 is located on the suction side. The numerically predicted jet/wake effect is seen to be significantly stronger in the exit than in the midplane. For comparison, experimental nondimensional through flow results are included.

Parametric Study of Reynolds Number. Computational parametric studies are performed to evaluate the relative influence of the nondimensional quantities on the torque converter pump core-to-shell side jet/wake flow from the simplified 180 deg bend flow model. Of particular interest is the effect on the flow field of varying the Reynolds number. For this model the Reynolds number is the only relevant nondimensional force parameter since there is no rotation in the model (no Rossby number influence). Changing only the working fluid's viscosity in the model varied the Reynolds number.

In an actual automotive torque converter the Reynolds number is in a constant state of flux; namely, as the speed ratio and the input (pump) speed of the torque converter changes so does the Reynolds number. Hence, the influence of the Reynolds number over a range of realistic operating conditions (Re=500–12,000) is discussed. The geometry used for all parametric studies was again the 230 mm torque converter pump with $R = 0.0661$ m, $h = 0.040,61$ m, $L_i = 0.0155$ m, $L_o = 0.024,96$, and $r = 0.0203$ m.

Figures 6–8 show the pump exit plane (shell side) jet peak velocity, the (core side) wake area, and the binormal vorticity component, respectively, as a function of the Reynolds number. For comparison, a limited number of experimental results are also included. Both the exit jet peak velocity and the wake area are seen to increase with increasing Reynolds numbers. For example, the wake area (as a percentage of the total passage area) increases from ~23% at Re=500 to 41% at Re=12,000. These trends are consistent with flow in a 180 deg rectangular bend experimental results by Mori et al. [8] and Rowe [9]. Hence, a strong correlation between the core-to-shell jet/wake flow and the Reynolds number is observed; namely, increasing the Reynolds number increases the jet/wake flow.

Parametric Study of Geometry. Computational parametric flow studies were performed to analyze the influence of changing the torque converter pump geometry on the core-to-shell side jet/wake flow. The pump radius of rotation, R, and the passage length, h, were varied and the jet/wake parameters were determined from the stationary 180 deg flow bend model for a range of Reynolds numbers from 500 to 12,000.

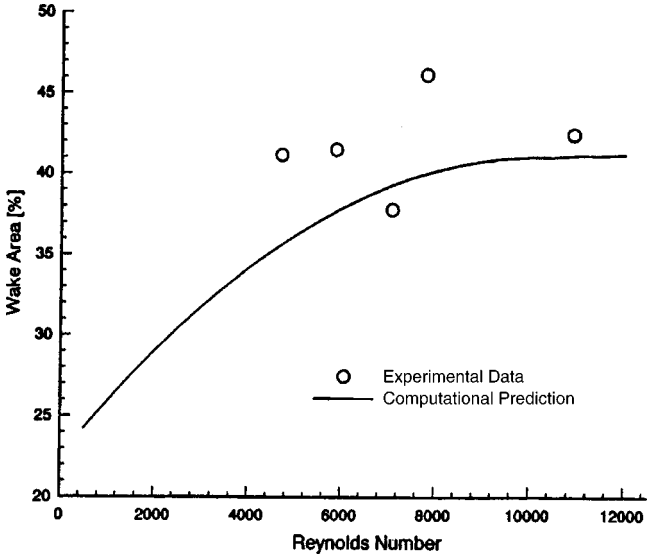

Fig. 7 Exit wake area

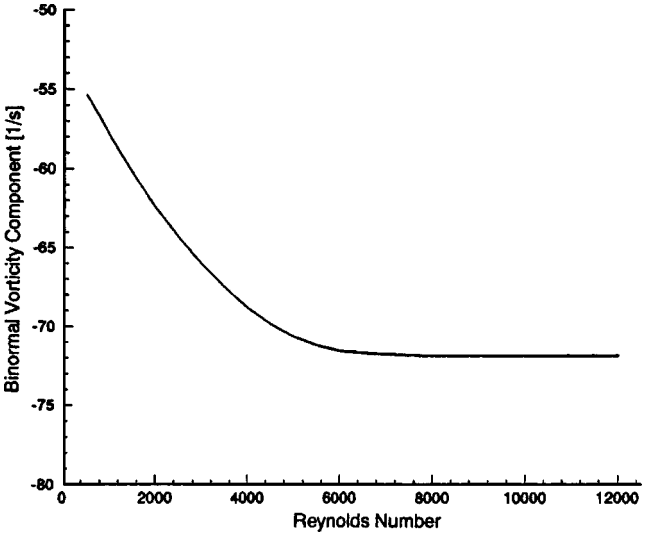

Fig. 8 Exit binormal vorticities

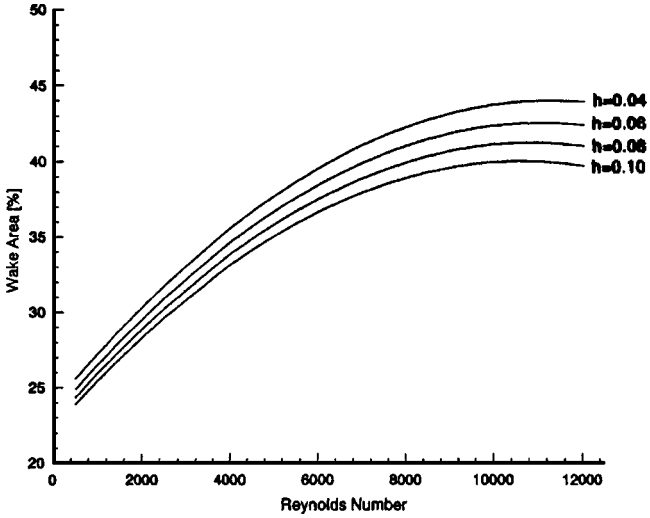

Fig. 10 Exit wake area

Radius of Rotation. The effect on the core-to-shell side jet/wake flow of changing the radius from the inlet plane to the center of rotation (pump shaft), *R*, was studied using stationary 180 deg bend flow model. Radii from 0.05 to 0.10 m were tested over the entire range of Reynolds numbers. Since there was no rotation in this simple flow model, changing the radius to the centerline only affected the axis-symmetry assumption and the associated passage three-dimensional (3D) dimensions; namely, a change in *R* is similar to changing the passage exit to inlet area ratio. As a consequence of this, the relationship between jet/wake parameters and the radius, *R*, was seen to be very weak.

Passage Length. The effect of changing the passage length, *h*, on the core-to-shell side jet/wake flow was evaluated from the 180 deg flow bend 2(D) model. The passage length, *h*, was varied from 0.04 to 0.10 m and jet/wake parameters were obtained for Reynolds numbers from 500 to 12,000. One should note that the radius of curvature of the passage, *r*, is directly related to the passage length, *h*, by $h=2r$, since a circular passage was assumed for this model. Thus, increasing the passage length, *h*, affected both the radial curvature and the exit to inlet area ratio (by the axis-symmetry assumption). Results for this parametric study are presented in Figs. 9 and 10.

Figure 9 shows that the pump exit plane jet peak velocity and thus, the jet/wake phenomenon significantly increases with decreasing passage length. For example, the maximum wake area (at Re=12,000) increases from 39% to 43% as *h* decreases from 0.10 to 0.04 m. This is explained by the fact that in a shorter passage the radius of curvature is smaller and, thus, the core side unfavorable boundary layer gradient becomes more severe. Also, in a shorter passage, the exit to inlet area ratio increases, causing the passage streamwise pressure gradient to become more unfavorable (this effect is probably very small compared to the curvature effect). Similar results are seen when observing the wake area relations in Fig. 10; namely, an increasing wake is seen for a decreasing passage length.

General Jet/Wake Flow Trends. To summarize the earlier observations, Tables 2 and 3 show qualitatively how the more relevant jet/wake flow parameters are affected by increasing the Reynolds number, the modified Rossby number, and the geometric parameters. Here, ⇑, indicates increasing, ⇓, decreasing, and, ⇔, negligible, affect on jet/wake flow parameter. The relative strength of the effect is indicated by the number of symbols. For example, Table 2 shows the normal vorticity to first increase, ⇑,

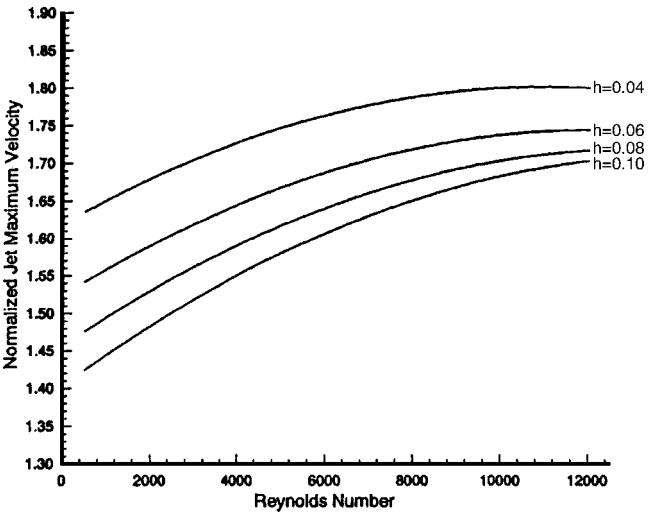

Fig. 9 Exit nondimensional jet velocities

Table 2 Summary of influences on the pressure-to-suction side jet/wake flow

	Peak Jet Velocity	Wake Area	Blockage Area	Normal Vorticity
Ro_m	⇑⇑⇑	⇑⇑⇑	⇑⇑⇑	⇓⇓⇓
Re	⇔	⇔	⇔	⇔
β	⇑⇓	⇓⇑	⇓⇑	⇑⇓
L_i/R	⇓	⇓	⇓	⇑
h/R	⇑	⇑	⇑	⇓

Table 3 Summary of influences on the core-to-shell side jet/wake flow

	Peak Jet Velocity	Wake Area	Blockage Area	Binormal Vorticity
Ro_m	⇔	⇔	⇔	⇔
Re	⇑⇑	⇑⇑	⇑⇑	⇓⇓
h/R	⇓⇓	⇓⇓	⇓⇓	⇑⇑

with the backsweeping angle (β), and then to decrease, $\Downarrow$, with the backsweeping angle (β) at higher angles (β>30 deg).

Secondary Flow Model

Secondary flows in the torque converter pump were seen to circulate counterclockwise in the midplane and clockwise in the exit plane for all experimental conditions tested. Hence, in the torque converter pump, very strong secondary flows are generated and, also, the secondary flows completely reverse rotational direction as they pass through the passage geometry (between the mid- and exit planes).

Streamwise vorticity and, hence, rotating secondary flows will develop whenever a moving fluid with a gradient of the reduced stagnation pressure ($P_{rs}=P+1/2\rho(V^2-\omega^2R^2)$) turns around a bend or is rotated about a fixed axis (Johnson [10]). A gradient in the reduced stagnation pressure, P_{rs}, can result from a nonuniform velocity profile or a reduction of P_{rs} due to boundary layer viscous dissipation. In the torque converter pump, the flow field is highly nonuniform because of the jet/wake flow phenomena, and the nonuniform flow field is both turned around a bend with a radius of curvature r, and is rotated around the shaft at an angular speed of ω. Hence, high values of streamwise vorticity and strong associated circulatory secondary flows are anticipated. The average streamwise vorticity can be calculated from the experimental results with the experimental secondary velocity components. For example, the 0.800 speed ratio case the average streamwise vorticity was determined to be 11.5 and -55.1 s^{-1} for the mid- and exit planes, respectively. These results confirm the experimental observations of strong counterclockwise circulation in the mid plane (positive streamwise vorticity) and strong clockwise circulation (negative streamwise vorticity) in the exit plane.

Streamwise Vorticity Generation Equations. Equations for the generation of streamwise vorticity, and, thus, circulatory secondary flows, in an intrinsic rotating coordinate system were first derived by Hawthorne [11], Smith [12], Smith [13], and Ellis [14]. The equations were then generalized to include viscous terms and compressibility effects by Howard [15] and Lakshminarayana and Horlock [16]. The equations as derived by Lakshminarayana and Horlock were employed for the analysis herein.

The fundamental generation of streamwise vorticity equation for a rotating system (Lakshminarayana and Horlock [16]) is given by

$$\frac{\partial}{\partial s}\left(\frac{\xi_s}{|V|}\right)=2\frac{\xi_n}{|V|r}-2\frac{s\cdot(\omega\times\xi)}{|V|^2}, \tag{2}$$

where s is in streamwise direction, n is in the normal direction, b is in the binormal direction (see Fig. 11), V is the meridional velocity, ξ_n is the normal vorticity component, ξ_s is the streamwise vorticity component, ξ is the total vorticity vector, and r is the radius of curvature. The first term in Eq. (2) is a streamline curvature term and the second is a Coriolis force term. For an impeller with a fixed axis of rotation (such as the torque converter) this equation can be further reduced to

$$\frac{\partial}{\partial s}\left(\frac{\xi_s}{|V|}\right)=2\frac{\xi_n}{|V|r}-2\frac{\omega\xi_b\sin\kappa}{|V|^2}, \tag{3}$$

where κ is the meridional flow angle relative to the axial direction and ξ_b is binormal component of vorticity. The streamwise vorticity, and thus secondary flows, is directly related to the normal and binormal vorticity via the equation for generation of streamwise vorticity in a rotating frame (Lakshminarayana and Horlock [16]) and as also discussed in modeling in part I of this paper. Note that the normal and binormal components of vorticity in Eq. (3) can be directly determined from the numerical analysis (pressure-to-suction side jet/wake flow: normal vorticity component, ξ_n; core-to-shell side jet/wake flow: binormal vorticity component, ξ_n).

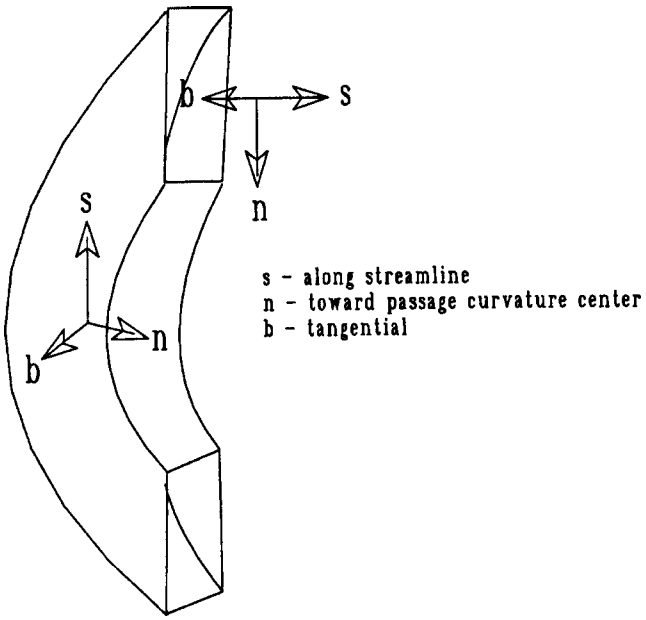

Fig. 11 Normal, binormal, and streamwise directions

Equation (3) shows that there are two relevant force terms that contribute to the generation of streamwise vorticity in a centrifugal impeller: The first term shows that streamwise vorticity is generated whenever a flow that is nonuniform in the pressure-to-suction direction, and thus, has a normal vorticity component, ξ_n, follows a curved bend with a radius of curvature, r. The second term shows streamwise vorticity generation whenever flow that is non-uniform in the core-to-shell direction (ξ_b) is rotated around a centerline (shaft). The sine term indicates that streamwise vorticity is only generated by the second term when a radial flow component ($\kappa\neq0$ deg) exists.

One should note that streamwise vorticity can also be generated by compressibility and viscosity; analytical terms for these effects can be found in Lakshminarayana and Horlock [16] but are not discussed herein for the sake of brevity. For the torque converter pump flow, the viscous influence on the generation of streamwise vorticity was estimated for a limited number of cases and was found to be negligible (2.1% of the total exit plane streamwise vorticity for the 0.800 speed ratio case).

Thus, in the torque converter pump, the pressure-to suction side jet/wake flow, modeled earlier by flow in a simple rotating straight-walled duct, only contributes to the first term of Eq. (3) and the core-to-shell side jet/wake flow, modeled by flow in a stationary 180 deg bend, only contributes to the second term of Eq. (3). The meridional flow angle in Eq. (3) can be closely approximated by $\kappa=\pi s/s_{\text{total}}$ for a circular pump torus (one should note that because of the meridional flow angle, the second term of Eq. (3) will have a significantly stronger influence on the pump exit plane secondary flow than on the midplane secondary flow). Consequently, Eq. (3), with the normal and binormal vorticities obtained from the simple 2D flow models, can be numerically integrated to calculate the streamwise vorticity in the torque converter pump and, thus, can be used to approximately predict the pump secondary flow circulation.

For the pump at the 0.065 and 0.800 speed ratio the streamwise vorticity was calculated. Results of the streamwise, the normal, and the binormal vorticity are included in Fig. 12 for the 0.800 speed ratio (Re=5055, $\text{Ro}_m=2.661$, $V_i=1.442$ m/s, $\omega=115.2$ rad/s). Experimental results for the 0.065 and 0.800 speed ratio streamwise vorticities are also included for a comparison. All vorticities are presented as functions of the pump percent chord distance from the inlet plane.

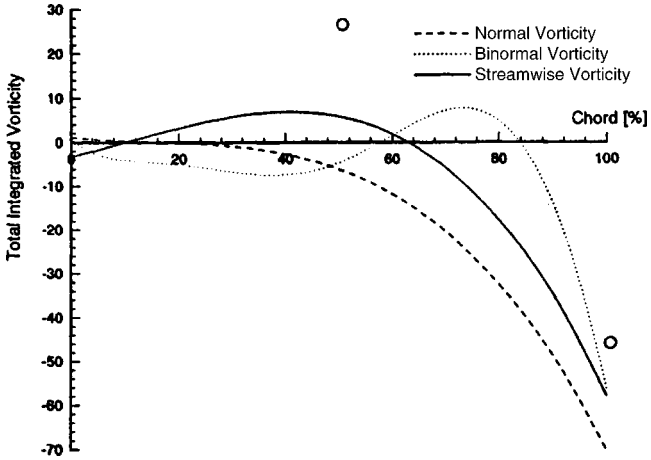

Fig. 12 Vorticities at SR=0.80

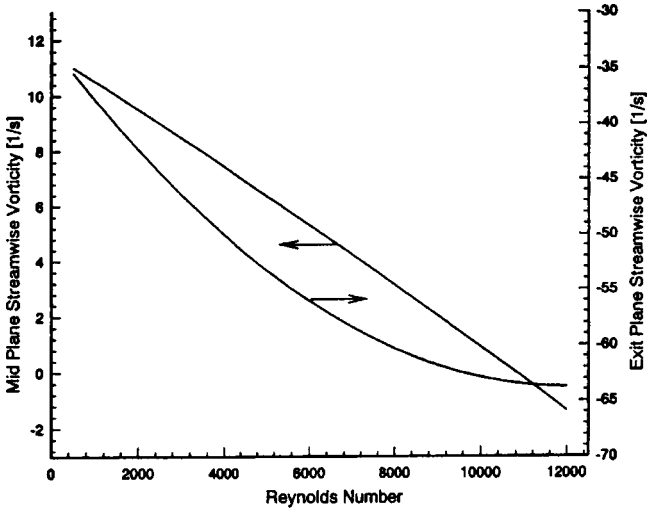

Fig. 13 Streamwise vorticity for $Ro_m=2.5$

A direct comparison of experimental and analytical results shows that the streamwise vorticity trends are well predicted (counterclockwise circulatory secondary flow in midplane, $\xi_s > 0$; clockwise circulating secondary flow in the exit plane, $\xi_s < 0$), but the model underpredicts the vorticity in the midplane and overpredicts it in the exit plane. Since the jet/wake flow was also underpredicted in the mid and overpredicted in the exit plane by the models above, and since jet/wake flow and vorticity are closely related by Eq. (3), this behavior is consistent. It is interesting to note that the midplane counterclockwise secondary flow circulation is primarily driven by the first term of Eq. (3) (bending of nonuniform flow) while the exit plane clockwise secondary flow circulation is primarily driven by the second term of Eq. (3) (Coriolis rotation of nonuniform flow).

Parametric Study of Nondimensional Parameters. Parametric studies are performed to evaluate the relative influence of the nondimensional jet/wake parameters on the torque converter pump streamwise vorticity and subsequent secondary flows. Of particular interest is the effect on the flow field of varying the nondimensional force parameters: the Reynolds number and the modified Rossby number. Also, the influence of the impeller backsweeping angle on the secondary flow is studied for a range of Reynolds and modified Rossby numbers. For these studies, normal and binormal vorticity results from the pressure-to-suction and core-to-shell jet/wake flow studies in Chap. 10 are used in Eq. (3) to determine the streamwise vorticity component. The geometry employed for all parametric studies is again the torque converter pump with $R=0.0661$ m, $h=0.040{,}61$ m, $L_i=0.0155$ m, $L_o=0.024{,}96$ m, and $r=0.0203$ m.

Reynolds Number. The relative influence of the Reynolds number on the torque converter pump streamwise vorticity was determined using the jet/wake models and Eq. (3). Since the Reynolds number was seen to only influence the core-to-shell side jet/wake flow, the streamwise vorticity is only affected through the second term (rotational Coriolis force term) of Eq. (3). The streamwise vorticity was determined for a range of Reynolds numbers from 500 to 12,000 while the modified Rossby number was fixed at 3.0 ($\omega=90.1$ rad/s$=860$ rpm, $V_i=1.0$ m/s). Figure 13 shows the pump mid- and exit plane analytical average streamwise vorticity as a function of the Reynolds number. Decreasing vorticity values in both planes for increasing Reynolds numbers are seen. This trend is consistent with increasing core-to-shell side jet/wake behavior for increasing Reynolds numbers, and, thus increasing binormal vorticity, ξ_b. Since the second term of Eq. (3) is negative, an increasing binormal vorticity will result in a decreasing streamwise vorticity, which is consistent with the observations from Fig. 13. Hence, increasing the pump Reynolds number will result in stronger clockwise circulating secondary flows in the exit plane and weaker counterclockwise circulating flows in the mid plane.

Modified Rossby Number. The modified Rossby number was previously seen to strongly affect the pressure-to-suction side jet/wake flow (and the normal vorticity, ξ_n) and, therefore, should have an equally strong effect on the first streamwise vorticity generation term in Eq. (3). The binormal vorticity [second term Eq. (3)] is not affected by the modified Rossby number, but during actual torque converter operation the modified Rossby number typically changes with pump speed, ω. Hence, the second term in Eq. (3) is also affected by the modified Rossby number via changes in the pump rotational speed.

To study this influence, a parametric study was performed in which the modified Rossby number was varied over a range from 0.5 to 4.0 (this corresponds approximately to a pump rotational speed range from 140 to 1200 rpm for the 230 mm torque converter at the 0.800 speed ratio) while the Reynolds number was held constant at 5000 ($V_i=1.0$ m/s). Figure 14 shows the pump mid- and exit plane average streamwise vorticity, obtained from Eq. (3) as a function of the modified Rossby number. Some experimental results for the pump exit plane are also included. Results in Fig. 14 show that by increasing the modified Rossby num-

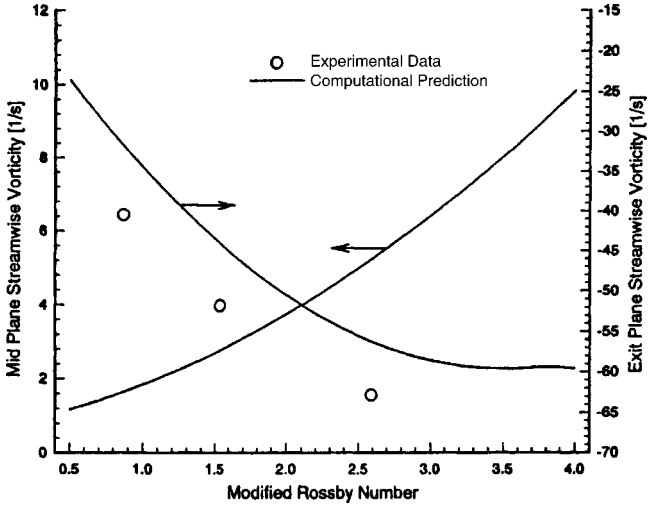

Fig. 14 Streamwise vorticity for Re=5000

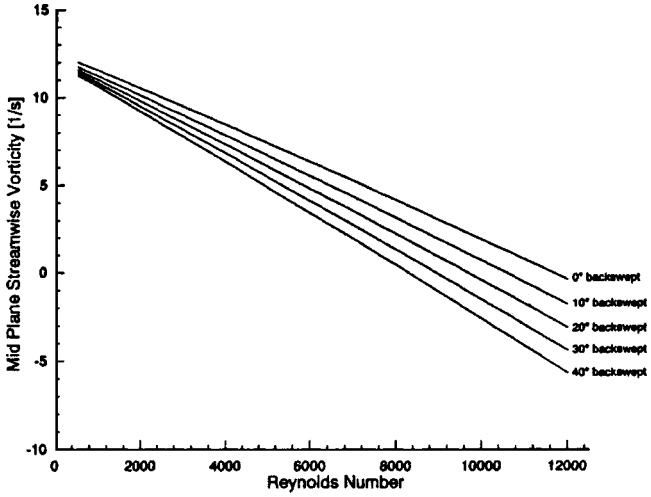

Fig. 15 Mid-plane streamwise vorticity for five backswept angles

ber, the positive streamwise vorticity in the midplane is increased and the negative streamwise vorticity in the exit plane is decreased. Experimental results are seen to agree well. This is consistent with observations of stronger jet/wake flow for larger modified Rossby numbers. Thus, by increasing the modified Rossby number (effectively increasing the pump speed) the counterclockwise circulating mid plane and the clockwise circulating exit plane secondary flows are significantly amplified.

Backsweeping Angle. Earlier the effect of changing the pump backsweeping angle on the pressure-to-suction side jet/wake phenomenon was studied. The results are utilized here to study the effect of backsweeping on the average streamwise vorticity generation and the associated circulatory secondary flows. For five different backsweeping angles the Reynolds and modified Rossby number were varied (Ro_m: 0.5–4.0, Re: 500–12,000) and the mid- and exit plane streamwise vorticity was determined from Eq. (3). Vorticity results are presented in Fig. 15 for the Reynolds number variation and in Fig. 16 for the modified Rossby number variation.

Figure 15 shows the mid plane average streamwise vorticity versus Reynolds number for the series of backsweeping angles, while the modified Rossby number was fixed at 3.0. The magnitude of the midplane streamwise vorticity is seen to decrease with increasing backsweeping angle. Since the backsweeping angle significantly affects the pressure-to-suction side jet/wake flow (Sec. 10.3.5) and, thus, the normal vorticity component, ξ_n, a strong influence on the first term of equation (flow bending) is expected. This is confirmed by the above observations; namely, a more uniform flow field (less jet/wake) decreases the generation of positive streamwise vorticity (counterclockwise circulatory secondary flows).

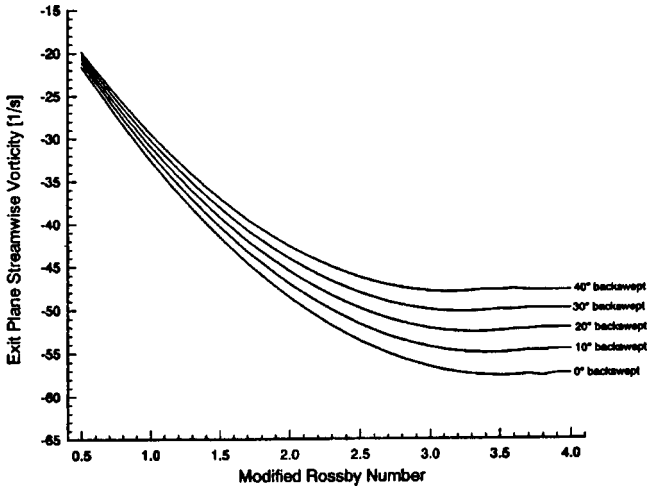

Fig. 16 Exit plane streamwise vorticity for five backswept angles

Table 4 Summary of influences on the pump circulatory secondary flow

	Mid Plane Vorticity	Mid Plane Flow	Exit Vorticity	Exit Plane Flow
Ro_m	⇑	CCW	⇓	CW
Re	⇓	CW	⇓	CW
β	⇓	CW	⇑	CCW
ω	⇓	CW	⇓	CW

Similarly, the pump exit plane average streamwise vorticity versus Reynolds number was studied. For this case, the influence of the backsweeping angle was seen to be weak; the streamwise vorticity magnitude slightly increases with an increasing backsweeping angle. This can be explained by the decreasing midplane vorticity causing the total integrated vorticity to decrease as well. Since the second term of Eq. (3) dominates in the exit plane secondary flow and since this term is not affected by the pressure-to-suction jet/wake, the influence of the backsweeping angle on the exit plane streamwise vorticity is weak.

Figure 16 present the pump mid plane average streamwise vorticity versus the modified Rossby number for the series of backsweeping angles. For this case the Reynolds number was held constant at 5000. Resulting streamwise vorticity trends are very similar to the observations from earlier. The physical explanations for decreasing midplane and increasing exit plane streamwise vorticity magnitudes are also identical to the ones given in the above paragraph; namely, the magnitude of the first term in Eq. (3) decreases with an increasing backsweeping angle (more uniform pressure-to-suction side flow) and less counterclockwise (positive) streamwise vorticity is generated. Hence, by increasing the backsweeping angle the midplane counterclockwise secondary flow circulation is reduced, while the exit plane clockwise flow circulation is increased.

General Secondary Flow and Streamwise Vorticity Trends Predicted secondary flows in the torque converter pump were seen to circulate in the counterclockwise direction (positive streamwise vorticity) in the pump mid plane and in the clockwise direction (negative streamwise vorticity) in the pump exit plane. These trends agree well with experimental observations. Both the Reynolds number and the modified Rossby number had a strong influence on the streamwise vorticity and, thus, on the magnitude of the secondary flow velocities.

The pump midplane counterclockwise secondary flow circulation was primarily caused by the interaction of the pressure-to-suction side jet/wake nonuniform flow (and the associated normal vorticity component) with the high radial/axial flow turning angle the flow undergoes while passing through a blade passage. Similarly, the pump exit plane clockwise secondary flow circulation was caused by the core-to-shell side jet/wake nonuniform flow (and the associated binormal vorticity component) being rotated around a fixed centerline (pump shaft). Hence, the pump streamwise vorticity, which was responsible for the generation circulatory secondary flows, was directly related to the pump jet/wake phenomena discussed earlier.

To summarize the earlier secondary flow observations, Table 4 shows qualitatively how the circulatory secondary flow is affected by increasing the Reynolds number, the modified Rossby number, the pump rotational speed, and the backsweeping angle. Here, ⇓,

indicates increasing and, ⇑, decreasing streamwise vorticity. Also, clockwise (CW) indicates increasing clockwise rotation and, counterclockwise (CCW), indicates increased counterclockwise secondary flow rotation.

Conclusions

The complex three-dimensional velocity field inside the automotive torque converter was previously experimentally determined using laser velocimetry. Results showed strong jet/wake including backflows and circulatory secondary flows in the pump. Particularly interesting was the sign change in rotation as the flow traversed from the midplane to the exit plane. For this paper to understand the fundamental flow behavior simplified analytical/numerical flow models, based on two-dimensional Navier-Stokes equation solutions and the streamwise vorticity generation equations, were developed to independently analyze the pump pressure-to-suction side jet/wake flow, the core-to-shell side jet/wake flow, and the circulating secondary flow phenomena. Parametric studies, based on the two-dimensional flow models, were undertaken to evaluate the effect that torque converter operating conditions and pump geometry had on the jet/wake flow parameters and the pump secondary velocities. Previous to this study the different mechanisms had not been separated to ascertain the magnitude and significance of the different effects on the jet-wake and secondary flows. Trends seen in the results from these studies compared favorably with experimental results.

To model and analyze the jet/wake phenomena observed in the pump, Navier-Stokes equation solutions for two simple two-dimensional flows (from a commercially available flow solver) were employed: (i) a rotating straight-walled duct to model the pressure-to-suction side jet/wake flow due to rotational Coriolis forces and (ii) a 180 deg flow bend to model the core-to-shell side jet/wake flow due to rapid radial/axial flow turning. Using the first of these two simple models the formation and development of the pump pressure-suction surface jet/wake flow was studied in detail in part I of this paper. In this second part the second model was be analyzed and added to the results from part I.

As indicated in part I, it is very important to recognize that the goal of these two papers is not to accurately predict the total flow field by superimposing the two results. Other authors have used full 3D models have been used to predict the total flow fields but using such models does not allow for the separation of different forces so that the fundamentals can be understood.

Results from the second model showed that the core side wake, which was due to flow separation caused by rapid radial flow turning, was primarily a function of the Reynolds number ($\mathrm{Re}=\rho V_i R/\mu$) and independent of the modified Rossby number ($\mathrm{Ro}_m=\omega R/2V_i$). For example, increasing the Reynolds number increased the core-to-shell side jet/wake flow. One of the most significant geometric parameters that was seen to affect the pump flow was the passage length (or curvature) for the core-to-shell jet/wake.

Using the modified equations for the generation of streamwise vorticity and the results from the two-dimensional jet/wake model for the normal and binormal vorticity components, trends for the secondary flows in the torque converter pump were predicted. Based on this simple model, a number of parametric studies were undertaken to evaluate the influence of the pump operating conditions and geometry on the secondary flows and the associated streamwise vorticities.

Predicted secondary flows in the torque converter pump circulated in the counterclockwise direction (positive streamwise vorticity) in the pump midplane and in the clockwise direction (negative streamwise vorticity) in the pump exit plane. These trends agreed with experimental observations. Both the Reynolds number and the modified Rossby number were seen to have a significant influence on the streamwise vorticity and, thus, on the magnitude of the secondary flow velocities.

The pump midplane counterclockwise secondary flow circulation was primarily caused by the interaction of the pressure-to-suction side jet/wake nonuniform flow (and the associated normal vorticity component) with the high radial/axial flow turning angle the flow underwent while passing through blade passage. Similarly, the pump exit plane clockwise secondary flow circulation was caused by the core-to-shell side jet/wake nonuniform flow (and the associated binormal vorticity component) being rotated about a fixed centerline (pump shaft). Thus, the pump streamwise vorticity, which was responsible for the generation circulatory secondary flows, was directly related to the pump jet/wake phenomena.

Acknowledgments

This research was sponsored by the General Motors Corporation Powertrain Division, the ROMAC Industrial Research Program at the University of Virginia, and by Blue Ridge Numerics, Inc.

References

[1] Krain, H., 1981, "A Study on Centrifugal Impeller and Diffuser Flow," J. Eng. Power, **103**, pp. 688–697.
[2] Moore, J., and Moore, J. G., 1981, "Calculations of Three-Dimensional Viscous Flow and Wake Development in a Centrifugal Impeller," J. Eng. Power, **103**, pp. 367–372.
[3] Eckardt, D., 1976, "Detailed Flow Investigations Within a High Speed Centrifugal Compressor Impeller," ASME J. Fluids Eng., **98**, pp. 390–402.
[4] Howard, J. H. G., and Lennemann, E., 1971, "Measured and Predicted Secondary Flows in a Centrifugal Impeller," J. Eng. Power, **103**, pp. 126–132.
[5] Gruver, J. K., Flack, R. D., and Brun, K., 1996, "Laser Velocimeter Measurements in the Pump of a Torque Converter Part I—Average Measurements," ASME J. Turbomach., **118**, pp. 562–569.
[6] Brun, K., and Flack, R. D., 1997, "Laser Velocimeter Measurements in the Turbine of an Automotive Torque Converter, Part I—Average Measurements," ASME J. Turbomach., **119**, pp. 646–654.
[7] Johnson, M. W., and Moore, J., 1982, "Secondary Flow Mixing Losses in a Centrifugal Impeller," 27th International Gas Turbine and Aeroengine Congress and Exposition, London, England, April 18–22, ASME paper no. 82-GT-44.
[8] Mori, Y., Uchida, Y., and Ukon, T., 1971, "Forced Convective Heat Transfer in a Curved Channel With a Square Cross-Section," Int. J. Heat Mass Transfer, **14**, pp. 1787–1793.
[9] Rowe, M., 1970, "Measurements and Computations of Flows in Pipe Bends," J. Fluid Mech., **43**, pp. 771–778.
[10] Johnson, M. W., 1978, "Secondary Flow in Rotating Bends," J. Eng. Power, **100**, pp. 553–560.
[11] Hawthorne, W. R., 1951, "Secondary Circulation in Fluid Flow," Proc. R. Soc. London, **206**, pp. 374–387.
[12] Smith, L. H., 1955, "Secondary Flow in Axial-Flow Turbomachinery," Trans. ASME, **77**, pp. 1065–1076.
[13] Smith, A. G., 1957, "On the Generation of the Streamwise Component of Vorticity for Flows in Rotating Passages," Aeronaut. Q., **8**, pp. 369–382.
[14] Ellis, G. O., 1964, "A Study of Induced Vorticity in Centrifugal Compressors," J. Eng. Power, **86**, pp. 63–76.
[15] Howard, J. H. G., 1966, "Analytical Theory of Secondary Flow in a Centrifugal Impeller," EIC Report, No. EIC-MECH 4, Waterloo, Ontario, Canada.
[16] Lakshminarayana, B., and Horlock, J. H., 1973, "Generalized Expressions for Secondary Vorticity Using Intrinsic Co-Ordinates," J. Fluid Mech., **59**, pp. 97–115.

Piotr Lampart
Institute of Fluid Flow Machinery,
Polish Academy of Sciences,
ul. Fiszera 14,
80-231 Gdańsk, Poland

Andrey Rusanov

Sergey Yershov

Ukrainian National Academy of Sciences,
2/10 Pozharsky,
61046 Kharkov, Ukraine,
also FLower Ltd.,
42/226 Tobolskaya,
61072 Kharkov, Ukraine

Stanislaw Marcinkowski

Andrzej Gardzilewicz

Institute of Fluid Flow Machinery,
Polish Academy of Sciences,
ul. Fiszera 14,
80-231 Gdańsk, Poland

Validation of a 3D RANS Solver With a State Equation of Thermally Perfect and Calorically Imperfect Gas on a Multi-Stage Low-Pressure Steam Turbine Flow

A state equation of thermally perfect and calorically imperfect gas is implemented in a 3D RANS solver for turbomachinery flow applications. The specific heats are assumed as linear functions of temperature. The model is validated on a five-stage low-pressure steam turbine. The computational results exhibit the process of expansion in the turbine. The computed and measured distributions of flow parameters in axial gaps downstream of subsequent turbine stages are found to agree reasonably well. It is also shown that the obtained numerical solution gives considerable improvement over the solution based on the thermally and calorically perfect gas model. [DOI: 10.1115/1.1852491]

1 Introduction

Navier–Stokes solvers for turbomachinery applications usually operate on the thermal and caloric equation of perfect gas, where the constants that link thermodynamic parameters, that is the individual gas constant R and specific heat ratio γ, remain unchanged in the entire flow region.

This approach is relatively well-grounded for one-component one-phase flow, which in steam turbines is believed to take place in high and intermediate pressure turbine stages where the steam is superheated. The approach requires determination of an individual gas constant and setting appropriate values of specific heats, or specific heat ratio. Unless the range of variation of flow parameters is too wide (exit/inlet pressure ratio too low as in multi-stage configurations), the scheme will converge and a reliable solution will be obtained.

The perfect gas equations cannot be accepted for solving the flow in low pressure (LP) turbines, where the steam expands across the saturation line, changing dramatically its properties. For a long time, a common practice of computational fluid dynamics (CFD) research engineers was to perform calculations of low pressure turbines individually for each stage, using the perfect gas equation and changing the constant values of the individual gas constant and specific heat ratio from stage to stage. Even this single-stage approach does not guarantee the correctness of the solution in the wet steam region. Another feature of flow computation is lost, as compared to the multi-stage approach, that is the automatic passing of flow parameters between the stages and allowing the mixing processes generated in one stage to be completed or continued in the subsequent stage(s). Single-stage computations would also require boundary conditions for each stage which have to be provided from a 0D/1D solver, or from pressure/temperature measurements in stage-to-stage gaps. Then, most likely, an opportunity is lost to validate the calculations using experimental investigations that are made in stage-to-stage gaps. This is usually due to a simple fact that there are no other sections available that were measured and not assumed as sections where computational boundary conditions are imposed.

Works are currently in progress to incorporate real gas effects into 3D turbomachinery flow solvers. Sturmayr and Hirsch [1] make use of IAPWS-95 steam tables (equilibrium steam properties) and a switched condensation model to account for transition between the metastable and equilibrium region. In addition to an array of Euler equations, a scalar convection-diffusion equation is solved for the condensation switch that is a measure of delay in transition from the subcooled dry to equilibrium wet steam until an appropriate level of subcooling is reached. In the paper by Bohn et al. [2], the flow field with homogeneous and heterogeneous condensation is calculated under metastable conditions as obtained from IAPWS-IF 97 steam tables. Dykas [3] estimates that computational costs of implementation of IAPWS-IF 97 tables are very high, possibly even as high as two orders of magnitude, as compared to the perfect gas equation. To reduce computational costs, Chmielniak et al. [4] and Wróblewski [5] propose to use a virial equation with three coefficients for superheated and subcooled steam

$$pv/RT = 1 + B(T)p + C(T)p^2 + D(T)p^3,$$

whereas Dykas [3] and Dykas et al. [6] propose the so-called local real gas equation of state similar to the above virial equation

$$pv/RT = A(T) + B(T)/v.$$

The virial coefficients are functions of temperature only and can be found from approximation of thermodynamic properties of water and steam IAPWS'97. The computational costs of flow solver using a virial equation are estimated in [3] to increase by a factor of 3–8 over the solver with the perfect gas equation. A set of additional differential convection-diffusion equations drawing on the classical nucleation theory is also used in [3–6] to describe the formation of the liquid phase (wetness fraction).

Contributed by the Fluids Engineering Division for publication in the JOURNAL OF FLUIDS ENGINEERING. Manuscript received by the Fluids Engineering Division December 11, 2003; revised manuscript received October 6, 2004. Review conducted by: W. Copenhaver.

The approach suggested in this paper is still a simpler and less costly modification of the perfect gas equation, that is the equation of thermally perfect and calorically imperfect gas, which makes specific heats c_v, c_p variable as linear functions of temperature. The effect of the introduced modification on the distribution of thermodynamic parameters is illustrated using a computational example of a five-stage LP steam turbine.

2 3D RANS Equations

In the code FlowER developed by Yershov and Rusanov [7], 3D viscous compressible flow through a turbine/compressor stage can be described by a set of unsteady Reynolds-averaged Navier–Stokes equations written in a curvilinear body-fitted coordinate system (ξ,η,ζ), rotating with an angular speed ϖ

$$\frac{\partial QJ}{\partial t}+\frac{\partial(E\xi_x+F\xi_y+G\xi_z)J}{\partial\xi}+\frac{\partial(E\eta_x+F\eta_y+G\eta_z)J}{\partial\eta}+\frac{\partial(E\zeta_x+F\zeta_y+G\zeta_z)J}{\partial\zeta}=HJ,$$

$$Q=\begin{bmatrix}\rho\\ \rho u\\ \rho v\\ \rho w\\ \rho h\end{bmatrix};\quad H=\begin{bmatrix}0\\ 2\rho v\varpi+\rho\varpi^2 r_x\\ -2\rho u\varpi+\rho\varpi^2 r_y\\ 0\\ 0\end{bmatrix};$$

$$E=\begin{bmatrix}\rho u\\ \rho u^2+p-\tau_{xx}\\ \rho uv-\tau_{xy}\\ \rho uw-\tau_{xz}\\ (\rho h+p)u-u\tau_{xx}-v\tau_{xy}-w\tau_{xz}+q_x\end{bmatrix};$$

$$F=\begin{bmatrix}\rho v\\ \rho uv-\tau_{xy}\\ \rho v^2+p-\tau_{yy}\\ \rho vw-\tau_{yz}\\ (\rho h+p)v-u\tau_{xy}-v\tau_{yy}-w\tau_{yz}+q_y\end{bmatrix};$$

$$G=\begin{bmatrix}\rho w\\ \rho uw-\tau_{xz}\\ \rho vw-\tau_{yz}\\ \rho w^2+p-\tau_{zz}\\ (\rho h+p)w-u\tau_{xz}-v\tau_{yz}-w\tau_{zz}+q_z\end{bmatrix};\qquad(1)$$

$$q=-\lambda\nabla T,\quad h=\varepsilon+\frac{u^2+v^2+w^2-\varpi^2r^2}{2}+\text{const}$$

$$\tau_{ij}=\tau_{mij}+\tau_{tij};\quad \tau_{mij}=2\mu_m(S_{ij}-S_{nn}\delta_{ij}/3),$$

$$\tau_{tij}=2\mu_t(S_{ij}-S_{nn}\delta_{ij}/3)-2\rho k\delta_{ij}/3$$

The symbols ε, p, ρ, u, v, w denote the internal energy, pressure, density, and components of the velocity; T is temperature; τ_{mij}, τ_{tij}, τ_{ij} are the molecular, turbulent, and total viscous stress; S_{ij} is the mean strain-rate tensor; $\mu=(\mu_m+\mu_t)$ is the effective (molecular+turbulent) viscosity; q is the heat flux; $\lambda=(\lambda_m+\lambda_t)=c_p(\mu_m/Pr_m+\mu_t/\mathrm{Pr}_t)$ is the effective (molecular+turbulent) heat conductivity; and Pr_m, Pr_t are molecular and turbulent Prandtl numbers.

The governing equations are supplemented with the two-equation turbulence model SST (shear stress transport) of Menter [8]. In this model, the standard k-ω model is activated in the near wall region, and then switched to the k-ε model in the wake region of the boundary layer and free shear layers. In order to more adequately predict strong adverse pressure gradient flows, the eddy viscosity is redefined so as to guarantee the proportional relationship between the principal turbulent shear stress and the turbulent kinetic energy in the boundary layer. A number of test cases given by Menter, including Driver's adverse pressure gradient flow, backward-facing step, NACA airfoil and transonic bump flows, show that the SST model yields a substantially better agreement with the experimental data, compared to those of other turbulence models. The Menter SST turbulence model in k-ω formulation can be written as

$$\frac{\partial U}{\partial t}+\frac{\partial R_i}{\partial x_i}=G-D+L;$$

$$U=\begin{bmatrix}\rho k\\ \rho\omega\end{bmatrix};\quad R_i=\begin{bmatrix}\rho k-(\mu+\sigma_k\mu_t)\dfrac{\partial k}{\partial x_i}\\ \rho\omega-(\mu+\sigma_\omega\mu_t)\dfrac{\partial\omega}{\partial x_i}\end{bmatrix};$$

$$G=\begin{bmatrix}\tau_{ij}S_{ij}\\ \gamma\dfrac{\omega}{k}\tau_{ij}S_{ij}\end{bmatrix};\quad D=\begin{bmatrix}\beta^*\rho\omega k\\ \beta\rho\omega^2\end{bmatrix};\qquad(2)$$

$$L=\begin{bmatrix}0\\ 2(1-F_1)\dfrac{\rho\sigma_{\omega2}}{\omega}\dfrac{\partial k}{\partial x_i}\dfrac{\partial\omega}{\partial x_i}\end{bmatrix};\quad \mu_t=\frac{\rho k/\omega}{\max[1;\Omega F_2/(a_1\omega)]}.$$

where k is the turbulent kinetic energy; $\omega=\varepsilon/k\beta^*$ is the specific dissipation rate and μ_t is turbulent viscosity. Blending functions F_1 (assuring smooth transition from the k-ω to the k-ε, and assuming one in the sublayer and logarithmic region and gradually switching to zero in the wake region of the boundary layer) and F_2 (assuring the proportional relationship between the principal turbulent shear stress and the turbulent kinetic energy in the boundary layer, and assuming one in the boundary layers and switching to zero in free shear layers) are

$$F_1=\tanh\{[\min(A_1;A_2)]^4\};\quad F_2=\tanh\{[\max(2B_1;B_2)]^2\}$$

$$A_1=\max(B_1;B_2);\quad A_2=\frac{4\rho\sigma_{\omega2}k}{CD_{k\omega}y^2};\quad B_1=\frac{\sqrt{k}}{\beta^*\omega y};$$

$$B_2=\frac{500\mu}{\rho y^2\omega};$$

$$CD_{k\omega}=\max\left(2\frac{\rho\sigma_{\omega2}}{\omega}\frac{\partial k}{\partial x_i}\frac{\partial\omega}{\partial x_i};10^{-20}\right)$$

A vector of constants $\phi=[\sigma_k,\sigma_\omega,\beta,\gamma]$ in the SST model can be written $\phi=F_1\phi_1+(1-F_1)\phi_2$, where ϕ_1 is this vector in the k-ω model, and ϕ_2 is in the k$-\varepsilon$ model written in k-ω formulation. The constants of the model are $a_1=0.31$, $\sigma_{k1}=0.85$, $\sigma_{k2}=1.0$, $\sigma_{\omega1}=0.5$, $\sigma_{\omega2}=0.856$, $\beta^*=0.09$; $\beta_1=0.075$, $\beta_2=0.0828$, $\gamma_1=0.553$, and $\gamma_2=0.44$. The distance function y is defined as a distance from the nearest wall in the 3D blade-to-blade passage. This function is important for switching between the k-ε and k-ω model. However, this function does not determine the turbulent length scale (as, e.g., for the Spalart–Allmaras model).

The boundary conditions for the set of equations (1) are at the walls—no-slip and no heat flux; at the inlet to the stage—spanwise distribution of the total pressure, total temperature, and flow angles; and at the exit—static pressure (either its spanwise distribution or a value at the mid-span with the radial equilibrium equation). The assumed boundary conditions impose the pressure drop across the flow domain and let the mass flow rate be resultant. For the set of Eqs. (2), the boundary conditions are at the walls—$k=0$; $\omega=60\mu_w/\rho_w\beta y^2$; at the inlet—$k=1.5(TuU_\infty)^2$; $\omega=[\max(S\Omega,\Omega^2)]^{0.5}$, where $S=(S_{ij}S_{ij}/2)^{0.5}$, Tu is the inlet free-stream turbulence, Ω is the vorticity (absolute value), and the subscript w denotes values at the wall; at the outlet—values of k and ω are extrapolated from the preceding cell centers.

The numerical solution is based on finite volume discretization and a Godunov-type upwind scheme where the inviscid fluxes at

the cell walls are calculated from the solution of the Riemann problem. Initial values for the Riemann problem are found from a series expansion around the cell center values where a high-order ENO (essentially nonoscillating) scheme is used to calculate spatial derivatives. The time-marching calculations converge to a steady state. To accelerate the process of convergence, a δ-form implicit operator of Beam and Warming is used. The viscous fluxes are calculated based on ENO interpolation. The numerical scheme assures second-order accuracy everywhere in space and time. For details of the numerical scheme, see Yershov [9] and also Yershov et al. [10]. The computations are carried out on an H-type multi-grid, refined near the endwalls, blade walls, and leading and trailing edges. One blade-to-blade passage from each blade row is computed. The mixing plane model is used where the distribution of flow parameters between the fixed/moving blade rows is transmitted in the radial direction and averaged circumferentially. The approach neglects the effect of stator/rotor interaction, which can be studied using sliding meshes at further expense of CPU time. The convergence of the calculations to a steady state is checked for the components of force acting at the blades of stator(s) and rotor(s) as well as for the difference in inlet and exit mass flow rates for each blade row. The calculations are stopped if the maximum deviations of current values of force components from the respective mean values for the latest 500 iterations do not exceed 0.1% of the mean values, and if the maximum discrepancy between the calculated mass flow rate at the inlet and exit of each stage is also less than 0.1% for the latest 500 iterations. The code has recently been validated on a number of turbomachinery test cases, including the Durham low speed turbine cascade, the NASA Rotor37, the NASA low speed centrifugal compressor, and the model air turbine of ITC Łódź (Poland) (see [11,12]).

3 State Equations

A standard equation of state closing the system of Navier–Stokes equations for CFD codes with turbomachinery applications is the state equation of thermally and calorically perfect gas, where the constants that link thermodynamic remain unchanged in the entire flow region

$$p = R\rho T; \quad i = \frac{\gamma}{\gamma - 1}\frac{p}{\rho} + \text{const}; \quad s = c_v \ln T - R \ln \rho + \text{const},$$
$$R = c_p - c_v; \quad \gamma = c_p / c_v; \quad c_p, c_v, R, \gamma = \text{const}. \tag{3}$$

The used symbols p, ρ, T, i, and s denote pressure, density, temperature, enthalpy and entropy; c_p, c_v are specific heats at constant pressure and volume, respectively; $R = c_p - c_v$ is the individual gas constant; $\gamma = c_p / c_v$ is the specific heat ratio. The above state equation is appropriate for solving the flow in high-pressure and intermediate-pressure turbines.

For multi-stage computations of low-pressure turbine flows, a modification of the above state equation, that is the state equation for thermally perfect and calorically imperfect gas, is suggested. The specific heats at constant volume and pressure c_v, c_p are assumed here to vary as linear functions of temperature, but the individual gas constant R does not change

$$p = R\rho T, \quad i = c_{v0} T + \frac{1}{2} c_v^t T^2 + \frac{p}{\rho} + \text{const};$$
$$s = c_{v0} \ln T - R \ln \rho + c_v^t T + \text{const},$$
$$c_v(T) = c_{v0} + c_v^t T, \quad c_p(T) = R + c_v(T); \quad R = \text{const}; \tag{4}$$
$$c_{v0}, c_v^t = \text{const}, \quad c_v^t \neq 0$$

The coefficients c_{v0}, c_v^t are found individually for each computation based on inlet/exit pressure, temperature and enthalpy, which is demonstrated in Sec. 8. This model of thermally perfect and calorically imperfect gas is implemented in the code FlowER.

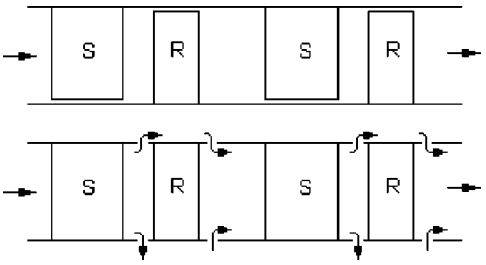

Fig. 1 Computational domains in code FlowER—computational domain with radial gaps over unshrouded blade tips (top), computational domain with source/sink-type permeable boundaries to simulate the effect of leakage over shrouded blade tips and windage flows (bottom); S—stator, R—rotor

4 Leakage Flows

In turbomachinery flows, to obtain reliable multi-stage predictions of flow patterns and efficiency estimates, it is also necessary to take into account the effects of leakage flows and extractions. Leakage flows do not yield stage work, and their mixing with the main stream adds to enthalpy losses in turbines. In the code FlowER, the computational domain may extend to the region over unshrouded blade tips, which enables direct computation of leakage over this type of blade. For shrouded blades, the leakage stream flows through labyrinth seal chambers, usually of complex geometry. Therefore, it looks reasonable to neglect, in the first approximation, the detailed structure of a leakage jet in the labyrinth seals or a windage flow between the fixed and rotating discs, and treat them as a source or sink of mass flow for the blade-to-blade passage. To model this type of leakage flows, the computational domain is modified at the endwalls where some places are permeable boundaries of the domain (see Fig. 1). The approach enables interaction of leakage flows with the main stream. It underlies the message that most of entropy creation due to leakage flows does not take place in the labyrinth seals or in passages between the fixed and rotating discs, but in the blade-to-blade passages during the leakage jet reentry when the leakage jet mixes with the main stream (see [13]). The idea of mass sink can also be extended on technological extractions at the extraction points.

One possible and convenient way of imposing boundary conditions for the source/sink approach is to prescribe a leakage mass flow rate G for an extraction; total temperature T_{0T}, mass flow rate G and flow direction of the leakage flow (meridional angle γ and swirl angle α) for an injection. Leakage mass flow rates of the injected/extracted fluid—equivalent to the intensity of sources/sinks—can be calculated either from simple 0D/1D studies of leakage and windage flows or from 2D/3D flow computations in labyrinth seals and windage flow passages, the latter possibly giving also the direction of leakage jet reentry. The mass flow rate condition is formulated to be satisfied integrally through each orifice. The mass flow rate is allowed to vary from node to node of the orifice, and its distribution in the orifice is affected by streamwise and pitchwise gradient of static pressure in the blading system near the endwalls. The velocity components at the source orifice are calculated based on the constant total pressure, input flow angles, and size of the orifice. The approach enables injection of the medium at arbitrary velocities and angles, determination of the effect of mixing of the injected fluid with the main flow, as well as evaluation of interaction of leakage flows with other vortex flows—secondary flows or separations (see [14]).

5 Object of Study—Five-Stage LP Turbine

The effect of modification of the state equation on flow patterns and distribution of thermodynamic parameters is studied on a five-stage low-pressure turbine (part of a 360 MW steam turbine).

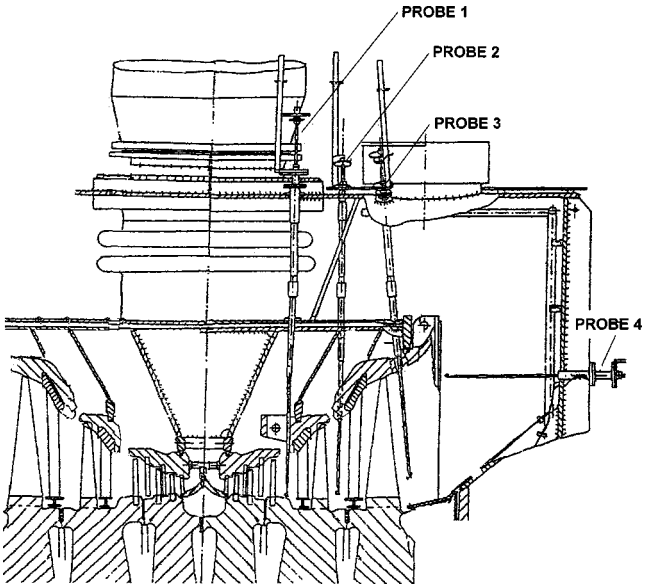

Fig. 2 LP part of 360 MW steam turbine in meridional view with measuring instrumentation

This drum-type reaction turbine has a radial inlet equipped with guide vanes and a radial outlet to the exhaust hood. Stators 2–5 and rotors 1–4 are shrouded and have typical labyrinth seals. Rotor 5 has unshrouded blades. Two regenerative extraction points are located downstream of stages 3 and 4. This LP turbine was experimentally investigated for some range of load by Marcinkowski [15]. These investigations are used in the present paper to define inlet/exit boundary conditions for the nominal load, and to validate the obtained computational results at the selected sections downstream of stages 3, 4, and 5 of the investigated turbine. A schematic diagram of the tested LP turbine in meridional view with measuring instrumentation is presented in Fig. 2.

6 LP Turbine Measurements

Measurements inside low-pressure steam turbines are known to be very difficult for several major reasons, including (1) unsteady operating conditions, (2) restricted access to the inside of the turbine, (3) choking of measuring probes with water, and (4) coincidence between isolines of pressure and temperature in the region of wet steam.

To investigate the flow field in selected sections of the LP turbine, multi-purpose probes and a measuring technique elaborated at the Institute of Fluid Flow Machinery were applied (see [16,17]). The multi-purpose probe enables (1) measurements of spanwise distribution of static and total pressure, temperature and flow angles between the blade rows at selected sections along the circumference where access is available, (2) determination of velocity distribution and evaluation of mass flow rate at characteristic control stations, and (3) determination of enthalpy drops and estimation of expansion lines for the subsequent stages.

The probes can be installed during nonstop operation into special seats prepared during an overhaul of the turbine. The installation of the probes does not disturb the turbine operation. The probes are usually 2–3 m long and perform only radial movements (with revolution). They are usually operated manually; however, in exceptional cases as well as during the calibration, their movement is motorized.

A view of the measuring probe is presented in Fig. 3. It can be classified as a disc probe. This type of probe is not sensitive to water films which form on it during the measurements. The probe head consists of four Pitot tubes inclined towards the flow at various pitch angles. It allows us to determine streamlines in the meridional plane and also to measure the total pressure, which is taken as the highest value from all tubes. Two holes are made on the side surface of the disc to determine the yaw angle. The holes are also used to measure the static pressure.

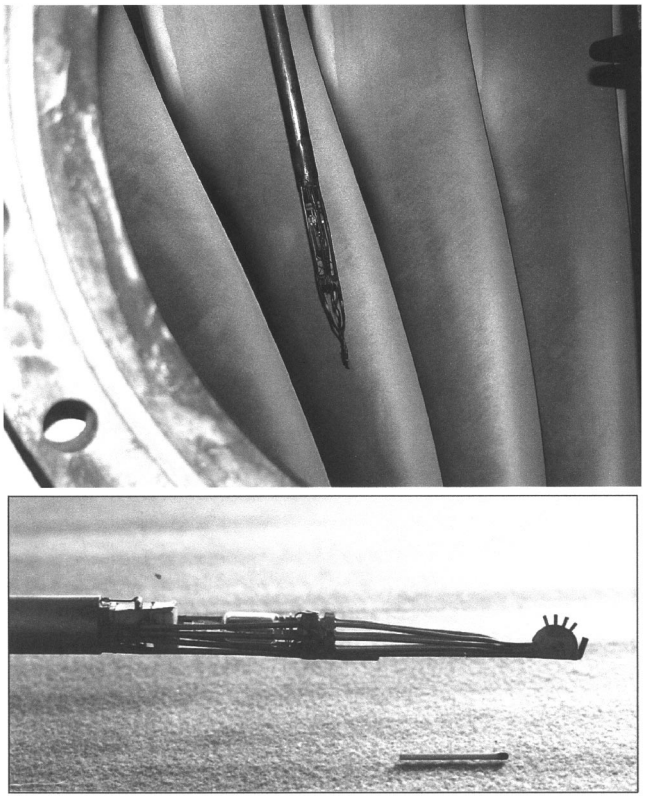

Fig. 3 Measuring probe inside the LP turbine downstream of the last stage rotor (top). Relative dimensions of the probe (bottom).

The microthermocouple for temperature measurements is mounted at the tip of the probe head. The whole tip of the probe is lined inside as well as covered outside with teflon to reduce watering of the probe and facilitate extraction of deposited water. The diameter of the probe disc is less than 20 mm. The diameter of the probe tubes at the tip is less than 1 mm. Smooth regular flow is assured at joints of tubes of different diameters. In order to perform blow-through to purge water from the probe before each measurement, a valve is installed which links all tubes with the atmosphere. After the blow-through when the measurement starts, the complete leak tightness is secured. After measurements, the probe tips have to be restored to their original condition due to large flow velocities and aggressiveness of steam, which destroys the teflon layer.

Before measurements the probe tips are calibrated in the wind tunnel. The calibration can be carried out in dry air or in wet steam with the wetness fraction less than 10% (see [18]). The position of the probe inside the turbine is determined with an accuracy of 1 mm. The pressure is measured with an accuracy of 0.5 mm Hg, which means that errors in determination of pressure in the LP turbine do not exceed 1%. Temperature readings are accurate to 0.2–0.5°C. Errors in determination of flow angles are less than 1 deg for the yaw angle and 10 deg for the meridional angle.

7 LP Turbine Efficiency

Both the computational model and measurement technique enable the evaluation of enthalpy losses in subsequent turbine stages and turbine efficiency. The enthalpy losses can be defined as

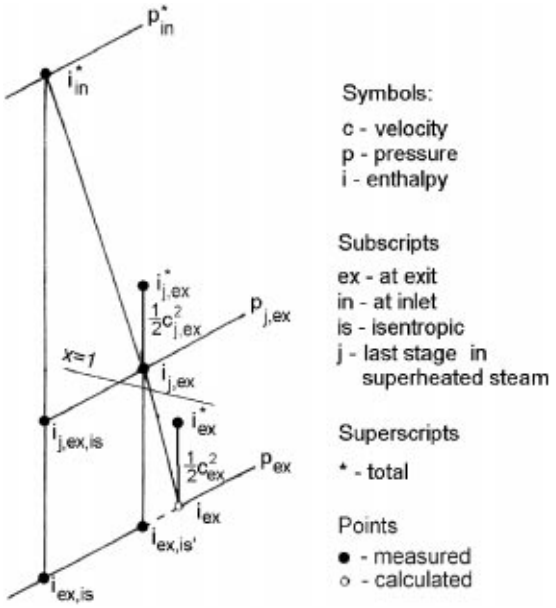

Fig. 4 Expansion line in an LP turbine for evaluation of efficiency from measurement data

$$\zeta = \frac{i_{ex} - i_{ex,is}}{i_{in}^* - i_{ex,is}}; \quad \zeta^* = \frac{i_{ex} - i_{ex,is} + c_{ex}^2/2}{i_{in}^* - i_{ex,is}}, \tag{5}$$

where ζ, ζ^* are the enthalpy losses without or with the leaving energy, respectively; c_{ex} is the exit velocity; and i_{in}^*, i_{ex}, $i_{ex,is}$ are the inlet total enthalpy, exit static enthalpy, and exit isentropic enthalpy referring to the exit pressure (superscript* denotes total values).

In the computational model, the isentropic enthalpy is given in the form $i_{ex,is} = i(p_{ex}, T_{ex,is}) = i(p_{ex}, \rho_{ex,is})$, where the isentropic temperature $T_{ex,is}$ or isentropic density $\rho_{ex,is}$ can be found from the zero entropy rise condition $s(p_{ex}, T_{ex,is}) = s(p_{in}^*, T_{in}^*)$ [see Eqs. (3) and (4)]. They can be derived analytically for the case of constant specific heats, and only numerically for the case of variable specific heats. The enthalpy losses are mass-averaged and take into account the presence of leakage streams and extractions—source/sink boundaries are treated here as inlet/exit boundaries, respectively.

The procedure of evaluation of enthalpy drops in subsequent turbine stages and efficiency of LP turbines based on the measurement data is explained in Fig. 4. It makes use of (1) measurements of distribution of static and total pressure and temperature at the inlet to the turbine and at the exit of subsequent turbine stages operating in superheated steam, (2) measurements of distribution of static and total pressure at the exit of turbine stages operating in the region of wet steam and measurement of the leaving energy, and (3) calculation of cascade losses for stages operating in wet steam. This method does not draw on measurements of dryness fraction. For superheated steam, the mass-averaged measured inlet/exit pressures and temperatures give enthalpy drops needed for Eq. (5). For wet steam, the measured inlet/exit pressures give the isentropic enthalpy drop (from the equilibrium steam tables). The real static enthalpy drop for the wet steam stages is then found assuming some value of cascade loss coefficient. This value is obtained from a 2D streamline curvature solver (see [19]). On the other hand, another considerable part of loss in LP turbines, that is the leaving energy (including also the energy connected with the tip leakage) needed for Eq. (5), is found from the measured distribution of exit velocity. Thus, of all loss components, only cascade losses in wet steam stages are calculated, whereas cascade losses in superheated steam stages and the leaving energy are measured. As a result of evaluation of cascade loss in wet steam, the equilibrium dry fraction can be found at the exit (from the equilibrium steam tables). For details of the method see [16]. A measurement method for evaluation of efficiency in wet steam turbines without measurements of dryness fraction is also described in [20].

Accuracy of determination of LP turbine efficiency based on the method presented above was studied by Krzyżanowski and Marcinkowski [21]. Errors in evaluation of efficiency for stages operating in superheated steam depend on errors in measurements of pressure and temperature distribution, errors in averaging of the obtained distribution, as well as on variation of these parameters during the measurement due to load fluctuations. Besides these factors, estimation of efficiency in exit stages operating in wet steam is charged with uncertainty over the measured leaving energy and calculated value of cascade losses, the latter found in [21] to be a prevailing error component. The error in efficiency estimation for the exit stage is $\Delta\eta = \pm 3\%$, for the LP turbine as a whole—$\Delta\eta = \pm 1.5$–2%.

8 Computational Domain and Input Data for 3D Computations

The five-stage LP turbine is calculated on a structured H-type grid of 4,600,000 cells in total refined near the endwalls, blade walls, trailing and leading edges—64 cells spanwise, 60 cells pitchwise, and 100–120 cells axially in each blade-to-blade passage. The number of cells in the axial direction varies with blade rows depending on the extension of axial diffusers. Grid refinements at the walls fulfill requirements of the assumed turbulence model in the boundary layer ($y^+ = 1$–2). In the course of investigations, grid-independence checks were made using a coarser grid of 3,800,000 cells and a more refined grid of 5,700,000 cells. With the observation that the results obtained on the three grids show no visible changes in flow patterns, and there are no changes in stage and turbine efficiencies, the calculations carried out on the grid of 4,600,000 cells were assumed as grid-independent. The flow-field results enclosed in this paper are obtained from this grid.

The gridded computational domain for the five-stage LP turbine in meridional view at mid-blade-to-blade distance and fragment of the grid in blade-to-blade view at mid-span are presented in Fig. 5. The figure exhibits also places at the endwalls where source/sink-type boundary conditions are imposed. These places numbered consecutively with the increasing axial coordinates from 1 to 18 correspond to injection or extraction of leakage flows (under the stators of stages 2 to 5 and above the rotors of stages 1 to 4), and to the extraction points downstream of stage 3 and 4.

Boundary conditions for calculations of the LP turbine are assumed based on values of parameters for nominal load obtained from the measurement technique described in the previous section—at the inlet: static temperature is $T_{in} = 538$ K, static pressure is $p_{in} = 5.14 \times 10^5$ Pa, static enthalpy is $i_{in} = 2992$ kJ/kg, dryness fraction is $x_{in} = 1.0$; at the exit: static temperature (saturation temperature) is $T_{ex} = 316$ K, static pressure is $p_{ex} = 0.086 \times 10^5$ Pa, $i_{ex} = 2352$ kJ/kg, and $x_{ex} = 0.905$ (subscripts *in* and *ex* denote inlet and exit values). Inlet/exit boundary conditions required by the solver are total temperature and total pressure at the inlet $T_{in}^* = 539$ K, $p_{in}^* = 5.19 \times 10^5$ Pa, and static pressure at the exit $p_{ex} = 0.086 \times 10^5$ Pa. The static temperatures and enthalpies at the inlet and exit are used to receive a proper linear relationship for variation of the specific heats. Values of c_{v0}, c_v^t can be found from the following system of linear equations (the third unknown is i_0)

$$i_{in} = c_{v0} T_{in} + \frac{1}{2} c_v^t T_{in}^2 + \frac{p_{in}}{\rho_{in}} + i_0;$$

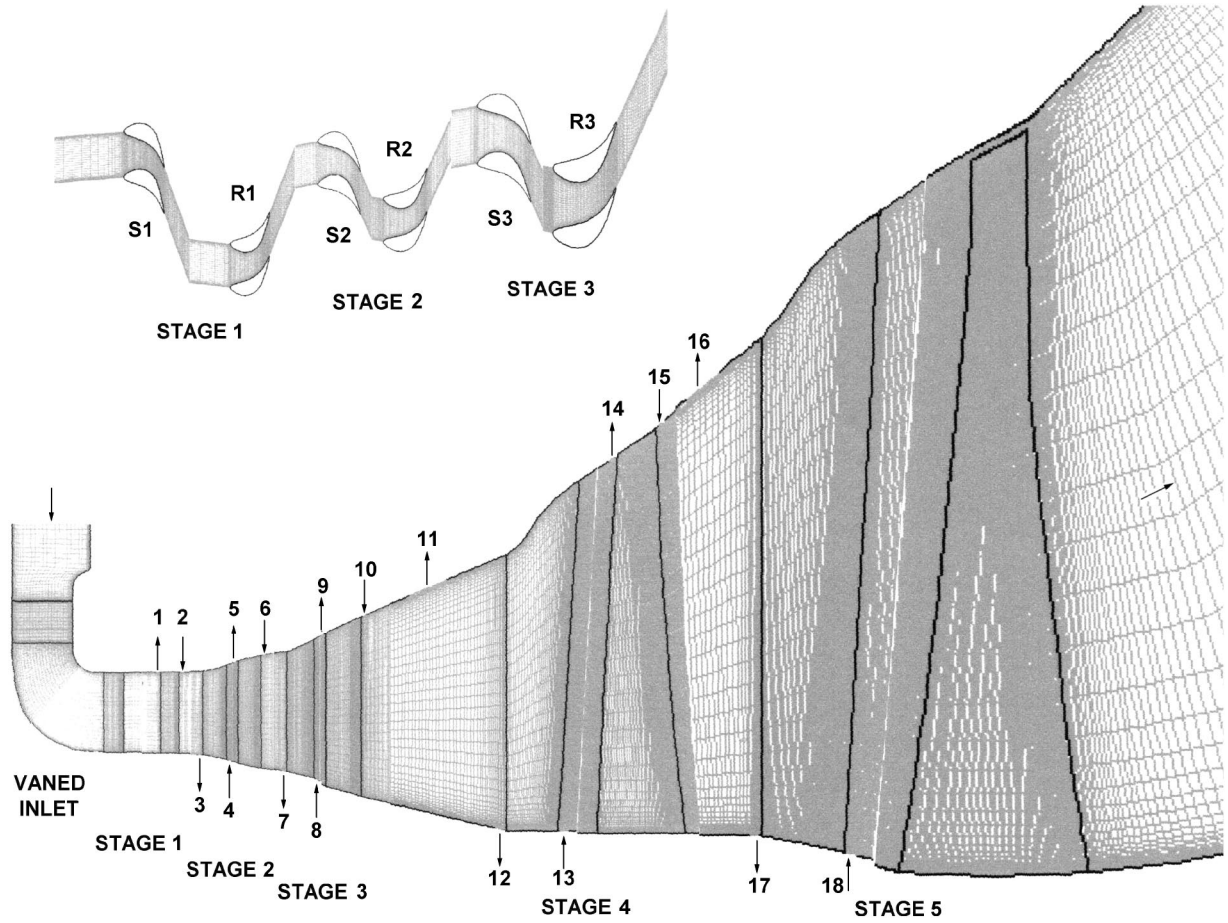

Fig. 5 Computational grid for the five-stage LP turbine in meridional view at mid blade-to-blade distance and fragment of the grid in blade-to-blade view at mid-span

$$i_{ex} = c_{v0} T_{ex} + \frac{1}{2} c_v^t T_{ex}^2 + \frac{p_{ex}}{\rho_{ex}} + i_0; \tag{6}$$

$$\gamma_{in} = \frac{c_{v0} + c_v^t T_{in} + R}{c_{v0} + c_v^t T_{in}}.$$

The individual gas constant R and specific ratio γ_{in} are assumed here to be values from the inlet in the region of superheated vapor ($R = 452$ J/kg K, $\gamma_{in} = 1.32$). Solving the system of equations (6) gives $c_{v0} = 6078$ J/kg K, $c_v^t = -8.67$ J/kg K^2, and $i_0 = 733$ kJ/kg. Thus, in the range of expected temperatures, c_v changes from 1413 J/kgK (for $T = 538$ K) to 3338 J/kg K (for $T = 316$ K), and c_p changes from 1865 to 3790 J/kgK, whereas the specific heat ratio γ changes from 1.32 to 1.135.

The computational domain extends on the region over unshrouded blade tips (rotor of stage 5), which enables direct computation of leakage over this type of blade. The labyrinth seal regions of shrouded blades and extractions are not in the computational domain, but the source/sink approach is used to tackle leakage flows and extractions. The needed boundary conditions for the source/sink approach such as mass flow rates and total temperatures of leakage flows and extractions are found from a system of 0/1D procedures that calculate a simplified heat-and-flow balance of the turbine [22]. These data for subsequent source/sink slots are collected in Table 1. Additionally, the meridional angle at injection slots, as measured counter-clockwise from the projection of the turbine axis on the meridional plane, was assumed -60 deg for the upper endwall (leakage over shrouded rotor blades) and 60 deg for the lower endwall (leakage under stator blades). The swirl angle of leakage jets, as measured clockwise from the projection of the turbine axis on the blade-to-blade plane, was assumed to be 60 deg at the upper endwall (this is to approximate the direction of the main flow downstream of the stators, assuming that there is little change of leakage jet direction in the rotor labyrinth seals). The swirl angle at the lower endwall was assumed to be 0° (this is due to the anticipated axial outflow from the rotors and also due to lack of further information on the behavior of leakage jets in stator labyrinth seals).

9 Computational Results

Figure 6 shows the axial distribution of mass flow rate in blade-to-blade passages of subsequent turbine blade rows. The mass flow rate at the inlet is equal to 104.8 kg/s. Changes of the mass flow rate at consecutively numbered source/sink slots along the

Table 1 Source/sink parameters for the five-stage LP turbine

Slot no.	1–2	3–4	5–6	7–8	9–10	11	12–13	14–15	16	17–18
Location	Rotor 1	Stator 2	Rotor 2	Stator 3	Rotor 3	Extraction 1	Stator 4	Rotor 4	Extraction 2	Stator 5
G (kg/s)	±3.31	±2.23	±1.82	±1.40	±1.10	−6.00	±0.51	±1.11	−5.50	±0.33
T_{0T} (K)	538	488	488	435	435	⋯	377	377	⋯	352

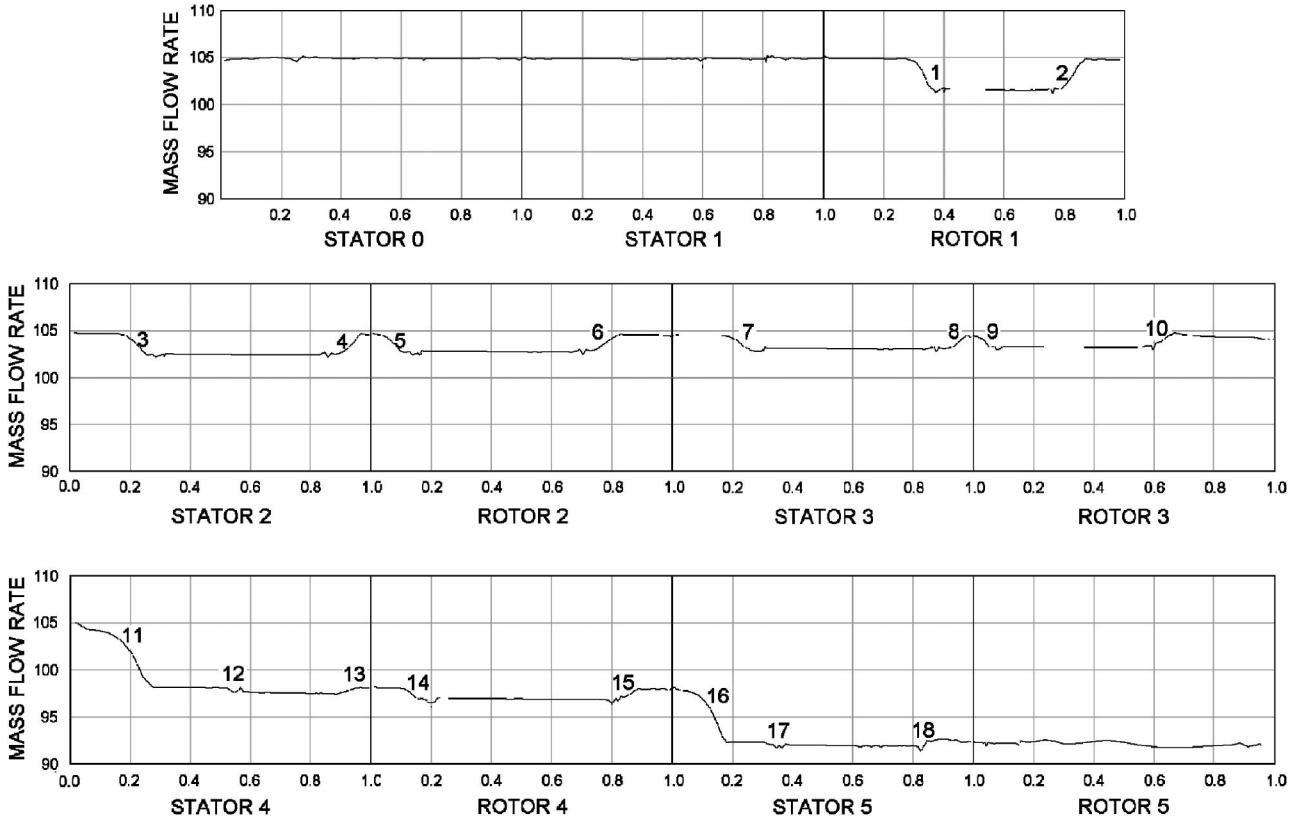

Fig. 6 Mass flow rate balance in blade-to-blade channels of subsequent turbine blade rows (numbers from 0.0 to 1.0 show nondimensional axial distance within subsequent blade rows)

turbine are due to tip and hub leakage flows, or due to steam extraction at two extraction points—slots 11 and 16 (note that the tip leakage over unshrouded blades of rotor 5 is not separated from the main stream, as the tip region belongs to the computational domain of the stage 5).

Figures 7–11 illustrate the process of expansion in the turbine. A plot of velocity vectors through the meridional section of the turbine at the mid-blade-to-blade distance is presented in Fig. 7 (note that a velocity vector is not an arrow but a dot with a stretch showing the direction of the velocity). The main flow through the turbine for nominal load seems to be regular and well-streamlined. There are no signs of massive separations. The flow remains attached to the endwalls, except for local regions of interaction of leakage flows with the main stream. Flow details in the region of

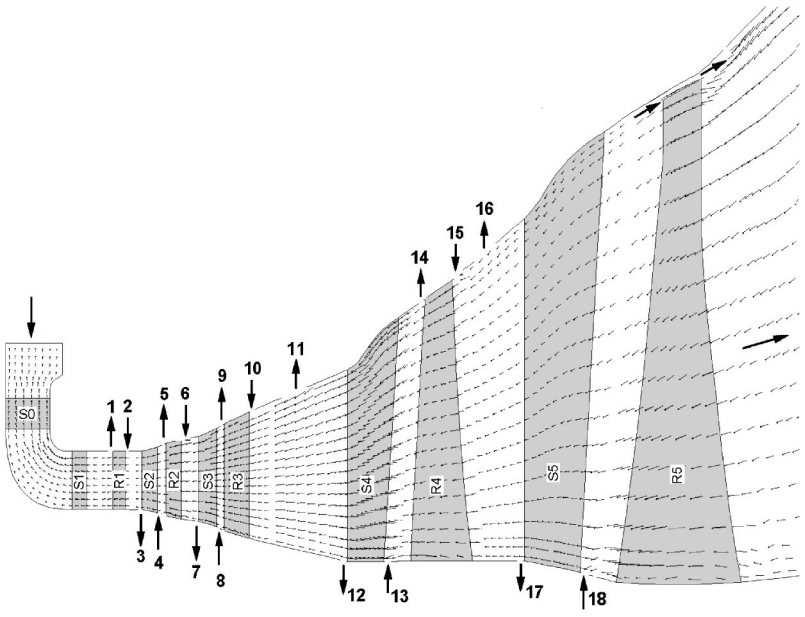

Fig. 7 Computed velocity vectors at mid blade-to-blade distance

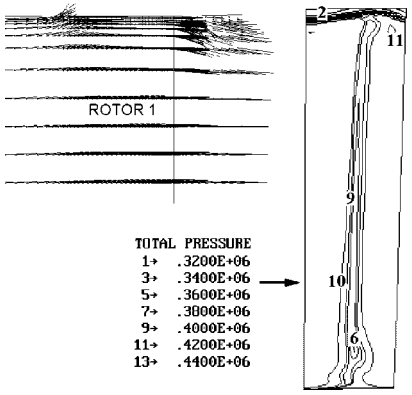

Fig. 8 Tip leakage flow over shrouded blades of rotor 1: velocity vectors in meridional view at mid blade-to-blade distance (left) and total pressure contours in circumferential view 25% of rotor axial chord downstream of the trailing edge (right)

tip leakage over/under shrouded/unshrouded blades are given in Figs. 8–10. Figure 8 shows velocity vectors and total pressure contours in the rotor of stage 1. Two endwall slots, that is one sink-type extraction slot upstream of the blade and one source-type injection slot located downstream, mark the entry to, and exit from, the labyrinth seal. Flow extraction in the sink affects little the velocity distribution in the main stream. However, sucking out some boundary-layer fluid at the tip endwall to the sink slot suppresses the development of secondary flow at the tip. Injection of the leakage flow into the main stream downstream of the rotor blade tip gives rise to mixing processes, being a significant source of total pressure or enthalpy loss at the tip. Figure 9 shows total pressure contours in the tip leakage region over unshrouded blades of rotor 5 at two circumferential sections—one section located still within the blade-to-blade passage of the rotor and the other section located 25% of the axial chord downstream of the trailing edge. Visible are the effects of a jet created in the gap between the blade tip and casing. After leaving the gap, the jet separates from the endwall and forms a clockwise rotating vortex where the tip leakage loss is concentrated. Figure 10 illustrates the injection of the hub leakage flow under stator 5. The extension of the mixing zone that can be seen from the velocity vectors is relatively small. This is partly due to the fact that the mass flow

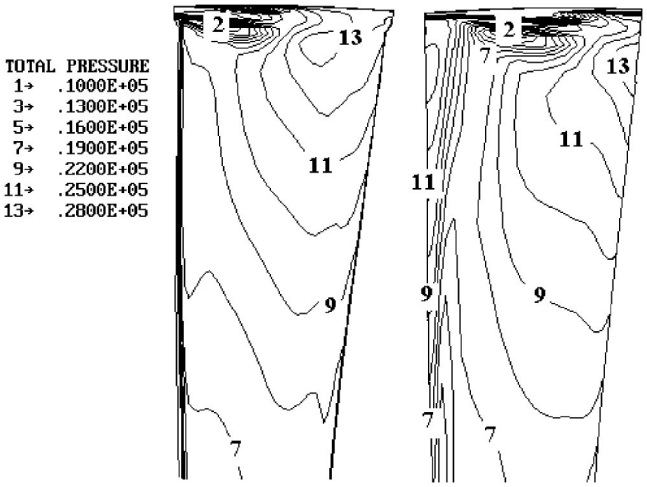

Fig. 9 Tip leakage flow over unshrouded blades of rotor 5: total pressure contours in circumferential view 5% of rotor axial chord upstream of the rotor trailing edge (left), and 25% of rotor axial chord downstream of the trailing edge (right)

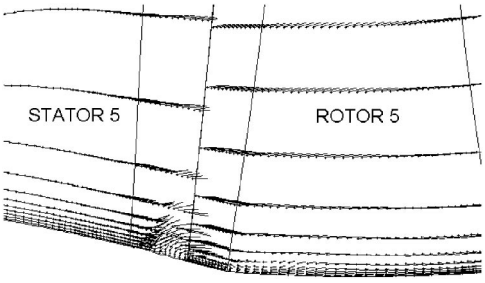

Fig. 10 Hub leakage flow under shrouded blades of stator 5: velocity vectors in meridional view at mid blade-to-blade distance

rate of this leakage flow is very low as the labyrinth seal is placed here some way down below the hub contour, and partly because the injected fluid also makes up for a mass flow deficit at the root of rotor 5.

Throughout the turbine, the velocity increases from the subsonic range to achieve supersonic values in passage throats of stages 3–5. Figure 11 shows sample Mach number distributions at mid-span sections of stage 3 and 5. The mean exit Mach number downstream of the stators of stages 1–3 is $M<0.75$, downstream of the stator of stage 5 is $M=1.2$. However, due to the large spanwise gradient of reaction as shown in Fig. 12, the Mach number reaches locally 1.6 at the root of stator 5 and near the tip of rotor 5. Figure 13 shows the calculated spanwise mass-averaged distribution of enthalpy losses in stage 3, 4, and 5 (the leaving energy not treated as a loss here) as captured 30% of the rotor

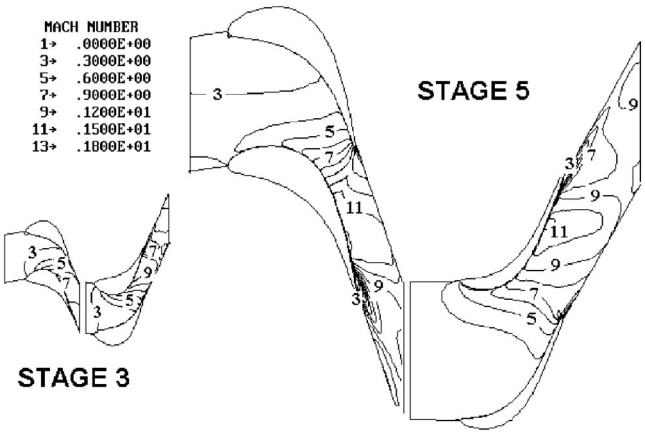

Fig. 11 Mach number contours in stages 3 and 5 in blade-to-blade view at mid-span

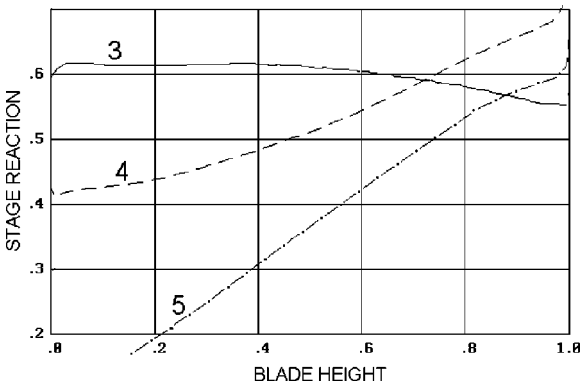

Fig. 12 Spanwise distribution of reaction in stages 3, 4, and 5

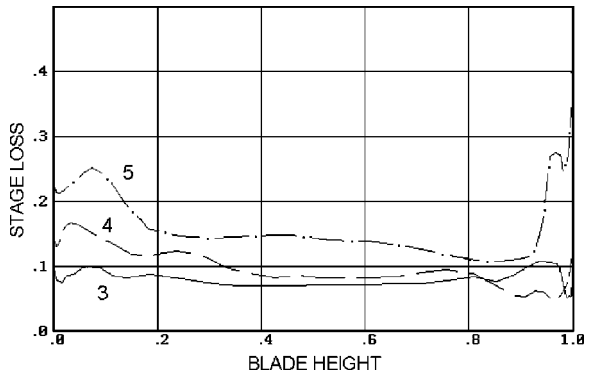

Fig. 13 Spanwise distribution of enthalpy losses in stages 3, 4, and 5 (the leaving energy not treated as a loss)

axial chord downstream of the rotor trailing edge. Conspicuous here are the increased values of enthalpy losses due to effects of tip leakage flows (especially in stage 5), secondary flows (in stage 3), and overloaded stator and underloaded rotor at the root (especially in stage 5) (see [23]). The enthalpy losses of the five-stage LP turbine as a whole (this time with the leaving energy treated as a loss) are estimated at 14.4%, giving the turbine efficiency of 85.6%.

10 Comparison With Available Experimental Data and With Computational Results From the Model of Thermally and Calorically Perfect Gas

In this section the computational results obtained based on the model of linearly variable specific heats are compared with the available experimental data and computational results from the constant specific heat model. Two cases of the perfect gas model with constant specific heats are considered: case A where the individual gas constant and specific heat ratio are those corresponding to steam conditions at the inlet—$R=452$, $\gamma=1.32$ (attempting the use of $\gamma=1.32$ for computation of the whole turbine may partly be justified by the fact that this value of isentropic coefficient is found in the vicinity of the saturation line, see [24]); and case B where the individual gas constant is an average from the inlet and exit values, and the specific heat ratio is calculated so as to satisfy the enthalpy drop through the turbine from the condition $i_{in}-i_{ex}=\gamma/(\gamma-1)(p_{in}/\rho_{in}-p_{ex}/\rho_{ex})$, see Eq. (3), yielding $R=436$, $\gamma=1.21$.

Table 2 gathers computed and experimental pressures, temperatures, enthalpies, and mass flow rates downstream of subsequent stages. There are minor differences downstream of stages 3, 4, and 5 between the measured pressure and pressure calculated in the variable specific heats model. The differences are larger for the model of constant specific heats. The temperature calculated in the model of variable specific heats agrees well with the measured value downstream of stage 5. The discrepancies are more significant downstream of stages 3 and 4. These calculations seem to underestimate the temperature drop for the first three stages and overestimate it for the two exit stages. The constant specific heats approach leads to erroneous determination of temperature downstream of stage 5. The most noticeable unphysical result is a drop of temperature below 230 K in case A downstream of stage 5. On the other hand, the temperature downstream of stages 3 and 4 in the constant specific heats model case B is closer to the experimental value than in the variable specific heats model. The observed differences in determination of temperature and pressure fields, as well as different ways of evaluation of the enthalpy in each computational model and in measurements, lead to differences in determination of enthalpy drops, power, and efficiency of subsequent stages. Of all computational variants, the variable specific heats model gives the best agreement with measurement data for enthalpies downstream of stages 3, 4, and 5 (downstream of stage 5, the enthalpy calculated in the model of variable specific heats is the same as the measurement value—Table 2). Case A of the constant specific heats model largely underestimates, whereas case B just underestimates, the enthalpy drop in the turbine. It seems that the variable specific heats model and constant specific heats model case B give similar prediction of thermodynamic parameters in the region of superheated steam (stages 1–3), but in the region of wet steam (stage 5) the results obtained from the variable specific heats model coincide with the measured values significantly better than those of the constant specific heats model. Note also that the overall turbine efficiency obtained from the variable specific heats model (as already mentioned equal to 85.6%) is very close to the efficiency obtained based on the measurements, which is 86%. At the same time the constant specific heats model gives a value of 88.5% in case A and 87.4% in case B. Table 2 shows also the calculated and measured mass flow

Table 2 Comparison of experimental and computed mass flow rate, pressure, temperature and enthalpy downstream of subsequent stages

Downstream of stage	Static pressure [bar]				Static temperature [K]			
	cp, cv *const*		cp, cv *var*	exp.	cp, cv *const*		cp, cv *var*	exp.
	A	B			A	B		
1	3.082	3.140	3.140	-	479.8	496.2	488.0	-
2	1.770	1.838	1.850	-	425.8	455.3	448.0	-
3	0.737	0.782	0.799	0.799	356.0	397.6	398.1	371.2
4	0.305	0.334	0.350	0.349	293.9	348.9	360.8	346.4
5	0.080	0.080	0.083	0.083	225.7	282.0	312.5	314.8
Downstream of stage	Static enthalpy [kJ/kg]				Mass flow rate [kg/s]			
	cp, cv *const*		cp, cv *var*	exp.	cp, cv *const*		cp, cv *var*	exp.
	A	B			A	B		
1	2881	2889	2886	-	105.9	105.6	104.7	-
2	2779	2786	2786	-	105.8	105.5	104.6	-
3	2660	2664	2640	2647	105.7	105.5	104.5	107.9
4	2531	2521	2517	2531	99.4	99.2	98.0	100.9
5	2412	2366	2350	2350	93.7	93.7	92.2	96.0

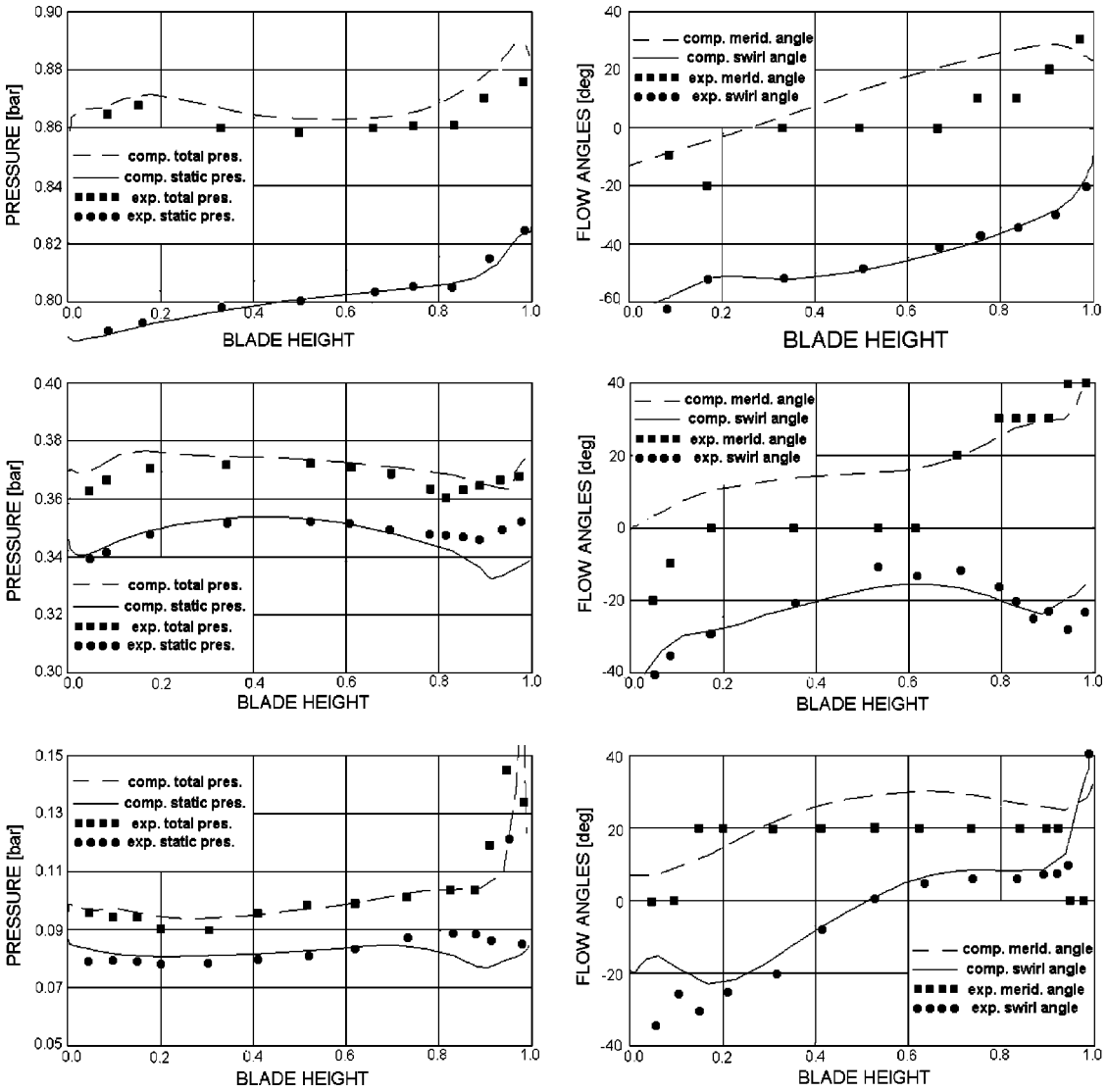

Fig. 14 Comparison of experimental and computed total and static pressure (left), meridional and swirl angle (right) downstream of stages 3 (top), 4 (center), and 5 (bottom)

rates in the LP turbine. The differences between the computed and measured values downstream of subsequent stages are relatively consistent. Unfortunately, the largest differences here are for the model of variable specific heats. The discrepancies do not exceed 4% of the measured values. Most likely they result from the single-phase flow model assumed in the computations.

Figure 14 shows a comparison of computed (based on the variable specific heats model) and measured spanwise pitch-averaged distribution of total and static pressure as well as meridional and swirl angle behind the stages 3, 4 and 5. In general, the computed distributions of static and total pressure downstream of subsequent stages follow the trends observed in the experiment. There is also a good qualitative agreement between the computed and measured distribution of the swirl angle. As for the meridional angle, the comparison is distorted due to weak accuracy of measurements of this parameter.

The calculations were carried out on a PC Pentium IV 2.4 GHz. In the case of variable specific heats, about 5000 iterations were needed on the highest level of multi-grid (4,600,000 cells) to reach the convergence of the solution to a steady state, amounting to 150 CPU hours. The variable specific heats model requires about 25% more CPU time than the constant specific heats model for a single iteration. Usually 10%–20% iterations more are needed to converge, which gives a total overhead of computational costs between 30% and 40% over the constant specific heats model.

11 Conclusions

A state equation of thermally perfect and calorically imperfect gas with variable specific heats defined as linear functions of temperature was implemented in a 3D RANS solver FlowER for multistage turbomachinery applications. The approach was validated on a five-stage LP steam turbine featuring different steam conditions from superheated to wet steam. It was found that the method yields reasonable determination of averaged thermodynamic parameters downstream of subsequent turbine stages as well as good estimation of turbine efficiency, as compared to the measurement results. The computed spanwise distributions of static and total pressure and swirl angle in stage-to-stage gaps were also found to agree relatively well with the available measured data. It was also shown in the paper that the method gives better solution over the model of thermally and calorically perfect gas, especially in the region of wet steam.

References

[1] Sturmayr, A., and Hirsch, Ch., 2003, ''Tabular IAPWS-95 Steam Properties Formulation With Switched Condensation Model in a 3D Navier-Stokes Solver,'' Proc. 5th European Conf. on Turbomachinery, Prague, Czech Republic, March 17–22, pp. 729–740.

[2] Bohn, D., Kerpicci, H., Ren, J., and Surken, N., 2001, ''Heterogeneous and Teterogeneous Nucleation in a Nozzle Guide Vane of an LP Steam Turbine,'' Proc. 4th European Conf. on Turbomachinery, Firenze, Italy, March 20–23, pp. 813–822.

[3] Dykas, S., 2001, ''Numerical Calculation of Steam Condensing Flow,'' TASK Quarterly, **5**(4), pp. 519–535.

[4] Chmielniak, T. J., Wróblewski, W., and Dykas, S., 1999, ''Stem Flow Calculations in Turbine Channels,'' Proc. 3rd European Conf. on Turbomachinery, March 2–5, London, UK, pp. 803–813.

[5] Wróblewski, W., 2000, ''Calculations of the Condensing Water Steam Flows in Turbine Blade Cascades,'' Turbulence, **6–7**, pp. 209–224.

[6] Dykas, S., Goodheart, K., and Schnerr, G. H., 2003, ''Numerical Study of Accurate and Efficient Modelling for Simulation of Condensing Flow in Transonic Steam Turbines,'' Proc. 5th European Conf. on Turbomachinery, Prague, Czech Republic, March 17–22, pp. 751–760.

[7] Yershov, S., and Rusanov, A., 1996, ''The Application Package FlowER for the Calculation of 3D Viscous Flows Through Multi-Stage Turbomachinery,'' Certificate of state registration of copyright, Ukrainian state agency of copyright and related rights, February 19.

[8] Menter, F. R., 1994, ''Two-Equation Eddy-Viscosity Turbulence Models for Engineering Applications,'' AIAA J., **32**(8), pp. 1598–1605.

[9] Yershov, S. V., 1994, ''The Quasi-Monotonous ENO Scheme of Increased Accuracy for Integrating Euler and Navier-Stokes Equations,'' Math. Model., **6**(11), pp. 58–64 (in Russian).

[10] Yershov, S. V., Rusanov, A. V., Shapochka, A., Lampart, P., Świrydczuk, J., and Gardzilewicz, A., 2002, ''Shape Optimization of Two Turbine Stages Using a Deformed Polyhedron Method and a 3D RANS Solver,'' Proc. Inst. Mech. Eng., Part A., J. Power Energy, **216(2)**, pp. 203–213.

[11] Lampart, P., Yershov, S., and Rusanov, A., ''Validation of Turbomachinery Flow Solver on Turbomachinery Test Cases,'' 2002, Cieplne Maszyny Przeplywowe (Turbomachinery), **122**, pp. 63–70.

[12] Lampart, P., Świrydczuk, J., and Gardzilewicz, A., 2001, ''On the Prediction of Flow Patterns and Losses in HP Axial Turbine Stages Using 3D RANS Solver and Two Turbulence Models,'' TASK Quarterly, **5**(2), pp. 191–206.

[13] Denton, J. D., 1993, ''Loss Mechanisms in Turbomachines,'' ASME J. Turbomach., **115**, pp. 621–656.

[14] Lampart, P., Yershov, S., Rusanov, A., and Szymaniak, M., 2004, ''Tip Leakage/Main Flow Interactions in Multi-Stage HP Turbines With Short Height Blading,'' ASME Paper no. GT2004-53882.

[15] Marcinkowski, S., 1998, ''Results of Extended Flow Measurements in the LP Part of 18K370 Steam Turbine in the Belchatów Power Station,'' Rep. Institute of Fluid Flow Machinery, Gdańsk, No. 292/98 (in Polish).

[16] Gardzilewicz, A., and Marcinkowski, S., 1995, ''Diagnosis of LP Steam Turbines. Prospects of a Measuring Technique,'' ASME PWR, **28**(3), pp. 349–358.

[17] Marcinkowski, S., 1985, ''Universal Measurement Probe for Tests on Wet Steam Flow in Turbines,'' Rep. Institute of Fluid Flow Machinery, Gdańsk, No. 50/85 (in Polish).

[18] Wiercíński, Z., 1998, ''Calibration of Disc Probes in the Wind Tunnel for Wet Steam Flow Measurements in Low-Pressure Turbines,'' Rep. Diagnostyka Maszyn Ltd., Gdańsk, No. 1/98 (in Polish).

[19] Gardzilewicz, A., Łuniewicz, B., and Stojanov, A., 1995, ''Streamline Curvature Calculation of Flow Through the Steam Turbines Stages With Diffusers,'' Proc. Int. Conf. SYMKOM'95, Łódż, Poland.

[20] Moore, M. J., Jackson, R., Wood, N. B., Langford, R. W., Walters, P. T., and Keeley, K. R., 1979, ''A Method of Measuring Stage Efficiency in Operational Wet Steam Turbines,'' Proc. Inst. Mech. Eng. C179/79.

[21] Krzyżanowski, J., and Marcinkowski, S., 1997, ''On Efficiency Measurements for Large Steam Turbine LP Stages,'' Proc. 2nd European Conf. on Turbomachinery, March 5–7, Antwerpen, Belgium, pp. 29–36.

[22] Gardzilewicz, A., 1984, ''Selected Problems of Computer-Aided Design of Steam Turbines and Heat Cycles,'' Rep. Institute of Fluid Flow Machinery, Gdańsk, No. 161/84 (in Polish).

[23] Lampart, P., 2000, ''The Application of Stator Blade Compound Lean at Root to Increase the Efficiency of LP Turbine Stages From Low to Nominal Load,'' ASME Paper no. IJPGC2000-15015.

[24] Gardzilewicz, A., 1977, ''Isentropic Expansion Coefficient in Wet Steam Near the Saturation Line,'' Trans. Inst. Fluid Flow Mach., **57**, pp. 31–44 (in Polish).

A Review of the History of the National Advisory Committee for Aeronautics Centrifugal Compressor Program and Arrival at Current Computational Design Procedures

Joseph T. Hamrick
Aerospace Research Corporation, 5454 Aerospace Road, Roanoke, VA 24014

Before and during World War II, the design and development of single stage high pressure ratio centrifugal compressors was essentially a cut-and-try exercise. To reach a high pressure without substantial experimentation required multiple stages of impellers and diffusers with pressure ratios in the 2:1 range. While such arrangements were satisfactory for commercial use where weight was not a major consideration, they were not suitable for jet engines. The centrifugal compressor for the Whittle engine, the first British jet engine, was developed by trial and error with numerous modifications of the hub-shroud profile. The centrifugal compressor section of the National Advisory Committee for Aeronautics (NACA) designed, built, and tested three compressor impellers during and after World War II. They were part of a program designed to evaluate various blade shapes, but encountered such instabilities at the design pressure ratios that the experimental results led to no definitive conclusions. In 1948, the Centrifugal Compressor Section was given the assignment to further investigate the three impellers. The investigation led to the development of a quasi-three-dimensional design procedure that eliminated the guesswork from the basic design of a centrifugal impeller. Since the 1948 to 1955 time period over which the procedure was developed, the advances in computers have allowed refinements in the original computational methods. It is the objective of this presentation to review the history of the NACA centrifugal compressor program and efforts that have led to the latest developments in computational design procedures. [DOI: 10.1115/1.1855326]

Introduction

The fact that the British had used a centrifugal compressor in the Whittle jet engine sparked a movement at the Cleveland Laboratory of the National Advisory Committee for Aeronautics (NACA) to perform further research on centrifugal compressors following World War II. During the war, the primary use of centrifugal compressors was supercharging piston engines. In addition, turbines driven by engine exhaust gases powered centrifugal compressors that were necessary for high altitude flight. For the pressures required for jet engines, it was clear that impeller design procedures that were used for the turbochargers and multistage compressors were not adequate. As a result, the Centrifugal Compressor Section of the Compressor and Turbine Division was assigned the task of deriving flow analyses of impellers of existing designs and arriving at effective design procedures for higher compression ratio impellers with predictable performance.

The numerical analysis attempt for one of three impellers that were available showed the deficiencies of the original design and in further developments of the numerical analysis method, a rapid design procedure resulted. It is the aim of this paper to relate the history of the NACA centrifugal compressor program and development of subsequent computational design procedures.

Contributed by the Fluids Engineering Division for publication on the JOURNAL OF FLUIDS ENGINEERING. Manuscript received by the Fluids Engineering Division August 25, 2004; revised manuscript received September 7, 2004. Review Conducted by: Y. Tsujimoto.

Numerical Analysis

For guidance in developing numerical analysis methods, a study of a textbook by Professor A. Stodola [1] (translation by Louis C. Loewenstein) of Germany was made. The contribution of that reference was significant. Professor Stodola drew from a number of theorists, one of whom was Flügel, who introduced the concept of stream filaments in the flow process. A method was devised [2] in which the average velocity distribution in stream tubes from the impeller hub to the shroud was obtained throughout the impeller. The computations were laborious and were done by operators of mechanical calculators. Those calculators were heavy and expensive, costing fifty to sixty times what a hand held electric calculator costs today. Additionally, tables had to be used for logarithmic and trigonometric functions. Use of computers was almost out of the question. They were extremely expensive and took up a whole room.

Three impellers with varying blade shapes [3] that had been tested were available for analysis. An impeller with parabolic blade shape was selected. An analysis of flow through the impeller was made. The analysis showed severely adverse velocity gradients along both hub and shroud surfaces. It was concluded that the adverse velocity gradients had resulted in flow separation, accounting for the poor performance of the impeller at pressure ratios above 2:1. As a result, an effort was made to design passages for an impeller with as few adverse velocity gradients as possible.

The impeller was designated MFI-1A. The blade for the impeller was designed by a method developed by Stanitz [4] in which a

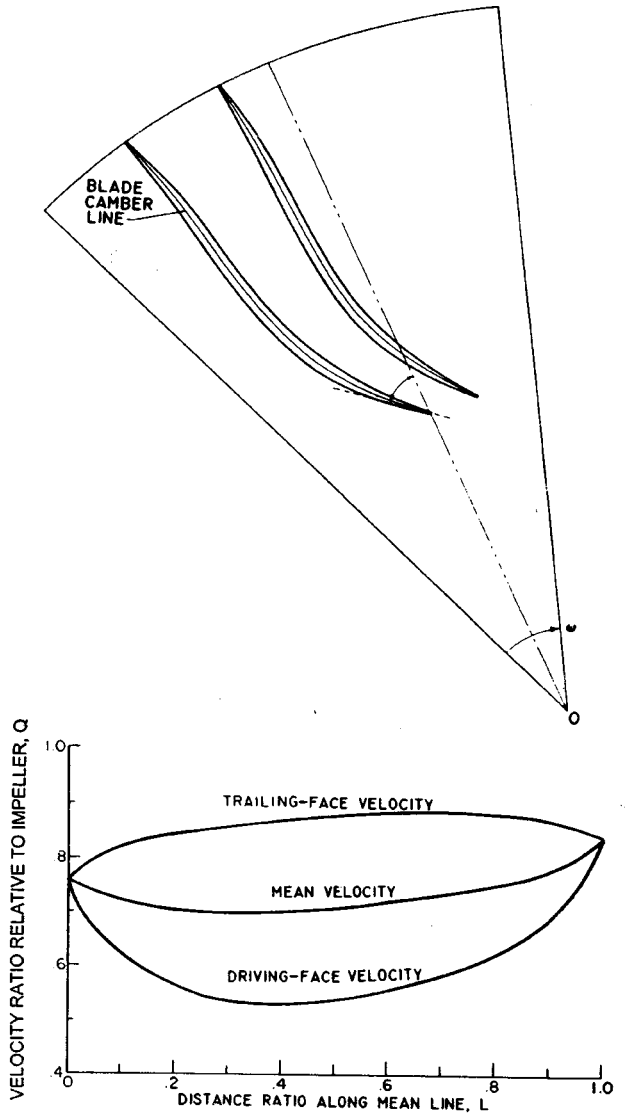

Fig. 1 Velocity distribution and blade shape for the MFI-1 impeller

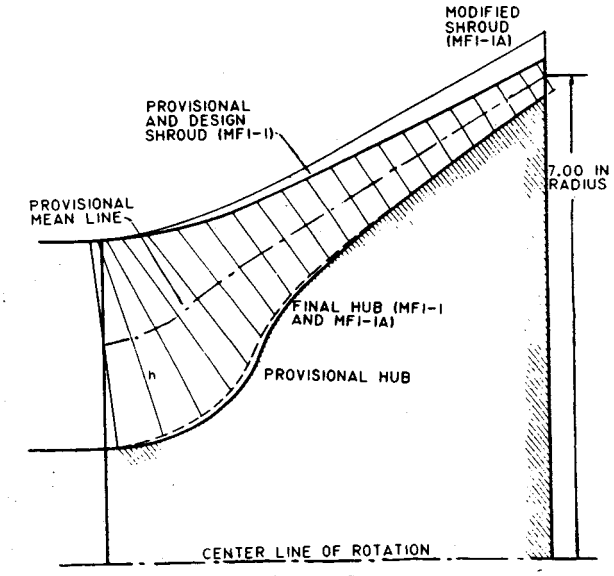

Fig. 2 The hub and shroud shape for the MFI-1

prescribed velocity distribution was used to determine the blade shape. Both velocity distribution and resulting blade shape are shown in Fig. 1.

The method of Hamrick et al. [2] was used iteratively to arrive at a hub-shroud profile for which the mean velocity, shown in Fig. 1, would be maintained from hub to shroud. To account for what were perceived as real fluid effects, the blade height was increased by a percentage of the outlet blade height varying linearly with distance along the shroud, from 0 at inlet to 74% at the outlet. The resulting hub and shroud shape is shown in Fig. 2. The performance of the MFI-1A is shown in Fig. 3.

For a second configuration, the percentage of the blade height increase was cut in half. The changed configuration was designated as the MFI-1B. There was little change in performance.

Diffuser vanes were added at the outlet of the MFI-1B impeller. The results proved the effectiveness of the numerical design. The 40-vane diffuser dropped the outlet velocity to Mach 0.2. The efficiency was 75.5% at 4.7/1 pressure ratio. Tests with a larger U. S. Army Air Force J-33 jet engine centrifugal compressor [5] showed that the compressors have an efficiency of 76% at a 4.7/1 pressure ratio. The J-33 was a copy of the Whittle engine. The compressor for that engine required testing of numerous modifications of the impeller before arrival at one with satisfactory performance. The good performance of the MFI-1 was attributed to minimizing the adverse velocity gradients in the impeller passages.

Past centrifugal impeller design efforts had been centered about the blade design. Three-dimensional flow considerations had somehow been neglected both in Europe and the U.S. With the arrival at what was, in effect, a quasi-three-dimensional numerical design method in the MFI-1 program, a much more predictable performance was possible. There was one drawback to the iterative design procedure undertaken for the MFI-1 in that approximately 500 h of calculating with hand calculators was required. An effort was put forth to arrive at a more rapid design method. A method for which the average velocity was prescribed at the hub for a base streamtube was developed for a prescribed blade shape [6]. Flows for succeeding layers of streamtubes were then calculated in the number needed to reach a shroud shape commensurate with the overall required flow rate. Blade surface velocities were computed based upon the assumption of a linear pressure variation across the passage between blades. The method proved to be straightforward and rapid.

With the development of a rapid design method, a return was possible to the original commitment to investigate the effect of blade curvature on centrifugal impeller performance. The shrouds

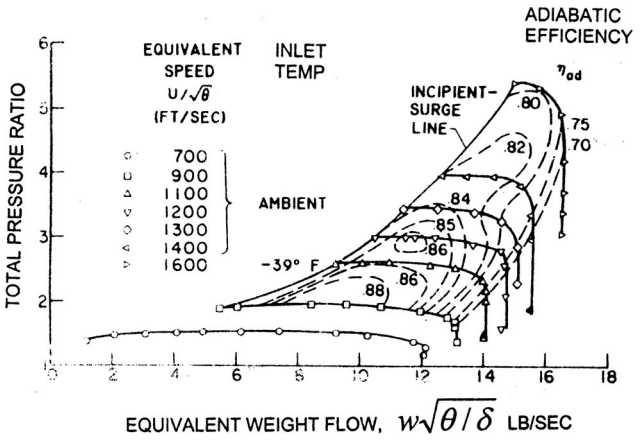

Fig. 3 Performance map for the MFI-1A

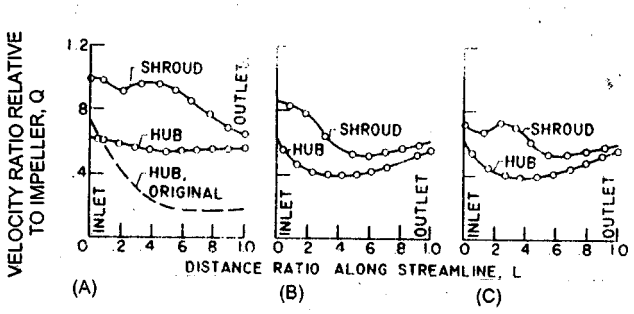

Fig. 4 Hub and shroud velocities for three impellers with modified shrouds

of the three impellers of reference [3] were modified by the method of reference [6] and tested. No allowance was made for viscous effects. The hub and shroud velocities for the modified shrouds are shown in Fig. 4.

The calculated hub velocity of the original parabolic bladed impeller is shown in Fig. 4. It was the only one of the three for which flow was analyzed. The performance maps, before and after, for the parabolic bladed impeller are shown in Fig. 5. Complete information on the results of tests on the three impellers is given in reference [7].

In 1956, there was no detailed information on the prediction of boundary layer behavior on the flow inside impellers. A 48 in. diameter radial flow impeller was instrumented to measure velocities in the impeller passages. The results are provided in reference [8]. At the time, velocity patterns at the passage surfaces could only be deduced. Some 30 years after the work on the 48 in. impeller was completed, John and Joan Moore made a detailed analysis of flow in the 48 in. impeller [9]. Their calculations were based upon methods contained in references [10] and [11]. The calculations included losses due to viscosity, secondary flow, and tip leakage. Calculations for off-design flows, as well as design flows, were in general agreement with NACA measurements.

In 1982, design of a 60 in. diameter impeller was initiated. It was later fabricated and tested at the National Aeronautic and Space Administration NASA, Cleveland laboratory. The method of references [10] and [11] was one of several methods to analyze the flow. The results of the analysis by the method of references [10] and [11] are contained in reference [12].

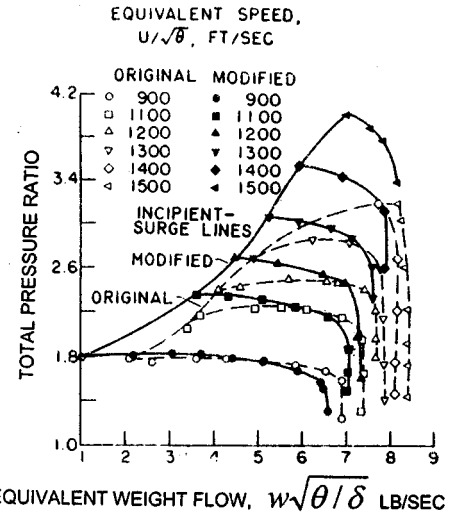

Fig. 5 Performance before and after modification for parabolic bladed impeller

In conversations with persons currently and previously involved with centrifugal compressor research, it appears that the rapid approximate design method of reference [6] stands somewhat alone for the initial design of impellers in the pressure ratio range of 2 or above. The initial design of an impeller application by reference [6] can be evaluated by the methods of reference [13].

In discussions with Kenneth Smith, former chief engineer at Cooper Bessemer Rotating Products Division (now, Rolls-Royce Energy Systems Inc.) and co-author, co-developer of reference [6], it was learned that Cooper Bessemer used the rapid approximate method of reference [6] with refinements based upon their in-house expertise to design a wide range of compressors for various applications, including natural gas pipe lines. The designs [14] were not checked by viscous flow analysis methods. Their primary concern was preparing designs having a minimum of adverse velocity gradients in the impeller passages. The designs were efficient ranging up to 92%. The method has been widely used and is recommended for use in compressor designs with compression requirements of 2/1 or above.

There are a number of viscous analysis methods. Among them are the lectures in 1985 presented by the NATO Advisory Group for Aerospace Research and Development (AGARD) [13]. The AGARD lecture series is on file in the library of Virginia Polytechnic Institute and State University, Blacksburg, Virginia.

Summary

A review of the published literature has revealed that a major effort has been made to develop computational flow procedures for calculating viscous flow effects. Current design procedures follow essentially those developed in the initial phase of the NACA centrifugal compressor program. Adjustments can be made in the designs by calculating viscous flow effects. However, in the use of viscous analysis methods, a point of flow separation is difficult to predict. Therefore, it is important to design for no deceleration on the trailing face of the blade.

Based upon the test results with the 48 inch impeller, separation on the driving face is not expected even with adverse velocity gradients. The design of a blade shape by prescribing the velocity distribution and arriving at the number of blades by the method of reference [4] followed by the design of the hub-shroud shape by the method of reference [6] is recommended. Although computer software can be written for the methods of references [4] and [6], it is still necessary to make a judicious prescription of velocity for the blade. The method of reference [13] may be used to analyze viscous effects.

References

[1] Stodola, A., 1927, *Steam and Gas Turbines*, Vol. II, McGraw–Hill, New York, pp. 990–997.

[2] Hamrick, J. T., Ginsburg, A., and Osborn, W. M., 1952, "Method of Analysis for Compressible Flow Through Mixed Flow Impellers of Arbitrary Design," NACA Report 1082, NACA, Washington, D.C.

[3] Anderson, R. J., Ritter, W. K., and Dildine, D. M., 1947, "An Investigation of the Effect of Blade Curvature on Centrifugal Impeller Performance," NACA TN 1313, NACA, Washington, D.C.

[4] Stanitz, J. D., 1951, "Approximate Design Method for High-Solidity Blade Elements in Compressors and Turbines," NACA TN 2408, NACA, Washington, D.C.

[5] Hamrick, J. T., and Beede, W. L., 1956, "Some Investigations With Wet Compression," Trans. ASME, **75**, pp. 409–418.

[6] Smith, K. J., and Hamrick, Joseph T., 1955, "A Rapid Approximate Method for the Design of the Hub-Shroud Profiles of Centrifugal Impellers of Given Blade Shape," NACA TN 3399, NACA, Washington, D.C.

[7] Kramer, J. J., Osborne, W. M., and Hamrick, J. T., 1960, "Design and Test of Mixed Flow and Centrifugal Impellers," J. Eng. Power, **82**, pp. 127–135.

[8] Hamrick, J. T., 1956, "Some Aerodynamic Investigations in Centrifugal Impellers," Trans. ASME, **78**, pp. 591–602.

[9] Moore, J., and Moore, J. G., 1988, "Secondary Flow, Separation, and Losses in the NACA 48-Inch Centrifugal Impeller at Design and Off-Design Conditions," ASME Paper 88-GT-101.

[10] Moore, J. G., 1985, "An Elliptic Calculation Procedure for 3D Viscous Flow," *3D Computational Techniques Applied to Internal Flows in Propulsion Systems*, Agard Lecture Series No. 140, NATO, Paris.

[11] Moore, J. G., 1985, ''Calculation of 3D Flow Without Numerical Mixing,'' *3D Computational Techniques Applied to Internal Flows in Propulsion Systems*, Agard Lecture Series No. 140, NATO, Paris.
[12] Moore, J., and Moore, J. G., 1990, ''A Prediction of 3D Viscous Flow and Performance of the NASA Low-Speed Centrifugal Compressor,'' ASME Paper 90-GT-234.
[13] Moore, J., 1985, ''3D Computation Techniques Applied to Internal Flow and Propulsion Systems,'' *3D Computational Techniques Applied to Internal Flows in Propulsion Systems*, Agard Lecture Series No. 140, NATO, Paris.
[14] Meier, R. H., and Schiller, R. N., 1976, ''Development and Testing of a New High Flow Centrifugal Pipeline Booster,'' *Proc. 6th Turbomachinery Symposium*, Gas Turbine Laboratories, Texas A&M University, College Station, TX.

Dong-Youn Shin
104-1 Munji-dong, Yoosung-ku,
Taejon, South Korea
Telephone: +82-42-870-6057
Fax: +82-42-861-2585
e-mail: wonwhale@lgehem.com

Paul Grassia
School of Chemical Engineering
and Analytical Science,
The University of Manchester, P.O. Box 88,
Sackville Street, Manchester M60 1QD,
United Kingdom
Telephone: +44-161-306-8851
Fax +44-161-306-4399
e-mail: paul.grassia@manchester.ac.uk

Brian Derby
Manchester Materials Science Center,
The University of Manchester,
Grosvenor Street, Manchester M1 7HS,
United Kingdom
Telephone: +44-161-200-3569
Fax: +44-161-200-8877
e-mail: brian.derby@manchester.ac.uk

Oscillatory Incompressible Fluid Flow in a Tapered Tube With a Free Surface in an Inkjet Print Head

Oscillatory incompressible fluid flow with a free surface occurs in an inkjet print head. Due to complex physical fluid behavior, numerical simulations have been a common approach to characterize the pressure and velocity development in time and space. However, the cost of a numerical approach is high in terms of computational time such that approximate analytic approaches have been developed. In this paper, an approximate analytic solution for a tapered nozzle section is described with a proper downstream boundary condition and the physical behavior of the meniscus deformation is modeled with a simple "window" theory. [DOI: 10.1115/1.1852474]

1 Introduction

Oscillatory incompressible fluid flow in a tapered tube with a free surface occurs in a general inkjet print head. Because of complex physical fluid behavior, numerical simulations have been a common approach to characterize fluid behavior such as pressure and velocity fields in time and space. Antohe and Wallace [1] and Khaskia [2] used the ANSYS finite element program (ANSYS Inc. Co., Canonsburg, PA, USA) to facilitate fluid–structure interaction computations. Their approach divides the inkjet operation into several discrete processes. These are modeled sequentially with the results of one fed into the next. Yeh [3,4] simulated a number of processes from drop generation to impact onto the substrate using the finite element (FEM) and volume of fluid (VOF) methods. He adopted ANSYS to compute equivalent force and chamber pressure, with a spring and piston model, and fed the corresponding flow rate to a subsequent drop generation stage. Pan et al. [5] integrated an implicit finite difference method with FLOW 3D (Flow Science, Inc., Los Alamos, NM, USA), as a user defined routine, to compute pressure change in a chamber. However, they reported difficulties in achieving convergence; the time step sizes chosen by FLOW 3D are too big for the convergence of the user programs. Therefore, the appropriate time step size selection is another challenge for them, which they determined by trial and error.

Some authors, however, have used simplified square wave pressure and axial velocity histories for their upstream boundary conditions to predict numerically the drop formation *at the nozzle*. Fromm [6] and Shield et al. [7] carried out numerical simulations of drop formation with extremely simplified upstream boundary conditions. Although Shield et al. [8] numerically computed pressure and velocity histories for their upstream boundary condition in their later work, it still appears unrealistic because of stepwise velocity histories in time. Adams and Roy [9] also used very simple but unrealistic boundary conditions for their numerical simulations of drop formation. Liou et al. [10] employed the finite volume method (FVM) to solve the continuity and Navier–Stokes equations coupled with VOF to track the liquid–air interface but the motion of a piezoelectric actuator was explicitly given, ignoring any influence of fluid pressure coupling on it. Only a few authors such as Khaskia [2], Yeh [3,4], Pan et al. [5], Shield et al. [8], Kyser et al. [11], Wallace [12] and Chen et al. [13] have taken into account the computation of pressure and velocity developments inside an inkjet print head chamber for their numerical simulation of the drop formation.

Despite successful numerical simulation results for the drop formation, which are capable of capturing key features of drop generation, the complete two-dimensional (2D) axisymmetric approach needs a huge computation time. If the driving mechanism, which involves a complex fluid–structure interaction, is also part of the computational domain, then the overall computation time dramatically increases. For example, Yeh [3,4] claimed his numerical approach took 24 h on a PC with a Pentium III (600 MHz) processor with 11,300 elements and 11,871 nodes in the finite element model. Wilkes et al. [14] reported a computational time of 6–48 h of CPU time on an IBM RS-6000 3BT with a 2D FEM model, for an analysis of the simpler drop formation process in the dripping faucet problem.

Analytical approaches have also been developed to characterize physical insights of fluid flow in a print head. These are attractive because of their inherent compactness and incomparably cheap computational cost, even though an analytical approach cannot cover all nonlinear and physical behaviors. Teng [15] and Koltay et al. [16,17] tried to solve fluid behavior in an inkjet print head by analytical means but to do this they oversimplified the real fluid behavior. Teng [15] assumed that a fluid behaves in a quasi-steady state manner. As a consequence, the solution for fluid flow becomes a well-developed Poiseuille flow, which cannot be true in an inkjet print head. Koltay et al. [16,17] presented a lumped model of a circular orifice but their solutions are primitive and the detailed developments of pressure and axial velocity were not presented.

The most successful analysis of oscillatory fluid flow in an inkjet print head using analytical methods was described by Dijks-

Contributed by the Fluids Engineering Division for publication on the JOURNAL OF FLUIDS ENGINEERING. Manuscript received by the Fluids Engineering Division September 23, 2002; revised manuscript received August 31, 2004. Review Conducted by: M. Plesniak.

man [18]. His analytical approach, using the Fourier series analysis to decompose the applied voltage waveform into a set of sinusoidal waves over time, succeeded in explaining the meniscus motion during drop formation, so that his descriptions of pressure and axial velocity history can be considered more realistic. However, the analytical treatment of a tapered tube in his work was based on successive discrete straight tubes, which have gradually descending radii. Although analytical results from the sectioning of a tapered tube may be regarded as correct when an infinite number of discrete tubes are used, the influence of the number of discrete tubes on the evolution of the fluid flow along the tube axis was not investigated and it is not known how many discrete tubes should be adopted for realistic results. Therefore, his work left some aspects to be improved.

The difficulty in achieving an adequate analytical treatment of a tapered tube has been found in other researchers' work. Baek et al. [19] converted a tapered tube into a single straight tube, of which the volume and length are the same as the tapered tube. Rembe et al. [20] derived a simple solution similar to the Bernoulli equation, based on the mean value theorem of calculus. These solutions are relatively primitive and do not give the detailed developments of pressure and axial velocity along the nozzle length. A better treatment of fluid behavior in a tapered nozzle is found in the work of Hart and Shi [21]. They achieved an approximate analytical solution based on an averaged axial flux from the continuity equation and this solution was utilized to obtain pressure and axial velocity with linearized Navier–Stokes momentum equations. Their solution, however, must be used with a very small taper angle (0.5 deg in their work), since the approximate function describing the area change of a tapered tube loses its accuracy as the taper angle increases. A similar procedure was used by Chakravarty and Mandal [22] but the taper angle is still very small at 0.5 deg and it is not clear whether their solution is suitable for a larger taper angle.

The downstream pressure boundary condition is another issue presented by Bogy and Talke [23] and Antohe and Wallace [1]. Bogy and Talke [23] described the end condition as an open-end pipe, where pressure becomes zero. Dijksman [18] also used zero pressure as the downstream pressure boundary condition at the nozzle tip. An open-end pipe implies that the reflecting pressure wave has the same magnitude as the incident pressure wave but with the opposite sign. However, Antohe and Wallace [1] stated that the downstream pressure boundary condition at the nozzle tip resembles a closed-end pipe, where the pressure derivative with respect to the nozzle axial direction becomes zero. Imposing a zero downstream pressure boundary condition certainly does not depict the fact that the axial velocity decreases as the nozzle orifice becomes smaller due to higher capillary pressure. From these contradictory findings by Bogy and Talke [23], and Antohe and Wallace [1], a better approximation for the downstream pressure boundary condition is required.

Finally we consider the modeling of meniscus deformation during inkjet printing. It was observed by Meinhart and Zhang [24] that the free surface of the meniscus deforms when a liquid is pushed outward during the deformation, in which case the central region of the meniscus inverts from concave to convex. This deformation and inversion process has not been modeled with previous analytic methods. Therefore, a so-called "window model" will be proposed here to take into account the meniscus deformation where mass transport takes place during the early stage of the meniscus development.

Our main goal is to achieve an acceptable and straightforward analytical solution for the nozzle part of an inkjet print head, which has a relatively steep taper angle compared to those used by authors such as Hart and Shi [21] and Chakravarty and Mandal [22]. A simple method to achieve a downstream pressure boundary condition with an oscillatory free surface will be described. Finally, the "window model," which describes the process of meniscus deformation, will be developed and its impact will be discussed in comparison with numerical simulations.

2 Mathematical Formulation

In this section, the governing equations for nozzle flow and the downstream boundary condition are introduced and the linearized z momentum Navier–Stokes equation is solved analytically. With the axial velocity histories thus described, the window model is developed to provide physical insight of meniscus deformation.

2.1 Analysis for the Nozzle Section. The analysis of a tapered nozzle uses a cylindrical coordinate system where r and z represent the radial and axial directions of a tapered nozzle. Five main assumptions are made throughout this paper: (1) Oscillatory fluid flow in a tapered tube is treated as an incompressible flow, (2) the walls are assumed to be rigid, (3) in axisymmetric cylindrical coordinates, pressure is assumed to be a z dependent function along the nozzle axis since in practice the pressure gradient along the r direction is small enough to be ignored compared to its gradient along the z direction, (4) convective acceleration terms are ignored since the z momentum Navier–Stokes equation is linearized, (5) the wavelength of the oscillation is assumed to be fairly long compared to the dimensions of the tapered nozzle.

With the above five main assumptions, the axial velocity function, $V_z(r,z)$, as shown in Eq. (2), can be obtained from the linearized z momentum Navier–Stokes equation as shown in Eq. (1) with the convective term discarded and also with $\partial^2 V_z/\partial z^2$ neglected, due to the long wave assumption. Here, V_r, ρ_f, and v are radial velocity, fluid density, and kinematic viscosity respectively. A no-slip boundary condition is applied to Eq. (1) and an assumed time dependence, $e^{i\omega t}$, where i and ω are the imaginary number and angular frequency, respectively, is omitted in all equations for convenience.

$$\frac{\partial V_z}{\partial t}+V_r\frac{\partial V_z}{\partial r}+V_z\frac{\partial V_z}{\partial z}=-\frac{1}{\rho_f}\frac{\partial P}{\partial z}+v\left(\frac{\partial^2 V_z}{\partial r^2}+\frac{1}{r}\frac{\partial V_z}{\partial r}+\frac{\partial^2 V_z}{\partial z^2}\right) \tag{1}$$

$$V_z(r,z)=-\frac{1}{\rho_f i\omega}\left(1-\frac{J_0(\lambda r)}{J_0(\lambda\cdot R(z))}\right)\frac{\partial P(z)}{\partial z} \tag{2}$$

In Eq. (2), $R(z)$ and λ are defined as $r_1-z\cdot\tan\theta$ and $\sqrt{-i\omega/v}$, where r_1, z, and θ are the inner radius at the upstream end of the nozzle, the axial coordinate, and the taper angle respectively. J_0 and $P(z)$ are a Bessel function of the first kind and a pressure function, the latter to be determined. Incompressibility and rigid wall assumptions yield Eq. (4) from the continuity equation as shown in Eq. (3)

$$\int_0^{R(z)}\frac{\partial}{\partial r}(rV_r)dr+\frac{\partial}{\partial z}\left(\int_0^{R(z)}rV_z dr\right)=0 \tag{3}$$

$$\frac{\partial^2 P(z)}{\partial z^2}+F_3(z)\cdot\frac{\partial P(z)}{\partial z}=0 \tag{4}$$

where $F_3(z)\equiv F_2(z)/F_1(z)$, and $F_1(z)$ and $F_2(z)$ are defined as follows:

$$F_1(z)=\int_0^{R(z)}r-\frac{r\cdot J_0(\lambda r)}{J_0(\lambda\cdot R(z))}dr,$$

$$F_2(z)=\int_0^{R(z)}r\cdot J_0(\lambda r)dr\cdot\frac{\lambda\cdot\tan\theta J_1(\lambda\cdot R(z))}{(J_0(\lambda\cdot R(z)))^2}$$

Equation (4) yields pressure and axial velocity functions as shown in Eqs. (5) and (6)

$$P(z)=C_1+C_2\cdot\int_{z_1}^{z}\exp\left(-\int_{z_1}^{\zeta}F_3(\xi)d\xi\right)d\zeta \tag{5}$$

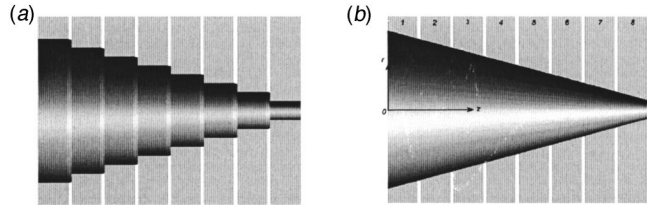

Fig. 1 Nozzle sectioning. (*a*) A set of discrete cylinders. (*b*) A set of continuous tapered nozzle sections

$$V_z(r,z)=\frac{1}{-\rho_f i\omega}\left(1-\frac{J_0(\lambda r)}{J_0(\lambda\cdot R(z))}\right)\cdot(C_2\exp(-\textstyle\int_{z_1}^{z}F_3(\xi)d\xi)) \tag{6}$$

The unknown coefficients, C_1 and C_2, will be determined with upstream and downstream boundary conditions.

Though exact formulas for the above pressure and axial velocity functions may exist, it is time-consuming to compute single and double integrals in the above solution, containing such a complicated function as $F_3(z)$. Therefore, an approximation of this complicated function is required using a series expansion. Assuming an arbitrary coordinate, z, located between z_1 and z_2 and that z_m is the mid point of the range $[z_1,z_2]$, $F_3(z)$ can be represented as shown in Eq. (7) from the first N terms of a series function. In a similar manner, the integrand of the outer integral of Eq. (5) can be replaced with a series function in Eq. (8). Capital letters A and B with subscripts, k, denote the series function coefficients and index number, while $T_1(z)$ and $T_2(z)$ denote the series functions themselves.

$$F_3(z)\approx T_1(z)\equiv\sum_{k=0}^{N-1}A_k\cdot(z-z_m)^k \tag{7}$$

$$\exp\left(-\int_{z_1}^{z}T_1(\xi)d\xi\right)\approx T_2(z)\equiv\sum_{k=0}^{N-1}B_k\cdot(z-z_m)^k \tag{8}$$

Finally, Eqs. (5) and (6) can also be approximated using two series functions as shown in Eqs. (9) and (10).

$$P(z)\approx C_1+C_2\cdot\int_{z_1}^{z}T_2(\xi)d\xi \tag{9}$$

$$V_z(r,z)\approx\frac{1}{-\rho_f i\omega}\left(1-\frac{J_0(\lambda r)}{J_0(\lambda\cdot R(z))}\right)\cdot(C_2\cdot T_2(z)) \tag{10}$$

These pressure and axial velocity functions, represented by approximate series functions, are only valid within the specified range of $[z_1,z_2]$. The advantage of the adoption of series functions representing the pressure and axial velocity functions is that their values are continuous within the specified range along the z direction and they can describe the evolution of a fluid flow along the tube axis. By preparing a sufficient number of successive nozzle pieces with equations analogous to Eqs. (9) and (10) on each piece, the inherent error of series functions can be easily reduced.

By plotting either pressure or axial velocity profiles against the axial direction after determining pairs of the unknown coefficients, C_1 and C_2, the smoothness of solutions on adjacent nozzle sections can be checked. Unknown coefficients are determined by applying continuity of pressure and mass flow at adjacent boundaries of each nozzle piece. If any distinct discontinuities in the z derivatives of the series functions are found at section boundaries, then the range of $[z_1,z_2]$ can be decreased and the number of nozzle sections can be increased to enhance the accuracy of the solutions.

A schematic drawing of the possible nozzle sectioning is shown in Fig. 1. Figure 1(*a*) shows a set of discrete cylinders describing the overall nozzle. However, pressure and axial velocity at each piece of a cylinder are treated as constant and they abruptly change at each adjacent boundary with this scheme. Figure 1(*b*) instead utilizes a set of continuous tapered nozzles which are series function approximated over the range $[z_{n1},z_{n2}]$ where n denotes the nth nozzle section and pressure and axial velocity develop continuously. We adopt this latter scheme.

2.2 Approximations of the Pressure Boundary Conditions

2.2.1 Upstream Pressure Boundary Condition. The upstream boundary condition at the inlet tube of an inkjet print head is commonly assumed to have zero pressure when ambient pressure is subtracted. This seems sensible when the inkjet print head is connected to a reservoir of radius much larger than that of the inkjet print head inlet tube, because it can be regarded as a flanged open-end condition. In this case, the inlet tube length is extended by the open-end correction factor given by Pierce [25] and Rossing and Fletcher [26]. If the radius and length of an inlet tube are r_i and l_i, respectively, then the open-end corrected length of the inlet tube becomes $l_i+0.82\times r_i$. However, in many cases, the radius of the connecting tube does not significantly differ from that of the inlet tube. In this case, the connecting tube can be considered as a semi-infinite compliant tube. The pressure function of a finite compliant tube is represented by two exponential functions with respect to the axial direction, z, with positive and negative argument, φ, in the form of $A\exp(\varphi z)+B\exp(-\varphi z)$, where A and B are arbitrary constants. The parameter, φ, can be written in terms of material properties of a compliant tube such as elastic modulus, Poisson's ratio and radial dimensions of a connecting tube, as well as fluid properties. One solution with either positive or negative φ is discarded and the other is retained, in order to make pressure and velocity decay from the nozzle inlet toward a reservoir. The analytical solution of oscillatory fluid flow in a compliant tube is not presented here since it is outside the scope of this paper. (See the work of Dijksman [18] or Shin et al. [27] for details.)

2.2.2 Downstream Pressure Boundary Condition With a Free Surface. As it may not be possible to obtain an exact downstream pressure boundary condition with a free surface by analytical means, the usual downstream pressure boundary condition used in numerical treatments is the implementation of zero pressure difference at the nozzle exit. Benjamin and Ursell [28] and Valha and Kubie [29], however, computed the pressure on an oscillatory free surface due to a vertical acceleration and their work is adapted here to obtain an approximate pressure condition for inkjet printing that is better than the usual zero pressure difference. A trapezoidal voltage waveform in the time domain is decomposed into a set of sinusoidal waveforms in the frequency domain. After solving the equations of the individual Fourier components, they are synthesized to represent pressure and velocity so that the resultant meniscus shape is assumed to be the sum of the meniscus shape from each Fourier series term. This implies that our treatment requires another additional assumption that weak nonlinearity enables the adoption of Fourier series analysis and linear superposition.

Without considering the shape of any liquid jet protruded out of the meniscus, only the meniscus location itself is considered, with the assumption that the meniscus rim remains at the nozzle tip all the time. The axial velocity of the nozzle exit is assumed to be a dominant factor for the determination of the meniscus shape and the influence of radial velocity is ignored for simplicity of analysis. Except for the area close to the meniscus rim, this assumption is valid, since the magnitude of the axial velocity is far larger than that of the radial velocity.

The location of the free surface and pressure can be approximated via Eqs. (11) and (12) if the meniscus motion is considered as the motion of a curved membrane. Here γ, μ, r_0, η, and V_z

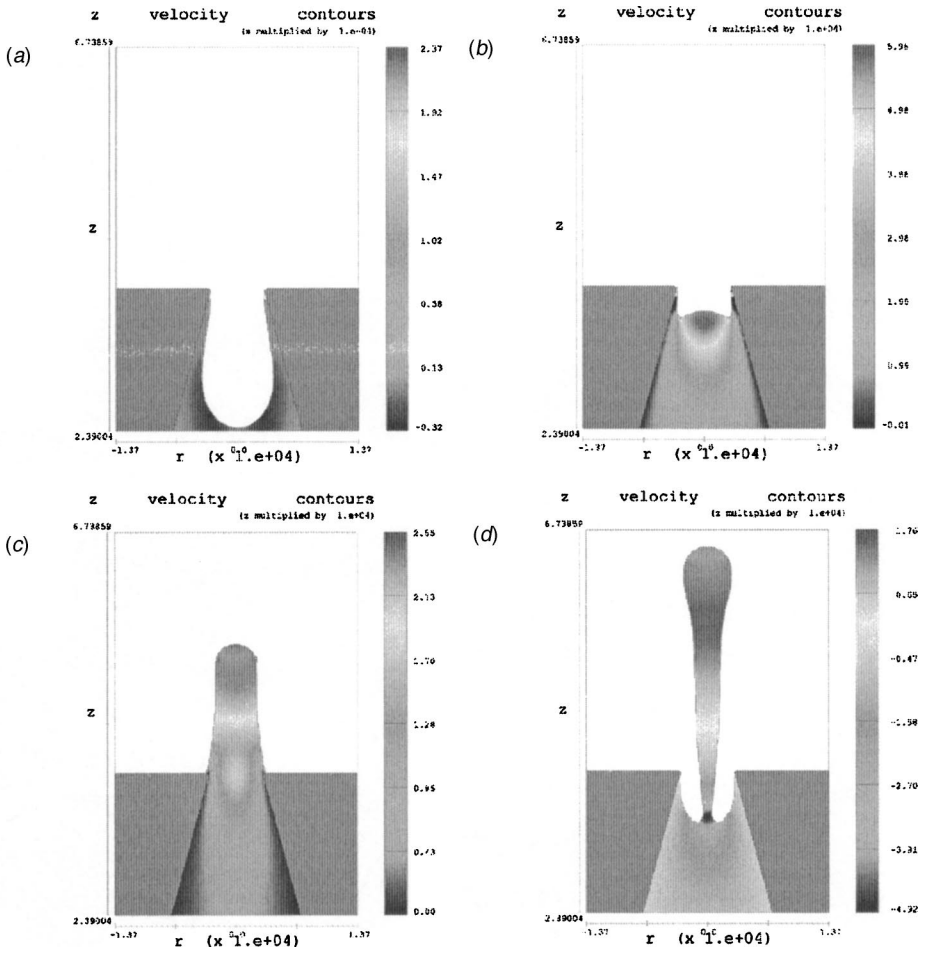

Fig. 2 Schematic of the drop formation stages illustrated by FLOW 3D simulations. (*a*) Meniscus motion without deformation. (*b*) Meniscus deformation. (*c*) Inception of necking. (*d*) Break-off. The different intensity of shading represents different axial velocities.

represent surface tension, dynamic viscosity, nozzle orifice radius, displacement of the meniscus from the tip of the nozzle, and axial velocity at the nozzle exit, respectively.

$$\eta = \int_0^t V_z dt' = \frac{V_z}{i\omega}, \tag{11}$$

$$\Delta P = \frac{2}{r_0^2} \int_0^{r_0} r \left\{ -\gamma \left(\frac{\partial^2 \eta}{\partial r^2} + \frac{1}{r} \frac{\partial \eta}{\partial r} \right) + 2\mu \frac{\partial V_z}{\partial z} \right\} dr \tag{12}$$

Equation (12), from the axial force balance, shows that the overall pressure difference at the liquid–air interface is controlled by the mean surface curvature, which depends on the meniscus shape, and the second term coming from the viscous normal stress, τ_{zz}. It is noted that nonlinearities have been ignored in computing the surface mean curvature. Equation (12) gives the average pressure along the hypothetical membrane surface and it is used as an approximate downstream boundary condition.

2.3 Meniscus Deformation and Extra Mass Transport. For convenience, the drop formation process can be divided into four main stages, which are experimentally observed (see Ref. [24]) and confirmed by numerical simulations. Figure 2 shows the simulation results of FLOW 3D, where these four main stages are represented. At the first stage, the meniscus velocity starts increasing with positive acceleration. From its minimum point in the axial direction, the meniscus moves outward with uniform curvature but without any other deformation as illustrated schematically in Fig. 2(*a*). Shortly after, however, the near center part of the meniscus starts bulging out. This meniscus deformation is assumed to be driven by the ratio of the rate of change of kinetic energy to the rate of change of surface energy. On simple physical grounds, if the rate of addition of kinetic energy is greater than the energy cost from the rate of growth of the surface, then the surface cannot be kept undeformed and meniscus deformation results. The radial position where the ratio is equal to unity is defined as the window radius through which fluid passes and creates a new surface. This deformed area grows outward in the radial and axial directions as shown schematically in Fig. 2(*b*) and extra mass clearly has been transported through the window, compared to an undeformed, uniformly curved meniscus. During this stage, the axial velocity of the meniscus surface approaches its maximum with positive acceleration.

During the third stage, following the peak axial velocity, the drop mass and kinetic energy are concentrated in the head of the jet and a reduced mass and associated kinetic-energy flux occurs at the nozzle exit compared to the second stage. Thus because of insufficient mass and kinetic energy flow to maintain a uniform ligament radius, a neck starts to form at the bottom of the jet as shown in Fig. 2(*c*). However, during this stage the drop still has a positive mass inflow.

At the fourth stage, when the axial velocity at the nozzle is negative, the radius of the jet ligament decreases more rapidly. As the ligament radius decreases, the mass outflow through the neck also decreases rapidly. Thus at this stage, the drop formation process consists of ligament stretching with little mass outflow at the

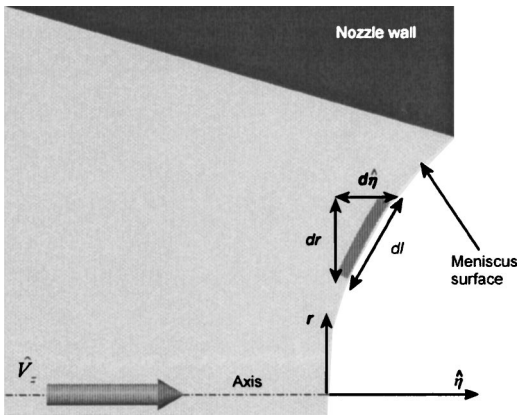

Fig. 3 Schematic drawing of the meniscus cross-section at the nozzle tip

nozzle. At the same time, the rest of the meniscus is pulled inward and forms a concave depression as shown in Fig. 2(*d*). Finally neck rupture occurs, releasing the drop.

To determine the window radius, the following assumptions are made. Only the influence of axial velocity on the rates of change of kinetic and surface energy is considered for simplicity, because the radial velocity is much smaller. We take the axial position, $\hat{\eta}$, and axial velocity, $\hat{V}_z$, to be sums over many Fourier components for the driving voltage signal considered earlier, as opposed to previous Eqs. (10)–(12) that considered a single Fourier component. A schematic drawing of the meniscus surface is shown in Fig. 3.

As is seen in the figure, the infinitesimal surface length, dl, can be represented by an infinitesimal radial length, dr, and axial distance, $d\hat{\eta}$. Formulas for dl and also for the surface area of the infinitesimal strip, dA, are shown in Eqs. (13) and (14).

$$dl = \sqrt{1+\left(\frac{\partial\hat{\eta}}{\partial r}\right)^2}\,dr \tag{13}$$

$$dA = 2\pi r\cdot dl = 2\pi r\sqrt{1+\left(\frac{\partial\hat{\eta}}{\partial r}\right)^2}\,dr \tag{14}$$

Surface energy on the infinitesimal strip, dA, is defined as $dS = \gamma\cdot dA$. If surface energy is differentiated with respect to time, then it yields a surface energy change rate, $d\dot{S}$ as shown in Eq. (15). Since $\hat{V}_z = d\hat{\eta}/dt$, Eq. (15) yields Eq. (16) upon exchanging the order of differentiation.

$$d\dot{S} = \gamma 2\pi r\frac{d}{dt}\left(\sqrt{1+\left(\frac{\partial\hat{\eta}}{\partial r}\right)^2}\right)\cdot dr$$

$$= \frac{\gamma 2\pi r}{\sqrt{1+\left(\frac{\partial\hat{\eta}}{\partial r}\right)^2}}\frac{\partial\hat{\eta}}{\partial r}\frac{d}{dt}\left(\frac{\partial\hat{\eta}}{\partial r}\right)dr \tag{15}$$

$$d\dot{S} = \gamma 2\pi r\frac{\frac{\partial\hat{\eta}}{\partial r}\cdot\frac{\partial\hat{V}_z}{\partial r}}{\sqrt{1+\left(\frac{\partial\hat{\eta}}{\partial r}\right)^2}}dr \tag{16}$$

The rate of change of kinetic energy, $d\dot{K}$, is rather simple to derive. The volumetric flow rate through the infinitesimal strip is $2\pi r\hat{V}_z dr$ and hence

$$d\dot{K} = \tfrac{1}{2}\rho_f 2\pi r\hat{V}_z dr\cdot\hat{V}_z^2 = \rho_f\pi r\hat{V}_z dr\cdot\hat{V}_z^2 \tag{17}$$

The infinitesimal rates of change of surface energy, $d\dot{S}$, and kinetic energy, $d\dot{K}$, at a given point on the meniscus surface are, therefore, defined as shown in Eqs. (16) and (17), respectively. Hence, the ratio, ζ, of the rate of change of kinetic energy to surface energy at a point on the meniscus surface is defined in Eq. (18)

$$\zeta = \frac{d\dot{K}}{d\dot{S}} = \frac{\rho_f\hat{V}_z^3}{2\gamma\frac{\partial\hat{\eta}}{\partial r}\cdot\frac{\partial\hat{V}_z}{\partial r}}\cdot\sqrt{1+\left(\frac{\partial\hat{\eta}}{\partial r}\right)^2} \tag{18}$$

If the axial velocity is positive and the absolute value of ζ is greater than unity, fluid at the interface breaks through the current surface and starts flowing outward. This simplified definition of a window ratio may have more than one singular point, especially where the radial gradient of either axial displacement or velocity becomes zero. When more than one window exists, then only the inner window will be taken for simplicity and convenience. In reality, adjacent windows are likely to spread along the surface of the meniscus and merge if the role of the radial velocity is taken into account.

3 Results and Discussion

Now, we analyze the model discussed in Sec. 2. First, in Sec. 3.1, physical parameters such as print head dimensions and properties, and fluid properties for computational works are introduced. Next, in Secs. 3.2 and 3.3, detailed information on computational parameters employed in the analytic and numerical calculations is covered.

FLOW 3D (Flow Science, Inc., Los Alamos, NM, USA) does not directly simulate the fluid–structure interaction and hence proper upstream pressure boundary conditions should be given by a user. For this purpose, upstream pressure boundary conditions are produced for a compliant inlet tube by the analytic model of Sec. 2.2.1, using MAPLE (Waterloo Maple, Inc., Waterloo, Ontario, Canada). In Sec. 3.4, by feeding these analytically achieved upstream pressure boundary conditions back to FLOW 3D and comparing analytical results with numerical results at an arbitrary point of the nozzle, the developed analytic model for descriptions of pressure and axial velocity history at the nozzle are validated.

In Sec. 3.5, local meniscus deformation, formulated in Sec. 2.3, is discussed and its impact on subsequent jet formation simulations are presented by demonstrating the difference of the inception times for the jet formation simulation with and without consideration of meniscus deformation.

All computations with MAPLE and FLOW 3D were run on a PC with AMD XP 2.2 GHz and 512 MBytes RAM.

3.1 Physical Parameters for Modeling. The overall print head dimensions of a MicroFab print head (MicroFab Technologies, Inc., Plano, TX, USA) are shown in Fig. 4. Material properties of PZT 5H, which surrounds a glass capillary tube, can be found in the data sheet of Morgan Matroc Electro Ceramics [30]. The elastic modulus and Poisson's ratio of a glass capillary tube are 46 GPa and 0.245, respectively. A connecting tube joins the inkjet print head to a reservoir and its material properties are assumed to be 0.34 GPa and 0.46 for elastic modulus and Poisson's ratio, respectively, which are typical for a PTFE-like elastic tube. Ethylene glycol is chosen as a fluid in an inkjet print head, of which density, viscosity, surface tension and speed of sound are 1113 $kg\cdot m^{-3}$, 20 mPa·s, 50 $mN\cdot m^{-1}$, and 1680 $m\cdot s^{-1}$, respectively; these values are taken from Dijksman's [18] paper.

Three trapezoidal voltage waveforms, applied to a piezoelectric actuator, are considered as shown in Fig. 5(*a*) with different voltage magnitudes, 20 V for case A, 40 V for case B and 60 V for case C, but all with the same frequency, 5 kHz. These voltage waveforms are fed to the analytic solution of Dijksman [18] to obtain pressure and velocity fields in time and space at the nozzle approximated with 50 Fourier terms. As shown in Fig. 5(*b*) for

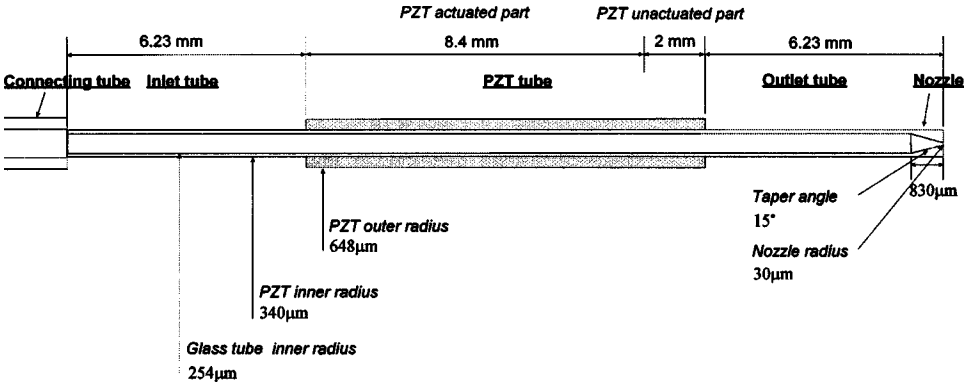

Fig. 4 Print head dimensions (Provided by MicroFab Inc.)

case C, 50 Fourier terms would be sufficient to describe the given waveforms: The root mean square relative errors for cases A, B, and C are all equal to 1.59%. The overall physical properties of materials and operating parameters are listed in Table 1.

3.2 Analytical Computations. In analytic computations, the nozzle is divided into eight sections equally spaced as shown in Fig. 1(*b*) and the first eight terms of the Taylor series in Eq. (7) are collected. Pressure and axial velocity functions on each section are series function approximated. Figures 6(*a*) and 6(*b*) show the comparison of $F_3(z)$ (computed analytically with MAPLE) and its series function approximated $T_1(z)$ of the first temporal Fourier component across the downstream quarter of the nozzle (here the 7th and 8th sections). The number of terms required for the series function approximation can be easily checked visually on a graph or computationally. By comparing eight nozzle sections and eight terms in each series with four nozzle sections and four terms in each series, it is found the root mean square relative errors of real and imaginary parts, e.g., on the final quarter section, are 0.0015% and 0.0031% with eight nozzle sections and 0.83% and 3.34% with four nozzle sections, respectively, comparing to $F_3(z)$ at the base frequency. Therefore, eight nozzle sections with eight Taylor series terms are chosen for the further analytic computation since this number of nozzle segments and terms does not significantly distort the original function, $F_3(z)$, but it needs less computation time than working with the original. An overall error is computed as the absolute magnitude of the difference squared between $F_3(z)$ and $T_1(z)$ normalized by the absolute magnitude

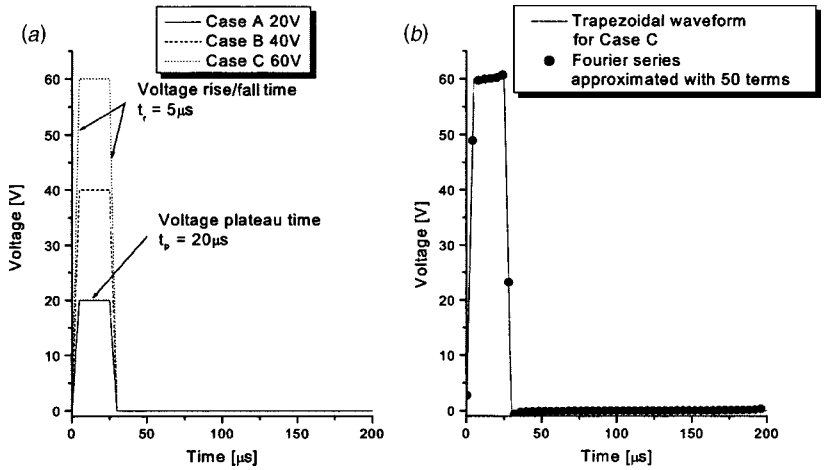

Fig. 5 Voltage waveforms. (*a*) Three voltage waveforms for cases A–C. (*b*) Fourier series approximated voltage waveform for case C with 50 Fourier terms.

Table 1 Physical properties of materials and operating parameters used for simulations

	Glass capilliary tube	PTFE connecting tube	
Elastic modulus	46 GPa	0.34 GPa	
Poisson's ratio	0.245	0.46	
	Ethylene glycol		
Density	1113 kg·m^{-3}	Viscosity	20 mPa·s
Surface tension	50 mN·m^{-1}	Speed of sound	1680 m·s^{-1}
	Case A	Case B	Case C
Voltage	20 V	40 V	60 V
Frequency	5 kHz	5 kHz	5 kHz
Voltage rise–fall time, t_r	5 μs	5 μs	5 μs
Voltage plateau time, t_p	20 μs	20 μs	20 μs

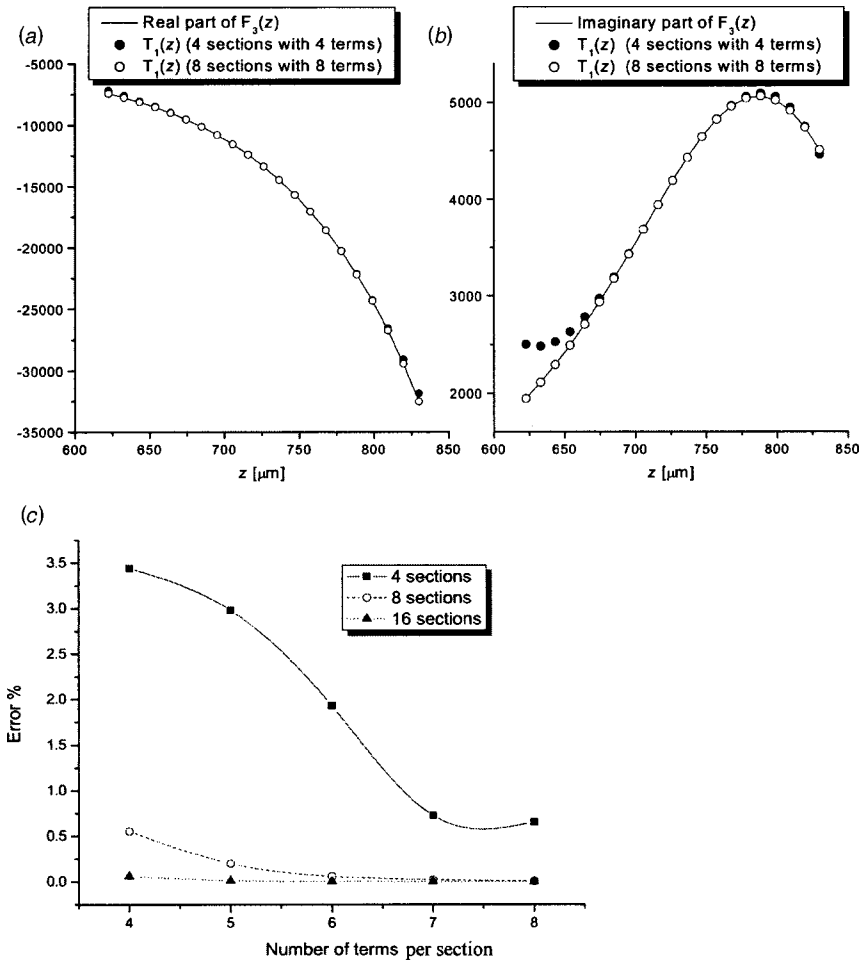

Fig. 6 Comparison of $F_3(z)$ and its series function approximation $T_1(z)$ with four nozzle sections and four terms per section, and eight nozzle sections and eight terms per section. (*a*) Real part of these functions. (*b*) Imaginary part of these functions. (*c*) Overall error of series approximations.

squared of $F_3(z)$, both integrated over the last quarter of the nozzle. The overall errors with different numbers of sections and terms are shown in Fig. 6(*c*).

The fluid–structure interaction of the composite tube and fluid inside an inkjet print head are solved as described in Dijksman's paper [18] with the analytic solution for the nozzle part and upstream and downstream pressure boundary conditions as described in Sec. 2. From this, pressure and velocity histories in time and space are obtained. Note that at the early stage when an emerging jet can be described by a single-valued function, $\hat{\eta}(r,t)$, this downstream pressure description given in Eq. (12) is valid. When a neck starts forming, the axial position of the jet surface becomes a multivalued function of radial coordinate and Eq. (12) is no longer an accurate description of the pressure condition at the nozzle tip but is employed nonetheless instead of assuming zero downstream pressure throughout the entire drop formation process.

3.3 Numerical Computations. Numerical simulations for cases, A, B, and C, were carried out using a full nozzle length with 20,000 cells and a Jacobi implicit scheme and then pressure results from FLOW 3D at the distance of 400 μm from the nozzle orifice on the axis (the full nozzle length being 830 μm) are produced as shown in Fig. 7.

3.3.1 Temporal Convergence. For numerical simulations, 10 successive pressure pulses are applied because the first several pressure waves show a transient response which comes from the initial cell conditions which are set to zero pressure and velocity. Numerical simulations with just the first pulse are likely to give inaccurate results. Regarding the transient influence on pressure histories, the 9th and 10th pressure pulses are compared and their root mean square relative differences are 3.97%, 3.20%, and 3.30% for cases A, B, and C, respectively. In addition, the root mean square relative differences of the 9th and 10th axial velocity are 1.34%, 4.79%, and 4.13%. These small differences indicate that transient responses have almost died away and hence the tenth pressure and axial velocity pulse histories on the nozzle axis are recorded hereinafter.

FLOW 3D allows only up to 200 time steps but this is not enough to describe a complex pressure waveform for 10 pulses. A special modification of FLOW 3D was made to allow up to 1000 pressure history data points in time by Flow Science, Inc. and the comparison between 500 and 1000 pressure history data points at the 10th pulse are made. The root mean square relative errors of 500 data point simulations with respect to 1000 data point simulations for cases A, B, and C at the distance of 400 μm from the nozzle orifice on the axis are 6.82%, 4.90%, and 3.50% for pressure histories, and 12.78%, 10.37%, and 12.74% for axial velocity histories, respectively. Hence 1000 data points are used hereinafter.

After the influences of any transient response and the number of time steps are checked, the comparison of numerical and analytical computations was done at the distance of 400 μm from the nozzle orifice on the axis. Numerical results differ from analyti-

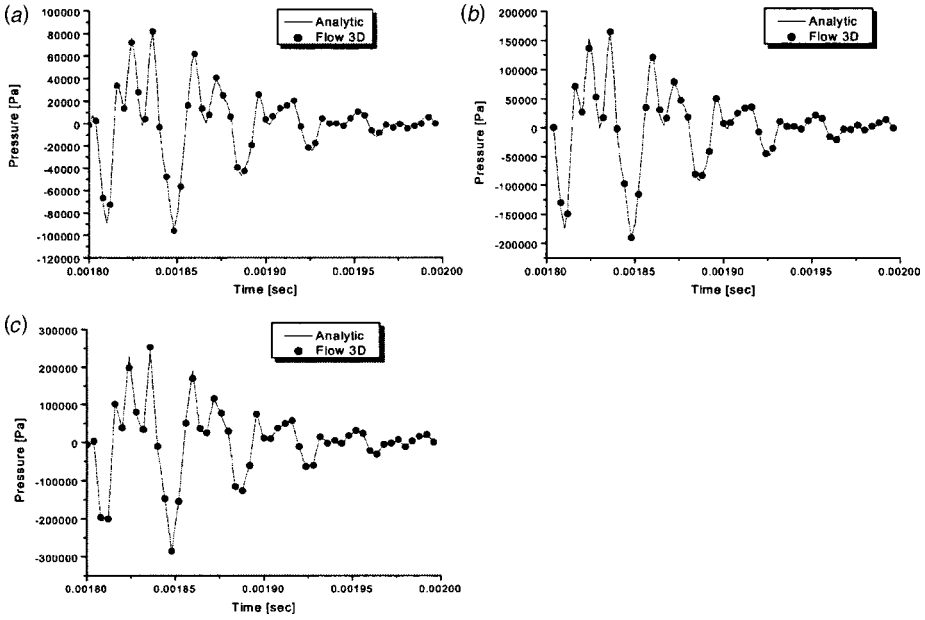

Fig. 7 Comparison of pressure results from numerical and analytical computations at 400 μm before the nozzle orifice on the axis. (*a*) Case A. (*b*) Case B. (*c*) Case C.

cally computed pressure results by 7.24%, 6.64%, and 7.33%, respectively, in terms of the root mean square relative error.

Hence, the full nozzle length simulation results show reasonable agreement with analytically computed pressure results at a distance of 400 μm from the nozzle orifice on the axis, but require a huge amount of computational time, 14,844, 22,040, and 27,620 s for cases A–C, respectively, compared to roughly 240 s for the analytical results. Therefore, numerical simulations with FLOW 3D have been carried out representing just the last 400 μm of a MicroFab print head of which the computational domain is shown in Fig. 8. Further simulations, therefore, will have analytic upstream pressure boundary conditions computed via Eq. (9) for cases A–C as shown in Fig. 7. Running simulations of this smaller domain allows improved spatial accuracy without sacrifice of computational time.

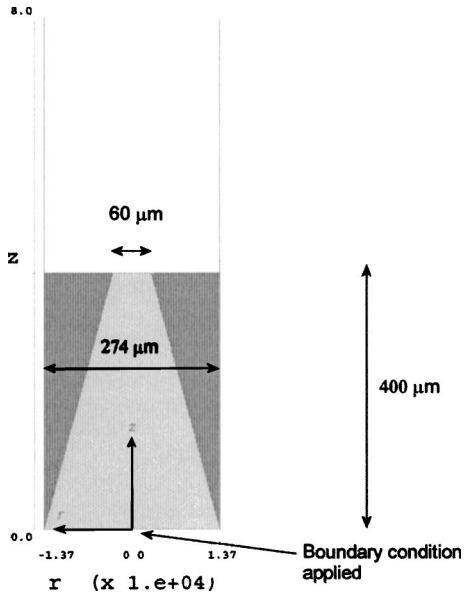

Fig. 8 Computational domain of the last 400 μm of the nozzle for numerical simulations with FLOW 3D

3.3.2 Spatial Convergence. Convergence tests in the refined computational domain shown in Fig. 8 were carried out with different cell numbers, 8000, 10,000, 20,000, and 40,000, and a constant cell aspect ratio in the *r* and *z* directions of unity. Hereinafter, all numerical and analytical results for the purpose of comparison will be obtained at the location of 100 μm before the nozzle orifice. Note that any axial location toward the nozzle tip is not suitable for extracting the pressure and axial velocity because of the meniscus retreat. There seems to be no significant differences among results with different cell numbers, though the peak axial velocities show slight mismatches. The axial velocity root mean square relative errors of 8000 cell simulations with respect to 40,000 cell simulations are 12.49%, 24.8%, and 19.52% for cases A–C, respectively. Pressure results from 8000 cells differ from 40,000 cells by 8.45%, 19.27%, and 6.51%, respectively. The axial velocity root mean square relative errors of 10,000 cell simulations with respect to 40,000 cell simulations are 7.21%, 11.58%, 37.03%, while the pressure root mean square relative errors are 3.98%, 6.84%, 10.9% for cases A–C, respectively. Regarding 20,000 cell simulations (compared to 40,000 cells), the axial velocity root mean square relative errors are 12.02%, 7.12% and 6.49%, while the pressure root mean square relative errors are 7.56%, 3.86%, and 3.25% for cases A–C, respectively.

However, when computational times are considered, yet higher cell numbers cost too much effort and time, compared to improvement of accuracy of the outputs and hence the number of cells has been fixed at 20,000.

3.4 Comparisons of Analytical and Numerical Results. Figure 9 shows the comparison between analytic and numerical results at the location of 100 μm before the nozzle orifice on the axis. No drop ejection is observed from the numerical simulation with FLOW 3D in case A but the other two cases have clear drop ejections.

The analytical pressure histories give better agreement with the numerical results from FLOW 3D than do the axial velocity histories. The root mean square relative errors in pressure for cases A–C are 15.14%, 21.10%, and 31.40% and axial velocity errors are 47.70%, 47.52%, and 42.66%, respectively. The comparison of volumetric flow rate may be another means to see globally the error of two methods, without restriction to a specific location in space, because the incompressible assumption gives the same

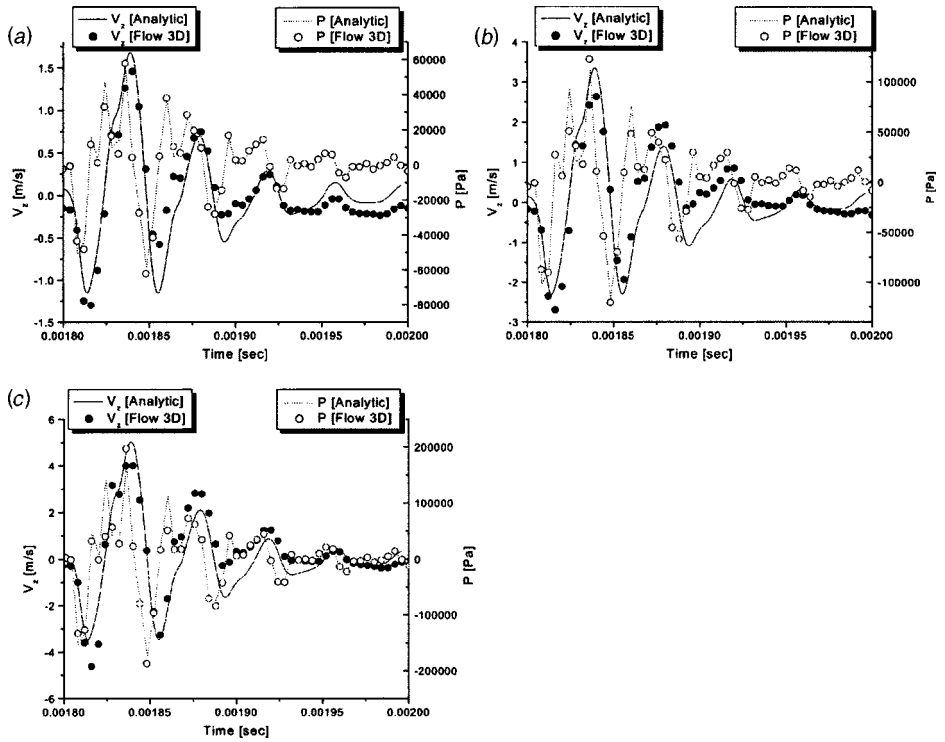

Fig. 9 Pressure and axial velocity comparisons. (*a*) Case A. (*b*) Case B. (*c*) Case C.

volumetric flow rate all through the nozzle length. As can be seen in Fig. 10, the root mean square relative errors of volumetric flow rate are 47.62%, 43.17%, and 39.68%, respectively.

Part of the reason for the discrepancies in axial velocity histories may result from the linearized Navier–Stokes z momentum equation. However, another source of these discrepancies may be from a secondary fluid flow induced by mass loss at the nozzle tip. When fluid is jetted from the nozzle, mass loss occurs. This mass loss is partly compensated by fluid returning from the exposed jet. However, the majority of the mass lost is replaced by fluid flow from the chamber side. This refilling process eventually sets fluid around the nozzle in motion and induces a secondary flow, implying refilling take place shortly after jetting. This secondary flow induced by refilling can be observed in the FLOW 3D results of Fig. 10(*c*) where volumetric flow rate after the first peak increases, compared to analytic results, but then gradually approaches the analytic predictions.

In the analytical results, the overall print head parts such as the nozzle, the chamber and the PZT actuator that surrounds the chamber are included in the model, following Dijksman's work [18]. Our numerical results, however, tend to be restricted to just the last 400 μm of the nozzle, with upstream pressure boundary

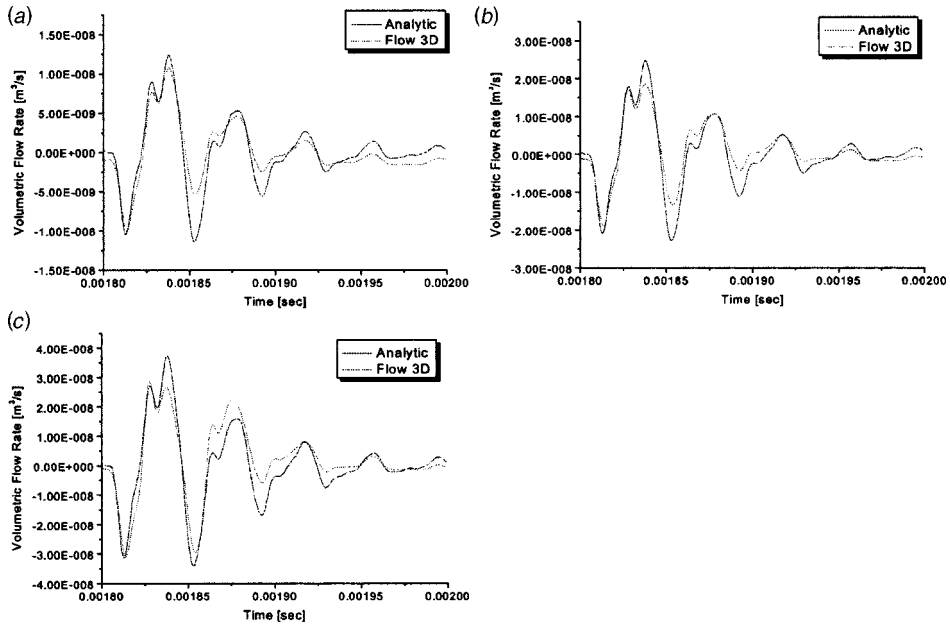

Fig. 10 Volumetric flow rate comparisons. (*a*) Case A. (*b*) Case B. (*c*) Case C.

Table 2 Comparison of computational times for analytic and numerical simulations on a PC with AMD XP 2.2 GHz and 512 MBytes RAM

	Analytical	Numerical	
Case A	240 s	8000 cells	4625s
		20,000 cells	17,500s
Case B	242 s	8000 cells	6171s
		20,000 cells	22,560s
Case C	242 s	8000 cells	7348s
		20,000 cells	27,310s

conditions determined by the analytical solution. Table 2 shows the comparison of computational times by analytic and numerical simulations. Note that if all print head parts were to be included in a numerical model, then the amount of computation time would increase dramatically above and beyond what is shown in Table 2.

3.5 Local Deformation of the Meniscus. The local meniscus deformation during the second stage, which was observed by experiments such as those done by Shield et al. [8], Meinhart and Zhang [24] and Chen and Basaran [31], has been formulated in Sec. 2.3 and its impact is discussed here.

In contrast to 2D axisymmetric numerical simulations, where this meniscus deformation window evolution is implicitly considered, the one dimensional (1D) numerical simulations of jet formation proposed by such authors as Shield et al. [7,8], Adams and Roy [9] and Chen et al. [13] did not implement this extra mass transport. The governing 1D equations can be found in the above works, but will not be discussed here because our immediate focus is on identifying the correct initial state to be used with a 1D system, and not on 1D systems *per se*. They assumed the meniscus in an emergent jet has uniform curvature, whereas the curvature of a drop forming in an inkjet print head is naturally nonuniform due to the inversion process as shown in Fig. 11. If the axial velocity is too low to create new surface, the meniscus protrudes without distinct local deformation but this is unlikely to produce any droplets.

The starting point of a 1D numerical simulation of jet formation is normally defined as the instant when an emerging jet, i.e., a uniformly curved meniscus, protruding from the nozzle would have a hemispherical shape. Therefore, the time interval from when the meniscus is fully retreated to when its volume would be equal to the volume of a hemisphere, assuming uniform curvature, implies a possible error, with less mass transport predicted at the start of 1D simulations in comparison to experimental data.

The inversion process of the meniscus implies that axial velocity should be accelerated to be faster within the window radius than in the remainder of the meniscus: This inversion being at the expense of the excess rate of change of kinetic energy. Though it is a highly nonlinear phenomenon, this conversion process can be approximated analytically by the help of a simple 1D approximation. When the axial velocity at the window radius, r_w, is equal to $\hat{V}_w$, the excess axial velocity, $\Delta\hat{V}_z$ at the point r ranging from 0 to r_w is assumed to be $\hat{V}-\hat{V}_w$ and hence the extra mass transport rate within the window is defined as shown in Eq. (19).

$$\Delta\dot{m}_w=\rho_f\int_0^{r_w}2\pi r\cdot\Delta\hat{V}_z dr \tag{19}$$

1D numerical simulations without the consideration of extra mass transport can lead to reduced kinetic energy of a droplet merely because the inception of a 1D numerical simulation without the window model is later than with the window model. For example, a sinusoidal velocity waveform of a frequency, f, is considered, the time, t_{hemi}, when an emerging jet has a hemispherical volume occurs after the moment of the peak axial velocity, i.e., $1/(4f)<t_{\text{hemi}}<1/(2f)$. However, the inception time with the window model is earlier than without window model, i.e., it can be $t_{\text{hemi}}\leq 1/(4f)$, although whether this actually occurs depends on the kinetic-energy rate put into the droplet. As a result, previous simulations most likely predicted a reduced kinetic energy.

The extra mass transported is computed and added via the window model beginning from when the meniscus is fully retreated, and ending when the net volume which has passed beyond the nozzle is equal to that of a hemisphere (with radius equal to that of the nozzle). The total transported volume at the end point is, therefore, the void volume of the retreated meniscus plus the

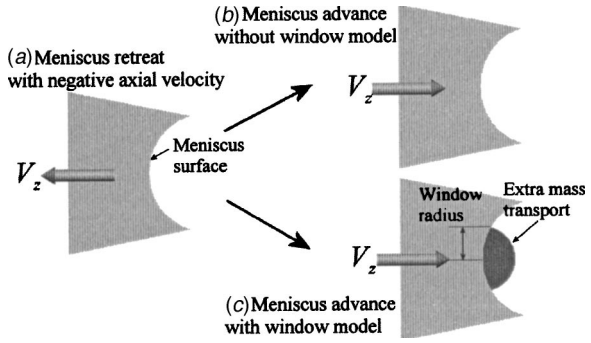

Fig. 11 Schematic based on experimental observations of meniscus inversion by local deformation and extra mass transport. (*a*) Meniscus retreat. (*b*) Meniscus advance without window model (conventional assumption). (*c*) Meniscus advance with window model (present model). Retreat and advance are clearly asymmetric in time.

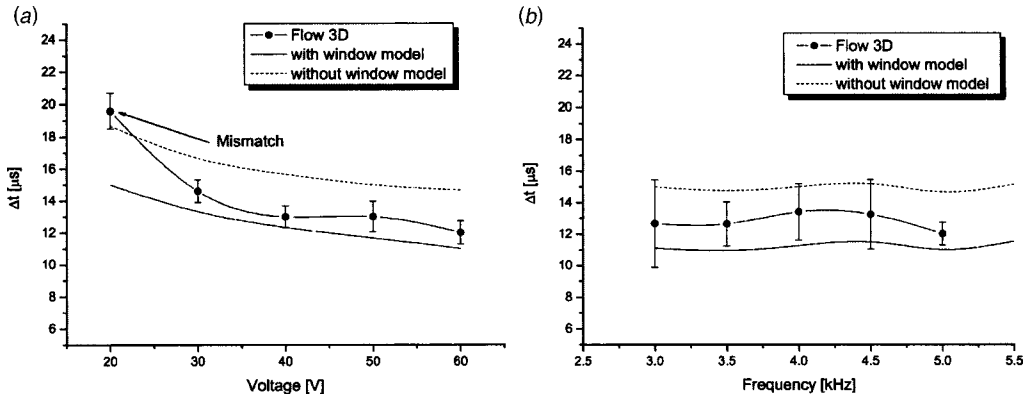

Fig. 12 Elapsed time, Δt, from the moment of maximum meniscus retreat to the moment when an emerging jet reaches a hemispherical volume. (*a*) Against voltage at 5 kHz. (*b*) Against frequency at 60 V.

hemisphere's volume. We introduce the symbol Δt to stand for the time interval between these start and end points. The analytically predicted and numerically predicted time intervals are shown in Fig. 12(*a*). Each Δt shows an error bar computed as follows. First, we calculate the square root of the sum of three relative errors (in axial velocity) squared, namely the transient response, temporal and spatial mesh truncations, all of which are specified in Sec. 3.3. Then the size of the error bar is reduced by the square root of the number of temporal steps required to accumulate the hemispherical volume, recognizing that (random) errors in axial velocity may tend to cancel one another during the accumulation of the said volume. Generally speaking, the analytic predictions with the window model give more accurate Δt values than those without.

However, a significant mismatch of Δt is found at the lowest driving voltage, 20 V (case A), where the numerically predicted Δt is closer to that without the window model. At 20 V, numerical simulations show there is no drop formation and an emerging jet forms a puddle near the nozzle orifice and hence the numerical axial velocity at the nozzle tip becomes slower by approximately 31.6% than the analytical axial velocity. This puddle formation by nozzle wetting is not considered in the present model. The analytically predicted and numerically predicted time intervals at various frequencies when the applied voltage is 60 V are shown in Fig. 12(*b*). It is noteworthy that numerical results are slightly higher than those from the window model. Generally speaking, void volumes from numerical results when the meniscus is fully retreated are bigger than void volumes from the analytical results. This is because meniscus retreat is generally both axial and radial (in cylindrical coordinates) in the former case, whereas only axial velocities are considered in the latter. These volume differences result in differing times to reach a net hemispherical volume.

4 Conclusion

To obtain pressure and axial velocity histories along the length of a tapered cylindrical nozzle with a relatively steep taper angle, an approximate analytical solution has been developed using series functions. When fluid jets out of the nozzle, a secondary axial velocity, which compensates the mass loss, may take place and the overall axial velocity observed from numerical results is the sum of the primary and secondary axial velocities. We postulate that as a consequence, subsequent velocity peaks after the initial highest positive peak axial velocities do not represent true axial velocity values as shown in Figs. 9(*c*) and 10(*c*). However, the influence of the secondary flow on pressure histories appears to be small. In addition, the effect of the secondary flow on the drop formation process is believed to be less significant than that of the primary flow, drop formation instead being governed by fluid deceleration at the nozzle.

A physical mechanism of the local deformation of a meniscus and creation of new surface due to an excess rate of addition of kinetic energy is proposed. This simple window model for new surface formation predicts the mass transported into the jet and good agreement with full numerical simulations is observed.

It is apparent that this analytical approach is much faster than numerical methods and produces reliable results within an acceptable range. The analytical solutions can be used for the pressure boundary data preparation in a subsequent numerical drop formation simulation with reasonable accuracy. This can then be used for drop formation simulation in the early stage of print head design.

Acknowledgments

We acknowledge the support of the EPSRC through project GR/N16969. D.-Y. Shin would like to give special thanks to the Rotary International for a postgraduate scholarship. We would also like to thank MicroFab Technologies, Inc. for information concerning the commercial ink jet heads used in this study.

Nomenclature

A_k, B_k = Series function coefficients
C_k = Unknown coefficient
F_k = z dependent function
J_0 = Bessel function of the first kind
$P(z)$ = Pressure function
$R(z)$ = $r_1 - z \cdot \tan\theta$
T_k = Taylor series expansion of z dependent function
V_r = Radial velocity
V_z = Axial velocity
$\hat{V}_w$ = Axial velocity at window radius $r = r_w$
$\hat{V}_z$ = The sum of overall axial velocity Fourier components
$d\dot{K}$ = Kinetic energy change rate
$d\dot{S}$ = Surface energy change rate
i = $\sqrt{-1}$
l_i = Inlet tube length
r_0 = Nozzle orifice radius
r_1 = Inner radius at the inlet of the nozzle
r_i = Inlet tube radius
r_w = Window radius
t_p = Voltage plateau time
t_r = Voltage rise/fall time
t_{hemi} = Time when the overall protruded volume equals a hemispherical volume
$\Delta\dot{m}_w$ = Extra mass transport rate
Δt = Time interval between the point the meniscus fully retreats and the point the overall protruded volume is equal to a hemispherical volume
ΔP = Membrane pressure
$\Delta\hat{V}_z$ = Accelerated axial velocity
φ = Decay constant for pressure in a compliant tube
γ = Surface tension coefficient
η = Meniscus displacement
$\hat{\eta}$ = The sum of meniscus displacement over all Fourier components
λ = $\sqrt{-i\omega/v}$
μ = Dynamic viscosity
v = Kinematic viscosity
θ = Taper angle
ρ_f = Fluid density
τ_{zz} = Viscous normal stress
ω = Angular frequency
ζ = Window ratio

References

[1] Antohe, B. V., and Wallace, D. B., 2002, "Acoustic Phenomena in a Demand Mode Piezoelectric Ink Jet Printer," J. Imaging Sci. Technol., **46**(5), pp. 409–414.
[2] Khaskia, A. M., 2002, "Static and Dynamic Modeling of Piezoelectric Drivers in Drop on Demand Printing," *FEMCI Workshop*, Maryland, USA.
[3] Yeh, J. T., 2000, "Simulation and Industrial Applications of Inkjet," *Proceedings of the 7th National Computational Fluid Dynamics Conference*, Kenting, Taiwan.
[4] Yeh, J. T., 2001, "A VOF-FEM and Coupled Inkjet Simulation," *Proceedings of ASME Fluids Engineering Division Summer Meeting*, The American Society of Mechanical Engineers, New York, USA.
[5] Pan, F., Kubby, J., and Chen, J., 2002, "Numerical Simulation of Fluid–Structure Interaction in a MEMS Diaphragm Drop Ejector," J. Micromech. Microeng., **12**, pp. 70–76.
[6] Fromm, J. E., 1984, "Numerical Calculation of the Fluid Dynamics of Drop-On-Demand Jets," IBM J. Res. Dev., **28**(3), pp. 322–333.
[7] Shield, T. W., Bogy, D. B., and Talke, F. E., 1986, "A Numerical Comparison of One-Dimensional Fluid Jet Models Applied to Drop-On-Demand Printing," J. Comput. Phys., **67**, pp. 327–347.
[8] Shield, T. W., Bogy, D. B., and Talke, F. E., 1987, "Drop Formation by DOD Ink-Jet Nozzles—A Comparison of Experiment and Numerical Simulation," IBM J. Res. Dev., **31**(1), pp. 96–110.
[9] Adams, R. L., and Roy, J., 1986, "A One-Dimensional Numerical Model of a Drop-On-Demand Ink Jet," ASME J. Appl. Mech., **53**, pp. 193–197.
[10] Liou, T. M., Shih, K. C., Chau, S. W., and Chen, S. C., 2002, "Three-Dimensional Simulations of the Droplet Formation During the Inkjet Printing Process," Int. Commun. Heat Mass Transfer, **29**(8), pp. 1109–1118.

[11] Kyser, E. L., Collins, L. F., and Herbert, N., 1981, ''Design of an Impulse Ink Jet,'' J. Appl. Photogr. Eng., **7**(3), pp. 73–79.
[12] Wallace, D. B., 1989, ''A Method of Characteristics Model of a Drop-on-Demand Ink-Jet Device Using an Integral Method Drop Formation Model,'' *Proc. ASME Winter Ann. Meeting*, San Francisco, CA, USA.
[13] Chen, P. H., Peng, H. Y., Liu, H. Y., Chang, S. L., Wu, T. I., and Cheng, C. H., 1999, ''Pressure Response and Droplet Ejection of a Piezoelectric Inkjet Printhead,'' Int. J. Mech. Sci., **41**(2), pp. 235–248.
[14] Wilkes, E. D., Phillips, S. D., and Basaran, O. A., 1999, ''Computational and Experimental Analysis of Dynamics of Drop Formation,'' Phys. Fluids, **11**(12), pp. 3577–3598.
[15] Teng, K. F., 1988, ''A Mathematical Model of Impulse Jet Mechanism,'' Math. Comput. Modell., **11**, pp. 751–753.
[16] Koltay, P., Moosmann, C., Litterst, C., Streule, W., Birkenmeier, B., and Zengerle, R., 2002, ''Modelling Free Jet Ejection on a System Level—an Approach for Microfluidics,'' *Technical Proceedings of the 2002 International Conference on Modeling and Simulation of Microsystems*, San Juan, Puerto Rico, pp. 112–115.
[17] Koltay, P., Moosmann, C., Litterst, C., Streule, W., and Zengerle, R., 2002, ''Simulation of a Micro Dispenser Using Lumped Models,'' *Technical Proceedings of the 2002 International Conference on Modeling and Simulation of Microsystems*, San Juan, Puerto Rico, pp. 170–173.
[18] Dijksman, J. F., 1984, ''Hydrodynamics of Small Tubular Pumps,'' J. Fluid Mech., **139**, pp. 173–191.
[19] Baek, S. H., Jeong, E. S., and Jeong, S., 2000, ''Two-Dimensional Model for Tapered Pulse Tubes. Part 1: Theoretical Modeling and Net Enthalpy Flow,'' Cryogenics, **40**, pp. 379–385.
[20] Rembe, C., Wiesche, S., and Hofer, E. P., 2000, ''Thermal Ink Jet Dynamics: Modeling, Simulation, and Testing,'' Microelectron. Reliab., **40**, pp. 525–532.
[21] Hart, V. G., and Shi, J., 1995, ''Governing Equations for Wave Propagation in Prestressed Joined Dissimilar Elastic Tubes Containing Fluid Flow: With an Example for a Tapered Section,'' Int. J. Eng. Sci., **33**(8), pp. 1121–1138.
[22] Chakravarty, S., and Mandal, P. K., 2000, ''Two-Dimensional Blood Flow Through Tapered Arteries Under Stenotic Conditions,'' Int. J. Non-Linear Mech., **35**, pp. 779–793.
[23] Bogy, D. B., and Talke, F. E., 1984, ''Experimental and Theoretical Study of Wave Propagation Phenomena in Drop-On-Demand Ink Jet Devices,'' IBM J. Res. Dev., **28**(3), pp. 314–321.
[24] Meinhart, C. D., and Zhang, H., 2000, ''The Flow Structure Inside a Microfabricated Inkjet Printhead,'' J. Microelectromech. Syst., **9**(1), pp. 67–75.
[25] Pierce, A. D., 1989, *Acoustics: An Introduction to Its Physical Principles and Applications*, The Acoustical Society of America, New York, USA, p. 348.
[26] Rossing, T. D., and Fletcher, N. H., 1998, *The Physics of Musical Instruments*, 2nd ed., Springer, New York, USA, p. 200.
[27] Shin, D. Y., Grassia, P., and Derby, B., 2003, ''Oscillatory Limited Compressible Fluid Flow Induced by the Radial Motion of a Thick-Walled Piezoelectric Tube,'' J. Acoust. Soc. Am., **114**(3), pp. 1314–1321.
[28] Benjamin, T. B., and Ursell, F., 1954, ''The Stability of the Plane Free Surface of a Liquid in Vertical Periodic Motion,'' Proc. R. Soc. London, Ser. A, **225**, pp. 505–515.
[29] Valha, J., and Kubie, J., 1996, ''Stability of a Gas–Liquid Interface in a Periodic Vertical Motion,'' Chem. Eng. Sci., **51**(22), pp. 4997–5006.
[30] Technical Publication TP-226: Properties of Piezoelectricity Ceramics, Morgan Electro Ceramics, http://www.morganelectroceramics.com/pdfs/tp226.pdf
[31] Chen, A. U., and Basaran, O. A., 2002, ''A New Method for Significantly Reducing Drop Radius Without Reducing Nozzle Radius in Drop-On-Demand Drop Production,'' Phys. Fluids, **14**(1), pp. L1–L4.

Kenji Oka
Associate Professor,
Department of Mechanical Engineering,
College of Engineering, Nihon University,
Kōriyama, 963-8642, Japan
e-mail: okak@mech.ce.nihon-u.ac.jp

Hidesato Itō
Former Professor, Nihon University,
Emeritus Professor, Tōhoku University,
3-5-13, Kuromatsu, Izumi-ku, Sendai,
981-8006, Japan

Energy Losses at Tees With Large Area Ratios

The loss coefficients for smooth, sharp-edged tees of circular cross-section with the area ratio of 11.44 were determined experimentally for five branch angles which ranged from 45 deg to 135 deg giving special consideration to all configurations of flow through the tees. The Reynolds number, in the leg carrying the combined flow, was kept to a constant value, i.e., 10^5 for the branch pipe and 3×10^4 for the main pipe, respectively. The equations for loss coefficients developed from the continuity, energy, and momentum principles give good agreement with the experimental results for tees with large area ratios provided that correction factors are introduced. The correction factors were determined by the analysis of the experimental data with the relative uncertainties from 0.9 to 3.3% according to the configurations of flow. The results constitute a useful guide to the determination of the loss coefficients for tees with large area ratios. [DOI: 10.1115/1.1852475]

Introduction

The determination of the energy losses caused by the combination and division of flow at tees with large area ratios are important in the design and analysis of piping systems such as manifolds, air-conditioning in buildings and tunnels, pipeline mixing in chemical engineering, fish bypass systems in hydraulic power plants, and so on. Although a considerable quantity of experimental research exists on loss coefficients for tees [1–16], only a few experimental results have been published on the loss coefficients for tees with large area ratios [3,4,8,14]. On the other hand, many authors [17–22] have proposed theoretical or empirical equations for the loss coefficients for tees, and Miller [23], as well as ESDU [24,25], have published charts for them. However, for lack of experimental data, most of the investigators have ignored the range of large area ratios. Apparently, no theoretical investigations have been published on the loss coefficients for the counter-dividing and counter-combining flow in tees.

The present work was undertaken to fill the need for information on this area of research, and to bridge a gap between the experimental and theoretical works on the loss coefficients for tees. The experiments were carried out for five smooth, sharp-edged tees of circular cross-section with the area ratio of 11.44, where the branch angles ranged from 45 deg to 135 deg. For all configurations of flow through the tees, the theoretical equations for loss coefficients developed from the continuity, energy, and momentum equations give good agreement with the experimental results provided that correction factors are introduced. A close examination of the experimental results of the previous workers also confirms the above relations for tees with large area ratios. The present investigations carried out both theoretically and experimentally, will constitute a useful guide to the determination of the loss coefficients for tees with large area ratios.

Definition of Loss Coefficient and Power-Loss Coefficient

The configurations of flow through a tee with a straight main pipe are shown in Fig. 1, where the heavy lines show the directions of flow under consideration. Six kinds of flow, that differ fundamentally from each other, are possible. With the upstream section as subscript 1 and the downstream section as subscript 3, the energy equation is

$$p_1+\frac{1}{2}\rho v_1^2=p_3+\frac{1}{2}\rho v_3^2+f_1\frac{l_1}{d_1}\frac{1}{2}\rho v_1^2+f_3\frac{l_3}{d_3}\frac{1}{2}\rho v_3^2+\Delta p_{13} \tag{1}$$

in which Δp_{13} is the energy loss due to the division or combination of flow between sections 1 and 3. The loss coefficient for dividing flow between sections 1 and 3 is defined by

$$(K_d)_{13}=\Delta p_{13}/(\rho v_1^2/2) \tag{2}$$

in which $v_1=Q_1/A_1$. Similarly, the loss coefficient for combining flow between sections 1 and 3 is

$$(K_c)_{13}=\Delta p_{13}/(\rho v_3^2/2) \tag{3}$$

in which $v_3=Q_3/A_3$. The continuity equation takes the form

$$Q_1=Q_2+Q_3 \tag{4}$$

for dividing flow, and

$$Q_1+Q_2=Q_3 \tag{5}$$

for combining flow. The power-loss coefficient for dividing flow is defined by [2,11,20]

$$\overline{K}_d=(K_d)_{12}Q_2/Q_1+(K_d)_{13}Q_3/Q_1 \tag{6}$$

Similarly, the power-loss coefficient for combining flow is [11,20]

$$\overline{K}_c=(K_c)_{13}Q_1/Q_3+(K_c)_{23}Q_2/Q_3 \tag{7}$$

In the following both the parentheses and the subscripts, to specify the loss coefficients, are ignored for brevity.

Experimental Apparatus

The experiments were carried out on smooth, sharp-edged tees with the area ratio of 11.44 ± 0.03. The branch angles tested were 45 deg, 60 deg, 90 deg, 120 deg, and 135 deg, respectively. The tees were gunmetal castings, made up of two pieces in the plane containing the main and the branch pipe axis. Their inner surfaces were machined and polished carefully with a P1200 abrasive paper and ceramic powder, so that the value of the arithmetical mean deviation of the roughness profile, Ra, was 0.03 μm. A typical arrangement of experimental apparatus is depicted in Fig. 2. The main pipe was 54.03 ± 0.02 mm ID, and the branch pipe was 15.97 ± 0.02 mm ID. These pipes were of a smooth drawn-brass tubing with the same internal diameter as the tees, and were sufficiently long to include the whole loss due to the division and combination of flow at tees.

The water, led from a surge tank or from a constant-level tank after passing through a honeycomb flow straightener and a con-

Contributed by the Fluids Engineering Division for publication on the JOURNAL OF FLUIDS ENGINEERING. Manuscript received by the Fluids Engineering Division October 3, 2002; revised manuscript received August 17, 2004. Review Conducted by: M. Otugen.

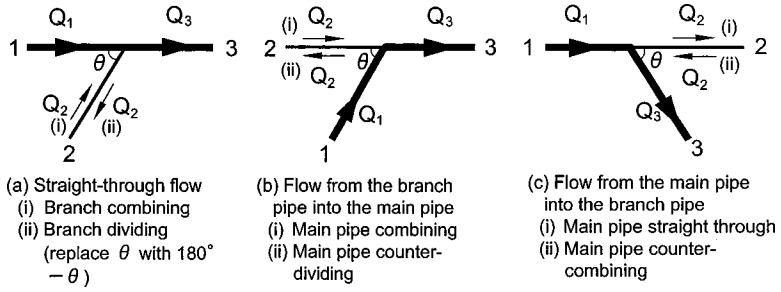

Fig. 1 Configurations of flow. Arrows indicate the direction of flow.

traction, enters the pipe under test. The details of pipe joints and piezometers are shown in Fig. 2. About 50 pipe diameters were used for the inlet length between the contraction and the upstream piezometer taps [26]. The downstream piezometer taps were located 55 pipe diameters downstream from the tee, where the hydraulic grade line practically coincides with the friction slope of a fully developed pipe flow [1–4,7,8,11,14]. In measuring the pressure difference p_1-p_3 between these two locations either a mercury–water or air–water multitube differential manometer was used, readings being made to the nearest 0.2 mm. For small pressure difference readings were made to the nearest 0.02 mm by the use of a cathetometer. The temperature of the water was measured to the nearest 0.1°C by a calibrated mercury thermometer inserted in the pipe of 68 mm ID in the downstream. The two parts of the flow were measured by a weighing tank and ISO 5167 orifice plates with corner tappings [27,28]. The latter had been calibrated accurately before the experiments, so that the relative uncertainty of discharge coefficient was 0.4%. The mean velocities in the pipe v_1 and v_3 were determined from discharge measurements. The friction factor for the experimental pipe was in good agreement with the Blasius resistance formula [26] and Prandtl's universal law of friction for smooth pipes [26]. Since the experimental data lie between these two equations [29], an experimental curve was drawn in the $f-\mathrm{Re}$ diagram so as to read f_1 and f_3 accurately. The relative uncertainty of the friction factor was 0.7%. The energy loss Δp_{13} was determined from Eq. (1). During the tests, the Reynolds number in the leg carrying the combined flow was kept to a constant value, i.e., 10^5 for the branch pipe and 3×10^4 for the main pipe, respectively.

Uncertainty analysis was carried out with reference to Coleman and Steele [30] and the ISO uncertainty guide [31]. The total uncertainties which considered both the measurement uncertainty and the uncertainty in the curve fit are given in Table 1 for both the correction factors and the regression equations for loss coefficients.

Experimental Results

Loss Coefficients for Straight-Through Flow in Tees. Figure 3 shows the loss coefficients for a straight-through flow. The combining flow case is shown in the right-hand side of the figure, where the loss coefficients divided by m are plotted against Q_2/Q_3. The loss coefficients are greatly influenced by the branch angle θ. In the case of $\theta>90$ deg where the flow from the branch pipe collides with the straight-through flow, the loss coefficients increase with the increasing of θ. The negative loss coefficients for the branch angles of 45 deg and 60 deg imply that the energy of the straight-through flow increases by a jet pump action of the high-velocity flow from the branch pipe.

The dividing flow case is shown in the left-hand side of the figure, where the scale of the ordinate is twice as large as that in the right-hand side. All the experimental results conform to a single curve regardless of the branch angle, taking negative values for small values of Q_2/Q_1. In the figure, the loss coefficients for a sharp-edged 90 deg equal the area tee at the Reynolds numbers of 10^5 and 2×10^5 reported by Ito and Imai [11] are also shown for a comparison. The difference between the two curves may be ascribed to the differences of both the area ratio and the Reynolds number. As found by Escobar [32], the occurrence of the negative loss for small values of Q_2/Q_1 may be attributed to the fact that the branch discharge comes from a region of low-velocity flow in the upstream of the main pipe.

In the case of 90 deg rectangular conduits Ramamurthy et al. [15] have shown that the dividing streamline profile, which bisects

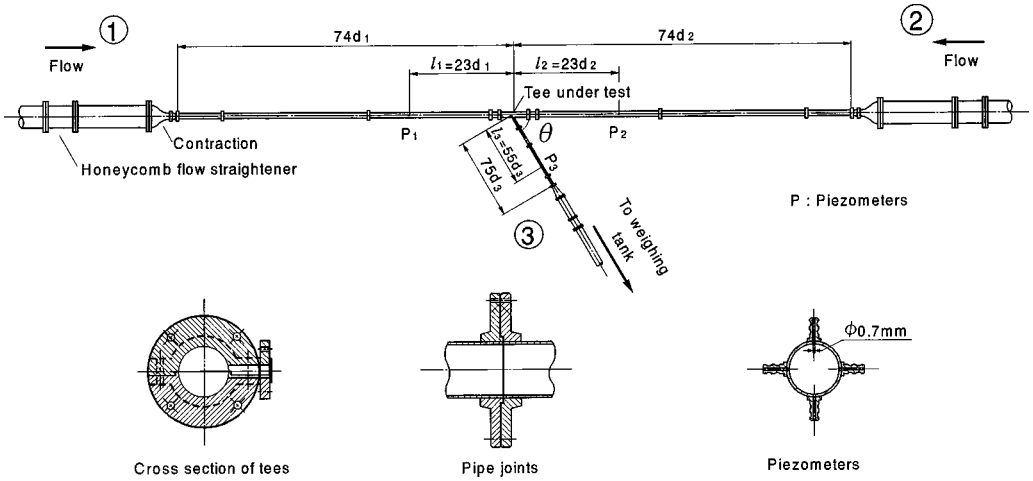

Fig. 2 Arrangement of experimental apparatus in the case of counter-combining flow, where θ=45 deg–135 deg and $d_1=d_2$.

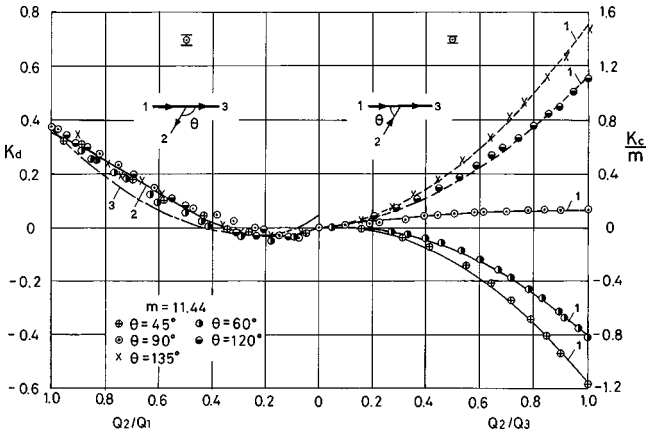

Fig. 3 Loss coefficients for straight-through flow in tees. $m=11.44$: 1 Eq. (8), 2 Eq. (15), 3 $\theta=90$ deg, $m=1$ [11].

two parts of flow is almost unaltered by the area ratio, and the energy loss associated with the expansion of the flow in the main is very weakly influenced by it. Similarly in the present experiments the dividing stream-surface profile [32] is almost unaltered by the branch angle, so that the energy loss for the straight-through flow is practically independent of the branch angle.

Loss Coefficients for Flow From Branch Pipe Into Main Pipe of Tees. The combining flow case is shown in the right-hand side of Fig. 4, where K_c/m^2 is used as the ordinate. The loss coefficients decrease with the increasing of Q_2/Q_3, and almost coincide with the theoretical value of -1 at $Q_2/Q_3=1$. The dividing flow case is shown in the left-hand side of the figure, where the loss coefficients are hardly influenced by the discharge ratio Q_2/Q_1. They increase with the increase in θ up to $\theta=90$ deg, and decrease with further increase in θ.

Loss Coefficients for Flow From Main Pipe Into Branch Pipe of Tees. The combining flow case is shown in the right-hand side of Fig. 5. With the increase in the discharge ratio Q_2/Q_3, the loss coefficients increase for $\theta<90$ deg, and decrease for $\theta>90$ deg. The loss coefficients for $\theta=90$ deg are hardly influenced by the discharge ratio. The dividing flow case is shown in the left-hand side of the figure, where K_d/m^2 is used as the ordinate. The loss coefficients decrease with the increasing of Q_2/Q_1, and almost coincide with the theoretical value of unity at $Q_2/Q_1=1$.

Power-Loss Coefficients for Tees. The power-loss coefficients obtained from the experiments are shown in Fig. 6 for all configurations of flow through the tees. The power-loss coefficients for the counter-dividing flow $\bar{K}_d$ are larger than those for the counter-combining flow $\bar{K}_c$, and in the case of $\theta=90$ deg, the former is about 2.3 times larger than the latter. In the figure the power-loss coefficients divided by m^2 are shown for both the dividing and combining flow with a straight-through flow, where the power-loss coefficients increase with increasing discharge through the branch pipe.

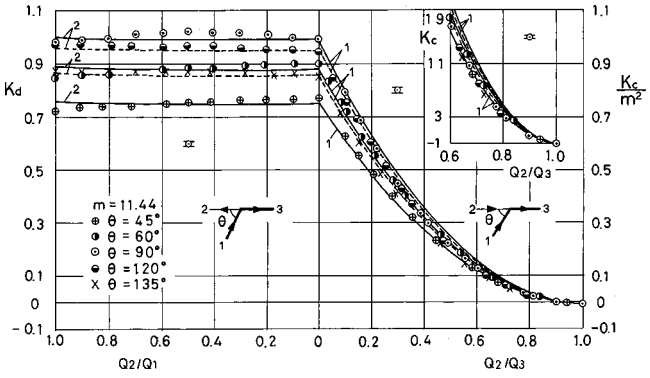

Fig. 4 Loss coefficients for flow from the branch pipe into the main pipe of tees. $m=11.44$: 1 Eq. (10), 2 Eq. (13).

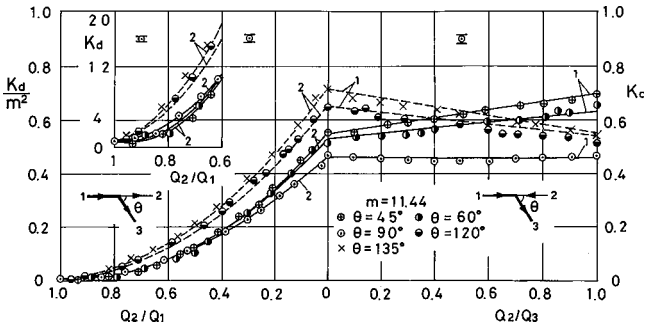

Fig. 5 Loss coefficients for flow from the main pipe into the branch pipe of tees. $m=11.44$: 1 Eq. (12), 2 Eq. (11).

Empirical Equations of Loss Coefficients for Tees With Large Area Ratios

The energy losses due to division and combination of flow at tees are assumed very nearly represented by the theoretical equations developed from the continuity, energy, and momentum equations. The following equations are proposed to express loss coefficients for tees with large area ratios, where k_c, k_d, and Λ are correction factors.

Straight-through flow in combining tees

$$K_c=k_c[2Q_2/Q_3-(1+2m\cos\theta)(Q_2/Q_3)^2] \tag{8}$$

Straight-through flow in dividing tees

$$K_d=k_d[2(\Lambda-1)Q_2/Q_1+(Q_2/Q_1)^2] \tag{9}$$

Branch flow in combining tees

$$K_c=-1+k_c[4Q_1/Q_3+(m^2-2m\cos\theta-2)(Q_1/Q_3)^2] \tag{10}$$

Branch flow in dividing tees

$$K_d=1+k_d[-2m\cos\theta Q_3/Q_1+m^2(Q_3/Q_1)^2] \tag{11}$$

Counter-combining flow in tees

$$K_c=k_c\left[1+\frac{2\cos\theta}{m}-\frac{4\cos\theta}{m}\frac{Q_1}{Q_3}+\frac{1}{m^2}\left(\frac{Q_1}{Q_3}\right)^2\right] \tag{12}$$

Counter-dividing flow in tees

$$K_d=k_d\left[1-\frac{2\cos\theta}{m}+\frac{1}{m^2}-\frac{2}{m^2}\frac{Q_2}{Q_1}+\frac{3}{m^2}\left(\frac{Q_2}{Q_1}\right)^2\right] \tag{13}$$

If $k_c=k_d=1$, Eqs. (8)–(13) reduce to the theoretical equations developed from the continuity, energy, and momentum equations, i.e., Eqs. (8) and (10) were developed by Favre [17], Eq. (9) by Sato [33] and Eq. (11) by Truckenbrodt [20]. Katz [19] also derived Eq. (9) for 90 deg equal area tees. Appendices A and B give the derivation of Eqs. (12) and (13), respectively.

The experimental data were analyzed to obtain the correction factors. The results determined by the method of least squares are presented in Table 1, and shown graphically in Fig. 7. In the case of the flow from the branch pipe into the main pipe shown in Fig. 4, k_d in Eq. (13) practically coincides with k_c in Eq. (10) for the same branch angle. Similarly, in the case of the flow from the

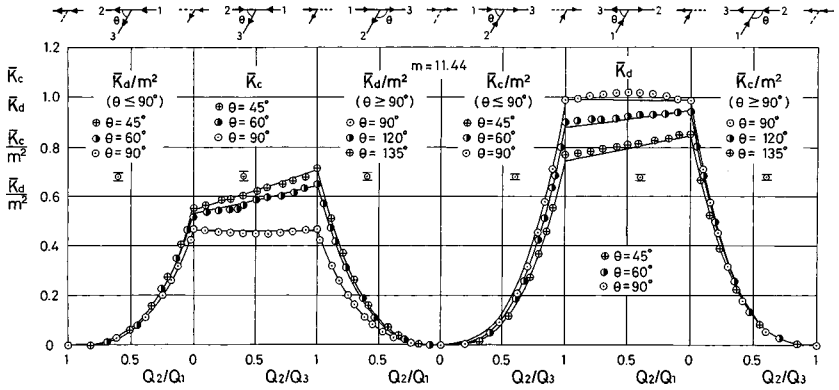

Fig. 6 Power-loss coefficients for tees. $m=11.44$: Full lines are given by Eqs. (6) and (7) together with Eqs. (8) to (13).

main pipe into the branch pipe shown in Fig. 5, k_c in Eq. (12) almost coincides with k_d in Eq. (11) for the same branch angle.

The correction factor Λ in Eq. (9) is given by the following empirical equation together with $k_d=0.354$ (see Appendix C).

$$\Lambda = 1 + (Q_2/Q_1 - 0.604)(1 - Q_2/Q_1) \tag{14}$$

Equation (9) becomes

$$K_d = -0.43Q_2/Q_1 + 1.49(Q_2/Q_1)^2 - 0.71(Q_2/Q_1)^3 \tag{15}$$

The foregoing equations for the loss coefficients with the correction factors shown in Table 1 are compared in Figs. 3–5 with the experimental results. The equations represent the experimental results very well.

Comparison With Results Obtained by Others

Representative experimental results for sharp-edged tees in the case of $m>8$ obtained by others [3,4,8,14] are compared in Figs. 8 and 9 with the proposed equations. The estimated Reynolds numbers in the main pipe in their experiments are also shown. In Fig. 9 since both the experimental results on the counter-dividing and counter-combining flow for $m>8$ are unavailable, the experimental results on the branch flow in dividing tees are presented together with those on the branch flow in combining tees. Although the uncertainties for K in their experiments are not clear, the experimental apparatus and procedures used were similar to those in the present experiments. The equations represent the experimental results very well. The values of k_c and k_d determined from the experimental data by the least-squares method are also shown in Fig. 7. Since the second term in the square brackets of Eq. (8) becomes independent of m for $\theta=90$ deg, the correction factor k_c in this case is greatly influenced by m, and as seen in the insert of Fig. 7(*a*) k_c increases with the increase in m. The k_c-value in Eq. (8) for $\theta=90$ deg is given by the following empirical equation:

$$k_c = 0.50m^{0.45} \tag{16}$$

This equation may be used in the range $8<m<20$.

The experimental results for sharp-edged tees obtained by others for $m<8$ were also analyzed to obtain the correction factors. However, the differences between the experimental data and the proposed equations increase with decreasing area ratio, and the equations give only qualitative agreement. Apparently, the proposed equations can be used for $m>8$. The reason may be attrib-

Table 1 Values of the correction factors. Uncertainties for the correction factors and for the equations of loss coefficients are also shown. $m=11.44$.

Equation	θ	45°	60°	90°	120°	135°
Eq. (8)	k_c	0.869	0.881	1.516	1.036	1.008
	U_{kc}	0.009	0.008	0.033	0.011	0.012
	$U_{Eq.(8)-regress}/m$	0.042	0.034	0.035	0.058	0.066
Eq. (10)	k_c	0.852	0.957	0.983	0.870	0.760
	U_{kc}	0.010	0.009	0.017	0.008	0.010
	$U_{Eq.(10)-regress}/m^2$	0.030	0.040	0.062	0.040	0.040
Eq. (11)	k_d	0.618	0.576	0.457	0.591	0.629
	U_{kd}	0.012	0.009	0.008	0.007	0.009
	$U_{Eq.(11)-regress}/m^2$	0.032	0.037	0.035	0.040	0.036
Eq. (12)	k_c	0.621	0.580	0.461	0.594	0.631
	U_{kc}	0.008	0.017	0.011	0.020	0.013
	$U_{Eq.(12)-regress}$	0.061	0.086	0.072	0.093	0.070
Eq. (13)	k_d	0.851	0.956	0.983	0.869	0.758
	U_{kd}	0.021	0.026	0.023	0.012	0.009
	$U_{Eq.(13)-regress}$	0.062	0.083	0.087	0.050	0.039
Eq. (15)	$U_{Eq.(15)-regress}$	0.034	0.040	0.036	0.042	0.035

Equation (16) for $\theta=90°$: $U_{Eq.(16)-regress}=0.087$

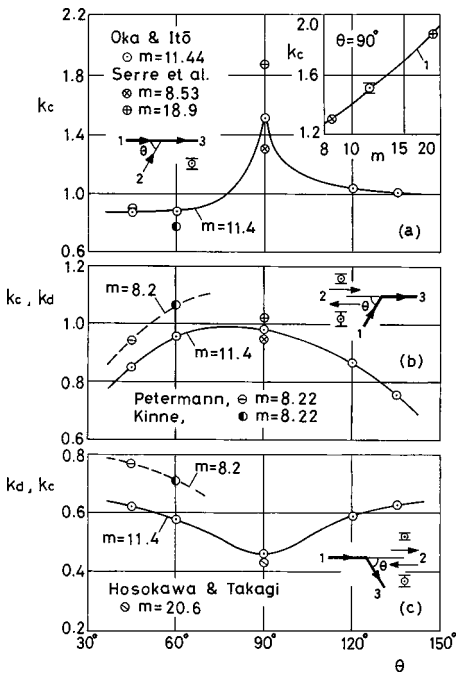

Fig. 7 Values of correction factors. (*a*) k_c for Eq. (8). 1 Eq. (16); (*b*) $k_c(\approx k_d)$ for Eqs. (10) and (13); (*c*) $k_d(\approx k_c)$ for Eqs. (11) and (12). The values of the uncertainties for k_c and k_d are given in Table 1.

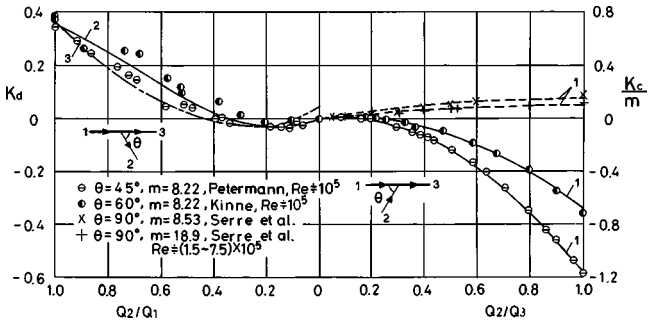

Fig. 8 Loss coefficients for straight-through flow in tees. Comparison with other investigators: 1 Eq. (8), 2 Eq. (15), 3 θ=90 deg, m=1 [11].

uted mainly to the fact that, as Ramamurthy and Zhu [16] have shown experimentally for the combining flow in 90 deg junctions of rectangular cross sections, the difference between the branch angle and the average angle for momentum transfer at the joining edge of the branch pipe increases with the decrease in the area ratio.

According to Figs. 7(*b*) and 7(*c*), which show the case of branch flow, both k_c and k_d decrease with the increase in the area ratio from 8 to 11. However, Eq. (12) in the case of $m \rightarrow \infty$ corresponds to the loss coefficient for flow from a large reservoir into a pipe with a square-edged entrance, in which k_c ranges from 0.4 to 0.5 for θ=90 deg [34,35]. Similarly, Eq. (13) in the case of $m \rightarrow \infty$ implies the loss coefficient for flow from the end of a pipe into a large reservoir, in which k_d is close to 1.0 [34,35]. The corresponding values of k_c=0.461 and k_d=0.983 for m=11.44 in Table 1 conform to the above-mentioned values. Thus, the k_c- and k_d-values for m=11.44 determined by the present experiments may be used to estimate approximately the loss coefficients for tees with the area ratio greater than 11.

Conclusions

1. The loss coefficients for tees with large area ratios are expressed by the equations developed from the continuity, energy, and momentum principles provided that the correction factors are introduced;
2. the correction factors determined by the present experiments are shown in Table 1 and Fig. 7. They may be used to determine the loss coefficients for smooth, sharp-edged tees of circular cross-section with the area ratio greater than 11;
3. the comparison of the proposed equations with the experimental results obtained by others shows that the proposed equations, with the correction factors shown in Fig. 7, give good agreement with the experimental results for the area ratio greater than 8;
4. the loss coefficients for straight-through flow in dividing tees are independent of the branch angle, and given by Eq. (15) for the area ratio greater than 8;
5. the loss coefficient for flow from a large reservoir into a pipe and that from the end of a pipe into a large reservoir agrees with the corresponding loss coefficient for a 90 deg tee with the area ratio of 11.

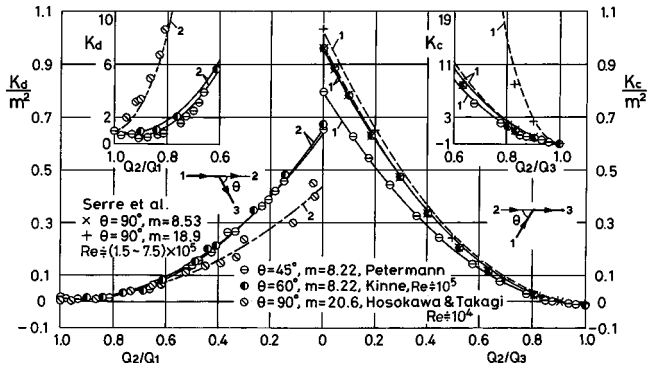

Fig. 9 Loss coefficients for branch flow in tees. Comparison with other investigators: 1 Eq. (10), 2 Eq. (11).

Acknowledgments

The authors wish to express their thanks to Messrs. K. Chida and A. Shibayama, students in the Master Course, and to the undergraduate students of the Department of Mechanical Engineering, College of Engineering, Nihon University, for their help during the course of this work.

Nomenclature

A = cross-sectional area of pipe
d = internal diameter of pipe
f = friction factor for straight pipe
$\underline{K}$ = loss coefficient
K = power-loss coefficient
k = correction factor
l = length of pipe
m = ratio of cross-sectional area of main pipe to that of branch pipe
p = static pressure
Q = discharge
U = uncertainty
v = mean axial velocity

Greek letters

θ = angle between branch pipe and main pipe
Λ = correction factor for straight-through flow in dividing tee
ρ = density
σ = standard deviation

Subscripts

1 = upstream of pipe under consideration
2 = side pipe
3 = downstream of pipe under consideration
c = combining flow
d = dividing flow
Eq.-regress = regression equation

Appendix A: Derivation of Equation of Loss Coefficients for Counter-Combining Flow

In the following, the flow is incompressible and one-dimensional. The friction loss can be neglected so that $f_1=f_3=0$ in Eq. (1). A control volume ABCD is selected as shown in Fig. 10, and a momentum balance is applied to the direction of the axis of the branch pipe. Since $A_1=A_2$

$$(p-p_3)A_3=\rho v_3^2 A_3+\rho(v_2^2-v_1^2)A_1\cos\theta \qquad (A\text{-}1)$$

where p is the average pressure in the tee. Since the friction loss is ignored, the pressure in the tee is approximately equal to the pressure in the upstream of the main pipe, i.e., $p=p_1$. If p_1 is eliminated from Eqs. (1) and (*A*-1)

$$\Delta p_{13}=\rho v_3^2/2+(1-2m\cos\theta)\rho v_1^2/2+\rho m v_2^2\cos\theta \qquad (A\text{-}2)$$

where $m=A_1/A_3$. Dividing each term in Eq. (*A*-2) by $\rho v_3^2/2$

$$K_c=1+(1-2m\cos\theta)(v_1/v_3)^2+2m\cos\theta(v_2/v_3)^2 \qquad (A\text{-}3)$$

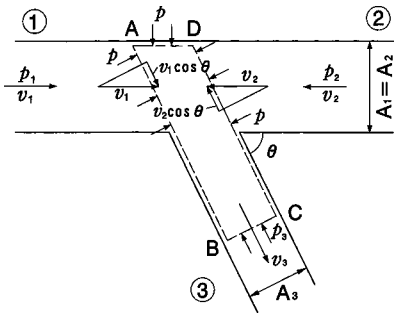

Fig. 10 Control volume for counter-combining flow in a tee.

From the continuity equation (5)

$$v_1/v_3 = Q_1/mQ_3 \tag{A-4}$$

and

$$v_2/v_3 = (1 - Q_1/Q_3)/m \tag{A-5}$$

With substitution of Eqs. (*A*-4) and (*A*-5) into Eq. (*A*-3), Eq. (12) results in the case of $k_c = 1$.

Appendix B: Derivation of Equation of Loss Coefficients for Counter-Dividing Flow

A control volume ABCD is selected as shown in Fig. 11, and a momentum balance is applied to the direction of the axis of the main pipe. Since $A_2 = A_3$

$$(p - p_3)A_3 = \rho(v_2^2 + v_3^2)A_3 - \rho v_1^2 A_1 \cos\theta \tag{B-1}$$

where p, the average pressure in the tee, is approximately equal to the pressure in the upstream of the branch pipe, i.e., $p = p_1$. If p_1 is eliminated from Eqs. (1) and (*B*-1)

$$\Delta p_{13} = (1 - 2\cos\theta/m)\rho v_1^2/2 + \rho v_2^2 + \rho v_3^2/2 \tag{B-2}$$

where $m = A_3/A_1$. Dividing each term in Eq. (B-2) by $\rho v_1^2/2$

$$K_d = 1 - 2\cos\theta/m + 2(v_2/v_1)^2 + (v_3/v_1)^2 \tag{B-3}$$

The continuity equation (4) leads to

$$v_2/v_1 = Q_2/mQ_1 \tag{B-4}$$

and

$$v_3/v_1 = (1 - Q_2/Q_1)/m \tag{B-5}$$

With substitution of Eqs. (*B*-4) and (*B*-5) into Eq. (*B*-3), Eq. (13) results in the case of $k_d = 1$.

Appendix C: Derivation of Equation of Loss Coefficients for Straight-Through Flow in Dividing Tees

A control volume ABCD is chosen as shown in Fig. 12, and a momentum balance is applied to the direction of the axis of the main pipe. On the assumption that the fluid, which flows into the branch pipe, carries away the momentum $\Lambda\rho Q_2 v_1$, where Λ is the correction factor

$$\rho v_3^2 A_3 + \Lambda\rho Q_2 v_1 - \rho v_1^2 A_1 = (p_1 - p_3)A_1 \tag{C-1}$$

where $A_1 = A_3$. If $p_1 - p_3$ is eliminated from Eqs. (1) and (C-1)

$$\Delta p_{13} = \rho v_3^2/2 + \Lambda\rho Q_2 v_1/A_1 - \rho v_1^2/2 \tag{C-2}$$

The continuity equation (4) leads to

$$v_3/v_1 = 1 - Q_2/Q_1 \tag{C-3}$$

Dividing each term in Eq. (*C*-2) by $\rho v_1^2/2$, and making use of Eq. (*C*-3), Eq. (9) results in the case of $k_d = 1$.

If $Q_2/Q_1 = 1$, then $\Lambda = 1$, because in this case the whole fluid flows into the branch pipe. With substitution of the values in Eq. (9), $K_d = k_d$ at $Q_2/Q_1 = 1$. On the assumption that $k_d = 0.354$, which is the mean value of K_d at $Q_2/Q_1 = 1$, the experimental values of $(\Lambda - 1)/(1 - Q_2/Q_1)$ were plotted against Q_2/Q_1 in Fig. 13. As seen from the figure, the experimental results are approximately expressed by a straight line, and we obtain Eq. (14). Λ is smaller than unity for small values of Q_2/Q_1. This fact supports the view that the branch discharge comes from a region of low-velocity flow in the upstream of the main pipe.

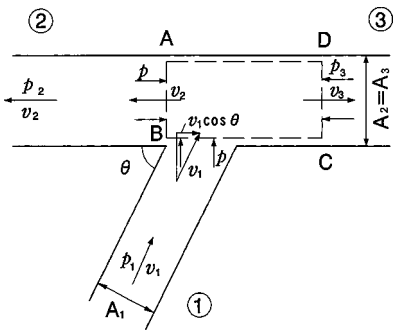

Fig. 11 Control volume for counter-dividing flow in a tee.

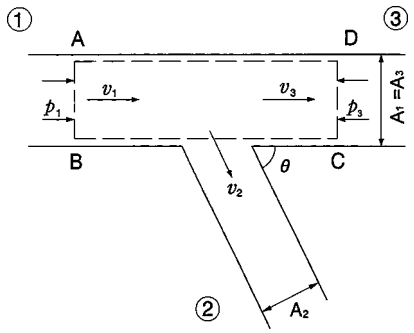

Fig. 12 Control volume for straight-through flow in a dividing tee.

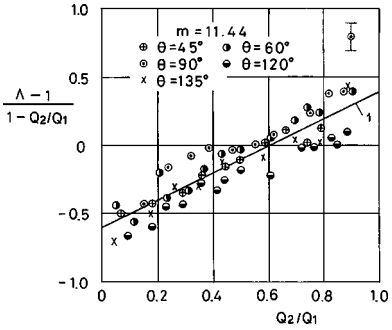

Fig. 13 Comparison of experimental data with Eq. (14). 1 Eq. (14).

References

[1] Vogel, G., 1926, "Untersuchungen über den Verlust in rechtwinkligen Rohrverzweigungen," Mitteilungen des Hydraulischen Instituts der Technischen Hochschule München, **1**, pp. 75–90.

[2] Vogel, G., 1928, "Untersuchungen über den Verlust in rechtwinkeligen Rohrverzweigungen," Mitteilungen des Hydraulischen Instituts der Technischen Hochschule München, **2**, pp. 61–64.

[3] Petermann, F., 1929, "Der Verlust in schiefwinkligen Rohrverzweigungen," Mitteilungen des Hydraulischen Instituts der Technischen Hochschule München, **3**, pp. 98–117.

[4] Kinne, E., 1931, ''Beiträge zur Kenntnis der hydraulischen Verluste in Abzweigstücken,'' Mitteilungen des Hydraulischen Instituts der Technischen Hochschule München, **4**, pp. 70–93.
[5] McNown, J. S., 1954, ''Mechanics of Manifold Flow,'' Trans. Am. Soc. Civ. Eng., **119**, pp. 1103–1142.
[6] Gardel, A., 1957, ''Les Pertes de Charge dans les Écoulements au Travers de Branchements en Té,'' Publication, No. 44, École Polytechnique de l'Université de Lausanne, Lausanne, Switzerland.
[7] Blaisdell, F. W., and Manson, P. W., 1963, ''Loss of Energy at Sharp-Edged Pipe Junctions in Water Conveyance Systems,'' Technical Bulletin, No. 1283, U.S. Department of Agriculture, Washington, D.C.
[8] Hosokawa, Y., and Takagi, S., 1966, ''Energy Loss Caused by the Flow Through a Pipe Line Which Has a Branch Pipe Jutting Into the Main Pipe (in Japanese),'' Reports of the Faculty of Engineering, Himeji Institute of Technology, **19A**, pp. 106–113.
[9] Miller, D. S., 1971, *Internal Flow. A Guide to Losses in Pipe and Duct Systems*, The British Hydromechanics Research Association, Cranfield, Bedford, UK, pp. 197–253.
[10] Gardel, A., and Rechsteiner, G. F., 1971, ''Les Pertes de Charge dans les Branchements en Té des Conduites de Section Circulaire,'' Publication, No. 118, École Polytechnique Fédérale de Lausanne, Lausanne, Switzerland.
[11] Itō, H., and Imai, K., 1973, ''Energy Losses at 90° Pipe Junctions,'' J. Hydraul. Div., Am. Soc. Civ. Eng., **99**, pp. 1353–1368.
[12] Abou-Haidar, N. I., and Dixon, S. L., 1992, ''Pressure Losses in Combining Subsonic Flows Through Branched Ducts,'' ASME J. Turbomach., **114**, pp. 264–270.
[13] Abou-Haidar, N. I., and Dixon, S. L., 1994, ''Measurement of Compressible Flow Pressure Losses in Wye-Junctions,'' ASME J. Turbomach., **116**, pp. 535–541.
[14] Serre, M., Odgaard, A. J., and Elder, R. A., 1994, ''Energy Loss at Combining Pipe Junction,'' J. Hydraul. Eng., **120**, pp. 808–830.
[15] Ramamurthy, A. S., Zhu, W., and Carballada, B. L., 1996, ''Dividing Rectangular Closed Conduit Flows,'' J. Hydraul. Eng., **122**, pp. 687–691.
[16] Ramamurthy, A. S., and Zhu, W., 1997, ''Combining Flows in 90° Junctions of Rectangular Closed Conduits,'' J. Hydraul. Eng., **123**, pp. 1012–1019.
[17] Favre, H., 1937, ''Sur les Lois Régissant le Mouvement des Fluides dans les Conduites en Charge avec Adduction Latérale,'' Revue Universelle des Mines, Ser. 8, **13**, pp. 502–512.
[18] Vazsonyi, A., 1944, ''Pressure Loss in Elbows and Duct Branches,'' Trans. ASME, **66**, pp. 177–183.
[19] Katz, S., 1967, ''Mechanical Potential Drops at a Fluid Branch,'' ASME J. Basic Eng., **89**, pp. 732–736.
[20] Truckenbrodt, E., 1980, *Fluidmechanik*, Vol. 1, Springer-Verlag, Berlin, pp. 278–283.
[21] Hager, W. H., 1984, ''An Approximate Treatment of Flow in Branches and Bends,'' Proceedings of the Institution of Mechanical Engineers, **198C**, pp. 63–69.
[22] Idelchik, I. E., (Translated by Malyavskaya, G. R.), 1994, *Handbook of Hydraulic Resistance*, 3rd ed., CRC Press, Boca Raton, pp. 413–501.
[23] Miller, D. S., 1990, *Internal Flow Systems*, 2nd ed., BHRA (Information Services), The Fluid Engineering Center, Cranfield, Bedford, UK, pp. 303–361.
[24] E.S.D.U., 1973a, ''Pressure Losses in Three-Leg Pipe Junctions: Dividing Flows,'' No. 73022, Engineering Sciences Data Unit, London.
[25] E.S.D.U., 1973b, ''Pressure Losses in Three-Leg Pipe Junctions: Combining Flows,'' No. 73023, Engineering Sciences Data Unit, London.
[26] Schlichting, H., (Translated by Kestin, J.), 1979, *Boundary-Layer Theory*, 7th ed., McGraw-Hill, New York, pp. 596–611.
[27] ISO 5167-1, 2003, *Measurement of Fluid Flow by Means of Pressure Differential Devices Inserted in Circular Cross-Section Conduits Running Full—Part 1: General Principles and Requirements*, International Organization for Standardization (ISO), Geneva, Switzerland, pp. 1–33.
[28] ISO 5167-2, 2003, *Measurement of Fluid Flow by Means of Pressure Differential Devices Inserted in Circular Cross-Section Conduits Running Full—Part 2: Orifice Plates*, International Organization for Standardization (ISO), Geneva, Switzerland, pp. 1–28.
[29] Richter, H., 1971, *Rohrhydraulik*, 5th ed., Springer, Berlin, pp. 138–139.
[30] Coleman, H. W., and Steele, Jr., W. G., 1999, *Experimentation and Uncertainty Analysis for Engineers*, 2nd ed., Wiley, New York, pp. 202–234.
[31] ISO, 1995, *Guide to the Expression of Uncertainty in Measurement. Corrected and Reprinted 1995*, International Organization for Standardization (ISO), Geneva, Switzerland, pp. 9–78.
[32] Escobar, J., 1954, ''Discussion to 'Mechanics of Manifold Flow,' by McNown, J. S.,'' Trans. Am. Soc. Civ. Eng., **119**, pp. 1119–1123.
[33] Sato, Y., 1963, ''Separating and Uniting Flows in Branch Pipes (in Japanese),'' J. Jpn Soc. Mechanical Engineers, **66**, pp. 1347–1353.
[34] Daily, J. W., and Harleman, D. R. F., 1966, *Fluid Dynamics*, Addison-Wesley, Reading, Massachusetts, pp. 314–319.
[35] Street, R. L., Watters, G. Z., and Vennard, J. K., 1996, *Elementary Fluid Mechanics*, 7th ed., Wiley, New York, pp. 359–364.

Yuichi Murai
Division of Mechanical Science,
Hokkaido University,
N13W8, Kitaku, Sapporo 060-8628, Japan
e-mail: murai@eng.hokudai.ac.jp
Phone: +81-11-706-6372,
Fax: +81-11-706-7889

Toshio Sasaki
Fiber Amenity Engineering Course,
University of Fukui,
Bunkyo 3-9-1, Fukui 910-8507, Japan
e-mail: toshio-s@fv.mech.fukui-u.ac.jp

Masa-aki Ishikawa
Department of Mechanical System Engineering,
The University of the Ryukyus,
Senbaru 1, Nishihana 903–0213, Japan
e-mail: ishi8614@tec.u-ryuku.ac.jp

Fujio Yamamoto
Fiber Amenity Engineering Course,
University of Fukui,
Bunkyo 3-9-1, Fukui 910-8507, Japan
e-mail: yamamoto@fv.mech.fukui-u.ac.jp

Bubble-Driven Convection Around Cylinders Confined in a Channel

This paper is concerned with flow visualization and image measurement of bubbly flows around various shapes of cylinders. A coaxial confined double rectangular chamber is constructed in order to provide a wide two-dimensional uniform bubble distribution upstream. The experiment shows that a wide two-phase convection is induced around the obstacle, though such an effect is not observed in research on the single-phase flow around objects. The spatial scale of the two-phase convection depends sensitively on the shape of the obstacle. Dense arrangement of cylinders is also investigated to find the interaction among the convection. The measurement results of void fraction, bubble velocity and liquid phase flow, which are obtained by image processing including particle tracking velocimetry, explore the detailed mechanism of generating the convection. [DOI: 10.1115/1.1852478]

Introduction

When an obstacle is installed in a bubbly flow where only bubbles rise up (called free-rising bubbly flow), a large scale two-phase convection is induced around the obstacle. The convection has a liquid single-phase region behind the obstacle since all the bubbles separate from the side part of the obstacle. This region is named the ''single-phase wake region'' in this paper. The typical length scale of the single-phase wake region is always much larger than the obstacle (see Fig. 3 for typical examples). The authors have succeeded in observing this phenomenon with good reproducibility using the experimental device generating uniform spatial void fraction and uniform bubble size in the planner test section.

This convection has not been found and discussed yet in previous papers regarding the bubbly flow around obstacles or cylinders while the flow around a cylinder is investigated by a number of researchers [1–5]. Also, the zone affected by inserting an object is relatively big in comparison with ordinary knowledge from single-phase viscous flow around various shapes of objects. The present results may contribute to the improvement of the design such as for steam generating pipes in nuclear power technologies and for pipe alignment in chemical systems and bioreactors.

This paper deals first with visualization and its image processing of two-phase flow around single cylinders with various shapes. After the mechanism of generating a wide two-phase convection is discussed for single cylinder system, the interaction of their convection is investigated using densely arranged circular cylinders as the second objective.

Experimental Apparatus

In order to generate a bubbly flow, which has a spatially uniform distribution of the bubble number density, two rectangular chambers are combined as a test channel as shown in Fig. 1. Liquid is filled up in the channel of the two chambers, which have different sizes in width but the same in height. This channel is only for gas injection and generating a free-rising bubbly flow from the bottom. There are several merits in the employment of this design.

First, the three-dimensionality of the flow is restricted using the double chamber with a narrow gap. Even though a two-dimensional geometry is provided with a sufficiently long span width, buoyancy-governed bubbly flow will naturally induce local three-dimensional convection in the open space. For instance, an inverse energy cascade phenomenon in free-rising bubbly flow [6] is observed and explains this flow characteristic. Hence, using parallel confined plates, which reduce the motion degree of freedom, is a reasonable way to observe the two-dimensional structure though additional frictional stress causes on the wall surface to slow the flow down. This concept was also employed in the past by, e.g., Bukhari and Lahey [7] and Murai et al. [8]. Second, the advantage of the rectangular double chamber—not a single planner channel—is that it enables simulation of a so-called ''unbounded system'' which does not have any solid boundary such as sidewalls. The boundary condition in the horizontal direction becomes periodic by adopting this structure.

The outline of the test chamber used in this experiment is as follows (see Fig. 1). The length of the rectangular chamber is 480 mm for the inner and 500 mm for the outer one. The maximum height of filling liquid is 1000 mm and the channel interval depth is 10 mm, which is larger than the bubble diameter in any case. All the walls of the chamber are made of transparent acrylic resin. The bubbly flow is observed from all the four planes of the rectangular chamber, and one plane is chosen as the test section where the cylinders are fixed. The bubbles for the chosen test section are generated from 123 injection nozzles, and 492 injection nozzles are installed in total. The inner and outer diameters of each nozzle are 0.3 and 1.5 mm, respectively. All the nozzles are located at interval distances of 4 mm in each plane. They are activated simultaneously while the experiment is performed. It has been confirmed by our observation that there is no remarkable secondary flow induced in the corner regions where the flow bends 90 deg as it passes. According to this evidence, the uniform void fraction is formed for a wide area of the section. The liquid is initially filled

Contributed by the Fluids Engineering Division for publication in the JOURNAL OF FLUIDS ENGINEERING. Manuscript received by the Fluids Engineering Division May 27, 2003; revised manuscript received September 14, 2004. Review Conducted by: S. Ceccio.

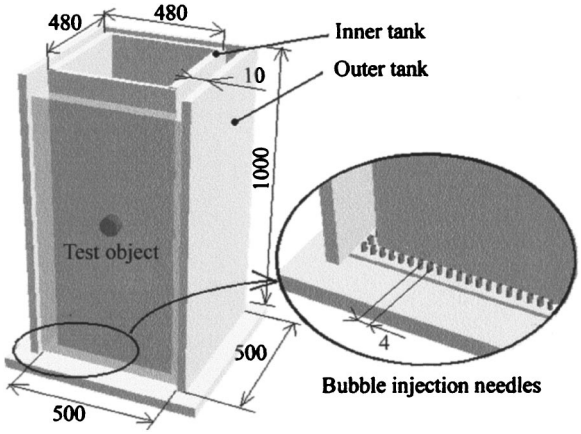

Fig. 1 Schematic diagram of double rectangular tank

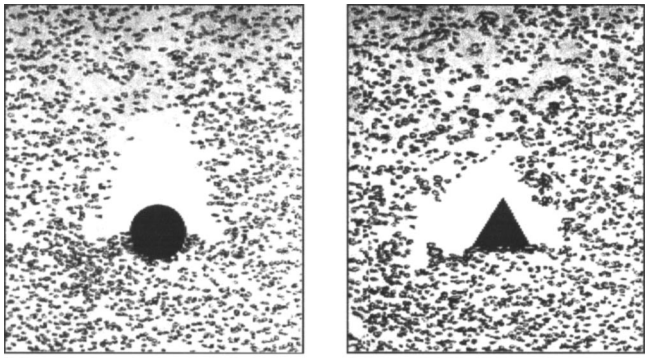

Fig. 3 Photograph of bubble distribution. (*a*) Circular cylinder. (*b*) Triangular cylinder.

up to 500 mm in height in the channel of the chamber. Room air is pressurized by a compressor and supplied to all the bubble injection nozzles through a pressure controller (Yokogawa Ltd, Standard pressure regulator 2657) and a floating-sphere type of gas flowmeter. For illuminating the bubbles, two metal halide lights with 500 W in total (Photron Ltd, HVC-SL) are used from the back of the test section. A light-diffusing translucent sheet is located in the center space of the rectangular chamber in order not to project the shadows of the bubbles, which rise in the opposite plane of the test section plane.

Image Analysis Method

There are many kinds of tools to measure the structure of bubbly flows including electric and optical fiber probes. Image processing, in particular, has been already utilized widely with two well-known major advantages, i.e., contact-free measurement and whole field measurement. The bubbly flow to be discussed in this paper has low speed and a high probability to enhance unstable flow when a probe is inserted, so that a contact-free measurement is required. Furthermore, the image processing provides simultaneous measurements of void fraction, bubble size, and bubble velocity. The detailed method of the image measurement is explained below (see Fig. 2).

Measurement Method for the Void Fraction. Figure 3 shows samples of an instantaneous picture of the bubble distribution. The following procedures are implemented to measure the time-averaged void fraction distribution from this image. (1) The image is binarized into 0 and 255 in brightness with 8 bit gray level. The threshold value for the binarization is determined by an automatic threshold method [9], provided that the upper and lower limitations are introduced in order to consider the illumination bias and the bubble's overlapping in the measurement area. The local bubble shadow fraction is obtained from the binarized image. (2) The void fraction is estimated from the bubble shadow fraction. The time-averaged value of the bubble shadow fraction is calculated using consecutive time serial images (named average shadow fraction). The average shadow fraction is calculated with a real number between 0 and 1. (3) The next equation is used to calculate the void fraction from the average shadow fraction:

$$\beta = 1 - \exp(-C\alpha). \tag{1}$$

Here, α is the void fraction, and β is the average shadow fraction. This equation is theoretically derived as an expected statistic value considering the bubble's overlapping probability, which was reported by Murai et al. [10] for the measurement of a bubble plume. The coefficient C is the dimensionless parameter obtained by a least square approximation of experimental calibration. In the present experiment, all the optical setup is fixed through all the flow conditions, and the value of C was 5.47 from the calibration experiment for $0<\alpha<0.25$. For example, as the void fraction is 20%, the average shadow fraction is 0.66. Equation (1) is unavailable for nonbubbly flow regime over $\alpha>0.25$.

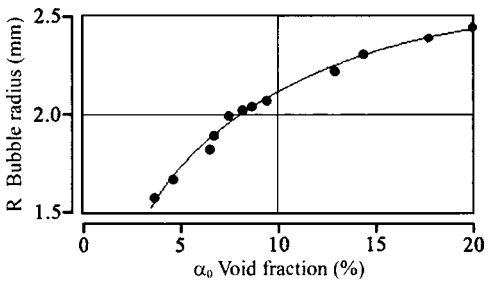

Fig. 2 Equivalent bubble radius versus void fraction

Particle Tracking Velocimetry for Bubbles. The bubble velocity is measured using particle tracking velocimetry (PTV) after the image is preprocessed to remove the background and the cylinders. In the preprocessing, the bubbles are heavily overlapped in the shadow image, therefore, the individual bubble's center of gravity is hardly obtained from the image directly. In this study, the thinning processing is introduced in order to solve the interface of the bubbles. For the thinning process Duff's pixel matrix [11] is utilized but an improvement is added to adjust the condition of the present image. The chain-coding process [12] is next employed for the interface pixel to calculate the center of gravity and the equivalent radius of each bubble. The equivalent radius is defined by the radius, which has equal volume of a spherical bubble. Using this method, 90% of the bubbles' velocities are extracted from the overlapped image. For instance, the local motion of the bubbles near the cylinders is validly measured while the bubbles are usually contacting frequently with the surface of the cylinders. The binary image cross-correlation method [13] is adopted as the basic algorithm of the PTV.

Particle Tracking Velocimetry for Tracer Particles. The carrier phase flow field through the cylinders is also measured by particle tracking velocimetry using tracer particles mixed in the medium. The tracer particles have 200–600 μm in diameter, and 1020 kg/m^3 in density. The particle diameter is set relatively large in order to avoid electro-chemical absorption on the gas-liquid interface and the liquid-solid interface. As the particles are seeded in the flow, the images consist of three objects, i.e., the bubbles, the particles, and the cylinders. The particle's velocity, which expresses the liquid flow field, is measured with PTV after the images are separated to the particle-only images. The criterion of the particle's identification is the size of the object, because the size is

larger for the bubbles and smaller for the particles. The binary image cross-correlation method [13] is adopted as the basic algorithm of the PTV as well as for the bubbles. The present PTV can evaluate not only time-average flow velocity but also fluctuation components caused by bubble-induced turbulence. This time the velocity fluctuation within a frequency of 30 Hz can be extracted but that of the higher frequency cannot be measured.

Measurement Uncertainty. Measurement error for the bubble shadow fraction is caused by optical disturbance such as the bubble's deformation and overlapping. It belongs to random error since bias error was removed by calibration experiment. With Eq. (1), therefore, the error of local void fraction is given by

$$\delta\alpha = \{C(1-\beta)\}^{-1}\delta\beta. \quad (2)$$

Assuming the error $\delta\beta=0.10$, the error $\delta\alpha$ is estimated as 0.018 in maximum case.

The measurement error of the bubble's velocity via PTV is caused by random error of the bubble centroid coordinate in the image processing. Assuming the centroid error of 20% of the bubble diameter (since the bubble's constitution pixel is more than 10), displacement error of bubbles during two consecutive images is 0.8 mm, and thereby the velocity error is estimated as 24.0 mm/s, which is 15% of the typical bubble rise velocity. The time-averaged bubble velocity obtained by 256 frames $\times 50$ sampled bubbles per frame has an uncertainty of $15\%/113=0.14\%$ relative to the typical bubble rise velocity.

In the same way, the measurement error of the liquid velocity obtained by the tracer particle's motion is estimated as 10% for instantaneous data and as 0.10% for time-averaged data.

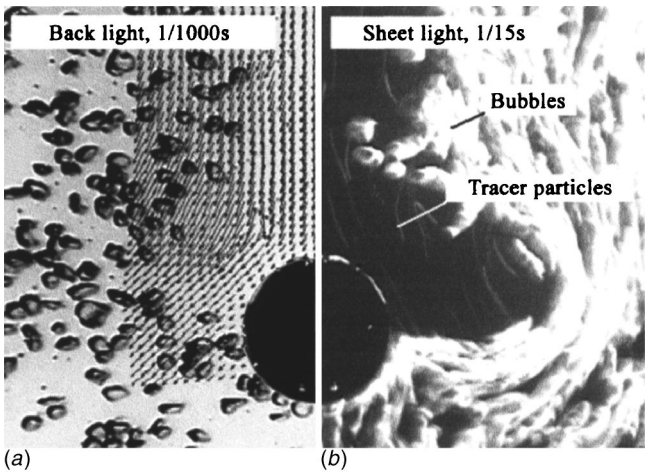

Fig. 4 Local behavior of bubbles and tracer particles. (*a*) Liquid velocity vectors obtained by PTV. (*b*) Pathlines of bubbles and particles.

Results and Discussion

Figure 2 shows the relationship between the bubble radius and the void fraction in this experiment, namely indicating the performance of the bubble generator. The void fraction is defined by the volume-averaged gas fraction in the control volume of $100\times100\times10$ mm^3, which is located 50 mm upstream of the inserted object. The bubble radius increases as the void fraction increases. The standard deviation of the bubble radius which is normalized by the average bubble radius is always lower than 0.15. The Reynolds number of the bubble ranges from 500 to 1800 in this experiment.

Visualization of the Bubble Motion. As shown in Fig. 3, the bubbles contact with the bottom surface of the cylinder first, then separate from the side surface or the edge, migrate for a while in the horizontal direction, and rise up again. Once this distribution occurs the flow pattern keeps stably for a long time with high reproducibility. Figure 4 shows the enlargement picture of the local bubble distribution around the circular cylinder, including tracer particles. The right-hand side shows the photograph of pathlines for 1/15 s. The left-hand side shows the velocity distribution of the tracer particles obtained by PTV with its interpolation. These pictures imply that the separation of the bubble from the side surface of the circular cylinder is induced by the local downward flow of the liquid above the cylinder. The speed of the downward flow is on the order of 0.3 m/s, and it is comparable to the terminal rise velocity of the bubbles. Thus the bubbles stop rising in this zone and advance in the horizontal direction. This means that the separation is governed by the local liquid flow and hence depends on the shape of the cylinder.

In the process of the bubble's collision with the cylinder surface, some bubbles show slight bouncing due to the bubble's deformation and its wake behind it. However, the bouncing effect only remains within a lengthscale of the bubble diameter after collision, and rapidly attenuates due to viscosity before traveling to separation point. Therefore, the bouncing or surface tension is not a major factor to enhance the single-phase wake region.

Void Fraction Around Single Cylinder. Figure 5 shows the time-averaged void fraction distribution formed around three types of objects, i.e., circular, square, and triangular cylinders, obtained by the method mentioned before. The void fraction upstream of the cylinder is 7.4% and the averaged bubble radius is 2.0 mm in these cases. The diameter of the circular cylinder and the side lengths of the square and triangular cylinders are all 50

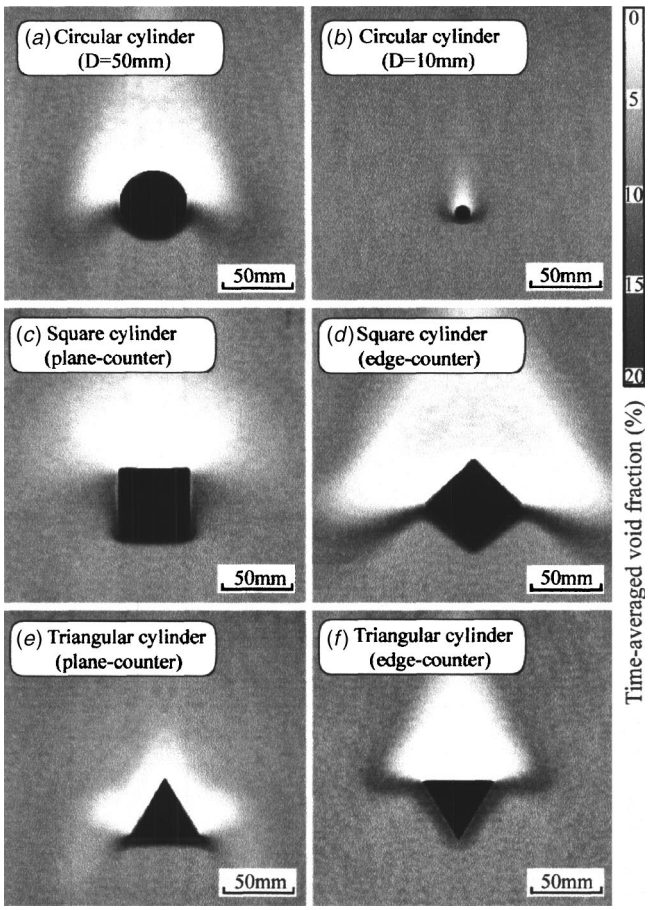

Fig. 5 Time-averaged void fraction distribution for basic shapes

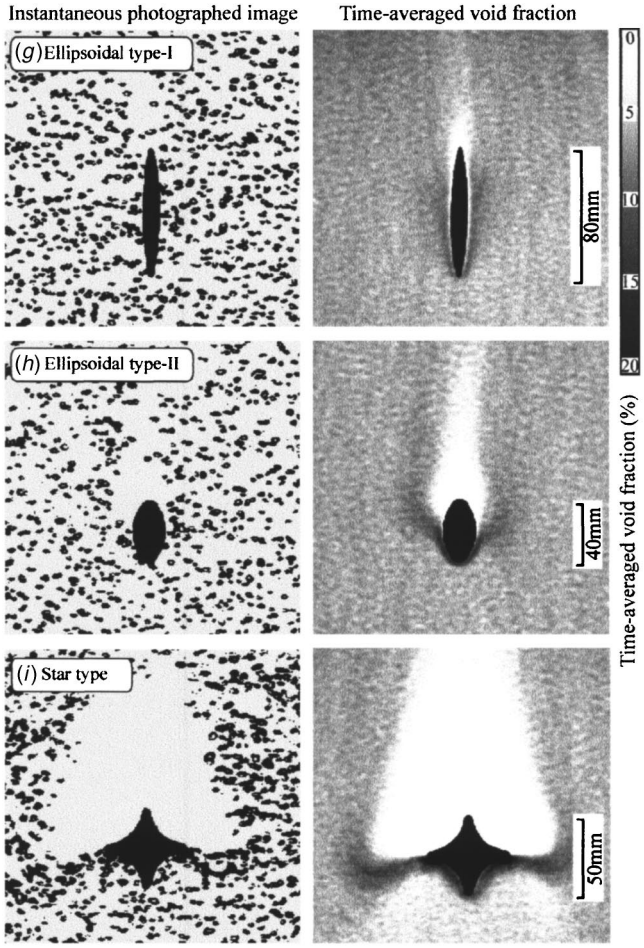

Fig. 6 Time-averaged void fraction distribution for other shapes

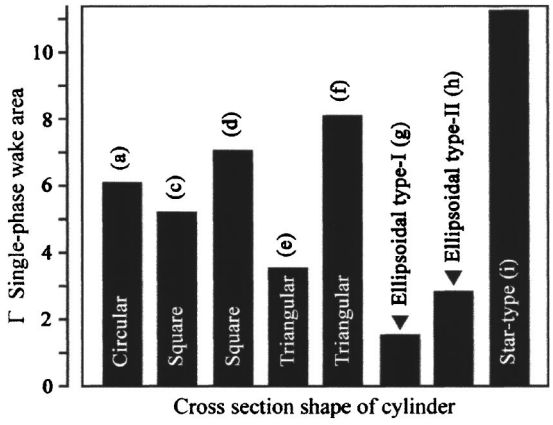

Fig. 7 Effect of cylinder's shape on the wake area

mm except for the case shown in Fig. 5(*b*). The number of image frames used for time averaging is 256 at an interval time of 1/30 s.

In the case of the circular cylinder (*a*), all the bubbles separate from the surface and move in the horizontal direction until the angle of 90 deg from the front point. Then, a single-phase region with triangular area is formed downstream of the cylinder. Hereafter, this region is called the single-phase wake region. The length scale of the single-phase wake region is around twice the diameter of the cylinder in the horizontal direction, and three times in the vertical direction. The single-phase wake region converges with decreasing diameter as shown in Fig. 5(*b*). This indicates that the bubbles' collision frequency is one of the parameters to determine the spatial scale of the single-phase wake region. In the case of the square cylinder (*c*), the bubbles leave the surface mainly at the rear edges. As the square cylinder is arranged by edge-counter angle (*d*), the bubbles' separation is enhanced so that the zone of the single-phase wake region expands quite widely. In the case that the regular triangular cylinder is fixed at a plane-counter angle (*e*), the bubbles separate at the front edges and do not make a wide single-phase wake region. For an edge-counter installation of the triangular cylinder (*f*), a single-phase wake region with beautiful regular triangular shape appears due to the stable bubble separation at the rear edges.

Figure 6 shows additional visualization results for ellipsoidal and starfish-type cylinders. The left column is the photographed image and the right column is the time-averaged void fraction. For the cases using ellipsoidal cylinders, the longitudinal direction of the ellipse corresponds to the flow direction. Around the ellipsoidal cylinder (*g*) with an aspect ratio of 8, a single-phase wake region is not formed clearly. The void fraction increases at the side surface of the cylinder and reduces slightly downstream. The reason for the increase at the side part is simply the fact that the bubbles have a relative downward velocity against the liquid. Lift and pressure gradient forces on the bubbles are not the reason because there is no main given flow in the liquid phase in this experiment so that they are sufficiently weak compared to the buoyant force of the bubbles. On the other hand, in the case of the ellipse (*h*), which has an aspect ratio of 2, bubble separation occurs and a relatively large single-phase region is formed similar to the case of the circular cylinder. The purpose of testing the starfish-type cylinder comes from the question of how to expand the convection structure. A big effect is observed in the case of the edge-counter square cylinder as shown in Fig. 5(*d*), so that an improved design to enhance the structure is given by the starfish type. As we expected, a wide single-phase wake region was generated as shown in Fig. 6(*i*). This shape helps to concentrate many bubbles gradually along the upstream curved surface and to change smoothly the bubble motion from the vertical to the horizontal direction. The liquid flow also accelerates gradually along the curved upstream surface. Furthermore, the downward flow behind the cylinder smoothly changes to a horizontal flow at the side edges and gives strong impulse to the bubbles. After the bubbles move to left and right parts, the buoyant force gradient behind the cylinder gets stronger and makes the downward liquid flow accelerate again. This cyclic phenomenon enhances to generate large scale convection in the case of the starfish-type cylinder.

As a summary of the aforementioned results, Fig. 7 represents the comparison of the area of the single-phase wake regions among eight types of the cylinder. Γ is the nondimensional area of the single-phase wake region with respect to the solid cross-section area of the cylinder. The area of the single-phase wake region itself is calculated by integrating the element area, which has a void fraction lower than half of the upstream void fraction. The note in each bar corresponds to those shown in Figs. 5 and 6. According to this comparison, the area of the single-phase wake region varies significantly depending on the shape. The area is least for the ellipsoidal type I (*g*), which is a streamlined shape like an airfoil. The area expands the widest for the starfish-type (*i*) cylinder, which is partly similar to the edge-counter square cylinder but the straight plane is altered to curved plane to adjust the streamline of the flow near the cylinder surface.

Void Fraction Around Plural Cylinder Arrangement. Figure 8 shows the time-averaged void fraction around plural arrangement of the circular cylinders, whose diameters are 30 mm, and the interval distances between the centers of gravity are twice the diameter. For the vertical in-line arrangement (*a*), the single-phase wake region of the upstream cylinder is smaller than that of a single cylinder, and it expands widely behind the downstream cylinder. For the horizontal arrangement (*b*), a high void fraction

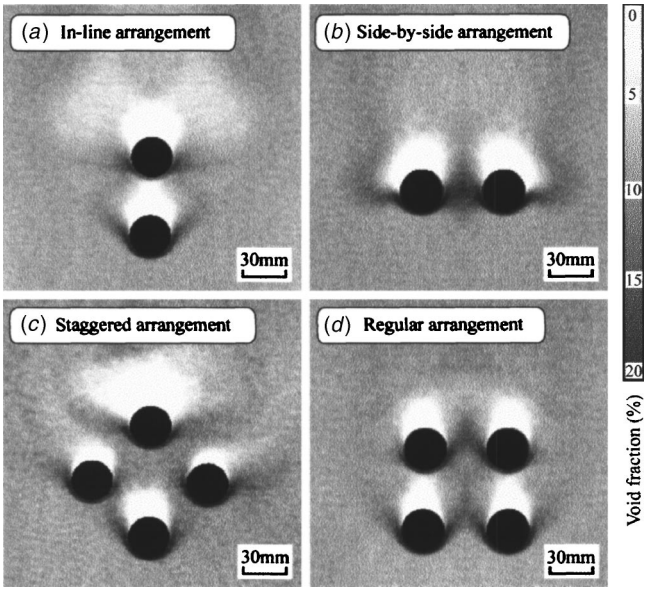

Fig. 8 Time-averaged void fraction around cylinders

region appears between the cylinders, and the single-phase wake region inclines outside. For the case (*c*), the single-phase wake region of the upstream cylinder is small, and that of the most downstream one gets the biggest. The arrangement (*d*) is showing combined characteristics of (*a*) and (*b*).

Bubble Motion Through Arrangement of Cylinders. The void fraction distribution around the cylinder depends on the bubble behavior in the vicinity of the cylinder surface. The bubbles near the cylinder involve two kinds of motion patterns. One is the transportation due to the liquid flow, and another is the intrinsic bouncing motion of individual bubble. The bouncing phenomenon is well known and investigated by Tsao and Koch [14] for a horizontal flat wall. The combination of the transportation by the liquid and the bouncing provides unpredictable response of the bubble near the surface of the cylinder. Therefore, the bubble motion is directly measured using PTV to obtain the following results.

Figure 9 shows the image measurement process of the bubble motion rising through the arrangement of circular cylinders. Figure 9(*a*) shows the raw image at a moment, and (*b*) shows the bubble distribution identified by the present image processing, where the position and the equivalent radius are reexpressed. Figure 9(*c*) shows the velocity vectors of bubbles, and (*d*) shows the velocity vectors of tracer particles. Table 1 shows the details of the experimental conditions for the parametric study.

Figure 10 shows the time-averaged rising velocity of the bubbles for five different conditions in the gas flow rate supplied from the bottom plane. The data are compared with four kinds of arrangement patterns of the cylinder including the cylinder-free condition. This result implies the following things. (1) The bubble rising velocity is reduced by the presence of the cylinder compared with the terminal velocity of the bubble in quiescent liquid, owing to the time loss for the bubble's collision on the cylinder. (2) The bubble rising velocity without the cylinder is faster than the terminal velocity since the bubbles will drive the upward liquid flow to result in raising the bubble's velocity. (3) Random arrangement of the cylinder reduces the bubble rising velocity the most while the regular arrangement yields the least reduction. (4) The reduction for the staggered arrangement is medium between the random and the regular ones, although the collision frequency is estimated the highest.

Figure 11 shows the measured averaged bubble radius versus the gas flow rate for the same set of the experiment. The bubble

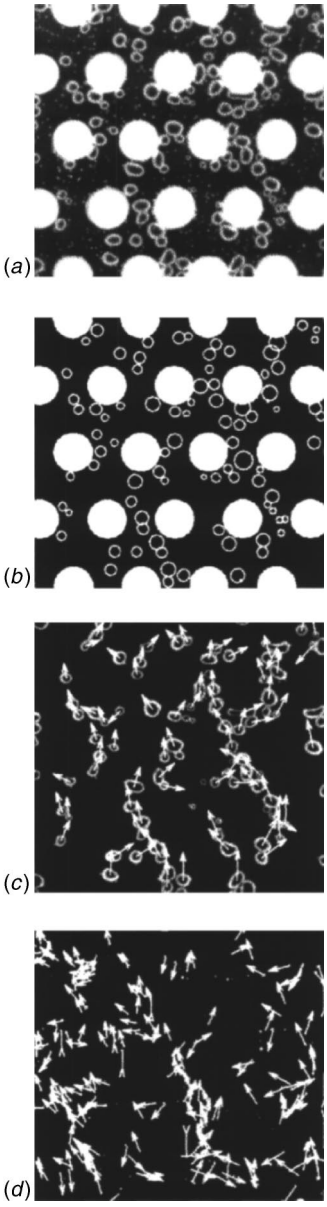

Fig. 9 Velocity vectors of each phase obtained by PTV. (*a*) Original image. (*b*) Identification of bubbles. (*c*) PTV for bubbles. (*d*) PTV for liquid phase.

radius increases with the gas flow rate for the no-cylinder case, which is the characteristic of the bubble generator. On the contrary, the bubble radius is kept small for the presence of the cylinder as the flow rate increases since the bubbles are divided by the collision on the cylinder. In the case of the staggered arrangement the bubble radius is minimum owing to the most frequent collision. After considering the relationship between the radius and the rising velocity, it can be said that the correlation is negative between the two for the staggered arrangement, i.e., the bubble collision frequency is the highest among three types of the arrangement but the rising velocity is not reduced the most. It indicates that there is a certain effect of the convection of the liquid, which will be discussed next.

Figure 12 shows the time-averaged void fraction and the time-averaged liquid velocity vector for case 5 shown in Table 1. Figure 13 shows the time-averaged void fraction and the kinetic energy distribution of the liquid phase. The void fractions in these figures are drawn with dimensionless value using the given void fraction at the bottom. With these results, the following points are

Table 1 Experimental conditions for dense arrangement

Gas: Nitrogen
Density=17.1 kg/m^3, Temperature=283–284 K
Morton no.=1.01×10^{-10}
Liquid: Water
Density=1000.5 kg/m^3, Temperature=283–284 K
Kinematic viscosity=1.44×10^{-6} m^2/s
Cylnder: Epoxy resin
Volume fraction=22.74%

Case no.	Q_G $\times10^{-5}$ m^3/s	R_G (mm)	α_G (%)	Re_G	Re_L	Eo
1	0.33	1.23	0.81	320.2	151.6	0.79
2	0.67	1.41	1.87	383.0	196.0	1.03
3	1.00	1.48	3.21	546.1	325.9	1.14
4	1.33	1.56	4.28	616.8	357.6	1.27
5	1.67	1.62	5.13	610.7	368.5	1.36

Q_G : Gas flow rate, R_G : Average radiation, a_G : Void fraction
Re_G : Bubble Re, Re_L : Liquid Re, Eo: Eötvös number

clarified. (1) The void fraction is commonly low behind each cylinder, which is a similar phenomenon to the flow around a single cylinder, except the fact that the area of the single-phase wake region of each cylinder is converged compared to that of single-cylinder. (2) The liquid driven by bubbles rises straight upward for the regular arrangement, rises with one-side oblique advection for the staggered arrangement, and rises through uncertain paths for the random arrangement. (3) The liquid has high kinetic energy similar to the bubble velocity distribution. This implies that the bubble rising velocity is strongly affected by the liquid flow pattern.

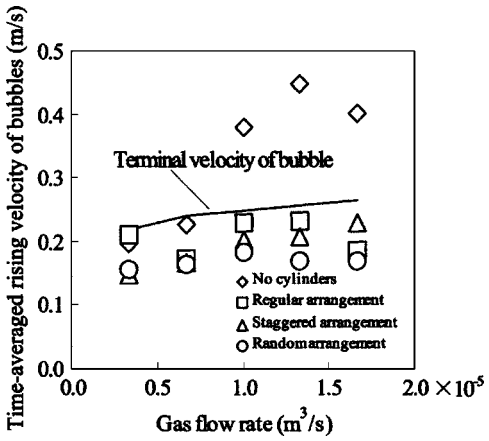

Fig. 10 Time-averaged rising velocity of bubbles

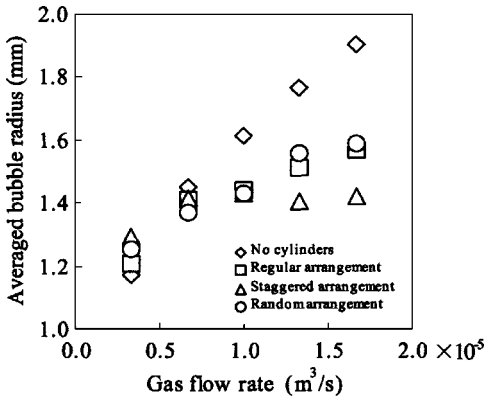

Fig. 11 Time-averaged equivalent radius of bubbles

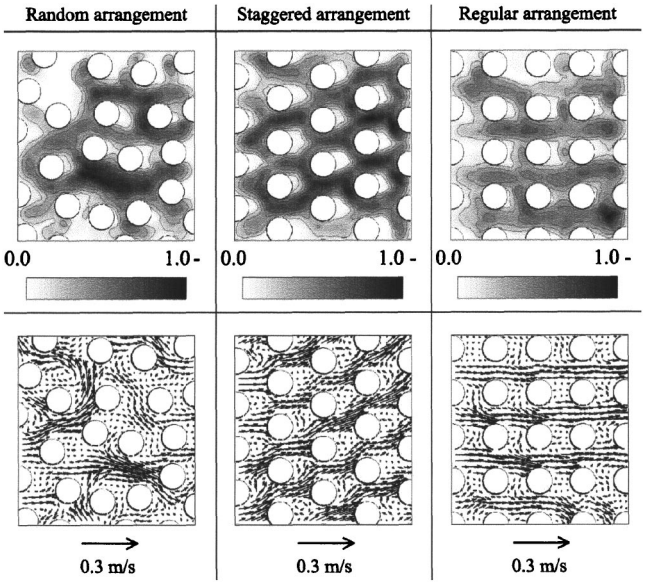

Fig. 12 Time-averaged void fraction and liquid velocity

By the way, there is a question why the liquid flows up in the oblique direction for the staggered arrangement. This is one of the stable flow patterns observed in this system. There is no clear evidence to explain the stability but at least the local liquid flow behind each cylinder enhances the one-way bubble rising phenomenon as if it were a gear. This has to be set as our future target of research.

Concluding Remarks

On the bubbly flow structure rising around single and multiple arranged cylinders in confined plates, the following points are newly found with experiments based on image processing.

1. Any type of cylinder induces a wide single-phase wake region behind it, whose spatial scale is much larger than the size of the cylinder. This phenomenon is governed by the collision frequency of the bubble to the solid surface, and also by the local liquid flow pattern. Hence, the area of the single-phase wake region sensitively depends on the shape of the cylinder.

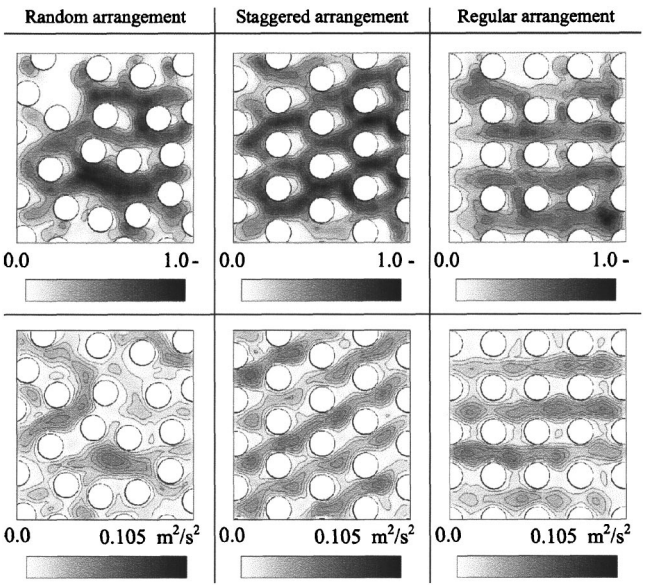

Fig. 13 Time-averaged void fraction and kinetic energy

2. The average rising velocity of the bubble through arrangement of a circular cylinder is reduced compared with the terminal rising velocity in quiescent liquid; however, the degree of the reduction is the least for the regular arrangement, and the biggest for the random arrangement.

3. The rising velocity and the size of the bubble are affected by the internal liquid flow pattern, i.e., straight upward flow is induced for the regular arrangement, one-side oblique flow is generated for the staggered arrangement, and irregular flow is formed for the random arrangement.

References

[1] Inoue, A., Kozawa, Y., Yokosawa, M., and Aoki, S., 1986, ''Studies on two-phase cross flow. Part I: Flow characteristics around a cylinder,'' Int. J. Multiphase Flow, **12**(2), pp. 149–167.

[2] Yokosawa, M., Kozawa, Y., Inoue, A., and Aoki, S., 1986, ''Studies on two-phase cross flow. Part II: Transition Reynolds number and drag coefficient,'' Int. J. Multiphase Flow, **12**(2), pp. 169–202.

[3] Serizawa, A., Huda, K., Yamada, Y., and Kataoka, I., 1997, ''Experiment and numerical simulation of bubbly two-phase flow across horizontal and inclined rod bundles,'' Nucl. Eng. Des., **175**, pp. 131–146.

[4] Sugiyama, K., Takagi, S., and Matsumoto, Y., 1999, ''Three-dimensional numerical analysis for bubbly flow around a circular cylinder,'' Trans. Jpn. Soc. Mech. Eng., Ser. B, **65**(638), pp. 3260–3267.

[5] Uchiyama, T., 2000, ''Numerical analysis of air-water two-phase flow across a staggered tube bundle using an incompressible two-fluid model,'' Nucl. Sci. Eng., **134**, pp. 281–292.

[6] Murai, Y., Song, X., Takagi, T., Ishikawa, M., Yamamoto, F., and Ohta, J., 2000, ''Inverse Energy Cascade Structure of Turbulence in a Bubbly Flow,'' JSME Int. J., Ser. B, **43**(2), pp. 188–196.

[7] Bukhari, K. M., and Lahey, R. T., 1987, ''An experimenal study of two-dimensional phase separation phenomena,'' Int. J. Multiphase Flow, **13**(3), pp. 387–402.

[8] Murai, Y., Matsumoto, Y., and Yamamot, F., 2000, ''Qualitative and Quantitative Flow Visualization of Bubble Motions in a Plane Bubble Plume,'' J. Visual., **3**(1), pp. 27–35.

[9] Otsu, N., 1979, ''A threshold selection method from gray-level histograms,'' IEEE Trans Syst., **SMC-9**, pp. 62–66.

[10] Murai, Y., Matsumoto, Y., and Yamamoto, F., 2001, ''Three-dimensional measurement of void fraction in a bubble plume using statistic stereoscopic image processing,'' Exp. Fluids, **30**(1), pp. 11–21.

[11] Duff, M. J. B., 1978, ''A large scale integrated circuit array parallel processor,'' Proc. 3rd IJCPR, pp. 728–733.

[12] Song, S., Yamamoto, F., Iguchi, M., Shen, L., Ruan, X., and Ishii, K., 1998, ''A method for measuring particle size in overlapped particle images,'' ISIJ Int., **38**(9), pp. 971–976.

[13] Uemura, T., Yamamoto, F., and Ohmi, K., 1989, ''A high speed algorithm of image analysis for real time measurement of two-dimensional velocity distribution,'' ASME-FED, **85**, pp. 129–133.

[14] Tsao, H. K., and Koch, D. L., 1997, ''Observations of high Reynolds number bubbles interacting with a rigid wall,'' Phys. Fluids, **9**(1), pp. 45–56.

M. A. Habib
Professor
email: mahabib@kfupm.edu.sa

H. M. Badr
Professor

S. A. M. Said
Professor

I. Hussaini
Lecturer

Mechanical Engineering Department, King Fahd University of Petroleum & Minerals, Dhahran 31261, Saudi Arabia

J. J. Al-Bagawi
Engineering Specialist, Saudi Aramco, Saudi Arabia

On the Development of Deadleg Criterion

Corrosion in deadlegs occurs as a result of water separation due to the very low flow velocity. This work aims to investigate the effect of geometry and orientation on flow field and oil/water separation in deadlegs in an attempt for the development of a deadleg criterion. The investigation is based on the solution of the mass and momentum conservation equations of an oil/water mixture together with the volume fraction equation for the secondary phase. Results are obtained for two main deadleg orientations and for different lengths of the deadleg in each orientation. The considered fluid mixture contains 90% oil and 10% water (by volume). The deadleg length to diameter ratio (L/D) ranges from 1 to 9. The results show that the size of the stagnant fluid region increases with the increase of L/D. For the case of a vertical deadleg, it is found that the region of the deadleg close to the header is characterized by circulating vortical motions for a length $l \approx 3$ D while the remaining part of the deadleg occupied by a stagnant fluid. In the case of a horizontal deadleg, the region of circulating flow extends to 3–5 D. The results also indicated that the water volumetric concentration increases with the increase of L/D and is influenced by the deadleg orientation. The streamline patterns for a number of cases were obtained from flow visualization experiments (using 200 mW Argon laser) with the objective of validating the computational model. [DOI: 10.1115/1.1852481]

1 Introduction

Deadleg is a term used to describe the inactive portion of a pipe, where the fluid is stagnant or having very low velocity, in various piping systems. This inactive pipe is normally connected to an active pipe that carries the main stream. Deadlegs represent regions prone to corrosion in oil piping systems due to stagnant or low velocity flow that causes emulsified water precipitation out of the crude. As described by Craig [1] and Lotz et al. [2], once water begins to drop out of solution onto the metal surface, wettability would become the controlling factor in corrosion. When metal becomes water wet, corrosion potential increases significantly. Internal corrosion was found to be predominant in low-velocity piping where emulsified water had precipitated out of the crude oil [3,4]. In order to maintain the integrity of the connecting main pipe, internal corrosion of deadlegs must be prevented, since it is very difficult to control and usually requires a major shut down to fix. In the oil and gas industry, deadleg corrosion presents the highest percentage of internal damage to pipelines or in-plant piping systems that are normally considered to operate in a non-corrosive environment. Deadlegs should be avoided whenever possible in the design of piping for fluids containing or likely to contain corrosive substances. When deadlegs are unavoidable, the length of the inactive pipe must be as short as possible to avoid stagnant or low velocity flows.

To date, there is no research published on the effect of deadleg geometry and flow velocity on the concentration of water or other corrosive agents in deadlegs. Most of the relevant published work focused on the effect of the oil-to-water ratio on the flow pattern and pressure drop in straight pipes. An experimental investigation [5] was conducted to study the effect of the oil-water ratio on the pressure gradient in a horizontal pipe. In this work, it was found that at a high oil-water ratio, oil formed the continuous phase and a water-drops-in-oil regime was observed. As the oil-water ratio was decreased, the flow patterns changed to concentric oil in water, oil-slugs-in-water, oil-bubbles-in-water, and finally oil-drops-in-water. The measured pressure gradient was found to be strongly dependent on the oil-water ratio. Pressure gradient data obtained from three different sets of experiments for stratified flow of two immiscible liquids in laminar-turbulent regime was presented [6]. This investigation was based on the parameters introduced by Lockhart and Martinelli [7]. The Lockhart and Martinelli parameters were used [6] for correlating the pressure gradient data in case of gas-liquid mixture flows. Unified models that incorporate the effect of the angle of inclination on the transition from annular flow to intermittent flow and from dispersed bubble flow were presented [8]. The models showed a smooth change in mechanisms as the pipe inclination varies over the whole range of upward and downward inclinations.

The stability of a stratified liquid-liquid two-phase system was investigated [9] and it was found that subzones of stratified-dispersed patterns might appear in regions where stable stratification is expected. The reduction of density differential, as the case in liquid-liquid systems, tended to extend the regions of dispersed flow patterns on the account of the range of the continuous stratified patterns. The formation of a stratified-dispersed/stratified pattern was attributed to the moderate buoyancy forces in case of reduced density differential. Due to the limited available experimental data, the model was not fully validated. A practical and sufficiently accurate method for calculating the pressure drop in a tee junction with combining conduits using a semiempirical approach was provided [10].

The experimental investigation [11] on the effect of influx in a two-phase, liquid-liquid flow system on the pressure drop behavior proved that the Brill and Beggs correlation method [12] was able to provide adequate pressure gradient predictions for oil-water flow. On the other hand, the acceleration confluence model [13] was found to be inadequate in predicting the pressure drops. Experimental results on the effect of the water volume fraction in an oil-water system on the pressure gradient in pipe flow were reported [14]. The pressure gradient measurements showed that the liquid-liquid dispersions exhibited a flow behavior that diverged from a single-phase flow. The measured values of the pressure gradient were much lower than those predicted from the homogeneous model. Similar studies for pressure losses in other pipe fittings were carried out [15] for both sudden pipe expansion and sudden contraction and by Schabacker et al. [16] for a sharp 180 deg bend.

A mathematical model for oil/water separation in pipes and tanks was recently proposed [17]. The model describes the pro-

Contributed by the Fluids Engineering Division for publication on the JOURNAL OF FLUIDS ENGINEERING. Manuscript received by the Fluids Engineering Division June 2, 2003; revised manuscript received September 30, 2004. Review Conducted by: I. Celik.

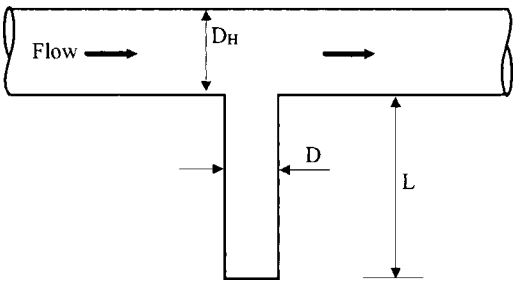

Fig. 1 The geometry of the deadleg configuration

cess of water separation in oil systems based on the two mechanisms of coalescence and settling. The separation of oil and water can be considered as a combination of emulsification and separation. It was observed [17] that the separation rate for water in oil systems increases with the increase in water cut, and that some water remains in the oil even after long settling times. These features may be qualitatively understood by a combination of coalescence and settling. A mathematical-numerical model that describes these mechanisms qualitatively was developed [17]. This model calculates the quality of the output oil as a function of system dimensions, flow rates, fluid physical properties, fluid quality, and drop size distribution at inlet. The computation of a continuous flow of a mixture of two immiscible fluids using the most general model for multiphase flows, the Eulerian approach, is difficult for large-scale industrial applications. On the other hand, the Lagrangian approach, which is used for continuous phase (liquid or gas) and a discrete secondary phase (particles, drops or bubbles), is only suitable for low discrete phase concentrations. The algebraic slip mixture model [18–22], which is a simplified version of the Eulerian model, allows the phases to be interpenetrating and allows the volume fraction of the two fluids to be between 0 and 1.

After a comprehensive literature search, it was found, to the best of our knowledge that no research was published on the effect of deadleg length and orientation on water separation in deadleg regions that are widely used in oil piping systems. This study aims at investigating the effect of deadleg geometry and orientation on the velocity field and water separation in deadlegs. The present work also aims to establish a deadleg criterion based on deadleg orientation and length-to-diameter ratio.

2 Problem Statement and Formulation

The problem considered is that of flow of an oil/water mixture having 90% oil and 10% water (by volume) in a tee junction with the deadleg forming one branch. The configuration considered for the deadleg is shown in Fig. 1. In this configuration, the deadleg may take either a horizontal or vertical position. The calculations were carried out for various lengths of the deadleg where the length-to-diameter ratio ranged from L/D=1 to 9 with the objective of obtaining the details of the flow velocity field as well as the changes in the water volumetric concentration inside the deadleg. This water concentration is important for corrosion prediction [1–4]. The average inlet flow velocity is 1 m/s in all cases. The length of the main tube (header) upstream the deadleg is 4.5 m, thus a length of 15 header diameters developing region is considered to eliminate the effect of the inflow velocity profile. This has

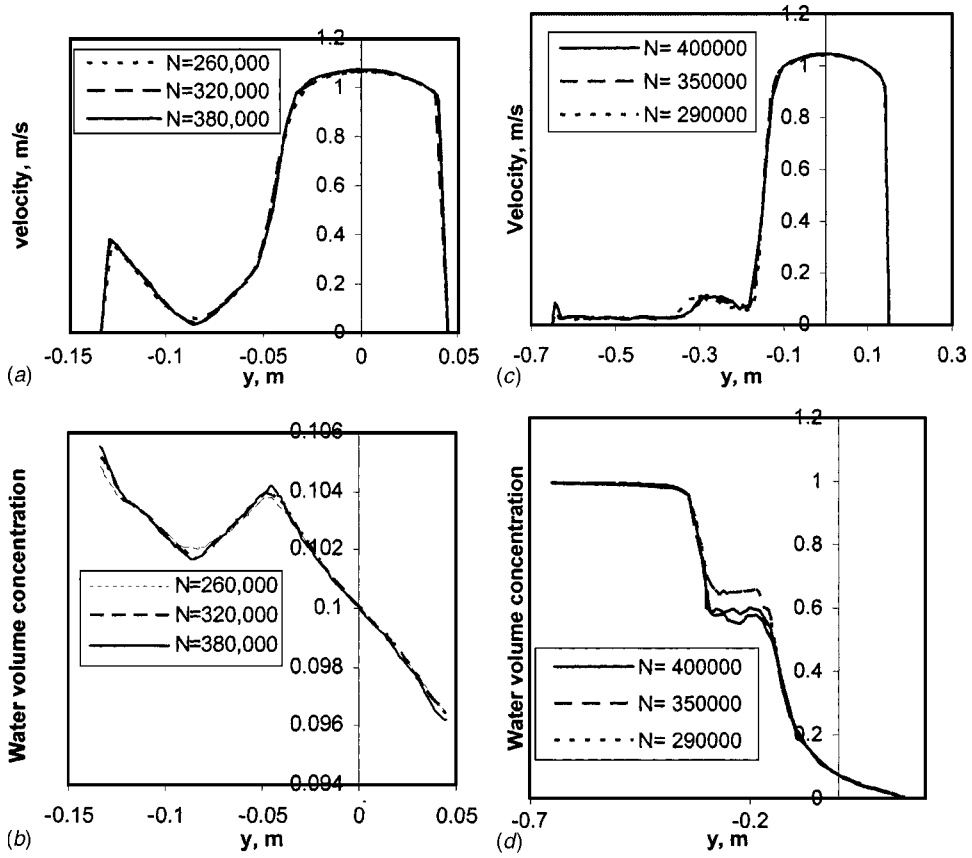

Fig. 2 The influence of mesh refinement on the velocity magnitude and volumetric water concentration along the axis of the deadleg, (*a*) Velocity magnitude L/D=1, $d=10^{-4}$ m (*b*) Volumetric water concentration L/D=1, $d=10^{-4}$ m (*c*) Velocity magnitude, L/D=5, $d=10^{-3}$ m (*d*) Volumetric water concentration L/D=5, $d=10^{-3}$ m

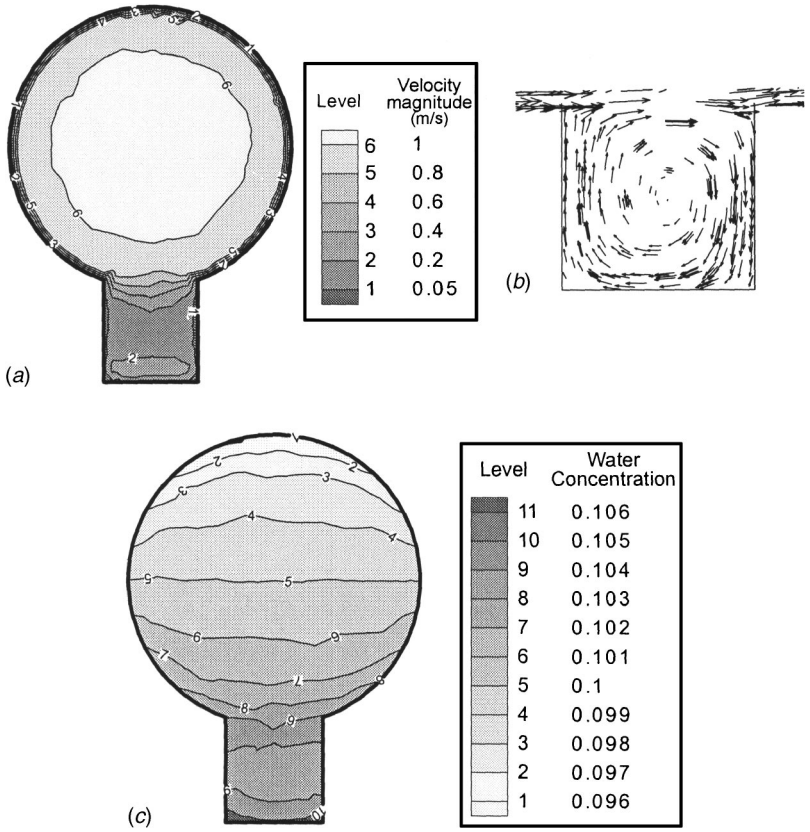

Fig. 3 Velocity contours, velocity vectors, and contours of the volumetric concentration of water for the vertical deadleg; L/D=1. (*a*) Velocity contours, (*b*) velocity vectors, and (*c*) Water concentration.

been justified by comparing profiles at different sections of the header tube upstream of the deadleg. The mathematical formulation for the calculation of the fluid flow field has been established. The fluid flow model is based on the time-averaged governing equations of three-dimensional (3D) turbulent flow. The algebraic slip mixture model [15] is utilized for the calculation of the two immiscible fluids (water and crude oil). The model solves the continuity equation for the mixture, the momentum equation for the mixture, and the volume fraction equation for the secondary phase (water), as well as an algebraic expression for the relative velocity. The slip mixture model [18,23] allows the phases to be interpenetrating. Therefore, the volume fraction of the primary and secondary flows for a control volume can take any value between 0 and 1. The model is based on the assumption of local momentum equilibrium. This occurs when the relative velocity between phases is small and the inertia associated with the drift is insignificant.

2.1 Continuity and Momentum Equations. The continuity and momentum equations [24–26] are described in the following.

2.1.1 Mass Conservation. The steady-state time-averaged equation for conservation of mass of the mixture can be written as

$$\frac{\partial}{\partial x_j}(\rho \overline{U}_{m,j}) = 0 \tag{1}$$

2.1.2 Momentum Conservation. The equation of momentum involves terms representing convection, diffusion, pressure gradient, body force, and frictional drag force. The drag force is given in terms of density and drift velocity. The steady-state time-averaged equation for the conservation of momentum of the mixture in the i direction can be obtained by summing the individual momentum equations for both phases. It can be expressed as

$$\frac{\partial}{\partial x_j}(\rho_m \overline{U}_{m,i}\overline{U}_{m,j}) = -\frac{\partial p}{\partial x_i} + \frac{\partial}{\partial x_j}\left(\mu_m \frac{\partial \overline{U}_{m,i}}{\partial x_j}\right) - \frac{\partial}{\partial x_j}(\rho \overline{u_{m,i}u_{m,j}}) + \rho_m g + \frac{\partial}{\partial x_j}\sum_{k=1}^{2} \alpha_k \rho_k u_{DK,i} u_{DK,j} \tag{2}$$

where p is the static pressure and the stress tensor $\rho \overline{u_{m,i}u_{m,j}}$ is given by

$$-\rho \overline{u_{m,i}u_{m,j}} = \left[\mu_{\text{eff}}\left(\frac{\partial \overline{U}_{m,i}}{\partial x_j} + \frac{\partial \overline{U}_{m,j}}{\partial x_j}\right)\right] - \frac{2}{3}\rho_m k_m \delta_{ij} \tag{3}$$

where δ_{ij} is the Kronecker delta which is equal to 1 for $i=j$ and equals 0 for $i \neq j$ and $\mu_{\text{eff}} = \mu_t + \mu_l$ is the effective viscosity. The turbulent viscosity μ_t is calculated using the high-Reynolds number form as

$$\mu_t = \rho_m C_\mu \frac{k_m^2}{\varepsilon_m} \tag{4}$$

with $C_\mu = 0.0845$ [16], and k_m and ε_m are the kinetic energy of turbulence of the mixture and its dissipation rate, respectively. These are obtained by solving their conservation equations as given below.

ρ_m and μ_m in Eq. (2) are the density and viscosity of the mixture that can be obtained from

$$\rho_m = \sum_{k=1}^{n} \alpha_k \rho_k \tag{5}$$

$$\mu_m = \sum_{k=1}^{n} \alpha_k \mu_k \tag{6}$$

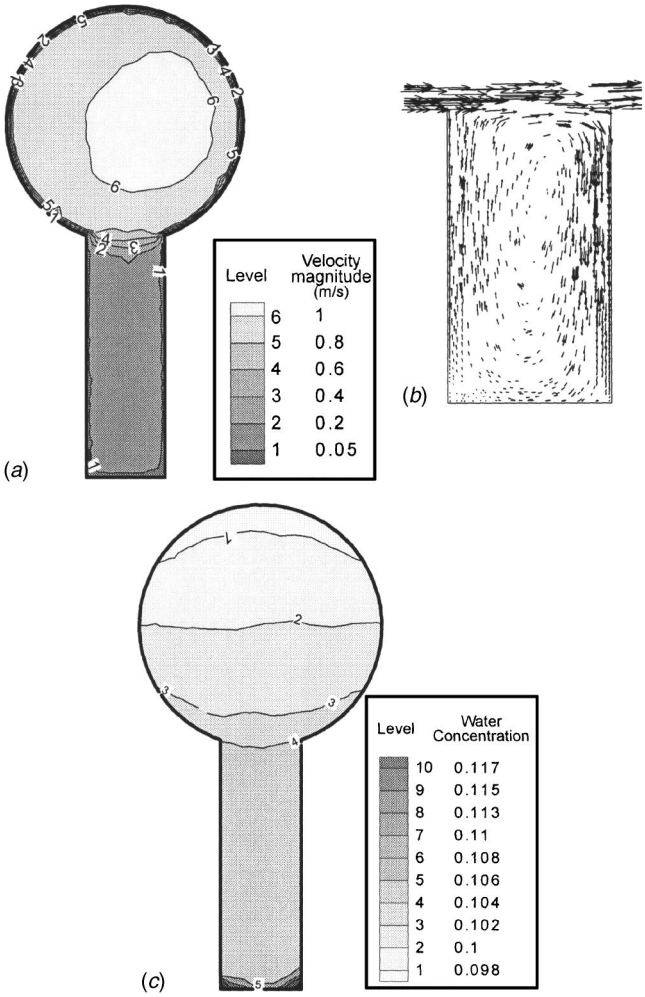

Fig. 4 Velocity contours, velocity vectors, and contours of the volumetric concentration of water for the vertical deadleg; L/D=3. (*a*) Velocity contours, (*b*) velocity vectors, and (*c*) water concentration.

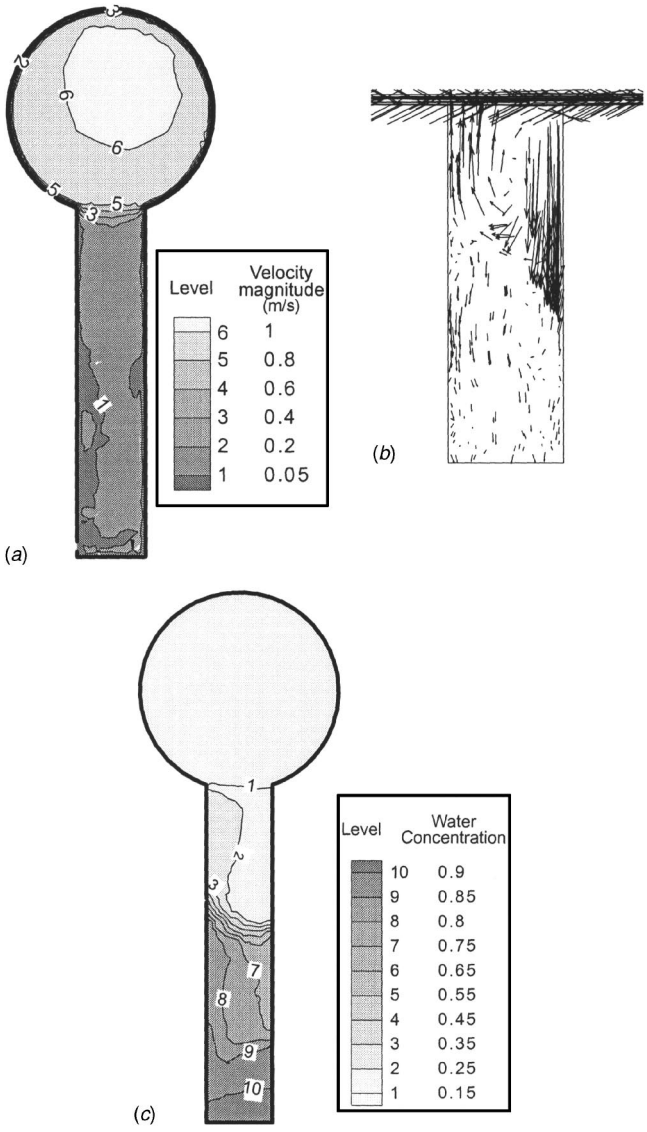

Fig. 5 Velocity contours, velocity vectors, and contours of the volumetric concentration of water for the vertical deadleg; L/D=5. (*a*) Velocity contours, (*b*) velocity vectors, and (*c*) water concentration.

$\overline{U}_m$ is the mass-averaged velocity

$$\overline{U}_m = \frac{\Sigma_{k=1}^{n} \alpha_k \rho_k \overline{U}_k}{\rho_m} \tag{7}$$

and $\overline{U}_{Dk}$ are the drift velocities and are given by

$$\overline{U}_{Dk} = \overline{U}_k - \overline{U}_m \tag{8}$$

The drift velocity is related to the relative (slip) velocity $\overline{U}_{ps}$ as

$$\overline{U}_{Ds} = \overline{U}_{ps} - \sum_{k=1}^{n} \frac{\alpha_k \rho_k}{\rho_m} \overline{U}_{pk} \tag{9}$$

with $\overline{U}_{ps}$ is given by

$$\overline{U}_{ps} = \overline{U}_s - \overline{U}_p \tag{10}$$

The slip velocity is a function of the density difference, droplet diameter, body force per density, and droplet Reynolds number. The body force includes gravitational and rotational forces. The slip velocity is expressed [18,23] as

$$\overline{U}_{ps} = \frac{(\rho_m - \rho_s) d_s^2}{18 \mu_p f_{\text{drag}}} \left[g - \overline{U}_m \frac{\partial}{\partial x_j} \overline{U}_{m,j} \right] \tag{11}$$

The drag function f_{drag} in the above equation is given by

$$f_{\text{drag}} = 1 + 0.15\,\text{Re}_d^{0.687} \quad \text{for Re} \leqslant 1000$$

and

$$f_{\text{drag}} = 0.0183\,\text{Re}_d \quad \text{for Re} > 1000 \tag{12}$$

The droplet Reynolds number

$$\text{Re}_d = \frac{\rho_p \overline{U}_{ps} d_s}{\mu_p} \tag{13}$$

2.2 Volume Fraction Equation for the Secondary Phase From the continuity equation for the secondary phase, the volume fraction equation for the secondary phase can be written as

$$\frac{\partial}{\partial x_j} (\alpha_s \rho_s \overline{U}_{m,j}) = - \frac{\partial}{\partial x_j} (\alpha_s \rho_s \overline{U}_{Ds}) \tag{14}$$

2.3 Conservation Equations for the Turbulence Model The conservation equations of the turbulence model [[17] and [18]] are given as follows.

2.3.1 Kinetic Energy of Turbulence.

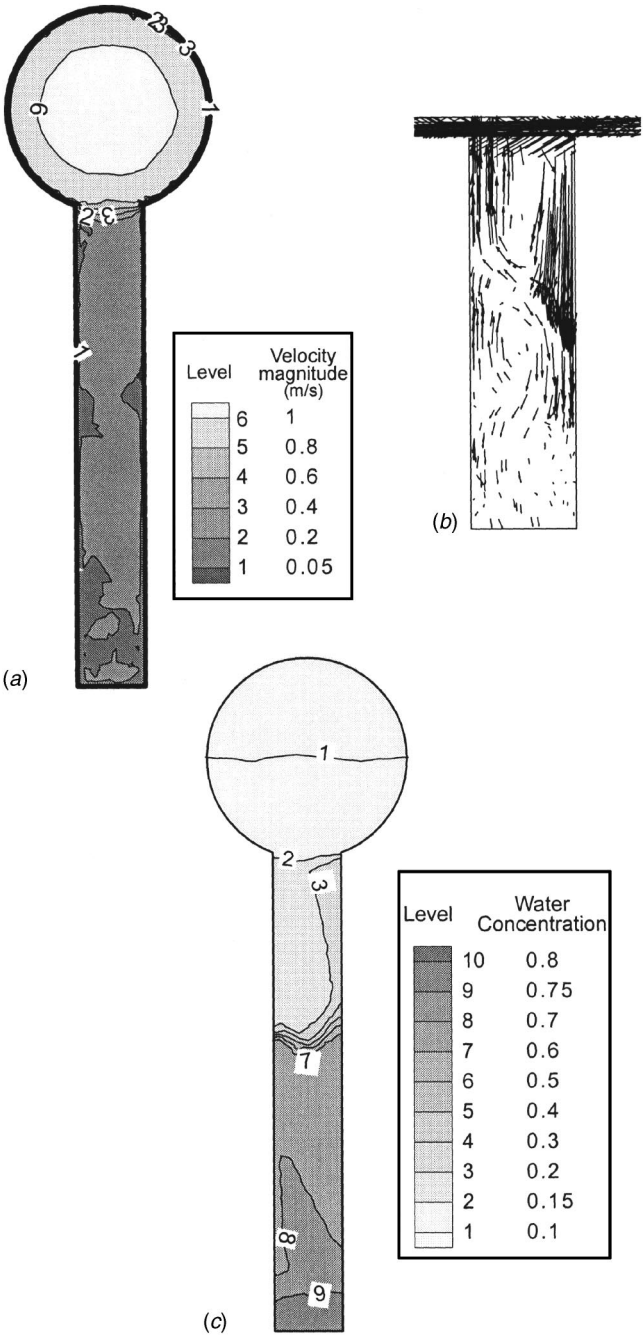

Fig. 6 Velocity contours, velocity vectors, and contours of the volumetric concentration of water for the vertical deadleg; L/D=7. (*a*) Velocity contours, (*b*) velocity vectors, and (*c*) water concentration.

$$\frac{\partial}{\partial x_j}(\rho \overline{U}_j k) = \frac{\partial}{\partial x_j}\left(\frac{\mu_{\text{eff}}}{\sigma_k}\frac{\partial k}{\partial x_i}\right) + G_k - \rho\varepsilon \tag{15}$$

2.3.2 Rate of Dissipation of the Kinetic Energy of Turbulence

$$\frac{\partial}{\partial x_j}(\rho \overline{U}_j \varepsilon) = \frac{\partial}{\partial x_i}\left(\frac{\mu_{\text{eff}}}{\sigma_\varepsilon}\frac{\partial \varepsilon}{\partial x_i}\right) + C_1 G_k \frac{\varepsilon}{k} - C_2 \rho \frac{\varepsilon^2}{k} \tag{16}$$

where G_k represents the generation of turbulent kinetic energy due to the mean velocity gradients and is given by

$$G_k = -\rho \overline{u_{mi} u_{mj}} \frac{\partial \overline{U}_{mj}}{\partial x_i} \tag{17}$$

The quantities σ_k and σ_ε are the effective Prandtl numbers for k and ε, respectively, and C_2 is given [27] as a function of the term k/ε and, therefore, the model is responsive to the effects of rapid strain and streamline curvature and is suitable for the present calculations. The model constants C_1 and C_2 have the values; $C_1 = 1.42$ and $C_2 = 1.68$.

The wall functions establish the link between the field variables at the near-wall cells and the corresponding quantities at the wall. These are based on the assumptions introduced [28] and have been most widely used for industrial flow modeling. The details of the wall functions are provided by the law-of-the-wall for the mean velocity [29].

2.4 Boundary Conditions. The velocity distribution is considered uniform at the inlet section. Kinetic energy and its dissipation rate are assigned through a specified value of $\sqrt{k/U^2}$ equal to 0.1 and a length scale L equal to the diameter of the inlet section. The boundary condition applied at the exit section (outlet of the heat exchanger tubes) is that of fully developed flow. At the wall boundaries, all velocity components are set to zero in accordance with the no-slip and impermeability conditions. Kinetic energy of turbulence and its dissipation rate are determined from the equations of the turbulence model. The secondary-phase volume fraction is specified at the inlet and exit sections of the flow domain.

2.5 Solution Procedure. The calculations were obtained using the FLUENT CFD-5.5 package. The conservation equations are integrated over a typical volume that is formed by dividing the flow field into a number of control volumes, to yield the solution. The equations are solved simultaneously using the solution procedure described by Patankar [30]. Calculations are performed with at least 300,000 finite volumes. Convergence is considered when the maximum of the summation of the residuals of all the elements for U, V, W and pressure correction equations is less than 0.01%. The grid independence tests were performed by increasing the number of control volumes from 260,000 to 380,000 ($h_{\min} = 0.16$ to 0.18 cm and $h_{\max} = 0.46$ to 0.51 cm) for the case of L/D=1 and from 290,000 to 400,000 ($h_{\min} = 0.27$ to 0.32 cm and $h_{\max} = 1.7$ to 2.0 cm) for a case of L/D=5 in two steps for each case. Figures 2(*a*) and 2(*b*) show the effect of mesh refinement on the variation of the velocity and volumetric water concentration along the axis of the deadleg. The influence of refining the grid on the velocity is very negligible. The grid independence test resulted in a maximum difference of less than 2.5% in the volumetric water concentration as the number of finite volumes increased from 260,000 to 320,000 and less than 0.8% as the number of volumes further increased from 320,000 to 380,000. Similar results are shown in Figs. 2(*c*) and 2(*d*) for the case of L/D=5 where the change of the number of control volumes from 350,000 to 400,000 has a negligible influence on both the velocity and the water volumetric concentration and has a maximum influence of 3% on the volumetric water concentration in a limited region of

Table 1 Range of local water concentration and length of regions with circulating flow for different orientations and length-to-diameter ratios

Deadleg orientation	L/D	Range of water concentration	Length of regions with circulating flow
Vertical	1	10.2%–10.4%	None
	3	10.2%–11.7%	2.8 D
	5	14.0%–86.7%	2.3 D
	7	13.2%–82.2%	2.8 D
Horizontal	1	9.0%–11.0%	Whole region, 1D
	3	8.2%–11.6%	Whole region, 3D
	5	6.5%–12.9%	3.3–4.5 D
	7	4.7%–16.0%	3.5–4.5 D
	9	4.2%–17.7%	4–5 D

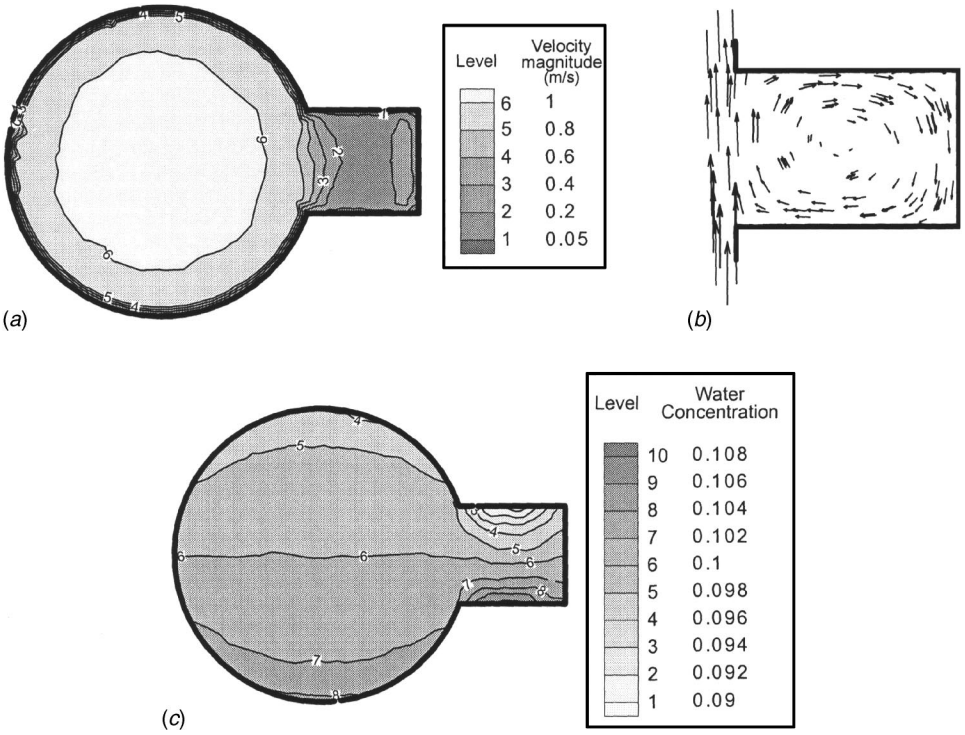

Fig. 7 Velocity contours, velocity vectors, and contours of the volumetric concentration of water for the horizontal deadleg; L/D=1. (*a*) Velocity contours, (*b*) velocity vectors, and (*c*) water concentration.

the deadleg. The abovementioned figures and percentage differences indicate that more mesh refinement will result in negligible changes in the accuracy of the computational model.

3 Results and Discussion

The details of the flow velocity field were obtained for different deadleg geometries and two orientations. The fluid at the inlet section in all of the considered cases is a homogeneous mixture containing 90% crude oil, by volume, and 10% water and the average flow velocity at inlet is 1 m/s. This concentration ratio represents a typical value in most of the crude oil wells. The header and branch diameters are $D_H=0.3$ and $D=0.1$ m for all cases. The deadleg length L is defined as the distance from the header to the end of the branch tube. Hafskjold et al. [17] show that, for a fully developed flow of two immiscible fluids, the droplet size ranges from 20 and 300 μm. The model is found to be only sensitive to droplets of diameters in the range of 10–25 μm and is less sensitive at larger droplet sizes. Therefore, the droplet size was taken to be 10^{-4} m for the cases considered in the present study.

The results are presented in terms of velocity contours, velocity vectors, and contours of water concentration. The velocity and water concentration contours are presented for a section in the deadleg that includes the branch (deadleg) tube centerline and is perpendicular to the header axis. The velocity vectors are presented for a section of the deadleg that contains the centerlines of the branch and header tubes. The first case is that of a vertical deadleg where four values of the lengths to diameter ratios (L/D=1, 3, 5, and 7) are considered. The contours of velocity magnitude and velocity vectors in addition to the volumetric water concentration are presented for each L/D ratio. Figure 3(*a*) shows the contours of velocity magnitude for the case of L/D=1. In this case, the core region of the main pipe has an almost uniform velocity distribution with a large velocity gradient near the wall as what one would expect in the case of a fully developed turbulent flow in a pipe. The velocity is high at the top and bottom regions of the deadleg (about 0.2 m/s) while low velocity exists at the middle. This distribution suggests the existence of a circulating flow zone similar to that occurring in a rectangular cavity with an upper moving boundary [31]. The velocity vectors in the deadleg (viewed from the side) are shown in Fig. 3(*b*). It is clear from the figure that a circulating flow zone exists in the deadleg that acted as a cylindrical cavity with its upper boundary open to the main stream. Such a circulating flow pattern tended to eliminate the stagnant fluid zone in the vertical deadleg. The effect of deadleg length on the variation of local water concentration in the vertical deadleg is shown in Fig. 3(*c*) for the same case of L/D=1. The local water concentration is found to be slightly higher than 10% (ranging between 10.2% and 10.5%) with the maximum concentration at the top and bottom regions of the deadleg as shown in Fig. 3(*c*). Having this maximum water concentration at the bottom is quite expected because of gravity effects but having the same value at the top may create some confusion. Actually, the maximum water concentration should occur at the bottom of the deadleg in the case of a stagnant fluid, however, because of the strong vortical motion [see Fig. 3(*b*)], the same concentration reaches the top region.

Figure 4(*a*) shows the contours of velocity magnitude in the case of L/D=3 and the corresponding velocity vectors for the same case are shown in Fig. 4(*b*). Figure 4(*c*) shows the contours of the water volumetric percentage for the same case. It is clear from these figures that the circulating flow zone extends over most of the entire length of the deadleg, however, with low velocity in the lower portion (about 0.05 m/s). Figure 4(*a*) also shows an asymmetric velocity profile in the main pipe as a result of the deadleg. Figure 4(*c*) shows that the water concentration varies from 10.2% to 11.7% with the maximum occurring in a very small region at the bottom of the deadleg.

The contours of velocity magnitude and velocity vectors as well as the water concentration for L/D>3 are shown in Figs. 5 and 6. The asymmetry of the velocity in the main pipe exists for L/D=5. Similar to the case of L/D=1, a circulating flow region occurs in

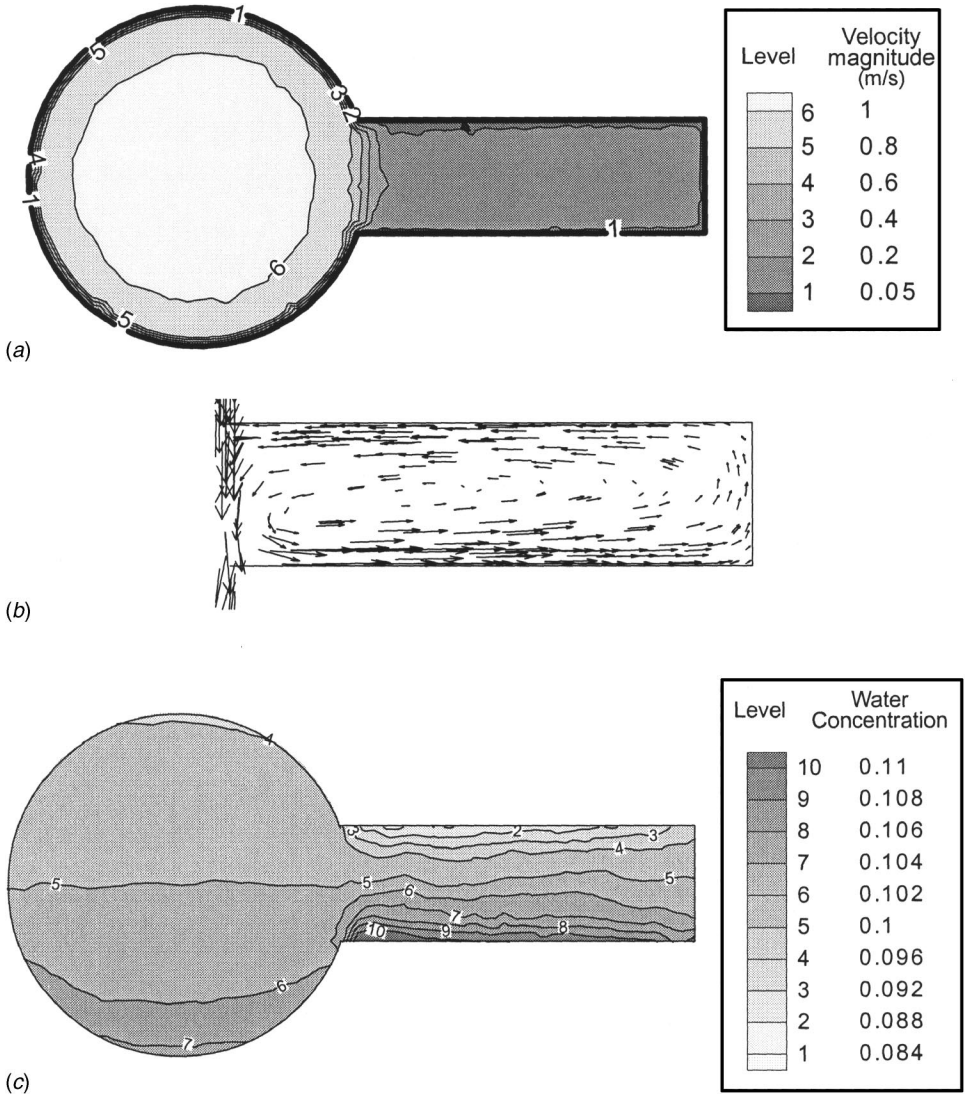

Fig. 8 Velocity contours, velocity vectors, and contours of the volumetric concentration of water for the horizontal deadleg; L/D=3. (*a*) Velocity contours, (*b*) velocity vectors, and (*c*) water concentration.

the upper part of the deadleg. The length of this part is equal to 2.3 D. A stagnant fluid zone appears in the middle and lower portions of the deadleg in cases of L/D>3 as shown in Figs. 5 and 6. Figure 5(*a*) shows a stagnant fluid region appearing near the wall in the case of L/D=5. That region extends, in a scattered fashion, in the lower part of the deadleg. The size of that region is found to increase with increasing L/D as can be seen in Figs. 5(*a*) and 6(*a*). Figure 6(*a*) shows an interesting flow pattern in which the upper section of the deadleg ($0<y<2.8$ D) is characterized by a circulating flow zone similar to that found in the case of L/D=3. This is followed by the middle section ($2.8\,\mathrm{D}<y<5.2$ D) that is occupied by some counter-rotating vortices. The lower section ($5.2\,\mathrm{D}<y<7$ D) is occupied by a stagnant fluid. The total length of the deadleg occupied by a stagnant fluid is 4.2 D that corresponds to 60% of the deadleg length. Considering the fact that the vortices in the middle region are too weak with negligible velocity magnitudes, it can be concluded that almost 70% of the deadleg is occupied by stagnant fluid.

Increasing L/D from 3 to 5 is found to create very high values of water concentration that reaches 86.7% at the bottom region as shown in Fig. 5(*c*). In this case, the upper half of the deadleg has a water concentration in the range from 14% to 39% while the lower half has a concentration in the range from 40% to 86.7% with maximum value at the bottom of the deadleg. The part of the deadleg that has high water concentration of more than 20% is about 46% of the deadleg length (about 2.3 D). The situation is almost the same in the case of L/D=7 [see Fig. 6(*c*)], however, the region of high water concentration (more than 20%) occupies about 40% of the deadleg length (about 2.8 D). Table 1 shows the range of local water concentration in the deadleg for different values of length-to-diameter ratios. Thus, for the case of vertical deadleg, it is clear that there is no stagnant fluid zone in all cases so long as L/D<3. For the cases of L/D>3, it is also clear that the region of the deadleg close to the header is characterized by circulating vortical motions for a length $l\approx 3$ D while the remaining part of the deadleg occupied by stagnant fluid.

The case of a horizontal deadleg was investigated for the same geometry of the vertical deadleg ($D_H=0.3$, $D=0.1$ m) but with different orientation. The problem was solved for five length-to-diameter ratios (L/D=1, 3, 5, 7, and 9) and the obtained contours of velocity magnitude, velocity vectors and concentration of liquid water are shown in Figs. 7–11. The only difference between this case and the one presented in Figs. 3–6 is the direction of gravity forces. In the previous case the gravity was acting in line with the deadleg axis while perpendicular to it in the present case. Figure 7(*a*) shows the velocity contours in case of L/D=1. The

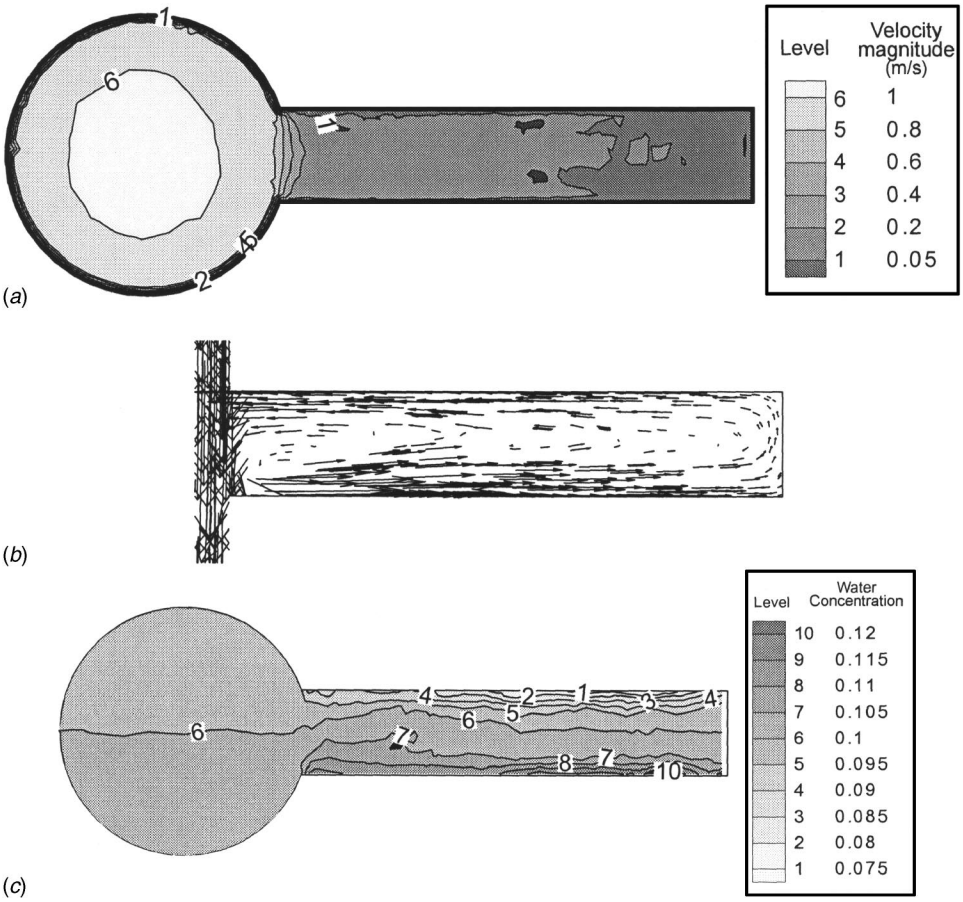

Fig. 9 Velocity contours, velocity vectors, and contours of the volumetric concentration of water for the horizontal deadleg; L/D=5. (*a*) Velocity contours, (*b*) velocity vectors, and (*c*) Water concentration.

fluid is stagnant only at the deadleg walls (the no-slip condition) while a circulating vortical motion occupies the entire deadleg region similar to that presented in Fig. 3(*a*). The outer and inner regions of the deadleg have higher velocity (≈0.2 m/s) with the lowest velocity in the central part (≈0.05 m/s). The velocity vectors for the same case are shown in Fig. 7(*b*). It is shown that the entire region is occupied by a recirculating flow region and confirms the contours of the velocity vectors in Fig. 7(*a*). Figure 8(*a*) shows the contours of velocity magnitude for the case of L/D=3. The velocity in the deadleg ranges from 0.01 m/s in the central region to about 0.05 m/s in the inner region (close to the header) with the stagnant fluid zones limited to the deadleg walls. The velocity vectors are shown in Fig. 8(*b*) and indicate circulating vortical flow with the vortex center at the pipe center line. As the length-to-diameter ratio increases to L/D=5, the circulating flow zone is found to occupy about 65%–80% of the deadleg length (about 3.2 D) leaving the remaining 20%–35% as stagnant fluid as shown in Fig. 9(*a*). As L/D increases further to L/D=7 and L/D=9, the length of the stagnant fluid zone increases as shown in Figs. 10(*a*) and 11(*a*). The figures show a stagnant fluid zone of length 3–3.5 D in the case of L/D=7 and of length 4–5 D in the case of L/D=9. Based on the obtained results, it is quite clear that there is no stagnant fluid zone in all cases of this orientation (horizontal deadleg configuration) so long as L/D<5. For the cases of L/D>5, it is also clear that the region of the deadleg close to the header is characterized by circulating vortical motions for a length $L=3-5$ D while the remaining part of the deadleg occupied by stagnant fluid.

To show the effect of deadleg orientation on the water concentration fields, we now compare the water concentration contours for a vertical deadleg presented in Figs. 3–6 with those of a horizontal deadleg presented in Figs. 7–11. For a horizontal deadleg of L/D=1, the water concentration varies from 9% in the upper region to 11% in the lower region as shown in Fig. 7(*c*). Although the range is very much the same as in the case of a vertical deadleg having the same geometry, the distribution is quite different [see Fig. 3(*c*) for comparison] due to the change of direction of gravity forces. In the horizontal deadleg case, the water concentration increases from top to bottom with an approximate symmetry about a vertical axis due to the circulating vortical fluid motion. As L/D increases to 3, the range of water concentration in the horizontal deadleg becomes slightly wider (from 8.2% to 11.6%) with a low concentration at the top and a high concentration at the bottom as can be seen in Fig. 8(*c*). For the cases of L/D=5, 7, and 9, the water concentration contours follow the same pattern as that of L/D=3, however with a wider range as L/D increases as shown in Table 1. The water concentration varies in the range 6.5% to 12.9% in the case of L/D=5 and becomes 4.7% to 16% in the case of L/D=7 and finally attains the range 4.2% to 17.7% in the extreme case of L/D=9.

4 Flow Visualization Procedure and Results

4.1 Experimental Setup. The experimental setup which is composed of two main parts, namely, the flow loop and the test section, is designed and constructed to carry out the flow visualization experiments. Descriptions of the two parts are given in the following subsections.

4.2 Flow Loop. The flow loop, which is a closed-type loop,

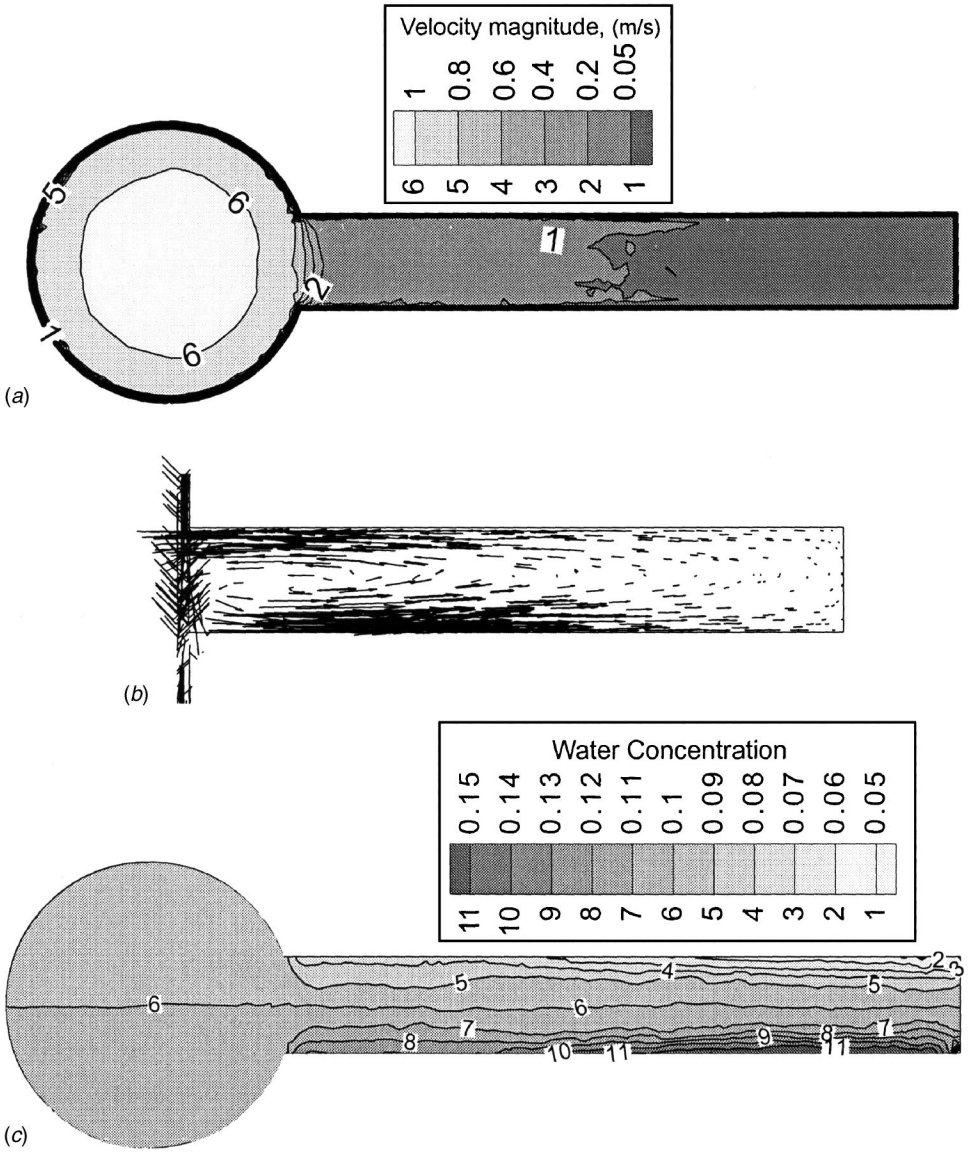

Fig. 10 Velocity contours, velocity vectors, and contours of the volumetric concentration of water for the horizontal deadleg; L/D=7. (*a*) Velocity contours, (*b*) velocity vectors, and (*c*) water concentration.

consists of a pump, a piping system, and two reservoirs. The lower reservoir has a total volume of 1 m^3. The upper reservoir is used as a settling chamber that is utilized to minimize the lateral flow fluctuations and unsteady flow oscillations in order to provide a steady uniform flow at the inlet of the header tube. The pump is a centrifugal-type water pump that has a rated power of 5 hp. The piping system is made of 2-in. PVC pipes and is equipped with three valves and a number of 90° bends. The two gate valves are used as pump suction and delivery valves and the ball valve is installed downstream of the deadleg. Water is pumped from the lower reservoir to the settling chamber and back to the lower reservoir through the test section. The pump delivery valve together with the ball valve (installed downstream of the test section) are used to control the volume flow rate in the test section.

4.3 Test Section. The test section that simulates the flow process in the deadleg region is designed to provide flexibility for the variation of the deadleg length. The detailed design drawings of the test section including construction details are shown in Fig. 12. The test section consists of an inlet section, an outlet section, and the deadleg region. The deadleg region contains a piston that can be moved in or out to provide a mechanism for varying the deadleg length. All the components of the test section are made out of plexiglas. It should be noted that the deadleg region is the main region of interest in this study. The deadleg geometry can be changed by installing the piston at the end of the header tube or the branch tube.

4.4 Instrumentation. The flow visualization experiments were performed utilizing a two-dimensional laser light sheet to illuminate the middle section (plane of symmetry) of the deadleg region. The flow visualization was accomplished by utilizing a 200 mW argon laser source. The laser beam was forced to pass through a vertical cylindrical glass rod of 8 mm diameter to produce a two-dimensional laser-light sheet. The horizontal laser sheet was diverted to the vertical plane using a 45° mirror. The laser sheet was aligned to pass through the plane of symmetry of the tube and deadleg region. The seeding particles used in the flow visualization experiments were small wooden particles that are almost of neutral buoyancy. The particle trajectory traces were photographed using a high-speed digital camera.

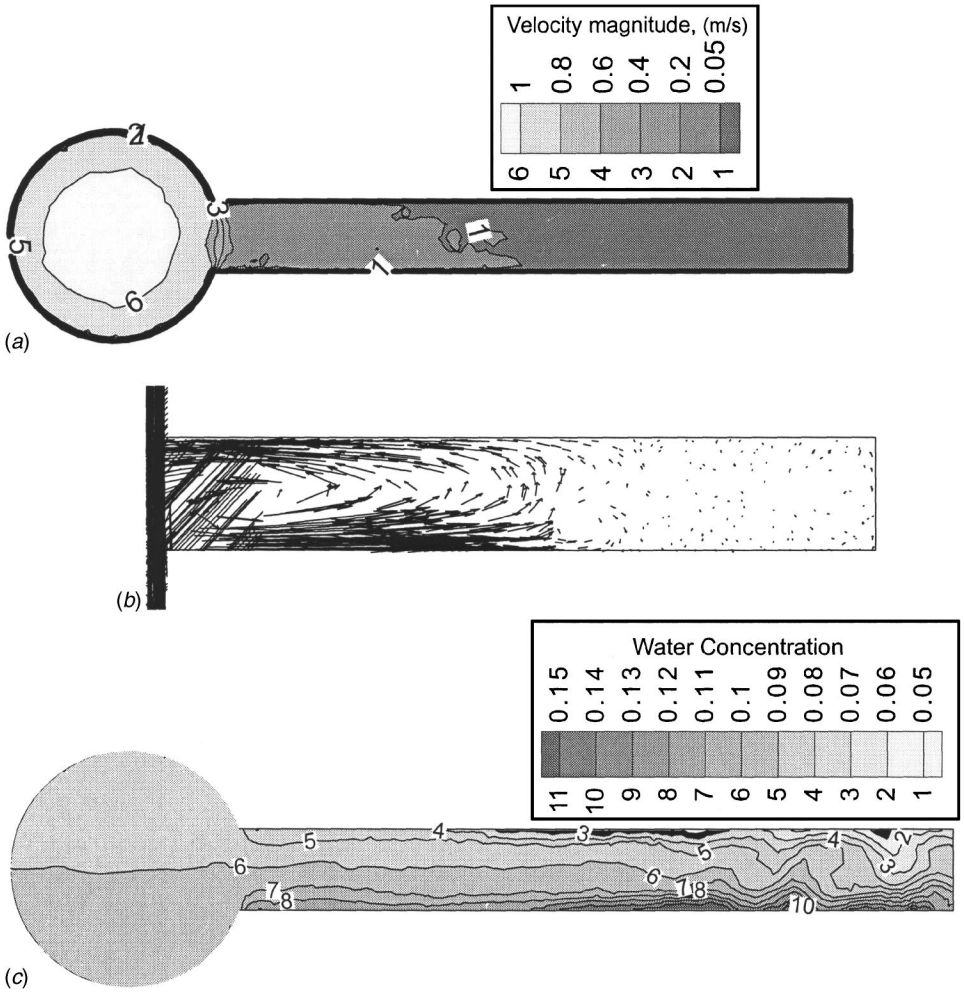

Fig. 11 Velocity contours, velocity vectors, and contours of the volumetric concentration of water for the horizontal deadleg; L/D=9. (*a*) Velocity contours, (*b*) velocity vectors, and (*c*) water concentration.

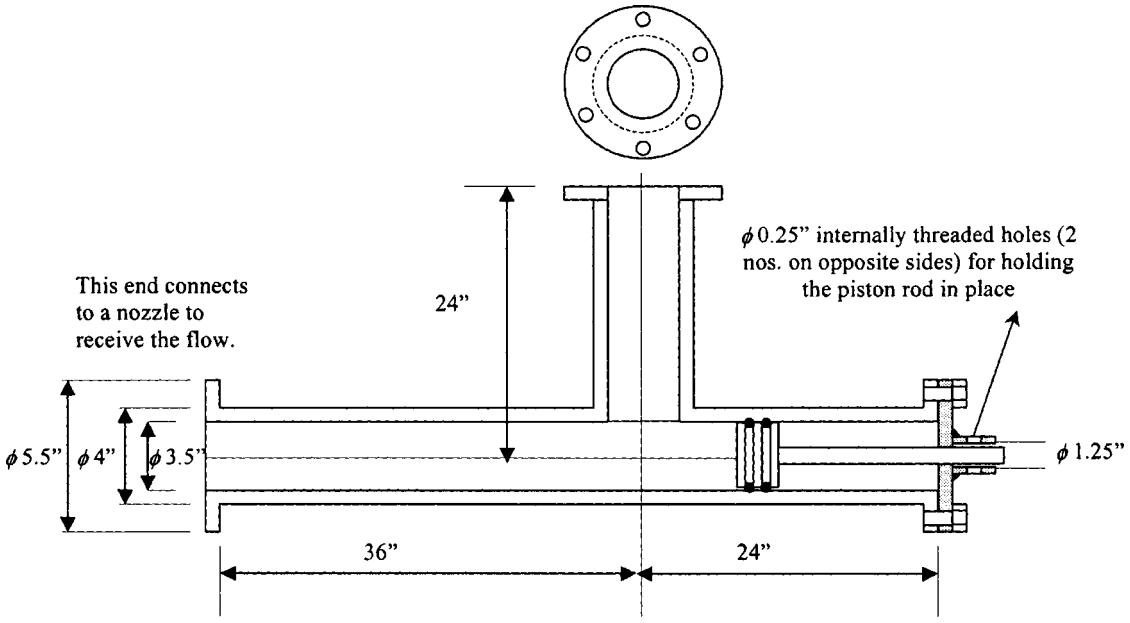

Fig. 12 Detailed construction of the test section

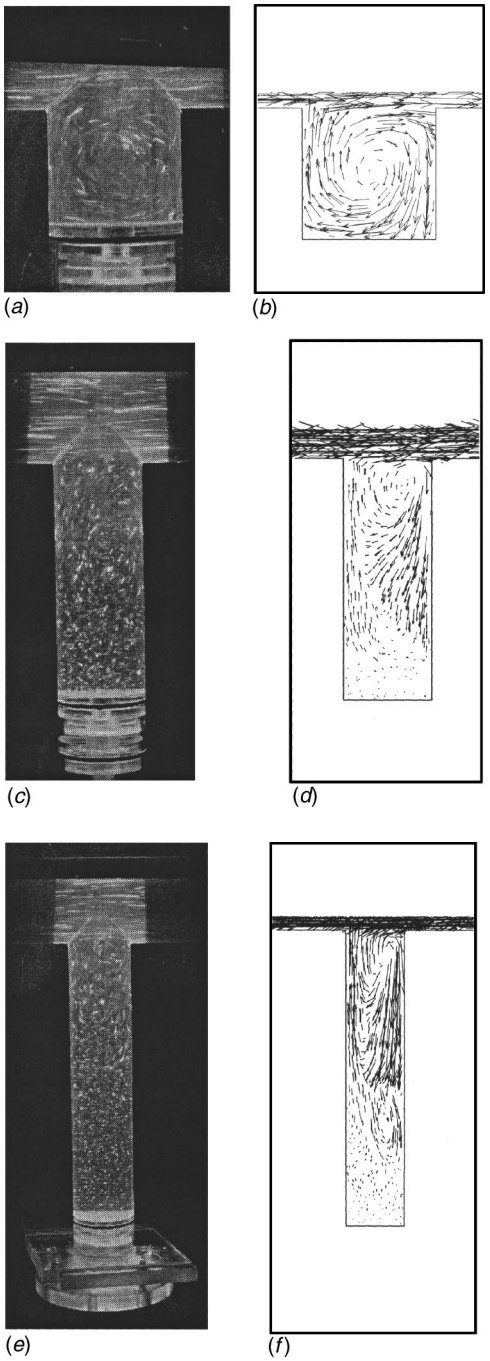

Fig. 13 Calculated and measured velocity vectors inside the deadleg. (a) Flow visualization results L/D=1, (*b*) calculated results L/D=1, (*c*) flow visualization results L/D=3, (*d*) calculated results L/D=3, (*e*) flow visualization results L/D=5, and (*f*) Calculated results L/D=5.

4.5 Flow Visualization Results. The details of the flow velocity field were visualized and photographed for the vertical deadleg geometry with different deadleg lengths (L/D equal to 1, 3, and 5) and are shown in Fig. 13. The case considered is that of a vertical deadleg with equal header and branch diameters of $D = 0.0889$ m. The details of the flow field for the case of L/D=1 are shown in Fig. 13(*a*). The computed velocity vectors for the same case are shown in Fig. 13(*b*). A very similar trend of flow pattern is observed between the flow visualization and calculated results. Figure 13(*c*) shows the velocity field for the case of L/D=3. It is clear from the figure that the circulating flow zone extends over most of the entire length of the deadleg, however, with low velocity in the lower portion. This is in good agreement with the computed velocity vectors for the same case as shown in Fig. 13(*d*). The velocity flow field for L/D=5 is shown in Figs. 13(*e*) and 13(*f*) for the computed and visualized velocity vectors and very similar flow patterns are observed in both figures. The good comparison between the computed and visualized flow patterns provide another verification of the accuracy of the computational model.

5 Conclusions

The effect of deadleg geometry and orientation on oil/water separation is investigated. The investigation is based on the solution of the mass and momentum conservation equations of an oil/water mixture together with the volume fraction equation for the secondary phase. Results are obtained for two main deadleg orientations and for length-to-diameter ratios ranging from 1 to 9 in each orientation. The considered fluid mixture contains 90% oil and 10% water (by volume) and the inlet flow velocity is kept constant (1 m/s). The results show that the size of the stagnant fluid region increases with the increase of L/D. For the case of a vertical deadleg, it is found that the region of the deadleg close to the header is characterized by circulating vortical motions for a length $l \approx 3$ D while the remaining part of the deadleg occupied by a stagnant fluid. The results also indicated that the water volumetric concentration increases with the increase of L/D and influenced by the deadleg orientation. Maximum value of the water concentration increases from 10.4% in the case of L/D=1 to more than 80% in the case of L/D=7 for the vertical deadleg orientation. In the case of a horizontal deadleg, the region of circulating flow extends to 3–5 D and the maximum concentration increases from 11% in the case of L/D=1 to 17.7% in the case L/D=9. The flow visualization experiments for the case of the vertical deadleg were carried out using a laser sheet. The visualized flow patterns provide an important verification of the accuracy of the calculated velocity field and also validate the present calculation procedure.

Acknowledgments

The authors wish to acknowledge the support received from King Fahd University of Petroleum & Minerals and Saudi Aramco during the course of this study.

Nomenclature

C = inlet concentration of water liquid
D = diameter of the deadleg (branch tube)
D_H = diameter of the header (main tube)
d = droplet diameter
L = Length of the deadleg
V = Inlet mixture velocity
C_μ = constant defined in Eq. (4)
C_1 = constant defined in Eq. (16)
C_2 = constant defined in Eq. (16)
G_k = generation of turbulent kinetic energy
g = gravitational acceleration
h = representative grid size, ($h = \text{cell\_volume}^{1/3}$)
k = turbulent kinetic energy
N = number of control volumes
p = pressure
Re = Reynolds number
$\overline{U_j}$ = mass-average velocity component
u_j = fluctuating velocity component
x_j = space coordinate
y = vertical distance, measured from the header tube center

Greek letters

α = volume fraction
ε = dissipation rate of turbulent kinetic energy

μ = dynamic viscosity
ρ = density
σ_k = effective Prandtl number for k
σ_ε = effective Prandtl number for ε

Superscripts

— = time average

Subscripts

D = drift
d = droplet
eff = effective
k = species
l = laminar
p = primary flow
max = maximum
min = minimum
m = mixture
s = secondary flow
t = turbulent

References

[1] Craig, B. C., 1996, ''Corrosion in Oil/Water Systems,'' Mater. Selection Design, Aug.
[2] Lotz, U., Van Bodegom, L., and Ouwehand, C., 1990, ''Effect of Type of Oil or Gas Condensate on Carbon Acid Corrosion,'' *Corrosion/90*, Paper no. 41, NACE, Houston TX.
[3] Ricca, P. M., 1991a, ''Ultrasonic Inspection Prompts Chemical Inhibitor Program,'' Oil & Gas Journal, **22**, pp. 73–82.
[4] Ricca, P. M., 1991b, ''Control of Deadleg Corrosion in a Crude Oil Pipeline,'' PD-Vol. 34, *Pipeline Engineering*, ASME, pp. 34–39.
[5] Charles, M. E., Govier, G. W., and Hodgson, G. W., 1961, ''The Horizontal Pipeline Flow of Equal Density Oil-Water Mixture,'' Can. J. Chem. Eng., **39**(1), pp. 27–36.
[6] Charles, M. E., and Lilleleht, L. U., 1966, ''Correlations of Pressure Gradients for the Stratified Laminar-Turbulent Pipeline Flow of Two Immiscible Liquids,'' Can. J. Chem. Eng., **44**(1), pp. 47–49.
[7] Lockhart, R. W., and Martinelli, R. C., 1949, Chem. Eng. Prog., **45**, pp. 39–48.
[8] Barnea, D., 1986, ''Transition From Annular Flow and From Dispersed Bubble Flow-Unified Models for the Whole Range of Pipe Inclinations,'' Int. J. Multiphase Flow, **12**, 5, pp. 733–744.
[9] Brauner, N., and Maron, D. M., 1992, ''Stability Analysis of Stratified Liquid-Liquid Flow,'' Int. J. Multiphase Flow, **18**, 1, pp. 103–121.
[10] Schmidt, H., and Loth, R., 1994, ''Predictive Methods for Two-Phase Flow Pressure Loss in Tee Junctions With Combining Ducts,'' Int. J. Multiphase Flow, **20**, 4, pp. 703–720.
[11] Plaxton, B. L., 1995, ''Pipeflow Experiments for Analysis of Pressure Drop in Horizontal Wells,'' *SPE Annual Technical Conference and Exhibition*, October 22–25, Dallas, TX, SPE Int L. Stdnt. Pap. Cntst., pp. 635–650.
[12] Brill, J., and Beggs, H., 1994, *Two-Phase Flow in Pipes*, University of Tulsa Press, Tulsa, OK.
[13] Asheim, H., Kolnes, J., and Oudeman, P., 1992, ''A Flow Resistance Correlation for Completed Wellbore,'' J. Pet. Sci. Eng., **8**, 2, pp. 97–104.
[14] Angeli, P., and Hewitt, G. F., 1996, ''Pressure Gradient Phenomena During Horizontal Oil-Water Flow,'' 1996 OMAE—*Pipeline Technology*, Vol. V, ASME, pp. 287–295.
[15] Hwang, C. J., and Pal, R., 1997, ''Flow of Two-Phase Oil/Water Mixtures Through Sudden Expansions and Contractions,'' Chem. Eng. J., **68**, pp. 157–163.
[16] Schabacker, J., Bolcs, A., and Johnson, B. V., 1998, ''PIV Investigation of the Flow Characteristics in an Internal Coolant Passage With Two Ducts Connected by a Sharp 180° Bend,'' ASME Paper No. 98-GT-544, Fairfield, NJ.
[17] Hafskjold, B., Celius, H. K., and Aamo, O. M., 1999, ''A New Mathematical Model for Oil/Water Separation in Pipes and Tanks,'' SPE Prod. Facil., **14**, 1, pp. 30–36.
[18] Fluent, 1988, *CD-Rom Fluent 5, User's Guide*, section 14.2.
[19] Wilson, W., 1999, ''The Development of a Droplet Formation and Entrainment Model for Simulations of Immiscible Liquid-Liquid Flows,'' MS thesis, Weat Virginia University.
[20] Celik, I. B., Badeau, A. E., Burt, A., and Kandil, S., 2001, ''A Single Fluid Transport Model for Computation of Stratified Immiscible Liquid-Liquid Flows,'' *Proceedings of the XXIX IAHR Congress*, Sep., Beijing, China, pp. 1–18.
[21] Dluska, E., Wronski, S., and Rudnaik, L., 2001, ''Two-Phase Gas-Liquid Coutte-Taylor Eccentric Reactor. Computational Calculation of Reactor Hydrodynamics,'' *Proceedings of the 2nd International Conference on Computational Heat and Mass Transfer* COPPE/UFRJ, Federal University of Rio de Janeiro, Brazil, Oct. 22–26.
[22] Vigil, R. D., and Zhu, X., 2001, ''Banded Liquid-Liquid Taylor-Coutte-Posuille Flow,'' AICHE J., **47**(9), pp. 1932–1940.
[23] Manninen, M., Taivassalo V., and Kallio, S., 1996, *On the Mixture Model for Multiphase Flow*, Technical Research Center of Finland, VTT Publication No. 288.
[24] Maron, D. M., 1992, ''Flow Pattern Transitions in Two-Phase Liq-Liq Flow in Horizontal Tubes,'' Int. J. Multiphase Flow, **18**, 1, pp. 123–140.
[25] Versteeg, H. K., and Malalasekera, W., 1995, *An Introduction to Computational Fluid Dynamics: The Finite Volume Method*, Longman Scientific and Technical, Essex, England.
[26] Reynolds, W. C., 1987, ''Fundamentals of Turbulence for Turbulence Modeling and Simulation,'' Lecture Notes for Von Karman Institute, Agard Report No. 755, pp. 1–11.
[27] Shih, T. H., Liou, W. W., Shabbir, A., and Zhu, J., 1995, ''A New k-ε Eddy-Viscosity Model for High Reynolds Number Turbulent Flows—Model Development and Validation,'' Comput. Fluids, **24**, 3, pp. 227–238.
[28] Launder, B. E., and Spalding, D. B., 1974, ''The Numerical Computation of Turbulent Flows,'' Comput. Methods Appl. Mech. Eng., **3**, pp. 269–289.
[29] Habib, M. A., Attya, A. M., and McEligot, D. M., 1989, ''Calculation of Turbulent Flow and Heat Transfer in Channels With Streamwise Periodic Flow,'' ASME J. Turbomach., **110**, pp. 405–411.
[30] Patankar, S. V., 1980, *Numerical Heat Transfer and Fluid Flow*, Hemisphere Publishing Corporation, New York.
[31] Chiang, T. P., Sheu, W. H., and Hwang, R. R., 1998, ''Effect of Reynolds Number on the Eddy Structure in a Lid-Driven Cavity,'' Int. J. Numer. Methods Fluids, **26**, pp. 557–579.

Numerical Procedure for the Laminar Developed Flow in a Helical Square Duct

V. D. Sakalis

P. M. Hatzikonstantinou
e-mail: hatzikon@upatras.gr

P. K. Papadopoulos

Department of Engineering Science,
University of Patras,
GR 26500 Patras, Greece

The incompressible fully developed laminar flow in a helically duct of square cross section is studied expressing the governing equations in terms of an orthogonal coordinate system. Numerical results are obtained with the described continuity, vorticity, and pressure (CVP) numerical method using a colocation grid for all variables. Since there are not approximations, the interaction effects of curvature, torsion and axial pressure gradient on the velocity components and the friction factor are presented. The results show that the torsion deforms substantially the symmetry of the two centrifugal vortices of the secondary flow, which for large values of torsion combined with small curvature tend to one vortex covering the whole cross section. The friction factor decreases for torsion in the range 0 to 0.1 and increases as the torsion increases further, a behavior which is more profound as the Dean number increases. Our results are stable for the calculated Dean numbers. [DOI: 10.1115/1.1852483]

Keywords: Helical Internal Flow, Numerical CVP Method, Incompressible Flow

1 Introduction

The flow through a helical duct is used extensively in various industrial applications, as in heat transfer equipment, chemical processes, propulsion systems, medical equipment, and centrifugal compressors. The characteristic feature of flow in curved and helical ducts is the development of the secondary flow which produces the increase of the heat and mass transfer rates particularly in the case of laminar flows. The extensive study of the flow through helical ducts is of importance for the design of industrial apparatus.

A helical duct such as that shown in Fig. 1(*a*) is characterized by the width a of the cross section, the curvature κ, and the torsion τ, which is related to the pitch h of the duct. If the torsion tends to zero, it means that the pitch h tends to zero and a toroidal duct is obtained, whereas if the curvature tends to zero, for finite torsion, a straight twisted duct is produced. The curvature causes the development of a centrifugal force, thus generating the secondary flow. This flow is characterized mainly by two stable, symmetric, counter-rotating vortices. The torsion causes the distortion in the symmetry of the flow, enlarging the lower vortex of the secondary flow at the expense of the upper vortex.

Analytical and numerical studies of the laminar incompressible flow through a helical duct have been restricted to cases of small curvature and pitch. The effect of the centrifugal force on the friction loss and the enhancement of the heat transfer rate has been studied numerically by Cheng et al. [1], Ghia et al. [2], Hwang and Chao [3], Hatzikonstantinou and Sakalis [4], and Sakalis and Hatzikonstantiou [5]. However, the study of the effect of the torsion on the flow through a helical duct has been limited, mainly because of the complex analysis required for the geometry of the duct. The flow through a circular helical duct has been well studied [6–12], as has that of elliptical cross section [13]. However, only a few works have been carried out with respect to the helical square ducts [14–18].

The existence of torsion requires the expression of the position and velocity vectors, as well as of the governing equations in terms of the coordinates $(\tilde{s},\tilde{x},\tilde{y})$ and the associated Frenet system on the centerline of the duct [Fig. 1(*b*)] with the unit axial tangent, normal, and binormal vectors denoted as $\vec{T}$, $\vec{N}$, and $\vec{B}$, respectively. The coordinate $\tilde{s}$ is measured along the helical axis of the duct and the coordinates $\tilde{x}$, $\tilde{y}$ are along the vectors $\vec{N}$ and $\vec{B}$, respectively. However, the coordinates $(\tilde{s},\tilde{x})$ and $(\tilde{s},\tilde{y})$ are nonorthogonal to each other except at the centerline. The use of nonorthogonal coordinates and tensor analysis, followed by authors like Wang [6] and Chen and Fan [11], express the governing equations in terms of covariant and contravariant velocity components, but do not describe the physical picture of the flow. Thus, these velocity components must be transformed into the physical velocity components $(\tilde{u}_1,\tilde{u}_2,\tilde{u}_3)$, corresponding to the physical orthogonal basis $(\vec{T},\vec{N},\vec{B})$, for a clear visualization of the developed flow. On the other hand, the use of an orthonormal coordinate system, which can be produced by a rotating mechanism of the $\vec{N}$, $\vec{B}$ cross-section plane [9], or by a straightforward use of the tensor analysis [14] produces the physical velocity components, revealing the correct physical behavior of the helical flow under the influence of the various geometric and dynamic parameters. Thus the dispute between the results of Wang [6] and Germano [7] who estimated that the torsion effect in the helical circular ducts are of first and second order, respectively, has been explained by [9,14,17], where it was found that these differences are due to the velocity components calculated by different coordinate systems. The studies of a helical square duct by Chen and Jan [17], expressed the governing equations in a nonorthogonal coordinate system, solved by the Galerkin finite element method and transformed their contravariant velocity components to the physical ones. Bolinder [15] solved the governing equations obtained using a physical basic vector and tensor analysis, with the SIMPLEC algorithm.

In a helical duct the centrifugal force plays a prominent role in creating a pair of vortices. However, above a critical value of the Dean number, the secondary flow is changed from the appearance of an additional two-vortex structure, due to the balance of the acting centrifugal and pressure gradient forces on the flow. This transition is usually denoted as Dean's instability. Authors including Joseph et al. [19] and Cheng et al. [1] have discovered a fully developed secondary flow with four vortices when the Dean number was above a critical Dean value. Contrary to Bolinger, Chen and Jan [17] conclude that the Dean instability can be avoided.

Contributed by the Fluids Engineering Division for publication on the JOURNAL OF FLUIDS ENGINEERING. Manuscript received by the Fluids Engineering Division August 8, 2003; revised manuscript received October 14, 2004. Review Conducted by: J. Marshall.

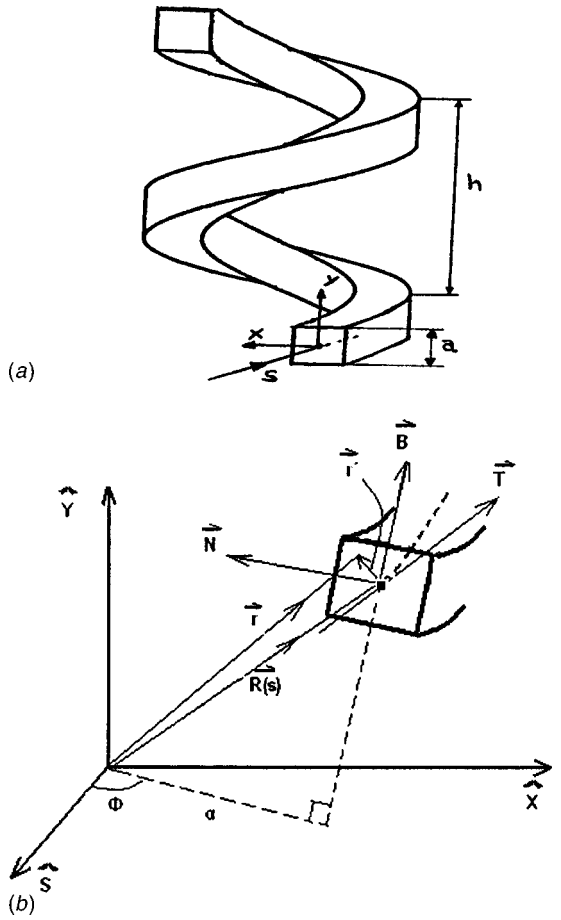

Fig. 1 (*a*) Helical duct. (*b*) Coordinate system.

However the present study shows that for predominant centrifugal forces over the effect of torsion the main pair of vortices of the secondary flow still appears, and as the torsion or the Dean number increases these vortices are substantially deformed. Winters [20], and Bolinder [14,15] showed that the four-vortex branch is unstable to perturbations, breaking the apparent symmetry of the cross section. This is confirmed by the present study, where transient calculations performed in the full cross section found only two-vortex solutions for limited Dean number intervals. Between these intervals nonconverged ''solutions'' oscillate between a two-vortex and a four-vortex structure as time iterations proceed. If one performs calculations in the half of the cross section imposing boundary conditions along the horizontal symmetry line, stable four-vortex solutions also appear. Other studies concerning the instabilities of the fully developed flow are discussed by Daskopoulos and Lenhoff [21].

In the present work, the incompressible laminar fully developed flow through a helical square duct is studied over a wide range of the parameters of the problem. The governing equations and the velocity components are expressed in an orthogonal coordinate system obtained by rotation. The results have been obtained applying a computational method [4,5,22]. The method, except the governing equations, introduces three additional variational representations of the continuity, vorticity, and pressure equations and is denoted as the CVP method by their acronym. The method is illustrated below, its validity is examined, and its predictions are compared with those obtained by other methods. The fact that a helical duct is the most complex duct, for which a fully developed flow can be established, indicates the importance of this flow problem for the study of the validity of any numerical method. The main advantages of the CVP method is its simplicity for application to complex mathematical equations and complex geometries using a collocation grid without introducing spurious oscillations. The method is compact and converges for a much wider range of the parametric values and less dense grids than those required by the pressure linked equation methods.

2 Mathematical Analysis

The position vector of the helical center line of the duct, in the Cartesian coordinate system (S,X,Y), is written

$$\vec{R}(\tilde{s}) = \alpha \cos\Phi \vec{i} + \alpha \sin\Phi \vec{j} + b\Phi \vec{k},$$

where

$$\Phi = \tilde{s}A, \quad A = (\alpha^2 + \mathrm{b}^2)^{-1/2}, \quad b = h/(2\pi) \tag{1}$$

$\tilde{s}$ is the arc length along the curve, and α and Φ are shown in Fig. 1(*b*). The unit tangent $\vec{T}$, normal $\vec{N}$ and binormal $\vec{B}$ vectors to the curve $\vec{R}(\tilde{s})$ are given by the relations

$$\vec{T}(\tilde{s}) = \frac{d\vec{R}}{d\tilde{s}} = -\alpha A \sin(\tilde{s}A)\vec{i} + \alpha A \cos(\tilde{s}A)\vec{j} + bA\vec{k}$$

$$\vec{N}(\tilde{s}) = \frac{1}{\mathrm{k}}\frac{d\vec{T}}{d\tilde{s}} = -\cos(\tilde{s}A)\vec{i} - \sin(\tilde{s}A)\vec{j} \tag{2}$$

$$\vec{B}(\tilde{s}) = \vec{T}\times\vec{N} = bA \sin(\tilde{s}A)\vec{i} - bA \cos(\tilde{s}A)\vec{j} + \alpha A\vec{k}$$

The curvature κ and the torsion τ are determined by the Frenet formulas

$$\frac{d\vec{B}}{d\tilde{s}} = -\tau'\vec{N} \Rightarrow \tau' = \frac{b}{\alpha^2 + b^2} \Rightarrow \tau' = bA^2$$

$$\frac{d\vec{T}}{d\tilde{s}} = \kappa'\vec{N} \Rightarrow \kappa' = \frac{\alpha}{\alpha^2 + b^2} \tag{3}$$

$$\frac{d\vec{N}}{d\tilde{s}} = \tau'\vec{B} - \kappa'\vec{T}$$

The position vector of any point in the duct is written in terms of the physical basic vectors $(\vec{T},\vec{N},\vec{B})$ as

$$\vec{r} = \vec{R} + \tilde{x}\vec{N} + \tilde{y}\vec{B}, \quad \vec{R} = (bA)^2\tilde{s}\vec{T} - \alpha\vec{N} + \alpha \mathrm{b}A^2\tilde{s}\vec{B} \tag{4}$$

The coordinate system $(\tilde{s},\tilde{x},\tilde{y})$ is nonorthogonal as it can be seen from the infinitesimal relation

$$d\vec{r} = (1 - \kappa'\tilde{x})\vec{T}d\tilde{s} + (d\tilde{x} - \tau'\tilde{y}d\tilde{s})\vec{N} + (d\tilde{y} + \tau'\tilde{x}d\tilde{s})\vec{B} = d\tilde{s}\vec{e}_s + \mathrm{d}\tilde{x}\vec{e}_x + d\tilde{y}\vec{e}_y \tag{5}$$

and the appearance, in the product $d\vec{r}\cdot d\vec{r}$, of the terms $d\tilde{s}\,d\tilde{x}$ and $d\tilde{s}\,d\tilde{y}$. In this system, the so-called natural base vectors, which are tangents to the coordinate axes $\tilde{s}$, $\tilde{x}$, $\tilde{y}$ are given, respectively, by

$$\vec{e}_s = \frac{\partial\vec{r}}{\partial\tilde{s}} = (1 - \kappa'\tilde{x})\vec{T} - \tau'\tilde{y}\vec{N} + \tau'\tilde{x}\vec{B}, \quad \vec{e}_x = \frac{\partial\vec{r}}{\partial\tilde{x}} = \vec{N},$$

$$\vec{e}_y = \frac{\partial\vec{r}}{\partial\tilde{y}} = \vec{B} \tag{6}$$

and are nonorthogonal for the points off the $\tilde{s}$ axis. When $\tau' = 0$, the coordinate system reduces to a toroidal one. However for the correct visualization of the flow, it is necessary to express the governing equations in terms of the orthogonal physical basic vectors $(\vec{T},\vec{N},\vec{B})$. The $\vec{N}$ and $\vec{B}$ vectors coincide, respectively, with the $\tilde{x}$ and $\tilde{y}$ axes of the cross section of the duct, keeping invariant the required boundary conditions. Then the contravariant velocity components $\overline{u_1} = d\tilde{s}/dt$, $\overline{u_2} = d\tilde{x}/dt$, and $\overline{u_2} = d\tilde{y}/dt$, are related to the physical velocity components $\tilde{u}_1$, $\tilde{u}_2$, $\tilde{u}_3$ through the relations

$$\vec{V}=\overline{u}_1\vec{e}_1+\overline{u}_2\vec{e}_2+\overline{u}_3\vec{e}_3=\tilde{u}_1\vec{T}+\tilde{u}_2\vec{N}+\tilde{u}_3\vec{B} \tag{7}$$

$$\overline{u}_1=J\tilde{u}_1, \quad \overline{u}_2=\tilde{u}_2+\tau\tilde{y}J\tilde{u}_1, \quad \overline{u}_3=\tilde{u}_3-\tau\tilde{x}J\tilde{u}_1 \tag{8}$$

These $\tilde{x}$- and $\tilde{y}$-coordinate axes are appropriate for nonrotated cross sections. However as we proceed along the $\tilde{s}$ axis of the duct, with a finite torsion, the $\tilde{x}$ and $\tilde{y}$ coordinate axes are rotating. Thus at each $\tilde{s}$, rotating the vectors $\vec{N}$, $\vec{B}$ around $\vec{T}$ with an angle $\phi(\tilde{s})=\tau'\tilde{s}+\phi_0$ and letting for convenience, the arbitrary constant angle $\phi_0=0$, we obtain an orthogonal coordinate system (s',x',y') with the basic unit vectors $(\vec{T},\vec{a}_n,\vec{a}_b)$. In this case $\tilde{s}=s'$, whereas the coordinates $\tilde{x}$, $\tilde{y}$ and the vectors $\vec{N}$, $\vec{B}$ are related with the coordinates x', y' and the unit vectors $\vec{a}_n$, $\vec{a}_b$, respectively, through the transformations

$$\tilde{x}=x'\cos\phi(\tilde{s})+y'\sin\phi(\tilde{s}), \quad \tilde{y}=-x'\sin\phi(\tilde{s})+y'\cos\phi(\tilde{s}) \tag{9}$$

$$\vec{N}=\vec{a}_n\cos\phi(\tilde{s})+\vec{a}_b\sin\phi(\tilde{s}) \quad \vec{B}=-\vec{a}_n\sin\phi(\tilde{s})+\vec{a}_b\cos\phi(\tilde{s}) \tag{10}$$

so that the relations $\partial\tilde{x}/\partial\tilde{s}=\tau'\tilde{y}$ and $\partial\tilde{y}/\partial\tilde{s}=-\tau'\tilde{x}$ are held.

Using the relations (9) and (10), the infinitesimal $d\vec{r}$ is written

$$d\vec{r}=J^{-1}\vec{T}d\tilde{s}+\vec{N}d\tilde{x}+\vec{B}d\tilde{y}=J^{-1}\vec{T}ds'+\vec{a}_n dx'+\vec{a}_b dy' \tag{11}$$

where $J^{-1}=1-\kappa'\tilde{x}=1-\kappa' x'\cos\phi-\kappa' y'\sin\phi$.

At first, defining the velocity $\vec{V}'=u_1'\vec{T}+u_2'\vec{a}_n+u_3'\vec{a}_b$, the continuity and the Navier-Stokes momentum equations for the incompressible flow, are easily expressed in the orthogonal coordinate system (s',x',y'), and are given by

$$\vec{\nabla}\vec{V}'=0 \tag{12}$$

$$\frac{\partial\vec{V}'}{\partial t'}+(\vec{V}'\vec{\nabla})\vec{V}'=-\frac{1}{\rho}\vec{\nabla}P'-\nu\vec{\nabla}\times\vec{\nabla}\times\vec{V}'=-\frac{1}{\rho}\nabla P'+\nu\nabla^2\vec{V}'$$

where t' is the time, ρ is the density, ν is the kinematic viscosity, and P' is the pressure. Considering the character of the fully developed flow, the variation of the axial pressure gradient $\partial P'/\partial s'$ in the (x',y') plane is negligible whereas the pressure gradients $\partial P'/\partial x'$, $\partial P'/\partial y'$ depend only on x' and y'. Thus the pressure may be split into two terms, so that $P'=p_a'(s')+p'(x',y')$, where the axial pressure gradient $P_s'\equiv\partial p_a'/\partial s'$ is assumed to be a known constant and all other s' derivatives are neglected.

The continuity and the momentum component Eqs. (12) along the coordinates s', x', y' are given, respectively, by

Continuity equation

$$\frac{\partial u_1'}{\partial s'}+\frac{\partial}{\partial x'}\left(\frac{u_2'}{J}\right)+\frac{\partial}{\partial y'}\left(\frac{u_3'}{J}\right)=0 \tag{13}$$

Momentum equations

$$\rho\frac{\partial u_1'}{\partial t'}+\rho J u_1'\left(\frac{\partial u_1'}{\partial s'}-\kappa' u_2'\cos\phi-\kappa' u_3'\sin\phi\right)+\rho u_2'\frac{\partial u_1'}{\partial x'}+\rho u_3'\frac{\partial u_1'}{\partial y'}$$
$$=-JP_s'+\mu\left\{J^2\left(\frac{\partial^2 u_1'}{\partial s'^2}-\kappa'^2 u_1'-2\kappa'\cos\phi\frac{\partial u_2'}{\partial s'}+\kappa'\tau'\sin\phi u_2'-2\kappa'\sin\phi\frac{\partial u_3'}{\partial s'}-\kappa'\tau'\cos\phi u_3'\right)\right.$$
$$\left.+\kappa'\tau' J^3 y\left(\frac{\partial u_1'}{\partial s'}-\kappa' u_2'\cos\phi-\kappa' u_3'\sin\phi\right)+\frac{\partial^2 u_1'}{\partial x'^2}-\kappa' J\cos\phi\frac{\partial u_1'}{\partial x'}-\kappa' J\sin\phi\frac{\partial u_1'}{\partial y'}+\frac{\partial^2 u_1'}{\partial y'^2}\right\} \tag{14}$$

$$\rho\frac{\partial u_2'}{\partial t'}+\rho J u_1'\left(\frac{\partial u_2'}{\partial s'}+\kappa' u_1'\cos\phi\right)+\rho u_2'\frac{\partial u_2'}{\partial x'}+\rho u_3'\frac{\partial u_2'}{\partial y'}$$
$$=-\frac{\partial p'}{\partial x'}+\mu\left\{J^2\left(2\kappa'\cos\phi\frac{\partial u_1'}{\partial s'}-\kappa'\tau' u_1'\sin\phi+\frac{\partial^2 u_2'}{\partial s'^2}-\kappa'^2 u_2'\cos^2\phi-\kappa'^2 u_3'\sin\phi\cos\phi\right)\right.$$
$$\left.+J^3\kappa'\tau' y'\left(\kappa' u_1'\cos\phi+\frac{\partial u_2'}{\partial s'}\right)+\frac{\partial^2 u_2'}{\partial x'^2}-\kappa' J\cos\phi\frac{\partial u_2'}{\partial x'}+\frac{\partial^2 u_2'}{\partial y'^2}-\kappa' J\sin\phi\frac{\partial u_2'}{\partial y'}\right\} \tag{15}$$

$$\rho\frac{\partial u_3'}{\partial t'}+\rho J u_1'\left(\frac{\partial u_3'}{\partial s'}+\kappa' u_1'\sin\phi\right)+\rho u_2'\frac{\partial u_3'}{\partial x'}+\rho u_3'\frac{\partial u_3'}{\partial y'}$$
$$=-\frac{\partial p'}{\partial y'}+\mu\left\{J^2\left(2\kappa'\sin\phi\frac{\partial u_1'}{\partial s'}-\kappa'\tau' u_1'\cos\phi+\frac{\partial^2 u_3'}{\partial s'^2}-\kappa'^2 u_2'\cos\phi\sin\phi-\kappa'^2 u_3'\sin^2\phi\right)\right.$$
$$\left.+\kappa'\tau' J^3 y'\left(\kappa' u_1'\sin\phi+\frac{\partial u_3'}{\partial s'}\right)+\frac{\partial^2 u_3'}{\partial x'^2}-\kappa' J\cos\phi\frac{\partial u_3'}{\partial x'}+\frac{\partial^2 u_3'}{\partial y'^2}-\kappa' J\sin\phi\frac{\partial u_3'}{\partial y'}\right\} \tag{16}$$

The obtained equations, without any further transformation, can be used only for the description of the flow along a duct with circular cross section, because in this case of symmetry, the use of coordinates along the unit vectors $\vec{a}_n$, $\vec{a}_b$ or $\vec{N}$, $\vec{B}$ is equivalent. However in the case of noncircular cross sections like the square cross section, it is necessary to project the velocity components in the physical orthogonal vectors $\vec{N}$, $\vec{B}$, which coincide with the main axes of symmetry of the cross section. In this case the velocity is given by $\vec{V}=\tilde{u}_1\vec{T}+\tilde{u}_2\vec{N}+\tilde{u}_3\vec{B}$ and the change of variables is achieved by utilizing a rotating transformation to undo the initial rotation of the Frenet basic vectors.

The transformation of the governing equations from the coordinate system (s',x',y') to the system $(\tilde{s},\tilde{x},\tilde{y})$, is achieved using the coordinate transformations (9) and the transformations for the velocity and the derivative operator components which are given by

$$u_2'=\tilde{u}_2\cos\phi-\tilde{u}_3\sin\phi, \quad u_3'=\tilde{u}_2\sin\phi+\tilde{u}_3\cos\phi \tag{17}$$

$$\frac{\partial}{\partial s'}=\frac{\partial}{\partial\tilde{s}}+\tau'\tilde{y}\frac{\partial}{\partial\tilde{x}}-\tau'\tilde{x}\frac{\partial}{\partial\tilde{y}}, \quad \frac{\partial}{\partial x'}=\cos\phi\frac{\partial}{\partial\tilde{x}}-\sin\phi\frac{\partial}{\partial\tilde{y}},$$
$$\frac{\partial}{\partial y'}=\sin\phi\frac{\partial}{\partial\tilde{x}}+\cos\phi\frac{\partial}{\partial\tilde{y}} \tag{18}$$

The transformation of Eqs. (13)–(17) via the relations (9), (17), and (18) produces a set of equations where each of the momentum equations along the $\tilde{x}$ and $\tilde{y}$ directions, depends on both the pressure gradients $\partial p'/\partial\tilde{x}$ and $\partial p'/\partial\tilde{y}$. Thus, after some algebraic manipulations of these equations, two new $\tilde{x}$ and $\tilde{y}$ momentum component equations are obtained, each one of which depends

only on the corresponding pressure gradient $\partial p'/\partial \tilde{x}$ and $\partial p'/\partial \tilde{y}$. Finally substituting into these equations the nondimensional variables

$$t=\frac{t'\nu}{D_h^2},\quad s=\frac{\tilde{s}}{D_h},\quad x=\frac{\tilde{x}}{D_h},\quad y=\frac{\tilde{y}}{D_h},\quad u_i=\frac{\tilde{u}_i D_h}{\nu}\quad i=1,2,3 \tag{19}$$

$$J=(1-\kappa'\tilde{x})^{-1}=(1-\kappa x)^{-1},\quad P=\frac{P'}{\rho\nu^2/D_h^2},\quad \kappa=\kappa' D_h,$$

$$\tau=\tau' D_h$$

where D_h is the hydraulic diameter of the duct, and the nodimensional governing equations take the conservative form

Continuity equation

$$\tau\left(\mathrm{y}\frac{\partial}{\partial x}-\mathrm{x}\frac{\partial}{\partial y}\right)u_1+\frac{1}{J}\left(\frac{\partial \mathrm{u}_2}{\partial x}+\frac{\partial u_3}{\partial y}\right)-\kappa u_2=0 \tag{20}$$

The s-momentum equation

$$\begin{aligned}&\frac{\partial u_1}{\partial t}+\frac{\partial(u_2+\tau \mathrm{J}y u_1)u_1}{\partial x}+\frac{\partial(u_3-\tau J x u_1)u_1}{\partial y}-2\kappa J u_1 u_2\\&\quad=-J\left(P_s+\tau y\frac{\partial p}{\partial x}-\tau x\frac{\partial p}{\partial y}\right)+J^2\left[-2\kappa\tau\left(y\frac{\partial}{\partial x}-x\frac{\partial}{\partial y}\right)u_2\right.\\&\quad\quad-\tau^2\left(y\frac{\partial}{\partial y}+\mathrm{x}\frac{\partial}{\partial x}\right)\mathrm{u}_1+\tau^2\left(y\frac{\partial}{\partial x}-x\frac{\partial}{\partial y}\right)^2 u_1\\&\quad\quad\left.-\kappa(\kappa u_1+\tau u_3)\right]+\kappa\tau^2 J^3 y\left(y\frac{\partial}{\partial x}-x\frac{\partial}{\partial y}\right)u_1\\&\quad\quad-\kappa^2\tau J^3 y u_2+\left(\frac{\partial^2}{\partial x^2}+\frac{\partial^2}{\partial y^2}\right)u_1-\kappa \mathrm{J}\frac{\partial u_1}{\partial x}\end{aligned} \tag{21}$$

The x-momentum equation

$$\begin{aligned}&\frac{\partial u_2}{\partial t}+\frac{\partial(u_2+\tau \mathrm{J}y u_1)u_2}{\partial x}+\frac{\partial(u_3-\tau \mathrm{J}x u_1)u_2}{\partial y}-\tau \mathrm{J}u_1 u_3+\kappa J u_1^2\\&\quad\quad-\kappa \mathrm{J}u_2^2\\&\quad=-\frac{\partial \mathrm{p}}{\partial x}+J^2\left[2\kappa\tau\left(y\frac{\partial}{\partial x}-x\frac{\partial}{\partial y}\right)u_1+\tau^2\left(y\frac{\partial}{\partial x}-x\frac{\partial}{\partial y}\right)^2 u_2\right.\\&\quad\quad-\tau^2\left(y\frac{\partial}{\partial y}+x\frac{\partial}{\partial x}\right)u_2+2\tau^2\left(\mathrm{x}\frac{\partial}{\partial \mathrm{y}}-\mathrm{y}\frac{\partial}{\partial \mathrm{x}}\right)\mathrm{u}_3\\&\quad\quad\left.-(\kappa^2+\tau^2)\mathrm{u}_2\right]+\kappa\tau^2 \mathrm{J}^3\mathrm{y}\left(y\frac{\partial}{\partial x}-x\frac{\partial}{\partial y}\right)u_2\\&\quad\quad-\kappa\tau \mathrm{J}^3 y(\kappa u_1-\tau u_3)+\left(\frac{\partial^2}{\partial y^2}+\frac{\partial^2}{\partial x^2}\right)u_2-\kappa \mathrm{J}\frac{\partial u_2}{\partial x}\end{aligned} \tag{22}$$

The y-momentum equation

$$\begin{aligned}&\frac{\partial u_3}{\partial t}+\frac{\partial(u_2+\tau \mathrm{J}y u_1)u_3}{\partial x}+\frac{\partial(u_3-\tau \mathrm{J}x u_1)u_3}{\partial y}+\tau \mathrm{J}u_1 u_2-\kappa \mathrm{J}u_2 u_3\\&\quad=-\frac{\partial p}{\partial y}+J^2\left[2\tau^2\left(y\frac{\partial}{\partial x}-x\frac{\partial}{\partial y}\right)u_2+\tau^2\left(-y\frac{\partial}{\partial x}+x\frac{\partial}{\partial y}\right)^2 u_3\right.\\&\quad\quad-\tau^2\left(\mathrm{y}\frac{\partial}{\partial y}+x\frac{\partial}{\partial x}\right)u_3+\tau(\kappa u_1-\tau u_3)\Big]+\kappa\tau^2 J^3 y\left(y\frac{\partial}{\partial x}\right.\\&\quad\quad\left.-x\frac{\partial}{\partial y}\right)u_3+\kappa\tau^2 J^3 y u_2+\left(\frac{\partial^2}{\partial y^2}+\frac{\partial^2}{\partial x^2}\right)u_3-\kappa J\frac{\partial u_3}{\partial x}\end{aligned} \tag{23}$$

The system of equations is subjected to the boundary conditions

$$\begin{aligned}&u_1=u_2=u_3=0\quad \text{at the walls for } t\neq 0\\&u_2=u_3=0,\quad u_1(x,y)=\text{parabolic profile for } t=0\end{aligned} \tag{24}$$

The parabolic profile of $u_1(x,y)$ at $t=0$ is obtained as a solution of Eq. (21) with $u_2=u_3=0$, for given values of the parameters $P_s=\partial p_a/\partial s$, κ, and τ.

The average axial velocity $\tilde{U}_{\mathrm{av}}$, over the cross-section area S of the duct with width $a=1$, is defined by

$$\tilde{U}_{\mathrm{av}}=\frac{1}{S}\int_{-1/2}^{1/2}\int_{-1/2}^{1/2}\tilde{u}_1 d\tilde{x}\,d\tilde{y} \tag{25}$$

The Reynolds (Re) and Dean (De) numbers are defined by

$$\mathrm{Re}=\tilde{U}_{\mathrm{av}}D_h/\nu=U_{\mathrm{av}}\quad\text{and}\quad \mathrm{De}=\mathrm{Re}\,\kappa^{1/2} \tag{26}$$

and the friction factor $\mathrm{f_h}$ is given by

$$f_h=\left(-\frac{\partial p'}{\partial \tilde{s}}\right)/(2\rho\tilde{U}_{\mathrm{av}}^2)=\left(-\frac{\partial p}{\partial s}\right)/(2\ \mathrm{Re}\ U_{\mathrm{av}})$$

$$\text{or}\quad f_h\,\mathrm{Re}=-\frac{\partial p}{\partial s}\Big/(2U_{\mathrm{av}}) \tag{27}$$

3 CVP Computational Method

The system of Eqs. (20)–(27) under the boundary conditions (24) will be solved with the CVP computational method, which has been described in detail [4,5,22]. Illustrating the method, we first linearize, for simplicity, the nonlinear terms of the equations by lagging the coefficients. Then at each time level $n+1$, the axial velocity u_1 is calculated solving Eq. (21) and subsequently the transverse velocity components u_2 and u_3 are calculated solving Eqs. (22) and (23), for given values of the parameters $P_s\equiv\partial p_a/\partial \mathrm{s}$, κ, τ and the prescribed values of p^n at the nth level. Equations (21), (22), and (23) are solved by the (ADI) iterative method. The estimated values denoted as u_2^*, u_3^* do not satisfy the continuity equation. Thus the velocity components and consequently the pressure are corrected so that

$$u_2^{n+1}=u_2^*+\delta u_2,\quad u_3^{n+1}=u_3^*+\delta u_3,\quad p^{n+1}=p^n+\delta p \tag{28}$$

Subtracting the momentum equations for u_2^*, u_3^* from the corresponding initial Navier-Stokes equations, we obtain the following equations which are used for the calculation of the pressure gradient corrections, defined as $f_2\equiv\partial\delta p/\partial x$, and $f_3\equiv\partial\delta p/\partial y$

$$\frac{\partial\delta u_b}{\partial t}+A_b^c(\delta u_b)+A_b^d(\delta u_b)\equiv -f_b,\quad b=2,3 \tag{29}$$

where the terms $A_b^c(\delta u_b)$ and $A_b^d(\delta u_b)$ are given, respectively, by

$$A_2^c(\delta u_2)=\frac{\partial(u_2+\tau J y u_1)\delta u_2}{\partial x}+\frac{\partial(u_3-\tau J x u_1)\delta u_2}{\partial y}-\kappa J u_2\delta u_2 \tag{30}$$

$$\begin{aligned}A_2^d(\delta u_2)=&-J^2\left[\tau^2\left(y\frac{\partial}{\partial x}-x\frac{\partial}{\partial y}\right)^2\delta u_2-\tau^2\left(y\frac{\partial}{\partial y}+x\frac{\partial}{\partial x}\right)\delta u_2\right.\\&\left.-(\kappa^2+\tau^2)\delta u_2\right]-\kappa\tau^2 J^3 y\left(y\frac{\partial}{\partial x}-x\frac{\partial}{\partial y}\right)\delta u_2\\&-\left(\frac{\partial^2}{\partial y^2}+\frac{\partial^2}{\partial x^2}\right)\delta u_2+\kappa J\frac{\partial\delta u_2}{\partial x}\end{aligned}$$

$$A_3^c(\delta u_3)=\frac{\partial(u_2+\tau J y u_1)\delta u_3}{\partial x}+\frac{\partial(u_3-\tau J x u_1)\delta u_3}{\partial y}-\kappa J u_2\delta u_3 \tag{31}$$

$$A_3^d(\delta u_3) = -J^2\left[\tau^2\left(-y\frac{\partial}{\partial x}+x\frac{\partial}{\partial y}\right)^2\delta u_3-\tau^2\left(y\frac{\partial}{\partial y}+x\frac{\partial}{\partial x}\right)\delta u_3 - \tau^2\delta u_3\right]-\kappa\tau^2J^3y\left(y\frac{\partial}{\partial x}-x\frac{\partial}{\partial y}\right)\delta u_3 - \left(\frac{\partial^2}{\partial y^2}+\frac{\partial^2}{\partial x^2}\right)\delta u_3+\kappa J\frac{\partial\delta u_3}{\partial x}$$

In the terms $A_b^c(\delta u_b)$ and $A_b^d(\delta u_b)$, with $b=2$, 3, the velocities u_1, u_2, and u_3 are considered at the n time level.

In our method, for the determination of the corrections δu_2 and δu_3, a system of variational equations is required which is constructed as follows. At first the continuity variational equation is obtained from Eq. (20) using Eq. (28) so that

$$\frac{\partial\delta u_2}{\partial x}+\frac{\partial\delta u_3}{\partial y}-\kappa J\delta u_2=G$$

where

$$G=-\left(\frac{\partial u_2^*}{\partial x}+\frac{\partial u_3^*}{\partial y}\right)+\kappa J u_2^*-\tau J\left(y\frac{\partial u_1}{\partial x}-x\frac{\partial u_1}{\partial y}\right) \tag{32}$$

Secondly, differentiating Eq. (29) for $b=2$ and $b=3$ with respect to y and x, respectively, and subtracting the produced equations, the vorticity variational equation is obtained.

Substituting into the produced equation, the vorticity correction $\delta\vec{\omega}$ defined by

$$\vec{\nabla}\times\delta\vec{U}=\delta\vec{\omega}=\delta\omega\vec{k},\quad \delta\omega=\frac{\partial\delta u_3}{\partial x}-\frac{\partial\delta u_2}{\partial y} \tag{33}$$

and neglecting the terms depending on higher degrees of κ, τ, and the product $\kappa\tau$, as well as the quantity $(\partial A_3(\delta u_3)/\partial x - \partial A_2(\delta u_2)/\partial y)$ as particularly small, the vorticity variational equation is obtained, which takes the form

$$\frac{\partial\delta\omega}{\partial t}-\nabla^2\delta\omega+\kappa J\frac{\partial\delta\omega}{\partial x}=0 \quad \text{with boundary condition} \quad \delta\omega\big|_c = \left(\frac{\partial\delta u_3}{\partial x}-\frac{\partial\delta u_2}{\partial y}\right)\Bigg|_c \tag{34}$$

where c is the contour enclosing the cross section area.

Theoretically, solving the system of Eqs. (32) and (33) in conjunction with Eq. (34), we could evaluate the corrections δu_2 and δu_3. However the solutions of these two first-order partial differential equations could not satisfy all the required boundary conditions at the contour enclosing the cross-section area. To approach this problem, we use a theorem proved by Hatzikonstantinou [22], that states that instead of solving, Eqs. (32) and (33), we can solve an equivalent system of second-order partial differential equations. These equations are obtained by differentiating Eq. (32) with respect to x and y, respectively, and expressing the apparent first-order and mixed derivatives, using Eq. (33), in terms of $\delta\omega$. Thus δu_3 and δu_2 are determined solving the Poisson variational equations

$$\nabla^2\delta u_3-\kappa J\frac{\partial\delta u_3}{\partial x}=\frac{\partial G}{\partial y}+\frac{\partial\delta\omega}{\partial x}-\kappa J\delta\omega \tag{35}$$

$$\nabla^2\delta u_2-\kappa\frac{\partial(J\delta u_2)}{\partial x}=\frac{\partial G}{\partial x}-\frac{\partial\delta\omega}{\partial y} \tag{36}$$

where $\nabla^2=\partial^2/\partial x^2+\partial^2/\partial y^2$, under the boundary conditions

$$\delta u_2=\delta u_3=0 \quad \text{at the wall.} \tag{37}$$

For the restriction of the numerical violation of the theoretical Eqs. (32) and (33), calculated using the solutions of Eqs. (35) and (36), we apply the following technique. First solving Eq. (35) we obtain δu_3. Consequently, calculating the second-order derivative of δu_2 with respect to its nonparallel coordinate y from Eq. (33) and substituting its value into Eq. (36), we obtain the Poisson equation

$$\frac{\partial^2\delta u_2}{\partial x^2}-\kappa\frac{\partial(J\delta u_2)}{\partial x}=\frac{\partial G}{\partial x}-\frac{\partial\delta\omega}{\partial y}-Q$$

$$\text{where}\quad Q=\frac{\partial^2\delta u_2}{\partial y^2}=\frac{\partial^2\delta u_3}{\partial y\partial x}-\frac{\partial\delta\omega}{\partial y}. \tag{38}$$

Substituting δu_2 and δu_3 into Eq. (29) the pressure gradient corrections f_2 and f_3 are evaluated and the correction δp is obtained by solving the pressure variational equation

$$\nabla^2\delta p=\frac{\partial f_2}{\partial x}+\frac{\partial f_3}{\partial y}\quad \text{where}\quad \frac{\partial\delta p}{\partial x}=\frac{\partial\delta p}{\partial y}=0\quad \text{at the wall.} \tag{39}$$

The boundary conditions on δp are obtained from the fact that the normal to the walls pressure gradients $\partial p/\partial x$ and $\partial p/\partial y$ are zero in accordance with the boundary layer theory. Knowing δu_2 and δu_3 the required variables u_2^{n+1}, u_3^{n+1} are derived from Eq. (28). However the pressure and its space gradients are derived by the relations $p^{n+1}=p^n+\lambda\,\delta p$, $p_b^{n+1}=p_b^n+\lambda\,\delta p_b$, $b=x$, y, where λ is an underrelaxation parameter. Inserting the quantities u_2^{n+1}, u_3^{n+1}, and p^{n+1} into Eqs. (21), (22), and (23) the iterative procedure is repeated until convergence is achieved.

We consider three versions of the method denoted as CVP(i), CVP(ic), and CVP(r) respectively. The CVP(i) version relates the irrotational correction of the velocity components so that $\delta\omega\approx 0$. In this case the algorithm is simplified because Eq. (34) is not involved, while Eqs. (35) to (38) are simplified. In this version the convection and diffusion terms are also neglected from the pressure gradient correction Eqs. (29). The CVP(ic) version is also an irrotational version like the CVP(i); however, the convection and diffusion terms are taken into account in Eq. (29). The CVP(r) version relates the rotational correction of the velocity components, $\delta\omega\neq 0$. In this case the convection and the diffusion terms in Eq. (29) are also taken into account.

4 Numerical Accuracy

4.1 Criteria of Convergence. For the numerical solution of the presented equations we use a colocated uniform grid, where all the variables, velocity components, and pressure are defined at the same grid points. Let the symbol Φ represents any one of the dependent variables. Then at the points t_n, x_i, y_j, and s_k we have $\Phi_{i,j,k}^n=\Phi(t_n,x_i,y_j,s_k)$. For the space discretization of the derivatives within the finite difference formulation, three point central difference formulas are used for the internal nodes of the flow region, and one-sided three-point inward formulas of second order of accuracy are used for the nodes at the boundaries. The time derivatives are approximated by two-point backward-difference formulas of first order of accuracy, and the nonlinear terms of the equations are linearized by lagging the coefficients for simplicity. Thus at the time level $n+1$ we have $(vu)^{n+1}\approx v^n u^{n+1}$ where v and u stand for two velocity components. The solution of Eq. (34) using $\partial\delta\omega/\partial t=(\delta\omega^{n+1}-\delta\omega^n)/\Delta t$ with $\delta\omega^n=0$ can be accelerated, if instead of $\delta\omega^n=0$, $\delta\omega^n$ is calculated via Eq. (33) using the known values of δu_2^n and δu_3^n.

The time dependent momentum equations Eqs. (21), (22), and (23) are solved applying the ADI iterative method, using a time step Δt which satisfies the relation

$$\Delta t\leqslant\frac{1}{6}\left(\frac{\Delta x^2+\Delta y^2}{2}\right) \tag{40}$$

Then, the values of the truncation errors vary less than 1% when the chosen value of Δt is doubled or tripled.

Table 1 Effect of the CVP(ic) and CVP(r) versions on the f_h Re and De factors in flows with $P_s=-20{,}000$, $\kappa=0.25$, and $\tau=0.1$

Grid	CVP(ic) De	CVP(ic) f_h Re	CVP(r) De	CVP(r) f_h Re	Percent difference in f_h Re
41×41	207.834	24.057	208.32	24.001	0.23
61×61	209.16	23.906	209.51	23.866	0.16
81×81	212.72	23.505	212.615	23.517	0.05
101×101	214.904	23.266	214.256	23.337	0.30

Because of the complexity of the momentum differential equations, the time iterative procedures for the evaluation of the variables u_1, u_2, u_3 are completed when the following conditions are satisfied, respectively:

$$\sqrt{\frac{1}{I^*J}\sum_{i=1,j=1}^{I,J}\left(\frac{(u_1^{n+1}-u_1^n)^2}{(u_1^{n+1})^2}\right)_{i,j}} \leqslant e_1 = 6^*10^{-5}$$

$$\sqrt{\frac{1}{I^*J}\left(\sum_{i=1,j=1}^{I,J}\frac{|(u_2^{n+1}-u_2^n)|}{(V_{\text{total}}^{n+1})}\right)_{i,j}} \leqslant e_1 \qquad (41)$$

$$\sqrt{\frac{1}{I^*J}\left(\sum_{i=1,j=1}^{I,J}\frac{|(u_3^{n+1}-u_3^n)|}{(V_{\text{total}}^{n+1})}\right)_{i,j}} \leqslant e_1$$

where $V_{\text{total}}=\sqrt{u_2^2+u_3^2}$ and I, J are the number of nodes along the x and y axes, respectively.

In the rotational version CVP(r), at each $n+1$ level, the internal iteration procedure for the calculation of $\delta\omega$, δu_2, and δu_3, solving the coupled Eqs. (34), (35), and (36), is repeated until the following convergence criterion is satisfied:

$$\left[\left(\sum_{i,j=1}^{I,J}\delta w\right)^{n+1}-\left(\sum_{i,j=1}^{I,J}\delta w\right)^{m}\right]\Big/\left(\sum_{i,j=1}^{I,J}\delta w\right)^{m+1} \leqslant e_2 \qquad (42)$$

where δw stands for $\delta\omega$, δu_2, and δu_3. For optimal values $e_2 \approx 0.1$, the number of internal iterations m, at each time level $n+1$, does not exceed the number $m=2$, except from the first ten time iterations for which $m=3$. The use of smaller values for e_2 results in a drastic increase of the internal iterations without a significant variation of the accuracy of the method.

The Poisson Eqs. (31), (32), (35), and (36) are solved with the Gauss-Seidel iterative algorithm, until the corresponding convergence criterions for $\delta M=\delta\omega$, δu_3, δu_2 are satisfied

$$\sqrt{\frac{1}{I^*J}\left(\sum_{i=1,j=1}^{I,J}\left(\frac{(\delta M^{\lambda+1}-\delta M^{\lambda})^2}{(\delta M^{\lambda+1})^2}\right)\right)} \leqslant e_3. \qquad (43)$$

For $\delta M=\delta\omega$, δu_3, δu_2 we choose $e_3 \cong 0.05$ and for $\delta M=\delta p$ we choose $e_3 \cong 0.5$.

The computational time for the overall convergence of the solution can be reduced if, instead of using the criteria of Eq. (40), the iterations of the Poisson correction equations are executed for a limited number of times. It is clear that the reduced accuracy of the solutions of the Poisson equations and of the internal iteration does not affect the accuracy of the method, which is governed by the criterion Eq. (41), but reduces drastically the time of convergence.

4.2 Accuracy of the Methodology. For the convergence of the computational procedure, the use of an under-relaxation parameter λ in the pressure gradient relations is necessary, because of the high complexity of the governing equations of the problem and the lack of symmetry of the flow. It is noted that in simpler cases, such as flows within straight or curved ducts, and high Dean numbers [4,5,22], the CVP method always converges without using any under-relaxation parameter. In the present study, for the under-relaxation parameter, we have given the value $\lambda=0.1$ for Dean numbers De<200 and ratio $\epsilon=\tau/\kappa \ll 1$ and $\lambda=0.0025$ for De>200 and ratio $\epsilon=\tau/\kappa \approx 1$.

The computational domain is the square cross section of the duct ($-0.5<x<0.5, -0.5<y<0.5$). The effects of the grid size on the friction product f_h Re and the Dean number are shown in Table 1, for a flow with $P_s=-20{,}000$, $\kappa=0.25$, $\tau=0.1$.

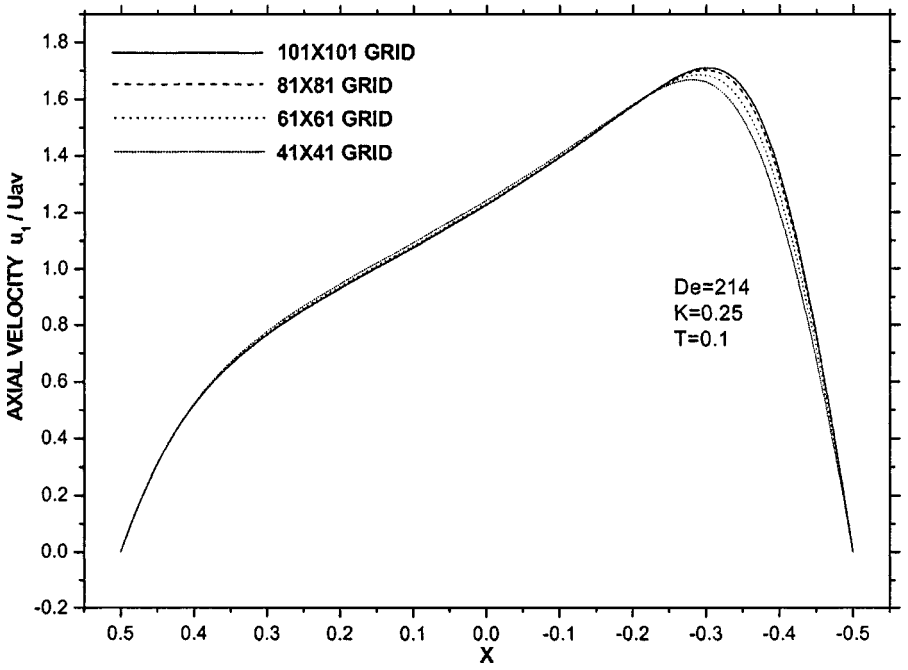

Fig. 2 Effect of the grid on the axial velocity u_1/U_{av} along the x ($y=0$) axes, when $\kappa=0.25$, $\tau=0.1$, and De=214

Table 2 Results for f_h/f_s and De when $\kappa=0.01$, $\tau=0.01$ with the CVP(ic) and other methods

Grid	P_s	U_{av}	Dean number	f_h/f_s	f_h/f_s Chen [18]	f_h/f_s Bolinder and Sunden [16]
61×61	−20,000	591.34	59.13	1.188	⋯	1.235
61×61	−40,000	1304.00	103.40	1.359	⋯	1.416
61×61	−60,000	1425.76	142.57	1.479	⋯	1.550
61×61	−80,000	1807.80	180.78	1.555	⋯	1.663
81×81	−100,000	2182.00	218.20	1.610	⋯	1.768
81×81	−120,000	2427.70	242.77	1.737	1.73	1.837

The results indicate also the effect of the irrotational [CVP(ic)] or of the rotational character [CVP(r)] of the velocity corrections on the formation of the flow field. In the CVP(ic) version, the percentage differences of the results for the friction product f_h Re are 0.63% for those obtained using 41×41 and 61×61 grids, 1.7% for those obtained using 61×61 and 81×81 grids, 1.02% for those obtained using 81×81 and 101×101, and a total of 3.4% for those obtained using 41×41 and 101×101 grids. Similar results are obtained for the CVP(r) version. The effect of the grid size on the profile of the axial velocity u_1/U_{av} along the x axes is shown in Fig. 2, for $\kappa=0.25$, $\tau=0.1$, and De=214. The accuracy of the results is established for numerical Peclet numbers $u_3(j,i)*\Delta y<2$ and $u_2(j,i)*\Delta x<2$, for avoiding oscillations in the solutions. Consequently as De increases the optimum grid size also increases.

Table 3 Results for f_h/f_s and De when $\kappa=0.01$, $\tau=0.1$ with the CVP(ic) and other methods

Grid	P_s	U_{av}	Dean number	f_h/f_s	f_h/f_s Chen [18]	f_h/f_s Bolinder and Sunden [16]
61×61	−10,000	329.58	32.96	1.066	1.06	⋯
61×61	−30,000	799.24	79.92	1.319	⋯	⋯
61×61	−50,000	1193.40	119.34	1.472	⋯	⋯
61×61	−70,000	1578.00	157.80	1.559	⋯	⋯

Table 6 Results for f_h/f_s and De when $\kappa=0.25$, $\tau=0.1$ with the CVP(ic) and other methods

Grid	P_s	U_{av}	Dean number	f_h/f_s CVP (ic)	f_h/f_s Chen [18]	f_h/f_s Bolinder and Sunden [16]
61×61	−20,000	413.53	209.5	1.680	⋯	1.737
61×61	−40,000	706.98	353.5	1.988	⋯	2.123
81×81	−60,000	943.0	471.5	2.235	⋯	2.403
101×101	−80,000	1161.93	581.0	2.419	⋯	2.642

The difference between the results obtained for f_h Re with the CVP(ic) and CVP(r) versions is, on average, about 0.19% for various grids from 41×41 to 101×101. This indicates that the version CVP(ic) may be preferred, considering that it is three times faster in the convergence time than the CVP(r) version, which includes an additional internal iteration for the solution of the variational velocity corrections, at each time level. Hereafter all the presented results have been obtained with the CVP(ic) version, if not noted otherwise.

5 Results and Discussion

5.1 Torsion Effect on the Friction Factor. Tables 2–6 show the variations in the ratio of the friction factor of a helical duct f_h Re to that of a straight duct f_s Re, the average velocity U_{av} and the Dean number for various values of the axial pressure gradients P_s, curvature, torsion, and grid size.

The results are then compared with those obtained by Chen [18] and Bolinder and Sunden [16]. For a straight duct the value f_s Re=14.23 has been determined analytically by Kays and Crawford [23]. Results obtained with $\kappa=0.01$, $\tau=0.01$ and $\kappa=0.01$, $\tau=0.1$ are shown in Tables 2 and 3, respectively, and the results

Table 4 Results for f_h/f_s and De when $\kappa=0.1$, $\tau=0.05$ with the CVP (ic) and other methods

Grid	P_s	U_{av}	Dean number	f_h/f_s CVP (ic)	f_h/f_s Chen [18]	f_h/f_s Bolinder and Sunden [16]
61×61	−10,000	265.9	84.086	1.324	1.33	1.343
61×61	−20,000	467.34	147.79	1.503	⋯	1.565
81×81	−30,000	659.58	208.58	1.598	⋯	1.74
81×81	−40,000	805.74	254.8	1.744	⋯	1.87
81×81	−50,000	949.8	300.35	1.850	⋯	1.99
81×81	−60,000	1083.4	342.6	1.945	⋯	2.096
81×81	−70,000	1200.1	379.78	2.048	⋯	2.189
81×81	−80,000	1322.9	418.33	2.125	⋯	2.28
81×81	−90,000	1435.8	454.04	2.202	⋯	2.364
81×81	−100,000	1555.0	491.7	2.260	⋯	2.45
101×101	−110,000	1667.7	527.4	2.318	⋯	2.53
101×101	−120,000	1771.6	560.23	2.38	2.38	2.60

Table 5 Results for f_h/f_s and De when $\kappa=0.1$, $\tau=0.1$ with the CVP(ic) and other methods

Grid	P_s	U_{av}	Dean number	f_h/f_s CVP (ic)	f_h/f_s Chen [18]	f_h/f_s Bolinder and Sunden [16]
61×61	−10,000	265.024	83.80	1.325	1.33	1.343
61×61	−20,000	462.2	146.16	1.520	⋯	1.558
81×81	−30,000	659.02	208.4	1.600	⋯	1.74
81×81	−40,000	817.86	258.63	1.719	⋯	1.877
81×81	−50,000	967.18	305.85	1.817	⋯	2.003
81×81	−60,000	1086.4	343.56	1.941	⋯	2.10
101×101	−70,000	1239.6	392.0	1.984	⋯	2.22
101×101	−80,000	1315.04	415.85	2.138	⋯	2.275
101×101	−90,000	1436.7	454.32	2.201	⋯	2.365
101×101	−100,000	1562.12	494.0	2.250	⋯	2.454
101×101	−120,000	1786.6	565.0	2.36	2.41	2.608

Table 7 Effect of torsion on f_h/f_s and De when $P_s=-1\times10^4$, -3×10^4

$\kappa=0.1$	$P_s=-10{,}000$		$P_s=-30{,}000$	
τ	f_h/fs	De	f_h/fs	De
0.00	1.317	84.38	1.637	203.66
0.01	1.292	85.98	1.593	209.26
0.05	1.324	84.09	1.598	208.58
0.10	1.325	83.80	1.600	208.40
0.15	1.330	83.50	1.633	204.13
0.20	1.335	83.20	1.629	204.65
0.25	1.334	83.30	1.689	197.33

indicate that the increase of torsion increases the values of friction factor. Results obtained with $\kappa=0.1$, $\tau=0.05$, and $\kappa=0.1$, $\tau=0.1$ are shown in Tables 4 and 5, respectively.

Their results show that as $|P_S|$ varies from 10^4 to 1.2×10^4, the friction ratio f_h/f_s increases on average about 78%. However, Table 5 shows, that for $\kappa=0.1$, as τ increases from 0 to 0.1, in the range of $|P_S|$ from 10^4 to 3×10^4, the factor f_h/f_s decreases by about 20%, and in the range 3×10^4 to 1.2×10^4, the factor f_h/f_s increases by about 48%. Our results show that the decrease in the function $f_h/f_s(\tau)$ for $\tau\ll0.01$ tends to disappear as $|P_S|$ becomes larger than 1.2×10^5, in agreement with the findings of Chen and Jan [17]. Results obtained with $\kappa=0.25$ and $\tau=0.1$ are also shown in Table 6.

From Tables 3, 5, and 6, it is observed that for $\tau=0.1$, as $|P_S|$ ranges from 10^4 to 5×10^4, the ratio f_h/f_s increases about 38% when $\kappa=0.01$, about 20% when $\kappa=0.1$, and about 26% when $\kappa=0.25$. The clear effect of the torsion on the ratio f_h/f_s is very small; it is shown in Table 7 for results obtained with $\kappa=0.1$ and $P_s=-10^4$, -3×10^4.

For $P_s=-10^4$ as τ increases from 0–0.1, the ratio f_h/f_s decreases about 2% and subsequently as τ increases from 0.1–0.25, the ratio f_h/f_s increases about 3.25%. Similarly for $P_s=-3\times10^4$ as τ increases from 0–0.1, the ratio f_h/f_s decreases about 2.7% and subsequently as τ increases from 0.1–0.25, the ratio f_h/f_s increases about 6%. These results are enhanced as P_s increases further. The decrease of f_h as τ increases for $\tau<0.01$, is the result of the increase of the axial velocity from the deformation of the toroidal axial velocity profile ($\tau=0$) produced by the centrifugal forces. The appearance of torsion destroys the pairs of vortices of the secondary flows, increasing the circulation of the flow around the walls of the duct. However, the further increase of torsion substantially increases the swirl of the flow, which leads to a decrease in the axial velocity, and increase in the transverse velocity components and consequently, the increase in the friction factor. Careful observation shows that the effect of torsion is of first order.

Our results for f_h/f_s compared with those obtained by Chen and Jan [17], with a finite element method, differ in average only about 0.55%, with a maximum difference of 2% when De=565 ($\kappa=\tau=0.1$, Table 5). However our results compared with those obtained by Bolinder and Sunden using a scheme based on the SIMPLE method [16], differ on average by 6.55%, with a maximum difference of 10% when De=392 ($\kappa=\tau=0.1$, Table 6). The significant discrepancy in agreement may be attributed to the latter's use of a hybrid difference scheme employing an appropriate combination of the SIMPLEC and SIMPLE methods. This scheme incorporates four under-relaxation parameters which evidently affect not only the convergence but the solution itself, whereas for the time step Δt, which also seriously affects the calculation, no-one information is given.

5.2 Torsion Effect on the Secondary Flow. For a better understanding of the balance between the centrifugal forces and the action of torsion, it is necessary to determine the most important terms and their effects on the momentum equations. The most important terms representing the centrifugal forces are the terms $-2\kappa Ju_1u_2$ and $\kappa J\partial u_1/\partial x$ in Eq. (21), the terms $\kappa J(u_1^2-u_2^2)$ and $-\kappa J\partial u_2/\partial x$ in Eq. (22) and the terms κJu_2u_3 and $-\kappa J\partial u_3/\partial x$ in Eq. (23). However in a helical flow with a finite pitch, the most important terms representing the effect of torsion are the coefficients $u_2+\tau Jyu_1$ and $u_3-\tau Jxu_1$, of the convection terms in Eqs. (22) and (23), which are responsible for the circulation of the fluid around the duct's wall, and deforming the pairs of vortices which are produced by the centrifugal forces. In addition, the torsion effect, to first order, in τ and $\kappa\tau$ is represented by the term P_s

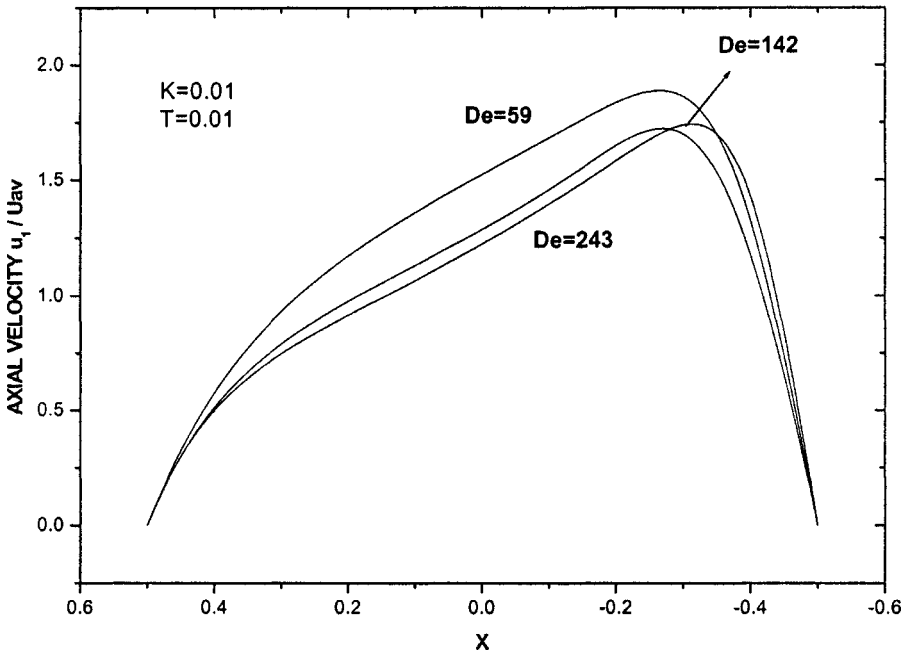

Fig. 3 Profiles of u_1/U_{av} along the x ($y=0$) axes when $\kappa=0.01$, $\tau=0.01$, and De=59, 142, 243

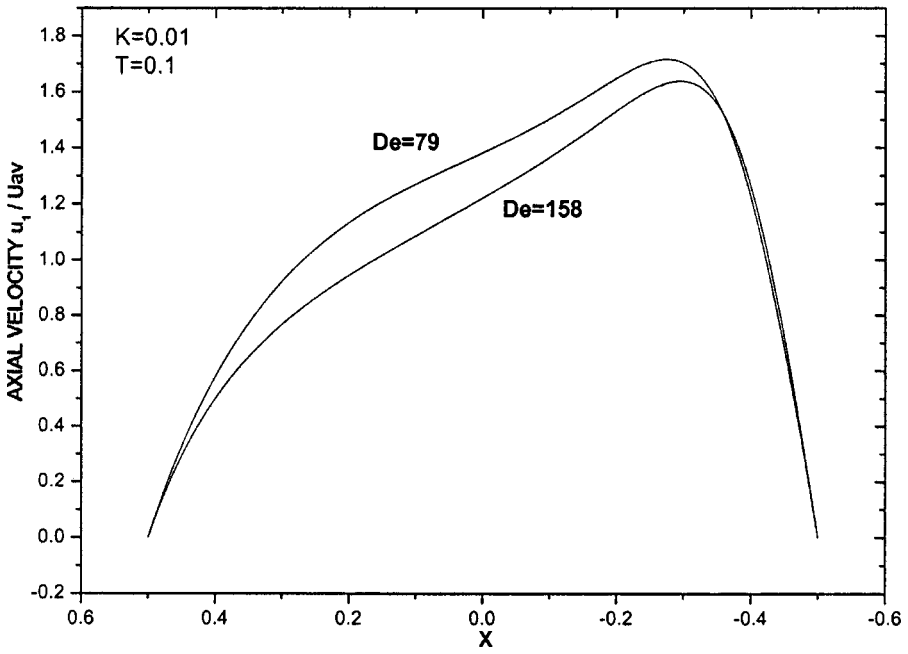

Fig. 4 Profiles of u_1/U_{av} along the x ($y=0$) axes when $\kappa=0.01$, $\tau=0.1$, and De=79, 158

$+\tau y\partial p/\partial x-\tau x\partial p/\partial y$ in Eq. (21), by the terms $\tau J u_1 u_3$ and $2\kappa\tau J^2(y\partial/\partial x-x\partial/\partial y)u_1$ in Eq. (22), and by the terms $\tau J u_1 u_2$ and $\tau\kappa J^2 u_1$ in Eq. (23).

The profiles of u_1/U_{av} along the x ($y=0$) axes are shown in Fig. 3, for $\kappa=0.01$, $\tau=0.01$ and De=59, 142, and 243 and in Fig. 4, for $\kappa=0.01$, $\tau=0.1$ and De=79 and 158. Similar profiles along the y ($x=0$) axes are shown in Figs. 5 and 6, respectively. For $\kappa=0.01$, as τ increases the parabolic profile of u_1/U_{av} along the x axis slightly increases particularly toward the inner part of the duct (Figs. 3, 4). However Figs. 5 and 6 show that as τ increases the symmetric profile of u_1/U_{av} along the y axis is strongly deformed. The peak of the axial velocity in the upper half of the cross section increases and is shifted to the upper wall of the duct, whereas the corresponding pick in the lower half of the cross section decreases substantially, due to the transferring of kinetic energy and the increase in the transverse velocity components. These changes are due to the convection terms and the $P_s+\tau y\partial p/\partial x-\tau x\partial p/\partial y$ term in Eq. (21), which redistribute the swirl of the flow. This trend is intensified as the ratio $\epsilon=\tau/\kappa$ increases from 1 to 10. It is noted that for $\epsilon=1$, that is $\tau=\kappa$, the pitch takes its maximum value. The variations of the axial velocity profiles along a helical duct when $\kappa=0.1$, $\tau=0.05$ are shown better in the contour diagrams of Fig. 7. Similar patterns are obtained for other parametric values, with various Dean numbers.

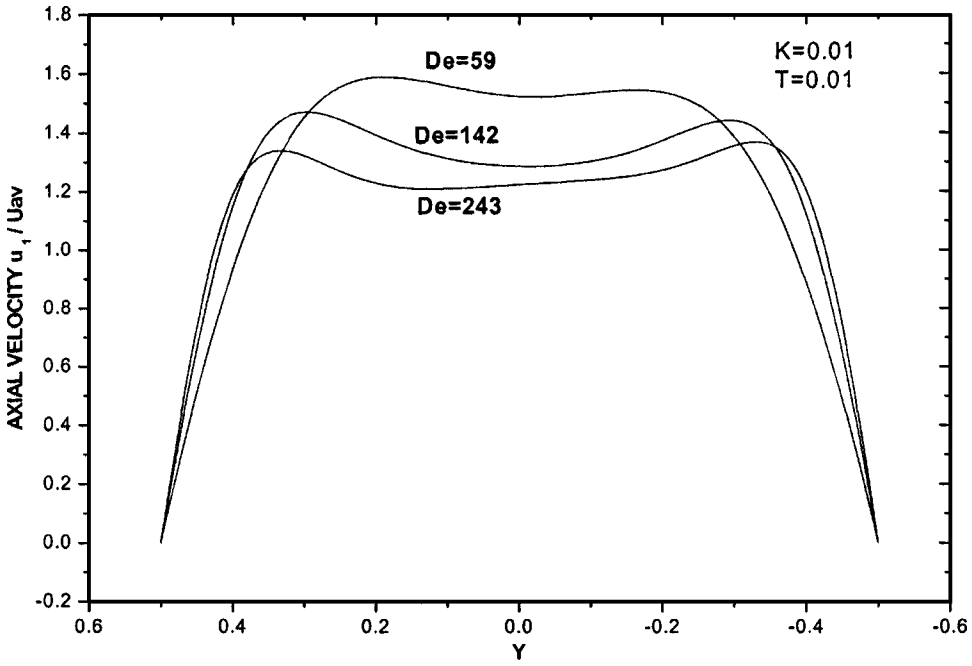

Fig. 5 Profiles of u_1/U_{av} along the y ($x=0$) axes when $\kappa=0.01$, $\tau=0.01$, and De=59, 142, 243

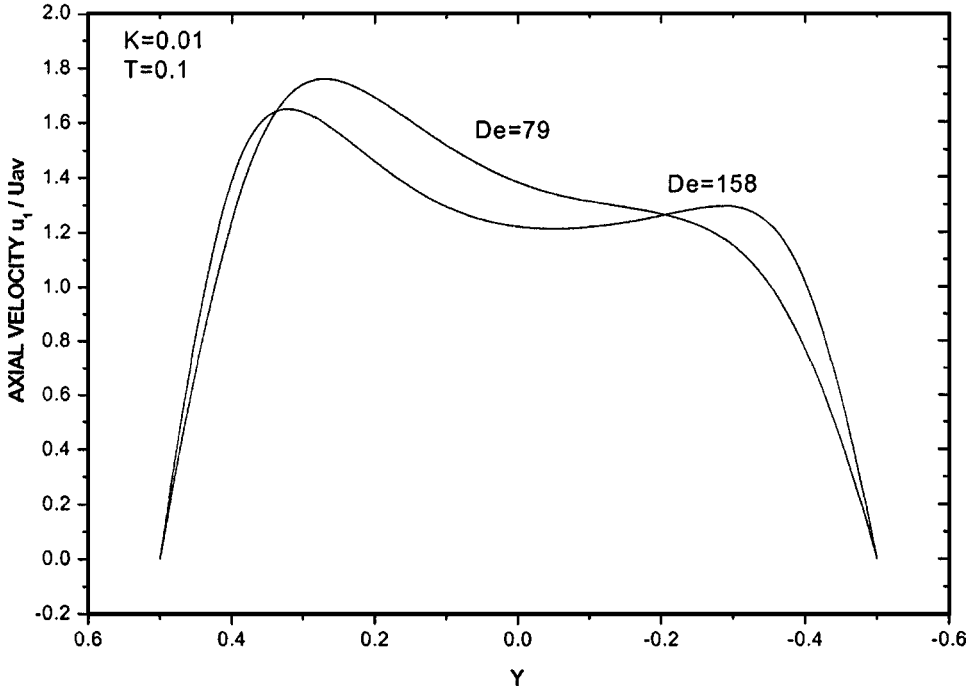

Fig. 6 Profiles of u_1/U_{av} along the y ($x=0$) axes when $\kappa=0.01$, $\tau=0.1$, and De=79, 158

For better understanding of the development of the flow, we construct the contour plots of the stream function Ψ of the transverse velocity defined by the equations $u_2=-\partial\Psi/\partial y$ and $u_3=\partial\Psi/\partial x$ and calculated by solving the Poisson equation $\nabla^2\Psi=\partial u_3/\partial x-\partial u_2/\partial y$.

The contour plots of the transverse velocity, for $\kappa=0.1$ and $\tau=0.15$, 0.2 when $P_s=-10{,}000$ are shown in Fig. 8, and the contour plots as the torsion increases from 0.01 to 0.25 are shown in Fig. 9 for $P_s=-30{,}000$. The increase in torsion yields the distortion of the symmetry of the flow, enlarging the lower vortex at the expense of the upper vortex. This is due to an increase in the transverse velocities at the expense of the axial velocity at the lower part of the cross section. The increase of the swirling area of the flow is due mainly to the role of the coefficients $u_2+\tau Jyu_1$ and $u_3-\tau Jxu_1$ of the convection terms. The increase of P_s intensify the phenomenon. Figure 9(*a*) shows that when the centrifugal forces are dominated with $\epsilon=0.1$, the secondary flow preserves the main pair of the centrifugal vortices. However as the torsion increases so that $\epsilon=0.1$, 1.5, 2, 2.5, the increasing swirl of the flow dominates the main two centrifugal vortices and increases the tendency of the squeezed upper vortex to separate into smaller vortices moving in the opposite direction. A careful observation of the contour plots shows that for large values of torsion [Figs. 9(*c*), 9(*d*)] an additional small squeezed vortex is created near the upper duct wall. However, an important observation is the interchange of mass flow between the lower and upper vortices. The streams of fluid which are interchanged between the two vortices are merged with the rotating fluid of the vortices. This phenomenon is more clearly shown in vector plots.

The effect of the Dean number on the flow with $\kappa=0.1$ and $\tau=0.05$ is shown in Fig. 10. Here again with small torsion and Dean numbers the main pair of the centrifugal vortices persists

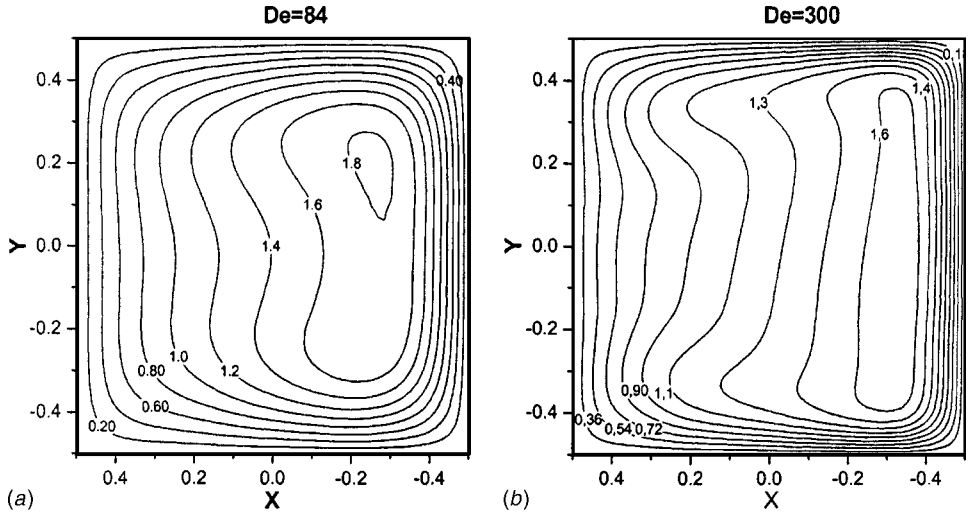

Fig. 7 Contours of u_1/U_{av} when $\kappa=0.1$, $\tau=0.05$, and De=84, 300

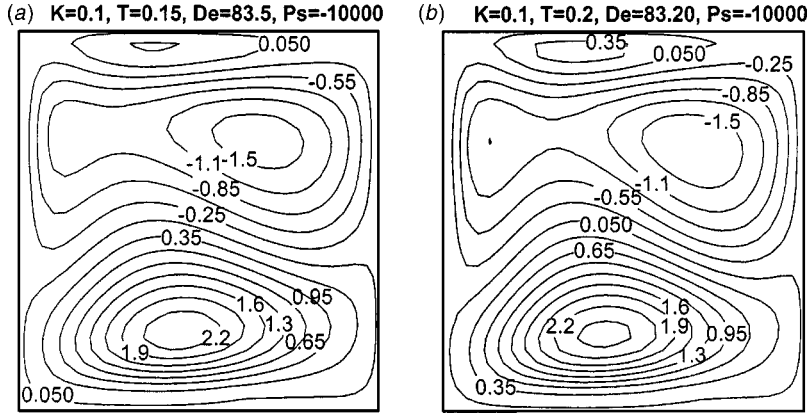

Fig. 8 Contours of the transverse velocity, shown the effect of torsion on the secondary flow when κ=0.1, τ=0.15, and 0.2 for p_s=−10,000

[Fig. 10(*a*)]. These results for low values of torsion are in closer agreement with the results obtained by Bolinder and Sunden [16], and in disagreement with the results obtained by Chen [18]. However, as the Dean number increases, the lower vortex enlarges at the expense of the upper velocity vortex. As De increases to large values strong swirl flows are generated, particularly along the corners and the walls of the duct. The increase of the torsion intensifies this trend and large flow quantities tend to be exchanged near and along the vertical walls of the duct. Comparing Figs. 9 and 10 it is concluded that a more uniform stirring of the flow may be achieved by increasing the torsion, keeping relatively low Dean numbers. This is particularly evident from Fig. 9(*d*) with the largest torsion τ=0.25 and the slightly lower Dean number De =197.33 from the other figures of Fig. 9. This reveals that in the dynamic evolution of the flow, as the torsion increases the average time of stirring of fluid clusters, around the wall of the duct, increases. This phenomenon is of particular importance in various chemical processes.

The contour plots of flows with κ=0.01, τ=0.01, De=183 having ϵ=1 and κ=0.01, τ=0.1, De=158 having ϵ=10>1 are shown in Fig. 11. These results show that for small curvature and very large values of ϵ, which corresponds to the domination of the torsion, the lower vortex is enlarged substantially, its center is moved toward the center of the duct, and the circulation of its flow becomes homogeneous. The upper vortex is squeezed strongly and is divided into two much smaller vortices moving in

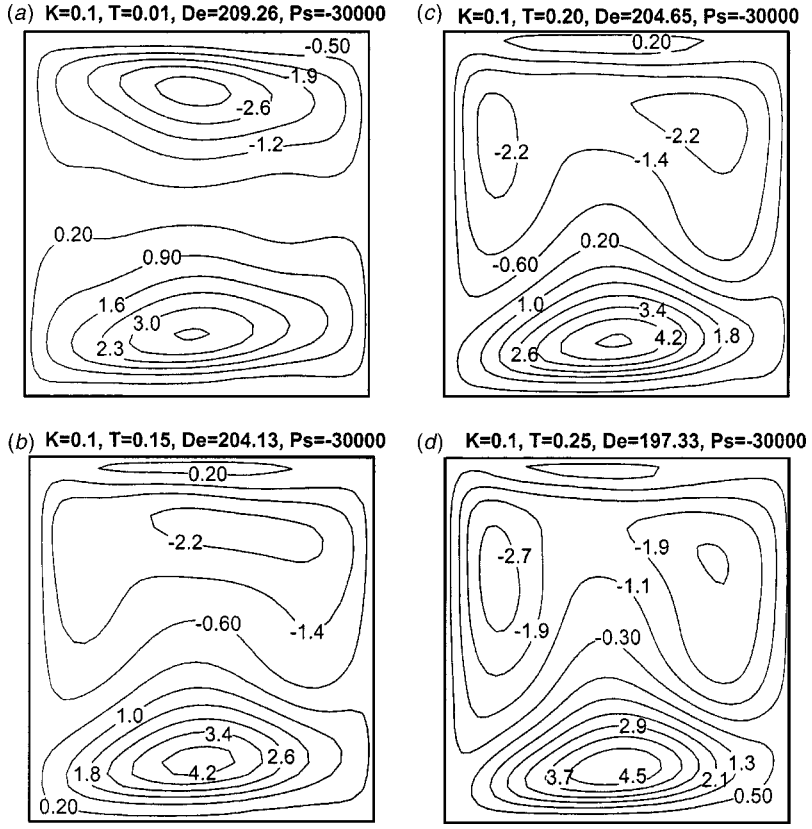

Fig. 9 Contours of the transverse velocity, shown the effect of torsion on the secondary flow when κ=0.1, τ=0.01, 0.15, 0.2, 0.25 for p_s=−300,000

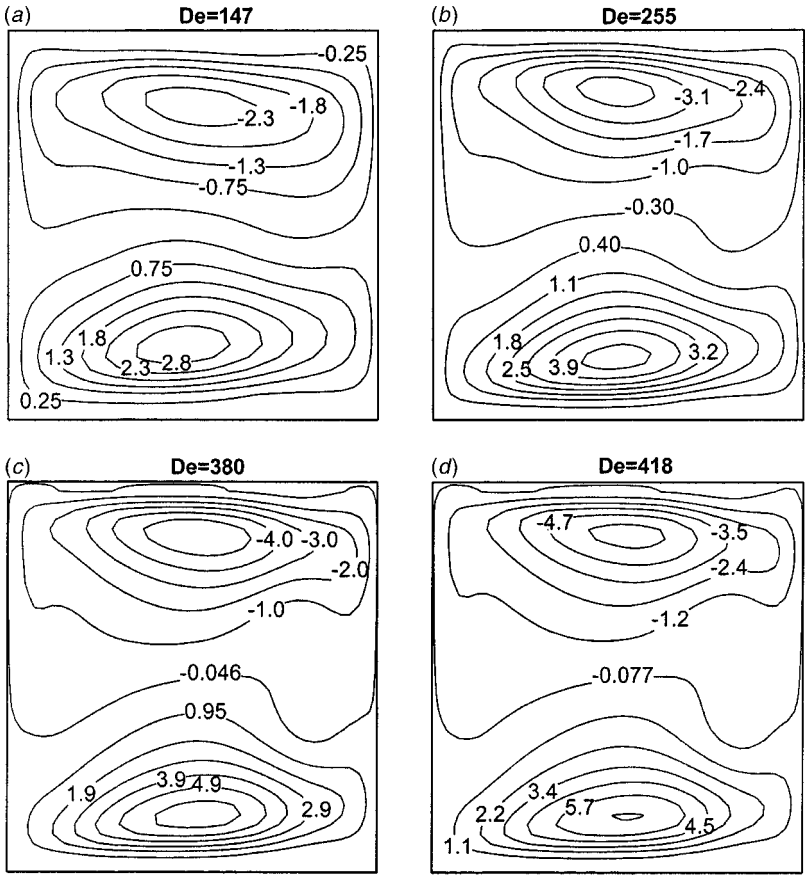

Fig. 10 Contours of the transverse velocity shown the effect of Dean number on the secondary flow when κ=0.1 and τ=0.05

opposite directions to the vertical walls of the duct. Thus as $\kappa \rightarrow 0$ and $\epsilon \gg 1$ the flow tends to that of a twisted duct with a much weaker secondary flow and an axial flow shifted to the inside of the helical duct, in agreement with the conclusions of Bolinder and Sunden [16] and Chen [18].

6 Concluding Remarks

The incompressible fully developed laminar flow in a helical square duct is studied for various values of curvature, torsion, and axial pressure gradients. Numerical results are obtained with the CVP computational procedure, using a colocation grid for all the variables of the problem. The method is more easily applicable to complex internal flows than other methods, without the introduction of spurious oscillations in the solutions.

The transient computations reveal that for very small values of torsion the centrifugal forces are dominant and two stable vortices in the secondary flow are still appeared. The increase of torsion and particularly for high Dean numbers, deforms the overall velocity symmetry of the flow, so that large flow quantities of the two main vortices tend to be exchanged near and along the verti-

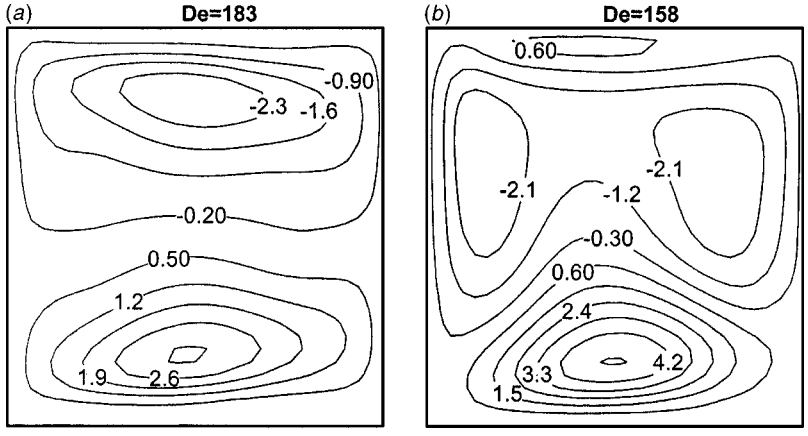

Fig. 11 Contours of the transverse velocity shown the effect of torsion on the secondary flow when (*a*) ϵ=1 with κ=0.01, τ=0.01, and De=183 and (*b*) ϵ=10 with κ=0.01, τ=0.1, and De=158

cal walls of the duct. It is proved that for large values of the torsion and yet moderate values of the Dean number there is a substantial swirling of the flow. The results indicate that the effect of torsion is of ''first order'' and results to the destruction of the symmetry of the internal secondary flow, enlarging the lower vortex to the expense of the upper vortex. However for the complete determination of the possible bifurcation structure, a detailed and may be direct method is needed.

Nomenclature

a = width of the duct ($=1$)
b = $h/(2\pi)$
D_h = hydraulic diameter
De = Dean number ($=\mathrm{Re}\,\kappa^{1/2}$)
f_h = friction factor of helical duct
f_s = friction factor of straight duct
h = pitch of helical duct ($=2\pi$b)
$\vec{i}, \vec{j}, \vec{k}$ = Cartesian unit vectors
P' = total dimensional pressure
P_s = axial pressure gradient ($=\partial p_a/\partial s$)
p = nondimensional pressure
$\vec{R}$ = describes the center line of the helical duct
Re = Reynolds number ($=\tilde{U}_{\mathrm{av}} D_h/\nu = U_{\mathrm{av}}$)
$\tilde{s},\tilde{x},\tilde{y}$ = dimensional non-orthogonal coordinate axes
s',x',y' = dimensional orthogonal coordinate axes
s, x, y = nondimensional orthogonal coordinate axes
$\vec{T},\vec{N},\vec{B}$ = Frenet's unit vectors
$\tilde{u}_1,\tilde{u}_2,\tilde{u}_3$ = dimensional velocity components along $(\tilde{s},\tilde{x},\tilde{y})$
u_1',u_2',u_3' = dimensional velocity components along (s',x',y')
u_1,u_2,u_3 = nondimensional velocity components (s,x,y)
$\tilde{U}_{\mathrm{av}}$ = average axial velocity
U_{av} = average nondimensional axial velocity
ϵ = τ/κ
κ = dimensionless curvature
λ = relaxation parameter
ν = kinematic viscosity
ρ = density
τ = dimensionless torsion
ω = vorticity

References

[1] Cheng, K. C., Lin, R., and Ou, J. W., 1976, ''Fully Developed Laminar Flow in Curved Rectangular Channels,'' ASME J. Fluids Eng., **98**, pp. 41–48.
[2] Ghia, K. N., Ghia, U., and Shih, C. T., 1987, ''Study of Fully Developed Incompressible Flow in Curved Ducts Using a Multigrid Technique,'' ASME J. Fluids Eng., **109**, pp. 226–235.
[3] Hwang, G. J., and Chao, C. H., 1991, ''Forced Laminal Convection in a Curved Isothermal Duct,'' ASME J. Heat Transfer, **113**, pp. 48–56.
[4] Hatzikonstantinou, P. M., and Sakalis, V. D., 2004, ''A Numerical-Variational Procedure for a Laminar Flow in Curved Square Ducts,'' Int. J. Numer. Methods Fluids, **45**, pp. 1269–1289.
[5] Sakalis, V. D., and Hatzikonstantinou, P. M., 2002, ''Predictions and Accuracy of the CVP Numerical Method for the Developed Laminar Flow in Curved Ducts,'' *Proceedings of the 4th GRACM Congress on Computational Mechanics*, University of Patras, Patras, Greece, Tsahalis, D., ed., **IV**, pp. 1400–1410.
[6] Wang, C. I., 1981, ''On the Low Reynolds Number Flow in a Helical Pipe,'' J. Fluid Mech., **108**, pp. 185–194.
[7] Germano, M., 1982, ''On the Effect of Torsion in a Helical Pipe Flow,'' J. Fluid Mech., **125**, pp. 1–8.
[8] Kao, H. C., 1987, ''Torsion Effect on Fully Developed Flow in a Helical Pipe,'' J. Fluid Mech., **184**, pp. 335–356.
[9] Tuttle, E. R., 1990, ''Laminar Flow in Twisted Pipes,'' J. Fluid Mech., **219**, pp. 545–570.
[10] Xie, D. E., 1990, ''Torsion Effect on Secondary Flow in a Helical Pipe,'' Int. J. Heat Mass Transfer, **11**, pp. 114–119.
[11] Chen, W. H., and Fan, C. N., 1986, ''Finite Element Analysis of Incompressible Viscous Flow in a Helical Pipe,'' J. Computational Mech., **1**, pp. 281–292.
[12] Liu, S., and Masliyah, J. H., 1993, ''Axially Invariant Laminar Flow in Helical Pipes With a Finite Pitch,'' J. Fluid Mech., **251**, pp. 315–353.
[13] Germano, M., 1989, ''The Dean Equations Extended to a Helical Pipe Flow,'' J. Fluid Mech., **203**, pp. 289–305.
[14] Bolinder, C. J., 1995, ''Numerical Visualization of the Flow in a Helical Duct of Rectangular Cross Section,'' ASME FED, presented at the *Third Symposium on Experimental and Numerical Flow Visualization*, New Orleans, USA, **172**, pp. 329–338.
[15] Bolinder, C. J., 1995, ''The Effect of Torsion on the Bifurcation Structure of Laminar Flow in a Helical Square Duct,'' ASME J. Fluids Eng., **117**, pp. 242–248.
[16] Bolinder, C. J., and Sunden, B., 1996, ''Numerical Prediction of Laminar Flow and Forced Convective Heat Transfer in a Helical Square Duct With a Finite Pitch,'' Int. J. Heat Mass Transfer, **139(15)**, pp. 3101–3115.
[17] Chen, W. H., and Jan, R., 1993, ''The Torsion Effect on Fully Developed Flow in Helical Square Ducts,'' J. Fluid Mech., **115**, pp. 292–301.
[18] Chen, W. H., 1993, ''The Torsion Effect on Fully Developed Laminar Flow in Helical Square Ducts,'' ASME J. Fluids Eng., **115**, pp. 292–301.
[19] Joseph, B., Smith, E. P., and Adler, R. J., 1975, ''Numerical Treatment of Laminar Flow in Helically Coiled Tubes of Square Cross Section,'' AIChE J., **121(5)**, pp. 965–974.
[20] Winters, K. H., 1987, ''A Bifurcation Study of Laminar Flow in a Curved Tube of Rectangular Cross Section,'' J. Fluid Mech., **180**, pp. 343–369.
[21] Daskopoulos, P., and Lenhoff, A. M., 1976, ''Flow in Curved Ducts, Bifurcation Structure for Stationary Ducts,'' ASME J. Fluids Eng., **98**, pp. 41–48.
[22] Hatzikonstantinou, P., 2002, ''A Computational Procedure for the Incompressible Three-Dimensional Parabolic Flows,'' *Proceedings of the 4th GRACM Congress on Computational Mechanics*, University of Patras, Patras, Greece, Tsahalis, D., ed., pp. 68–79.
[23] Kays, W. M., and Crawford, E. M., 1993, *Convective Heat and Mass Transfer*, McGraw-Hill, New York.

Self-Excited Oscillations of Flow Past a Perforated Plate: Attenuation Via Three-Dimensional Surface Elements

C. Ozalp

A. Pinarbasi

Department of Mechanical Engineering,
Cukurova University,
01330 Balcali Adana, Turkey

D. Rockwell

Department of Mechanical Engineering
and Mechanics,
354 Packard Laboratory, 19 Memorial
Drive West,
Lehigh University
Bethlehem, PA 18015 USA
e-mail: dor0@lehigh.edu

It is known that flow past a perforated plate can give rise to purely hydrodynamic, self-sustained oscillations, which have a wavelength of the order of the plate length. The present investigation demonstrates that these oscillations can be effectively attenuated by three-dimensional surface elements in the form of vortex generators. A technique of high-image-density particle image velocimetry is employed to characterize the patterns immediately adjacent to the surface of the perforated plate. These patterns are interpreted in conjunction with pressure spectra at the trailing-end of the plate, as well as velocity spectra determined from cinema sequences of images. In the absence of the three-dimensional surface elements, a well-defined front of the unstable oscillation propagates along the surface of the plate. In the presence of an appropriate surface element, the front is no longer detectable, and instantaneous and averaged defects of the streamwise velocity and surface-normal vorticity exist along the span of the plate. The magnitudes and spanwise wavelengths of these defects are directly related to the extent of attenuation of the oscillation. Since the magnitudes of these defects decay significantly with distance along the plate, the most effective attenuation typically occurs for plate lengths less than or equal to a critical length. An appropriate measure of the degree of attenuation is a reduction in the magnitude of the coherent component of the fluctuating pressure. For all cases, even in the presence of effective attenuation, a low magnitude spectral peak at the frequency of the inherent oscillation is still discernible; it may be either sharp or broadband, and is indicative of the robust nature of the self-sustained oscillation.
[DOI: 10.1115/1.1852477]

1 Introduction

Flow past a perforated plate can give rise to short wavelength instabilities that scale on the diameter of the perforation (hole), and a recently documented long wavelength instability that scales on the length of the plate. Brief summaries of these classes of instabilities, as well as related investigations of flow control of oscillation via three-dimensional surface elements, typically in the form of vortex generators, are given in the following.

1.1 Short Wavelength Instabilities and Broadband Fluctuations Due to Flow Past a Perforated Plate. Flow past a circular perforation, among an array of perforations, which are usually bounded on the backside by a defined cavity(ies), has been addressed by Meyer [1], Dean [2], Adams [3], Tsui and Flandro [4], and Bauer and Charpkis [5]. In this series of studies, the generation of tones was generally attributed to the hydrodynamic instability of the shear layer past a single hole. Related investigations involve those of Ronneberger [6], who experimentally addressed the physics of the unsteadiness past a circular hole, as well as Nelson [7] and Howe [8], who focused on the broadband generation of fluctuations (noise). A still further aspect of this class of investigations is determination of the impedance of a perforated plate, with the aid of external excitation, as pursued by Dickey et al. [9]. Flow past inclined slats, i.e., louvers, with a cavity on their backside, can give rise to oscillations and noise generation that are analogous to those arising from flow past a perforated plate, as characterized by Bruggeman et al. [10] and Looijmans and Bruggeman [11]. Furthermore, Zoccola [12] recently investigated the instabilities arising from one to three spanwise obstacles located along the mouth of a resonant cavity.

The present investigation focuses on the particular situation of a long wavelength instability past a perforated plate, as given in the synopsis of the next section.

1.2 Long Wavelength Instabilities Past Perforated Plates. Celik and Rockwell [13] showed, for the case of a laminar inflow boundary layer, existence of purely hydrodynamic, self-sustained oscillations of flow past a perforated plate of relatively high area ratio, which was bounded on its backside by a closed cavity. Ozalp et al. [14] demonstrated that even in the case where the inflow boundary layer is fully turbulent, this type of long-wavelength instability persists and, in fact, gives rise to strongly coherent oscillations with sharply defined peaks of both pressure and velocity spectra. The dimensionless frequency of these oscillations has values of the order $f_oL/U=0.5$ to 0.6, in which f_o is the coherent frequency of oscillation, L is the length of the perforated plate, and U is the freestream velocity. Remarkably, this dimensionless frequency, as well as other features of the oscillation, have direct analogies with purely hydrodynamic oscillations of flow past a cavity in absence of a perforated plate along its opening as addressed, for example, by Rockwell and Naudascher [15], Gharib and Roshko [16], and Howe [17,18]. If the cavity is allowed to undergo resonance in a standing wave mode, then the self-excited oscillation of the shear flow is substantially affected, for cases both without and with a perforated plate along the cavity opening, as described by Ekmekci and Rockwell [19].

Ozalp et al. [14] show that long wavelength hydrodynamic oscillations involve the propagation of coherent concentrations of velocity, vorticity, and Reynolds stress correlations along the surface of a perforated plate. Moreover, by observation of a plane of the flow immediately adjacent to the surface of the plate, they

Contributed by the Fluids Engineering Division for publication in the JOURNAL OF FLUIDS ENGINEERING. Manuscript received by the Fluids Engineering Division October 28, 2003; revised manuscript received July 9, 2004. Review conducted by: H. Johari.

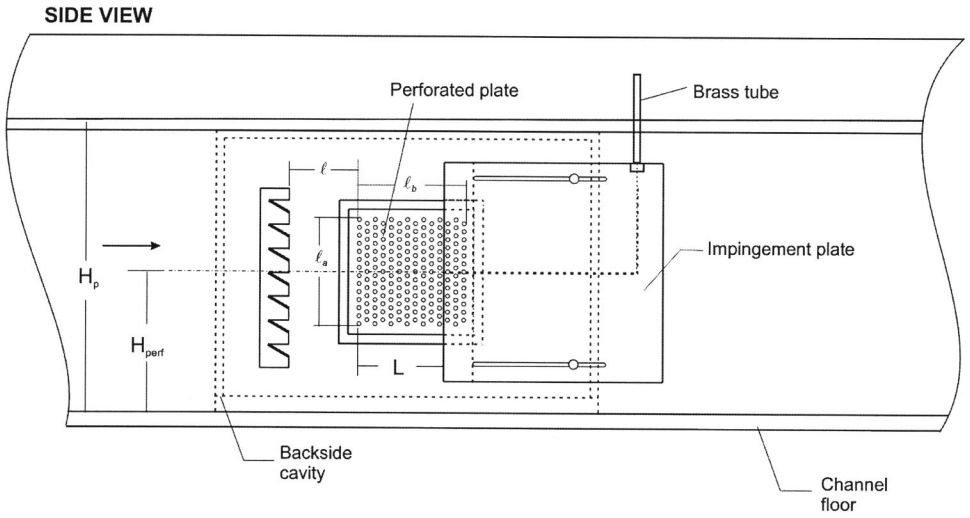

Fig. 1 View of perforated plate, impingement plate, and vortex generator

showed that such oscillations involved propagation of a well-defined front, i.e., an interface between relatively high and low regions of velocity along the plate surface. This front was reasonably well correlated, in a large-scale sense, along the span of the perforated plate.

1.3 Alteration of Flow Structure Due to Three-Dimensional Surface Elements. Although three-dimensional surface elements, such as vortex generators, have not been employed for the type of flow instability addressed herein, investigations of such elements or generators for attenuation of self-excited

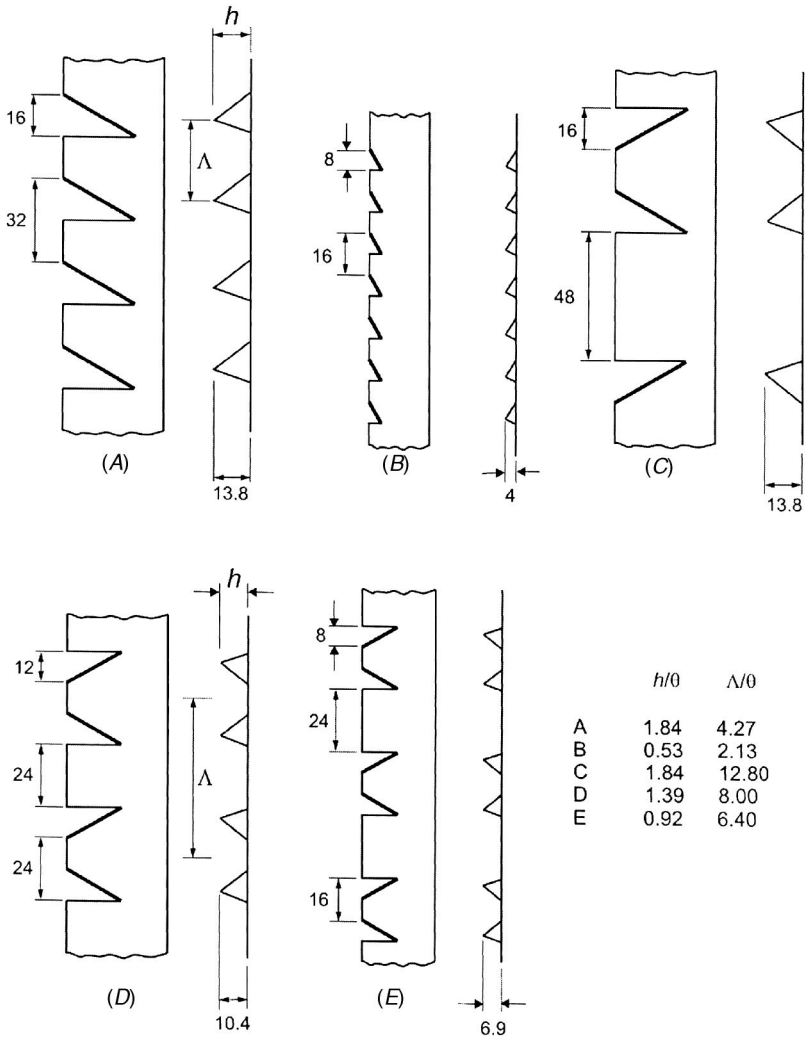

Fig. 2 Plan and side views and dimensions of vortex generators

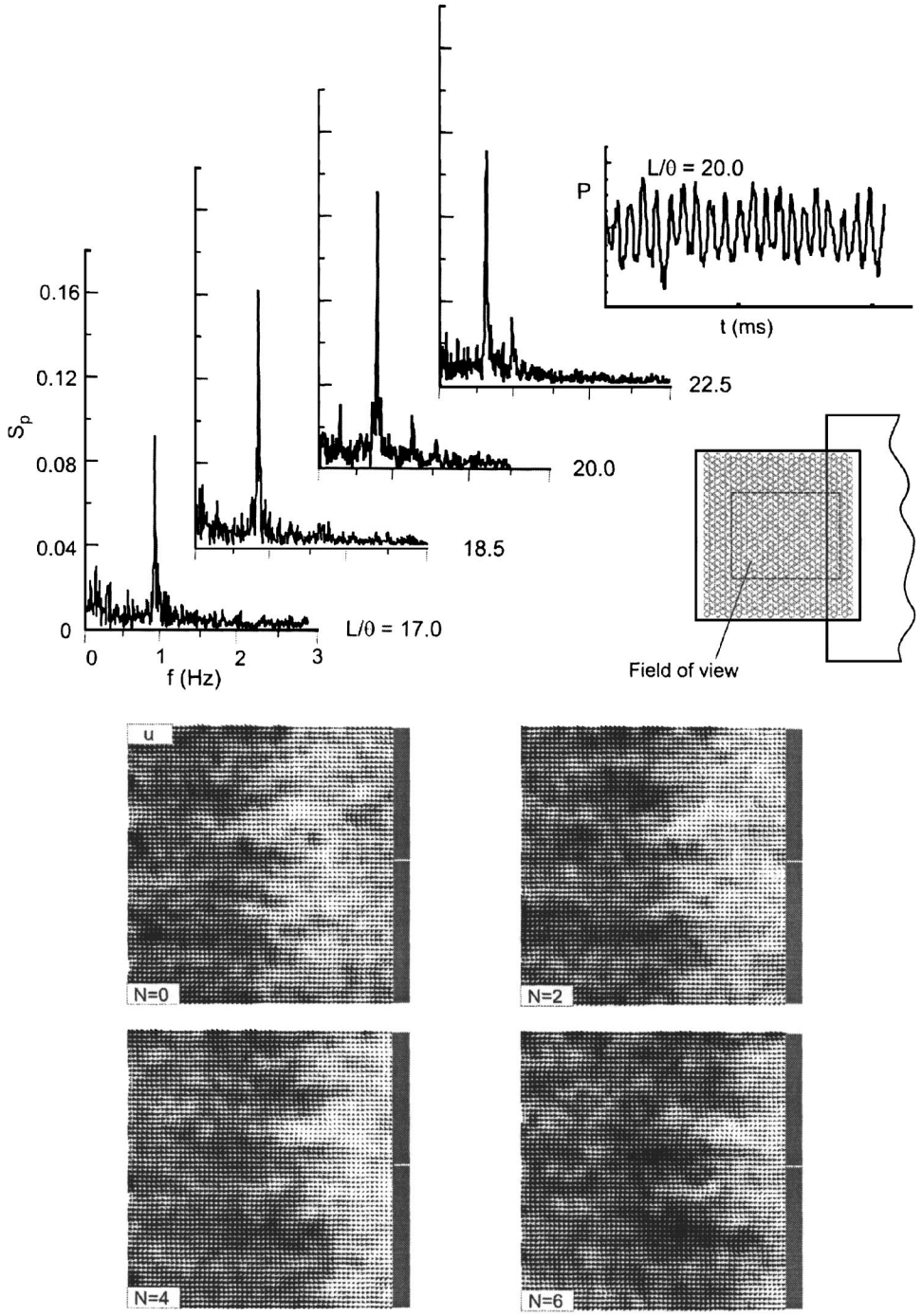

Fig. 3 Spectra of pressure fluctuation S_p at tip of impingement edge without vortex generator for various L/θ values. Images show the patterns of instantaneous vectors of the longitudinal (streamwise) component of velocity u for $L/\theta=20$. N represents the frame number of cinema sequence. (Images were selected from Ref. [14].)

oscillations in related configurations can provide guidance. They have been effectively used for alterations of the structure of separated flows of finite streamwise extent, in the absence of a perforated or slotted plate along the cavity opening. Keller and Escudier [20] demonstrated the attenuation of self-sustained oscillations of flow past a cavity, with emphasis on the effect of incidence angle of the generators. Karadogan and Rockwell [21] characterized the effect of dimensionless height and wavelength of vortex generators for attenuation of the self-sustained oscillations of an axisymmetric jet flow through a cavity. Bruggeman et al. [22] attained effective attenuation of the self-excited oscillations arising from flow past a deep cavity by deployment of ramp-type elements along the leading-edge of the cavity.

1.4 Unresolved Issues. Consideration of the foregoing observations of self-sustained oscillations, as well as methods for their attenuation, leads to the definition of central, unresolved issues for the present case of self-excited oscillations past a perforated plate.

a. Recent observations of highly coherent, self-sustained oscillations of flow past a perforated plate, which is bounded on

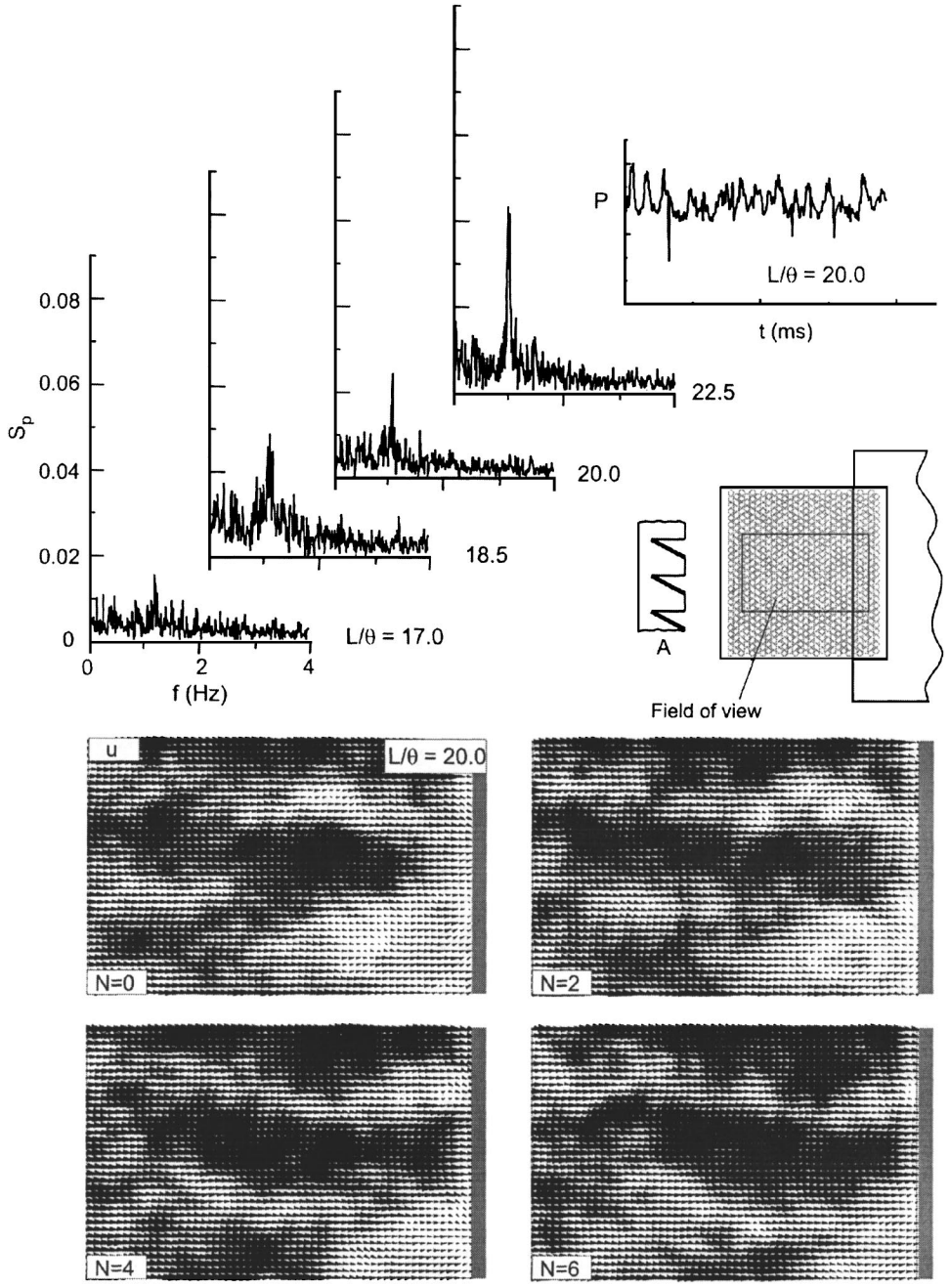

Fig. 4 Spectra of pressure fluctuation S_p at tip of impingement edge for type *A* vortex generator for various L/θ values. Images show the patterns of instantaneous vectors of the longitudinal (streamwise) component of velocity *u* for effective plate length $L/\theta=20$ and for effective plate width $w/\theta=19$, which is the same for all subsequent images. *N* represents the frame number of cinema sequence.

its backside by a closed cavity, raises the issue whether modification of the spanwise coherence of the shear flow on the high-speed (front side) of the perforated plate can lead to effective mitigation of the self-sustained oscillation. That is, it is not yet known whether an appropriate type of surface treatment, which would induce localized velocity and vorticity defects along the span of the plate, can lead to attenuation of this type of robust oscillation.

b. In the event that attenuation can be achieved, the minimum effective height of the three-dimensional elements, as well as the most effective spanwise wavelength between them, has not been characterized.
c. The magnitude of the local velocity defect, and thereby the vorticity, is expected to decay with streamwise distance along the perforated plate. If this is the case, the question is whether oscillations are attenuated only when the streamwise length of the plate is smaller than a critical value.

The intent of the present investigation is to address these features, using patterns of instantaneous and averaged velocity and vorticity, in conjunction with pressure measurements.

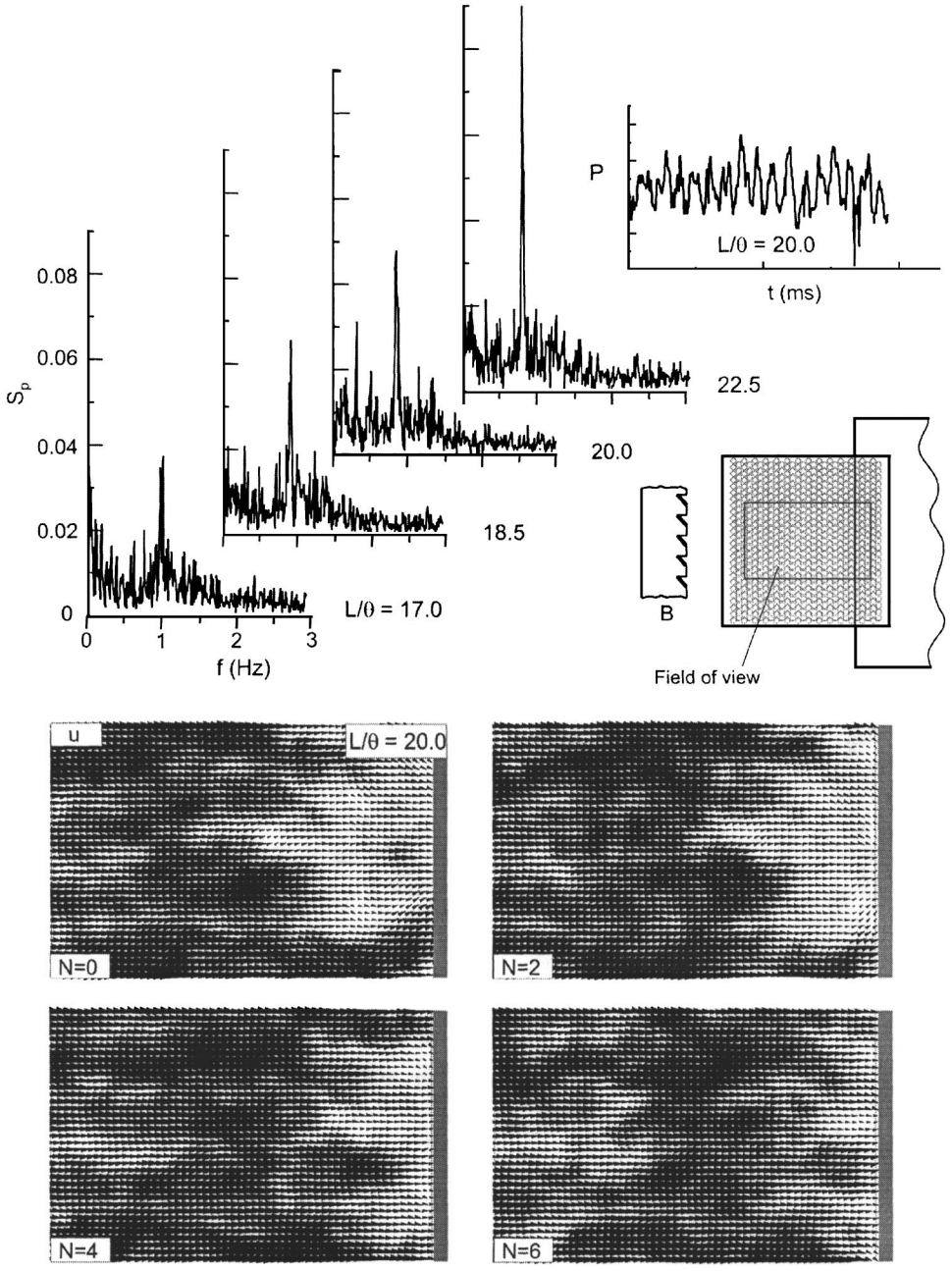

Fig. 5 Spectra of pressure fluctuation S_p at tip of impingement edge for type *B* vortex generator for various L/θ values. Images show the patterns of instantaneous vectors of the longitudinal (streamwise) component of velocity *u* for $L/\theta=20$. *N* represents the frame number of cinema sequence.

2 Experimental System and Techniques

The experimental system employed for the present investigation was essentially that of Ozalp et al. [14], who investigated self-sustained oscillations in the absence of three-dimensional surface elements. The reader is referred to that work for a detailed description of the facility. The central features of the flow system and perforated plate arrangement are described in the following.

All experiments were performed in the large-scale water channel. Its test section was 4928 mm long, 610 mm deep, and 927 mm wide. A test section insert was constructed within this main test section, as defined by Ozalp et al. [14]. It allowed generation of a fully evolved, turbulent boundary layer approaching the perforated plate, which is shown in the present Fig. 1. For all experiments, the free-stream velocity was $U=240$ mm/s and the momentum thickness θ of the inflow turbulent boundary layer was $\theta=7.5$ mm, which corresponds to a value of Reynolds number based on θ of $\mathrm{Re}_\theta=1800$. The perforated plate of Fig. 1 was mounted vertically in a continuous vertical plate, which had a height $H_p=457$ mm. The streamwise length of the plate was $\ell_b=183$ mm and its spanwise width was $\ell_a=197$ mm. The perforated plate had a thickness of 11 mm, holes of diameter $D=6.4$ mm, and an open area ratio of 69%, which corresponds to the areas of all of the holes normalized by the area of the plate. On the basis of the investigation of Ozalp et al. [14], it is known that these parameters give rise to highly coherent oscillations, and, for this reason, they were selected for the present investigation. The effective length L of the plate, as defined in Fig. 1, could be varied by translating an impingement plate along its surface. For the

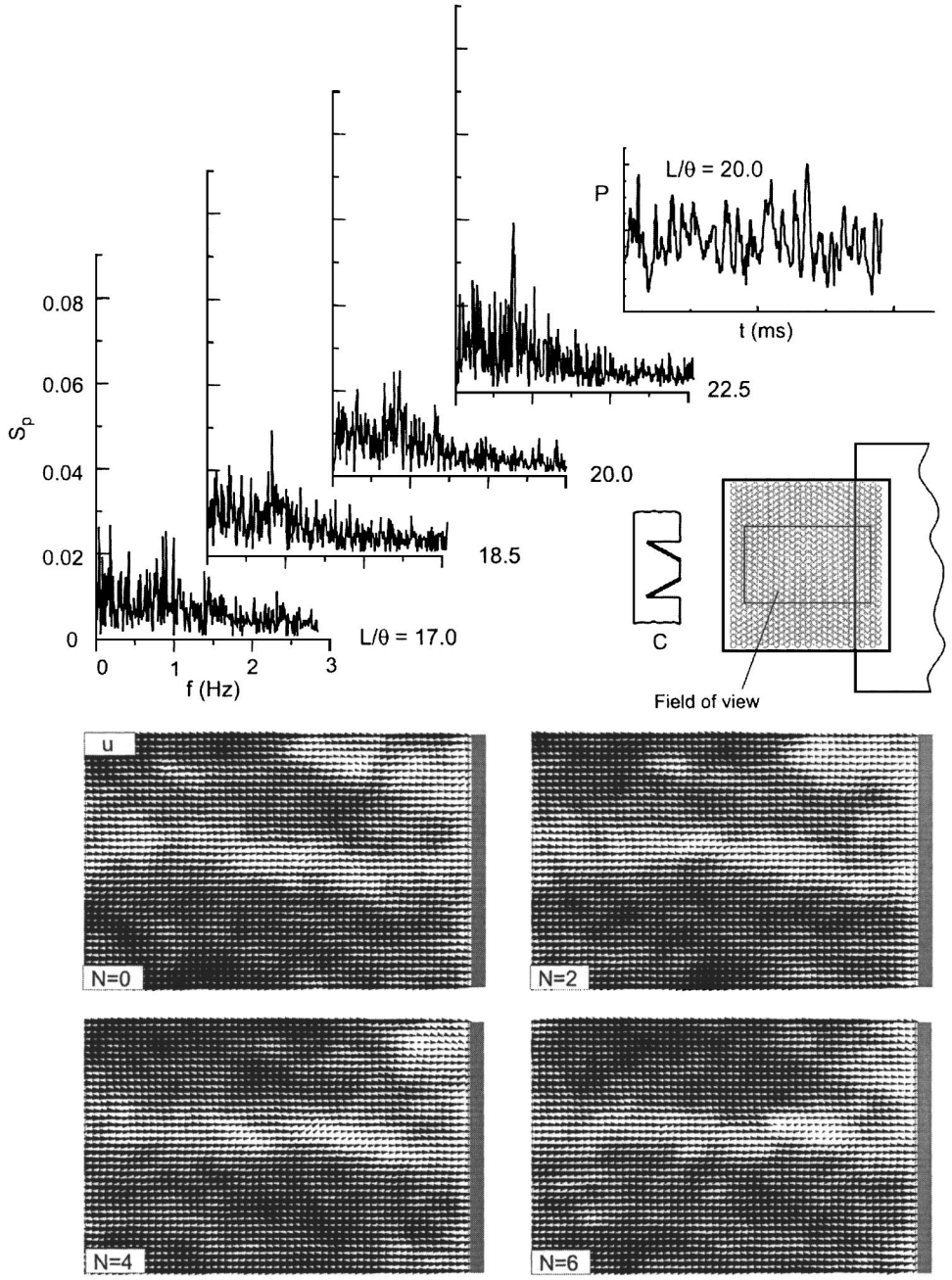

Fig. 6 Spectra of pressure fluctuation S_p at tip of impingement edge for type *C* vortex generator for various L/θ values. Images show the patterns of instantaneous vectors of the longitudinal (streamwise) component of velocity *u* for $L/\theta=20$. *N* represents the frame number of cinema sequence.

investigation herein, various plate lengths L are expressed in normalized form using the momentum thickness θ of the inflow boundary layer, i.e., L/θ.

The perforated plate system of Fig. 1 was open to the freestream on its front side and bounded by a large-scale cavity on its back side. The boundary of this cavity is defined in the schematic using a pattern of dashed lines. This cavity was firmly bolted to the vertical plate of the test section and, furthermore, sealed with silicone rubber such that there was no possibility for leakage. The cavity was much larger than the width and length of the perforated plate, in order to ensure that local zones of recirculation were not influential. The dimensions of the cavity are as follows: Streamwise length of 610 mm, height of 432 mm, and depth of 432 mm. In order to ensure that elastic wall effects were not significant, the walls were of 12.5 mm thick Plexiglas. Furthermore, for the frequencies of the coherent spectral peaks of the velocity and pressure fluctuations generated in this investigation, the corresponding values of acoustic wavelength were approximately two orders of magnitude larger than the representative dimensions of the cavity. As a consequence, acoustic resonance effects were precluded. Furthermore, this limiting condition means that any upstream influence from the trailing-edge to the leading-edge of the plate is essentially instantaneous, i.e., purely hydrodynamic.

Pressure measurements were made using a watertight PCB transducer, which was mounted within the brass tube shown in Fig. 1. As verified by independent transient response tests, this

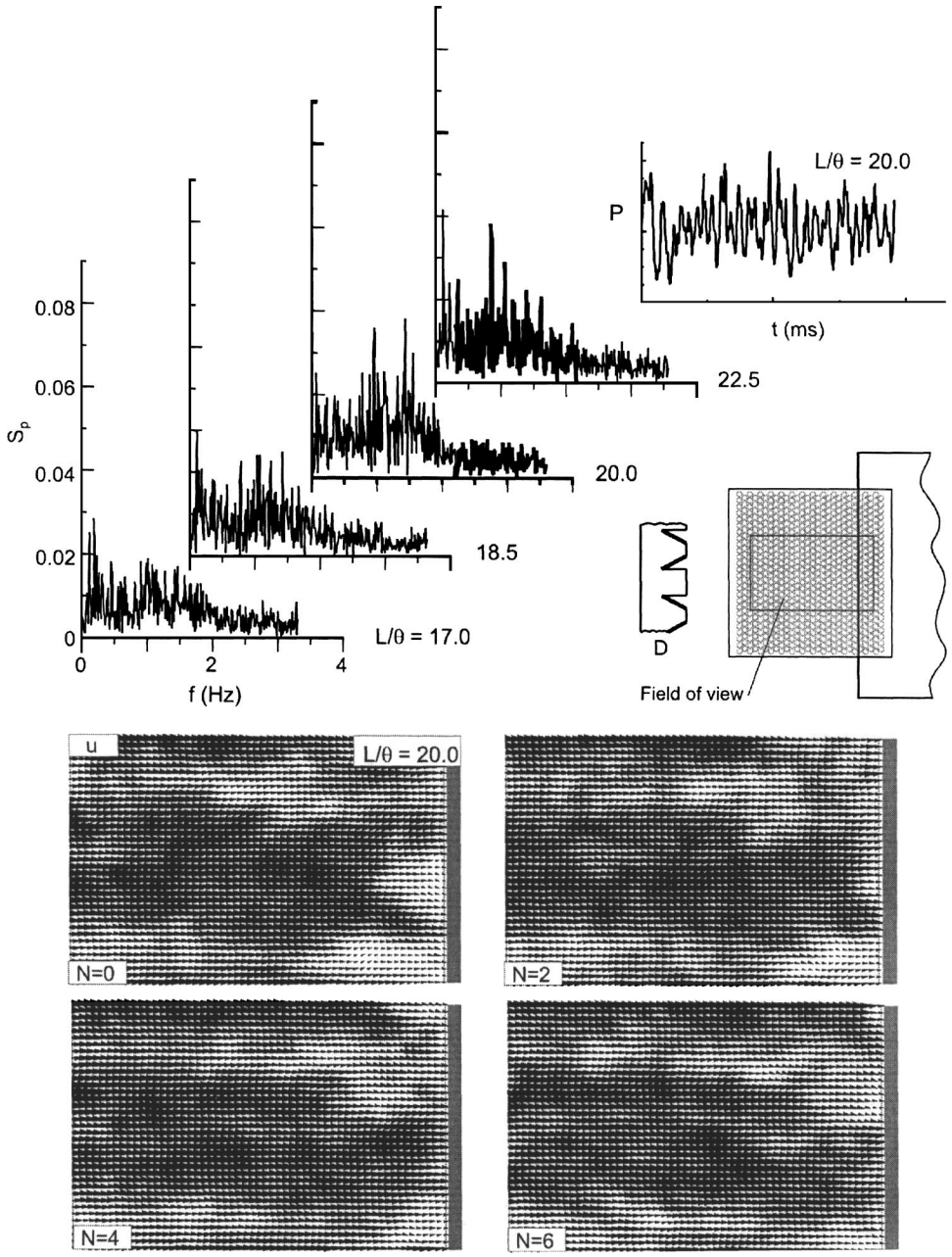

Fig. 7 Spectra of pressure fluctuation S_p at tip of impingement edge for type *D* vortex generator for various L/θ values. Images show the patterns of instantaneous vectors of the longitudinal (streamwise) component of velocity *u* for $L/\theta=20$. *N* represents the frame number of cinema sequence.

arrangement allowed measurement of the fluctuations at the tip of the impingement plate with minimal amplitude and phase distortions; both were within 1% of the actual values.

Quantitative patterns of the flow structure were obtained using a technique of high-image-density particle image velocimetry. Two pulsed Yag lasers, which were fitted with a cylindrical-spherical lens system, provided a 1 mm thick laser sheet. For all imaging employed herein, this laser sheet was located parallel to, and at a distance of 1 mm from, the surface of the perforated plate. This orientation and location of the laser sheet provided patterns of instantaneous flow structure over the field of view of the surface of the perforated plate.

Imaging of the flow structure requires effective seeding. Metallic coated, hollow plastic spheres having a diameter of 12 μ were employed. The seeding density resulted in a minimum of 15 to 20 particle images within the interrogation window. Patterns of particle images were recorded with a high resolution camera having a CCD array of 1024×1024 pixels. During interrogation, the size of the window had two different values, 32×32 pixels and 16×16 pixels. An overlap of 50% was used in order to satisfy the Nyquist criterion. The uncertainty of velocity and vorticity are estimated respectively to be less than 1.5 and 6%.

Spectral analysis of the pressure and velocity signals was carried out in accord with the procedures outlined by Newland [23]. In essence, the definition for the spectrum is

$$S_k \frac{1}{N f_s} X_k^* X_k$$

in which N is the number of data points, f_s is the sampling fre-

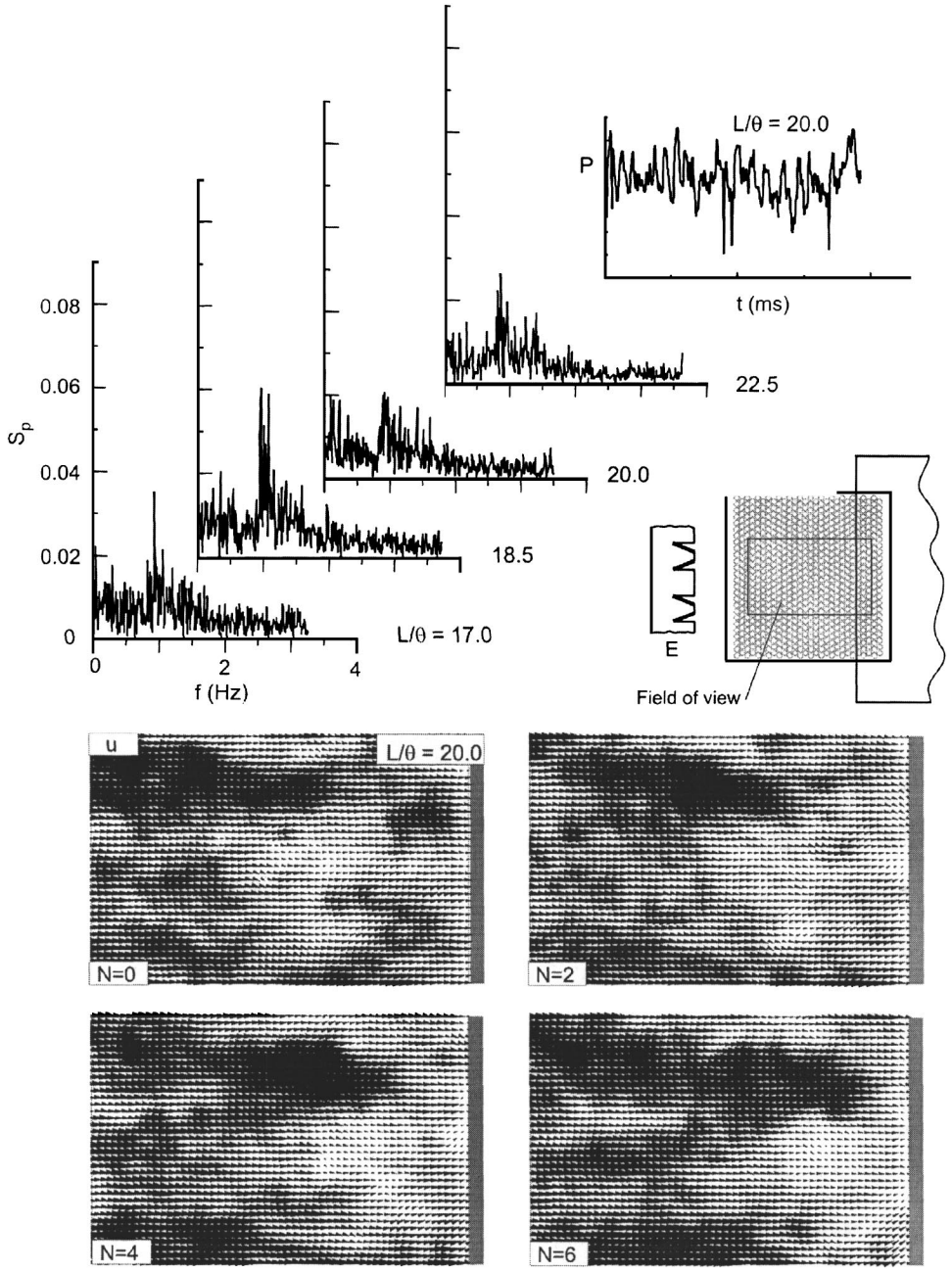

Fig. 8 Spectra of pressure fluctuation S_p at tip of impingement edge for type *E* vortex generator for various L/θ values. Images show the patterns of instantaneous vectors of the longitudinal (streamwise) component of velocity *u* for $L/\theta=20$. *N* represents the frame number of cinema sequence.

quency, X_k is the fast Fourier transform (FFT) of time series, and X_k^* is its complex conjugate. For evaluation of S_p and S_u, the values of sampling frequency f_s had values of 10 and 7.5, respectively. These spectra allow identification of both the relative amplitude and frequency of the predominant spectral peak. In this investigation, the inflow velocity U was maintained constant while the effective length L of the plate was varied. Values of frequency of the spectral peak were in the range $f=0.8402$ to 0.997, which corresponds to values of Strouhal number $fL/U=0.55$ to 0.57.

A schematic of a representative three-dimensional surface element, which can be generally referred to as a row of vortex generators, is given in Fig. 1. The trailing-edge of this unit was located a distance of $\ell=89$ mm upstream of the first row of perforations in the plate, as designated in the schematic of Fig. 1. Five different configurations of the three-dimensional triangular surface elements were employed. They are designated as elements $A-E$ in Fig. 2. For each type of element, the absolute values of element height and wavelength are given in dimensions of mm on each schematic. Furthermore, the table at the inset of Fig. 2 provides dimensionless values of the height h/θ and wavelength Λ/θ. As indicated, the values of dimensionless height range from $h/\theta=0.3$ to 1.4, while the values of spanwise wavelength are essentially from $\Lambda/\theta=2.13$ to 12.80. As will be demonstrated, small values of h/θ are relatively ineffective.

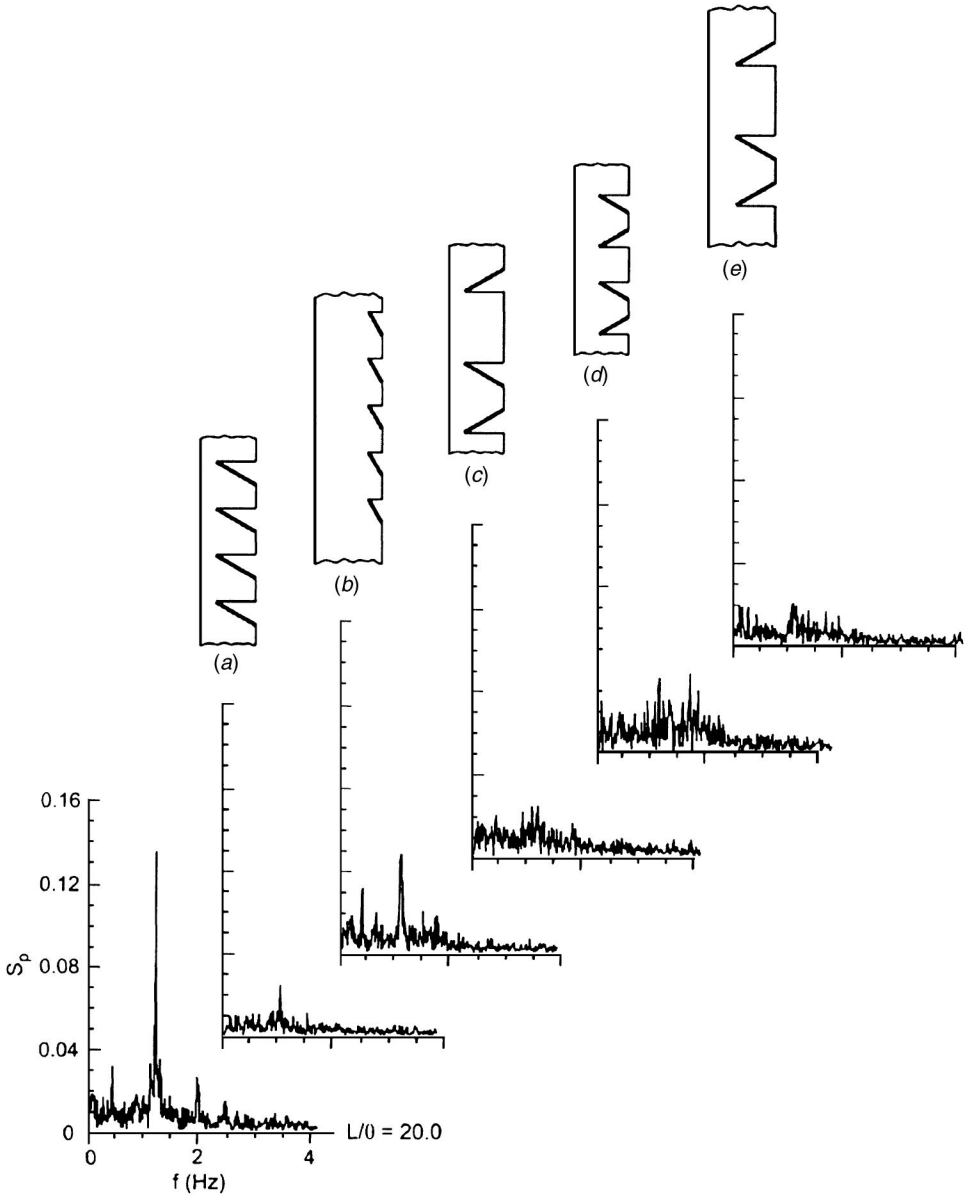

Fig. 9 Comparison of spectra of pressure fluctuation S_p at tip of impingement edge with and without vortex generators for $L/\theta=20$. The first spectrum corresponds to the case of no vortex generator, while others represent spectra with vortex generators shown in the figure.

3 Oscillations in the Absence of a Three-Dimensional Surface Element

Figure 3 shows pressure spectra and images of the instantaneous flow structure along the span of the plate in absence of a three-dimensional surface element. It serves as a reference case for the mitigation of self-sustained oscillations, which is addressed in subsequent figures. Images were taken over a square field of view with dimensions 92.63×92.63 mm^2. The pressure spectra $S_p(f)$ shown at the top of Fig. 3 indicate sharply defined peaks for the range of cavity length extending from $L/\theta=17.0$ to 22.5. Correspondingly, the sequence of instantaneous images of streamwise velocity u is given in the cinema sequence $N=0$, 2, 4 and 6. Darker regions correspond to larger magnitude vectors, and lighter regions to relatively small magnitude vectors. It is evident that a front, defined as the interface between regions of high (dark) and low (light) regions of u, propagates from left to right. In the section that follows, the consequences of the three-dimensional surface elements on both the pressure spectra and the surface patterns of Fig. 3 will be addressed. Images in Figs. 4–8 were taken in a field of view with dimensions 86.83×137.48 mm^2.

4 Attenuation of Self-Sustained Oscillations Via Three-Dimensional Surface Elements

4.1 Pressure Spectra and Patterns of Instantaneous Velocity. The effect of the three-dimensional surface element A is shown in Fig. 4. It involves, in essence, a series of triangular elements, all having the same angle of inclination (see Fig. 2). The set of pressure spectra shown at the top of Fig. 4 indicate that, in all cases, the amplitude of the spectral peak is smaller than the corresponding reference values of Fig. 3. Substantial attenuation occurs up to $L/\theta=20$ and, at this value, the time trace of the pressure signal intermittently shows regions of both ordered and

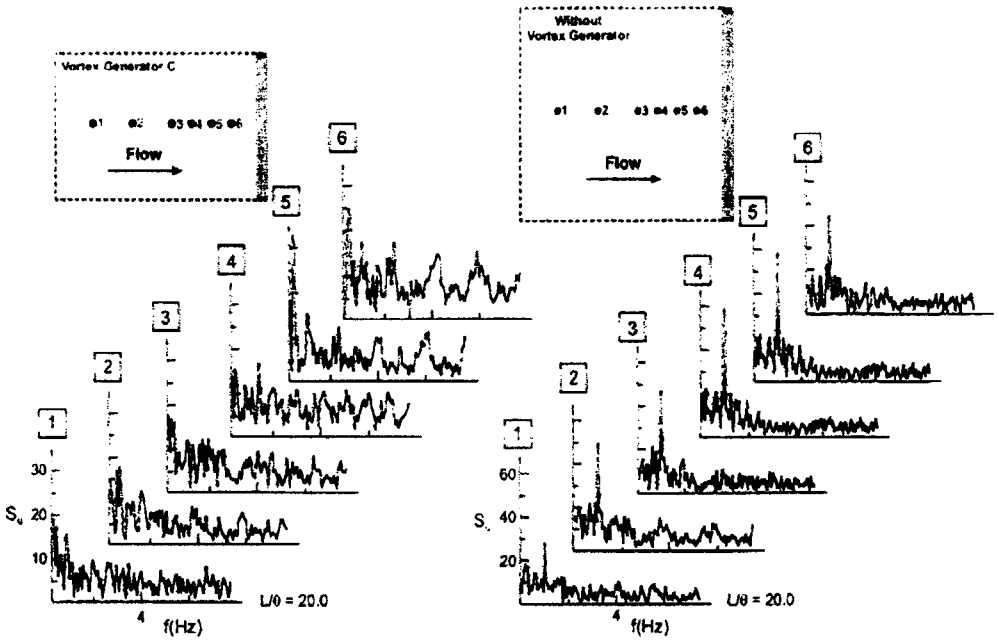

Fig. 10 Spectra of velocity fluctuation S_u for various longitudinal (streamwise) locations for type *C* vortex generator and without vortex generator. The field of view indicated by the rectangular region at the top of each spectra has dimensions of 138 mm length and 86 mm width and 138 mm length and 142 mm width, respectively. Impingement length corresponds to $L/\theta=20$.

less organized fluctuations. At the largest value of $L/\theta=22.5$, the magnitude of the peak is sharply defined, but still is less than half the reference value given in Fig. 3.

The physical basis for mitigation of the spectral peaks of Fig. 4 is given in the cinema sequence of instantaneous streamwise velocity u at the bottom of Fig. 4. Regions of significant velocity defects (light-colored regions) form alternately with regions of higher velocity (dark-colored regions) across the span of the plate. Furthermore, adjacent regions of larger velocity are connected, for example, as evident at the middle of the image $N=0$ in Fig. 4. Viewing the patterns at all values of N at the bottom of Fig. 4, then comparing with the patterns of Fig. 3 in the absence of a three-dimensional surface element, it is evident that Fig. 4 does not show a clearly defined front that propagates from left to right.

The spectra and velocity patterns of Fig. 5 correspond to a three-dimensional element B that is geometrically similar to the element of Fig. 4. As indicated in the overview of Fig. 2, however, this element has a height h/θ that is more than a factor of 3 smaller than the element A given in Figs. 2 and 4. The spectra at the top of Fig. 5 indicate that this configuration is, in most cases, marginally effective. At the largest value of $L/\theta=22.5$, the attenuation of the peak is minimal. Furthermore, the trace of the pressure signal $p(t)$ at $L/\theta=20$ indicates a reasonably organized oscillation over the entire time interval.

The corresponding patterns of instantaneous streamwise velocity u of Fig. 5 show regions of lower velocity interspersed in an irregular fashion among regions of higher (dark) velocity, but the well-defined longitudinal regions of lower and higher velocity evident in the images of Fig. 4 are not present. Furthermore, viewing together all of the images at values of $N=0-6$ in Fig. 5, it is possible, in an approximate sense, to witness the propagation, from left to right, of the highly irregular front. This front, however, is not as well defined as in the reference case of Fig. 3 in the absence of the three-dimensional element.

A fundamentally different three-dimensional element, geometry C, is represented in Fig. 6. Generally speaking, the spectra shown at the top of Fig. 6 indicate reasonable reduction of the predominant spectral peak. For the largest plate length $L/\theta=22.5$, the attenuation is less effective. Nevertheless, at this value of L/θ, the amplitude of the spectral peak is of the order of one-third the value in the absence of the three-dimensional element (see Fig. 3).

This attenuation is accompanied by the appearance of a well-defined, longitudinal band of velocity defect (light region) in all of the images of instantaneous streamwise velocity u, i.e., images $N=0$ through $N=6$ of Fig. 6. The persistence of this band of low velocity over the entire streamwise extent of the image is similar in form to the case shown in Fig. 4, for which effective attenuation was also achieved. Furthermore, the lack of a well-defined front, of the type shown in Fig. 3, is also apparent in the patterns of velocity of Fig. 6. Again, this feature is in accord with that observed in conjunction with the attenuation concept of Fig. 4.

The same overall form of the three-dimensional surface element of Fig. 6, but with successively decreasing values of dimensionless height h/θ and wavelength Λ/θ, are represented by the configurations D and E, respectively, of Figs. 7 and 8. As indicated by the corresponding spectra therein, element D of Fig. 7 is essentially as effective as the element C in Fig. 6 in reducing peak amplitudes of the spectra over the given range of L/θ. On the other hand, element E of Fig. 8 is not as effective as configuration C of Fig. 6 for the lowest values of $L/\theta=17.0$ and 18.5. On the other hand, it is remarkably effective at longer values of $L/\theta=20.0$ and 22.5. This observation may, at least in part, be explained by the patterns of instantaneous streamwise velocity u at the bottom of Fig. 8. Consider, for example, the image $N=6$. At the left edge of this image, several distinct bands of high velocity (dark regions) are evident. On the other hand, towards the middle of the image $N=6$, the top two bands appear to coalesce, or merge together, to form a single band. The consequence is that, in the right half of the image, only two distinct high velocity (dark region) bands are evident. This larger spanwise spacing may promote more effective attenuation at larger streamwise lengths, as observed for the larger spacing of the low velocity (light regions) of Fig. 6.

Comparison of spectra of the pressure fluctuation at the tip of the edge with and without the three-dimensional surface elements (vortex generators) is shown in Fig. 9 for a representative value of $L/\theta=20$. It is evident that all configurations $A-E$ can lead to attenuation, to varying degrees, of the large amplitude spectral

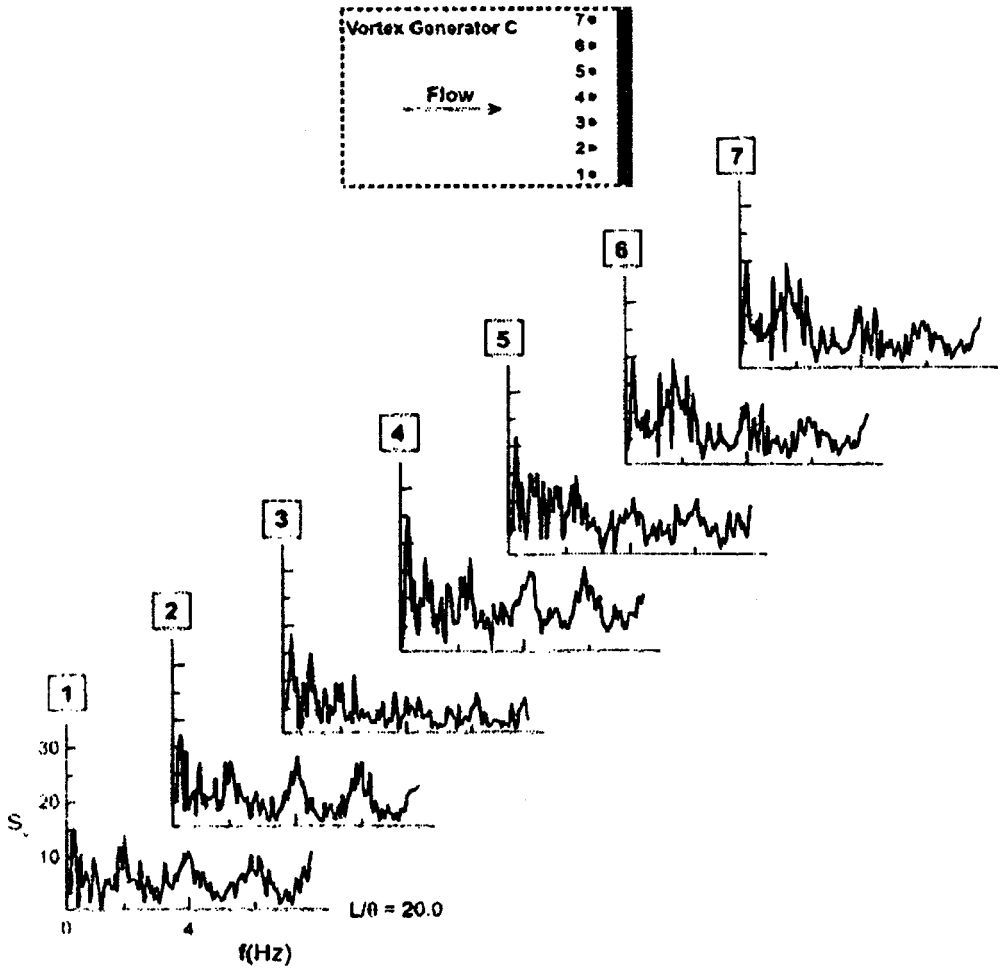

Fig. 11 Spectra of velocity fluctuation S_u for various spanwise positions across the impingement plate for type *C* vortex generator. The field of view by the rectangular region of the top of each set of spectra has dimensions of 128 mm length and 86 mm width. Impingement length corresponds to $L/\theta=20$.

peak, at least for this value of L/θ. The element *B* is clearly the least effective of these configurations. As indicated in the foregoing, it is necessary, however, to consider the entire range of L/θ when assessing the performance of these three-dimensional surface elements.

4.2 Velocity Spectra. Spectra S_u of the streamwise velocity fluctuation u were evaluated at various locations in the streamwise and spanwise directions along the perforated plate with and without vortex generators. The spectra S_u on the left-hand side of Fig. 10 indicate that the sharply defined peak in the corresponding spectra S_u without a vortex generator, given at the right of Fig. 10, as well as the peak in the pressure spectra S_p of Fig. 3, is substantially attenuated along the entire streamwise extent of the image. For purposes of reference, the locations of the points of evaluation, 1–6, are shown to scale in the field of view, which has a length of 138 mm and a width of 86 mm. A similar type of representation, but across the span of the plate, is shown in Fig. 11. Again, a generally similar level of attenuation occurs over this spatial extent. Taken together, the spectra of Figs. 10 and 11 show that the organized peak of the oscillation is globally attenuated over the surface of the plate.

4.3 Patterns of Averaged Velocity and Vorticity. Time-averaged patterns of the near-surface velocity and vorticity fields are shown in Figs. 12–14; they are complements to the corresponding instantaneous representations given in the foregoing figures. Figure 12 shows well-defined bands of lower (light region) and higher (darker region) velocity for the configurations *A*, *C*, *D*, and *E*, for which effective attenuation was achieved. The distinct feature of the pattern of time-averaged streamwise velocity $\langle u \rangle$ of image *A* is the fact that the light and dark bands are substantially inclined relative to the direction of the freestream velocity. Such inclination does not occur for the patterns of *C*, *D*, and *E*. Correspondingly, surface element *A* yielded the least effective attenuation of the configurations represented in Fig. 12; details of this attenuation are shown in Fig. 4.

Patterns of time-averaged velocity vectors at various streamwise locations are shown in Fig. 13 for two representative configurations *C* and *E*. As indicated in the foregoing Figs. 6 and 8, both of these configurations yielded effective attenuation. These velocity vectors show two major features. First of all, the magnitude of the velocity defect in the leftmost profile is of the order of one-third of the maximum velocity away from the defect. In other words, this defect magnitude is apparently adequate to induce sufficient spanwise dephasing of the oscillation, which yields attenuation. The second point is that the magnitude of this defect decays with streamwise distance along the plate, which is evident from inspection of the patterns corresponding to both configurations *C* and *E*. This decay is most likely the origin of the less effective attenuation at the largest values of L/θ for each of the three-dimensional elements investigated herein. That is, when L/θ is sufficiently large, the magnitude of the defect has decayed sufficiently at larger streamwise distances, such that effective attenuation may not be possible.

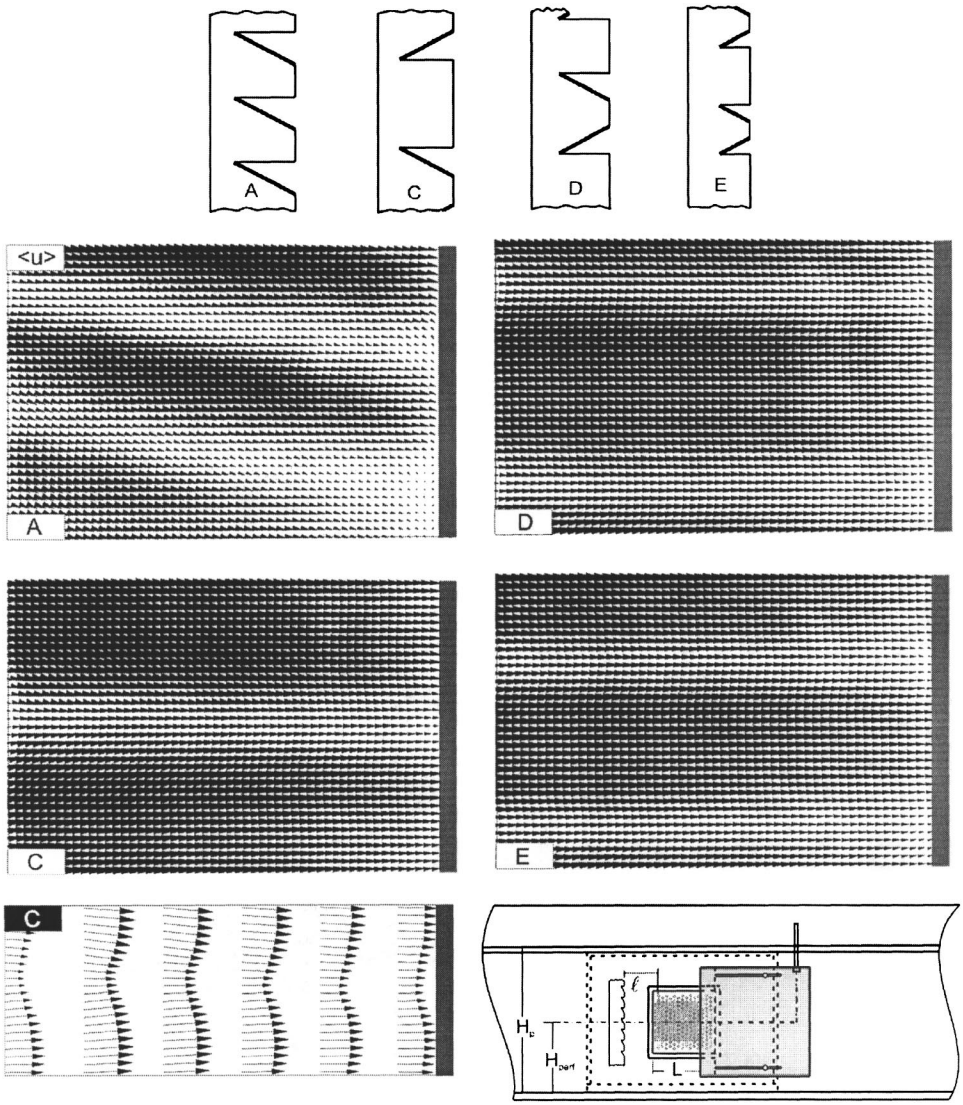

Fig. 12 Patterns of average vectors of the longitudinal (streamwise) component of velocity *u* for various vortex generators for $L/\theta=20$ and $L=152.4$ mm

Corresponding patterns of time-averaged vorticity $\langle\omega\rangle$ are given in Fig. 14 for elements *C* and *E*. The peak values of vorticity in images *C* and *E* are respectively $\omega\theta/U=0.31$ and 0.22. In other words, generation of this magnitude of dimensionless surface-normal vorticity appears to be adequate to effectively attenuate the coherent oscillation.

5 Concluding Remarks

Robust, self-sustained, purely hydrodynamic oscillations of shear flow past a perforated plate have recently been observed. These oscillations, which occur in the presence of a cavity on one side of the plate, do not involve any acoustic resonance or elastic effects. Such oscillations involve a well-defined front, which propagates along the high speed surface of the plate. The aim of the present investigation has been to induce localized velocity and vorticity effects along the span of the propagating front, such that the oscillation is attenuated. The primary findings are as follows:

a. The time records and spectra of the fluctuating pressure at the effective trailing-edge of the plate provide global indicators of the strength of the shear layer oscillation. In the presence of a three-dimensional surface element, it is possible to attain a substantial reduction in the degree of organization of the pressure fluctuation and the amplitude of its spectral peak. This indicator of attenuation is reinforced by spectra of the fluctuating velocity in regions upstream of the effective trailing-edge of the plate. The attenuation can involve either a reduction in amplitude of a sharply defined spectral peak, or transformation of the sharp spectral peak to a relatively broadband, low level peak.
b. The most effective mitigation of the oscillation, i.e., reduction in amplitude of the spectral peak, is achieved with dimensional heights h of the three-dimensional surface elements, i.e., vortex generators, of $h/\theta=1-2$, in which θ is the momentum thickness of the inflow boundary layer. Furthermore, the most effective spanwise wavelength Λ of the generators is in the range $\Lambda/\theta=4-12$.
c. The mechanism of attenuation of the self-excited oscillation involves, first of all, streamwise striations of instantaneous velocity u and time-averaged velocity $\langle u\rangle$ at spanwise locations corresponding to the deployment of the vortex generators. The maximum value of the local defect of the time averaged velocity $\langle u\rangle$ is of the order of one-third the undisturbed region of velocity away from the defect. These defects of $\langle u\rangle$ are associated with corresponding peaks of vorticity ω normal to the surface of the plate. These peaks are in the range $\omega\theta/U=0.22-0.43$; they can have either a positive or negative sign. Furthermore, it is shown that when

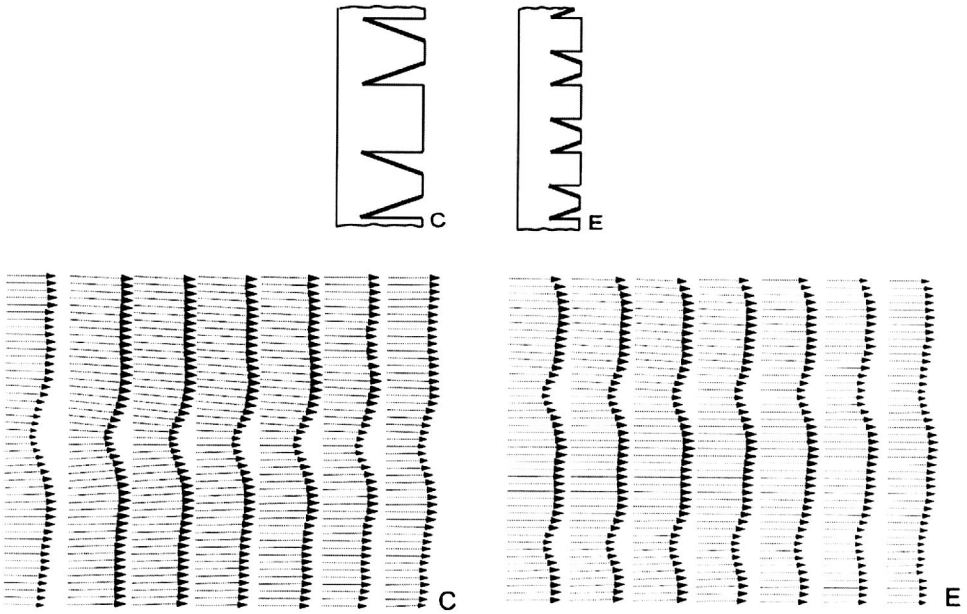

Fig. 13 Patterns of the averaged velocity vectors at various streamwise locations for different vortex generators. $L/\theta=20$, $L=152.4$ mm and width w of field of view is $w/\theta=19$.

the striations of $\langle u \rangle$ or $\langle \omega \rangle$ are angled substantially with respect to the freestream, the attenuation is less effective compared to cases where the induced striations are parallel to the freestream.

d. A critical length L of the perforated plate exists, beyond which effective attenuation is not possible; it has a value of approximately $L/\theta=20$. This critical length is due to the decay of the defect of $\langle u \rangle$ with streamwise distance along the perforated plate, such that, at sufficiently large value of L/θ, the defect becomes small. For the analogous case of self-sustained oscillations of shear flow along a cavity in the absence of a perforated plate, it is well known that the re-

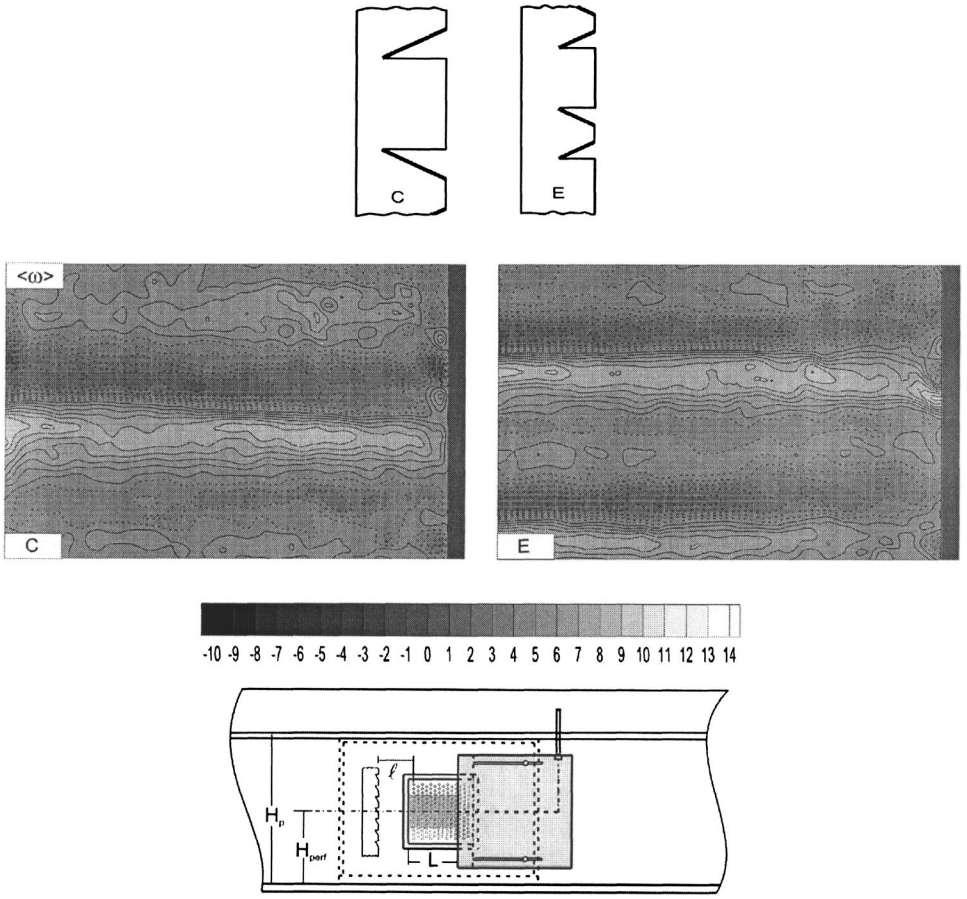

Fig. 14 Contours of averaged vorticity for various vortex generators for $L/\theta=20$

gion of upstream influence that sustains highly coherent oscillations occurs at the trailing (impingement) edge of the cavity. If this concept is extended to the present case, then spanwise defects of $\langle u \rangle$ (and u) would correspond to decreased spanwise correlation of the shear-flow–trailing-edge interaction, thereby resulting in a less effective upstream influence and amplitude of oscillation; conversely, this defect becomes small at the trailing-edge when L/θ is adjusted to larger values; the spanwise variations of $\langle u \rangle$ (and u) are not as large, and attenuation is no longer possible.

e. When the length of the perforated plate downstream of the vortex generators exceeds a certain value, two-dimensional oscillations reappear in the flow over the perforated plate. These observations suggest that the height h of vortex generators should be more than 5% of the length of the perforated plate, i.e., $h/L > 0.05$, in order to disrupt the two-dimensional character of the flow over the entire length of the perforated plate. This criterion, however, must be further considered before it is taken as a design guideline.

Acknowledgments

The authors gratefully acknowledge the financial support of the Office of Naval Research under Grant No. N00014-01-1-0606, monitored by Dr. Pat Purtell and Dr. Ron Joslin. Supplemental support in the form of facilities and instrumentation was provided by Air Force Office of Scientific Research Grant No. F49620-02-1-0061. The continuing advice of Dr. Ted Farabee of the Naval Surface Warfare Center, Carderock, is appreciated.

References

[1] Meyer, E., Mechel, F., and Kurtze, G., 1958, ''Experiments on the Influence of Flow on Sound Attenuation in Absorbing Ducts,'' J. Acoust. Soc. Am., **30**, pp. 165–174.

[2] Dean, P., 1972, ''On the Measurement of the Local Acoustic Impedance of the Walls of Flow Ducts and Its Use in Predicting Sound Attenuation,'' Ph.D. thesis, University of Southampton.

[3] Adams, W. J., 1974, ''The Design of Reactive Silencers for Internal Combustion Engines,'' Institute of Sound and Vibration Research, Interim Report, University of Southampton.

[4] Tsui, C. Y., and Flandro, G. A., 1977, ''Self-Induced Sound Generation by Flow Over Perforated Duct Liners,'' J. Sound Vib., **50**, pp. 315–331.

[5] Bauer, A. B., and Chapkis, R. L., 1977, ''Noise Generated by Boundary Layer Interaction With Perforated Acoustic Liners,'' J. Aircr., **14**, pp. 157–160.

[6] Ronneberger, D., 1980, ''The Dynamics of Shearing Flow Over a Cavity—a Visual Study Related to the Acoustic Impedance of Small Orifices,'' J. Sound Vib., **71**, pp. 565–581.

[7] Nelson, P. A., 1982, ''Noise Generated by Flow Over Perforated Surfaces,'' J. Sound Vib., **83**, pp. 11–26.

[8] Howe, M. S., 1997, ''Sound Produced by Turbulent Flow Over a Perforated Inlet,'' J. Sound Vib., **139**, pp. 227–240.

[9] Dickey, N. S., Selamet, A., and Ciray, M. S., 2001, ''An Experimental Study of the Impedance of Perforated Plates With Grazing Flow,'' J. Acoust. Soc. Am., **110**, pp. 2360–2370.

[10] Bruggeman, J. C., Velekoop, J. C., Van Der Knapp, F. G. P., and Keuning, P. J., 1991, ''Flow-Excited Resonance in a Cavity Covered by a Grid: Theory and Experiments,'' NCA-Vol.11/FED-Vol.130, Flow Modeling, Measurement and Control ASME, pp. 135–144.

[11] Looijmans, K. N. H., and Bruggeman, J. C., 1997, ''Simple Vortex Models for Vibration and Noise Caused by a Flow Over Louvers in a Cavity Opening,'' *Proceedings Fluid-Structure Interactions, Aeroelasticity, Flow-Induced Vibration and Noise Symposium*, **1** ASME AD-Vol. 53-1, pp. 351–359.

[12] Zoccola, P. J., 2002, ''Excitation by Flow Over an Obstructed Opening,'' ASME IMECE2002/NCA-33374.

[13] Celik, E., and Rockwell, D., 2002, ''Shear Layer Oscillation Along a Perforated Surface: A Self-Excited Large-Scale Instability,'' Phys. Fluids, **14**(**12**), pp. 4444–4448.

[14] Ozalp, C., Pinarbasi, A., and Rockwell, D., 2003, ''Self-Excited Oscillations of Turbulent Inflow Along a Perforated Plate,'' J. Fluids Struct., **17**(7), pp. 955–970.

[15] Rockwell, D., and Naudascher, E., 1978, ''Review—Self-Sustaining Oscillations of Flow Past Cavities,'' ASME J. Basic Eng., **100**, pp. 152–165.

[16] Gharib, M., and Roshko, A., 1987, ''The Effect of Flow Oscillations on Cavity Drag,'' J. Fluid Mech., **117**, pp. 501–530.

[17] Howe, M. S., 1997, ''Edge, Cavity and Aperture Tones at Very Low Mach Numbers,'' J. Fluid Mech., **330**, pp. 61–84.

[18] Howe, M. S., 1998, *Acoustics of Fluid-Structure Interactions*, Cambridge University Press, New York.

[19] Ekmekci, A., and Rockwell, D., 2003, ''Self-Sustained Oscillations of the Shear Flow Past a Slatted Plate Coupled With Cavity Resonance,'' J. Fluids Struct., **17**(8), pp. 1237–1245.

[20] Keller, J. J., and Escudier, M. P., 1979, ''Periodic-Flow Aspects of Throttles, Cavities, and Diffusers,'' Brown-Boveri Research Center Report RLR-79-144 S, November.

[21] Karadogan, H., and Rockwell, D., 1983, ''Toward Attenuation of Self-Sustained Oscillations of a Turbulent Jet Through a Cavity,'' ASME J. Fluids Eng., **105**(3), pp. 335–340.

[22] Bruggeman, J. C., Hirschberg, A., van Dongen, M. E. H., Wijnands, A. P. J., and Gorter, J., 1991, ''Self-Sustained Aero-Acoustic Pulsations in Gas Transport Systems: Experimental Study of the Influence of Closed Side Branches,'' J. Sound Vib., **150**(3), pp. 371–393.

[23] Newland, D. E., 1993, *An Introduction to Random Vibrations, Spectral and Wavelet Analysis*, 3rd ed., Longman Singapore Publishers, Singapore.

Flow Past a Spinning Sphere With Surface Blowing and Heat Transfer

H. Niazmand

M. Renksizbulut*

Mechanical Engineering Department, University of Waterloo, Waterloo, Ontario, Canada N2L 3G1

Computations are performed to determine the transient three-dimensional heat transfer rates and fluid forces acting on a stream-wise spinning sphere for Reynolds numbers in the range $10 \leqslant Re \leqslant 300$ and angular velocities $\Omega_x \leqslant 2$. In this Re range, classical flow past a solid sphere develops four different flow regimes, and the effects of particle spin are studied in each regime. Furthermore, the combined effects of particle spin and surface blowing are examined. Sphere spin increases drag in all flow regimes, while lift shows a nonmonotonic behavior. Heat transfer rates are not influenced by spin up to a certain Ω_x but increase monotonically thereafter. An interesting feature associated with sphere spin is the development of a special wake regime such that the wake simply spins without temporal variations in its shape. For this flow condition, the magnitudes of the lift, drag, and heat transfer coefficients remain constant in time. Correlations are provided for drag and heat transfer. [DOI: 10.1115/1.1852471]

Introduction

Flow over spheres is a fundamental problem encountered in many engineering devices. It is well known that the motion of spherical particles in some applications also involves rotation and surface blowing, such as the motion of fuel droplets in combustors. Although particle rotation typically occurs around an arbitrary axis in space, investigation of cases with rotation axes normal and parallel to the principal flow direction can provide fundamental information. The characteristics of the flow field for particle rotation in the streamwise direction (*spin*) are quite different from that in the transverse direction (*rotation*). Rotation displaces and reduces the recirculation region of the wake such that at sufficiently high rotational speeds it is completely suppressed [1], while spin has the opposite effect. The structure of the near wake region has a strong influence on the behavior of the drag and lift forces as well as the heat transfer characteristics of the particle, and therefore, deserves close examination.

For uniform flow past a sphere, the wake forms at $Re \cong 20$ and undergoes several well-defined transitions as the Reynolds number is increased. First transition occurs at $Re \cong 212$, where the axisymmetric steady wake becomes planar symmetric yet steady and attached. In the second transition, the steady planar-symmetric wake becomes unsteady at $Re \cong 270$ forming a periodic wake with vortex shedding. The details of the wake structure in each wake regime have been investigated both experimentally and theoretically [2–8]. However, a review of the relevant literature provides limited information on the effects of particle spin. In particular, the simultaneous effects of particle spin and nonuniform surface blowing (e.g., droplet evaporation) have not been addressed yet.

The case of particle rotation has attracted some attention in the literature, where the experimental studies of Sakamoto and Haniu [9], Oesterle and Dinh [10], and Best [1], and the numerical studies of Salem and Oesterle [11], and Kurose and Komori [12] in the range of low- to moderate-Reynolds numbers ($1 < Re < 300$) can be mentioned among others. However, for the case of a spinning sphere much less information is available in this Re range. The only known work is the numerical study of Kim and Choi [13]. They considered $Re = 100$ in the steady symmetrical regime, $Re = 250$ in the steady nonsymmetrical regime, and $Re = 300$ in the unsteady wake regime, for angular velocities of $\Omega_x \leqslant 1$. It is reported that the forces acting on the sphere are influenced by spin, and the vortical structures behind the particle are significantly modified. For higher Re flows over spinning spheres, Clift et al. [14] have summarized previous studies and pointed out that the transition to turbulence, which is identified by a sudden drop in the standard drag curve, occurs at lower Re with increased spin. Similar behavior is observed in the present study at moderate Re, such that increasing particle spin reduces the transitional Re between the different wake regimes.

Information regarding the heat transfer characteristics of flow over a spinning sphere is also limited and mainly for high Re flows. Eastop [15] conducted an experimental investigation of the influence of spin on heat transfer from a sphere to an air stream for $4640 < Re < 11{,}590$ and $\Omega_x \leqslant 2$. It was found that the average heat transfer rates are affected only when $\Omega_x \geqslant 0.5$. Furuta et al. [16] performed similar experiments to evaluate mass transfer rates at higher spinning speeds. Measurements were made over the Ω_x range of 0.2 to 25 at four values of Re (0,2000,3800,10,000). They also found that the local and average mass transfer coefficients are almost unaffected by spin up to about $\Omega_x \approx 0.5$, gradually increasing with Ω_x thereafter.

Vaporization of a spinning fuel droplet in an otherwise quiescent environment has been studied analytically by Lozinski and Matalon [17]. It is shown that the vaporization rate is enhanced by spin due to the creation of a secondary flow toward the droplet poles and outward from the equator. This finding is supported by the experimental results of Pearlman and Sohrab [18]. Recently, Niazmand and Renksizbulut [19,20] carried out numerical investigations of the flow and temperature fields around rotating spheres with surface blowing. It is shown that transient behavior of important flow parameters such as the lift and drag coefficients are significantly influenced by particle rotation and surface blowing. However, the surface-averaged heat transfer rates are not influenced appreciably by particle rotation even at high rotational speeds, whereas the local heat transfer rates are drastically affected.

The aim of the present study is to examine the transient flow field and thermal effects around a spinning sphere numerically. The range of Reynolds numbers considered here are 10 to 300, and the dimensionless angular velocity will be varied up to 2. The combined effects of particle spin and surface blowing will also be

*Corresponding author; email: metin@uwaterloo.ca

Contributed by the Fluids Engineering Division for publication on the JOURNAL OF FLUIDS ENGINEERING. Manuscript received by the Fluids Engineering Division November 2, 2003; revised manuscript received September 20, 2004. Review Conducted by: S. Ceccio.

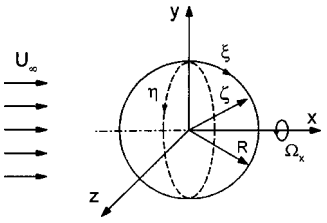

Fig. 1 Flow geometry and coordinates

addressed. Important features of the spinning-sphere flow will be compared to their counterparts for rotating spheres reported in [19,20].

Problem Formulation

The flow geometry and sphere in generalized coordinates (ξ,η,ζ), which in the present problem lie along the spherical coordinates (θ,φ,r) respectively, are shown in Fig. 1. A uniform stream in the positive x direction flows over a sphere spinning with constant angular velocity ω_x around the principal flow axis. The laminar, constant property, viscous flow under study is governed by the usual set of continuity, momentum and energy equations as follows:

$$\int_A \vec{V}\cdot\vec{n}dA=0 \tag{1}$$

$$\frac{\partial}{\partial\tau}\int_\forall \vec{V}d\forall+\int_A \vec{V}\vec{V}\cdot\vec{n}dA=-\int_A p\vec{n}dA+\frac{1}{\mathrm{Re}}\int_A \nabla\vec{V}\cdot\vec{n}dA \tag{2}$$

$$\frac{\partial}{\partial\tau}\int_\forall Td\forall+\int_A T\vec{V}\cdot\vec{n}dA=\frac{1}{\mathrm{Re}\,Pr}\int_A \vec{\nabla}T\cdot\vec{n}dA \tag{3}$$

These equations have been nondimensionalized using D, U_∞, and (D/U_∞) as the characteristic length, velocity, and time scales, respectively. The nondimensional fluid temperature is defined as $T=(T_f-T_\infty)/(T_s-T_\infty)$.

Inflow boundary conditions are simply $u=1$ and $v=w=T=0$. For outflow, zero gradients along the streamlines are applied for $\theta\geqslant 120$ deg to all variables such that $\vec{V}\cdot\vec{\nabla}f=0$, where $f=u$, v, w, T. On the surface of a solid sphere, the flow satisfies the no-slip boundary condition, $u=v=w=0$. In the case of a porous sphere with surface mass efflux, the blowing velocity normal to the surface is prescribed as $\vec{V}_n=C(1+\cos\theta)\vec{n}$, where θ is measured form the front stagnation point. Coefficient C is a measure of the strength of the surface blowing and it is chosen in the range $0.01\leqslant C\leqslant 0.04$, which corresponds to conditions encountered in many droplet vaporization processes. On the surface of a sphere, spinning with a nondimensional angular velocity of $\Omega_x=R\omega_x/U_\infty$ around the x axis in the counterclockwise direction, the velocity components are

$$u=0,\quad v=\Omega_x\sin\varphi\sin\theta,\quad w=\Omega_x\cos\varphi\sin\theta \tag{4}$$

With the simultaneous application of surface blowing and spin, the velocity components at the surface become

$$u=\vec{V}_n\cdot\vec{e}_x,\quad v=\Omega_x\sin\varphi\sin\theta+\vec{V}_n\cdot\vec{e}_y,$$
$$w=\Omega_x\cos\varphi\sin\theta+\vec{V}_n\cdot\vec{e}_z \tag{5}$$

where $\vec{e}_x$, $\vec{e}_y$, and $\vec{e}_z$ are unit vectors in the x, y, and z directions, respectively.

Initial conditions correspond to a sudden introduction of a spinning sphere with or without surface blowing into an otherwise uniform free stream. The initial pressure is specified as zero over the whole computational domain.

The resultant force acting on the particle is obtained by integrating the normal and tangential stresses on the sphere surface

$$\vec{F}=-\int_A p\vec{n}dA+\int_A \vec{\vec{\tau}}\cdot\vec{n}dA \tag{6}$$

which is nondimensionalized as $\vec{C}_F=\vec{F}/(\pi R^2\rho U_\infty^2/2)$. The component of $\vec{C}_F$ along the x axis is the drag coefficient C_D. The contribution to drag arising from non-uniform surface blowing is negligible. For flow over a spinning sphere the components of $\vec{C}_F$ along the y and z axes have finite values, and therefore, the lift coefficient is defined as $C_L=\sqrt{C_y^2+C_z^2}$. This is in contrast to the flow over a rotating sphere, where only one $\vec{C}_F$ component normal to the principal flow direction exists due to the presence of a plane of symmetry for the range of parameters considered here [5,20]. The dimensionless average heat taransfer coefficient is the Nusselt number defined as

$$\mathrm{Nu}(\tau)=\frac{hD}{k}=\frac{1}{A}\int_A \vec{\nabla}T\cdot\vec{n}dA \tag{7}$$

Solution Method and Accuracy

The governing equations given above were solved numerically. A control-volume-based integration technique was used in performing the discretization process in a generalized coordinate system (ξ,η,ζ). Based on Taylor-series expansion, the discretized equations are second order accurate in time and space. The transient terms were discretized using a three-point backward scheme. Central differencing is used in the evaluation of diffusion fluxes at the control volume faces. For convective terms, a central differencing scheme with a deferred correction is employed after linearizing using the best available estimates of velocity components from the previous iteration.

The numerical method employed has been described in detail by Dwyer [21] and further improved by Niazmand and Renksizbulut [19] to properly capture the vortex shedding process at moderate Reynolds numbers, and will be only briefly outlined here. The method consists of two steps. The velocity components are first calculated from the momentum equations using an alternating-direction predictor-corrector scheme. Since the pressure field is not known at this stage, values from the previous time step are used. Then the pressure correction is calculated from the correction equation designed to satisfy the continuity equation. This pressure correction equation is of Poisson type and is solved by the predictor-corrector line-relaxation method. Thus, new estimates for the pressure and velocities are obtained until the solution converges at each time step. The converged velocity field is then used in the energy equation to determine the new temperature field.

The details of the grid independence study, as well as evidence of accuracy in predicting wake features, fluid forces, and heat transfer rates in the range of parameters considered here are given elsewhere [19,20], and therefore, will not be repeated here. In order to assess the temporal accuracy of the present numerical scheme, the time histories of the drag coefficient and separation angle for the classical problem of flow over an impulsively started solid sphere have been compared with the semi-analytical results of Dennis and Walker [22] at Re=100. As shown in Fig. 2, present calculations are in excellent agreement with their results. In this figure, the separation angle is measured from the rear stagnation point. Flow separation begins at $tU_\infty/R=0.834$ as compared to 0.854 calculated by Dennis and Walker [22]. Obviously, there are inherent temporal singularities associated with nonphysical initial conditions such as impulsive or sudden starts, and therefore, the computations always start with very small time steps, which gradually expand to prespecified maximum values. The comparison shown in Fig. 2 clearly demonstrates that all intrinsic inaccuracies involved in a sudden startup disappear very quickly and do not affect the overall temporal accuracy of the solution.

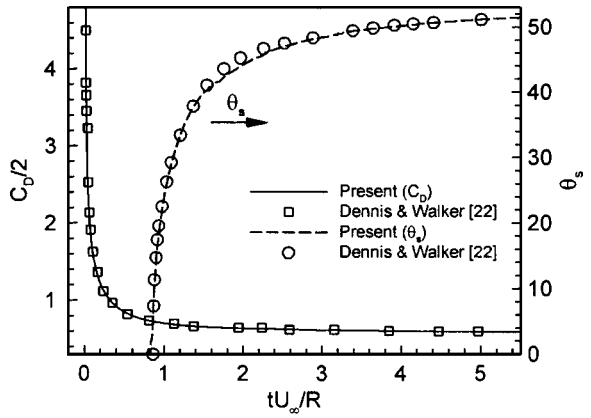

Fig. 2 Drag coefficient and separation angle histories for an impulsively started solid sphere

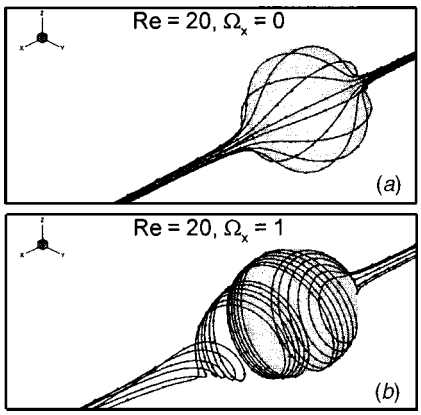

Fig. 3 (*a*)–(*b*). Streamlines at Re=20: (*a*) no spin, (*b*) $\Omega_x=1$.

Results and Discussion

Simulations are performed in the range $10\leqslant Re\leqslant 300$ covering the four different flow regimes of classical flow past a stationary solid sphere: (1) steady attached flow for $Re\leqslant 20$; (2) steady axisymmetric flow with separation for $20<Re<212$; (3) steady planar-symmetric flow for $212\leqslant Re\leqslant 270$, and (4) unsteady planar-symmetric flow with vortex shedding for $Re>270$. The effects of particle spin will be considered for Re=10, 20, 100, 200, 250, and 300 as representative of each flow regime. Transient behavior of the lift, drag, and heat transfer coefficients will be presented for spin in the range $\Omega_x\leqslant 2$, with Pr=1. Computations with surface blowing in combination with particle spin will also be discussed.

For most cases considered here, a numerical grid of $(\xi_{max},\eta_{max},\zeta_{max})=(71,50,71)$ has been used, and the far-field boundary has been set at 20 radii from the center of the sphere. The grid points are expanded only in the radial direction with an expansion ratio of about 1.09 and a dimensionless time step of $\Delta\tau=0.0025$ is used to initiate the calculations. However, this time step is increased by a factor of 1.02 to a maximum value in the range of $0.01\leqslant\Delta\tau_{max}\leqslant 0.05$ depending on the Reynolds number, spin speed, and surface blowing strength.

1. The $Re\leqslant 20$ range: Present calculations confirm that, up to $Re\cong 20$, uniform flow past a motionless sphere does not separate despite the pressure asymmetry around the particle. Particle spin enhances this asymmetry, and if spin is strong enough, a separated flow can form at much lower Re. Present calculations at Re=10 with $\Omega_x=0.25$ indicate the onset of a small separation region, which increases in length to about $0.14D$ at $\Omega_x=1$. At Re=20 with the same spinning speed, the wake length is about $0.41D$, which is equal to the wake length of a nonspinning sphere at Re=50. The wake length is defined as the distance from the rear stagnation point to the end of the separated zone along the main flow axis. The steady state flow patterns at Re=20 are shown in Figs. 3(*a*) and (*b*). In Fig. 3(*a*), the streamlines for a nonspinning sphere indicate an orderly axisymmetric flow, which leaves the surface very close to the rear stagnation point. In Fig. 3(*b*), the streamlines for a spinning sphere show that the fluid particles are dragged around the sphere several times before leaving the surface at an angle of $\theta_s=133$ deg. In this flow regime, the drag increases with particle spin by 4.6% and 7.4% at $\Omega_x=1$ for Re=10 and 20, respectively, while the heat transfer rates are essentially unaffected.

2. The $20<Re<212$ range: In this range, flows at Re=100 and 200 will be considered. Global views of the effects of spin and surface blowing on the flow structure at Re=100 are presented in Figs. 4(*a*)–(*c*). In all cases shown, the streamlines pass through the *same* grid points in the flow field around the front stagnation point. As expected, in the absence of surface blowing [Figs. 4(*a*) and (*b*)], the streamlines passing through these grid points originate far upstream around the main flow axis. However, with surface blowing [Fig. 4(*c*)], the streamlines passing through the same grid points originate from the sphere surface around the front stagnation point. Flow over a nonspinning sphere [Fig. 4(*a*)], forms a closed-bubble recirculating wake of length $L=0.87D$, which separates at $\theta_s=127$ deg. Particle spin, as shown in Fig. 4(*b*), drags the fluid around the sphere and forms a spinning wake with a larger size and an earlier flow separation. Table 1 shows that the wake length increases while the separation angle decreases with increasing spin for Re=100. The same is almost true for Re=200 except at $\Omega_x=1$, when the wake becomes unsteady and its length varies slightly in time. The physical reason for this behavior is related to the centrifugal forces acting on the fluid, which have the same effect as an additional adverse pressure gradient in the wake region. The centrifugal effects are more profound at higher spinning speeds and the present calculations at $\Omega_x=2$ indicate more than 200% increase in the wake length as

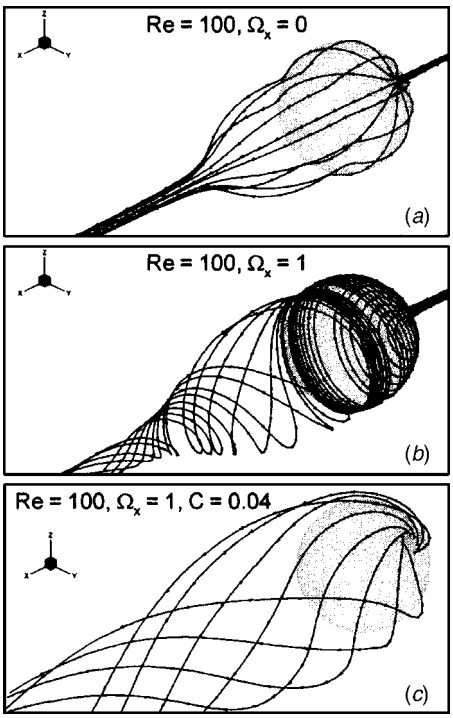

Fig. 4 (*a*)–(*c*). Streamlines at Re=100: (*a*) no spin or blowing, (*b*) spin only, and (*c*) spin and blowing.

Table 1 Wake length and separation angle with increasing particle spin

	Re = 100		Re = 200	
Ω_x	L/D	θ_s	L/D	θ_s
0	0.87	126.8	1.37	116.6
0.25	0.90	125.7	1.38	116.4
0.5	1.01	122.6	1.49	114.4
1	1.32	115.8	1.45	110.5

compared to flow over a nonspinning sphere. As shown in Fig. 4(*c*), the combined effects of spin ($\Omega_x=1$) and surface blowing ($C=0.04$) cause the boundary layer to be pushed strongly away from the surface, resulting in a much larger recirculation zone ($L=1.60D$), which influences the surface forces and heat transfer rates considerably, as will be discussed later.

Figure 5 shows the temporal behavior of the drag coefficient with increasing spin at Re=100. The fact that higher spin causes the flow to separate sooner accounts for the increase in C_D with increasing Ω_x. An examination of the pressure and viscous contributions to total drag indicates that the changes are essentially all due to pressure drag. The effect of spin on C_D is more significant at higher Ω_x such that C_D is 13% larger at $\Omega_x=1$, and 37% larger at $\Omega_x=2$ as compared to the $\Omega_x=0$ case. The case with $\Omega_x=2$ is considered to determine if the wake shows any signs of unsteadiness or lack of axisymmetry at higher spinning speeds. A study of the temporal behavior of the wake and the drag coefficient at $\Omega_x=2$ indicates that the wake is still steady and axisymmetric despite its considerable enlargement and streamwise stretching. The steady-state values of C_D at $\Omega_x=0.5$ and 1 compare very well with the numerical results of Kim and Choi [13].

In Fig. 5, an oscillatory behavior in C_D is observed with increasing spin at very early times ($\tau\approx1.5$). This is related to the sudden introduction of the spinning sphere into the uniform and steady free stream. Initial drag behavior is strongly affected by the onset of flow separation and the rate of subsequent wake growth. In an impulsive start, the effects of spin on flow separation and wake growth are immediate whereas the effects of the background flow are delayed (see Fig. 2) by about $\tau\approx\pi/2$, which is approximately the transit time of a fluid particle over the sphere. This delayed synergistic action coupled with the contribution of sphere spin to the rapid expansion of the wake (to almost twice its nonspinning size at $\Omega_x=2$) leads to the sudden but temporary increase in the drag coefficient at $\tau\approx1.5$ seen in Fig. 5.

Figure 6 shows the temporal variation of the surface-averaged Nusselt number for the same conditions as in Fig. 5. It is clear that the heat transfer rates are almost unaffected by spin up to about $\Omega_x=0.5$, increasing thereafter. The increase in Nu is about 8% at $\Omega_x=2$ as compared to a nonspinning sphere. At much higher Reynolds numbers, Eastop [15] and Furuta et al. [16] also observed (experimentally) that the heat transfer rates are not influenced by spin at relatively low angular velocities $\Omega_x\leqslant0.5$. The distribution of Nu over most of the sphere surface is almost unaffected by particle spin, that is, the heat transfer rate is at a maximum around the front stagnation point, decreases gradually to a minimum around the separation point, then shows some recovery toward the rear stagnation point due to advection in the recirculation zone. The changes in the local Nu due to spin occur mainly in the wake region. For a spinning sphere, the wake not only becomes larger in size but also gains angular momentum, which increases the convective effects in this region, leading to higher heat transfer rates.

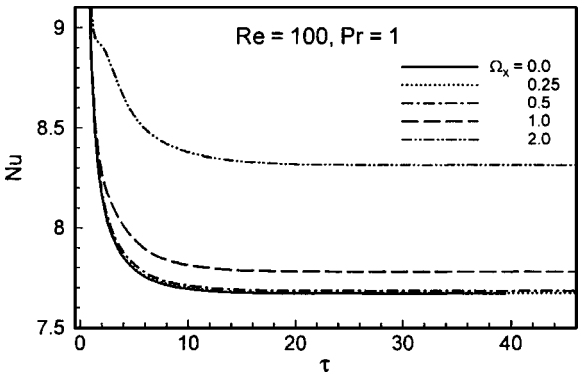

Fig. 6 Nusselt number histories at Re=100 for different spinning speeds

Figure 7 shows the simultaneous effects of surface blowing and particle spin on the heat transfer rates. As expected, there are major reductions in Nu due to surface blowing. However, a comparison of the transient Nu with surface blowing at $\Omega_x=0.5$ and 1 with their counterparts without blowing (Fig. 6) indicates that surface blowing does not alter the temporal patterns. Surface blowing also reduces the drag coefficients by about 10% from their corresponding values for a spinning sphere.

Next, the case of Re=200 is studied, which is close to the Re=212 wake transition for flow past a solid sphere. Since both sphere spin and surface blowing have destabilizing effects on the boundary layer, they are expected to influence this transition significantly. Figures 8 and 9 show the temporal behavior of the drag and lift coefficients at several spinning speeds. To study the effects of surface blowing, a case with $\Omega_x=0.5$ and $C=0.04$ is also included. Similar to the previous case (Re=100), particle spin gradually increases the drag coefficient, however unlike the previous case, the wake structure undergoes severe changes as the

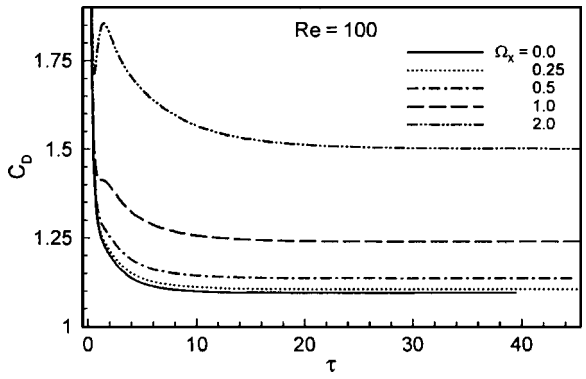

Fig. 5 Drag coefficient histories at Re=100 for different spinning speeds

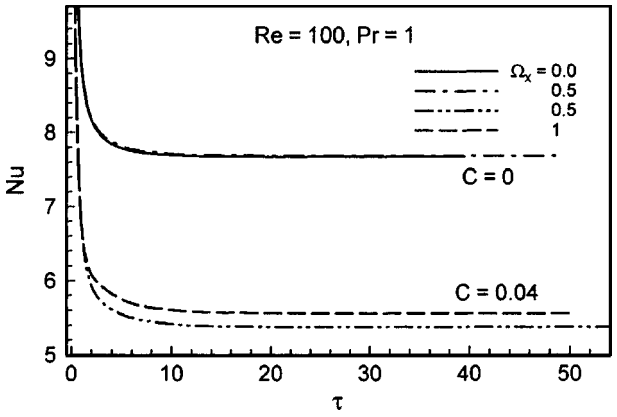

Fig. 7 Nusselt number histories at Re=100 for different spinning speeds and surface blowing

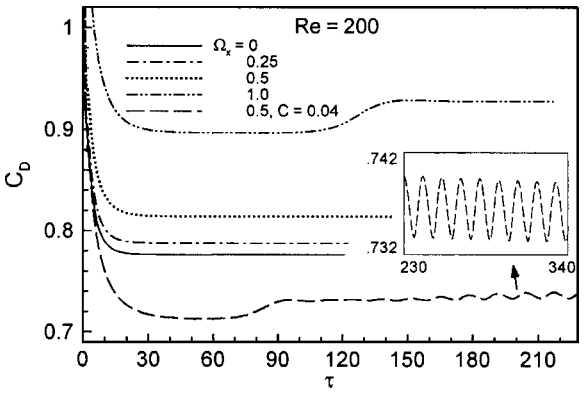

Fig. 8 Drag coefficient histories at Re=200 for different spinning speeds and surface blowing

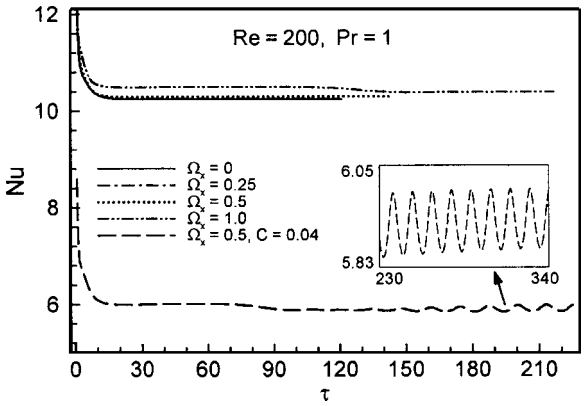

Fig. 10 Nusselt number histories at Re=200 for different spinning speeds and surface blowing

spinning speed increases. For the case of $\Omega_x=0.5$, the fact that the drag coefficient converges to a constant value while lift is zero indicates that the wake structure is steady and axisymmetric. Increasing the spin to $\Omega_x=1$ makes the wake unsteady, but very different than that of a rotating sphere [19,20]. In the present case, the wake simply spins at a constant speed (different from Ω_x) with no temporal variation in its shape. The best indicator of this kind of unsteadiness is the constant values of the lift and drag forces, while the lift components show strong sinusoidal variations with a zero time-averaged values. Note that the constant values of lift and drag are reached after the establishment of the organized periodic wake flow. Kim and Choi [13] refer to this as a *frozen wake*, since the wake remains essentially steady around a coordinate rotating at constant velocity.

Surface blowing in the absence of particle spin or rotation results in the development of a nonaxisymmetrical wake at Re=200 similar to the wake pattern that forms in the range $212 \leqslant Re \leqslant 270$ for flow over a solid sphere. In combination with sphere rotation, this non-symmetrical wake transforms into an unsteady wake with vortex shedding [19]. Similar behavior is observed here when both surface blowing with $C=0.04$ and sphere spin with $\Omega_x=0.5$ are applied simultaneously. The reduction in the drag coefficient is mainly due to surface blowing that reduces friction drag. The unsteadiness in the wake manifests itself as fluctuations in the lift and drag coefficients, which appears after the formation of a symmetrical wake (where $C_L=0$) and its subsequent transformation to a steady but nonsymmetrical wake, resulting in the sudden increase in lift as seen in Fig. 9.

In Fig. 10, the temporal variations of the Nusselt number for the same flow parameters as in Fig. 8 are shown. Similar to the flow at Re=100, for $\Omega_x \leqslant 0.5$, heat transfer is essentially unaffected by particle spin, while Nu increases at higher Ω_x. The case with the combined effects of surface blowing and particle spin indicates an unsteady thermal wake with periodic behavior in the heat transfer rate. As expected, a major reduction in heat transfer occurs because of the thickening of the thermal boundary layer due to surface blowing. It is noted that for the case with $\Omega_x=1$, Nu reaches a constant value despite the unsteady behavior of the thermal wake as shown in Fig. 11, due to the frozen wake structure indicated earlier. In Fig. 11, the instantaneous isotherms in the *x*-*y* plane at five time levels evenly distributed through one complete cycle are plotted. The complete similarity of the isotherms in the first and last panels confirms the periodicity of the thermal field. The isotherms in all panels show a thin thermal boundary layer around the front half of the sphere up to the separation point, which is basically not affected by the unsteadiness in the thermal wake. Similar thermal patterns appear in the *x*-*z* plane with a phase lag, which indicates that the whole thermal wake is spinning around the *x*-axis at a constant angular speed while conserving its shape.

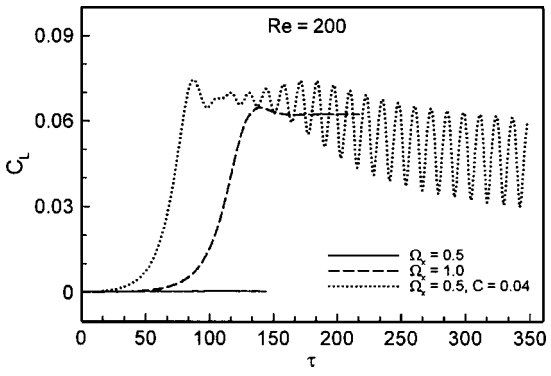

Fig. 9 Lift coefficient histories at Re=200 for different spinning speeds and surface blowing

3. The $212 \leqslant Re \leqslant 270$ range: In this wake regime, Re=250 will be considered. Unlike the previous regime, which features a closed axisymmetric recirculating wake for flow over a solid sphere, the wake here develops a flow in the azimuthal direction on either side of the symmetry plane. Despite the breakdown of the axisymmetric wake structure, there is no vortex shedding. However, any source of instability in the boundary layer, such as sphere spin, rotation, or surface blowing can trigger the shedding process and cause an unsteady wake flow to develop. The present study shows that even a low level of spin such as $\Omega_x=0.1$ can initiate an unsteady wake structure. The same is true for surface blowing and sphere rotation [19].

Figures 12(*a*) and (*b*) show the temporal behavior of the drag and lift coefficients for three different spinning speeds. For the case of $\Omega_x=0.25$, the drag and lift coefficients approach constant values after the initial temporal variations, which can be interpreted as the formation of a steady planar symmetric wake flow, similar to that of a nonspinning sphere. However, it is interesting to note that the wake structure at this Ω_x develops an unsteady pattern similar to the case with Re=200 and $\Omega_x=1$. The periodic behavior of the components of the lift coefficient with a zero time average, shown in Fig. 13, is an indication of the unsteady wake flow with a frozen state at $\Omega_x=0.25$. The numerical results of Kim and Choi [13] also show similar wake patterns for $0.1 \leqslant \Omega_x \leqslant 0.3$.

The drag coefficients in Fig. 12(*a*) show a gradual but nonlinear increase with increasing spin. The time-averaged drag coefficients at $\Omega_x=0.5$ and 1 are 0.748 and 0.858, respectively, which are about 5% and 21% higher than that of a nonspinning sphere at Re=250. Both values are in excellent agreement with the results of Kim and Choi [13]. The unsteady behavior of the wake at $\Omega_x=0.5$ is more clear in the time variation of the lift coefficient in

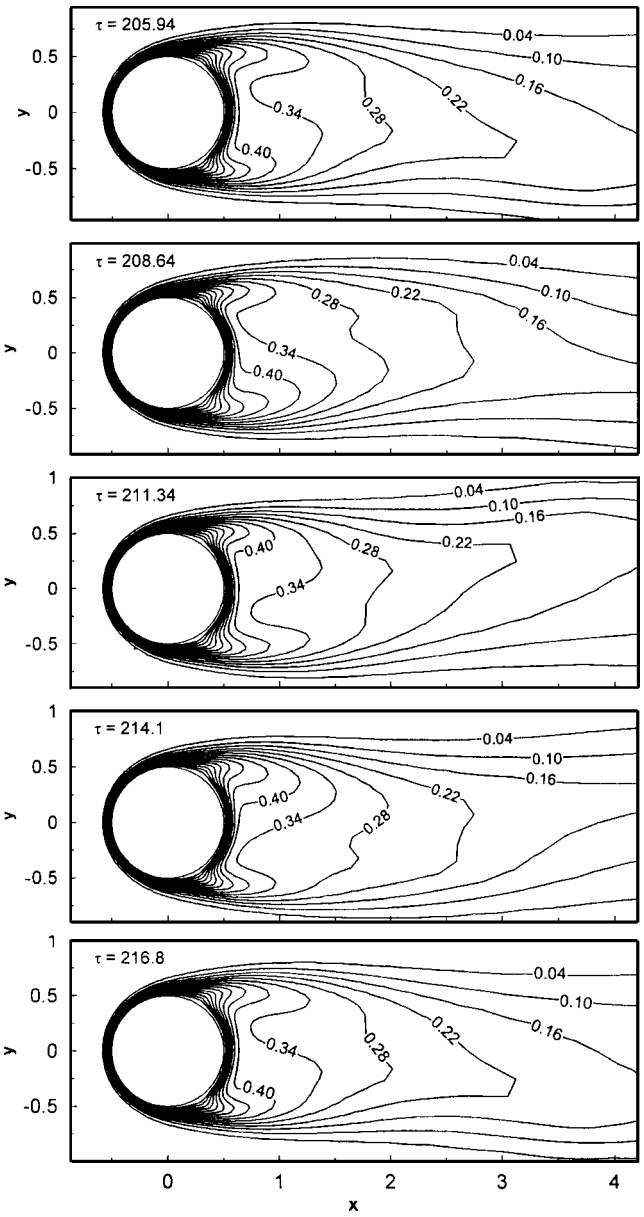

Fig. 11 Isotherms in one cycle for flow over a spinning sphere at Re=200 with $\Omega_x=1$

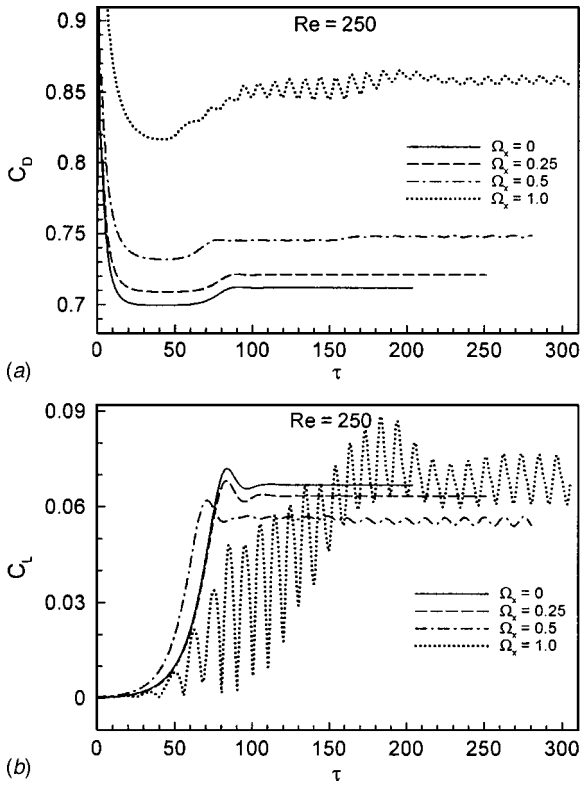

Fig. 12 (a)–(b). Drag and lift coefficients at Re=250 for different spinning speeds.

Fig. 12(b). On the other hand, the temporal behavior of the lift coefficient at $\Omega_x=0.25$ is similar to the non-spinning sphere, where C_L is zero at early times due to the formation of an axisymmetric wake, while it increases sharply to its maximum value when the wake loses its axisymmetry. Later, the vortex shedding process begins and the wake develops an organized periodic structure as evidenced by the oscillatory behavior of the lift coefficient. Note that at a higher spinning speed $\Omega_x=1$, the vortex shedding begins immediately after the formation of the axisymmetric wake, which causes the establishment of the final organized periodic wake to occur in a longer time span. From Fig. 12(b), the non-monotonic behavior of the time-averaged lift coefficient with increasing Ω_x can also be inferred. Numerical results of Kim and Choi [13] also indicate a decrease in lift up to $\Omega_x \cong 0.5$ followed by a gradual increase thereafter.

In Fig. 14, the Nusselt number variations are shown for the same flow conditions as in Fig. 12. The development of an unsteady periodic thermal wake is clear for cases with $\Omega_x=0.5$ and 1, while the presence of a frozen wake structure at $\Omega_x=0.25$ leads to a constant Nu despite its unsteady nature. It is clear that particle spin gradually increases the time-averaged heat transfer rates due to enhanced convection in the wake region, yet its effect is limited to about 3% even at high Ω_x.

Surface blowing also leads to the development of a periodic wake at this Reynolds number. Clearly, the combined effects of particle spin and surface blowing are expected to create even greater unsteadiness. Consider, for example, the case of $\Omega_x=0.25$ and $C=0.04$ for surface blowing. The wake structure at this flow condition in the absence of blowing is unsteady but frozen. The superposition of surface blowing leads to the development of an unsteady wake with associated temporal fluctuations in the lift and drag coefficients, as shown in Fig. 15. However, these fluctuations die out in time, and after a long period of time, the wake almost attains an unsteady frozen state, in which the lift and drag coefficients approach constant values.

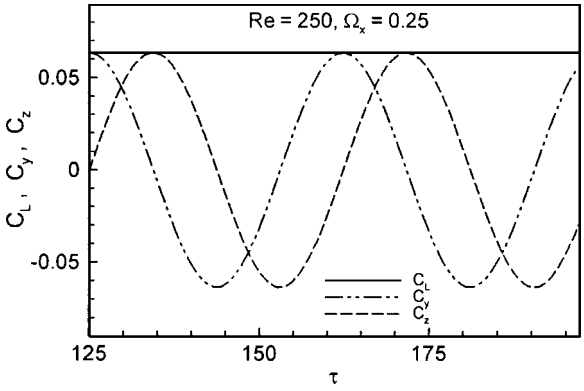

Fig. 13 The components of the lift coefficient at Re=250 with $\Omega_x=0.25$

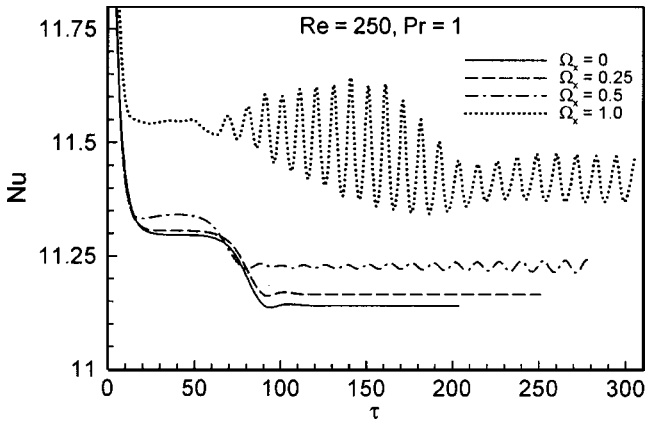

Fig. 14 Nusselt number histories at Re=250 for different spinning speeds

4. The Re>270 range: Computations at Re=300 indicate a loss of axial symmetry and the development of a time periodic wake with vortex shedding. However, the wake contains a plane of symmetry, which remains fixed in time. Sphere rotation does not affect the planar symmetry of the wake flow, while sphere spin causes the planar symmetry to be destroyed, which in turn delays the establishment of the fully developed shedding process.

In Figs. 16(*a*) and (*b*), time histories of the drag and lift coefficients at Re=300 and several Ω_x are shown. A comparison of the amplitudes of the C_D and C_L oscillations shows a dramatic drop at $\Omega_x=0.16$, which indicates that the wake is close to a frozen state. This finding is different from the results of Kim and Choi [13], which indicate a frozen wake at $\Omega_x=0.5$ and 0.6. It is also noticed that the amplitude of the C_L oscillations for $\Omega_x=0.05$ is about 0.01, which is a 37% reduction as compare to a nonspinning sphere. The C_L oscillations first die out at the frozen-wake state and then increase gradually but not monotonically. This is in contrast to the effects of particle rotation, which monotonically increase the amplitude of the C_L as compared to a sphere at rest [19]. The same is true for the C_D oscillation amplitudes. This can be attributed to the fact that the frozen-wake pattern does not exist for a rotating sphere.

As shown in Fig. 17, the time-averaged drag coefficient $\overline{C_D}$ increases monotonically with increased spin. The numerical results of the Kim and Choi [13] are also shown for comparison. At $\Omega_x=0.8$, $\overline{C_D}=0.762$, which is 16% higher than that for flow over a sphere at rest. Sphere rotation also causes an increase in $\overline{C_D}$, but in a more dramatic way. For example, at this Re with $\Omega_z=0.25$,

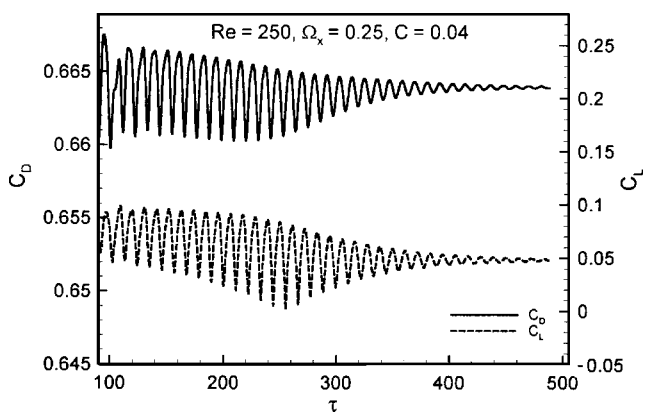

Fig. 15 Lift and drag coefficient histories at Re=250 with surface blowing

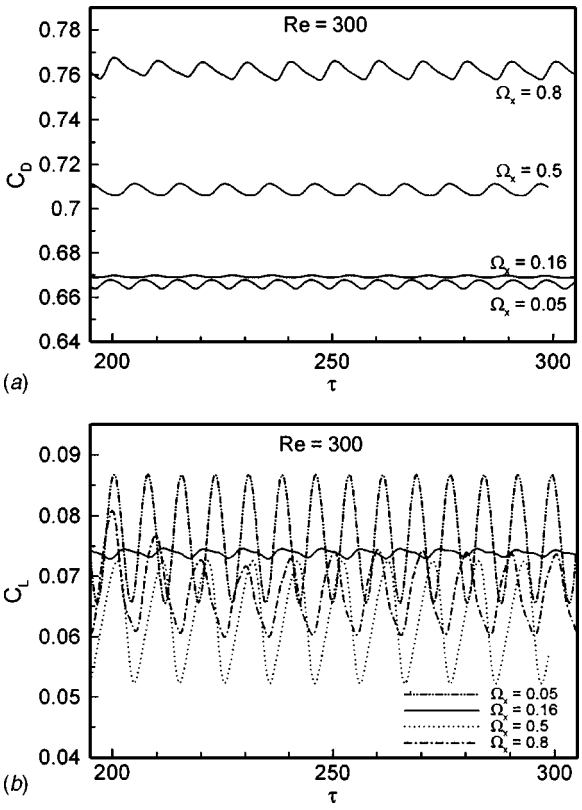

Fig. 16 (a)–(b). Drag and lift coefficient histories at Re=300 for different spinning speeds.

rotation leads to a 12% increase in $\overline{C_D}$ [19], while the corresponding increase with a spin velocity of $\Omega_x=0.25$ is only 3%. On the other hand, the time-averaged lift coefficient $\overline{C_L}$ shows a non-monotonic behavior similar to the previous case (Re=250), with a minimum located at $\Omega_x=0.5$. A similar trend is shown in [13], however the minimum $\overline{C_L}$ value reported is much below the one in the present study. No straightforward explanation can be offered for this discrepancy.

Figure 18 shows the time evolution of the surface-averaged Nu for the same Ω_x as in Fig. 15. At $\Omega_x\cong 0.16$, the frozen-wake effect damps out the heat transfer oscillations, but otherwise, the amplitudes increase with spin. At $\Omega_x=0.8$, the oscillation amplitude is about 100% larger than that of a nonspinning sphere. Considering

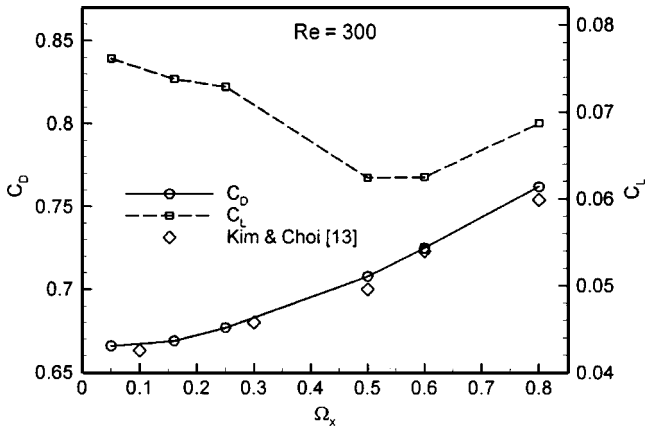

Fig. 17 Effects of particle spin on the time-averaged lift and drag coefficients at Re=300

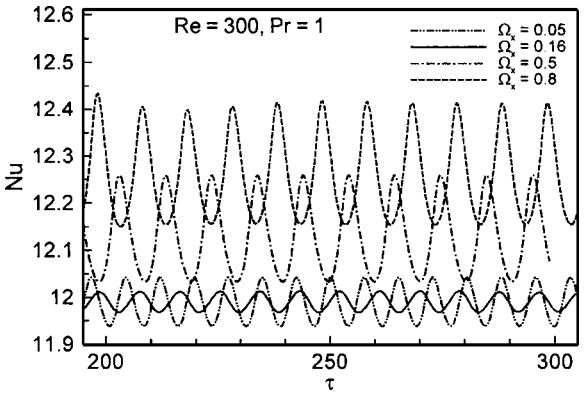

Fig. 18 Nusselt number histories at Re=300 for different spinning speeds

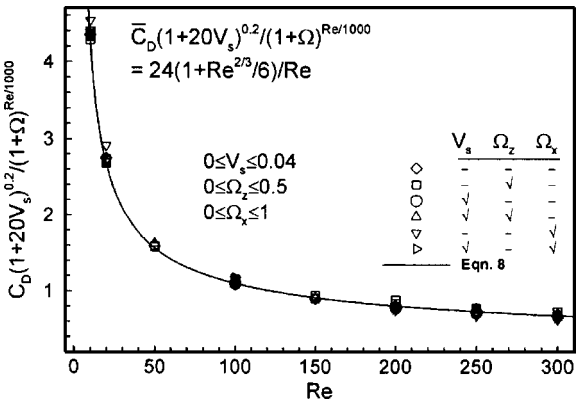

Fig. 20 Drag coefficient correlation and numerical data

the fact that at this Re, the time-averaged Nu for a nonspinning sphere is Nu≅12, it appears that particle spin barely influences heat transfer. Even at a high spin velocity of $\Omega_x=0.8$, Nu=12.28, which is only 2.3% larger.

In Fig. 19, the combined effects of particle spin and surface blowing on the temporal behavior of the lift and drag coefficients are presented. These two effects bring further complications to the complex process of vortex shedding at this Re. For flow over a solid sphere in the absence of these effects, the unsteady near-wake structure includes the formation of a vortex eye, growth of the vortex close to the sphere, and then the motion of vortex downstream (vortex shedding) [5,19]. The vortices are always formed and shed from the same orientation. For a spinning sphere, the wake also spins, however, surface blowing somewhat reduces the angular velocity of the wake, and therefore, increases the time required to complete one wake spin cycle. During this time, the wake goes through the stages indicated above, while spinning. Depending upon the wake stage, the wake spinning speed is affected by the amount of the fluid entrained into it. The spinning speed of the wake decreases when the vortex is growing in size, and increases during the time that the full size vortex moves away from the sphere and leaves behind a shear layer that rolls up and forms a new vortex eye. This nonuniform spin of the near-wake structure affects the surface forces acting on the sphere and creates the rather complicated behavior of the lift and drag coefficients as shown in Fig. 19. The time-averaged drag coefficient is basically the same as that of the flow over a solid sphere without spin or surface blowing. This means that the increase in drag due to particle spin is compensated by the reduction in drag due to surface blowing. On the other hand, the time-averaged lift coefficient $\overline{C}_L$ is about 15% greater than that for flow over a motionless sphere. Since particle spin reduces $\overline{C}_L$ at this Ω_x, the increase must be due to blowing effects.

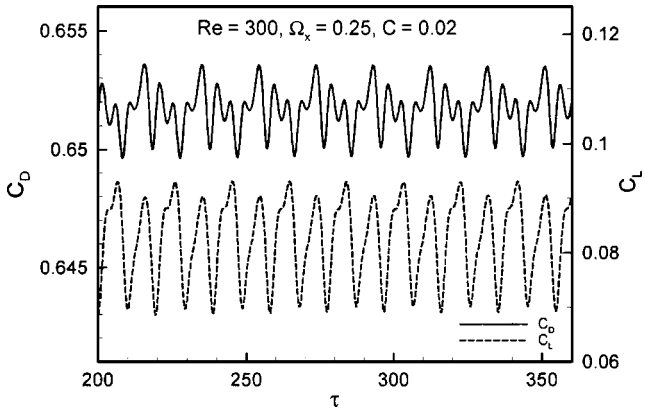

Fig. 19 Lift and drag coefficient histories at Re=300 with surface blowing

Drag and Heat Transfer Correlations

As shown in Fig. 20, the present data for the drag coefficients of spinning spheres can be accommodated (within ±10%) in the following correlation previously developed by the authors for rotating spheres [19]:

$$\frac{\overline{C}_D(1+20V_s)^{0.2}}{(1+\Omega)^{\mathrm{Re}/1000}} = \frac{24}{\mathrm{Re}}\left(1+\frac{\mathrm{Re}^{2/3}}{6}\right) \tag{8}$$

where V_s is the average nondimensional blowing velocity, and $\Omega=\Omega_z$ for rotation, $\Omega=\Omega_x$ for spin, and $\Omega^2=\Omega_x^2+\Omega_z^2$ when both are simultaneously present. This correlation is based on 87 cases and is valid for $0\leqslant V_s\leqslant 0.4$, $0\leqslant\Omega_z\leqslant 0.5$, $0\leqslant\Omega_x\leqslant 1$ and $10\leqslant\mathrm{Re}\leqslant 300$.

In general, sphere spin unlike rotation does not generate lift at lower Reynolds numbers. However, particle spin promotes flow separation and transition to an unsteady wake at higher Re, which leads to the development of lift forces. As demonstrated earlier, in such cases the lift coefficient does not show a monotonic behavior with increasing spin. Given its rather erratic behavior, no attempt has been made in the present work to develop a lift correlation.

As for heat transfer, it has been established that sphere rotation has negligible effects on the Nusselt number for $\Omega_z<0.5$ and limited influence thereafter [20]. Present calculations for spinning spheres indicate a similar trend, and the correlation suggested for rotating spheres with surface blowing [20] is found to be applicable (within ±8%) for spinning spheres as shown in Fig. 21. This

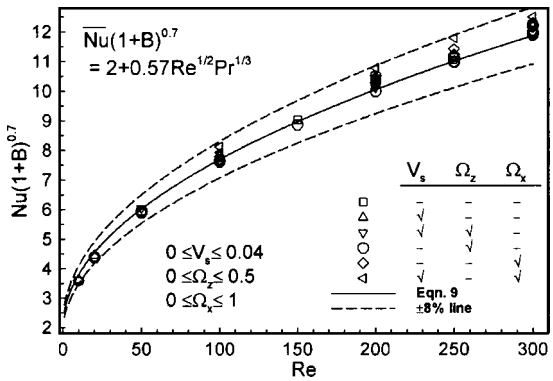

Fig. 21 Heat transfer correlation and numerical data

correlation was originally developed for the convective droplet evaporation in high temperature flows by Renksizbulut and Yuen [23]:

$$\overline{\mathrm{Nu}}(1+B)^{0.7}=2+0.57\,\mathrm{Re}^{1/2}\,\mathrm{Pr}^{1/3} \tag{9}$$

where B is the transfer number, $B=\mathrm{Pe}_s/\mathrm{Nu}$ for cases with surface blowing.

Summary and Conclusions

Fluid dynamics and heat transfer characteristics of laminar flows past spinning spheres have been studied with and without nonuniform surface blowing (simulating droplet evaporation) in the range $10\leqslant \mathrm{Re}\leqslant 300$. In contrast to sphere rotation, which causes the wake to shrink in size and even vanish at high rotational speeds, particle spin (stream-wise rotation) increases the wake size due to centrifugal effects and changes the near-wake structure dramatically. Sphere spin promotes early flow separation, and depending on the spin velocity, the flow can separate at Reynolds numbers much less than $\mathrm{Re}=20$ corresponding to classical flow past a motionless solid sphere. Particle spin (as well as rotation) also promotes earlier transition to unsteadiness in the wake. An interesting case is the development of an unsteady wake at $\mathrm{Re}=200$ with $\Omega_x=1$, which is not apparent from the temporal behavior of the lift, drag, and heat transfer coefficients, since they are invariant in time. The components of the lift coefficient develop periodic behavior with zero time-averaged values such that their net result is constant in time. The same conditions in combination with surface blowing demonstrate strong time variations in fluid flow and heat transfer characteristics, even at lower spinning velocities.

Surface-averaged global parameters such as the drag and lift coefficients are also influenced by particle spin. The drag coefficient increases with spin, while the lift coefficient behavior depends on the Re. At $\mathrm{Re}=10$, 20, and 100, a spinning sphere has zero lift with an axisymmetric wake at all Ω_x studied here. For $\mathrm{Re}=250$ and 300, the lift coefficients display nonmonotonic behavior with the minima at about $\Omega_x=0.5$. On the other hand, surface-averaged heat transfer rates are less influenced by particle spin. The Nusselt number remains unaffected by increasing spin for $\Omega_x<0.5$ in all flow regimes, increasing slowly thereafter.

Acknowledgment

The financial support of the Natural Sciences and Engineering Research Council of Canada is gratefully acknowledged.

Symbols and Abbreviations

A = area
B = transfer number, $B=\mathrm{Pe}_s/\mathrm{Nu}$
D = diameter of sphere
h = heat transfer coefficient
k = thermal conductivity
L = wake length
Nu = Nusselt number, $\mathrm{Nu}=hD/k$
$\overline{\mathrm{Nu}}$ = time-averaged Nu
$\vec{n}$ = normal unit vector
p = pressure
Pe = Peclet number, $\mathrm{Pe}=\mathrm{Re}\,Pr$
Pr = Prandtl number, $\mathrm{Pr}=\nu/\alpha$
r, θ, φ = spherical coordinates
R = radius of sphere
Re = Reynolds number, $\mathrm{Re}=U_\infty D/\nu$
t = time
T = temperature, $T=(T_f-T_\infty)/(T_s-T_\infty)$
u, v, w = velocity components in the x, y, z directions
U_∞ = free stream velocity
$\vec{V}$ = velocity vector

Greek symbols

ν = kinematic viscosity
θ_s = separation angle
τ = nondimensional time, $\tau=tU_\infty/D$
$\overleftrightarrow{\tau}$ = viscous stress tensor
Ω_x = spin speed, $\Omega_x=R\omega_x/U_\infty$
Ω_z = rotational speed, $\Omega_z=R\omega_z/U_\infty$
ω = angular velocity

Subscripts

f = fluid
s = surface
∞ = free-stream

References

[1] Best, J. L., 1998, "The Influence of Particle Rotation on Wake Stability at Particle Reynolds Numbers, $\mathrm{Re}_P<300$—Implications for Turbulence Modulation in Two-Phase Flows," Int. J. Multiphase Flow, **24**, pp. 693–720.
[2] Kim, I., and Pearlstein, A., 1990, "Stability of the Flow Past a Sphere," J. Fluid Mech., **211**, pp. 73–93.
[3] Natarajan, R., and Acrivos, A., 1993, "The Instability of the Steady Flow Past Spheres and Disks," J. Fluid Mech., **254**, pp. 323–344.
[4] Tomboulides, A. G., and Steven, A. O., 2000, "Numerical Investigation of Transitional and Weak Turbulent Flow Past a Sphere," J. Fluid Mech., **416**, pp. 45–73.
[5] Johnson, T. A., and Patel, V. C., 1999, "Flow Past a Sphere up to a Reynolds Number of 300," J. Fluid Mech., **378**, pp. 19–70.
[6] Bagchi, P., and Balachandar, S., 2002, "Steady Planar Straining Flow Past a Rigid Sphere at Moderate Reynolds Number," J. Fluid Mech., **466**, pp. 365–407.
[7] Magarvey, R. H., and Bishop, R. L., 1961, "Transition Ranges for Three-Dimensional Wakes," Can. J. Phys., **39**, pp. 1418–1422.
[8] Sakamoto, H., and Haniu, H., 1990, "A Study on Vortex Shedding From Spheres in a Uniform Flow," ASME J. Fluids Eng., **112**, pp. 386–392.
[9] Sakamoto, H., and Haniu, H., 1995, "The Formation Mechanism and Shedding Frequency of Vortices From a Sphere in Uniform Shear Flow," J. Fluid Mech. , **287**, pp. 151–171.
[10] Oesterle, B., and Dinh, B., 1998, "Experiments on the Lift of a Spinning Sphere in a Range of Intermediate Reynolds Numbers," Exp. Fluids, **25**, pp. 16–22.
[11] Salem, M. B., and Oesterle, B., 1998, "A Shear Flow Around a Spinning Sphere: Numerical Study at Moderate Reynolds Numbers," Int. J. Multiphase Flow, **24**, pp. 563–585.
[12] Kurose, R., and Komori, S., 1999, "Drag and Lift Forces on a Rotating Sphere in a Linear Shear Flow," J. Fluid Mech., **384**, pp. 183–206.
[13] Kim, D., and Choi, H., 2002, "Laminar Flow Past a Sphere Rotating in the Streamwise Direction," J. Fluid Mech., **461**, pp. 365–385.
[14] Clift, R., Grace, J. R., and Weber, M. E., 1970, *Bubbles, Drops and Particles*, Academic, New York.
[15] Eastop, T. D., 1973, "The Influence of Rotation on the Heat Transfer From a Sphere to an Air Stream," Int. J. Heat Mass Transfer, **16**, pp. 1954–1957.
[16] Furuta, T., Jimbo, T., Okazaki, M., and Toei, R., 1975, "Mass Transfer to a Rotating Sphere in an Axial Stream," J. Chem. Eng. Jpn., **8**(6), pp. 456–462.
[17] Lozinski, D., and Matalon, M., 1992, "Vaporization of a Spinning Fuel Droplet," *24th Symposium (Int.) on Combustion*, Institute, Pittsburgh, PA, pp. 1483–1491.
[18] Pearlman, H. G., and Sohrab, S. H., 1991, "The Role of Droplet Rotation in Turbulent Spray Combustion Modeling," Combust. Sci. Technol., **76**, pp. 321–334.
[19] Niazmand, H., and Renksizbulut, M., 2003, "Surface Effects on Transient Three-Dimensional Flows Around Rotating Spheres at Moderate Reynolds Numbers," Comput. Fluids, **32**, pp. 1405–1433.
[20] Niazmand, H., and Renksizbulut, M., 2003, "Transient Three-Dimensional Heat Transfer From Rotating Spheres With Surface Blowing," Chem. Eng. Sci., **58**, pp. 3535–3554.
[21] Dwyer, H. A., 1989, "Calculations of Droplet Dynamics in High Temperature Environments," Prog. Energy Combust. Sci., **15**, pp. 131–158.
[22] Dennis, S. C. R., and Walker, J. D. A., 1972, "Numerical Solutions for Time-Dependent Flow Past an Impulsively Started Sphere," Phys. Fluids, **15**(4), pp. 517–525.
[23] Renksizbulut, M., and Yuen, M. C., 1983, "Experimental Study of Droplet Evaporation in a High-Temperature Air Stream," J. Heat Transfer, **105**, 384–388.

Computational Study of the Flow Around a Ducted Tip Hydrofoil

Hildur Ingvarsdottir

Carl Ollivier-Gooch

Sheldon I. Green
e-mail: green@mech.ubc.ca

Department of Mechanical Engineering,
The University of British Columbia,
2324 Main Mall, Vancouver BC,
V6T 1Z4, Canada
[DOI: 10.1115/1.1852489]

Introduction

All lifting surfaces that terminate in a moving fluid create tip vortices as a by-product. Tip vortices on marine propellers have two undesirable effects: they reduce the efficiency of the blade and they may cause tip vortex cavitation. Tip vortex cavitation can cause pitting and erosion of the propeller and surrounding equipment and is also a source of vibration and noise.

Several devices and methods have been studied to reduce the effects of tip vortices on propellers, including the Kort Nozzle, bulbous blade tips [1], porous blade tips [2], small bladelets [3], and injecting a dilute polymer solution at the tip of a hydrofoil [4,5].

This study focuses on ducted blade tips. In this geometry, flow-through ducts, aligned approximately with the chord, are affixed at the hydrofoil/blade tips [6]. Water and wind tunnel hydrofoil tests have shown that ducts suppress tip vortex rollup, substantially delaying the onset of tip vortex cavitation with little change in the lift to drag ratio [7]. Sea trials on a ducted tip propeller and a conventional one showed that the cavitation inception index could be reduced by approximately 50% by installing the ducted tips, without a concomitant loss of efficiency [8].

A number of computational studies have been done on tip vortices, both in aerodynamic and marine applications. Studies of the most relevance to the current work include computational studies by Dacles-Mariani et al. [9] and Hsiao and Pauley [10,11]. Those studies showed qualitative agreement with experiments, but differed in quantitative measures such as tip vortex size and strength.

In this paper, our objective is *not* to advance the state of the art in computational techniques for tip vortex flows, but rather to use existing tools to perform a comparative study of hydrofoils with and without ducted tips. While we do not expect precise quantitative results, we do expect to observe correct trends in flow behavior with changes in geometry. As such, this work should provide good physical insight and a basis for later optimization of a ducted tip propeller blade.

Modeling Considerations

The current study considers a uniform flow past two hydrofoils with a modified National Advisory Committee for Aeronautics (NACA) 64–309 cross section. One of the hydrofoils has a rounded tip whereas the other has a duct attached to its tip as described below. The hydrofoils, their computational domains, and the flow properties of the surrounding fluid were chosen with comparison to the experimental data of Green [12] in mind.

Geometry

Both hydrofoils are without twist and taper and have an aspect ratio of 1.17 based on the semi-span (s)[1]. The semi-span of the rounded tip hydrofoil is measured from the root of the hydrofoil to the spanwise station where the rounding of the tip starts. The rounded tip is formed by joining semi-circles of diameter equal to the local foil thickness, placed at regular intervals along the chord (c).

The semi-span of the ducted tip hydrofoil (Fig. 1) is based on the average spanwise distance between the root of the foil and the intersection curve between the duct and the hydrofoil (the change in span chordwise is less than $\pm 0.5\%$). The duct has an outside diameter of 0.19 c and is 0.67 c long and is attached flush with the hydrofoil trailing edge, with its central axis aligned with the camber line. The duct has thus a slight curvature to it. The thickness of the wall is 0.013 c at the front top and bottom of the duct, but tapers off to almost no thickness along the whole outboard side of the duct as well as towards the trailing edge of the duct. The shape of the duct and its attachment to the foil have been made to resemble as closely as possible the original ducted tip hydrofoil for which the experimental results are available. It is however impossible to replicate the original hydrofoil perfectly; the greatest difference between the two occurs in the area where the duct and the hydrofoil meet. On the original hydrofoil a fillet was added to smooth the intersection but that fillet has not been replicated in the computational model due to the difficulty in creating and meshing a hydrofoil with such a fillet.

The dimensions of the computational domain were chosen so that the cross section perpendicular to the freestream flow would be the same as the corresponding cross section of the tunnel in which the experiments were performed. The flow domain is 2 chord lengths high and wide. The domain extends 2 chord lengths downstream of the trailing edge and 1.25 chord lengths upstream of the leading edge of the hydrofoil. The hydrofoils are tilted around the quarter chord line when run at a non-zero angle of attack.

Grid Generation

This study uses multiblock grids with structured hexahedral, semi-structured prismatic, and unstructured tetrahedral blocks, generated with *CFD-GEOM* [13] from CFD Research Corporation (Huntsville, AL).

Gridding the Rounded Tip Hydrofoil

A C mesh is wrapped around a two-dimensional section of the hydrofoil and extruded along the foil from the symmetry plane to the opposite side of the domain to form a C-H mesh. The surface mesh on the tip of the foil is primarily a H mesh with triangular meshes near the leading and trailing edges to avoid mesh quality problems. This surface mesh is extruded, forming a H-H block and two conforming prismatic blocks.

Gridding the Ducted Tip Hydrofoil

This geometry is more challenging to mesh than the rounded tip. The inflow plane of the duct is gridded with a H grid in the center of the duct and an O grid along the duct wall. These two grids are extruded out through the duct to the outlet boundary of the flow domain. The region just upstream of the duct and outboard of the foil tip is filled with a tetrahedral mesh. The remainder of the gridding is similar to the gridding of the rounded tip hydrofoil. A C grid is extruded from the root wall along the surface, part way around the top of the duct, then straight across the

Contributed by the Fluids Engineering Division for publication in the JOURNAL OF FLUIDS ENGINEERING. Manuscript received by the Fluids Engineering Division November 16, 2001; revised manuscript received April 12, 2004. Review conducted S. Ceccio.

[1]Note that, because we are working with half of a symmetric hydrofoil, our semi-span is approximately equivalent to the hub-to-tip distance for a propeller blade.

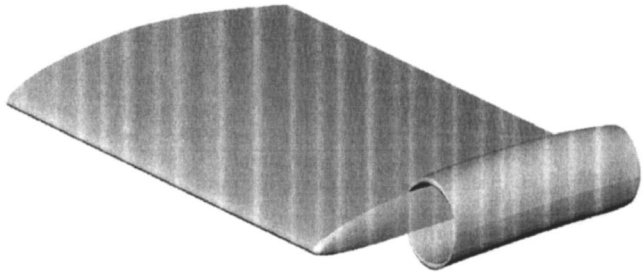

Fig. 1 Ducted tip hydrofoil

flow domain to the opposite tunnel wall. This leaves a gap outboard of the foil tip, the duct, and the extrusion of the duct mesh. This gap is filled with a prism mesh and an H-H mesh, extruded from existing surface meshes in the gap. Note that this meshing scheme results in several nonconforming block interfaces. A cutaway of a complete ducted-tip mesh is shown in Fig. 2.

Grid Density

Based on a convergence study reported elsewhere [14], the primary grid used for the rounded tip hydrofoil in this study was generated with approximately 536,000 cells. The C-H grid has $209\times34\times73$ grid points. 151 of the 209 streamwise grid points and 44 of the 73 spanwise grid points are on the hydrofoil. The first grid spacing at the hydrofoil surface is 0.0006 c, resulting in typical wall y^+ values of 15–35. Because the k-ϵ turbulence model in CFD-ACE(U) uses wall functions, y^+ cannot be made too small (less than about 11.5) without causing solution divergence. Grid dependence was studied and it was shown that grid independence could be achieved for the majority of the flow.

The ducted tip hydrofoil calculations used a grid of approximately 402,000 cells, including about 64,000 tetrahedra and 8700 prisms. The first cell above the solid surfaces generally extends 0.001 c into the flow domain.

Numerical Method

The pressure-based, finite-volume flow solver *CFD-ACE(U)* [15] from CFDRC was used in this study. The code uses unstructured/hybrid grids to integrate the Navier-Stokes equations. Cases were run using a second-order accurate scheme with upwinding for the convective terms and a k-ϵ turbulence model with wall functions for the near-wall region.

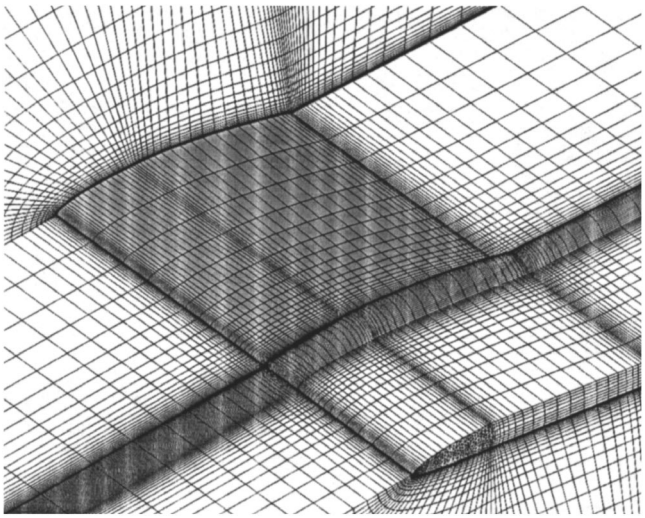

Fig. 2 Grid topology for the ducted tip hydrofoil

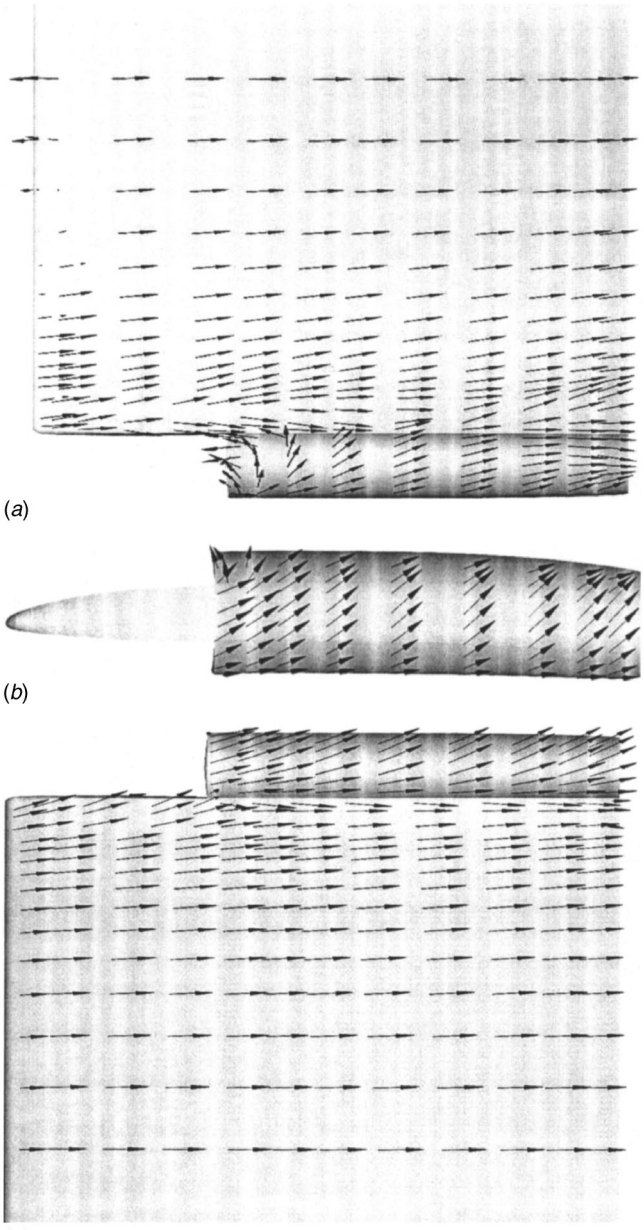

(*a*)

(*b*)

(*c*)

Fig. 3 Surface vector pictures of the (*a*) suction side, (*b*) tip, and (*c*) pressure side of the ducted tip hydrofoil at α=12 deg

The freestream velocity was specified for the inlet. At the outlet, constant pressure was specified; the outflow velocity need not be specified for an upwind scheme. A no-slip flow condition was used for the solid hydrofoil surface. Boundaries corresponding to the walls of the tunnel were specified as slip walls.

Results

The ducted and rounded tip hydrofoils were studied at angles of attack α=7 deg and α=12 deg and a Reynolds number $\mathrm{Re}=1.2\times10^6$. Due to space limitations, only the α=12 deg results will be discussed in detail.

Our primary comparison is between surface velocity vectors obtained from the computations and surface flow visualization (SFV) photographs from experiments done by Green [12]. Surface flow vectors for the rounded tip hydrofoil (not shown) are in very good overall agreement with experiment. One significant difference was near the hydrofoil root, where the interference vortex

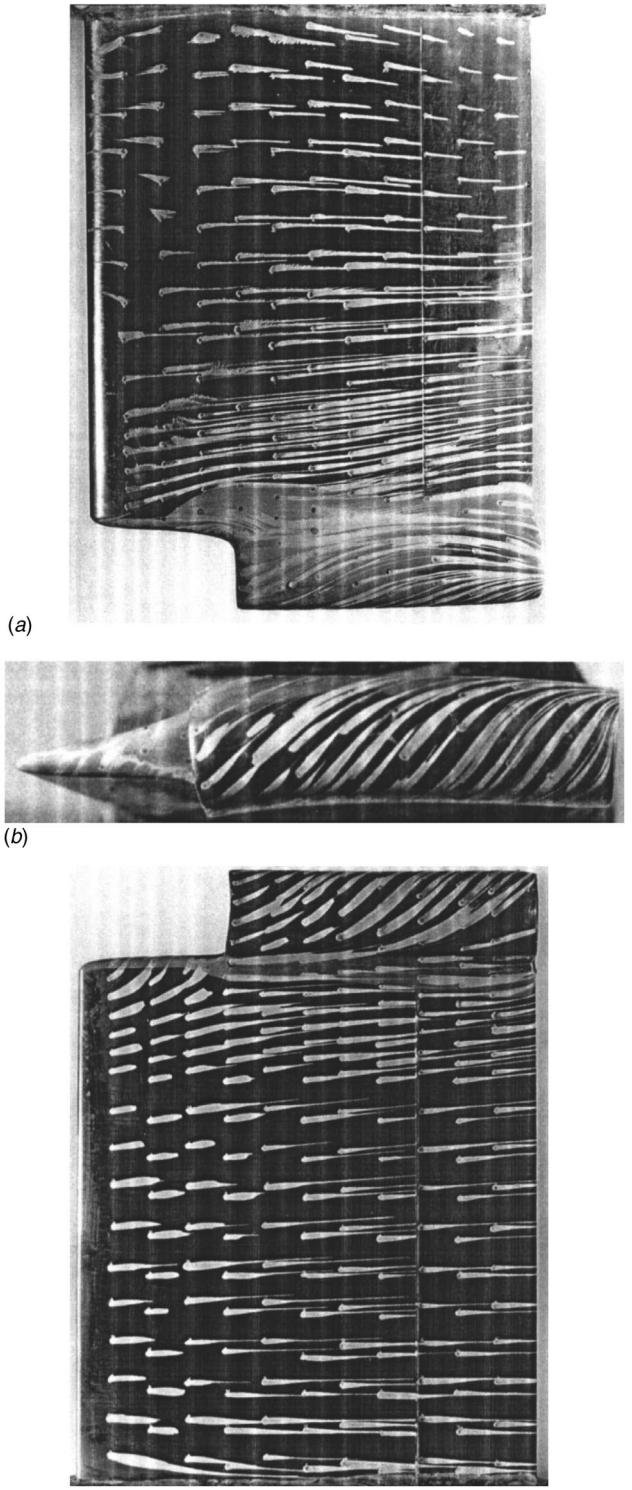

(*a*)

(*b*)

(*c*)

Fig. 4 SFV photographs of the (*a*) suction side, (*b*) tip, and (*c*) pressure side of the ducted tip hydrofoil at α=12 deg

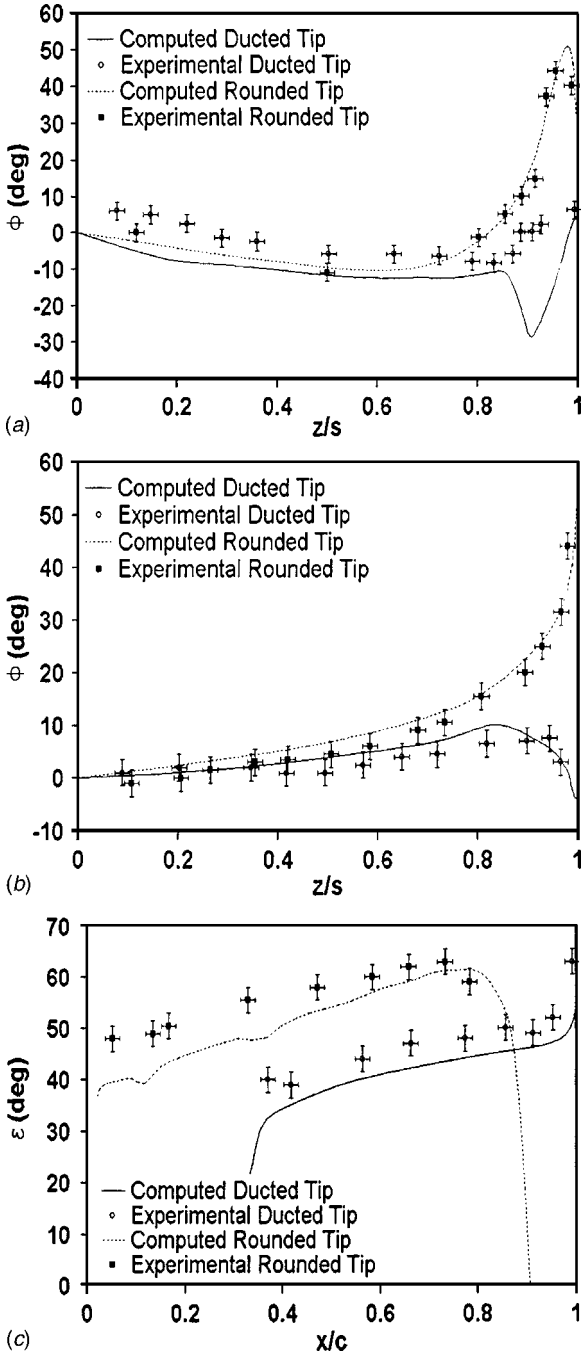

Fig. 5 Flow angles at α=12 deg. (*a*) Outboard flow angles at the trailing edge on the suction side. (*b*) Outboard flow angles at the trailing edge on the pressure side. (*c*) Downwash flow angles at the tip.

was not captured by the computation, which modeled the wall with a slip boundary condition. Another difference is significantly lower flow angles, relative to the chordline, around the tip for the computed hydrofoil than the experimental one. This difference is especially great toward the leading edge tip. This discrepancy can be largely attributed to the poorly resolved interaction between the vortex rollup and the boundary layer.

The agreement between computations and experiments for the ducted tip hydrofoil is also overall quite good, as may be seen in Figs. 3 and 4. The agreement between the SFV photographs and the surface vector pictures is excellent on the pressure side and very good on the duct of the hydrofoil as well. The agreement was also very good for the α=7 deg case. The surface flow on the suction side is very well predicted at the front part of the hydrofoil but less so toward the trailing edge, as can be seen clearly in Fig. 5(*a*), where the flow angles toward the tip at the trailing edge are much different from those measured from the SFV photographs. This difference was believed to be caused by a lack of a fillet between the duct and the hydrofoil in the computational model. In

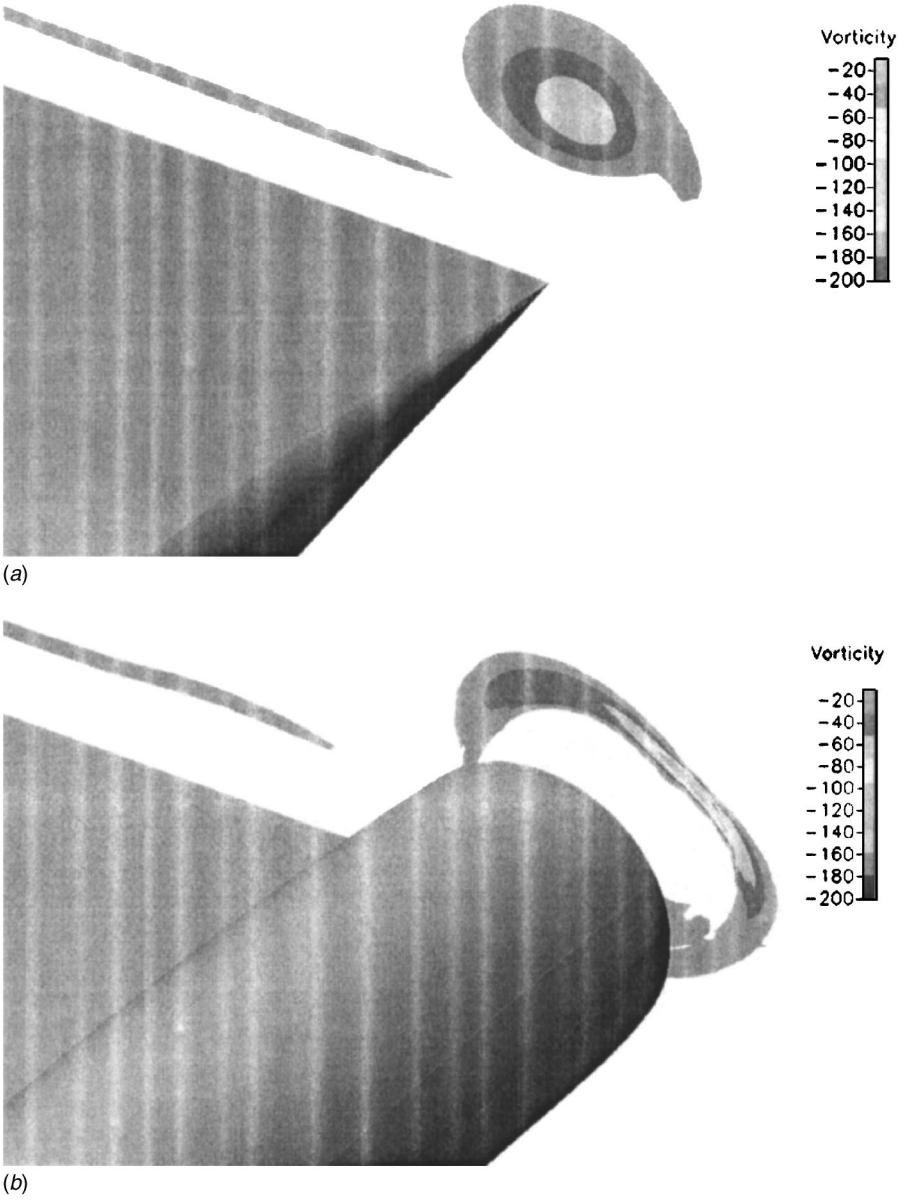

Fig. 6 Streamwise (x) component of vorticity in the x-z plane right behind the trailing edge ($x/c=1.05$) of the (a) rounded tip and (b) ducted tip hydrofoil at $\alpha=12$ deg and $Re=1.2\times10^6$

order to test that hypothesis, the flow angles measured from a SFV photograph of a ducted tip hydrofoil with less fillet were also compared to the computational flow angles. The hydrofoil with the smaller fillet has significantly greater (negative) values of σ near the tip on the suction side. This observation supports the argument that the difference between experiments and computation is largely due to the absence of a fillet in the computational model. Referring to Figs. 3(a) and 4(a), separation is seen at the leading edge of the computational and experimental hydrofoils at $\alpha=12$ deg. The separation occurs toward the root of the hydrofoil and the agreement between computation and experiment is remarkably good. Leading edge separation was experimentally determined to extend from the root to between 57% and 64.5% of span. For the computed result, this extent is 63% of span.

After validating the computational results with experimental data through surface flow visualization on the ducted and rounded tip hydrofoils, the axial and tangential velocities of the trailing vortex were studied. Computations were performed on the

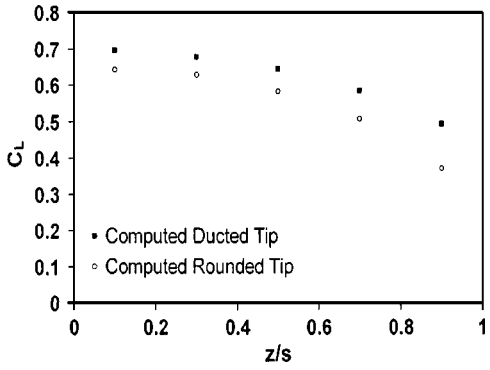

Fig. 7 Sectional lift along spanwise stations of the computational hydrofoils at $\alpha=7$ deg and $Re=1.2\times10^6$

rounded tip hydrofoil at $\alpha=10$ deg and $\mathrm{Re}=5.2\times10^5$ with comparison to the experimental data of Green [12] in mind. The computed axial velocity U_x/U_∞ in the vortex core immediately downstream of the hydrofoil was 1.47, which compares well to a mean axial velocity of $U_x/U_\infty=1.53\pm0.17$, measured in the center of a vortex core of a rounded tip hydrofoil of similar shape (NACA 66-209 cross section) and same aspect ratio at the same operating conditions. The corresponding maximum tangential velocities were $(U_\theta/U_\infty)_{\text{computational}}=0.83$ and $(U_\theta/U_\infty)_{\text{experimental}}=0.80$.

Discussion

Comparing the surface flow over the rounded and ducted tip hydrofoils is a good way to assess qualitatively the performance of the different geometries. It is observed from the computations in Fig. 5, as was seen earlier in experiments, that the spanwise velocity component at the trailing edge pressure and suction side, despite the fillet problem, is substantially less than that of the rounded tip. The difference in the spanwise velocity component suggests that the ducted tip hydrofoil sheds less circulation over the hydrofoil surface than does the rounded tip hydrofoil. The tangential velocities on the duct suggest that vorticity is shed from the duct. Computations of vorticity confirm this. The streamwise component of vorticity immediately downstream of the trailing edge of the hydrofoils ($x/c=1.05$) in the plane normal to the freestream flow direction is shown in Fig. 6. The tip vortex behind the rounded tip hydrofoil is concentrated in a circle with the highest vorticity in the center of the circle whereas the vorticity from the ducted tip hydrofoil is shed in a ring with the same shape as the duct, with the highest vorticity located on the outboard side of the duct. Given this, we would expect the lift along the ducted tip hydrofoil to be higher than for the rounded tip hydrofoil. Sectional lift coefficients at $\alpha=7$ deg (see Fig. 7) confirm that the ducted tip hydrofoil indeed generates greater lift at all spanwise stations, consistent with the hypothesis that the ducted tip geometry has greater bound circulation at the root and sheds its circulation only close to the tip.

Given the patterns of shed vorticity, we expect the minimum pressure in the trailing vortex of the ducted tip hydrofoil to be significantly higher than that of the rounded tip hydrofoil. This is in fact the case. The minimum computed pressure coefficients $C_{p,\min}$ in the y-z plane at $x/c=1.05$ and $\alpha=12$ deg are $(C_{p,\min})_{\text{ducted tip}}=-1.07$ and $(C_{p,\min})_{\text{rounded tip}}=-2.94$. While these results are not quantitatively precise, the trend is clear: the ducted tip should dramatically inhibit cavitation inception, a finding that is in agreement with experimental observations of Green and Duan [7].

Conclusions

The flow over two finite-span hydrofoils, one with a rounded tip and one with a ducted tip, was studied to gain a better understanding of the flow around the duct and provide a good basis for further optimization of the duct size and location for a propeller blade. The finite-volume flow solver *CFD-ACE(U)* from CFDRC was used, with a k-ε turbulence model and hybrid grids with 350,000–550,000 cells. Cases were run with a second-order accurate upwind scheme and the results compared to available experimental data. The aim of the study was to simulate the flow around a ducted tip hydrofoil with the hope of gaining a better understanding of the flow around the duct as well as providing a good basis for further optimization of the size and duct location on a propeller blade.

Near surface flow vector plots of the CFD-modeled hydrofoils at 12 deg angle of attack were compared to SFV photographs from experiments done by Green [12]. Qualitatively, the overall agreement in flow directions along the hydrofoil is very good. Flow angles measured along the trailing edge of the different geometry hydrofoils suggest that the ducted tip hydrofoil sheds less bound circulation over the majority of the wing span than does the rounded tip hydrofoil. This was confirmed by studying the x component of vorticity immediately downstream of the two hydrofoils, which showed that the vorticity is shed in the shape of a duct from the ducted tip hydrofoil instead of a concentrated circular vortex as is the case for the rounded tip hydrofoil. Also, the sectional lift along the span of the hydrofoils is higher for the ducted tip hydrofoil than for the rounded tip hydrofoil. The minimum pressure associated with the tip vortices is much lower for the rounded tip hydrofoil than the ducted tip hydrofoil, which is in agreement with experiments showing a reduced cavitation inception index for this geometry.

References

[1] Crump, S. F., 1948, "The Effects of Bulbous Blade Tips on the Development of Tip Vortex Cavitation on Model Marine Propellers," Report C-99, David Taylor Naval Ship Research and Development Center, Bethesda, MD.

[2] Mani, K., Sharma, S. D., and Arakeri, V. H., 1988, "Effect on Propeller Blade Modification and Cavitation Induced Noise," FED (Am. Soc. Mech. Eng.), **64**, pp. 64–67.

[3] Itoh, S., Ishii, N., Tagori, T., and Ide, T., 1987, "Study of the Propeller With Small Blades on the Blade Tips (1st Report)," J. Soc. Naval Architects Japan, **159**, pp. 82–90. (Published in Japanese with English abstract).

[4] Fruman, D. H., and Aflalo, S. S., 1989, "Tip Vortex Cavitation Inhibition by Drag Reducing Polymer Solutions," ASME J. Fluids Eng., **111**, pp. 211–216.

[5] Chahine, G. L., Frederick, G. F., and Bateman, R. D., 1993, "Propeller Tip Vortex Cavitation Suppression Using Selective Polymer Injection," ASME J. Fluids Eng., **115**, pp. 497–503.

[6] Green, S. I., Acosta, A. J., and Akbar, R., 1988, "The Influence on Tip Geometry on Trailing Vortex Rollup and Cavitation Performance," *ASME, Cavitation and Multiphase Flow Forum*, Cincinatti, OH, pp. 76–80.

[7] Green, S. I., and Duan, S. Z., 1995, "The Ducted Tip—A Hydrofoil Tip Geometry With Superior Cavitation Performance," ASME J. Fluids Eng., **117**, pp. 665–672.

[8] Hordnes, I., and Green, S. I., 1998, "Sea Trials of the Ducted Tip Propeller," ASME J. Fluids Eng., **120**, pp. 808–817.

[9] Dacles-Mariani, J., Zilliac, G. G., Chow, J. S., and Bradshaw, P., 1995, "Numerical/Experimental Study of a Wingtip Vortex in the Near Field," AIAA J., **33**(9), pp. 1561–1568.

[10] Hsiao, C., and Pauley, L. L., 1998, "Numerical Study of the Steady-State Tip Vortex Flow Over a Finite-Span Hydrofoil," ASME J. Fluids Eng., **120**, pp. 345–353.

[11] Hsiao, C., and Pauley, L. L., 1999, "Numerical Computation of Tip Vortex Flow Generated by a Marine Propeller," ASME J. Fluids Eng., **121**, pp. 638–645.

[12] Green, S. I., 1988, "Tip Vortices—Single Phase and Cavitating Flow Phenomena," Ph.D. thesis, California Institute of Technology.

[13] CFD Research Corporation, 2001, *CFD-GEOM User's Guide*, Huntsville, Alabama.

[14] Ingvarsdottir, H., 2001, "Computational Studies of the Flow Around Rounded and Ducted Tip Hydrofoils," M.A.Sc. thesis, University of British Columbia.

[15] CFD Research Corporation, 2001, *CFD-ACE(U) User's Guide*, Huntsville, Alabama.

Application of MATLAB Functions for Time Domain Simulation of Systems With Lines With Fluid Transients

Patompong Wongputorn
e-mail: patompong_wongputorn@whirlpool.com
Bangkok, Thailand

David Hullender
e-mail: Hullender@mae.uta.edu

Robert Woods
e-mail: Woods@mae.uta.edu
University of Texas Arlington, Arlington, TX 76019

John King
e-mail: John.King@FNC.Fujitsu.com
Fujitsu Network Communications, Richardson, TX 75082

[DOI: 10.1115/1.1852488]

Keywords: Time Domain Simulation, Hydraulic, Pneumatic, Fluid Transients in Lines, Transfer Functions

Introduction

Hydraulic and pneumatic fluid transmission lines are often internal components within a total dynamic system to be analyzed by time domain simulation. This paper introduces a new and simple approach utilizing MATLAB® computational tools for including the model for the line fluid transients in the model for the overall system. The fluid transients in the lines are based on a laminar flow distributed parameter model, which includes nonlinear frequency dependent viscous friction terms as well as heat transfer effects in gas lines.

Time domain simulation of a system containing fluid line transients is quite complex if the transfer functions for the fluid transients consist of hyperbolic Bessel functions, which is the case for the ''Dissipative'' model [1–26]. The total system simulation model formulation procedure is to first combine the equations for the system, including the transfer functions for the fluid transients, into a single transfer function for the system output variable of interest. By obtaining the output variable transfer function, it is a one step MATLAB® process to obtain the simulation for any system input of interest. For most systems, the ''solve'' algorithm in MATLAB® is needed to obtain this transfer function in terms of symbolic variables representing the system variables and the nonlinear transfer functions for the fluid transients. A least-squares curve fit algorithm named 'invfreqs' in the MATLAB® *Signal Processing Toolbox* is used to formulate a rational polynomial approximation for this complex transfer function in the frequency domain [27–32]. The approximation is very accurate over a designated frequency range corresponding to the bandwidth of the components of the total system and to the frequency content of the input disturbances. As will be demonstrated, the advantage of this new approach is the ability to include the distributed parameter model for the fluid transients without questionable assumptions associated with friction approximations and lumped parameter modeling techniques associated with fluid transients. The model formulation and approximation algorithm is demonstrated for a simple line terminating into a fluid tank and then for a complex hydraulic braking system containing several hydraulic lines [33].

Contributed by the Fluids Engineering Division for publication in the JOURNAL OF FLUIDS ENGINEERING. Manuscript received by the Fluids Engineering Division July 15, 2003; revised manuscript received September 13, 2004. Review conducted by Y. Tsujimoto.

Dissipative Model

Consider the schematic of a fluid transmission line shown in Fig. 1. It is assumed that the line is a tube with uniform and rigid circular cross section. Also, it is assumed that the fluid media (liquid or gas) flows though the line in one dimension with mean speed that is relatively slow compared to the speed of sound in the fluid. In Fig. 1, P_a and Q_a denote the pressure and volumetric flow at the left end of the line. Also, P_b and Q_b denote the pressure and volumetric flow at the right end of the line. The direction of the arrows represents the direction of the flows when positive.

Details of the derivation of the so-called ''dissipative'' distributed-parameter model for this transmission line are presented in numerous publications [11] and most recently in the work of Nursilo [19]. A particularly useful input–output expression representing the solution for this distributed-parameter model is presented in Eqs. (1) and (2), i.e.,

$$Q_a(s)=C_1(s)P_a(s)-C_2(s)P_b(s) \tag{1}$$

$$Q_b(s)=C_2(s)P_a(s)-C_1(s)P_b(s) \tag{2}$$

where

$$C_1(s)=\frac{\cosh\Gamma(s)}{Z(s)\sinh\Gamma(s)} \tag{3}$$

$$C_2(s)=\frac{1}{Z(s)\sinh\Gamma(s)} \tag{4}$$

$$\Gamma(s)=D_n s\frac{r^2}{\nu}\left[\frac{1+(\gamma-1)B_\sigma}{1-B}\right]^{1/2} \tag{5}$$

$$Z(s)=\frac{Z_0}{\sqrt{1-B}\sqrt{1+(\gamma-1)B_\sigma}} \tag{6}$$

The Bessel function ratios, B_σ and B are as follows:

$$B_\sigma(s)=\frac{2J_1(\mathrm{j}\sqrt{\sigma sr^2/\nu})}{j\sqrt{\sigma sr^2/\nu}J_0(j\sqrt{\sigma sr^2/\nu})} \tag{7}$$

$$B(s)=\frac{2J_1(\mathrm{j}\sqrt{sr^2/\nu})}{j\sqrt{sr^2/\nu}J_0(j\sqrt{sr^2/\nu})} \tag{8}$$

where, J_0 and J_1 are zero and first-order Bessel functions of the first kind. Note that the Bessel functions are functions of complex variables. Also, it is important to note that for a liquid, the specific heat ratio γ is one and thus, B_σ drops out of Eqs. (5) and (6). The next sections of this paper demonstrate ways to incorporate these equations for line fluid transients into a model for a total system.

Example 1: Hydraulic Line Terminating Into a Tank. Consider the hydraulic fluid line connected to a tank (fluid capacitance) shown in Fig. 2. There is a valve represented by a linear fluid resistance R at the connection to the tank. The input to this system is the pressure P_a and the output of interest is the pressure in the tank P_t. This first example represents a problem where the transfer function relationship between the input and the output can easily be obtained by manually combining the equations. The equation for a lumped fluid capacitance [34] for the tank is

$$Q_b(s)=C_t sP_t(s) \tag{9}$$

The equation for a lumped linear fluid resistance [34] is

$$P_b(s)=RQ_b(s)+P_t(s) \tag{10}$$

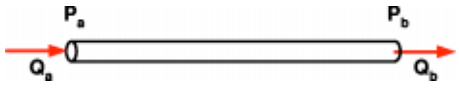

Fig. 1 Schematic of a fluid transmission line

Using Eq. (2) for the fluid transients in the line gives

$$Q_b(s)=C_2(s)P_a(s)-C_1(s)P_b(s) \tag{11}$$

Equations (9)–(11) represent three equations and three unknowns $Q_b(s)$, $P_b(s)$, and $P_t(s)$. Solving for $P_t(s)$ gives

$$P_t(s)=H(s)P_a(s) \tag{12}$$

where

$$H(s)=\left[\frac{C_2(s)}{[1+C_1(s)R]C_t s+C_1(s)}\right] \tag{13}$$

This transfer function is a very nonlinear function of the Laplace variable s. It is desired to approximate $H(s)$ by a simple ratio of rational polynomials in s representing a linear differential equation.

In general, the approach to achieving a transfer function approximation is to match the frequency response of the original transfer function, over a frequency range of interest, with the frequency response of a rational polynomial transfer function, which represents a linear ordinary differential equation [32]. This approach utilizes a least-squares curve fit algorithm named "invfreqs," provided in MATLAB® *Signal Processing Toolbox*, to obtain the polynomial coefficients associated with the transfer function frequency response curve fits. This m-file, "invfreqs," employs the least squares technique of Levi [27] along with an iteration algorithm, which utilizes the damped Gauss–Newton method.

Before generating a rational polynomial representation for $H(s)$, it necessary to determine the frequency range of interest for the system dynamics. The lower frequency is usually close to zero to preserve the dc gain of the transfer function. The upper bound on the frequency range is determined by the largest of either the frequency content of the input $P_a(t)$, by c/L, or by estimating the inverse of the time constant associated with pressurizing the tank, i.e.

$$\frac{1}{\tau}=\frac{1}{C_t(R_{sf}+R)} \tag{14}$$

Using MIL-H-5060 hydraulic fluid at 26.7°C (80°F), the approximate fluid properties [34] are $\beta=1.896\times10^9$ N/m^2, $\nu=2.0\times10^{-5}$ m^2/s, and $\rho=875$ kg/m^3. If the tank volume, V, is 0.00142 m^3, the line length, L, is 5 m, the inside radius, r, of the line is 0.005 m, and the valve resistance, R, is 1.776e8 Ns/m^5, then Eq. (14) gives 0.0004 s which corresponds to a frequency of 2500 rad/s.

An estimate of the order of the transfer function needed to accurately approximate $H(s)$ over the desired frequency range is determined from an examination of the frequency response of $H(s)$. At least two orders are needed for each apparent second order mode. Examination of the frequency response reveals that

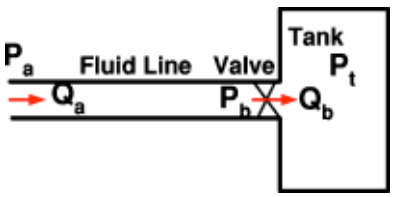

Fig. 2 Schematic for a fluid line, valve, and tank

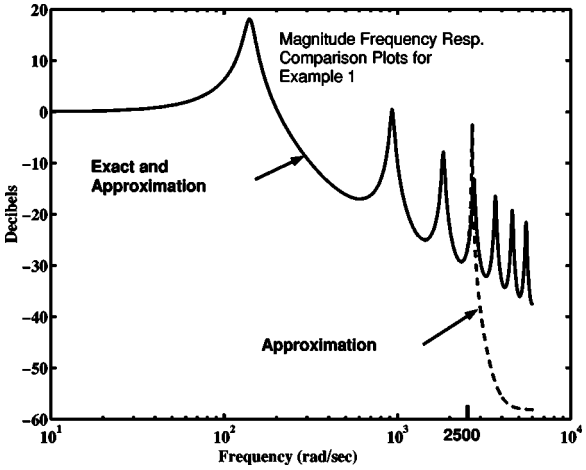

Fig. 3 Frequency response magnitude comparison plots for the system shown in Fig. 2

there are at least three second order modes over this frequency range; thus, the order of the approximation should be at least 8 and possibly 10. A tenth order transfer function was chosen for this example. The procedure of achieving an accurate curve fit is a significant contribution of this paper; so, the MATLAB® m-file, which uses "invfreqs" to generate the approximation for $H(s)$, is provided in the Appendix and on the Author's web site [33]. It is important to note that the number of frequency points and spacing must be determined by trial and error. Since all of the computations are in MATLAB®, the order is probably not a major issue since the transfer function will be stored in memory for further simulation and analysis. For this case, the result is a tenth order rational polynomial transfer function representing a linear ordinary differential equation, i.e.

$$H(s)\approx\frac{-3.398e^6s^9+1.041e^{10}s^8-\cdots+1.21e^{33}s+1.238e^{35}}{s^{10}+2.762e^9s^9+\cdots+7.631e^{30}s^2+1.281e^{33}s+1.235e^{35}}$$

As shown in Figs. 3 and 4, the inverse frequency algorithm generates a very accurate linear model out to the specified maximum frequency of interest, 2500 rad/s. The time response corresponding to a step pressure input at the left end of the line is shown in Fig. 5; note the pure time delay at the beginning of the response associated with the speed of sound and the time required for the first pressure changes to reach the tank.

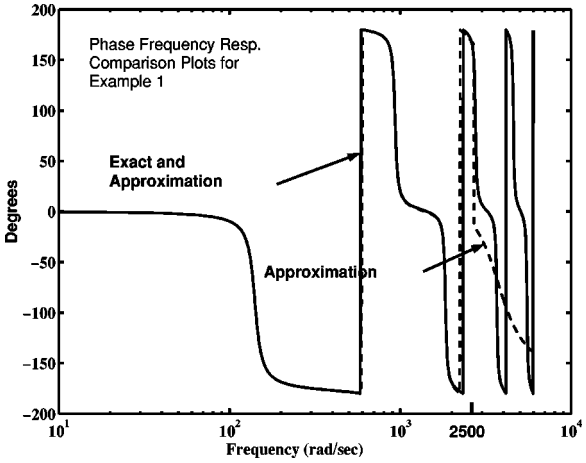

Fig. 4 Frequency response phase comparison plots for the system in Fig. 2

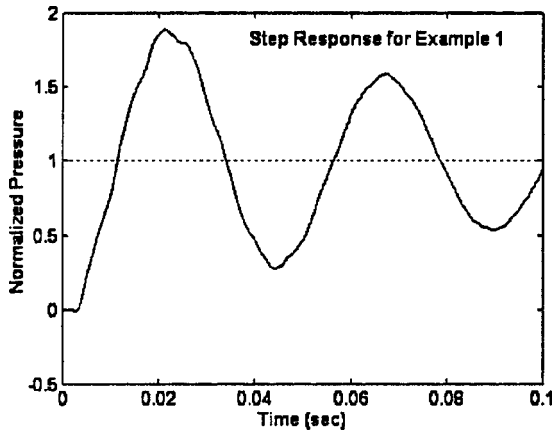

Fig. 5 Tank pressure step response for the system shown in Fig. 2

Example 2: Hydraulic Brake Actuation System. For a second example, consider the schematic of a hydraulic brake actuation circuit shown in Fig. 6 for a front-end loader. When the brake valve is opened by pressing on the brake pedal, hydraulic fluid passes through line "a" of length L_a to the "T" connector which diverts fluid to the front and rear brake cylinders. As shown, there are seven different hydraulic lines, which must be modeled in order to analyze the time domain response of the pressures in the brake cylinders. A typical reason for analyzing this system might be to determine how the time required to pressurize the brake cylinders is affected by the diameter of the lines and/or by the temperature of the oil.

Using Eqs. (1) and (2) for each of the line sections in Fig. 6, results in the following equations:

Line "a":

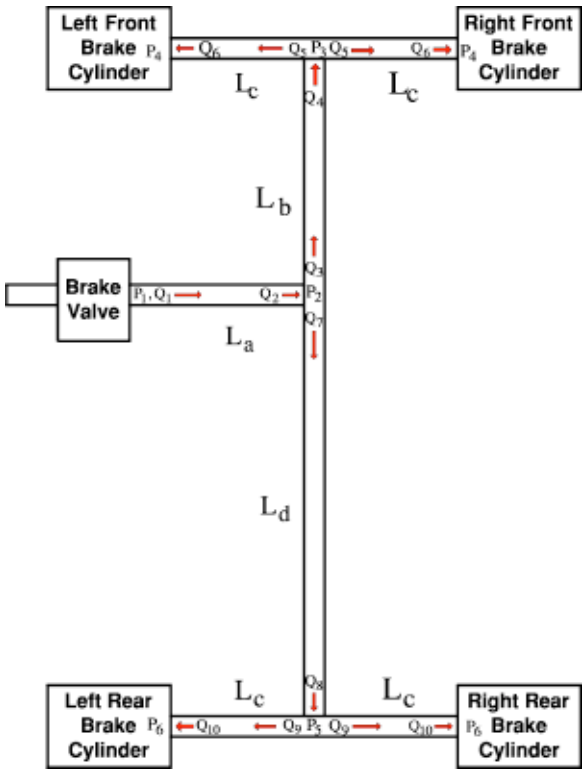

Fig. 6 Schematic of a hydraulic brake system for Example 2

$$Q_2 = C_{2a}P_1 - C_{1a}P_2 \tag{15}$$

Line "b":

$$\begin{aligned} Q_3 &= C_{1b}P_2 - C_{2b}P_3 \\ Q_4 &= C_{2b}P_2 - C_{1b}P_3 \end{aligned} \tag{16}$$

Line "c" front:

$$\begin{aligned} Q_5 &= C_{1c}P_3 - C_{2c}P_4 \\ Q_6 &= C_{2c}P_3 - C_{1c}P_4 \end{aligned} \tag{17}$$

Line "c" rear:

$$\begin{aligned} Q_9 &= C_{1c}P_5 - C_{2c}P_6 \\ Q_{10} &= C_{2c}P_5 - C_{1c}P_6 \end{aligned} \tag{18}$$

Line "d":

$$\begin{aligned} Q_7 &= C_{1d}P_2 - C_{2d}P_5 \\ Q_8 &= C_{2d}P_2 - C_{1d}P_5 \end{aligned} \tag{19}$$

For the "T" connectors, the equations are

$$Q_2 = Q_3 + Q_4 \tag{20}$$

$$Q_4 = 2Q_5 \tag{21}$$

$$Q_8 = 2Q_9 \tag{22}$$

For the brake cylinders, the equations are

$$Q_6 = C_b s P_4 \tag{23}$$

$$Q_{10} = C_b s P_6 \tag{24}$$

where the lumped parameter capacitance is given by

$$C_b = \left[\frac{V}{\beta} + \frac{A^2}{K}\right] \tag{25}$$

Equations (15)–(24) represent 14 equations with 14 unknowns: P_2, P_3, P_4, P_5, P_6, Q_2, Q_3, Q_4, Q_5, Q_6, Q_7, Q_8, Q_9, and Q_{10}. The input is P_1. Because of the complexity and number of equations, as compared to the first example, where the solution was easily obtained manually, it is advantageous to use symbolic math and the "solve" algorithm in MATLAB® to get the solution. The MATLAB® m-file which uses "solve" and "invfreqs" for solving these equations and then generating the rational polynomial transfer function for the total system is provided in the Appendix. When reviewing this m-file, it is important to note the symbolic variable substitution procedure for the hyperbolic Bessel functions and parameters. Also, the frequency increments will not always be obvious and must be determined by trial and error attempts to get reasonable curve fits at both the upper and lower frequency bounds.

Using the total line length from the brake valve to the rear brake cylinder divided into the speed of sound gives a frequency of 134 rad/s. The inverse of the time constant based on the steady flow resistance and brake cylinder capacitance is 45 rad/s. The frequency range of interest is selected to be 1 rad/sec to 300 rad/sec and the order of the transfer function approximation is chosen to be 10.

For the designated frequency range and system order, the magnitude and phase frequency response comparisons are shown in Figs. 7 and 8. The curve fit is observed to be extremely close to the exact out to 300 rad/s. This transfer function between the input pressure P_1 and the rear brake cylinder pressure P_6 is shown in Eqs. (26) and (27). Note that this transfer function represents a linear ordinary differential equation that is good for any assumed input $P_1(s)$.

$$P_6(s) = G(s)P_1(s) \tag{26}$$

where

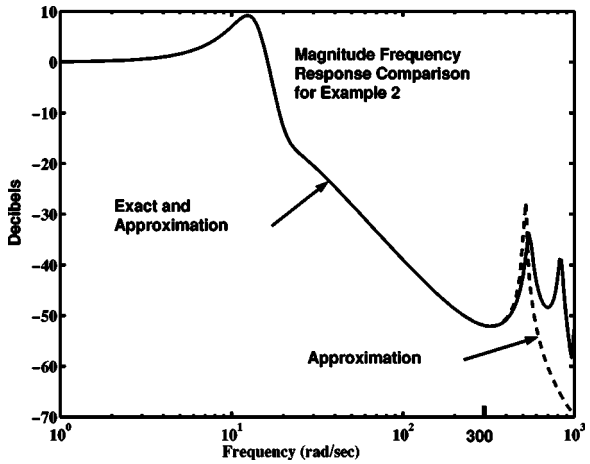

Fig. 7 Frequency response magnitude comparison plots for Example 2

$$G(s) \approx \frac{5.987e^{13}s^9 - 8.70e^{14}s^8 + \cdots + 3.674e^{35}s + 5.45e^{36}}{s^{10} + 1.35e^{17}s^9 + \cdots + 3.86e^{35}s + 5.45e^{36}} \tag{27}$$

Typical simulation results using this transfer function are shown in Figs. 9 and 10 for a step input.

As shown in Fig. 9, the performance of the brake system is very sensitive to the temperature of the oil with 0.00635 m (1/4 in.) diameter lines. The viscosity of ISO 46 oil at 10°C (50°F) is so high that it takes almost 4 s for the brake cylinder pressure to reach the desired level. For 79.4°C (175°F), the desired pressure is achieved in less than 0.2 s. As shown in Fig. 10, the performance of the brake system is sufficiently fast, even at the lower temperature, for a line diameter of 0.0127 m (1/2 in.).

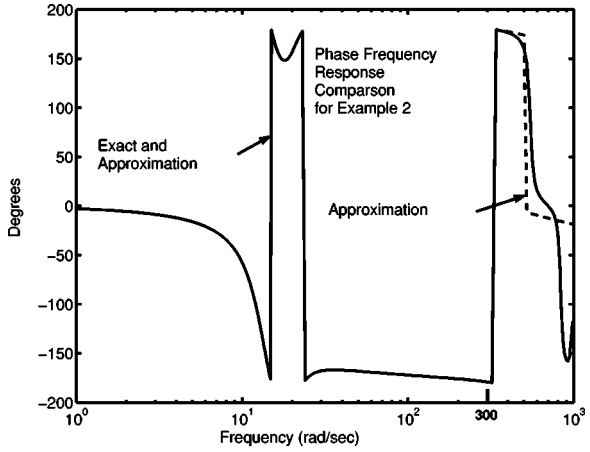

Fig. 8 Frequency response phase comparison plots for Example 2

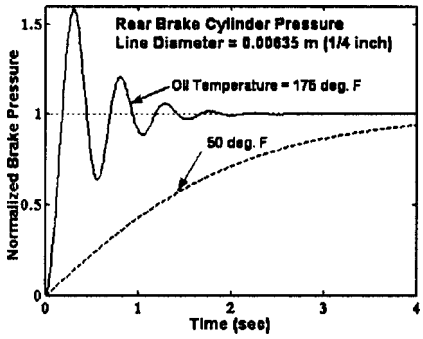

Fig. 9 Comparison of brake cylinder pressure response for different oil temperatures

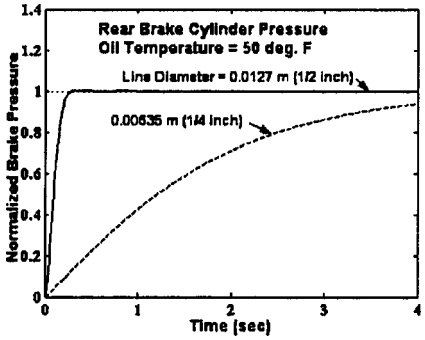

Fig. 10 Comparison of brake cylinder pressure responses for different line diameters

This second example demonstrates the simplicity of using the MATLAB® Symbolic Toolbox for solving very complex simultaneous equations. Because of the nonlinear properties of the model for the fluid line transients as represented by C_1 and C_2, it would be essentially impossible to formulate a simulation model for this system without having to simplify our friction model in the equations for the line fluid transients or resort to lumped parameter models for the lines or limit our analysis to methods requiring periodic inputs.

Summary and Conclusions

For problems where a fluid transmission line is an internal component within a total system to be simulated in the time domain, it is often desirable to be able to accurately model the fluid transients in the line with partial differential equations that include frequency dependent friction terms and heat transfer effects for gases. Thus, accuracy issues associated with friction model approximations and associated with lumped parameter modeling errors are avoided.

An algorithm has been introduced that generates very accurate rational polynomial transfer functions for a total system in which one or more lines are internal components. The transfer functions are generated in the MATLAB® working environment using symbolic variable solution algorithms. The contribution of this paper is the procedure for using MATLAB® to simulate dynamic systems with fluid lines in which the fluid transients are significant in the frequency range of interest without having to approximate the fluid transient friction model.

Nomenclature

A = Brake cylinder piston area, m^2
c = Speed of sound, m/s
C_t = Tank capacitance, V/β [34]
D_n = Dimensionless dissipative number, $\nu L/cr^2$
J = $\sqrt{-1}$
K = Brake cylinder piston return spring constant, N/m
L = Line length, m
P_t = Tank pressure
r = Internal radius of the line, m
R = Linear approximation for valve flow resistance, $\partial P/\partial Q$
R_{sf} = Steady laminar flow line resistance, $8\rho\nu L/\pi r^4$ [34]
S = Laplace variable
t = time, s
τ = time constant, s
V = Tank volume, m^3

Z_O = Characteristic impedance constant, $\rho c/\pi r^2$
β = Bulk modulus of fluid, N/m^2
γ = Ratio of specific heats
ρ = Mass density of fluid, kg
σ = Prandtl number for the fluid
ν = Kinematic viscosity of fluid, m^2/s
ω = Frequency, rad/s

Appendix

MATLAB® m-File for Example 1.

```
function [Ht]=Example1 % Fluid line terminating into a tank (fluid capacitance).
warning off Vis=2.0e-5; r=0.005; Be=1.896e9; Den=875;
c=sqrt(Be/Den); Zo=Den*c/(pi*r^2); V=0.00142; L=5;
Ct=V/Be; R=1.776e8; syms s C1 C2
B=2*besse1j(1,j*sqrt(r^2*s/Vis))/(j*sqrt(r^2*s/Vis)*
besse1j(0,j*sqrt(r^2*s/Vis))); Z=Zo/sqrt(1-B);
Dn=Vis*L/(c*r^2); G=Dn*(r^2*s/Vis)/sqrt(1-B);
H=C2/((1+C1*R)*Ct*s+C1); %Trans. fun. to be curve fitted. H=subs(H,'C1',cosh(G)/(Z* sinh(G)));
H=subs(H,'C2',1/(Z* sinh(G))); % Generate frequency data for the curve fit. Note, the last value is the range of interest.
w=[(10:1:195),(200:10:980),(1000:20:2500)];
N=length(w); % Generate a greater frequency range for an accuracy comparison
wc=[(10:1:195),(200:10:980),(1000:20:6000)];
NC=length(wc); for k=1:N sw=j*wc(k); TF(k) =subs(H,s,sw); TFc(k)=TF(k);
end
N1=N+1;
for k=N1:NC %Additional frequencies for accuracy comparisons.
sw=j*wc(k); TFc(k)=subs(H,s,sw); % Additional data for the accuracy comparison.
end
[Num,Den]=invfreqs(TF,w,9,10,[ ],100); Ht=tf(Num,Den)
step(Ht,0.03)
% Generate Freq. Resp. plots to determine the accuracy of curve fit.
figure
Hc=freqs(Num,Den,wc); MH=20* log 10(abs(Hc));
AH=angle(Hc)*180/pi; MTF=20* log 10(abs(TFc));
ATF=angle(TFc)*180/pi; semilogx(wc,MH,'r',wc,MTF,'b');
title('Magnitude Comparison Plots');
xlabel('Frequency rad/sec'); ylabel('Decibels'); figure
semilogx(wc,AH,'r',wc,ATF,'b'); title('Phase Comparison Plots');
xlabel('Frequency rad/sec'); ylabel('Degrees');
```

MATLAB® m-File for Example 2.

```
function [G]=example2
% Hydraulic brake system for a front-end loader.
Vis=10e-6; Den=820; % ISO 46 Oil at 175°F
% Vis=300e-6; Den=880; % ISO 46 Oil at 50°F
warning off; r=0.0032; Be=1.7235e8; c=sqrt(Be/Den);
Zo=Den*c/(pi*r^2);
V=2.46e-6; A=0.0111; K=3.78e6; La=.559;
Dna=Vis*La/(c*r^2); Ld=2.134; Dnd=Vis*Ld/(c*r^2);
Lb=0.762; Dnb=Vis*Lb/(c*r^2); Lc=0.7112;
Dnc=Vis*Lc/(c*r^2);
syms s
B=2*besse1j(1,j*sqrt(r^2*s/Vis))/(j*sqrt(r^2*s/Vis)*
B=2*besse1j(1,j*sqrt(r^2*s/Vis))/(j*sqrt(r^2*s/Vis)*
besse1j(0,j*sqrt(r^2*s/Vis))); Z=Zo/sqrt(1-B);
Ga=Dna*r^2*s/Vis/sqrt(1-B); Gd=Dnd*r^2*s/Vis/sqrt
(1-B);
Gc=Dnc*r^2*s/Vis/sqrt(1-B);
Gb=Dnb*r^2*s/Vis/sqrt(1-B);
Sol=solve('Q2=C2a*1-C1a*P2','Q3=C1b*P2
-C2b*P3','Q4=C2b*P2-C1b*P3','Q5=C1c*P3
-C2c*P4', ... 'Q6=C2c*P3-C1c*P4','Q7=C1d*P2
-C2d*P5','Q8=C2d*P2-C1d*P5','Q9=C1c*P5
-C2c*P6', ... 'Q10=C2c*P5-C1c*P6','Q2=Q3
+Q4','Q4=2*Q5','Q8=2*Q9','Q6=Cb*s*P4','Q10
=Cb*s*P6', ... 'P2,P3,P4,P5,P6,Q2,Q3,Q4,Q5,Q6,Q7,
Q8,Q9,Q10');
H=Sol.P6; collect(H,s);
H=subs(H,'C1a',cosh(Ga)/(Z* sinh(Ga)));
H=subs(H,'C2a',1/(Z* sinh(Ga)));
H=subs(H,'C1d',cosh(Gd)/(Z* sinh(Gd)));
H=subs(H,'C2d',1/(Z* sinh(Gd)));
H=subs(H,'C1c',cosh(Gc)/(Z* sinh(Gc)));
H=subs(H,'C2c',1/(Z* sinh(Gc)));
H=subs(H,'C1b',cosh(Gb)/(Z* sinh(Gb)));
H=subs(H,'C2b',1/(Z* sinh(Gb)));
H=subs(H,'Cb',(V/Be+A^2/K));
w=[(1:.1:9.9),(10:.2:19.8),(20:1:99),(100:5:195),
(200:20:300)];
N=length(w);
wc=[(1:.1:9.9),(10:.2:19.8),(20:1:99),(100:5:195),
(200:20:1000)]; NC=length(wc);
for k=1:N; sw=j*wc(k); TF(k)=subs(H,s,sw);
TFc(k)=TF(k); end
N1=N+1;
%Additional frequencies generated for accuracy comparisons.
for k=N1:NC; sw=j*wc(k); TFc(k)=subs(H,s,sw); end
%Create a transfer function by curve fitting.
[Num,Den]=invfreqs(TF,w,9,10,[ ],100); G=tf(Num,Den);
step(G)
figure
Hc=freqs(Num,Den,wc); MH=20* log 10(abs(Hc));
AH=angle(Hc)*180/pi; MTF=20* log 10(abs(TFc));
ATF=angle(TFc)*180/pi;
semilogx(wc,MH,'r',wc,MTF,'b'); title('Magnitude Comparison Plots');
xlabel('Frequency rad/sec'); ylabel('Decibels'); figure
semilogx(wc,AH,'r',wc,ATF,'b')
title('Phase Comparison Plots'); xlabel('Frequency rad/sec');
ylabel('Degrees').
```

References

[1] Yang, W. C., Glidewell, J. M., Tobler, W. E., and Chui, G. K., 1991, "Dynamic Modeling and Analysis of Automotive Multi-Port Electronic Fuel Delivery System," ASME J. Dyn. Syst., Meas., Control, **113**, pp. 143–151.

[2] Yang, W. C., and Tobler, W. E., 1993, "Dynamic Modeling and Analysis of Electronically Controlled Power Steering System," ASME Dynamic Systems and Control Division DSC, **52**, 1993, Advanced Automotive Technologies Proceedings of the 1993 ASME Winter Annual Meeting.

[3] Glidewell, J. M., Yang, W. C., and Chui, G. K., 1993, "On-Board Diagnostic Strategy for Multi-Port Electronic Fuel Injection Systems Using Fuel Transient Analysis," ASME Dynamic Systems and Control Division Publication DSC, **52**, Advanced Automotive Technologies, Proceedings of the 1993 ASME Winter Annual Meeting.

[4] Hullender, D. A., and Woods, R., 1981, "Evaluation of V/STOL Flying Quality With Fluidic Controls," final report to the Naval Air Systems Command for sponsored research under Contract No. N0019-80-C-0257.

[5] Watton, J., 1989, *Fluid Power Systems*, Prentice–Hall, New York.

[6] Hullender, D. A., 1990, "Effects of Fluid Transmission Lines in Pressure Measurement," Section 10.5, *Instrumentation and Control—Fundamentals and Applications*, John Wiley, Somerset, New Jersey, pp. 434–438.

[7] Holland, C. M., Blade, R. J., and Dorsch, R. G., 1965, "Attenuation of Sinusoidal Perturbations Superimposed on Laminar Flow of a Liquid in a Long Line," NASA TN D-3099.

[8] Proceedings of the ASME Biomedical Fluid Mechanics Symposium, Denver, Colorado, 1966.

[9] Brown, F. T., 1962, "The Transient Response of Fluid Lines," ASME J. Basic Eng., **84**, No. 4.

[10] Gerlach, C. R., 1969, "Dynamic Models for Viscous Fluid Transmission Lines," Proceedings of the 10th Joint Automatic Control Conference, Boulder.

[11] Goodson, R. E., and Leonard, R. G., 1972, "A Survey of Modeling Techniques for Fluid Transmission Line Transients," ASME J. Basic Eng., **94**, pp. 474–482.

[12] Woods, R. L., 1981, "The Effects of Source and Load Impedance Connected

to Fluid Transmission Lines,'' Fluid Transmission Lines Dynamics, ASME Special Publication, New York.
[13] Zielke, W., 1968, ''Frequency-Dependent Friction in Transient Pipe Plow,'' J. Basic Eng., **90**, No. 1, pp. 109–115.
[14] Trikha, A. K., 1975, ''An Efficient Method for Simulating Frequency-Dependent Friction in Transient Liquid Flow,'' J. Fluids Eng., **97**, pp. 97–105.
[15] Chaudhry, M. H., 1987, *Applied Hydraulic Transients*, Van Nostrand Reinhold, New York.
[16] Wylie, E. B., and Streeter, V. L., 1993, *Fluid Transients in Systems*, Prentice–Hall, New Jersey.
[17] Streeter, V. L., 1971, ''A Survey Paper on Numerical Methods as Applied to Fluid Transients,'' ASME Winter Annual Meeting, Washington, D.C.
[18] Wylie, E. B., and Streeter, V. L., 1978, *Fluid Transients*, McGraw–Hill, New York.
[19] Nursilo, Witrisnanto Sih, 2000, Fluid Transmission Line Dynamics, Ph.D. dissertation, The University of Texas at Arlington, Arlington, Texas.
[20] Woods, R. L., Hsu, C. H., Chung, C. H., and Keyser, D. R., 1983, ''Comparison of Theoretical and Experimental Fluid Line Responses With Source and Load Impedances,'' *Fluid Transmission Lines Dynamics*, ASME Special Publication, II, New York.
[21] Hullender, D. A., and Healey, A. J., 1981, ''Rational Polynomial Approximations for Fluid Transmission Line Models,'' *Fluid Transmission Lines Dynamics*, ASME Special Publication, New York.
[22] Healey, A. J., and Hullender, D. A., 1981, ''State Variable Representation of Modal Approximations for Fluid Transmission Line Systems,'' *Fluid Transmission Lines Dynamics*, ASME Special Publication, New York.
[23] Hsue, C. Y., and Hullender, D. A., 1983, ''Modal Approximations for the Fluid Dynamics of Hydraulic and Pneumatic Transmission Lines,'' *Fluid Transmission Lines Dynamics*, ASME Special Publication, II, New York.
[24] Hullender, D. A., and Woods, R. L., 1983, ''Time Domain Simulation of Fluid Transmission Lines Using Minimum Order State Variable Models,'' *Fluid Transmission Lines Dynamics, ASME Special Publication*, II, New York.
[25] Yang, Woong-Chul, 1983, ''Modal Approximation of Hydraulic Transmission Line Models by Using Simplified Bessel Function Ratio,'' M.Sci. thesis, The University of Texas at Arlington, Arlington, Texas.
[26] Wongputorn, P., Hullender, D. A., and Woods, R. L., 2003, ''A Simplified Method for Formulating the Simulation Diagram for Fluid Systems Containing Fluid Transmission Lines,'' FEDSM2003-45246, 4th ASME_JSME Joint Fluids Engineering Conference, Hawaii.
[27] Levi, E. C., 1959, ''Complex-Curve Fitting,'' IRE Transactions on Automatic Control, AC-4, pp. 37–43.
[28] Sanathanan, C. K., and Koerner, J., 1963, ''Transfer Function Synthesis as a Ratio of Two Complex Polynomials,'' IEEE Trans. Automatic Control, **AC-8**, pp. 56–58.
[29] Ljung, L., 1993, ''Some Results on Identifying Linear Systems Using Frequency Domain,'' 32nd IEEE Conference on Decision and Control, San Antonio, Texas, pp. 3534–3538.
[30] De Vries, D. K., and Van den Hof, P. M. J., 1995, ''Frequency Domain Identification With Generalized Orthonormal Basis Functions,'' Proceeding of the 34th IEEE Conference of Decision and Control, New Orleans, Louisiana.
[31] Bayard, D. S., 1994, ''High-Order Multivariable Transfer Function Curve Fitting: Algorithms, Sparse Matrix Methods and Experimental Results,'' Automatica, **30**, pp. 1439–1444.
[32] Wongputorn, P., 2001, ''Time Domain Simulation of Systems With Fluid Transmission Lines,'' M.Sci. thesis, The University of Texas at Arlington, Arlington, Texas.
[33] Internet web site for downloading fluid transmission line m-files: macpro.uta.edu/hullender.
[34] Woods, R. L., and Lawrence, K. L., 1997, *Modeling and Simulation of Dynamic Systems*, Prentice–Hall, New Jersey.

Transformation of a Polynomial for a Contraction Wall Profile

D. Brassard
e-mail: dan@brassard.com

M. Ferchichi
e-mail: mohsen.ferchichi@lakeheadu.ca
Phone: (807) 343-8571, Department of Mechanical Engineering, Lakehead University, 955 Oliver Road, Thunder Bay, ON P7B 5E1, Canada

[DOI: 10.1115/1.1852492]

Introduction

In the design of contractions for low-speed wind tunnels, several desirable characteristics of the wall profile are identified, primarily consisting of a wall profile described by a function having zero first- and second-order derivatives, and the radii of curvature at the inlet and outlet roughly proportional to the area [1]. This condition would be the most favorable to achieve flow uniformity, thin boundary layers, and negligible losses [2]. A contraction profile, described by a fifth degree polynomial, has been developed by Bell and Mehta [3] and has been repeatedly employed successfully in contraction design in two and three dimensions. This polynomial has proven so successful that it has largely become the design standard. However, because this polynomial is symmetrical and has identical radii of curvature at the inlet and outlet, an arrangement traditionally considered undesirable [1], many designers of wind tunnel contractions believe that a more qualitative, experimental design of contraction profiles, the so-called ''by-eye'' design, will produce better results. The purpose of this short note is to develop a transformation of Bell and Mehta's [3] polynomial such that any curve characteristics selected by a designer can be described by an analytical function that will have vanishing first and second derivatives at the inlet and outlet, and will have continuous first and second derivatives throughout. It is important that this be achieved as simply as possible so that it would be of maximum utility to the designer. Systematic manipulation of as few parameters as possible should produce the curve desired.

The Transformation

The transformation described herein is an attempt to provide an easy, systematic procedure allowing Bell and Mehta's [3] fifth-order polynomial to be fitted to a ''by-eye'' curve chosen by the designer of a wind tunnel contraction, satisfying the criteria described above.

The central fifth-order polynomial of Bell and Mehta [3] that describes a contraction wall profile as shown in Fig. 1 is the function chosen for transformation and is given by

$$h=[-10\xi^3+15\xi^4-6\xi^5]\left(1-\frac{H_o}{H_i}\right)+1, \tag{1}$$

where $h=y/H_i$ is the contraction wall height normalized by the contraction inlet height, H_i; H_o is the height of the contraction wall at the outlet, all measured from the axis of symmetry of the contraction; and $\xi=x/L$ is the downstream distance normalized by the contraction length, L. Defining Bell and Mehta's [3] core polynomial as

$$\eta=10\xi^3-15\xi^4+6\xi^5 \tag{2}$$

it has been defined as varying between 0 and 1 in order to present the resulting contraction profiles consistently and intuitively. In order to bias Eq. (1) in a consistent, smooth fashion to arbitrary inlet and outlet heights, while incorporating the change in the wall profile shape as desired by the designer, the following transformation is proposed:

$$h=\left\{-\eta\left[1-\left(\frac{H_o}{H_i}\right)^{1/f(\xi)}\right]+1\right\}^{f(\xi)} \tag{3}$$

where $f(\xi)$ is an arbitrary, continuous function of ξ defined for $0\leqslant\xi\leqslant1$ and normalized such that $0<f(\xi)<1$. Expressions for the first and second derivatives of h in Eq. (3), $dh/d\xi$ and $d^2h/d\xi^2$, respectively, provided in the Appendix may be used to show that any continuous function, $f(\xi)$, chosen in Eq. (3) will result in a contraction wall profile described by a continuous function, maintaining first and second derivatives equal to zero at the inlet and outlet.

Equation (3) is obviously very similar to Bell and Mehta's [3] transfer function; it is the functional nature of $f(\xi)$ which provides interesting results as demonstrated in the following examples performed for a 16:1 area contraction ratio.

Figure 2(*a*) shows the resulting contraction wall profiles for a constant $f(\xi)$, namely 0.3 and 0.5. It can be seen by inspection of Fig. 2(*a*) that selecting a constant $f(\xi)$ produces the desired larger inlet radius than outlet radius with zero first and second derivatives at inlet and outlet as shown in Figs. 2(*b*) and 2(*c*), respectively. Figure 3(*a*) shows contraction wall profiles corresponding to a linear and quadratic $f(\xi)$. Changing the functional form of $f(\xi)$ generates numerous contraction profiles that result in the desired characteristics described above as shown in Figs. 3(*b*) and 3(*c*).

Discussion and Conclusions

In this article, a transformation of a low-speed, wind tunnel contraction profile proposed by Bell and Mehta [3] was developed. The transformation guarantees that, for any continuous, smooth function $f(\xi)$ chosen in Eq. (3), the first- and second-order derivatives of the contraction wall profile vanish at the inlet and outlet. This transformation generates a wide range of contraction wall profiles described by a convenient continuous function for a designer to choose from as opposed to the purely ''by-eye'' design.

Based on the examples of $f(\xi)$ presented here, it can be argued that favorable wall characteristics, such as a larger radius at the inlet than at the outlet, can be generated by judicious selection of $f(\xi)$ either as a constant or as a function of ξ. For instance, if a

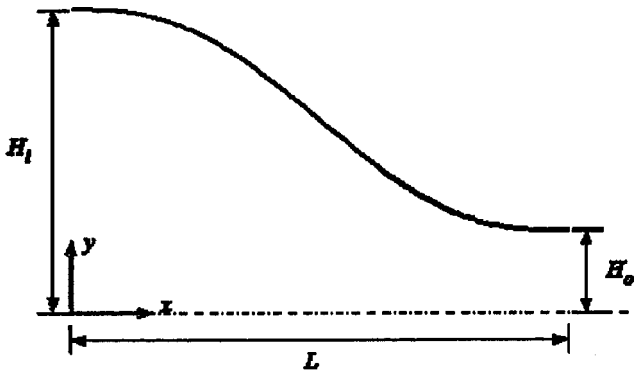

Fig. 1 Geometrical parameters of contraction profile

Contributed by the Fluids Engineering Division for publication in the JOURNAL OF FLUIDS ENGINEERING. Manuscript received by the Fluids Engineering Division January 13, 2004; revised manuscript received August 12, 2004. Review conducted by: H. Johari.

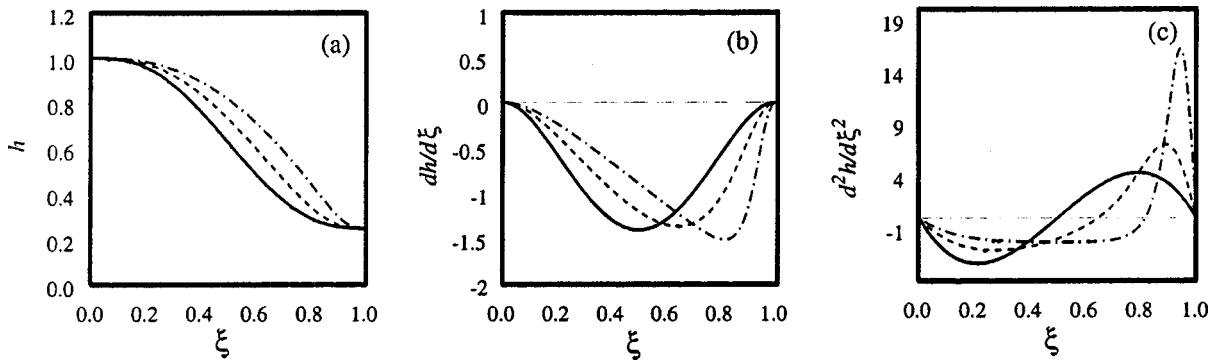

Fig. 2 Transformation with constant $f(\xi)$; (a) The transformed profiles (b) corresponding first derivatives (c) corresponding second derivatives. —— Untransformed; —·—·—·— $f(\xi)=0.3$; — — — $f(\xi)=0.5$.

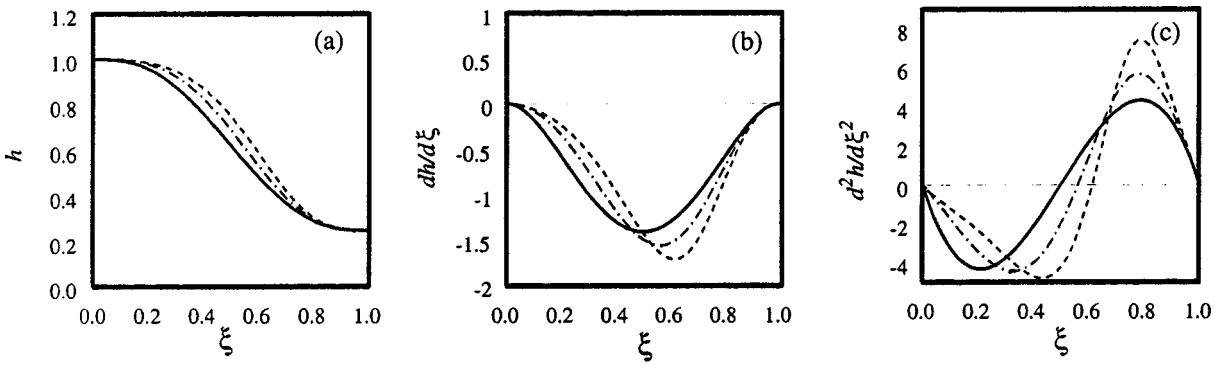

Fig. 3 Transformation with non-constant $f(\xi)$; (a) The transformed profile (b) corresponding first derivatives (c) corresponding second derivatives. —— Untransformed; —·—·—·— Linear $f(\xi)$; — — — Quadratic $f(\xi)$.

designer wishes to generate a large radius at the inlet, a smaller radius at the outlet while maintaining a longer transition of the outlet radius to the test section, linear or quadratic functions, $f(\xi)$, could be chosen.

When a researcher wishes to design a contraction wall curve using a Computational Fluid Dynamics (CFD) code, this transformation can be easily incorporated for optimizing the wall profile based on the flow characteristics resulting from each $f(\xi)$ selected.

It is hoped that the present work will provide designers with a tool that would facilitate the selection of contraction wall profiles that suit their research requirements.

Acknowledgments

The authors are grateful to Dr. J. H. Bell, Dr. P. Bradshaw, and Dr. R. D. Mehta for their assistance and comments on the original report. This work was financially supported by the Natural Sciences and Engineering Research Council of Canada.

Appendix

The primes and double-primes are the first and second derivatives of the variable with respect to ξ, respectively:

$$\frac{dh}{d\xi}=\left\{-\eta\left[1-\left(\frac{H_o}{H_i}\right)^{1/f}\right]+1\right\}^{f}\left[f'\ln\left[-\eta\left(1-\left(\frac{H_o}{H_i}\right)^{1/f}\right)+1\right]+\frac{f\left\{-\eta'\left[1-\left(\frac{H_o}{H_i}\right)^{1/f}\right]-\frac{\eta(H_0/H_i)^{1/f}f'\ln(H_o/H_i)}{f^2}\right\}}{-\eta\left(1-\left(\frac{H_o}{H_i}\right)^{1/f}\right)+1}\right]$$

$$\frac{d^2h}{d\xi^2}=\left\{-\eta\left[1-\left(\frac{H_o}{H_i}\right)^{1/f}\right]+1\right\}^{f}\left[f'\ln\left\{-\eta\left[1-\left(\frac{H_o}{H_i}\right)^{1/f}\right]+1\right\}+\frac{f\left\{-\eta'\left[1-\left(\frac{H_o}{H_i}\right)^{1/f}\right]-\frac{\eta(H_o/H_i)^{1/f}f'\ln(H_o/H_i)}{f^2}\right\}}{-\eta\left[1-\left(\frac{H_o}{H_i}\right)^{1/f}\right]+1}\right]^2$$

$$+\left\{-\eta\left[1-\left(\frac{H_o}{H_i}\right)^{1/f}\right]+1\right\}^{f}f''\ln\left\{-\eta\left[1-\left(\frac{H_o}{H_i}\right)^{1/f}\right]+1\right\}+2f'\left(\frac{-\eta'\left[1-\left(\frac{H_o}{H_i}\right)^{1/f}\right]-\frac{\eta(H_o/H_i)^{1/f}f'\ln(H_o/H_i)}{f^2}}{-\eta\left[1-\left(\frac{H_o}{H_i}\right)^{1/f}\right]+1}\right)$$

$$+f\left(\frac{-\eta''\left[1-\left(\frac{H_o}{H_i}\right)^{1/f}\right]-\frac{2\eta'(H_o/H_i)^{1/f}f'\ln(H_o/H_i)}{f^2}+\frac{\eta(H_o/H_i)^{1/f}(f'\ln(H_o/H_i))^2}{f^4}+\frac{2\eta(H_o/H_i)^{1/f}f'^2\ln(H_o/H_i)}{f^3}-\frac{\eta(H_o/H_i)^{1/f}f''\ln(H_o/H_i)}{f^2}}{-\eta\left(1-\left(\frac{H_o}{H_i}\right)^{1/f}\right)+1}\right)$$

$$-\frac{f\left(-\eta'\left(1-\left(\frac{H_o}{H_i}\right)^{1/f}\right)-\frac{\eta(H_o/H_i)^{1/f}f'\ln(H_o/H_i)}{f^2}\right)^2}{\left\{-\eta\left[1-\left(\frac{H_o}{H_i}\right)^{1/f}\right]+1\right\}^2}$$

References

[1] Mehta, R. D., and Bradshaw, P., 1979, ''Design Rules for Small Low Speed Wind Tunnels,'' Aeronaut. J., **73**, pp. 443–449.

[2] Bell, J. H., and Mehta, R. D., 1989, ''Boundary-Layer Predictions for Small Low Speed Contractions,'' AIAA J., **27**, pp. 372–374.

[3] Bell, J. H., and Mehta, R. D., 1988, ''Contraction Design for Small Low-Speed Wind Tunnels,'' NASA CR 177488, Contract NAS2-NCC-2-294.

Surface Flow Visualization Using Thermal Tufts Produced by Evaporatively Cooled Spots

Jason S. Smith and James W. Baughn
Department of Mechanical and Aeronautical Engineering, University of California, Davis, CA 95616 USA

Aaron R. Byerley
Department of Aeronautics, United States Air Force Academy, CO 80840 USA

[DOI: 10.1115/1.1852493]

Introduction and Background

Surface flow visualization is useful for understanding flow in many applications and can be used to complement and validate studies of complex flow using computational fluid dynamics (CFD). A recent development in non-intrusive surface flow visualization has been the development of ''laser thermal tufts''. Baughn et al. [1] first described this technique in a study to determine where flow separation had occurred on the suction side of a turbine blade. This technique was later patented by the USAF (Rivir et al. [2]). The principle behind this method was to use a laser to heat a spot on a surface coated with thermochromic liquid crystals (TLCs), showing up on an image of the surface as a round dot. This circular laser spot ($\sim$3 mm) heated the surface above the color play temperature, creating a distinct thermal tuft downstream. The thermal tuft was created by advection in the direction of surface airflow. The result was a teardrop shaped color change in the TLCs pointing in the downstream direction. Using this method, they were able to determine the location of boundary layer separation on a turbine blade model in a cascade wind tunnel. They pointed out that multiple spots could be obtained by using a laser tuft matrix (LTM). In the location of boundary layer separation or reattachment, the thermal tuft is circular and centered around the laser spot with no hint of a teardrop shape. Further demonstrations of the laser thermal tuft were done by Townsend [3]. Baughn et al. [4] presented the results for a laser thermal tuft created by an infrared (IR) laser on the flow separation and reattachment on a turbine blade at low Reynolds numbers. The IR laser produced a clear red spot at the center of the thermal tuft. Their results are shown in Fig. 1.

For their case where freestream turbulence is 0.5%, separation occurred at location 2, while reattachment occurred at location 4. In between locations 2 and 4 was a region of recirculation, indicated by the tail pointing in the opposite direction of freestream at location 3. At high freestream turbulence, they were able to show that the flow remained attached; the laser tuft images all point in the direction of freestream. Later in the same year a patent was granted to the USAF for the laser thermal tuft method (River et al. [2]).

Further applications of the laser thermal tuft were done by Butler et al. [5] and Byerley et al. [6]. These studies also used the laser thermal tuft to determine the location of flow separation and reattachment. In addition, Byerley et al. [6] introduced a dimensionless term to quantify the strength of the laser tuft called the eccentricity. Using a similar technique as the laser thermal tuft, Batchelder and Moffat [7] described a surface flow visualization technique using heat sinks with ''pin fins'' to create an array of small hot spots on a surface.

A ''cool'' thermal tuft was produced by Byerley et al. [8], where IR heaters were used to uniformly heat a black surface with reflective spots affixed to the surface. The reflective surface remained cool while the surrounding surface heated up and produced a thermal tuft downstream of the ''cool'' spot.

In the present work, a new evaporatively cooled thermal tuft method for surface flow visualization is described. The thermal tuft is a teardrop shaped surface temperature pattern pointing in the direction of the surface flow. In the present study, a wetted wicking material was embedded in a small hole on the surface of a low thermal conductivity substrate to produce evaporatively cooled spots which in turn produce the thermal tufts. When exposed to flow, evaporation occurs and each spot stabilizes at the wet bulb temperature. These thermal tufts are observed on a flat plate in the present study using infrared thermography.

Principles of Thermal Tufts

We define a thermal tuft here, in reference to surface flow visualization, as a teardrop shaped temperature pattern on a surface, originating from a heated or cooled spot, pointing in the direction of the surface flow. The thermal tuft is generated by advection, causing the heated or cooled air to interact with the surface downstream of the thermal spot. The region surrounding the thermal tuft involves heat transfer in both convection and conduction (see Fig. 2).

For boundary layer flow, the characteristics of the boundary layer play an important role in the shape and size of the thermal tuft. The two types of boundary layers affecting the thermal tuft are the velocity boundary layer and thermal boundary layer. The hydrodynamic- or velocity boundary layer begins upstream of the thermal tuft. The thermal boundary layer begins at the heated or cooled spot and decays downstream of the spot, creating the thermal tuft. It is thin compared to the velocity boundary layer. These boundary layers are illustrated in Fig. 3.

The size of the heated or cooled spot is small with respect to the change in thickness of the velocity boundary layer over the distance of the spot. This means that the velocity profiles at the beginning and at the end of the spot remain relatively unchanged.

Evaporatively Cooled Thermal Tuft Method (ECTT)

The purpose of the present research was to develop a new thermal tuft method using evaporatively cooled spots to produce the thermal tufts. The evaporative cooling uses the phase change between liquid and vapor to produce isothermal cooled spots. A 3×3 matrix of small cylinders containing wicking material (see Fig. 4) was imbedded in a wall to produce the cooled spots. The wall material consisted of a foam base covered by a foam-filled poster board. A black matte finish paint was applied to the wall surface to increase its emissivity. The cavity or hole with the wicking material was sealed by embedding an aluminum tube that was plugged on the bottom using plumber's putty.

The thermal tuft produced in this study works on the principle of evaporative cooling. If a wet spot on a surface is cooled by evaporation, the temperature stabilizes at a temperature at or slightly above the wet bulb temperature. The limiting factor in measurement time is the supply of water and wicking capability. The ideal design would consist of a small cavity or hole filled with a material that conveys liquid to the test surface easily by capillary action.

Some of the wicking materials considered for the present study were floral foam, baby diaper filling, and wicking string. A material called OASIS® Floral Foam was found to work well due to its high absorptive qualities and ease of fabrication. Technical data from the manufacturer reports that their floral foam holds over 40 times its weight in water. The capillary ability of the floral foam

Contributed by the Fluids Engineering Division for publication in the JOURNAL OF FLUIDS ENGINEERING. Manuscript received by the Fluids Engineering Division March 11, 2004; revised manuscript received August 12, 2004. Review conducted by: M. Otugen.

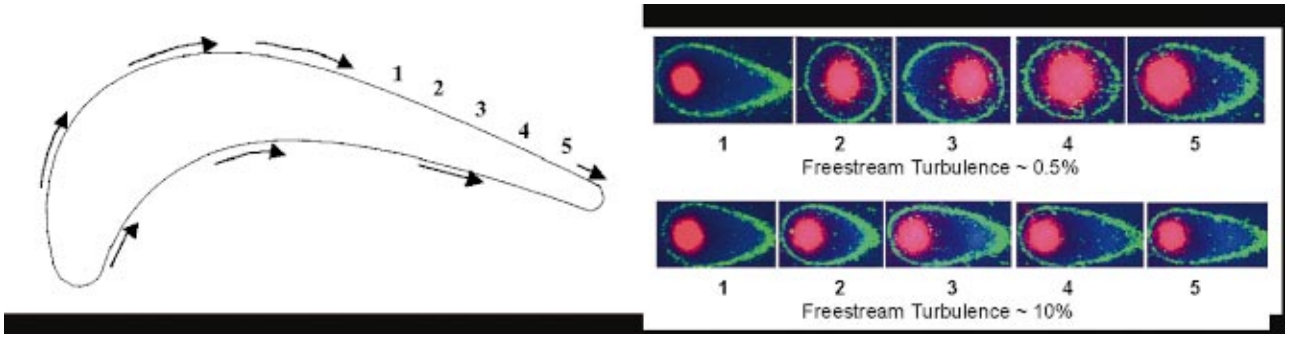

Fig. 1 Laser thermal tuft (IR) on a turbine blade [4].

was found to be more than adequate to keep up with the evaporation rate. It was easily cut to the desired shape using a thin-walled tube as a die punch.

Infrared Thermography

In the present study infrared thermography was used to detect the thermal tufts as an alternate approach to using liquid crystal thermography (as used with the earlier laser thermal tuft). The first clear advantage to using IR thermography is that no liquid crystals are needed to produce the thermal tufts. The model surface simply needs to be smooth and reasonably uniform in emissivity. Another advantage to IR thermography is that lighting of the model is not necessary.

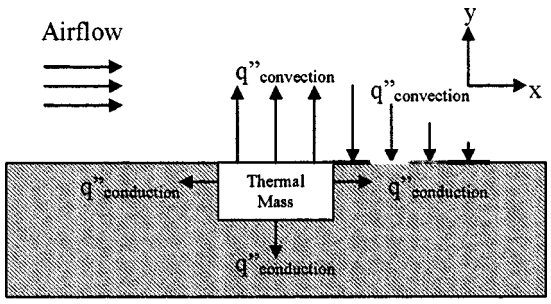

Fig. 2 Heat transfer involved in thermal tufts.

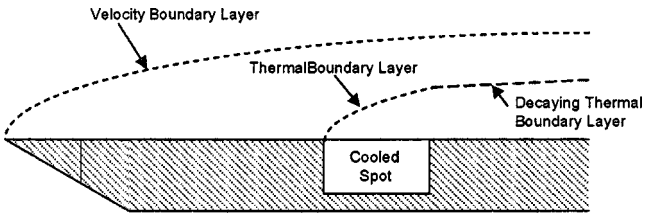

Fig. 3 Velocity and thermal boundary layer development.

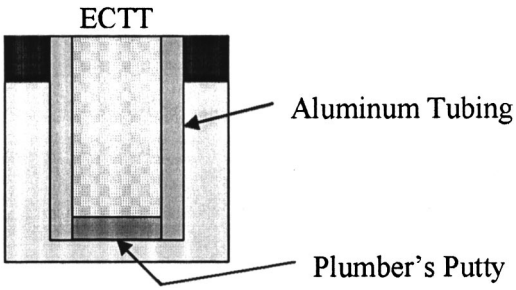

Fig. 4 Embedded ECTT cavity design.

The thermal resolution for IR cameras is known as the noise equivalent temperature difference (NETD). This is the temperature difference that two black body radiators need in order to produce a difference in the camera signal equal to signal noise. Lower-end IR cameras have a NETD on the order of 0.12 K while higher end cameras have a NETD as small as 0.02 K. The IR camera used here was a Mitsubishi IR-M700 with a NETD of 0.08 K. This camera has a relatively high resolution, 801×512 pixels. The IR wavelengths captured by this camera were in the 3–5 μm range. In this range a special window is required. A ruby-sapphire window was used with transmission up to 5 μm.

The software used to capture the images was Ulead Media Studio 6. The images captured by the IR camera were saved in the tiff format on the highest resolution setting. Gain and level control were adjusted in order to see a clear thermal tuft. The captured images were grayscale with values from 0 to 255 (8 bits) for each pixel to represent the surface temperatures. Postprocessing of the IR images was done using Photoshop. A color gradient map was applied to the grayscale image to produce a color thermal tuft.

Results and Discussion

A sample of the thermal tufts produced in a wind tunnel using the ECTT method is shown in Fig. 5. There are three consecutive thermal tufts with a freestream velocity of 5 m/s.

These thermal tufts show a very distinct difference between the edge of the hole or spot and the surrounding surface of the model. This suggests that the emissivity of the saturated foam is slightly different than the black paint coating on the model surface. This is good because the center of the thermal tuft is easily identified, making it easier to discern the thermal tuft direction. A color gradient map was applied to grayscale images of Fig. 5 and is shown in Fig. 6. The hole with the wicking material or circular spot outline was quite distinct and did not require any image enhancement.

Conclusions

Thermal tufts for surface flow visualization using evaporatively cooled spots were obtained successfully using an infrared camera. These thermal tufts clearly show the direction of the flow on the surface and with a matrix of spots can provide excellent surface flow visualization. The method is simple and easy to implement.

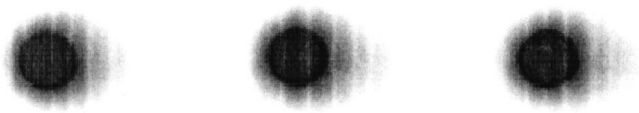

Fig. 5 IR image of ECTTs at freestream velocity of 5 m/s.

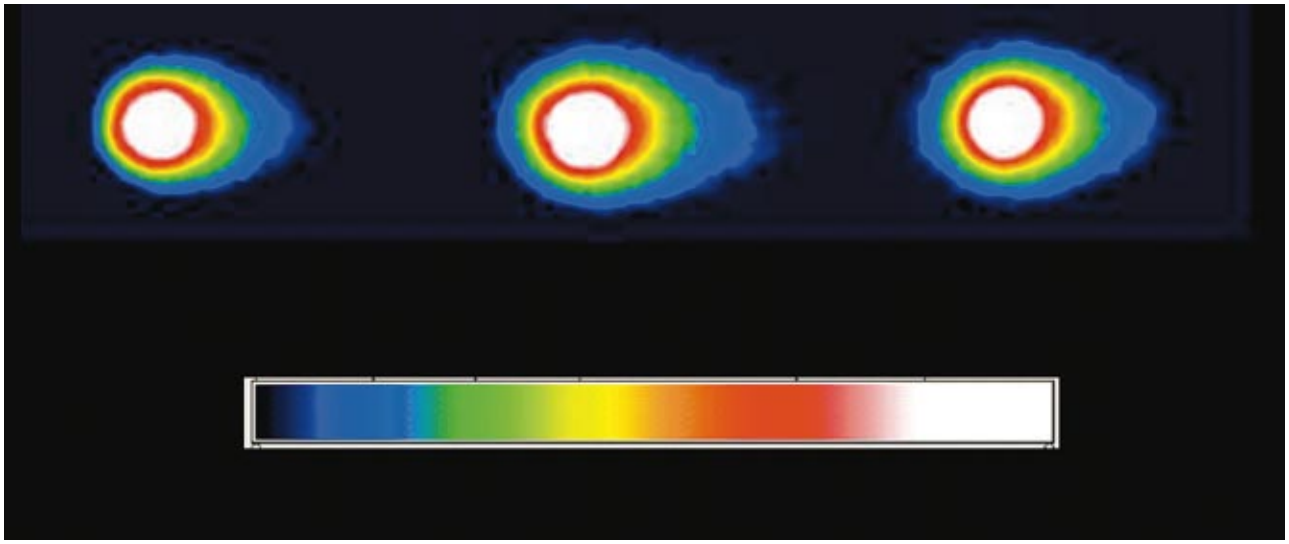

Fig. 6 Enhanced IR image of the thermal tufts shown in Fig. 5

In the present study the wicking material used was absorptive floral foam that was easily shaped and inserted into the model substrate. Any wicking material with similar characteristics should provide similar thermal tufts.

The thermal tufts produced by this method provide a nonintrusive measurement technique for surface flow visualization. With this new method, a matrix of spots can be used on a model of complex shape to provide surface flow direction at multiple locations on the model surface, thus providing surface flow visualization.

Although infrared thermography was used in this demonstration, it is expected that liquid crystal thermography would produce equally good thermal tufts with this method if the color play temperature range of the TLC was chosen carefully for the range of ambient and wet bulb temperatures during the measurements.

References

[1] Baughn, J. W., Butler, R. J., Byerley, A. R., and River, R. B., 1995, ''An Experimental Investigation of Heat Transfer, Transition and Separation on Turbine Blades at Low Reynolds Number and High Turbulence Intensity,'' ASME Paper no. 95-WA/HT-25.

[2] River, R. B., Baughn, J. W., Townsend, J. L., Butler, R. J., and Byerley, A. R., 1999, ''Thermal Tuft Fluid Flow Investigation Apparatus With A Color Alterable Thermally Responsive Liquid Crystal Layer,'' United States Patent No. 5963292.

[3] Townsend, J. L., 1996, ''A Laser Thermal Tuft Using Liquid Crystals for Flow Visualization,'' M.S. thesis, University of California, Davis.

[4] Baughn, J. W., Mayhew, J. E., Butler, R. J., Byerley, A. R., and Rivir, R. B., 1999, ''Turbine Blade Flow Separation and Reattachment at Low Reynolds Numbers,'' ASME J. Heat Transfer, **121**, August picture gallery.

[5] Butler, R. J., Byerley, A. R., Van Treuren, K., and Baughn, J. W., 2001, ''The Effect of Turbulence Intensity and Length Scale on Low-Pressure Turbine Blade Aerodynamics,'' Int. J. Heat Fluid Flow, **22**, pp. 123–133.

[6] Byerley, A. R., Stormer, O., Baughn, J. W., Simon, T. W., Van Treuren, K. W., and List, J., 2003, ''Using Gurney Flaps to Control Laminar Separation on Linear Cascade Blades,'' ASME J. Turbomach., **125**(1), pp. 114–120.

[7] Batchelder, K. A., and Moffat, R. J., 1998, ''Surface Flow Visualization Using the Thermal Wakes of Small Heated Spots,'' Exp. Fluids, **25**, pp. 104–107.

[8] Byerley, A. R., Stormer, O., Baughn, J. W., Simon, T. W., and Van Treuren, K. W., 2001, ''A Cool Thermal Tuft for Detecting Surface Flow Direction,'' ASME J. Heat Transfer, **124**, p. 594.